THE UNIVERSITY OF MANITOBA

A Study of Critical Phenomena and Viscous Properties in Several NiMn AuFe and CrFe Spin Glasses and Reentrant Ferromagnets

BY

WENXIN RUAN

A THESIS SUBMITTED TO
THE FACULTY OF GRADUATE STUDIES OF
THE UNIVERSITY OF MANITOBA
IN PARTIAL FULFILLMENT OF THE REQUIREMENTS OF
THE DEGREE OF DOCTOR OF PHILOSOPHY

DEPARTMENT OF PHYSICS
WINNIPEG, MANITOBA
FEBRUARY 1993

ISBN 0-315-81666-X

Canada

Name WENXIN RUAN

Dissertation Abstracts International is arranged by broad, general subject categories. Please select the one subject which most nearly describes the content of your dissertation. Enter the corresponding four-digit code in the spaces provided.

Solid State Physics
SUBJECT TERM

0611
SUBJECT CODE

UMI

Subject Categories

THE HUMANITIES AND SOCIAL SCIENCES

COMMUNICATIONS AND THE ARTS
Architecture 0729
Art History 0377
Cinema 0900
Dance 0378
Fine Arts 0357
Information Science 0723
Journalism 0391
Library Science 0399
Mass Communications 0708
Music 0413
Speech Communication 0459
Theater 0465

EDUCATION
General 0515
Administration 0514
Adult and Continuing 0516
Agricultural 0517
Art 0273
Bilingual and Multicultural 0282
Business 0688
Community College 0275
Curriculum and Instruction 0727
Early Childhood 0518
Elementary 0524
Finance 0277
Guidance and Counseling 0519
Health 0680
Higher 0745
History of 0520
Home Economics 0278
Industrial 0521
Language and Literature 0279
Mathematics 0280
Music 0522
Philosophy of 0998
Physical 0523
Psychology 0525
Reading 0535
Religious 0527
Sciences 0714
Secondary 0533
Social Sciences 0534
Sociology of 0340
Special 0529
Teacher Training 0530
Technology 0710
Tests and Measurements 0288
Vocational 0747

LANGUAGE, LITERATURE AND LINGUISTICS
Language
- General 0679
- Ancient 0289
- Linguistics 0290
- Modern 0291

Literature
- General 0401
- Classical 0294
- Comparative 0295
- Medieval 0297
- Modern 0298
- African 0316
- American 0591
- Asian 0305
- Canadian (English) 0352
- Canadian (French) 0355
- English 0593
- Germanic 0311
- Latin American 0312
- Middle Eastern 0315
- Romance 0313
- Slavic and East European 0314

PHILOSOPHY, RELIGION AND THEOLOGY
Philosophy 0422
Religion
- General 0318
- Biblical Studies 0321
- Clergy 0319
- History of 0320
- Philosophy of 0322

Theology 0469

SOCIAL SCIENCES
American Studies 0323
Anthropology
- Archaeology 0324
- Cultural 0326
- Physical 0327

Business Administration
- General 0310
- Accounting 0272
- Banking 0770
- Management 0454
- Marketing 0338

Canadian Studies 0385
Economics
- General 0501
- Agricultural 0503
- Commerce-Business 0505
- Finance 0508
- History 0509
- Labor 0510
- Theory 0511

Folklore 0358
Geography 0366
Gerontology 0351
History
- General 0578
- Ancient 0579
- Medieval 0581
- Modern 0582
- Black 0328
- African 0331
- Asia, Australia and Oceania 0332
- Canadian 0334
- European 0335
- Latin American 0336
- Middle Eastern 0333
- United States 0337

History of Science 0585
Law 0398
Political Science
- General 0615
- International Law and Relations 0616
- Public Administration 0617

Recreation 0814
Social Work 0452
Sociology
- General 0626
- Criminology and Penology 0627
- Demography 0938
- Ethnic and Racial Studies 0631
- Individual and Family Studies 0628
- Industrial and Labor Relations 0629
- Public and Social Welfare 0630
- Social Structure and Development 0700
- Theory and Methods 0344

Transportation 0709
Urban and Regional Planning 0999
Women's Studies 0453

THE SCIENCES AND ENGINEERING

BIOLOGICAL SCIENCES
Agriculture
- General 0473
- Agronomy 0285
- Animal Culture and Nutrition 0475
- Animal Pathology 0476
- Food Science and Technology 0359
- Forestry and Wildlife 0478
- Plant Culture 0479
- Plant Pathology 0480
- Plant Physiology 0817
- Range Management 0777
- Wood Technology 0746

Biology
- General 0306
- Anatomy 0287
- Biostatistics 0308
- Botany 0309
- Cell 0379
- Ecology 0329
- Entomology 0353
- Genetics 0369
- Limnology 0793
- Microbiology 0410
- Molecular 0307
- Neuroscience 0317
- Oceanography 0416
- Physiology 0433
- Radiation 0821
- Veterinary Science 0778
- Zoology 0472

Biophysics
- General 0786
- Medical 0760

EARTH SCIENCES
Biogeochemistry 0425
Geochemistry 0996
Geodesy 0370
Geology 0372
Geophysics 0373
Hydrology 0388
Mineralogy 0411
Paleobotany 0345
Paleoecology 0426
Paleontology 0418
Paleozoology 0985
Palynology 0427
Physical Geography 0368
Physical Oceanography 0415

HEALTH AND ENVIRONMENTAL SCIENCES
Environmental Sciences 0768
Health Sciences
- General 0566
- Audiology 0300
- Chemotherapy 0992
- Dentistry 0567
- Education 0350
- Hospital Management 0769
- Human Development 0758
- Immunology 0982
- Medicine and Surgery 0564
- Mental Health 0347
- Nursing 0569
- Nutrition 0570
- Obstetrics and Gynecology 0380
- Occupational Health and Therapy 0354
- Ophthalmology 0381
- Pathology 0571
- Pharmacology 0419
- Pharmacy 0572
- Physical Therapy 0382
- Public Health 0573
- Radiology 0574
- Recreation 0575
- Speech Pathology 0460
- Toxicology 0383

Home Economics 0386

PHYSICAL SCIENCES
Pure Sciences
Chemistry
- General 0485
- Agricultural 0749
- Analytical 0486
- Biochemistry 0487
- Inorganic 0488
- Nuclear 0738
- Organic 0490
- Pharmaceutical 0491
- Physical 0494
- Polymer 0495
- Radiation 0754

Mathematics 0405
Physics
- General 0605
- Acoustics 0986
- Astronomy and Astrophysics 0606
- Atmospheric Science 0608
- Atomic 0748
- Electronics and Electricity 0607
- Elementary Particles and High Energy 0798
- Fluid and Plasma 0759
- Molecular 0609
- Nuclear 0610
- Optics 0752
- Radiation 0756
- Solid State 0611

Statistics 0463

Applied Sciences
Applied Mechanics 0346
Computer Science 0984
Engineering
- General 0537
- Aerospace 0538
- Agricultural 0539
- Automotive 0540
- Biomedical 0541
- Chemical 0542
- Civil 0543
- Electronics and Electrical 0544
- Heat and Thermodynamics 0348
- Hydraulic 0545
- Industrial 0546
- Marine 0547
- Materials Science 0794
- Mechanical 0548
- Metallurgy 0743
- Mining 0551
- Nuclear 0552
- Packaging 0549
- Petroleum 0765
- Sanitary and Municipal 0554
- System Science 0790

Geotechnology 0428
Operations Research 0796
Plastics Technology 0795
Textile Technology 0994

PSYCHOLOGY
General 0621
Behavioral 0384
Clinical 0622
Developmental 0620
Experimental 0623
Industrial 0624
Personality 0625
Physiological 0989
Psychobiology 0349
Psychometrics 0632
Social 0451

A STUDY OF CRITICAL PHENOMENA AND VISCOUS PROPERTIES IN SEVERAL NiMn AuFe and CrFe SPIN GLASSES AND REENTRANT FERROMAGNETS

BY

WENXIN RUAN

A Thesis submitted to the Faculty of Graduate Studies of the University of Manitoba in partial fulfillment of the requirements for the degree of

DOCTOR OF PHILOSOPHY

Abstract

Measurements of the low field complex dynamic susceptibility of both reentrant ferromagnets and spin glasses of $Ni_{1-x}Mn_x$ (x = 0.22, 0.225, 0.236, 0.25). are presented. The real and imaginary parts of the a.c susceptibility were measured for alloys at low excitation frequencies (ω = 16 Hz) over the temperature range $4.2 \leq T \leq 250$ K in fixed static fields between $0 \leq H_a \leq 46$ Oe. For the reentrant configuration of NiMn, the real part of the a.c susceptibility exhibits a *triple*-peaked structure, consisting of a "high" temperature ferromagnetic critical peak which experiences a systematic suppression in amplitude and upward shift in temperature with increasing field, and two lower temperature reentrant peaks which are associated with strong irreversibility and also exhibit a similar systematic suppression in amplitude but downward shift in temperature with increasing field. A critical analysis of the ferromagnetic peak yields estimates for the critical exponent δ and γ which indicate extensive exchange bond disorder. A non-divergent anomaly in the temperature dependence of the amplitude of the leading nonlinear susceptibility in the vicinity of the reentrant temperature suggests the possibility of a genuine phase transition to a low temperature reentrant phase.

The decay of the low-field thermorement magnetization of both reentrant ferromagnets and spin glasses of $Ni_{1-x}Mn_x$ (x = 0.236, 0.25, 0.269), $Au_{1-x}Fe_x$ (x = 0.10, 0.17), $Cr_{1-x}Fe_x$ (x = 0.17, 0.22) and a canonical ferromagnet Pd-1.4 at.% Fe were measured over four decades of observation time (1 s $< t <$ 10^4 s), as a function of temperature and wait time. A crossover from low temperature *nonequilibrim* relaxation within the reentrant phase to high temperature *equi-*

librium dynamics in the ferromagnetic phase was observed in reentrant NiMn, AuFe and CrFe ferromagnets: the relaxation in the ferromagnetic phase shows no wait time dependence and is described by the supreposition of a weak power-law and a constant term, $M_R(t) = M_o + M_1 t^{-m}$; within the reentrant regime the relaxation function changes to the superposition of a stretched-exponential and a constant term, $M_R(t) = M_o + M_1 \exp\left[-(t/\tau)^{1-n}\right]$, with typical spin glass parameters and with strong wait time effects. The relaxation isotherms measured in pure spin glasses of these systems exhibit virtually identical nonequilibrium behaviour to that observed in the reentrant phase of the ferromagnets, and can be described by the same function; however, the superposition of a product of the stretched-exponential and the weak-power law and a costant term, $M_R(t) = M_o + M_1 t^{-m} \exp\left[-(t/\tau)^{1-n}\right]$, is required to describe relaxations at long wait times. The weak-power decay in the high temperature ferromagnetic phase in reentrant ferromagnets was confirmed by themoremanent relaxation measured in the Pd-1.4 at% Fe ferromagnet. The isothermal remanent magnetization (IRM) measurements in $Au_{90}Fe_{10}$ spin glass shows a fascinating memory behaviour observed for the first time in AuFe system, which reflects the existence of macroscopoically *long* relaxation times in spin glasses, and also proves the validity of linear response governing principle for the IRM relaxation. A temperature cycling experiments for the $Cr_{83}Fe_{17}$ spin glass show an new inflection points induced at short times in the thermoremanent magnetization decay and provided the compelling evidence for the existence of the overlap length between different "droplet domains" introduced in a droplet scaling theory and a mesoscopic domain picture.

Acknowledgements

I wish to express my very deep thank to my advisor Dr. Roy Roshko for bringing me into a such fascinating reserach field, for his invaluable guidance, for all of our intimate cooperation over the past six years. I want to thank Dr. F. Hawson(??), Dr. J. Page, Dr. G. Tabitz, Dr. G. Williams for being my committe member, especially I want to thank Dr. G. Williams for his many useful advices and help. Special thanks go to Dr. Henry Kunkel, Roy Gilles, Dr. Xuezhi Zhou, James Gould, Dr. Z. Wang, Patricia Mitchler, Ivan Yeung, Kirk Kornik, Guoqiang Yang, Dawei Li for their expert assistance and cooperations. I also greatly thank Dr. Robert Guardo who provide me time and space to finally finish this thesis in Institute de Génie Biomédical, École Polytechnique de Montreal.

I am greatly indebted to my family in China, without whose support during the past years this thesis would not have been possible. Finally, I want to thank my wife Sharon Tee for her great assistance, encouragements and supports.

To my wife *Sharon*

Contents

Chapter I

Experimental Overview of Bond Disordered Magnets

The purpose of this chapter is to provide a general description of disordered magnetic systems and to review some experimental properties of such systems.

For many decades since the discovery of X-ray diffraction by Bragg in 1912, magnetism in solids was exclusively concerned with "orderly" systems, with identical magnetic ions distributed throughout a regular crystalline lattice on equivalent atomic sites, and magnetic classification seemed to be straightforward, being one of *diamagnetism, paramagnetism, ferromagnetism, antiferromagnetism and ferrimagnetism.* This situation was dramatically altered about twenty years ago by a burst of theoretical and experimental activity involving two related types of systems: amorphous solids, in which no two atomic sites are equivalent, and disordered solids, in which different atoms occupy randomly the sites of a regular crystal lattice. Amorphous solids, which are normally made by rapid chilling a melt, have been studied extensively and are not the subject of this thesis (see review articles by Moorjani and Coey, 1984; also Wohlfarth, 1980). Our research focuses on the second category: site disordered crystalline magnets, and specifically on magnetic phase transitions in such systems.

The basic requirements for magnetic order in a solid are (i) the existence of magnetic moments associated with unpaired electrons on the atoms, and (ii) an interaction to couple them together. It is known that these microscopic magnetic moments interact mutually not only through the very weak ordinary magnetic dipole-dipole forces, but more importantly through quantum mechanical forces, which actually determine the magnetically ordered state in solids. The quantum mechanical forces are a consequence of the Coulombic repulsion of the electronic charge distributions of two adjacent atoms i and j, together with the Pauli exclu-

sion principle, and are known as the exchange interaction. They introduce a term into the Hamiltonian of a magnetic system of the form

$$H = -\frac{1}{2}\sum_{i,j} J_{ij}\vec{S}_i \cdot \vec{S}_j, \tag{1.1}$$

where μ_B is the Bohr magneton, $\vec{S}_i$ and $\vec{S}_j$ denote the spin magnetic moments of the ith and jth atoms respectively, and J_{ij} is the exchange integral (Morrish, 1965). Its strength depends on the amount of overlap between the two adjacent electronic wavefunctions. If $J_{ij} > 0$, parallel alignments of the two spin moments are favoured in minimizing the energy, which results in ferromagnetism. On the other hand, when $J_{ij} < 0$, antiparallel arrangements of the $\vec{S}_i$ and $\vec{S}_j$ are favoured, which causes antiferromagnetism or ferrimagnetism.

The magnetic interaction becomes complicated in a disordered magnetic system. Disordered magnetic systems, specifically site-disordered magnets, are solid solutions formed by substituting magnetic impurity atoms (Fe, Mn, Co, Ni, etc) randomly throughout the lattice sites of a non-magnetic host metal (such as Au, Ag, Cu etc). The solute magnetic impurities often tend to retain their magnetic moments even while in solution, and varying their concentration changes the separation between two impurity atoms. When the concentration of magnetic impurities is so low that the impurities are surrounded by non-magnetic host atoms, direct exchange interaction is impossible and the mechanism which couples these impurity magnetic moments is known as the RKKY (named after its principal investigators, Ruderman and Kittel, Kasuya and Yosida) indirect exchange interaction. The RKKY interaction is a long range interaction and is restricted to materials containing itinerant electrons, which are the intermediaries in the coupling. A localized magnetic moment, $\vec{S}_i$, polarizes the host's conduction electron spins in its neighborhood. This electron spin polarization oscillates up and down as a function of separation from the $\vec{S}_i$ moment, and the oscillations determine the orientation of the second magnetic moment $\vec{S}_j$; hence the impurity spins $\vec{S}_i$ and

$\vec{S}_j$ are indirectly coupled. This coupling may also be represented by an exchange term:

$$H_{RKKY} = J_{RKKY}\vec{S}_i \cdot \vec{S}_j, \tag{1.2}$$

but with an effective exchange integral J_{RKKY} given by

$$J_{RKKY}(R_{ij}) \sim \frac{\cos 2k_F R_{ij}}{{R_{ij}}^3}, \quad \text{as } \mathrm{R_{ij}} \to \infty \tag{1.3}$$

where k_F is the Fermi wavevector and $R_{ij} = \mid \vec{R}_i - \vec{R}_j \mid$ represents the distance between ith moment and jth moment.

The existence of RKKY coupling means that in a disordered metallic system, in which the separation between magnetic moments is random, both positive and negative exchange bonds between moments occur. This leads to possible conflicts in the system on a microscopic scale as magnetic moments try to respond to antagonistic constraints. Each of the impurity moments receives instructions from all the other impurity moments (by means of RKKY exchange bonds) as to the direction in which it should point. Positive bonds require parallel alignments and negative bonds require anti-parallel arrangements. Because the distances between the moments are random, the instructions for each individual impurity moment are in conflict with each other. This is called spin frustration. All of the impurity spin magnetic moments must cooperatively choose a configuration of random orientations, as shown in Figure 1-1, which simultaneously satisfies all the random exchange bonds. Therefore a frustrated system has no unique microscopic configuration for its ground state; there is an essentially infinite number of equivalent states that can be adopted. As a result, a frustrated magnetic system shows metastability, with hysteresis effects, time dependent relaxation towards an equilibrium state, and dependence on its thermal and magnetic histories.

Magnetic ordering in disordered magnets is highly concentration dependent, and considerably more complex than it is in pure metals. When the concentration of magnetic impurities is very low, such that the impurities are mainly

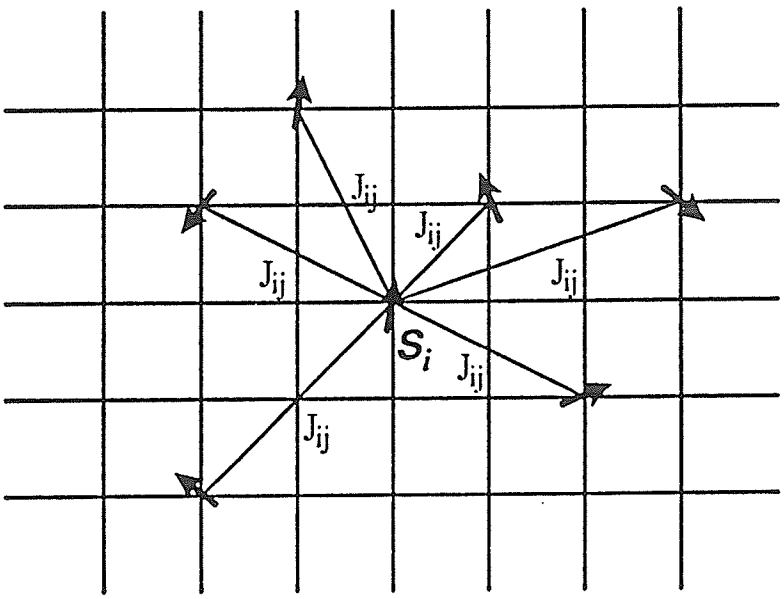

Figure 1-1: An illustration of spin frustration for spins located randomly on the lattice sites.

non-interacting, we have the "single impurity" limit which exhibits experimental properties describable within the framework of the Kondo Effect (Daybell, 1973 and Rizzuto, 1974). By increasing the concentration, the local moments begin to interact via the RKKY mechanism. As the temperature is lowered in zero external field, the impurity spins become "locked" in random orientations and form what is known as a spin glass state in which there is no long range magnetic order. As the concentration is further increased, there is a greater statistical chance of a given impurity being first or second nearest neighbor to another impurity, and short range correlations become important. Now small groups of impurities clusters, form at one temperature, interact with each other via the long range RKKY interaction, and then cooperatively freeze at a lower freezing temperature. The term "cluster glass" or "mictomagnetism" describe such a state. Finally, at some concentration specific to the crystal structure, each magnetic site will have at least one magnetic nearest neighbor. Such a macroscopic connection or uninterrupted chain extending from one end of the crystal to the other, corresponds to the percolation limit or that concentration for which there is a non-zero probability that a given occupied site belongs to an unbounded cluster , and if $J_{nearest-neighbour} > 0$, the system orders ferromagnetically. The above process is shown schematically in Figure 1-2 (Wohlfarth, 1980).

From a practical point of view, the fabrication of these systems demands that two criteria be met: (i) the impurity moment must be stable, i.e., the Kondo temperature should be less than $T_K \cong 1$ K, so cooperative ordering processes are not compromised by the weakening of the local moments at low temperatures, and (ii) a high solubility such that the impurities may be dissolved easily in the metal host. Wohlfarth (1980) has made a detailed compilation of a variety of well-studied spin glass systems which indicates the extent to which these criteria are satisfied in various combinations of noble metal hosts with transition metal impurities CuMn, AgMn, and AuFe, as well as transition metal hosts with transition metal impurities

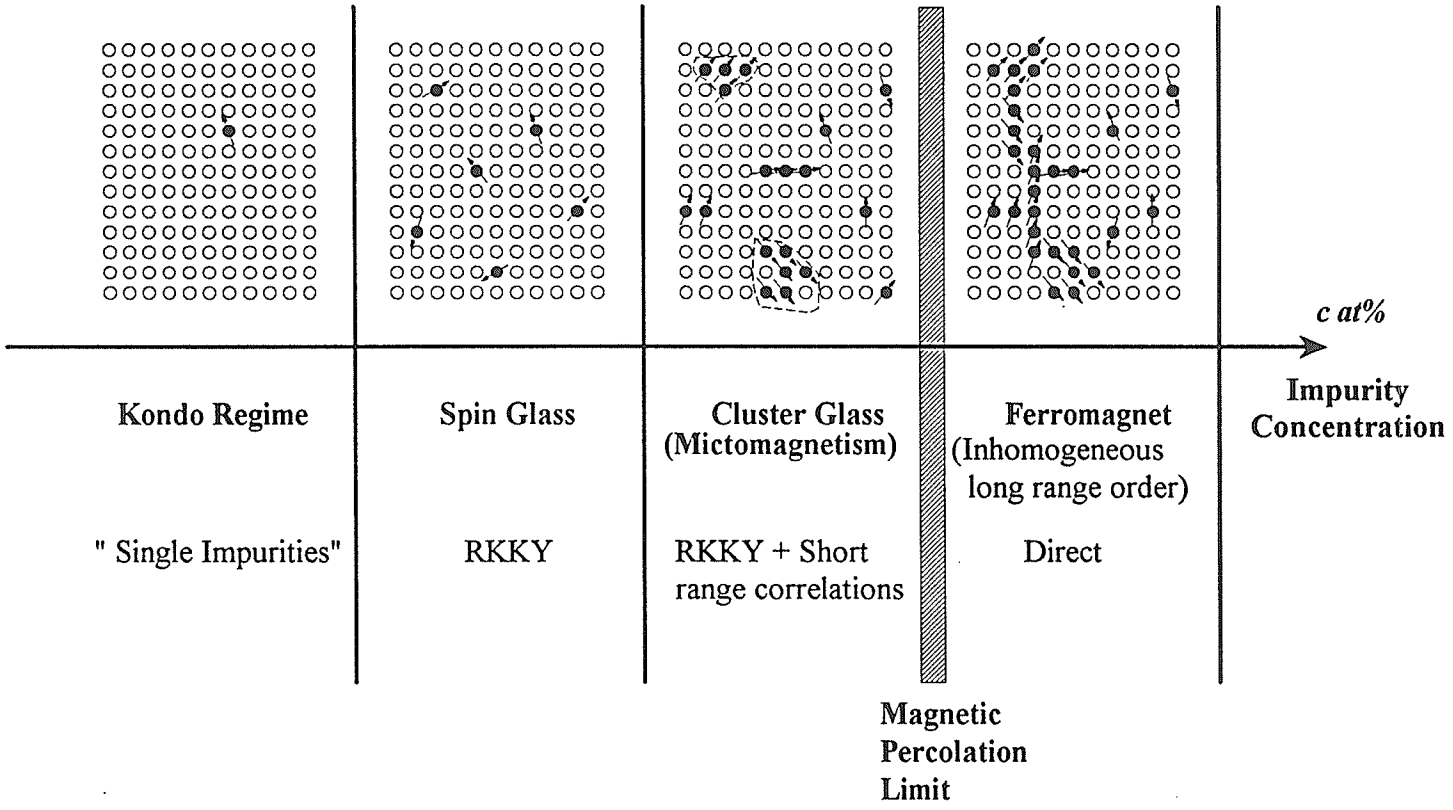

Figure 1-2: Four types of magnetic states: **Kondo Regime, Spin Glass, Cluster Glass, Ferromagnet,** with the magnetic impurity concentration increasing from left to right. From Wohlfarth (1980).

(PdFe, PdMn, PtMn, PdCo). In the latter case, the exchange enhancement of the host leads to giant moment behavior. The term giant moment means that when a single, localized, magnetic moment like Fe is dissolved in an almost magnetic host-like Pd, the net moment on the Fe impurity is much greater than that due to the bare magnetic impurity alone. These magnetic entities, which are the impurity moment plus the induced polarization cloud of the host's surrounding conduction electrons, can be considered as one magnetic moment which is then called "giant". A typical example of a giant moment is found in PdFe, in which the experiments (Crangle and Scott, 1965) reveal the Fe moments to be approximately 10 μ_B as compared to about 3 μ_B for Fe in non-enhanced hosts.

Figure 1-3 shows a typical example of an experimental magnetic phase diagram for a site disordered system, in this case $(Pd_{0.9965}Fe_{0.0035})_{1-c}Mn_c$. Such diagrams generally exhibit four magnetically ordered phases: paramagnet (P), ferromagnet (F), spin glass (SG) and re-entrant ferromagnet (RF) (Verbeek et al., 1978). (a) For Mn compositions $c \leq 3$ at.%, long range ferromagnetism due to a direct Fe-Fe giant moment interaction is found below the Curie temperature T_c, which initially rises with Mn concentration and then falls off above 2 at.% Mn. (b) At a higher concentrations $c > 6.0$ at.%, the competition between the direct ferromagnetic Fe-Fe and direct antiferromagnetic Mn-Mn interactions generates enough spin frustration to destroy the long-range ferromagnetism, and spin glass behavior sets in below T_{SG}. (c) For intermediate compositions $3 < c \leq 6.0$ at.%, there are apparent sequential transitions from paramagnet to ferromagnet, and then to a spin glass as the temperature is lowered further; such a phenomenon is known as re-entrant behavior.

Each regime is characterized by a very distinct magnetic response. Figure 1-4 shows the ac susceptibility as a function of temperature in zero static external field for three samples corresponding to the three different regimes discussed above (Verbeek et al., 1978). Curve (a) for $c = 1$ at.% Mn shows an abrupt knee-like

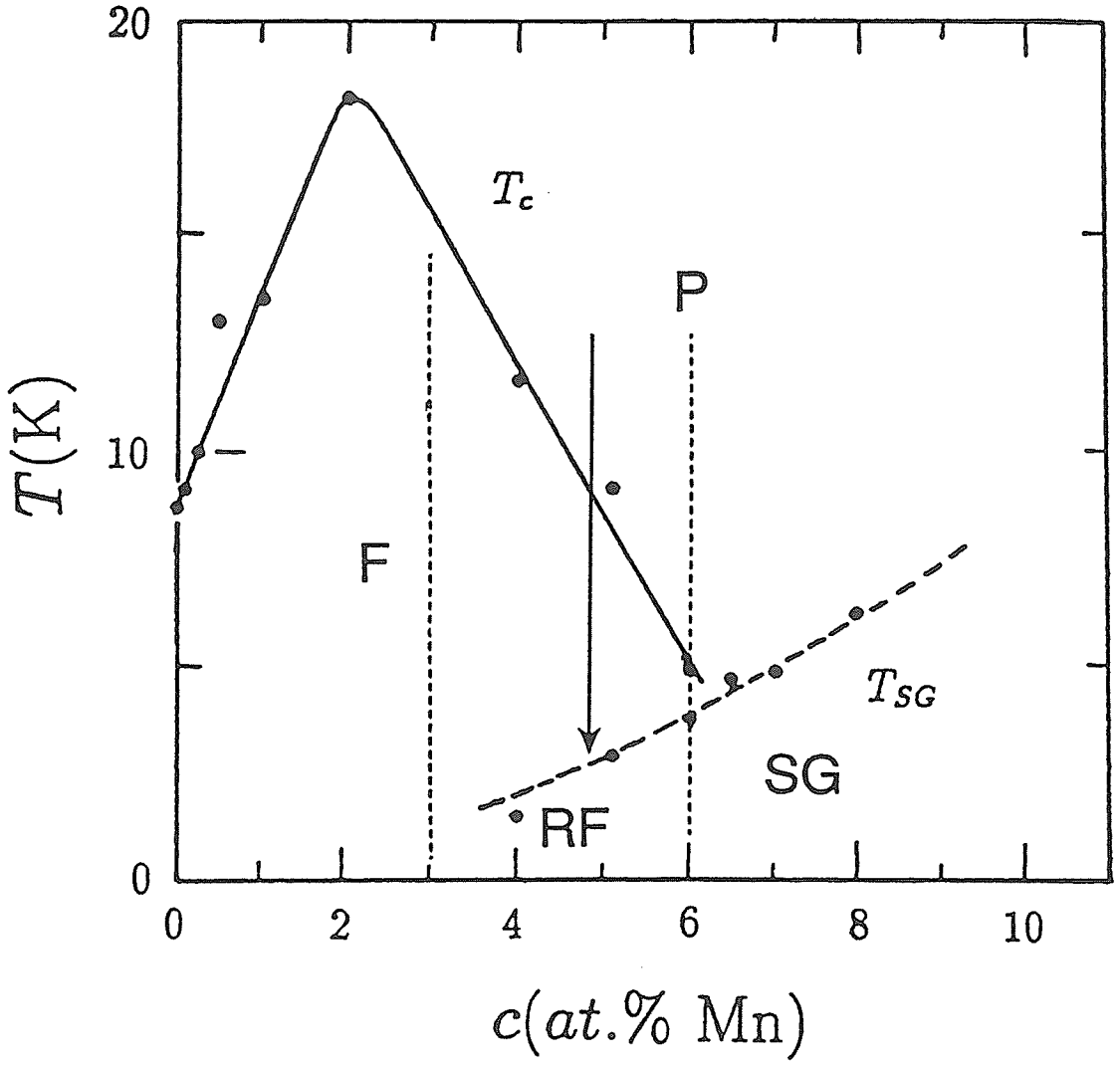

Figure 1-3: The magnetic phase diagram of $(Pd_{0.9965}Fe_{0.0035})$ + c at% Mn. The various phases are: paramagnetic (P), ferromagnetic (F), spin glass (SG), and the reentrant ferromagnet (RF) for $3 \leq c \leq 6$. From Verbeek et al. (1978).

profile at high temperature, typical of a transition from paramagnetism to ferromagnetism, and the susceptibility remains at a roughly constant value down to the lowest temperatures. The Curie temperature ($T_c \approx 13K$) is estimated to be the temperature at which $d\chi/dT$ is maximum. Curve (c) for $c = 6.5$ at.% exhibits a typical spin glass cusp at $T_{SG} \approx 4.7$ K. Notice that the ac susceptibility is substantially smaller than it is for the ferromagnet, indicating that spin glass ordering is a very weak magnetism. Curve (b) combines characteristics of both curves (a) and (c), and displays the typical re-entrant ferromagnetic signature. As the temperature is lowered, the system first exhibits a reasonably sharp high temperature knee, indicating a ferromagnetic transition, and then at lower temperatures($\sim$ 5 K), the susceptibility drops dramatically. Verbeek et al. (1978) associated such a rapid decrease in the susceptibility with the collapse of the ferromagnetic state and the onset of spin glass ordering.

It is important to point out that the temperature independent plateau in curves (a) and (b) is an artifact of the sample geometry, related to the large demagnetizing factor D which depends purely on the sample shape, and which imposes a maximum value on the measured susceptibility of $\chi_{meas} = 1/D$. This tends to enhance the abruptness of the transitions, particularly in the re-entrant case, so that the existence of such a plateau is not always a reliable indication of a genuine cooperative phase transition.

With application of a static magnetic field, a wealth of structure can be revealed in ac susceptibility measurements. Figure 1-5 is a typical example; it shows the temperature dependence of the ac susceptibility in various static fields for the disordered ferromagnets Pd-0.75 at.% Mn and Pd-2.5 at.% Mn (Ho et al., 1981a). A set of peaks, called ferromagnetic critical peaks, are clearly observed. The peak temperatures shift upwards, while peak heights are suppressed as the field is increased. This type of ferromagnetic critical behavior is predicted by scaling theory, and is reproduced by numerical calculation based on the Sherrington-Kirkpatrick

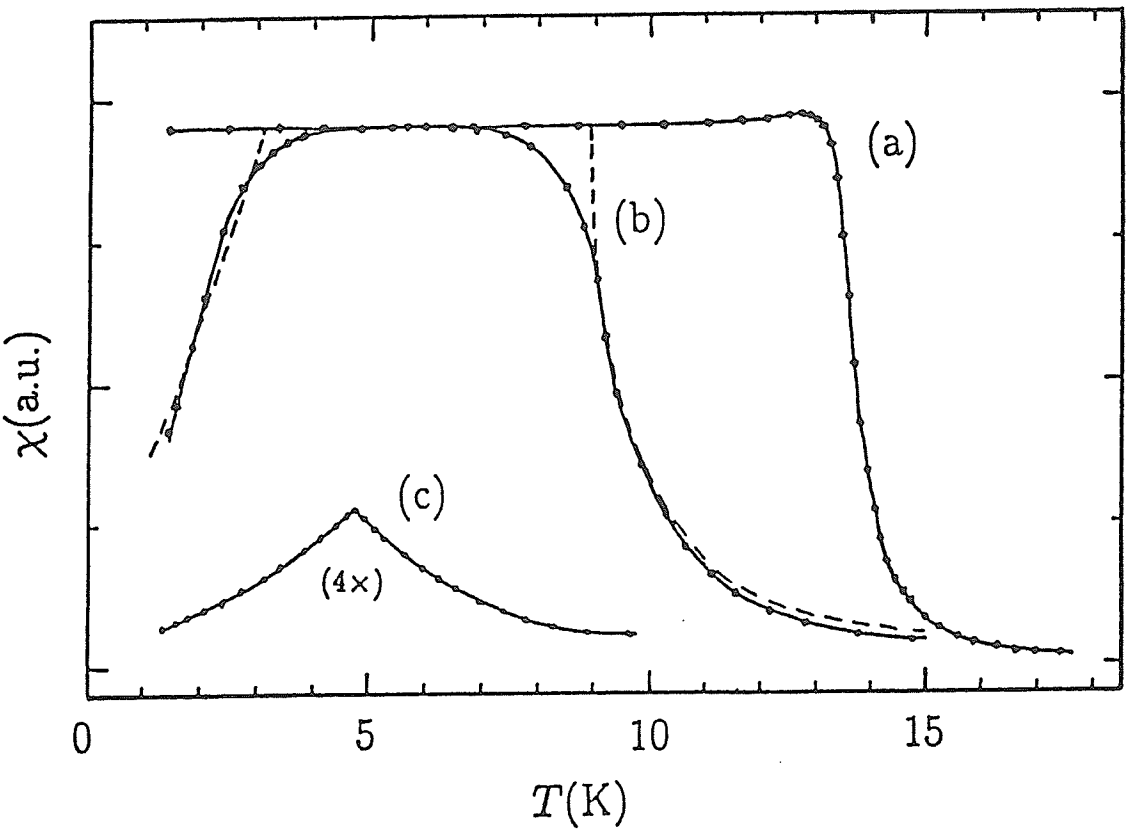

Figure 1-4: Zero-field ac susceptibility measurements (using a driving field of 0.1 Oe and 210 Hz) on three $(Pd_{0.9965}Fe_{0.0035})$ + c at% Mn alloys:
(a) ferromagnet (c=1.0).
(b) reentrant ferromagnet (c = 5.0)
(c) spin glass (c = 6.5).
The dashed line represents a theoretical re-entrant calculation (from the Sherrington-Kirkpatrick model) which has been artificially demagnetization limited. From Verbeek et al. (1978).

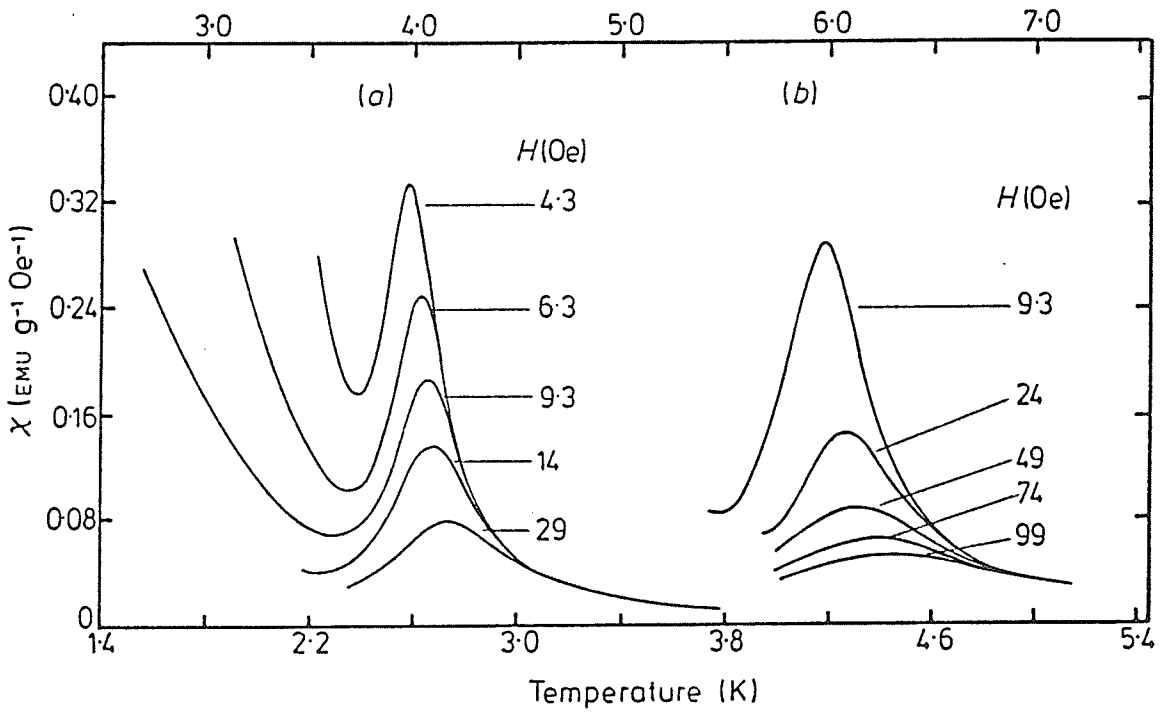

Figure 1-5: A close examination of the ac susceptibility as a function of temperature in the vicinity of the ac susceptibility peaks for (a) Pd-0.75 at% Mn (left curve) and (b) Pd-2.5 at% Mn (right curve), at low collinear biasing fields. From Ho et al.(1981a).

(SK) model. A detailed discussion of the SK model will be presented in the next chapter (section 2.2.1). Unlike ferromagnets, spin glasses show a different response. A good example is shown in Figure 1-6 where the ac susceptibility of the spin glass Pd-5.0 at.% Mn is plotted as a function of temperature in the vicinity of spin glass temperature $T_{SG} = 2.84$ K for various static fields (Zastre et al., 1985). (The exchange bond frustration in PdMn is similar in origin to that in PdFeMn). As the magnetic field is increased, the peak amplitude is suppressed, but the peak temperature is shifted downwards to lower temperatures (dashed line in Figure 1-6). Such behavior can also be qualitatively demonstrated by numerical calculations based on the SK model. In the case of re-entrant ferromagnets, one expects elements of both ferromagnetic and spin glass behavior to occur. Figure 1-7 displays the ac susceptibility measured as a function of temperature in several finite external fields for a re-entrant ferromagnet $(Fe_{0.65}Ni_{0.35})_{1-x}Mn_x, x = 0.113$ (Huck et al., 1988). Three distinct peaks are detected. The high temperature peaks near the Curie temperature $T_c \cong 160$ K are recognized as ferromagnetic critical peaks which are shifted upwards in temperature with increasing field. The two lower temperature peaks near the spin glass temperature $T_{SG} \cong 60$ K both show typical spin glass behavior with the peak temperatures moving downwards as the field increases. Some attempt has been made to correlate these two peaks with various instability lines predicted by vector spin models (section 2.2.2) which suggest that the lower peak is related to the onset of strong irreversibility, i.e., time dependence of the magnetic response.

Further quantitative tests can be performed on the ac susceptibility critical peaks in order to verify the existence of a ferromagnetic phase transition. A set of exponents γ, β, δ, called critical exponents, describe the critical behavior in a ferromagnetic phase transition, and, according to the scaling theory of ferromagnetism (discussed in section 2.3 of next chapter), magnetization and susceptibility

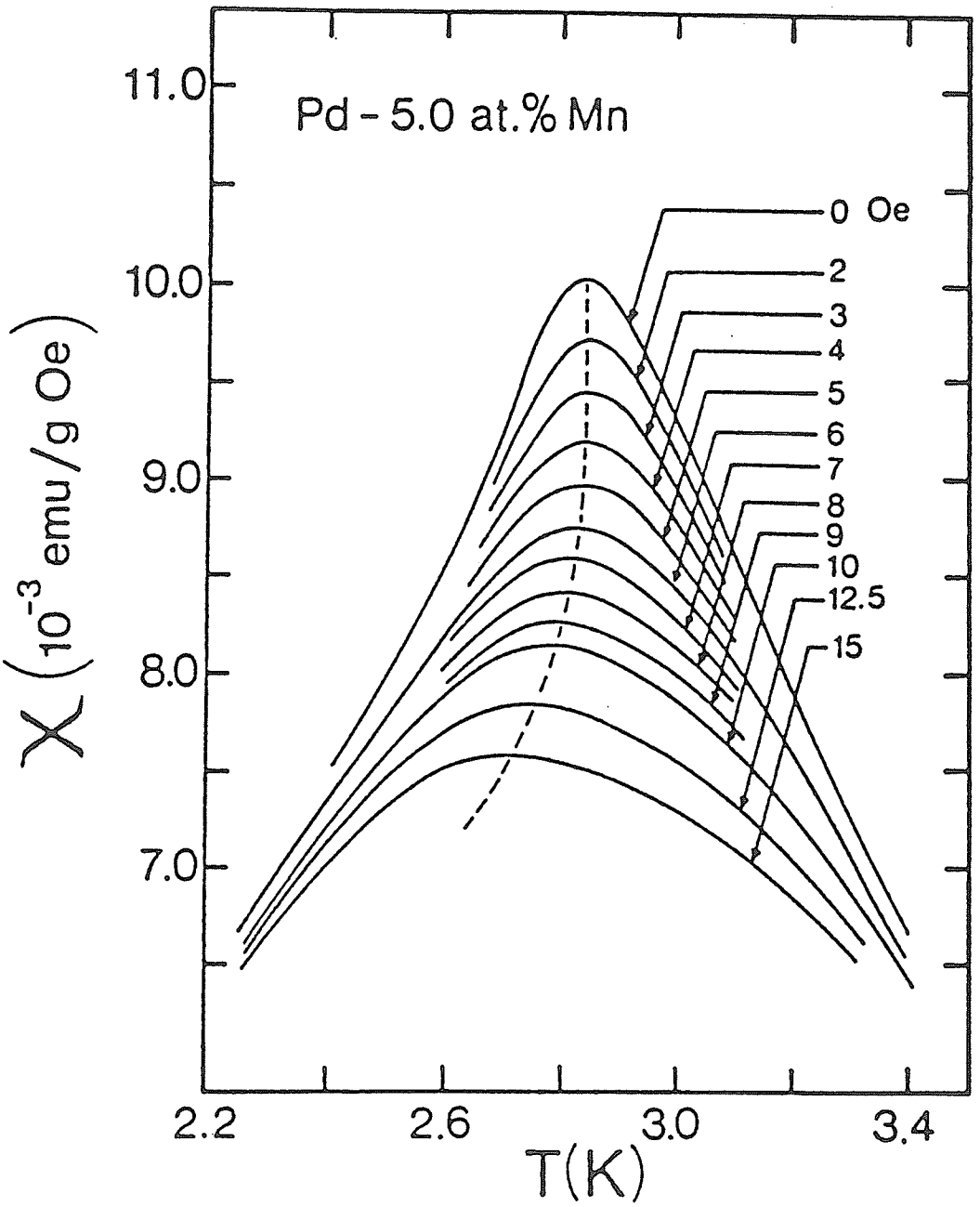

Figure 1-6: The field-dependence of the ac susceptibility of Pd-5.0 at%Mn plotted against temperature T in the vicinity of T_{SG} = 2.84 K. The numbers marked against each curve are the static biasing fields. From Zastre et al. (1985).

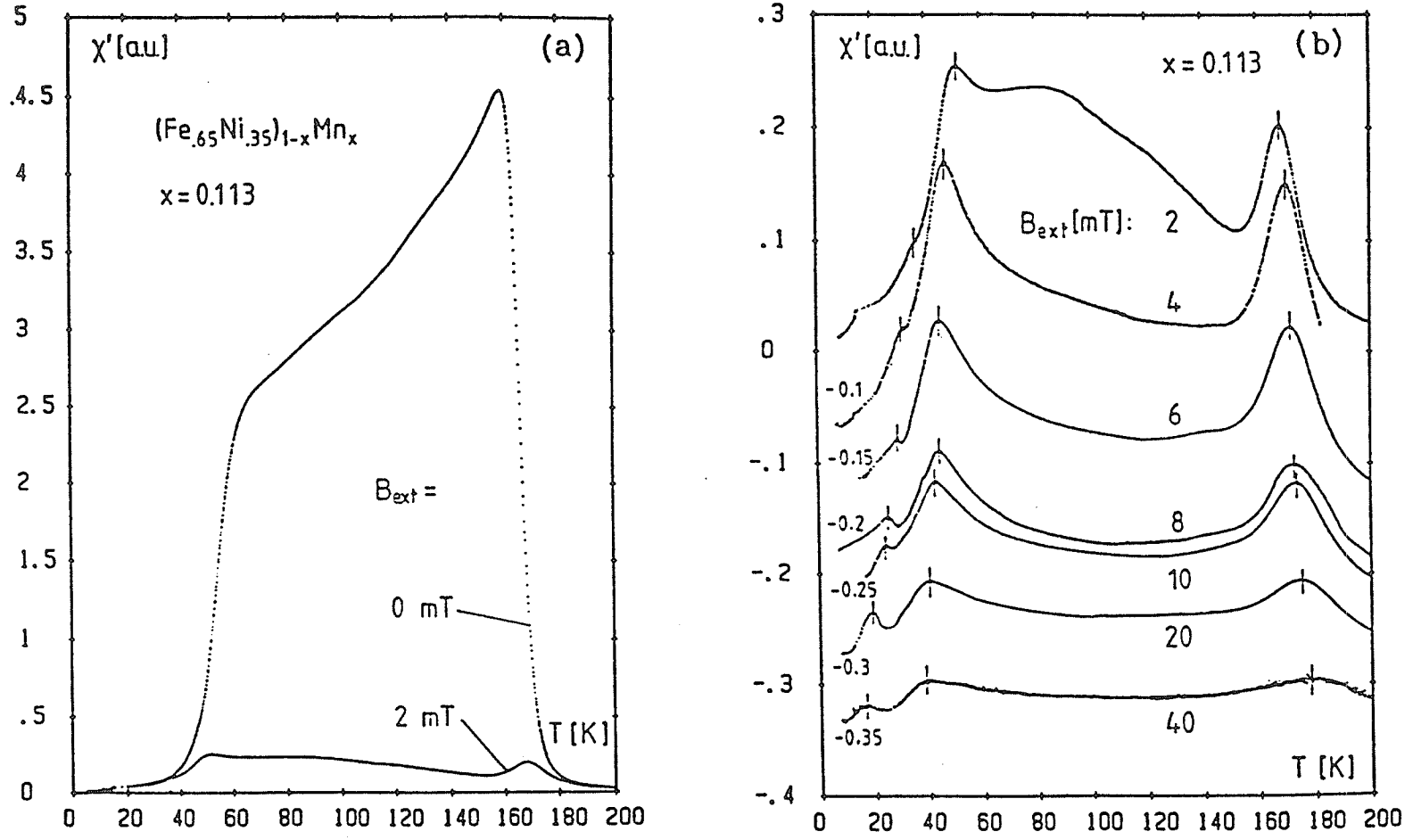

Figure 1-7: (a) ac Susceptibility vs. temperature (ν = 137 Hz, $H_{0,ac}$= 5.5 A/m). The measurement without an external dc field shows a ferromagnetic-like maximum just below $T_c$and an anomalous break down below 60 K. Note the large influence of the small external dc field on the amplitude of the χ'-signal. (b) ac Susceptibility vs. temperature in external dc fields. At 2 mT there are two well distinguished peaks at $T_{R,I}$and T_c With increasing external field the low temperature peak is split into two resolved peaks indicating a different field dependence of $T_i$and T_R. From Huck et al. (1988).

obey the following scaling equations of state

$$m(h,t) = t^{\beta} F\left(\frac{h}{t^{\gamma+\beta}}\right) \tag{1.4}$$

$$\chi(h,t) = h^{(1/\delta)-1} G\left(\frac{h}{t^{\gamma+\beta}}\right) \tag{1.5}$$

where h is the linear scaling field $h \sim H_a/T_c$, $t = \mid (T - T_c)/T_c \mid$ is the reduced temperature, and F and G are scaling functions whose form is unknown. One example of such a scaling test is shown in Figure 1-8 (Kunkel and Williams, 1988). They measured the ac susceptibility as a function of temperature in various dc biasing fields for a $(Pd_{0.9965}Fe_{0.0035}) + 5.0$ at.% Mn re-entrant ferromagnet in the vicinity of the upper paramagnetic-ferromagnetic transition. According to scaling theory, a plot of the normalized susceptibility $\chi(h,t)/\chi(h,t_{peak})$ versus $t/h^{(\gamma+\beta)^{-1}}$ (with choice of $(\gamma+\beta)^{-1} = 0.46$) should produce a universal curve for all static fields above the Curie temperature $T_c = 9.3$ K (Kunkel and Williams, 1988). The quality of the scaling plot in Figure 1-8 indicates a well defined paramagnetic-ferromagnetic transition.

In contrast to ferromagnets, the zero field ac susceptibility of spin glasses does <u>not</u> diverge at the spin glass temperature T_{SG}, and an expansion of the magnetization as a series in <u>odd</u> powers of the applied field

$$M(H,T) = \chi_o(T)H - a_2(T)H^3 + a_4(T)H^5 - ... \tag{1.6}$$

$$\chi(H,T) = \chi_o(T) - a_2(T)H^2 + a_4(T)H^4 - ... \tag{1.7}$$

yields a <u>finite</u> $\chi_o(T)$ at all temperatures, so that the <u>leading</u> divergence in $\chi(H,T)$ in spin glasses occurs in the coefficient $a_2(T)$ of the H^2 term. This means that only <u>non-linear</u> terms can be represented by a scaling function in spin glasses (Yeung et al., 1987). Since the non-linear response is typically much weaker than the linear response, the search for a genuine phase transition in spin glasses is more difficult than it is for ferromagnets. Critical divergences, universality and scaling relations in spin glasses can be found in analysing the non-linear terms. In fact, many typical

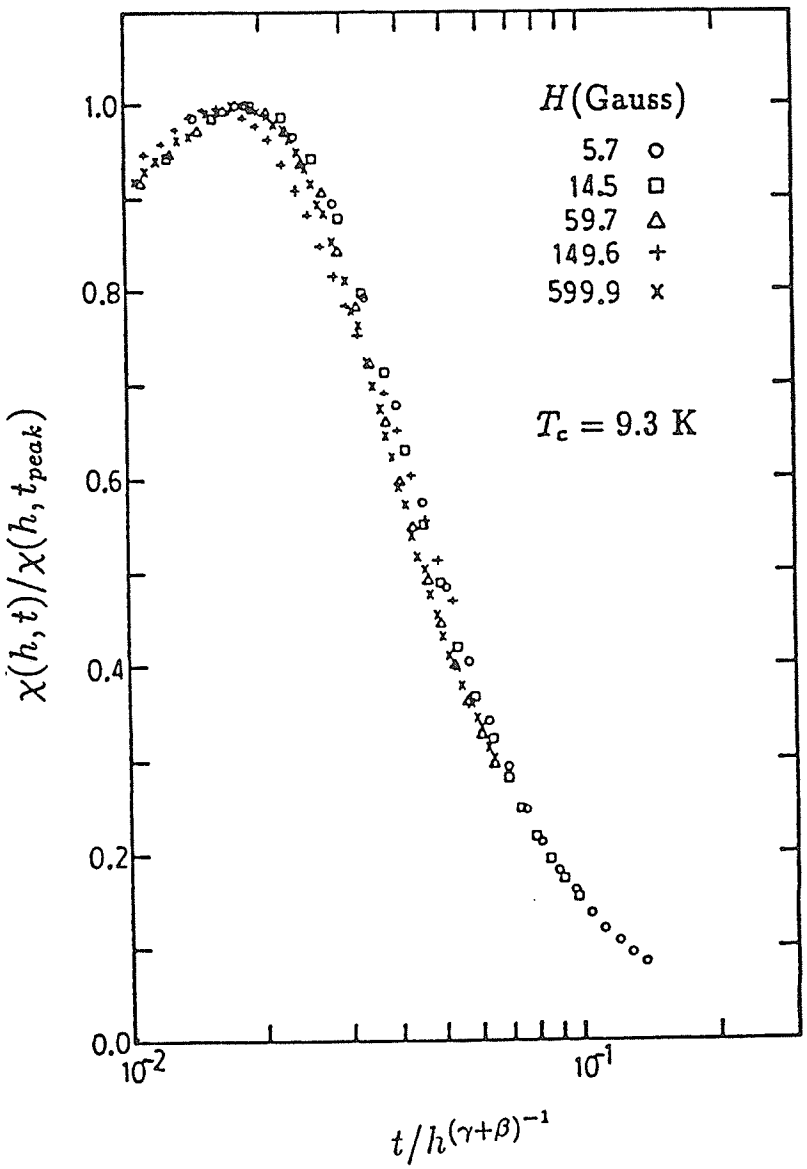

Figure 1-8: A scaling plot for the potentially re-entrant ($Pd_{0.9965}Fe_{0.0035}$) + 5 at% Mn system. Various internal fields are indicated, and the temperatures all lie above 9.3 K. The reduced temperature t_{pcak} represents the location of the high temperature peak in $\chi(t)$ for a particular field. The quality of the scaling illustrates that a well defined paramagnetic/ferromagnetic transition occurs at T_c = 9.3 K. From Kunkel and Williams (1988).

spin glasses exhibit such critical behavior. We illustrate here the critical properties of the non-linear susceptibility in spin glasses Pd-5.0 at.% Mn and Pd-5.5 at.% Mn (Zastre et al., 1985, see also Figure 1-6). By plotting the ac susceptibility χ as a function of H^2 or H^4 for various fixed temperatures, the coefficients $a_2(T)$ and $a_4(T)$ can be obtained from the initial slopes of these curves; the results are summarized in Figure 1-9 which clearly demonstrates nearly symmetric *divergence* in both $a_2(T)$ and $a_4(T)$ about T_{SG} for both Pd-5.0 at.% Mn and Pd-5.5 at.% Mn. Such observations are in good agreement with the predictions of effective field theory (section 2.3).

Although the critical nature of the direct paramagnetic to spin glass transition has been confirmed by non-linear response experiments, true non-linear critical behavior has not yet been verified in re-entrant systems near the lower ferromagnetic to spin glass transition. This is primarilly due to the complication of domains and the effects of domain wall motion. One of the few re-entrant systems which show an anomaly in the non-linear susceptibility is $(Pd_{0.9965}Fe0.0035)$ + 5.0at.% Mn (Kunkel and Williams 1988). Figure 1-10 shows the temperature dependence of the coefficient $a_2(T)$ near the lower transition temperature. A distinct peak is observed near $T = 4.07$ K, defined as T_{SG}, suggesting a possibly critical ferromagnet glass transition.

In addition to ac susceptibility measurements, a variety of other physical properties, such as specific heat, resistivity, Mössbauer effect and neutron scattering etc, have also been used to characterize the various magnetically ordered phases.

Specific heat measurements on ferromagnets can be used to determine the Curie temperature T_c. The excess specific heat $C_m = \Delta C = C_{alloy} - C_{host}$ will show an anomaly at T_c, as shown in Figure 1-11 for four bond disordered PdMn ferromagnets (Boerstoel et al., 1972). The sharp cusp at T_c indicates a well defined paramagnetic-ferromagnetic transition, and is in good agreement with the predictions of the mean-field-theory of ferromagnetism (Stanley, 1971).

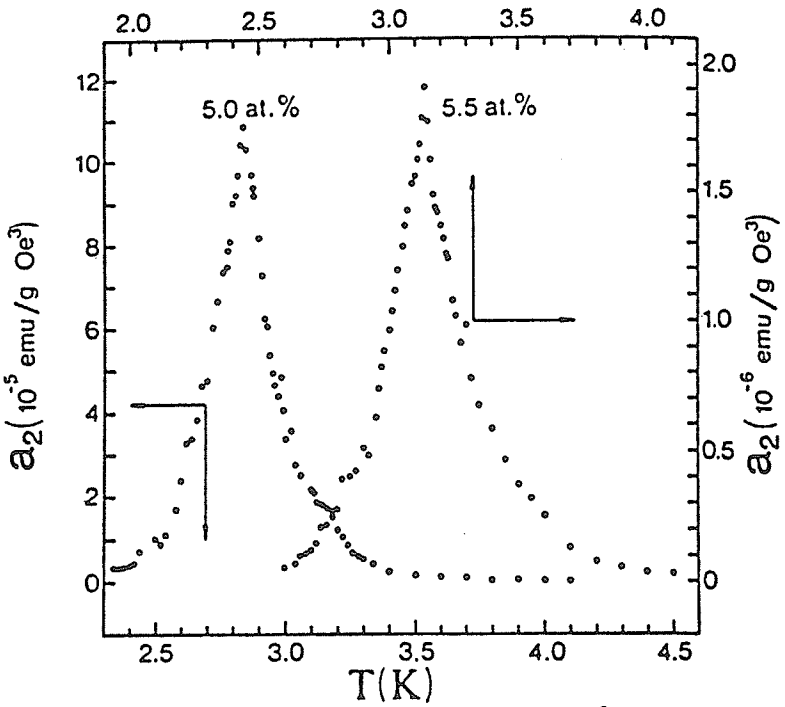

Figure 1-9: (a) The temperature dependence of the H^2 coefficient $a_2(T)$ for the Pd-5 and 5.5 at % Mn samples. From Zastre et al. (1985).

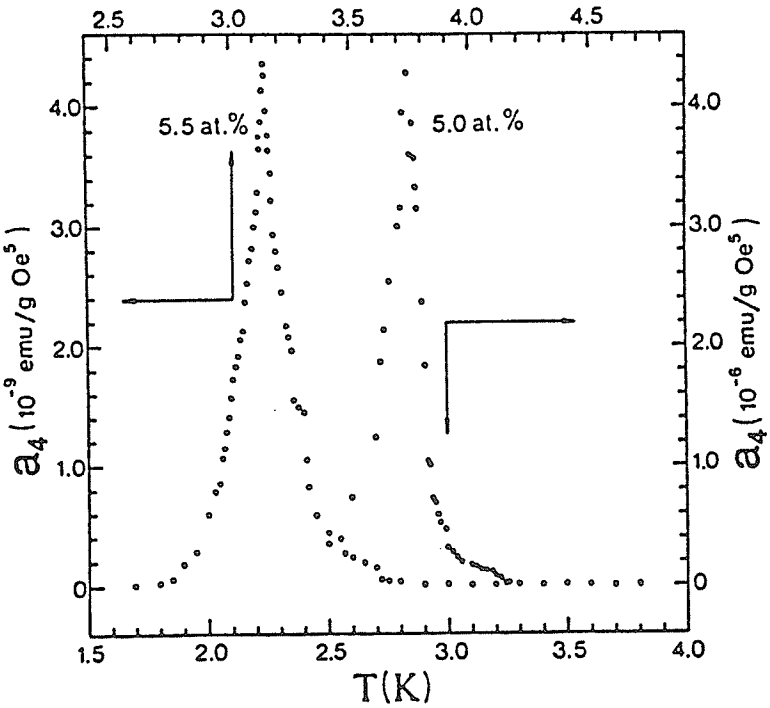

Figure 1-9: (b) The temperature dependence of the H^4 coefficient $a_4(T)$ for the Pd-5 and 5.5 at% Mn samples. From Zastre et al. (1985).

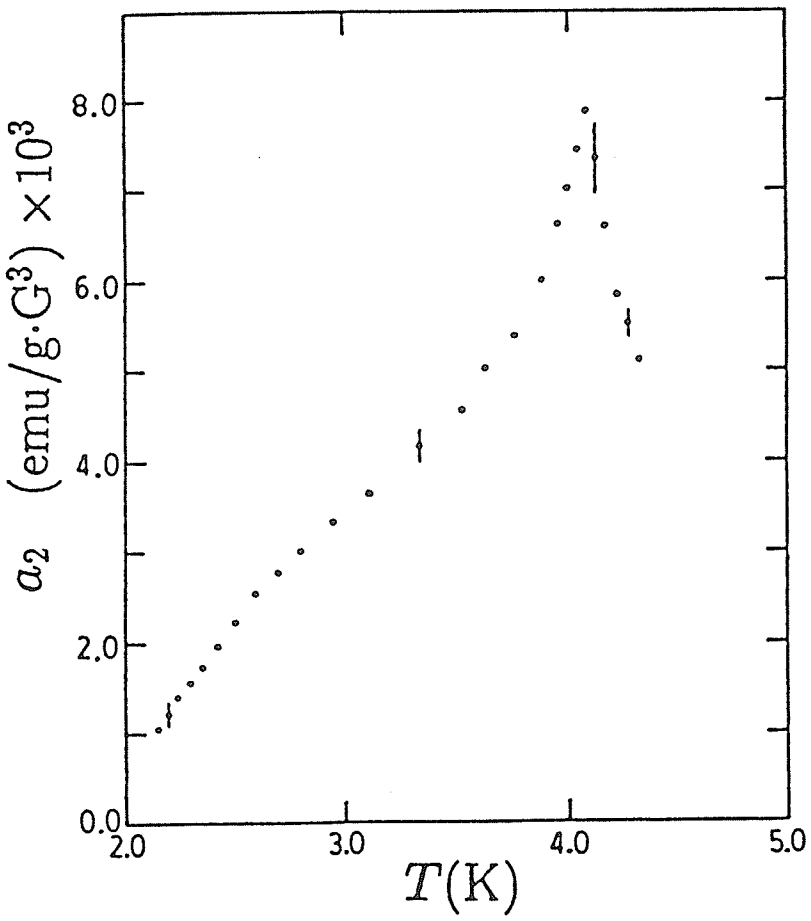

Figure 1-10: A peak in the quadratic field coefficient of the $(Pd_{0.9965}Fe_{0.0035})$ + 5.0 at% Mn susceptibility apparently occurs near 4.07 K. The anomaly is suggestive of critical re-entrant behaviour, and is used to identify the re-entrant transition temperature T_{SG}. From Kunkel and Williams (1988).

By contrast, the magnetic specific heat C_m of spin glasses generally displays a rather broad maximum (contrary to the predictions of the SK model, which predicts a cusp at T_{SG}) at temperatures higher than the glass freezing temperature T_{SG}. Figure 1-12 shows a typical example C_m as a function of temperature for three CuMn spin glasses (Martin, 1980). The vertical lines mark the spin glass temperatures T_{SG} from susceptibility measurements. Further analysis of the low temperature behavior of C_m shows $C_m(T) \approx C_1 T + C_2 T^2$ in these systems (where C_1 and C_2 are constants), although the leading temperature dependence of the magnetic specific heat of spin glasses often varies from one system to another system (Fischer 1985, and reference therein). While no abnormal behavior can be seen directly in C_m vs T plots, an anomaly is observed in the field dependence of the magnetic specific heat C_m (Fogle et al., 1981; Brodale et al., 1983). Fogle et al. (1981) measured the specific heat of a Cu-0.279 at.% Mn spin glass as a function of temperature in various fixed fields. The peak in the specific heat C_m broadened and shifted to higher temperatures as the field increased. The function $C_m/T = A + BH^2$ was used to fit the C_m/T vs H data (as shown in the insert of Figure 1-13) and the coefficient B of H^2 term shows a sharp negative minimum near T_{SG}, perhaps associated with the onset of the spin glass ordering. Whereas few specific heat measurements have been performed on re-entrant ferromagnets, one example is shown in Figure 1-14(a) for an insulating re-entrant ferromagnet $Eu_xSr_{1-x}S$ with $x = 0.54$ (Meschede et al., 1980). A broad maximum is observed near the ferromagnetic transition temperature T_c, and the magnetic specific heat varies linearly with temperature below the maximum. Although the magnetic specific heat C_m shows no singularity at T_{SG}, a tiny step is observed by plotting dC_m/dT versus log T in Figure 1-14(b).

Electrical resistivity measurements on spin glasses show similar behavior to the magnetic specific heat. The incremental electrical resistivity $\Delta\rho(T) = \rho_{alloy}(T)$ - $\rho_{host}(T)$ of several spin glasses has been measured as a function of

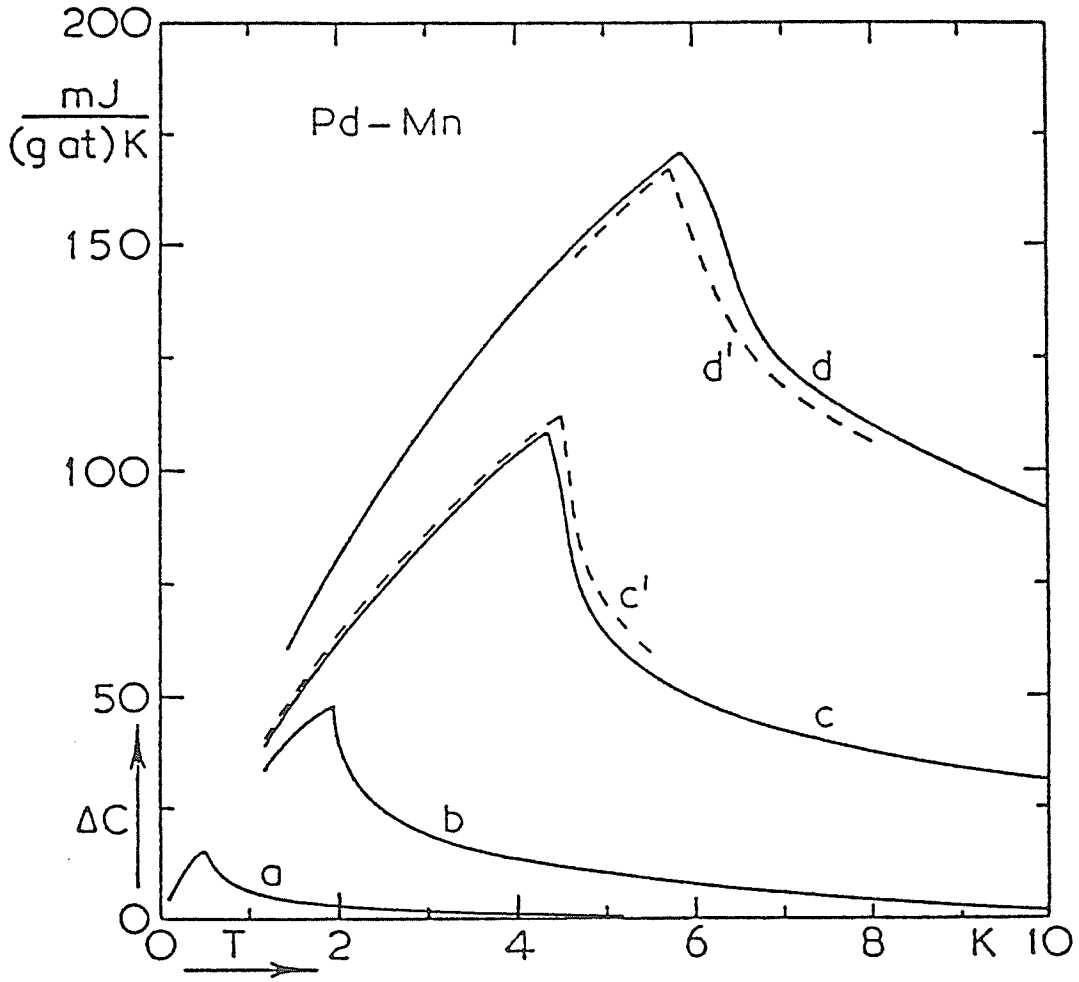

Figure 1-11: ΔC vs. T of Pd-Mn alloys containing 0.19 at% (a); 0.54 at.% (b); 1.35 at.% (c); 2.45 at.% Mn (d) at H = 0. Curves c′ and d′ represent measurements after 220 hours of homogenization at 1000°C subsequent to the usual homogenization (48 hours at 1025°C). From Boerstoel et al. (1972).

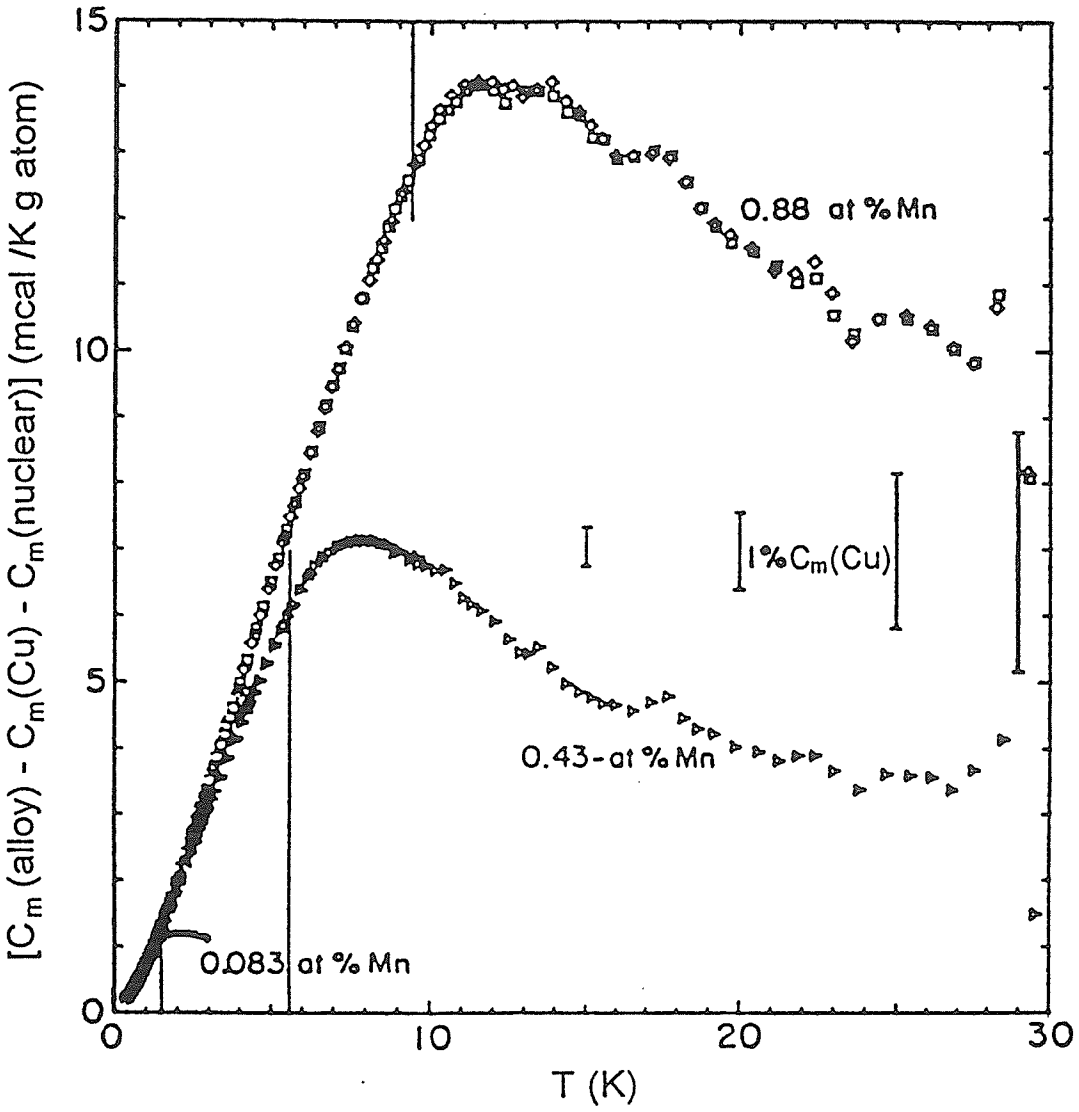

Figure 1-12: *Cu*Mn Spin glass specific heat plotted against temperature. The vertical bars intersecting the plots mark the estimate of T_{SG} for each composition. The bars in the center of the graph show the magnitude of 1% of the specific heat of copper. From Martin (1980).

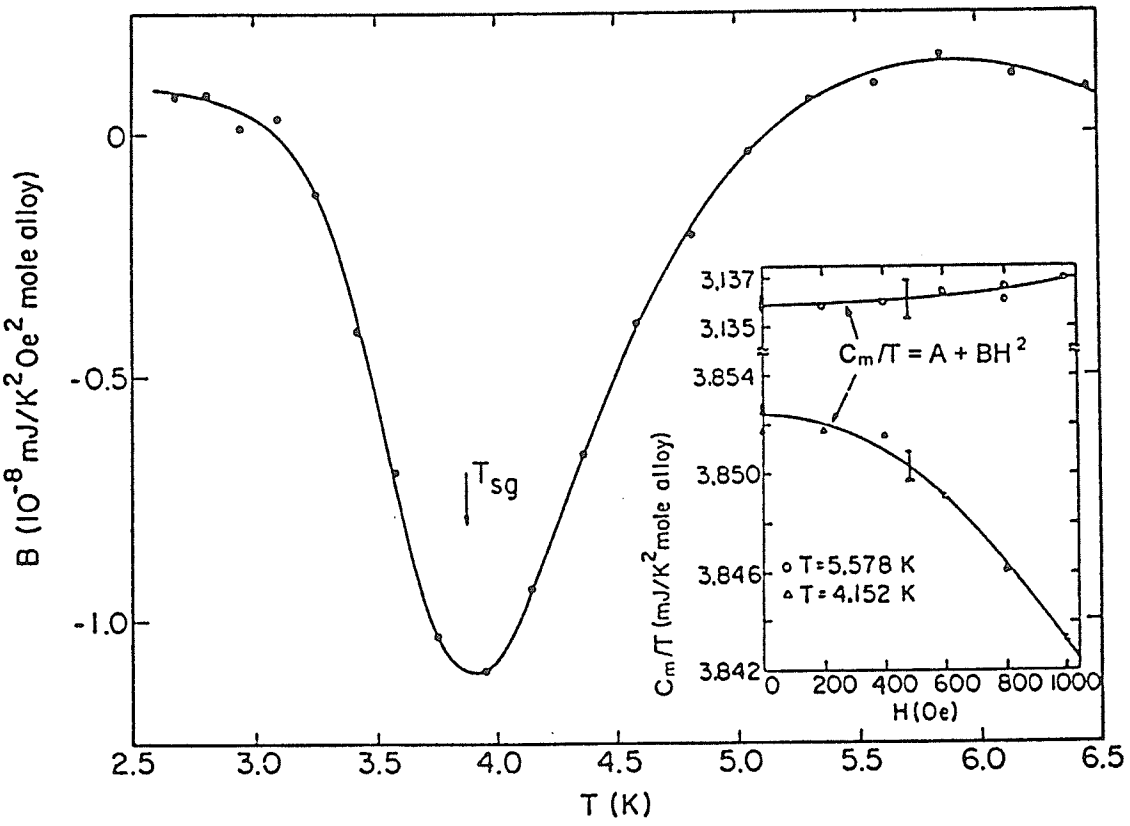

Figure 1-13: The field dependence of the specific heat $C_m/T = A + B H^2$, shown in the inset of the figure, and the coefficient B of the H^2 term. The error bars in the inset correspond to $\pm 0.01\%$ of the total measured specific heat. From Fogle et al. (1981).

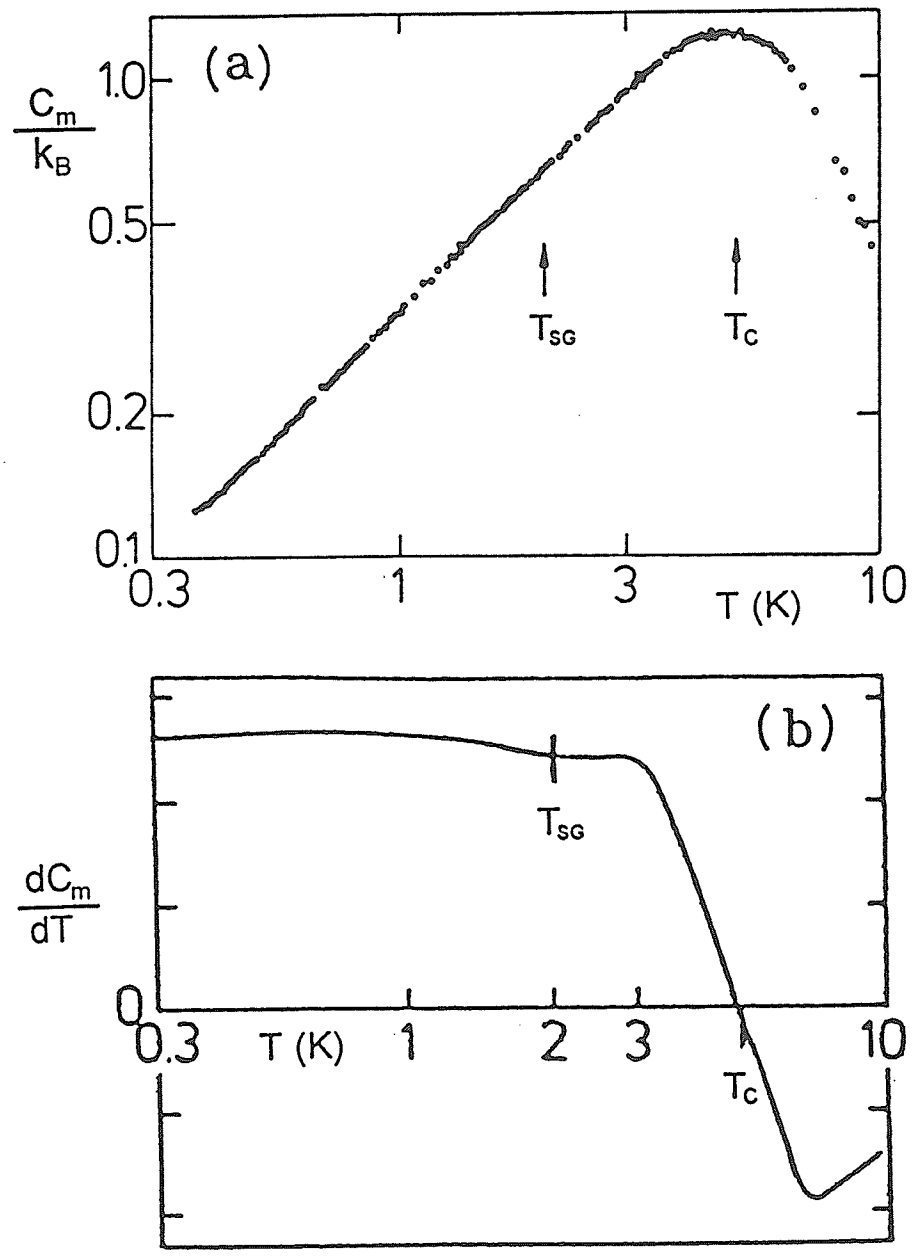

Figure 1-14: (a) Specific heat C_m per Eu atom divided by k_B vs temperature T in zero field for a re-entrant ferromagnet $Eu_xSr_{1-x}S$ (x=0.54). (b) The temperature derivative dC_m/dT of the specific heat in (a) vs temperature T on a logarithmic scale. From Meschede et al. (1980).

temperature by Ford and Mydosh (1976), and the results for AgMn are given in Figure 1-15. For all compositions there is a broad maximum at a temperature T_m higher than T_{SG}, with T_m proportional to the impurity concentration. Closer examination of the temperature dependence of $\Delta\rho(T)$ reveals a linear T-dependence near T_{SG}, and a $T^{3/2}$-dependence in the lowest temperature region. The absence of an anomaly in the electrical resistivity of spin glasses is consistent with the fact that no anomaly is generally observed in the magnetic specific heat. In ferromagnets, however, a sharp anomaly is normally observed. The incremental resistivity $\Delta\rho(T)$ of some disordered PdMn ferromagnets is plotted as a function of temperature in Figure 1-16 (Ho et al., 1981a). The temperature at which $d(\Delta\rho)/dT$ reaches a maximum coincides with the Curie temperature T_c obtained from ac susceptibility results (Figure 1-5). Such a sharp "knee" is indicative of a ferromagnetic phase transition. Below T_c, $\Delta\rho(T)$ varies linearly with temperature and obeys a ferromagnetic $T^{3/2}$-dependence at even lower temperatures.

Neutron scattering experiments and Mössbauer effect measurements can probe a magnetic system on microscopic time scales. Neutron scattering can provide information on magnetic short range order, the spin glass freezing process, as well as the dynamic relaxation of the spins (Binder and Young, 1986). However, the interpretation of the neutron scattering data is difficult. The absence of Bragg scattering indicates no long-range magnetic order in spin glasses. The frequency and wave-vector-dependent susceptibility $\chi(\vec{q},\omega)$ of Cu-8.0 at.% Mn, as computed for the broad quasi-elastic scattering peaks, exhibits a peak for small $\vec{q}$ at a temperature higher than the spin glass temperature obtained from ac susceptibility measurements (Fischer, 1985, and references therein). The neutron spin-echo technique was used to measure the time-dependent spin-spin correlation function in the spin glasses CuMn and $La_{0.7}Er_{0.3}Al_2$ (Binder and Young, 1986; and reference therein). These results indicate that there exists a broad spectrum of spin relaxation times which is temperature dependent and extends from at least 10^{-12}s

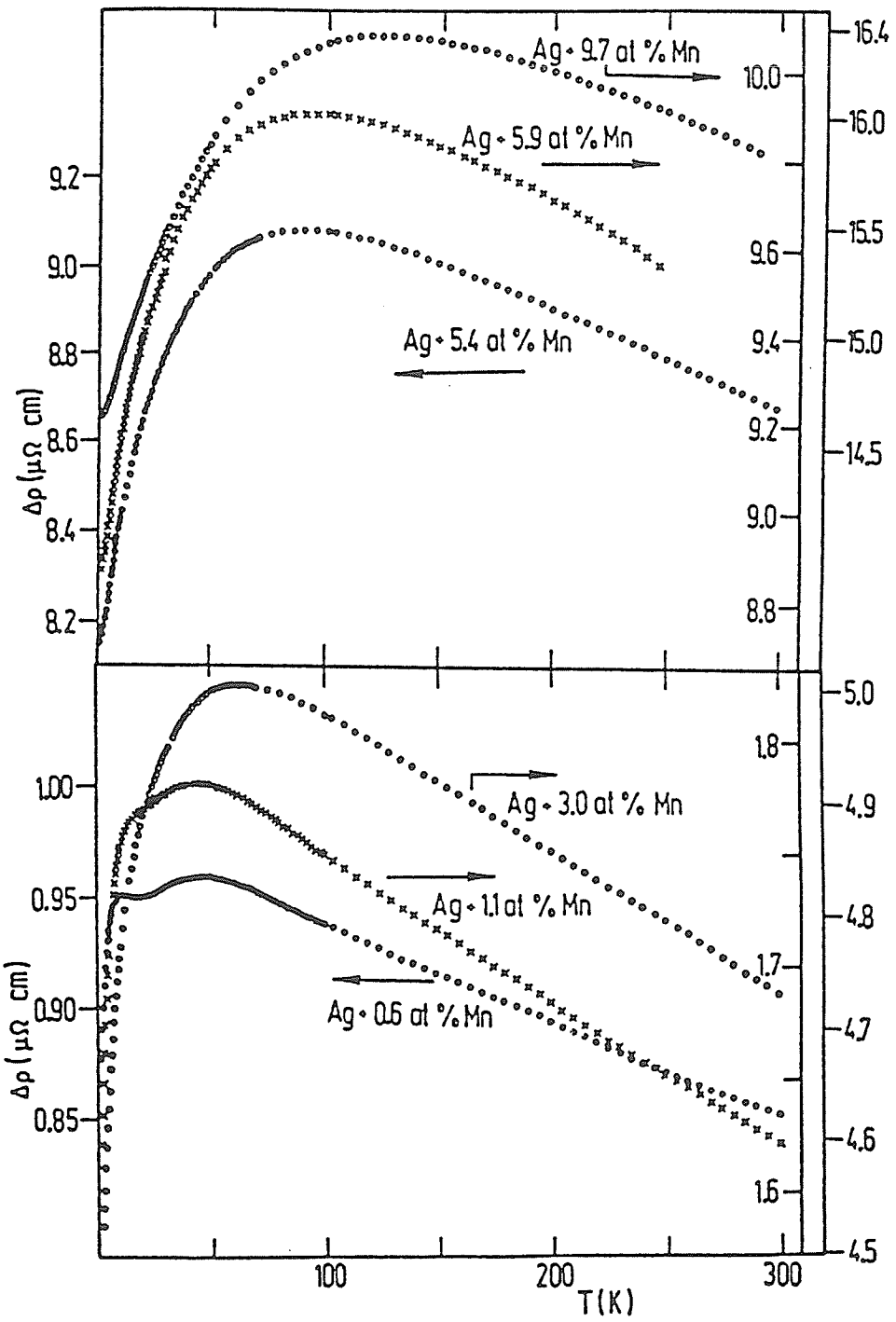

Figure 1-15: Over-all temperature variation of $\Delta\rho$ ($\mu\Omega$ cm) for *Ag*Mn alloys with concentrations between 0.6 and 9.7 at% Mn. Note the changes in scale as the concentration increases. From Ford and Mydosh (1976).

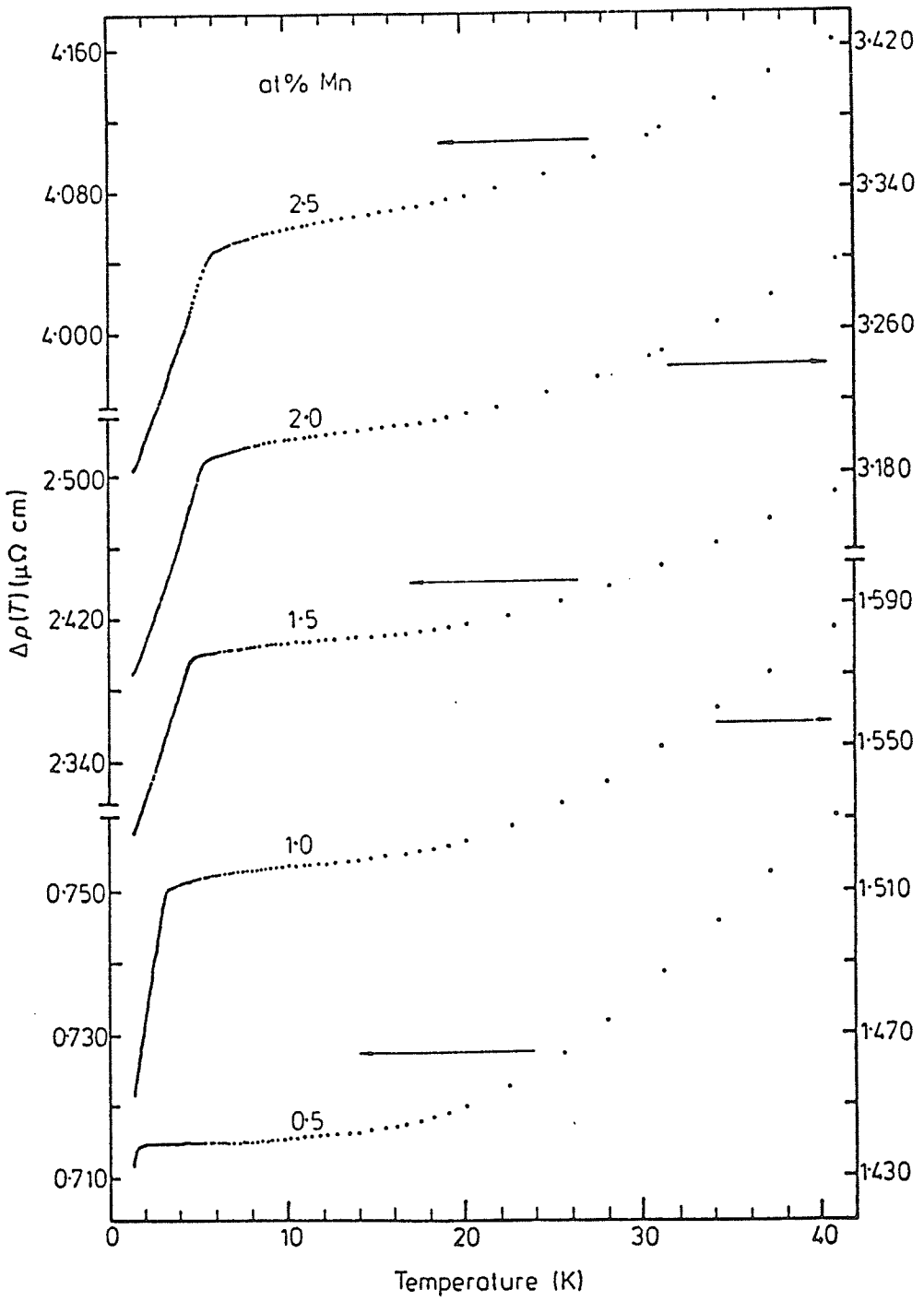

Figure 1-16: A summary of the resistivity data in the form of an incremental resistivity $\Delta\rho(T)$ against temperature plot below 40 K, for *Pd*Mn. From Ho et al. (1981a).

to 10^{-2}s below T_{SG}. Near T_{SG}, no sharp critical slowing down(Fischer, 1985); instead, the relaxation varies gradually with temperature. Thus it was concluded that the freezing of the spins in spin glasses is a gradual process with no sharp phase transition.

A dynamic freezing-in of spins was also indicated from the Mössbauer measurements. In studying the Mössbauer effect in spin glasses, the spin glass temperature can be identified by the "peak splitting" of the Mössbauer spectrum, caused by the formation of static or quasi-static internal fields due to spin freezing (Hunag, 1985; and reference therein). Thus the analysis of Mössbauer spectra can provide information on local arrangements of magnetic moments. Figure 1-17 presents zero-field Mössbauer spectra on an Au-3.0 at.% Fe spin glass between 1.9 K and 19 K (Meyer et at., 1985). An abrupt change of regime was observed at about 19.5 K, well above T_{SG} (= 16.4 K). Below 19 K, the spectra can be fitted by a static, inhomogeneously broadened field distribution $P(H)$. Mössbauer measurements on a Au-16.8 at.%Fe re-entrant ferromagnet (Lange et al., 1990) demonstrate the existence of a low temperature transition at $T_{SG} \sim 45$ K from ferromagnetism to a spin-glass like state, characterized by a freezing of the transverse components (with respect to a strong applied static field) of Fe spin magnetic moments, i.e, the spins are canted, supporting the prediction of a Gabay-Toulouse transition line (section 2.2.2). However, Violet and Borg (1983, 1984) disagreed with this conclusion. They observed two superposed six-line Mössbauer spectra at 4.2 K for AuFe alloys with Fe concentrations between 10.5 and 33 at.%, and argued that these lines are derived from Fe in two compositionally different phases.

Irreversibility is a striking feature of spin glasses, often studied by magnetization measurements, especially remanent magnetization measurements after an applied field has been switched off. Two types of remanent magnetization should be distinguished, depending on the order of cooling and the application of a magnetic field. (a) The Isothermal Remanent Magnetization (IRM) is obtained by

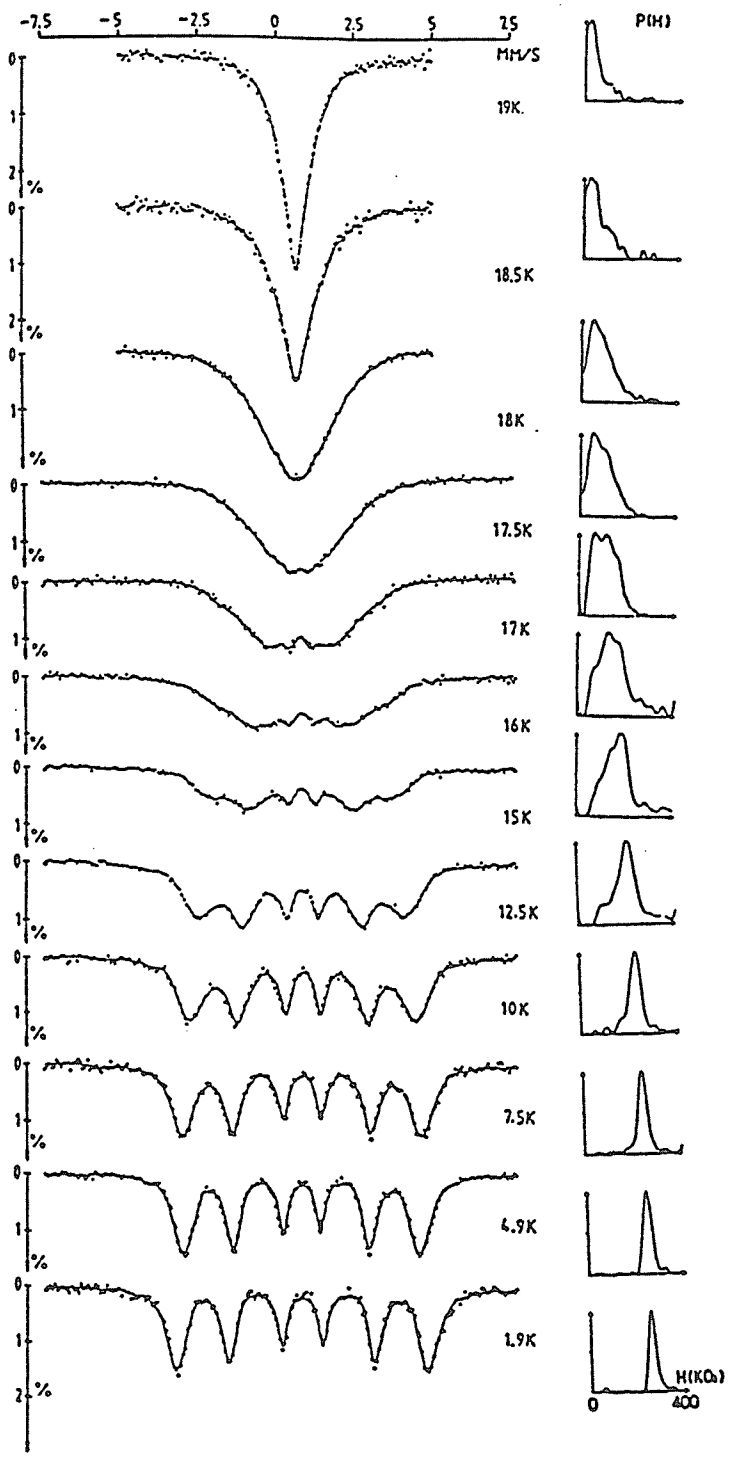

Figure 1-17: Thermal evolution of the Mössbauer spectra below 19 K for a Au-3.0 at% Fe spin glass. The spectra were fitted with an inhomogeneous hyperfine field distribution *P(H)*. From Meyer et al. (1985).

cooling the sample from above T_{SG} to a measurement temperature T_m (below T_{SG}) in zero field, then a static field is applied for a period of time and switched off. (b) The Thermoremanent Magnetization (TRM) is obtained by cooling the sample in a static field from a temperature above T_{SG} down to T_m, and after a wait time t_w has elapsed, the field is then turned off. Figure 1-18 displays the field dependences of the TRM and IRM at a temperature below T_{SG} for the spin glass Au-0.5 at.%Fe (Tholence and Tournier, 1974). There is a weak maximum in the TRM and a substantial difference between the TRM and IRM at lower fields due to a time dependent component in the magnetization. Both the TRM and IRM reach the same saturation value, but the TRM requires a lower field. Another example of irreversibility in spin glasses is given in Figure 1-19, which shows the zero-field-cooled (ZFC) and field-cooled (FC) magnetization of Pt-2400 ppm Mn as a function of temperature (Yeung et al., 1988). The ZFC curve was obtained by cooling the sample to the lowest temperature in zero field, then applying a field of 2 Oe and measuring the magnetization upon warming, while the FC curve was measured by first cooling the sample in a field of 2 Oe to the lowest temperature. As seen from Figure 1-19, the FC and ZFC magnetizations are identical above T_{SG} (defined by the cusp in the ZFC curve), but below their behavior differs dramatically due to irreversibility. The irreversibility appears in magnetic hysteresis measurements as well. A displaced magnetic hysteresis loop is shown in Figure 1-20 for Cu-25.0 at.%Mn at a temperature below T_{SG} when the sample was cooled initially in a field $H_c = 12.7$ kOe. The shape of the hysteresis loop depends on the magnetic history of the sample as well.

The time decay of the TRM in AuFe spin glasses was first studied by Holtzberg et al. (1977) and Guy (1978). Guy measured the decay of the TRM for a Au-2.0 at.% Fe for observation times 10 s $< t <$ 500 s, and found that the decay could be approximately represented by a logarithmic function

$$M_{TRM} = M_o - S \ln t \tag{1.8}$$

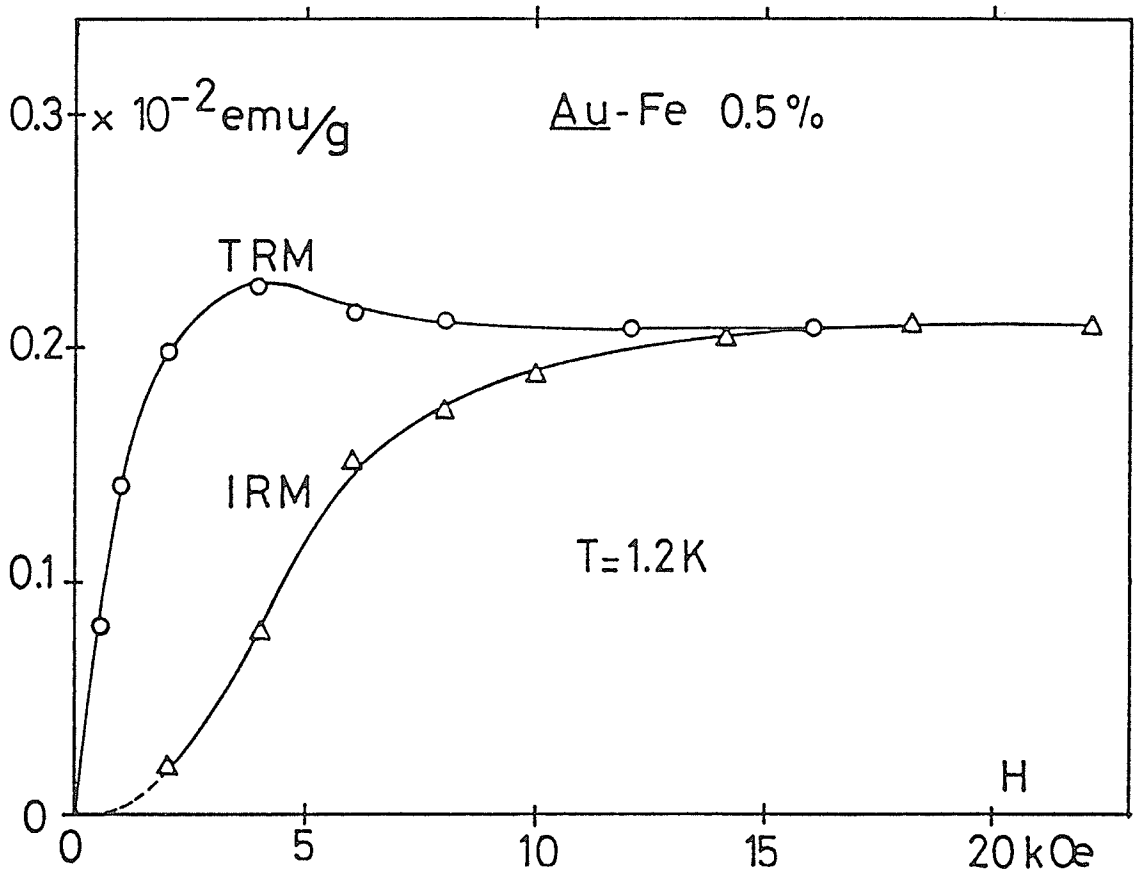

Figure 1-18: Field dependence of the thermoremanent magnetization (TRM) obtained after cooling from $T_i > T_{SG}$ to $T = 1.2$ K in a field H, and of the isothermal remanent magnetization (IRM) obtained when a field H applied at 1.2 K is suppressed. From Tholence and Tournier (1974).

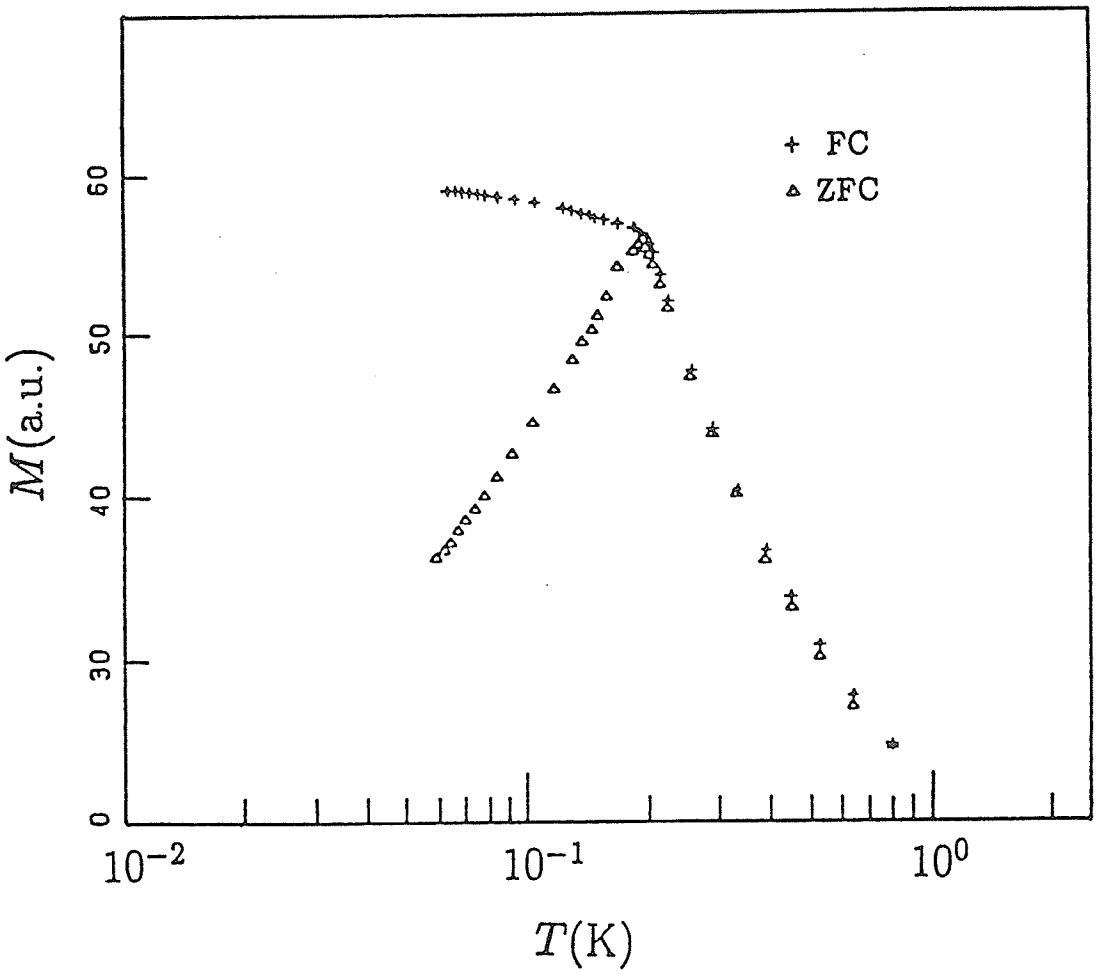

Figure 1-19: The FC and ZFC magnetization of the Pt+2400 ppm Mn spin glass, using an applied field of 2 Oe. The peak in the ZFC curve is at $T_{SG} \approx 200$ mK. From Yeung et al. (1988).

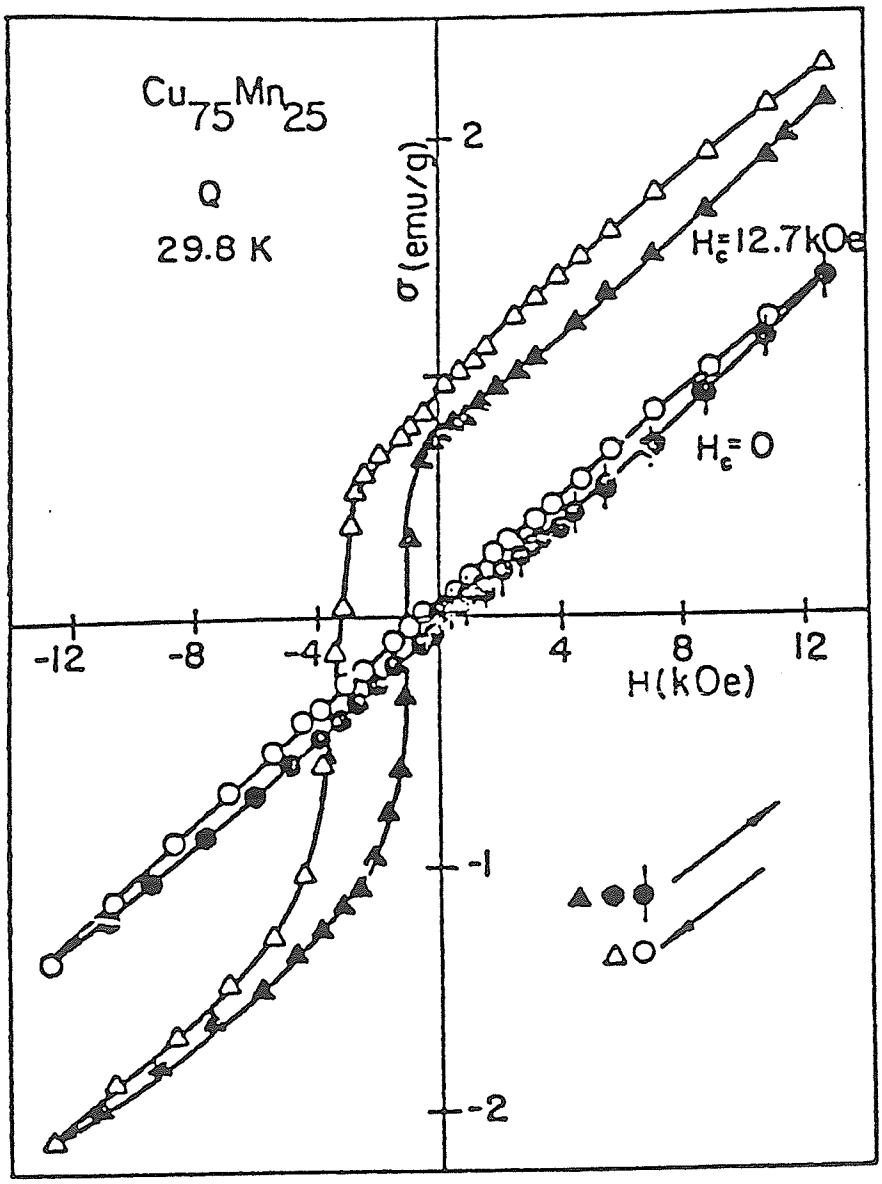

Figure 1-20: Magnetization of *Cu*Mn with 25 at.% Mn vs field after zero-field cooling (H_c = 0) and after cooling in a field of 12.7 kOe. From Beck (1978).

where M_o is a constant, and S depends on field, temperature and materials. A logarithmic time dependence was first used by Street and Woolley (1949) to describe magnetic viscosity, known as after-effects, in ferromagnetic alloys.

Ferré et al. (1981) measured the decay of the thermoremanent magnetization of the insulating spin glass $Eu_{0.4}Sr_{0.6}S$ over two full decades of time (1 s $\leq t \leq$ 100 s). Their data are more consistent with a power law rather than a logarithm function:

$$M_{TRM} = M_o t^{-m(H,T)} \tag{1.9}$$

where the parameter m depends both on field and temperature.

In order to find the true functional form of the relaxation in spin glasses, it is necessary to record the decay of the TRM over as long an interval as possible. Chamberlin et al. (1984), and Chamberlin (1984, 1985) measured the time decay of the TRM on three different spin glasses over 4 decades 0.2 s $< t <$ 1000 s , and found that for all measurement temperatures below T_{SG}, the decay could be described accurately by a stretched-exponential function for 5 s $\leq t \leq$ 1000 s:

$$M_{TRM} = M_o' \exp[-C(\omega t)^{1-n}/(1-n)] \tag{1.10}$$

where the prefactor M_o' and exponent n are temperature dependent constants, and the factor C and relaxation frequency ω can be chosen to be independent of temperature. Figure 1-21 shows the decay for Ag + 2.6at.%Mn + 0.46 at.%Sb at four temperatures below T_{SG}. A plot of M_{TRM} vs log t (Figure 1-21(a)) proves that M_{TRM} does not decay logarithmically, while a log-log plot of M_{TRM} vs t (Figure 1-21(b)) demonstrates a breakdown of the power law dependence. The solid lines represent the best fit using the stretched-exponential function Eq.(1.10). Further investigations of the wait time t_w dependence of the TRM by Chamberlin (1984) and Hoogerbeets et al. (1985, 1986) led to a rewriting of Eq.(1.10) in the form:

$$M_{TRM} = M_o \exp\left[-(\frac{t}{\tau_p})^{1-n}\right] \tag{1.11}$$

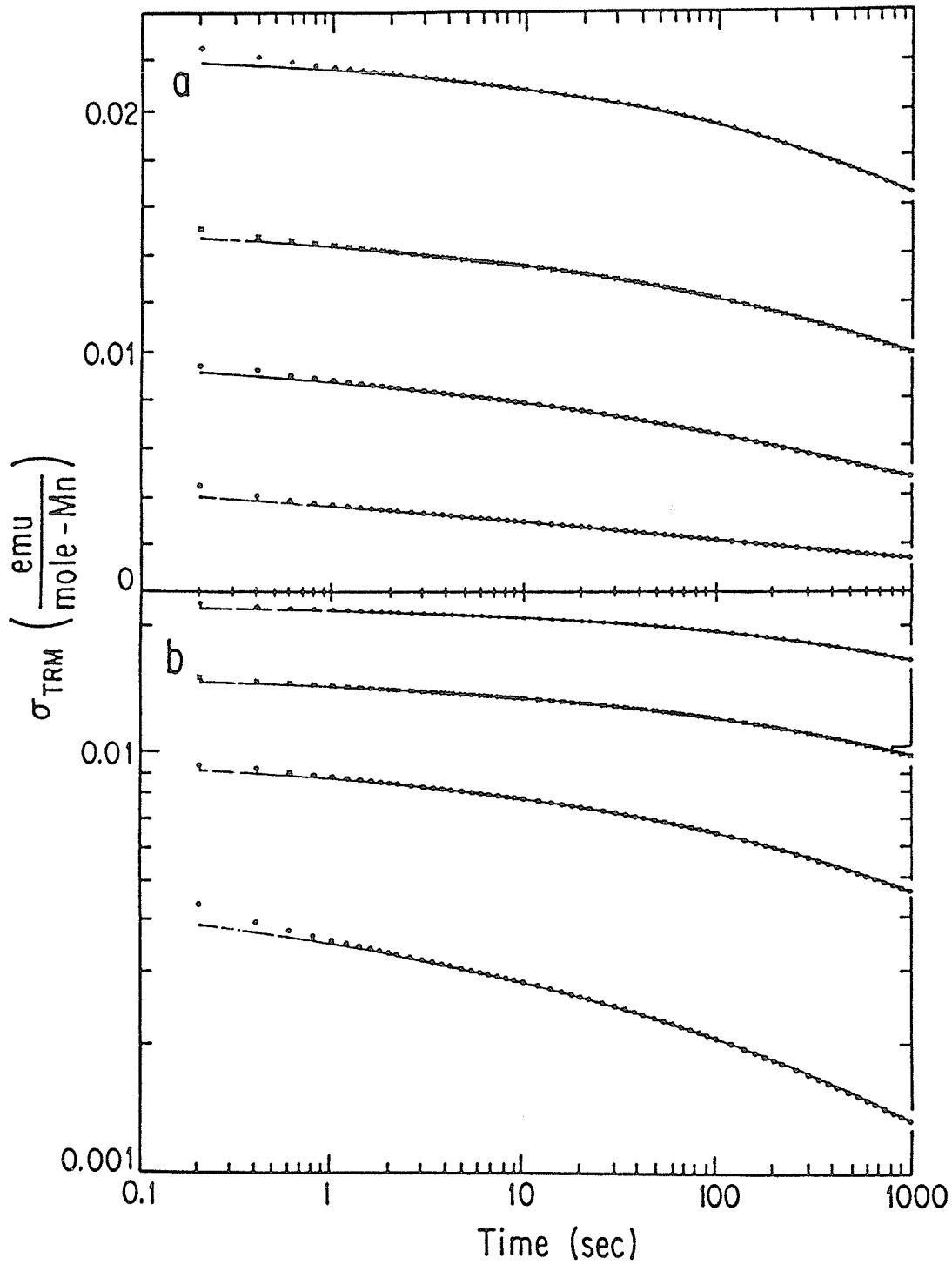

Figure 1-21: (a) Semi-log and (b) log-log plot of the thermoremanent magnetization as a function of time in 2.6% AgMn + 0.46% Sb at T/T_g = 0.771, 0.856, 0.897 and 0.966, from top to bottom, respectively. The solid lines are the best stretched-exponential fits (Eq.1.10) to the data. From Chamberlin et al. (1984).

where τ_p or $(1/\omega)$ is found to depend *both on the measurement temperature* T_m *and the wait time* t_w, while the initial TRM value of M_o and the exponent n are temperature dependent only. From the extensive studies of the decay of the TRM in several spin glasses, Hoogerbeets et al. (1986) found two empirical expressions to connect τ_p with T_m and t_w, and argued that the stretched-exponential time dependence of the TRM qualitatively agrees with the theoretical results from the infinite-range Ising model. Recent TRM measurements done by the same group (Bontemps and Orbach, 1988; Luo et al., 1988) on the insulating spin glasses $Eu_{1-x}Sr_xS$ (x=0.4, 0.54) showed two relaxation regimes. The decay is a power law at short time. Beyond a well-defined crossover time which increases with wait time (only for x=0.54; no detectable wait time dependence was found for x=0.4 sample), the decay is of the stretched-exponential form. They concluded that both the power law (Eq.(1.9)) and the stretched-exponential (Eq.(1.11)) function are essential ingredients of the equilibrium dynamics of a the spin glass.

The wait time dependence of the TRM decay in spin glasses, which is known as aging effect was first discovered by Nordblad et al. (1986). Figure 1-22 shows typical wait time effects for a Cu-5.0 at.%Mn spin glass. The sample was cooled in an applied field (H_a = 2 Oe) from a reference temperature (T_{ref} = 28.5 K) above the spin glass temperature (T_{SG} = 28 K) to the measurement temperature T_m = 25 K. After a wait time t_w at T_m, the applied field was turned off, and the relaxation of the TRM was recorded over the time interval 1 s $\leq t \leq 10^4$ s. The most striking feature in a plot of M_{TRM} vs. log t (Figure 1-22(a)) is the existence of an inflection point which shifts towards longer times as the wait time t_w increases. Such an effect can be clearly seen in Figure 1-22(b), where the relaxation rate $S(t)$, defined as

$$S(t) = -\frac{1}{H}\frac{\partial M_{TRM}}{\partial \ln t} \tag{1.12}$$

is plotted as a function of log t. Closer inspection of the influence of the wait time reveals that the maximum in $S(t)$ (or the inflection point in M_{TRM}) occurs at $t \approx$

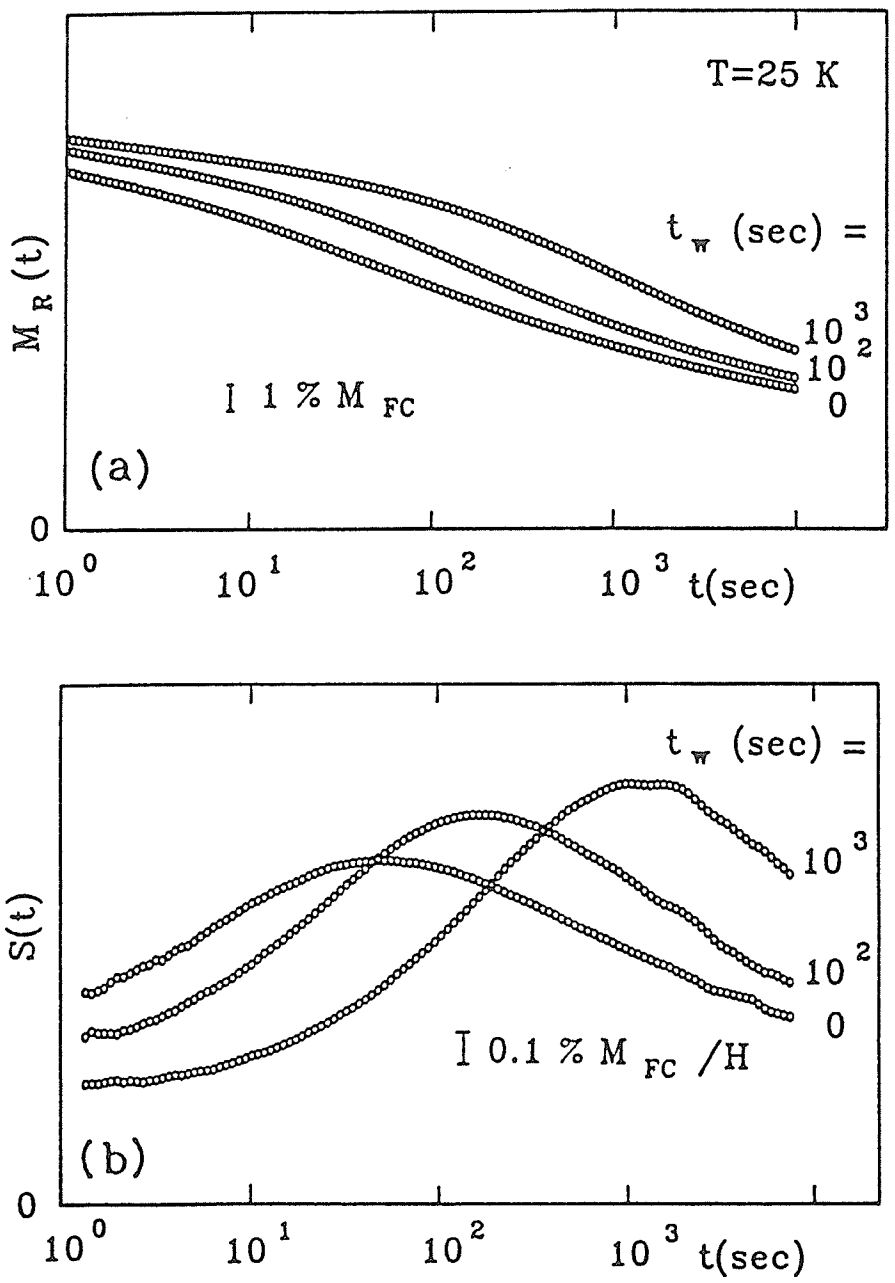

Figure 1-22: (a) Remanent magnetization curves of Cu-5 at.% Mn spin glass (T_{SG} = 28 K), measured at a temperature T_m = 25 K for different wait times t_w, plotted vs log_{10} *(t)*. 1% of the field-cooled magnetization value is indicated. (b) Relaxation rate S(t) corresponding to the remanent magnetization curves in (a) plotted vs log_{10} *(t)*. A relaxation rate of 0.1% of the field-cooled susceptibility value is indicated. From Nordblad et al. (1986).

t_w. These relaxation data could be fitted approximately by a nearly logarithmic function (Eq.(1.8)) superimposed on a stretched-exponential function (Eq.(1.11)) due to the aging process. The aging phenomena can also be observed in the zero-field-cooled (ZFC) magnetization relaxation, as shown in Figure 1-23 for a Cu-10 at.%Mn spin glass (Granberg et al., 1988). The sample was cooled in zero-field from T_{ref} to $T_m < T_{SG}$. After a wait time t_w at T_m, a small field of $H_a = 0.8$ Gs was applied and the magnetization M_{TRM} was measured over four decades. Figure 1-23(a) shows relaxation curves for a series of wait times t_w from 10^2 s to 10^4 s. The wave-like shape of $S(t)$ in Figure 1-23(b), with its maximum occurring near the corresponding wait time t_w, reflects the influence of the aging process on the relaxation of spin glasses.

The unique aging effect which characterize the dynamics in spin glasses implies that the spin glass phase is inherent nonequilibrium. Aging in spin glasses was first observed in low frequency ac susceptibility measurements on Cu-4 at.%Mn as a slow relaxation of both the real and imaginary parts of the susceptibility at constant temperature below T_{SG} (Lundgren et al., 1983). Nordblad et al. (1987b) pointed out that the spin glass dynamics are controlled by three fundamental physical quantities: the measurement temperature, the age of the spin glass state, and the magnitude of magnetic field being switched on (or off). In searching for the intrinsic equilibrium relaxation function of a spin glass from measurements of the TRM and ZFC magnetization, the following four essential requirements were emphasized by Nordblad et al.

(i) A wide observation time window.

(ii) Accurately controlled, stable temperature.

(iii) Appropriate consideration of the wait time.

(iv) Small cooling magnetic fields such that the system is in the linear response regime.

They argued that the stretched-exponential function Eq.(1.11) used by

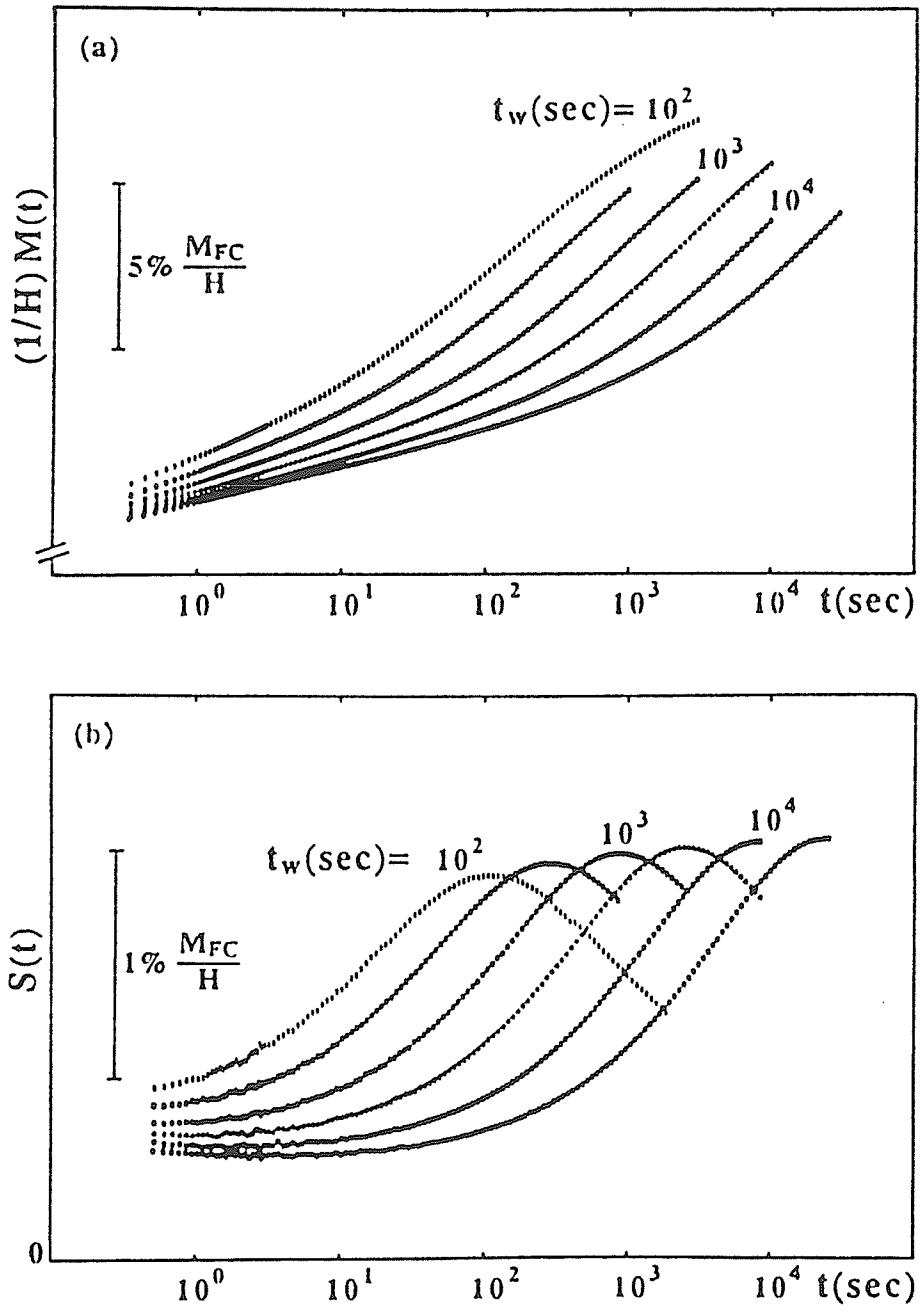

Figure 1-23: Zero-field-cooled susceptibility *(1/H) M(t)* and the corresponding relaxation rate S(t) at different wait times t_w = 10^2, 3×10^2, 10^3, 3×10^3, 10^4, and 3×10^4 s, plotted vs $log_{10}(t)$. T_m = 41.2 K, T_g = 45.3 K, H = 0.8 Gs. (a) *(1/H)M(t)*, 5% of $(1/H)M_{FC}$ indicated. (b) *S(t)*, 1% of $(1/H)M_{FC}$ indicated. From Granberg et al. (1988).

Hoogerbeets et al. (1986) is not the true functional form of equilibrium relaxation in spin glasses. The stretched-exponential is only a representation of the nonequilibrium relaxation caused by the influence of aging in spin glasses, and the true spin glass relaxation at thermal equilibrium obeys a weak power law (Eq.(1.9)); an apparent stretched-exponential relaxation imposed by the aging process can only be observed when the wait time t_w is within the experimental observation time window

Experimentally, the spin glass relaxation at thermodynamic equilibrium can only be observed for times t much less than the wait time ($t \ll t_w$) (Granberg et al., 1986 and reference therein), and is often difficult to acquire from the low field TRM measurements due to limitations of the experimental apparatus. However these data can be obtained from ac susceptibility measurements. The relaxation rate $S(t)$ can be obtained from the imaginary part of the ac susceptibility $\chi''(\omega)$ (Granberg et al., 1986; Lundgren et al, 1982, 1985) as follows

$$S(t) \simeq \frac{2}{\pi}\chi''(\omega), \qquad t = \frac{1}{\omega}. \tag{1.13}$$

Figure 1-24 shows the relaxation rate $S(t)$ plotted as a function of log t for the amorphous metallic spin glass $(Fe_{0.15}Ni_{0.85})_{75}P_{16}B_6Al_3$ (Svedlindh et al., 1987). The data points for $t < 10^{-1}$ s are calculated from $\chi''(\omega)$. The solid line through these points is the best fit using a weak power law $S(t) \propto t^{-0.05}$, and represents the equilibrium relaxation rate $S(t)$ ($t_w = \infty$) judging from the evolution of the curves for times $t_w = 10^2, 10^3, 10^4$ sec. We will present some theoretical justification of the power law and the stretched-exponential functions in section 2.4, and discuss this subject further in great detail in the last chapter.

Another way to study the thermodynamic equilibrium relaxation of spin glasses is to measure the time decay of the saturated remanent magnetization M_S. Based on the study of the field and wait time dependence of the TRM and the IRM in Cu-5 at.% Mn, Nordblad et al. (1987a; see also Granberg et al., 1987) found

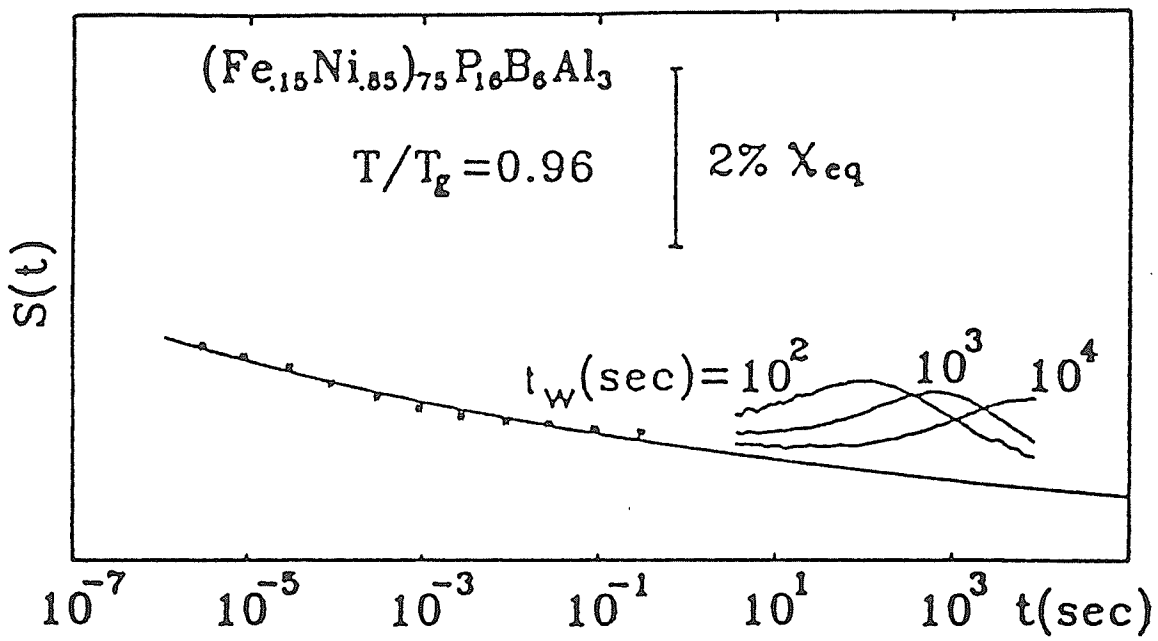

Figure 1-24: Relaxation rate *S(t)* vs. *log(t)* obtained from ac susceptibility (Eq.(1.13)) and zero-field-cooled susceptibility measurements (Eq.(1.12)), at a temperature $T = 0.96T_{SG}$. Two percent of the equilibrium susceptibility is indicated. The various ZFC curves refer to different wait times, $t_w = 10^2$, 10^3, and 10^4s. The solid line represents the best power-law fit ($S \propto t^{-0.05}$) to the ac susceptibility data. From Svedlindh et al. (1987).

that above a rather well-defined high field (H_S), a thermodynamic equilibrium state is imposed on the spin glass, and the decay of the TRM is *independent* of field and wait time. Figure 1-25 shows log-log plots of the time derivative of the saturated remanent magnetization $-dM_S/dt$ as a function of time at several temperatures below T_{SG} for the amorphous metallic spin glass $(Fe_{0.15}Ni_{0.85})_{75}P_{16}B_6Al_3$ (Granberg et al., 1987). For temperatures of $T/T_{SG} < 0.98$, the relaxation can be described accurately by the power law of Eq.(1.9) (straight lines in Figure 1-25). In the vicinity of T_{SG} ($0.98< T/T_{SG} <1.0$), the following empirical function consisting of the product of a power law and a stretched- exponential

$$M_S = M_o t^{-m} \exp\left[-\left(\frac{t}{\tau_p}\right)^{1-n}\right] \tag{1.14}$$

was used to fit the data accurately (solid curves in Figure 1-25); the pure stretched exponential was not sufficient to represent their data. A function in the form of a power law times a stretched-exponential was used in a scaling analysis of the aging process in a AgMn spin glass by Alba et al. (1986). They found that the relaxation curves for different wait times at a given temperature below T_{SG} could be superimposed on a unique universal curve. Van Hemmen and Nieuwenhuys (1986) measured the time decay of the saturated remanent magnetization at $T/T_{SG} = 0.8$ for a $CuMn_{0.05}Ni_{0.03}$ spin glass over a very long time ($10 < t < 2 \times 10^5$ s). Their data, however, followed an enhanced power law

$$M_S = M_o(\omega t)^{-A[\ln(\omega t)]^{y-1}} \tag{1.15}$$

where A, ω and y are fitting parameters with $y > 1$. The stretched-exponential Eq.(1.11) did not fit their data.

In concluding this chapter, we present two fascinating nonequilibrium phenomena in spin glasses: (i) memory behavior, and (ii) temperature cycling. The memory behavior of the spin glass was discovered by Lundgren et al. (1986a) in Cu-5.0 at.%Mn. The sample was cooled in zero field to a measurement temperature T_m, where a sequence of field reversal illustrated in Figure 1-26(a), was

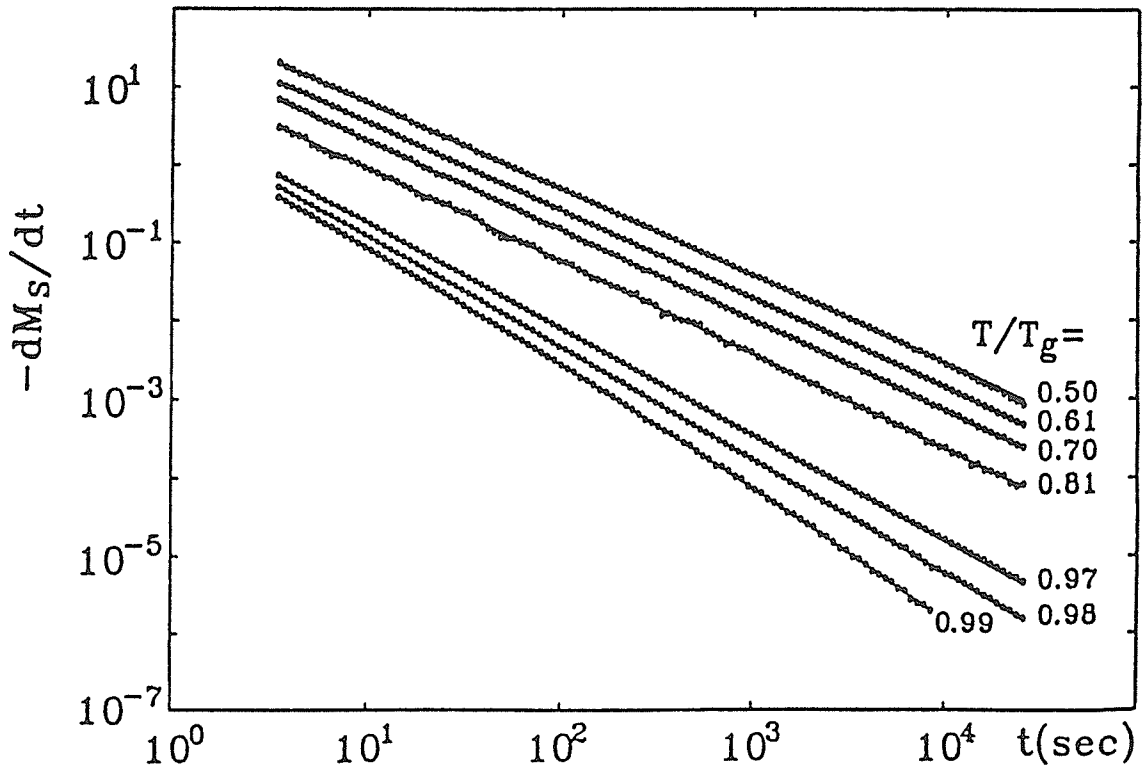

Figure 1-25: *log(- dM_s/ dt)* vs *log(t)* at several temperatures below T_{SG} for the amorphous metallic spin glass $(Fe_{0.15}Ni_{0.85})_{75}P_{16}B_6Al_3$. Solid curves are the best fits of the experimental data to Eq.(1.14). From Granberg et al. (1987).

applied after an initial wait time t_{w1}. The change of the magnetization is measured, starting after t_{w4}. The relaxation of the remanent magnetization for $t_{w1} = 0$ and 10^4 seconds is displayed in Figure 1-26(b) and (c), respectively. The common feature of these two curves is the oscillating behavior which appears to reflect a memory of the history of field cycling. For a long initial wait time $t_{w1} = 10^4$ s, the remanent magnetization changes sign. Lundgren et al. stated that the principle of superposition can be applied in this low field linear response regime, and the oscillating remanent magnetization (ORM) can be simulated (solid line of Figure 1-26(c)) by the superposition of the response functions corresponding to each field pulse.

The temperature cycling experiments in spin glasses (Lundgren 1988; Granberg et al., 1990, 1988) were inspired by two relaxation models proposed by Fisher and Huse (1988a, 1988b and Section 2.4.1) and Koper and Hilhorst (1988 and Section 2.4.2). The experimental procedure is as follows: the sample is cooled in zero field to a measurement temperature T_m below T_{SG}. After a long wait time t_w at T_m, the temperature cycling of $T_m \Rightarrow T_m + \Delta T \Rightarrow T_m$ is made. When T_m is recovered a small probing field is applied and the relaxation of the magnetization is recorded. Figure 1-27 shows the relaxation rate $S(t)$ versus log t for Cu-10 at.%Mn for a series of temperature cyclings done at $T_m = 0.9\ T_{SG}$ after $t_w = 10^4$ s (Lundgren, 1988). The pronounced feature in Figure 1-25 is that the relaxation rate displays <u>two</u> maxima for some intermediate values of ΔT ($\cong$ 0.71 K). According to the relaxation models, the maximum at short times is produced by the temperature cycling ΔT which impose a new <u>overlap length</u> $l_{\Delta T} \propto (\Delta T)^{-1}$. A cross-over from equilibrium to nonequilibrium relaxation will occur at $l_{\Delta T}$, which experimentally corresponds to the inflection point observed in the M_{TRM} vs log t curves.

While considerable effort has been devoted to studying the relaxation dynamics of pure spin glasses, bond disorder ferromagnets in general, and reentrant

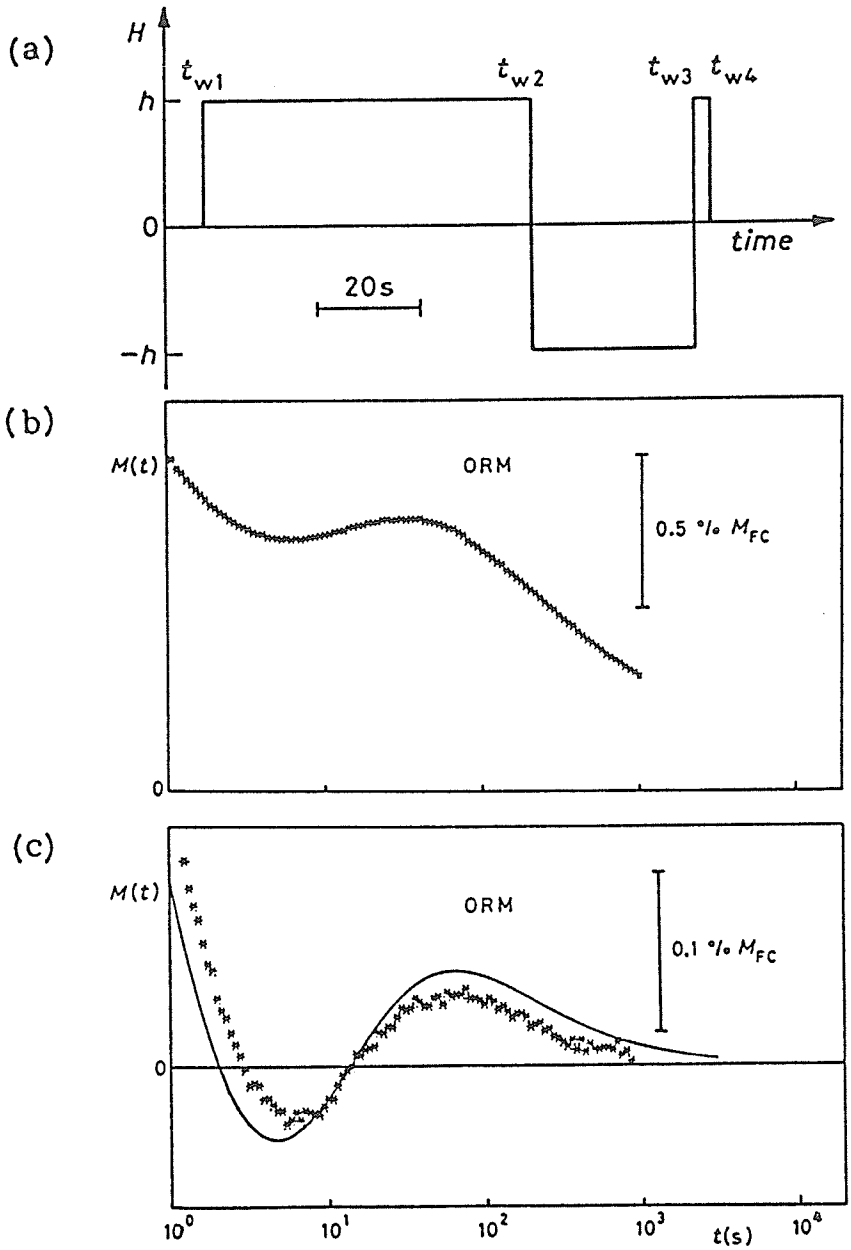

Figure 1-26: (a) The sequence of field changes (h = 1 Gs) applied after the sample is zero field cooled. The t_{wi}'s refer to the wait time at constant temperature prior to the ith field change. By definition, t equals zero at t_{w4}. The field changes are made at t = -100, -35, -3.2 and 0 s. (b) Time relaxation of the remanent magnetization obtained *after* the sequence of field variations illustrated in (a) for an initial wait time t_{w1} = 0 s. (c) initial wait time t_{w4} = 10^4 s. The solid curve represents the calculated behaviour of a memory function. Note the change in sign of the ORM. From Lundgren et al. (1986a).

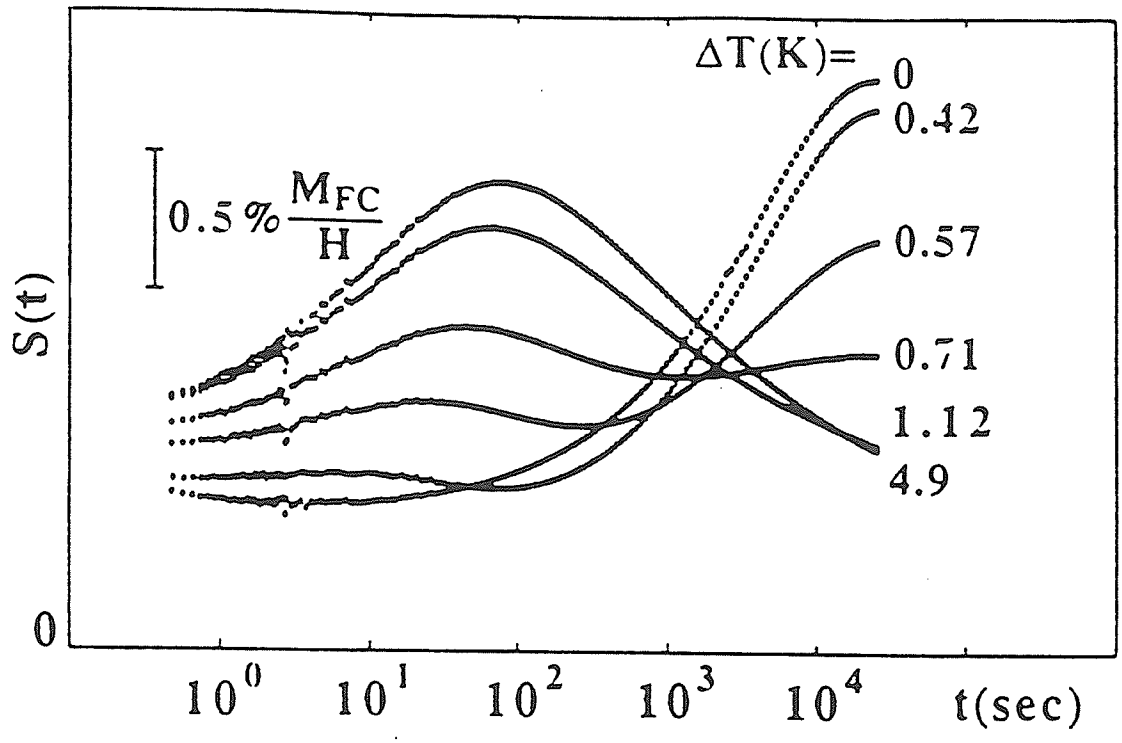

Figure 1-27: Relaxation rate *S(t)* vs. *log(t)* at T_m = 0.9 T_g (T_g = 45.3 K). The sample Cu-10 % Mn has been aged for 10^4 s at T_m. The different curves are recorded immediately after a positive *temperature cycling*, ΔT. From Lundgren (1988).

ferromagnets in particular, have received comparatively little attention. One of the principle goals of this thesis is to present a systematic study of the relaxation dynamics in reentrant ferromagnets, and to attempt to verify the existence of a ferromagnetic-to-spin glass transition by a comparison with the dynamical properties of pure spin glasses.

Chapter II

Theory of Disordered Magnets

An enormous amount of theoretical effort has been expended on studying spin glasses during the past two decades after Cannella and Mydosh (1972) discovered a cusp in the low field ac susceptibility of dilute AuFe alloys. The central issue is to understand if the cusp in the ac susceptibility signals the existence of a genuine thermodynamic phase transition. A number of challenging questions has been raised:

(i) Is a spin glass really a new kind of "ordered" phase, and if it is, what is the characteristic order parameter for such a phase?

(ii) A phase transition is associated with various critical phenomena; what are the appropriate critical quantities for the spin glass phase transition?

(iii) What are the dynamic properties (such as magnetic relaxation) in a (non-equilibrium) spin glass system?

These problems will be discussed in this chapter, and answers will be offered within the context of specific models.

2.1 General Theoretical Concepts

2.1.1 RKKY Indirect Exchange Interaction

I have mentioned in Chapter I that the RKKY interaction provides indirect long range coupling between magnetic impurities, and causes spin frustration in a dilute magnetic alloy. In this section, I will briefly outline the derivation of the RKKY interaction.

Consider a dilute magnetic alloy (for example AuFe) in which magnetic impurity atoms are immersed in a sea of conduction electrons. There will be a direct $s-d$ exchange interaction, $-J\vec{S}\cdot\vec{s}$, between the localized d-electrons of the im-

purity and the mobile conduction s-electrons of the host, where J is the exchange parameter. To simplify the problem without losing any essential features, we assume that the interaction between a magnetic impurity $\vec{S_\alpha}$ localized at $\vec{r} = 0$ and the conduction electrons $\vec{s_i}$ at $\vec{r_i}$ can be represented by a δ-function exchange interaction

$$-J\sum_i \vec{S_\alpha}\cdot\vec{s_i}\delta(\vec{r_i}) = -g\mu_B\sum_i \vec{s_i}\cdot\vec{H}_{eff}(\vec{r_i}) \tag{2.1}$$

where g is the electronic g-factor, and μ_B is the Bohr magneton. Each conduction electron spin thus experiences an effective magnetic field $\vec{H}_{eff}(\vec{r})$ due to the impurity spin $\vec{S_\alpha}$ given by

$$\vec{H}_{eff}(\vec{r}) = +\frac{J}{g\mu_B}\vec{S_\alpha}\delta(\vec{r}) \tag{2.2}$$

with the Fourier transform

$$\vec{H}_{eff}(\vec{q}) = +\frac{J}{g\mu_B}\vec{S_\alpha} \tag{2.3}$$

where $\vec{q}$ is a wavevector. The magnetization associated with this field can be expressed as a Fourier series:

$$\begin{aligned}\vec{M}(\vec{r}) &= \frac{1}{V}\sum_{\vec{q}}\vec{M}(\vec{q})e^{i\vec{q}\cdot\vec{r}} \\ &= \frac{1}{V}\sum_{\vec{q}}\chi(\vec{q})\vec{H}_{eff}(\vec{q})e^{i\vec{q}\cdot\vec{r}}\end{aligned} \tag{2.4}$$

with

$$\vec{M}(\vec{q}) = \chi(\vec{q})\vec{H}(\vec{q}) \tag{2.5}$$

where $\chi(\vec{q})$ is the Fourier component of the susceptibility of the conduction electron gas in the host metal, and V is the volume of the specimen. Thus the conduction electron spin polarization (the difference between the numbers of up spins and down spins per unit volume) due to the effective field $\vec{H}_{eff}(\vec{r})$ (from the impurity $\vec{S_\alpha}$) is (using Eqs.(2.4) and (2.3))

$$\vec{s}(\vec{r}) = \frac{1}{g\mu_B V}\sum_{\vec{q}}\chi(\vec{q})\vec{H}_{eff}(\vec{q})e^{i\vec{q}\cdot\vec{r}}$$

$$= \frac{J}{g^2 {\mu_B}^2 V} \sum_{\vec{q}} \chi(\vec{q}) e^{i\vec{q}\cdot\vec{r}} \vec{S}_\alpha. \tag{2.6}$$

For a free (non-interacting) electron gas, the susceptibility $\chi_0(\vec{q})$ is given by (Schwartz, 1976)

$$\chi_\circ(\vec{q}) = 2{\mu_B}^2 n(\epsilon_F) U(\vec{q}/2k_F) \tag{2.7}$$

where $n(\epsilon_F)$ is the density of states of conduction electrons of one spin per unit energy at the Fermi surface ϵ_F, k_F is the Fermi wavevector of the conduction electrons and $U(\vec{q}/2k_F)$ is given by

$$U(x) = \left[1 + \frac{1-x}{2x} \ln\left|\frac{1+x}{1-x}\right|\right]. \tag{2.8}$$

By substituting Eq.(2.7) into Eq.(2.6) and converting the sum over $\vec{q}$ into an integral (White, 1983), the free-electron spin polarization becomes

$$\vec{s}_{RKKY}(\vec{r}) = -\frac{3JN}{8\epsilon_F V} \frac{{k_F}^3}{\pi} \left[\frac{\cos(2k_F r)}{(2k_F r)^3} - \frac{\sin(2k_F r)}{(2k_F r)^4}\right] \vec{S}_\alpha \tag{2.9}$$

where N is total number of electrons in the crystal.

The Eq.(2.9) is known as the RKKY spin polarization and is plotted in Figure 2.1-1 (curve (a)) as a function of the distance from the impurity (Schwartz, 1976). It can be seen that a localized magnetic moment induces an oscillatory spin polarization of the conduction electrons in the vicinity of the magnetic moment. The sign of the net spin polarization depends both upon the sign of the exchange coupling constant J and the distance r from the impurity. For large values of r, the spin polarization oscillates with a period $(2k_F)^{-1}$ and the amplitude of the oscillations decreases rapidly as $1/r^3$. The reason why this spin polarization is oscillatory is that the conduction electrons try to screen out the magnetic moment on the impurity by means of their spins (just as, by means of their charge, conduction electrons screen out the charge on the impurity ion, which induces the Friedel charge-density oscillations (Kittel 1963, Chapter 18)), but their wavefunctions have a limited range of wavelengths. In the simplest case of a non-interacting electron gas, the highest wavenumber available is $2k_F$.

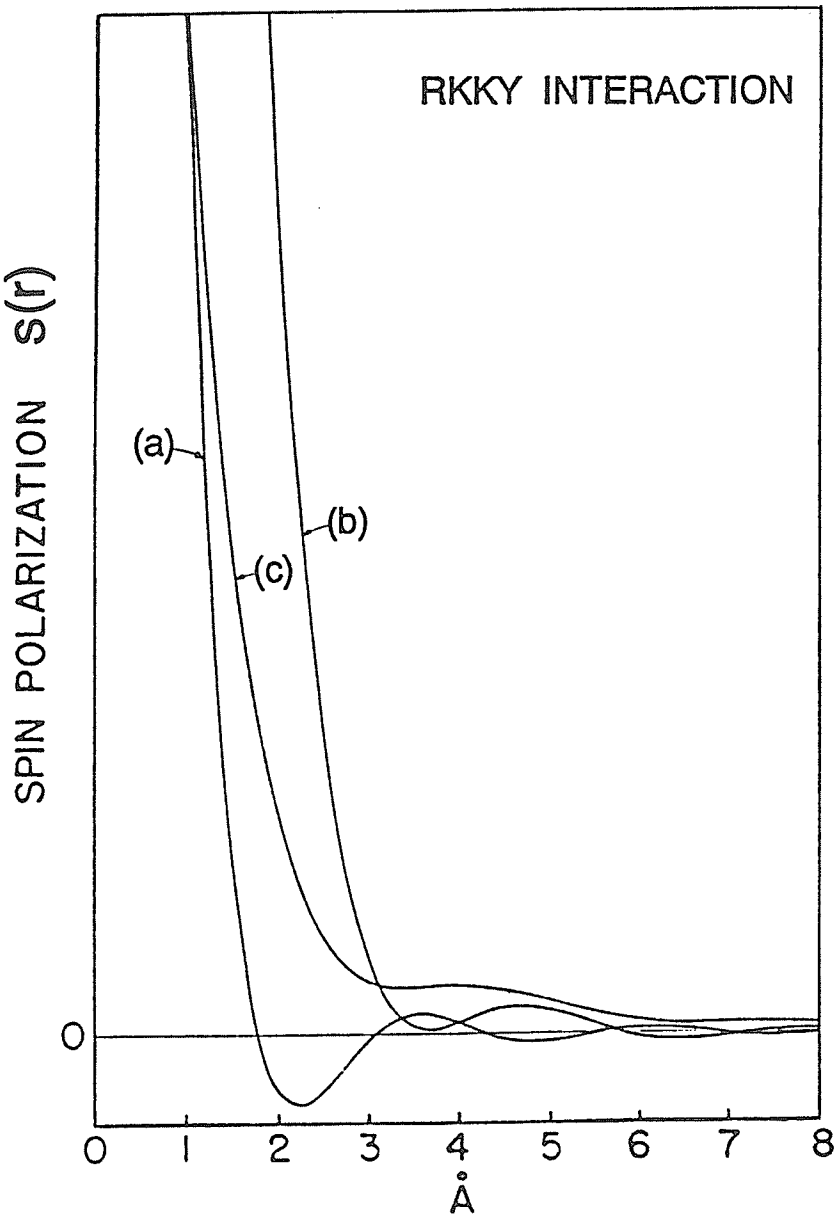

Figure 2.1-1: The spin polarization about a δ-function magnetic field probe for the (a) non-interacting electron gas, (b) interacting electron gas with $\nu n(\epsilon_F)U(0) = 0.9$ in Eq.(2.17) and (c) the interacting electron gas including finite range interaction with $\nu(0)n(\epsilon_F)U(0) = 0.9$. From Schwartz (1976).

The spin polarization due to the RKKY $s-d$ exchange interaction provides an indirect exchange coupling between two magnetic moments in dilute metallic alloys. Consider two magnetic impurities $\vec{S}_i$ and $\vec{S}_j$ localized at $\vec{R}_i$ and $\vec{R}_j$, respectively. The spin $\vec{S}_j$ will interact with spin $\vec{S}_i$ via the $\vec{S}_i$-induced polarized conduction electrons $s_{RKKY}(\vec{r}-\vec{R}_i)$ (given by Eq.(2.9)) at $\vec{R}_j$:

$$H_{RKKY} = -J\vec{S}_j \cdot \vec{s}(\vec{r}-\vec{R}_i) \cdot \delta(\vec{r}-\vec{R}_j). \tag{2.10}$$

Substituting Eq.(2.9) into Eq.(2.10), we can express Eq.(2.10) as

$$H_{RKKY} = J_{RKKY}(R_{ij})\vec{S}_i \cdot \vec{S}_j \tag{2.11}$$

where

$$J_{RKKY}(R_{ij}) = \frac{3J^2N}{8\epsilon_F V}\frac{{k_F}^3}{\pi}\left[\frac{\cos(2k_F R_{ij})}{(2k_F R_{ij})^3} - \frac{\sin(2k_F R_{ij})}{(2k_F R_{ij})^4}\right] \tag{2.12}$$

and $R_{ij} = \left|\vec{R}_i - \vec{R}_j\right|$. For a large separation ($R_{ij} \to \infty$), Eq.(2.12) becomes

$$J_{RKKY}(R_{ij}) \sim \frac{\cos(2k_F R_{ij})}{{R_{ij}}^3}. \tag{2.13}$$

The strength of the RKKY interaction falls off rapidly as $1/{R_{ij}}^3$ (Figure 2.1-1), for large values of R_{ij}, and the sign of the effective coupling constant J_{RKKY} oscillates as a function of R_{ij} with a period $(2k_F)^{-1}$.

In the discussion above, I have neglected the effects of the Coulomb interaction between electrons. The free-electron spin polarization Eq.(2.9) is appropriate for noble metal hosts such as Au and Cu, in which the conduction electrons are essentially non-interacting s electrons. For hosts such as Pd or Pt, where the conduction electrons are narrow d-band electrons, the effect of Coulomb interactions between the conduction electrons has to be taken into account and the free electron susceptibility $\chi_0(\vec{q})$ is replaced by the interacting electron susceptibility $\chi(\vec{q})$. For simplicity, the actual Coulomb interactions by δ-functions of strength ν localized at the lattice sites; the effect is equivalent to introducing an effective

exchange field proportional to $\vec{M}(\vec{q}) \propto \nu\vec{M}(\vec{q})$, in q-space. Eq.(2.5) is modified to (Kittel, 1968)

$$\vec{M}(\vec{q}) = \chi_0(\vec{q})\left[\vec{H}(\vec{q}) + \nu\vec{M}(\vec{q})\right] \tag{2.14}$$

or

$$\vec{M}(\vec{q}) = \vec{H}(\vec{q})\frac{\chi_0(\vec{q})}{1-\nu\chi_0(\vec{q})}. \tag{2.15}$$

Thus the susceptibility of an interacting electron gas is given by

$$\chi(\vec{q}) = \frac{\chi_0(\vec{q})}{1-\nu\chi_0(\vec{q})} \tag{2.16}$$

and

$$\begin{aligned}\frac{\chi(\vec{q})}{\chi_0(\vec{q})} &= [1-\nu\chi_0(\vec{q})]^{-1} \\ &= \left[1-2{\mu_B}^2\nu n(\epsilon_F)U(\vec{q}/2k_F)\right]^{-1}.\end{aligned} \tag{2.17}$$

As a result of the Coulomb interaction, the susceptibility of the interacting electron gas is enhanced when ν is positive, as anticipated; however, the enhancement is also $\vec{q}$-dependent (Figure 2.1-2). Notice that the enhancement is much greater for small $\vec{q}$, which indicates that the range of the spin polarization $\vec{s}(\vec{r})$ becomes longer in $\vec{r}$-space. The exchange enhancement pushes out the first zero of the RKKY oscillations and increases their amplitude (Figure 2.1-1 curve (b)). However, at sufficiently large distances from the impurity, the oscillations appear again. If the finite range of the Coulomb interaction is also taken into account, then ν becomes effectively $\vec{q}$-dependent. This fact causes an even more rapid decrease of $\chi(\vec{q})$ with increasing $\vec{q}$, and makes the range of the magnetic disturbance (spin polarization) even longer (Figure 2.1-1 curve (c)).

Some interesting results were obtained by Kim and Schwartz (1968) when they calculated the conduction-electron spin polarization around an impurity in a strongly magnetized host metal (e.g. Ni, Fe or PdFe,) which all have a spontaneous magnetization below their Curie temperature. For the ferromagnetic host

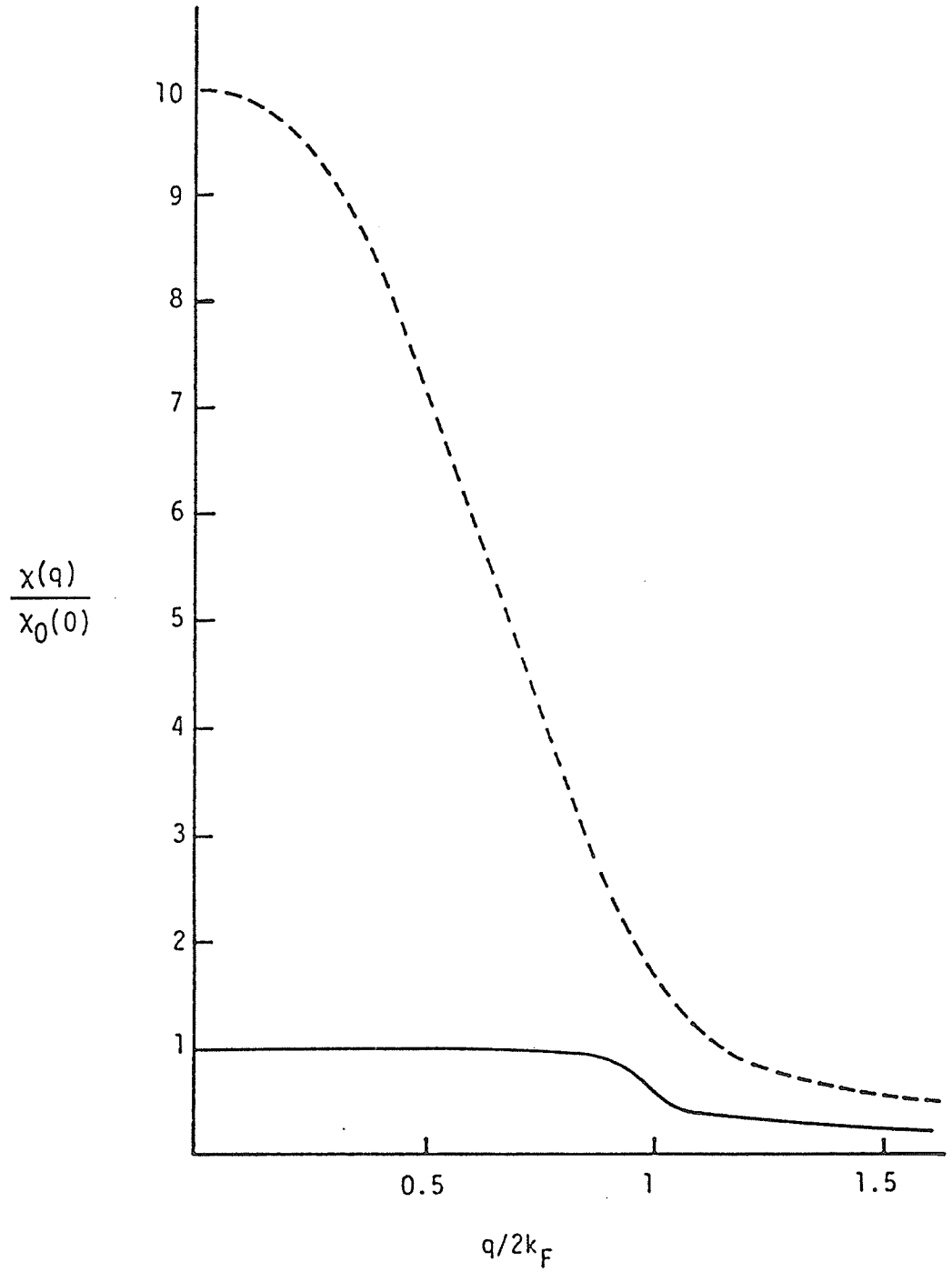

Figure 2.1-2: The normalized q-dependent susceptibility of an electron gas. The solid curve represents the free-electron susceptibility $\chi_o(q)$; the dashed curve represents the interacting-electron gas susceptibility for the case $\nu n(e_F) = 0.9$. From Roshko (1979).

metals like Fe or Ni, the electronic susceptibility $\chi(\vec{q})$ in Eq.(2.6) is replaced by the component of the susceptibility tensor in the direction of the spontaneous magnetization. The resulting spin polarization is shown in Figure 2.1-3 for various values of the relative magnetization of the host metal $p = (n_+ - n_-)/2n$, where $n_\pm$ are the number of electrons (holes) of each spin, and $2n$ is the total number of electrons (holes). For a ferromagnetic host like Ni, one spin d band is completely filled and $p \simeq 1$. The spin polarization becomes the simple RKKY oscillation without any exchange enhancement effects (Figure 2.1-3); the magnetic disturbance is almost confined to the impurity site (for example Mn in Ni). For a dilute ferromagnetic host like PdFe, the relative magnetization $p \ll 1$, which induces a long range spin polarization around magnetic impurities. Magnetic impurities in a ferromagnetic host like Fe produce a spin polarization with range intermediate between Ni and PdFe (Figure 2.1-3), since both up and down spin bands are partially filled.

2.1.2 Quenched Average and the Replica Method

Consider a magnetic system with spin magnetic moments $\vec{S}_i$ randomly located on the lattice sites of a non-magnetic host. At high temperature, the magnetic atoms will diffuse through the lattice, and come to thermal equilibrium very quickly. The free energy of this system is

$$F = -k_B T \ln [Z]_{av} \tag{2.18}$$

with the partition function Z given by

$$Z\{J_{ij}\} = Tr_{\{S_i\}} \exp[-\beta H(J_{ij}, S_i)], \qquad \beta = \frac{1}{k_B T}. \tag{2.19}$$

where $Tr_{\{S_i\}}$ is the trace over N spins S_i, $H(J_{ij}, S_i)$ is the Hamiltonian of the system, and J_{ij} describes the exchange interaction between $\vec{S}_i$ and $\vec{S}_j$. $[...]_{av}$ denotes the exchange bond average over the random variable J_{ij} (because of the diffusion of magnetic atoms). This kind of average is known as an *annealed average.*

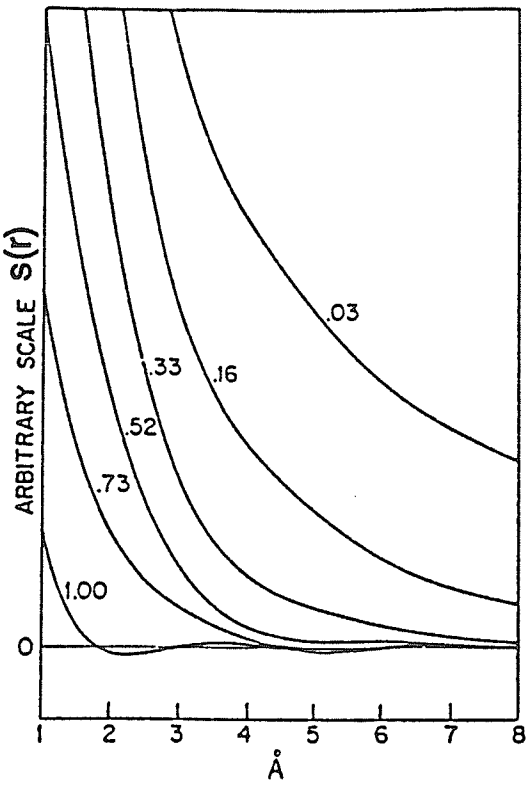

Figure 2.1-3: Plot of $s(r)$ vs r for various values of the relative magnetization p. The range is very large for small p. The $p=1$ curve is just the simple RKKY interaction. From Kim and Schwartz (1968).

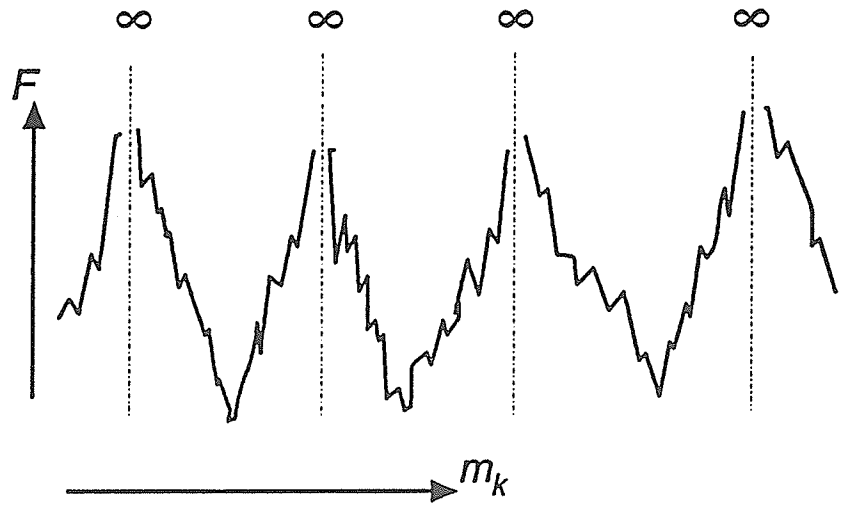

Figure 2.1-4: Schematic plot of the evolution of part of the free energy "hypersurface" (shown as a function of one phase space variable only).

When the system is quenched into a low temperature state in which all magnetic impurities are frozen at fixed lattice sites, the diffusion time for each atom to approach equilibrium is much longer than the experimental observation time and the exchange parameters J_{ij} become "quenched variables". The average over J_{ij} ($[Z]_{av}$ in Eq.(2.18)) is the wrong physics. Binder and Young (1986) suggested that one can generally average extensive variables, such as the free energy per spin

$$f = \frac{1}{N}[F]_{av} = -\frac{k_B T}{N}[\ln Z\{J_{ij}\}]_{av} \tag{2.20}$$

where N is number of spins in the system. The kind of average we deal with, i.e., $[\ln Z\{J_{ij}\}]_{av}$ rather than $[Z\{J_{ij}\}]_{av}$, is called a *quenched average.*

To perform the quenched average is not an easy task because the logarithmic function occurs inside $[...]_{av}$. In the presence of an external field H_0 along the z direction, we can write the Hamiltonian of the system as

$$H = -\sum_{(ij)} J_{ij}\vec{S}_i \cdot \vec{S}_j - H_0 \sum_i S_{iz} \tag{2.21}$$

where the $\sum_{(ij)}$ denotes a summation over the $N(N-1)/2$ distinct pairs of spins. If exchange parameters J_{ij} are randomly chosen according to a fixed distribution $P(J_{ij})$, Eq.(2.20) becomes

$$f = -\frac{k_B T}{N}\int \prod_{(ij)} P(J_{ij}) \ln Z\{J_{ij}\} dJ_{ij} \tag{2.22}$$

with

$$Z\{J_{ij}\} = Tr_{\{S_i\}} \exp\left\{\beta \sum_{(ij)} J_{ij}\vec{S}_i \cdot \vec{S}_j + \beta H_0 \sum_i S_{iz}\right\}, \quad \beta = \frac{1}{k_B T}. \tag{2.23}$$

As a first step we have to calculate the partition function with a Hamiltonian that contains a large set of quenched random variables $\{J_{ij}\}$, typically 10^{23}, with no translational invariance. Even though this calculation could be done, the partition function would be a function of typically 10^{23} variables. The final step, averaging over the exchange parameters J_{ij}, does not simplify the calculation since $Z\{J_{ij}\}$

appears inside a logarithm. The prohibitive difficulty in this computation comes from the random variables J_{ij}. If we could carry out the average over the exchange bonds before performing $Tr_{\{S_i\}}$, we then might be able to simplify our calculation. This implies that we have to decouple $Z\{J_{ij}\}$ from the logarithm, and this is the idea behind the replica method, which is widely used in the statistical mechanics of random systems.

The replica method was first applied to the spin glass problem by Edwards and Anderson (1975), and is based on the use of the exact relation

$$\ln Z = \lim_{n\to 0} \frac{1}{n}(Z^n - 1). \tag{2.24}$$

The average over $\ln Z$ is then

$$[\ln Z\{J_{ij}\}]_{av} = \lim_{n\to 0} \frac{1}{n}\left[[Z^n\{J_{ij}\}]_{av} - 1\right] = \lim_{n\to 0} \frac{\partial}{\partial n}[Z^n\{J_{ij}\}]_{av}. \tag{2.25}$$

For positive integer n, one can express $Z^n\{J_{ij}\}$ in term of n identical replicas of the system:

$$\begin{aligned} Z^n\{J_{ij}\} &= \prod_{\alpha=1}^{n} Z_\alpha\{J_{ij}\} = \prod_{\alpha=1}^{n} Tr_{\{S_i^\alpha\}} \exp\left[-\beta H\{J_{ij}, S_i^\alpha\}\right] \\ &= Tr_{\{S_i^1\}\{S_i^2\}\ldots\{S_i^n\}} \exp\left[-\sum_{\alpha=1}^{n} \beta H(J_{ij}, S_i^\alpha)\right] \end{aligned} \tag{2.26}$$

and

$$Z_n \equiv [Z^n\{J_{ij}\}]_{av} = \int \prod_{ij} P(J_{ij}) Z^n(J_{ij})\, dJ_{ij}. \tag{2.27}$$

The indices α which are attached to the spins are called replica indices. All the replicas of the system have the same set of random exchange bonds $\{J_{ij}\}$, but different spin configurations $\{S_i^\alpha\}$. In the next section, we can show that for a specific model, the average of $Z^n\{J_{ij}\}$ can be expressed as

$$Z_n = Tr_S \exp(-\beta H_{eff}) \tag{2.28}$$

where Tr_S denotes $Tr_{\{S_i^1\}\{S_i^2\}\ldots\{S_i^n\}}$, the trace over N spins in each of n replicas (total of Nn spins), H_{eff} is an effective Hamiltonian of a (fictitious) translationally invariant problem without the disorder parameters J_{ij}; conventional statistical

mechanical methods can now be applied.

2.1.3 Broken Ergodicity and Order Parameters

When a system undergoes a phase-transition from a disordered state to an ordered state, the symmetry of the system generally becomes lower; this is called broken symmetry. A simple example is a phase transition from a paramagnetic state to a ferromagnetic state in an Ising ferromagnet ($S_i = \pm 1$). When the phase transition occurs, the spin at each site is locked in either the up or down direction, and the symmetric orientation in the paramagnetic state therefore breaks down. Broken symmetry always leads to broken ergodicity (the converse may not be true) (Palmer, 1982). In the conventional Boltzman statistical mechanics, a physical system is ergodic if every allowed microstate which satisfies the macroscopic conditions can be visited by the system after a sufficient long time; the thermal average of a physical quantity is performed over all possible microstates. When broken ergodicity occurs in the system, only a portion of all possible microstates are allowed by the system, and the thermal average should be done only over these states. The general discussion on broken ergodicity was given by Palmer (1982). Fischer and Hertz (1991) pointed out that strictly speaking the broken symmetry and broken ergodicity can only occur in an infinite system (number of atoms $N \rightarrow \infty$), since, in a finite system all possible states are accessible at any finite temperatures. Experimentally a system is said to be effectively nonergodic if its maximum fluctuation time is beyond the experimental observation time scale (Binder and Young 1986, Section III B).

A phase transition (or broken symmetry) can be characterized by an order parameter, which measures the amount and kind of ordering built up in the neighbourhood of the critical point. The order parameter may vanish above the critical point, but it must be nonzero in the region just below the critical point. For a ferromagnetic transition, the order parameter is the zero-field spontaneous mag-

netization

$$\vec{M} = \frac{1}{N}\sum_i \left\langle \vec{S}_i \right\rangle_T \tag{2.29}$$

where $< \vec{S}_i >_T$ is the thermal average of spin $\vec{S}_i$. For spin glasses the spontaneous magnetization can no longer serves as an order parameter since $\vec{M}$ is also zero in the spin glass state due to frozen random spin orientations. To define an order parameter for spin glasses becomes a complicated task due to unique broken ergodicity in spin glasses. The origin of broken ergodicity in spin glasses can not be obviously traced to a broken symmetry (in the next section we show that this symmetry is called *replica-symmetry*). An extensive discussion about broken ergodicity and the order parameter in spin glasses has been given by Binder and Young (1986, section III, B and F), Fischer and Hertz (1991 section 2.4) and Palmer (1982), and here I only summarize the physical picture discussed by them.

There are very many stable states in the spin glass which are separated by energy barriers. For a system with N spins the free energy corresponding to these states has a broad distribution. Not all states are in a global minimum of the free energy; some of them are in local minima of the free energy. In the limit $N \to \infty$, some of these energy barriers between minima will become infinite, and the entire state space is then partitioned into very many mutually inaccessible "valleys" within which there exist many "subvalleys" separated by finite energy barriers. If we express the free energy as a function of the N local magnetizations m_i, $F = F(m_1, m_2, \ldots, m_N)$, and imagine a plot in $N+1$ dimensional space whose axes are labeled by $m_i (i = 1, \ldots, N)$ and F, this so-called many-valley picture can be schematically shown in Figure 2.1-4, which shows the evolution of part of the free energy hypersurface $F(m_i, m_2, \ldots, m_N)$ as a function of one variable m_k. Each of these valleys represents one thermodynamic state, so theoretically speaking, when an infinite system finds itself in one of these valleys, it will stay in this state forever, and exhibit properties which are in general specific to that

valley and different from true equilibrium properties which involve averaging over all valleys.

Corresponding to the many-valley picture in the spin glass, three common order parameters are defined:

(i) An order parameter q^{ll} for a single valley l

$$q^{ll} = \frac{1}{N}\sum_i \left(\left\langle \vec{S}_i \right\rangle_T^{(l)}\right)^2. \tag{2.30}$$

(ii) The Edwards-Anderson order parameter

$$q_{EA} = \left[\sum_l P_l \left(\left\langle \vec{S}_i \right\rangle_T^{(l)}\right)^2\right]_{av} \tag{2.31}$$

where

$$P_l = \frac{\exp\left(-Nf_l/k_BT\right)}{\sum_l \exp\left(-Nf_l/k_BT\right)} \tag{2.32}$$

is the statistical weight associated with the state l which has free energy f_l. q_{EA} is then a weighted average of q^{ll} over all valleys.

(iii) The statistical mechanics order parameter

$$q = \lim_{\tilde{H}\to 0}\lim_{N\to 0}\left[\sum_l P_l \left(\left\langle \vec{S}_i \right\rangle_T^{(l)}\right)^2\right]_{av} \tag{2.33}$$

where $\tilde{H}$ is a staggered field which breaks the spin-reversal symmetry ($S_i \Rightarrow -S_i$ for all i). The calculation of q now involves interference terms of the form $P_l P_{l'} \langle S_i\rangle_T^{(l)} \langle S_i\rangle_T^{(l')}$ between different valleys $l \neq l'$, then a weighted average $[\ldots]_{av}$.

It is useful to establish the relationship between q and q_{EA} and the order parameter matrix element $q_{\alpha\beta}(\alpha \neq \beta, \alpha, \beta = 1, \ldots, n)$ in the replica framework, as many of the calculations in the following section will be done by the replica method (the definition of $q_{\alpha\beta}$ will be deferred to section 2.2). It can be shown that

$$q = \lim_{n\to 0} \frac{1}{n(n-1)} \sum_{\alpha\beta} q_{\alpha\beta} \tag{2.34}$$

$$q_{EA} = \lim_{n\to 0}\lim_{\alpha\to\beta} q_{\alpha\beta}. \tag{2.35}$$

An overlap function $q^{ll'}$ can be defined to describe the correlation between different states l, l'

$$q^{ll'} = \frac{1}{N}\sum_i \langle S_i\rangle_T{}^{(l)}\langle S_i\rangle_T{}^{(l')}. \tag{2.36}$$

The probability distribution of $q^{ll'}$ is defined by

$$P(q) = \left[\sum_{ll'} P_l P_{l'}\delta(q - q^{(ll')})\right]_{av}. \tag{2.37}$$

In the replica framework, $P(q)$ becomes

$$P(q) = \lim_{n\to 0}\frac{1}{n(n-1)}\sum_{\alpha\neq\beta}\delta(q - q_{\alpha\beta}). \tag{2.38}$$

In the next section, I will show that $q_{\alpha\beta}$ is replaced by a continuous order parameter function $q(x)$ with $0 \leq x \leq 1$, which indicates that a spin glass cannot be described by a single order parameter, but rather requires many of them.

2.2 Mean Field Theory

In the historical study of phase transitions in magnetic systems, the first step has always been to define a mean-field-theory (MFT), the reasons being (i) it is simple, and (ii) its predictions usually agree fairly well with experiments. The mean-field theory of spin glasses is, however, much more difficult to establish than it is in ferromagnetism. The pioneering work in spin glass theory was done by Edwards and Anderson (1975) by solving the classical Heisenberg problem with random exchange interactions. The theory was then extensively developed by Sherrington and Kirkpatrick (S-K Model, 1975) and Gabay and Toulouse (Vector Model, 1981) with their infinite-range interaction model for which the solutions are exact.

In the short-range EA model, a system of N classical vector spins is placed on a regular lattice, the Hamiltonian of such a system is generally described as

$$H = -\frac{1}{2}\sum_{ij} J_{ij}\vec{S}_i\cdot\vec{S}_j - g\mu_B\sum_i \vec{H}_0\cdot\vec{S}_i. \tag{2.39}$$

Frustration is introduced through an exchange interaction J_{ij}, which is limited to Z neighbors and distributed according to a Gaussian distribution with zero mean value:

$$P(J_{ij}) = \frac{1}{J\sqrt{2\pi}} \exp\left(-\frac{{J_{ij}}^2}{2J^2}\right) \tag{2.40}$$

where J is the standard deviation.

The EA model uses a quantity

$$q \equiv \left\langle \vec{S}_i(t_0) \cdot \vec{S}_i(t) \right\rangle, \qquad \text{with} \quad t \gg t_0 \tag{2.41}$$

to describe the probability that a given spin $\vec{S}_i$ at time t_0 will point in the same direction at a much later time t. A nonvanishing probability after thermally averaging $< \ldots >$ will then indicate *spin freezing.* This quantity is therefore used as an order parameter to characterize the spin glass state ($q \neq 0$).

By using the replica technique to calculate an exchange bond average, Edward and Anderson found the zero-field susceptibility to be

$$\chi = \begin{cases} \frac{C}{T} & T > T_{SG} \\ \frac{C}{T_{SG}} - \vartheta(T_{SG} - T)^2 & T < T_{SG} \end{cases} \tag{2.42}$$

where C is the Curie constant. The model successfully predicts a cusp in the susceptibility at T_{SG}, as is observed experimentally. However, the EA model also predicts a cusp around T_{SG} in the specific heat, which has not been found experimentally. Nevertheless, this simple model marks the beginnings of spin glass theory.

2.2.1 The Sherrington-Kirkpatrick Model

By analogy with the mean field theory for ferromagnetism, Sherrington and Kirkpatrick (1975) introduced a mean-field theory for spin glasses. The Sherrington and Kirkpatrick model (SK model, Sherrington and Kirkpatrick, 1975, and Kirkpatrick and Sherrington, 1978) is an EA-like model in which each spin interacts equally with every other spin through an identical exchange distribution

$P(J_{ij})$. This is clearly an unphysical assumption; however, since the MFT of ferromagnetism leads to predictions that agree fairly well with experiment, it is worthwhile to choose the MFT as a starting point for developing spin glass theory. It turns out that, even in the mean-field theory of spin glasses, the problem is not easy to solve.

The SK model involves N Ising spins ($S_i = \pm 1$), with an external field H_0 applied in the direction of quantization, and interacting with each other through infinite-range exchange interactions J_{ij} which are independently distributed according to a Gaussian probability distribution with a non-zero mean value

$$P(J_{ij}) = \frac{1}{J\sqrt{2\pi}} \exp\left(-\frac{(J_{ij} - J_0)^2}{2J^2}\right). \tag{2.43}$$

The Ising Hamiltonian of the system is

$$H = -\sum_{(ij)} J_{ij} S_i S_j - h \sum_i S_i \tag{2.44}$$

where $h = g\mu_B H_0$, and $\sum_{(ij)}$ denotes a summation over the $N(N-1)/2$ distinct pairs of spins. Two intensive variables are introduced:

$$J_0 \equiv \frac{\overline{J_0}}{N}; \qquad J \equiv \frac{\overline{J}}{N^{1/2}} \tag{2.45}$$

to prevent infinite energy in the thermodynamic limit $N \to \infty$. The ratio $\eta = \overline{J_0}/\overline{J}$, which is related, in practice, to the concentration of magnetic impurities, is important in determining the properties of the system.

The free energy per spin is given by

$$f = \lim_{N\to\infty} \left(-\frac{k_B T}{N}\right) [\ln Z \{J_{ij}\}]_{av} \tag{2.46}$$

After introducing n identical replicas of the system, and using Eq.(2.25), Eq.(2.46) becomes

$$\begin{aligned} f &= \lim_{N\to\infty} \lim_{n\to 0} \left(-\frac{k_B T}{N}\right) \frac{1}{n} \left([Z^n \{J_{ij}\}]_{av} - 1\right) \\ &= \lim_{N\to\infty} \lim_{n\to 0} \left(-\frac{k_B T}{N}\right) \frac{1}{n} (Z_n - 1). \end{aligned} \tag{2.47}$$

We start by evaluating Z_n with Eq.(2.27). Replacing $H\left(J_{ij}, S_i^{\alpha}\right)$ by Hamiltonian Eq.(2.44), we have

$$Z_n = Tr_{\{S_i^1\}\ldots\{S_i^n\}} \int_{-\infty}^{+\infty} [\prod_{(ij)} P(J_{ij}) dJ_{ij}] \exp\left[\beta \sum_{(ij)} J_{ij} \sum_{\alpha=1}^{n} S_i^{\alpha} S_j^{\alpha} + \beta h \sum_i \sum_{\alpha=1}^{n} S_i^{\alpha}\right], \beta = \frac{1}{k_B T}. \quad (2.48)$$

Inserting Eq.(2.43) and Eq.(2.45), and averaging over the exchange bonds J_{ij} which leads to Gaussian integrals (Kirkpatrick and Sherrington, 1978)

$$\begin{aligned} Z_n &= Tr_S \exp\left\{N^{-1} \sum_{(ij)} \left[\frac{\overline{J_0}}{k_B T} \sum_{\alpha} S_i^{\alpha} S_j^{\alpha} + \frac{1}{2}\left(\frac{\overline{J}}{k_B T}\right)^2 \sum_{\alpha\beta} S_i^{\alpha} S_j^{\alpha} S_i^{\beta} S_j^{\beta}\right] \right. \\ &\quad \left. + \frac{h}{k_B T} \sum_{i\alpha} S_i^{\alpha}\right\}, \qquad \alpha, \beta = 1, \ldots, n \\ &\equiv Tr_S \exp\left[-\beta H_{eff}(n)\right], \end{aligned} \quad (2.49)$$

which can be interpreted as the trace of a fictitious Hamiltonian $H_{eff}(n)$ with n interacting replicas of a homogeneous system with translational invariance.

Noting that $(S_i^{\alpha})^2 = 1$, and dropping some $1/N$ correction terms as $N \to \infty$, one has (Fischer, 1983)

$$\begin{aligned} Z_n &= Tr_S \exp\left\{N^{-1} \frac{\overline{J_0}}{k_B T} \sum_{\alpha} \left(\sum_i S_i^{\alpha}\right)^2 + \frac{1}{2} N^{-1} \left(\frac{\overline{J}}{k_B T}\right)^2 \sum_{\alpha \neq \beta} \left(\sum_i S_i^{\alpha} S_i^{\beta}\right)^2 \right. \\ &\quad \left. + \frac{1}{2} N n \left(\frac{\overline{J}}{k_B T}\right)^2 + \frac{h}{k_B T} \sum_{i\alpha} S_i^{\alpha}\right\}. \end{aligned} \quad (2.50)$$

The first two squared terms in $\exp\{\ldots\}$ can be simplified using the identity

$$\exp\left(-\frac{1}{2}\lambda a^2\right) = \left[\frac{\lambda}{2\pi}\right]^{1/2} \int_{-\infty}^{+\infty} dx \exp\left[-\frac{\lambda x^2}{2} + a\lambda x\right] \quad (2.51)$$

and, performing Tr_S for $\sum_i$, Eq.(2.50) becomes (Kirkpatrick and Sherrington, 1978)

$$\begin{aligned} Z_n &= \exp\left[\frac{1}{4} N n \left(\frac{\overline{J}}{k_B T}\right)^2\right] \int \left[\prod_{\alpha} \left(\frac{N}{2\pi}\right)^{1/2} dx_{\alpha}\right] \left[\prod_{(\alpha\beta)} \left(\frac{N}{2\pi}\right)^{1/2} dy_{\alpha\beta}\right] \\ &\quad \cdot \exp\left\{-N\left[\frac{1}{2} \sum_{(\alpha\beta)} {y_{\alpha\beta}}^2 + \frac{1}{2} \sum_{\alpha} {x_{\alpha}}^2 - \ln Tr_n \exp h_{eff}\left(x_{\alpha}, y_{\alpha\beta}\right)\right]\right\} \end{aligned} \quad (2.52)$$

where the function

$$h_{eff}(x_\alpha, y_{\alpha\beta}) = \frac{\overline{J}}{k_B T} \sum_{(\alpha\beta)} y_{\alpha\beta} S^\alpha S^\beta + \left(\frac{\overline{J_0}}{k_B T}\right)^{1/2} \sum_\alpha x_\alpha S^\alpha + \frac{h}{k_B T} \sum_\alpha S^\alpha \qquad (2.53)$$

is a dimensionless effective single-spin Hamiltonian, $(\alpha\beta)$ in Eq.(2.52) and Eq.(2.53) refers to $\alpha \neq \beta$, and the trace Tr_n is now over n replicas at a single site, x_α and $y_{\alpha\beta}$ are integration variables.

The SK model assumes that the limit $N \to \infty$ can be taken before the limit $n \to 0$ (Kirkpatrick and Sherrington,1978), so the integration in Eq.(2.52) can be done by the method of steepest descents, in which the integrations can be replaced by the integrand evaluated at its maximum value. Combining Eq.(2.47) and (2.52) and performing $\lim_{n\to 0} \lim_{N\to\infty}$, the free energy becomes (de Almeida and Thouless, 1978)

$$f = -\frac{\overline{J}^2}{4k_B T} - k_B T \lim_{n\to 0} n^{-1} \max\{-G(x_\alpha, y_{\alpha\beta})\} \qquad (2.54)$$

with

$$\begin{aligned} G(x_\alpha, y_{\alpha\beta}) &= \frac{1}{2} \sum_{(\alpha\beta)} {y_{\alpha\beta}}^2 + \frac{1}{2} \sum_\alpha {x_\alpha}^2 \\ &\quad - \ln Tr_n \exp\left(h_{eff}\left(x_\alpha, y_{\alpha\beta}\right)\right) \end{aligned} \qquad (2.55)$$

and $h_{eff}(x_\alpha, y_{\alpha\beta})$ is given by Eq.(2.53). Applying the stationary point condition

$$\begin{cases} \left.\frac{\partial f}{\partial x_\alpha}\right|_{x=x_\alpha{}^0} = 0, \\ \left.\frac{\partial f}{\partial y_{\alpha\beta}}\right|_{y_{\alpha\beta}=y_{\alpha\beta}{}^0} = 0, \qquad \alpha \neq \beta; \end{cases} \qquad (2.56)$$

or

$$\begin{cases} \left.\frac{\partial G}{\partial x_\alpha}\right|_{x=x_\alpha{}^o} = 0, \\ \left.\frac{\partial G}{\partial y_{\alpha\beta}}\right|_{y_{\alpha\beta}=y_{\alpha\beta}{}^o} = 0, \qquad \alpha \neq \beta \end{cases} \qquad (2.57)$$

to Eq.(2.55), one obtains

$$\begin{cases} {x_\alpha}^0 = \left(\beta\overline{J_0}\right)^{1/2} \frac{Tr_n S^\alpha \exp\left[h_{eff}\left(x_\alpha, y_{\alpha\beta}\right)\right]}{Tr_n \exp\left[h_{eff}\left(x_\alpha, y_{\alpha\beta}\right)\right]} \equiv \left(\beta\overline{J_0}\right)^{1/2} < S^\alpha > \\ {y_{\alpha\beta}}^0 = (\beta\overline{J}) \frac{Tr_n S^\alpha S^\beta \exp\left[h_{eff}\left(x_\alpha, y_{\alpha\beta}\right)\right]}{Tr_n \exp\left[h_{eff}\left(x_\alpha, y_{\alpha\beta}\right)\right]} \equiv (\beta\overline{J}) < S^\alpha S^\beta > \end{cases} \qquad (2.58)$$

with

$$\beta\overline{J_0} = \frac{\overline{J_0}}{k_B T}, \qquad \beta\overline{J} = \frac{\overline{J}}{k_B T}.$$

It becomes apparent in the following section that solving Eq.(2.54) is quite difficult.

(i)Replica Symmetric Solution

Sherrington and Kirkpatrick (1978) took the simplest situation where they assumed that all of the replicas are indistinguishable, so that at the maximum of the integrand, all the ${x_\alpha}^0$ are equal, as are all the ${y_{\alpha\beta}}^0$ (*replica symmetry*); thus

$$\begin{cases} {x_\alpha}^0 &= x_n = \left(\beta\overline{J_0}\right)^{1/2} m_n \\ {y_{\alpha\beta}}^0 &= {y_{\beta\alpha}}^0 = y_n = \left(\beta\overline{J}\right) q_n, \qquad \alpha \neq \beta. \end{cases} \tag{2.59}$$

Substituting Eq.(2.59) into Eq.(2.54) and performing the rather complicated calculation, Sherrington and Kirkpatrick obtained (1978)

$$\begin{aligned} f &= k_B T \left(\frac{\overline{J_0}}{2k_B T} m^2 - \frac{1}{4}\left(\frac{\overline{J}}{k_B T}\right)^2 (1-q)^2 \right. \\ &\quad \left. - \frac{1}{\sqrt{2\pi}} \int_{-\infty}^{+\infty} dz \exp\left(-\frac{1}{2}z^2\right) \ln\left(2\cosh \Xi(z)\right) \right) \end{aligned} \tag{2.60}$$

with the new variables m and q given by

$$m = \frac{1}{\sqrt{2\pi}} \int_{-\infty}^{+\infty} dz \exp\left(-\frac{1}{2}z^2\right) \tanh \Xi(z) \tag{2.61}$$

$$q = \frac{1}{\sqrt{2\pi}} \int_{-\infty}^{+\infty} dz \exp\left(-\frac{1}{2}z^2\right) \tanh^2 \Xi(z) \tag{2.62}$$

where the variable $k_B T \Xi(z) = \left(\overline{J_0} m + \overline{J} q^{1/2} z + h\right)$ can be interpreted as the local random field acting on a site, and $h = g\mu_B H_0$ is the external field.

The physical significance of the variables m and q, given by Eqs.(2.61) and (2.62), has been shown by Kirkpatrick and Sherrington (1978) to be

$$m \equiv \langle \langle S_i \rangle_T \rangle_J \tag{2.63}$$

$$q \equiv \left\langle \langle S_i \rangle_T^{\,2} \right\rangle_J \tag{2.64}$$

where $< \ldots >_T$ denotes a thermal average and $< \ldots >_J$ denotes an exchange bond average. Thus m is the local magnetization (or magnetization per spin site)

and q represents an Edward-Anderson type order parameter. The spin glass state is characterized by $q \neq 0$ and $m = 0$.

The differential susceptibility can be obtained (Sherrington and Kirkpatrick, 1975) by

$$\chi = \lim_{h \to 0} \frac{\partial m}{\partial h} = \frac{1 - q(T)}{k_B T - \overline{J_0}\,(1 - q(T))} = \frac{\chi^{(0)}}{1 - \overline{J_0}\chi^{(0)}} \tag{2.65}$$

with

$$\chi^{(0)} = \beta(1 - q). \tag{2.66}$$

$\chi^{(0)}$ is the susceptibility for $\overline{J_0} = 0$ (Fischer, 1983). Above the spin glass temperature, where $q = 0$, Eq.(2.65) is just a Curie-Weiss law. The susceptibility as a function of T is plotted in Figure 2.2-1. A cusp is predicted at T_{SG}, which becomes rounded with the application of a finite field (represented by the dashed line). As in the EA model, the SK model also predicts a peak in the specific heat.

Numerically solving the coupled equations (2.61) and (2.62) as a function of temperature and the ratio $\eta = \overline{J_0}/\overline{J}$ with $h = 0$, yields the magnetic phase diagram in Figure 2.2-2. The three phases are distinguished by the behavior of the magnetization m and the order parameter q. These phases are paramagnetic with $m = q = 0$, ferromagnetic with $m \neq 0, q \neq 0$, and spin glass with $m = 0, q \neq 0$. For $\eta \geq 1.0$, the paramagnetic region gives way to ferromagnetic ordering below a Curie temperature $T_c = \overline{J_0}/k_B$. For $\eta \leq 1.0$, the SK model predicts a transition from paramagnet to spin glass at a spin glass temperature $T_{SG} = \overline{J}/k_B$. For $1 \leq \eta \leq 1.25$, the model predicts a so-called *"reentrant" phase transition* namely paramagnetic→ferromagnetic→spin glass as the temperature is decreased. It is now believed that the low temperature transition, which is represented by a broken line in Figure 2.2-2, does <u>not</u> appear in the correct SK solution. In fact, the SK calculation does not get the entropy $S \equiv -N\left(\frac{\partial f}{\partial T}\right)_M$ correct at low temperatures.

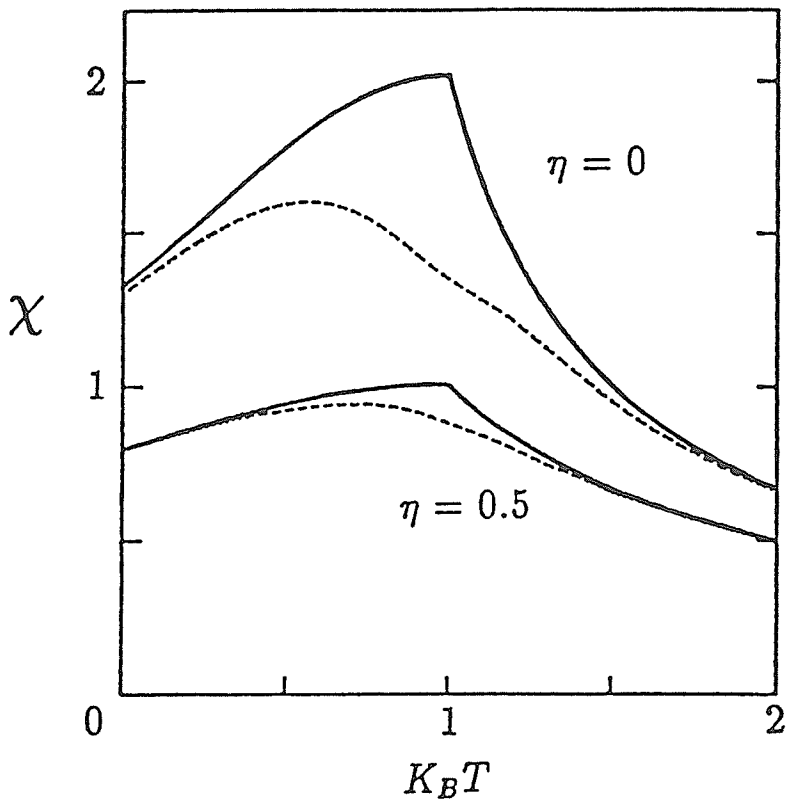

Figure 2.2-1: Differential susceptibilities of two spin glasses ($\eta = 0$ and $\eta = 0.5$), as calculated by the S-K solution. The zero-field spin glass cusps(solid curves) become rounded with the application of a field (dashed curves). From Sherrington and Kirkpatrick (1975).

The entropy S in the SK solution is $S(0) \approx -0.17$ at $T = 0$ (Sherrington and Kirkpatrick, 1975), which led other theorists to re-examine the SK solution at low temperatures.

(ii) Instability of the SK Solution at Low Temperatures: AT line

The stability of the SK solution was examined by de Almeida and Thouless (1978). Recall Eq.(2.55). The function $G(x_\alpha, y_{\alpha\beta})$ involves $n + n(n-1)/2 = n(n+1)/2$ variables x_α and $y_{\alpha\beta}$. Minimizing G requires all of the second partial derivatives with respect to x_α and $y_{\alpha\beta}$ at the saddle point ${x_\alpha}^0, {y_{\alpha\beta}}^0$ to be positive. In other words, the eigenvalues of the $\vec{G}$ matrix $[G_{nm}]$, called the Hessian matrix, must be positive. This condition will also ensure that the Gaussian integral in Eq.(2.52) converges at the saddle point in the limit $N \to \infty$. This can be seen schematically by making a Taylor expansion of G at its stationary point

$$G(y) = G(y_0) + \frac{1}{2}G''(y_0)(y - y_0)^2 + \dots$$

where $G'(y_0) = 0$ defines the saddle point y_0; then the Gaussian integral in Eq.(2.52) becomes

$$\int dy \exp\left[-NG(y)\right] = \int dy \exp\left[-NG(y_0) - \frac{1}{2}NG''(y_0)(y - y_0)^2 - \dots\right].$$

The second term can be ignored as $N \to \infty$, provided that $G''(y_0) > 0$; otherwise the resulting Gaussian integral diverges and the saddle point procedure is senseless.

The elements of the Hessian matrix

$$\frac{\partial^2 G}{\partial x_\alpha \partial x_\beta}, \qquad \frac{\partial^2 G}{\partial y_{\alpha\beta} \partial y_{\gamma\delta}}, \quad \text{and} \quad \frac{\partial^2 G}{\partial x_\alpha \partial y_{\gamma\delta}}, \quad \text{at} \quad {x_\alpha}^0, {y_{\alpha\beta}}^0 \tag{2.67}$$

with G defined by Eq.(2.55), were evaluated by de Almeida and Thouless (1978). By taking the replica-symmetric solution, they reproduced the phase boundaries separating the paramagnetic phase (P) from the spin glass (SG) and ferromagnetic (F) phases, respectively, in agreement with the SK solution; however, at low temperatures, they found an instability condition in zero field

$$\left(\frac{k_B T}{\overline{J}}\right)^2 \geq \frac{1}{\sqrt{2\pi}} \int dz e^{-\frac{1}{2}z^2} sech^4 \left[\frac{1}{k_B T}(\overline{J_0} m + \overline{J} q^{1/2} z)\right] \tag{2.68}$$

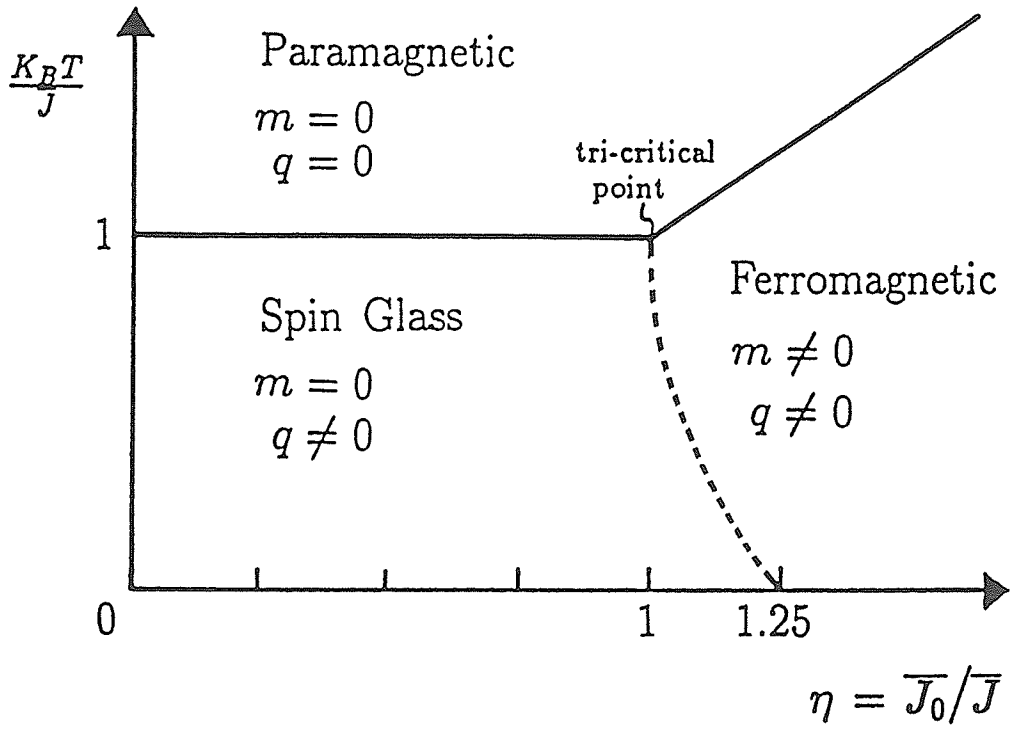

Figure 2.2-2: The zero-field magnetic phase diagram of the S-K model. The region $1 < \eta < 1.25$ (broken line) is "reentrant". From Sherrington and Kirkpatrick. (1975).

based on the requirement of the positive eigenvalues of the $[G_{nm}]$ matrix. By taking the equality in Eq.(2.68) and numerically solving Eq.(2.68), de Almeida and Thouless found the AT instability line (d) in Figure 2.2-3. The SK solution in the SK phase and in the ferromagnetic phase below the AT line is unstable; thus the SK-reentrant transition line (broken line in Figure 2.2-3) no longer exists in the correct SK solution.

For finite field with $\overline{J_0} = 0$, the instability AT line is also numerically plotted as line (b) in Figure 2.2-3, although there is no phase transition in the SK solution for non-zero field (de Almeida and Thouless,1978). Notice that the instability line (b) approaches lower temperatures as the field increases, so for high enough fields, the SK solution around the reentrant line becomes stable. In the region of small fields close to $T_{SG} = \overline{J}/k_B$, the AT stability line can be expressed as

$$H^2 > (4\overline{J}^2/3)(1 - T/T_{SG})^3. \tag{2.69}$$

De Almeida and Thouless suggested that the instability could be removed by breaking the permutation symmetry, i.e. $q_{\alpha\beta} \neq q_{\beta\alpha}$, between the replicas, but they were unable to offer an appropriate solution.

Notice that the positive eigenvalues of the $[G_{nm}]$ matrix in Eq.(2.54) actually maximize the free energy f, which is the reason why, in spin glass theory, one often sees the statement that the free energy in spin glasses should be maximized. This is rather a misleading statement, however; the correct statement should be that we are seeking the stable solution of Eq.(2.54) of the lowest free energy, so even though the negative eigenvalues of $[G_{nm}]$ minimize the free energy f, they nevertheless leads to an unstable solution.

(iii) Replica Symmetry Breaking: the Parisi Solution

In order to obtain the stable solutions for m and q for Eq.(2.59) and cure the negative entropy $S(0)$ in the SK model, the assumption of $q_{\alpha\beta} = q_{\beta\alpha}$, $\alpha \neq \beta$ in Eq.(2.59) has to be removed, in another words we have to break the replica

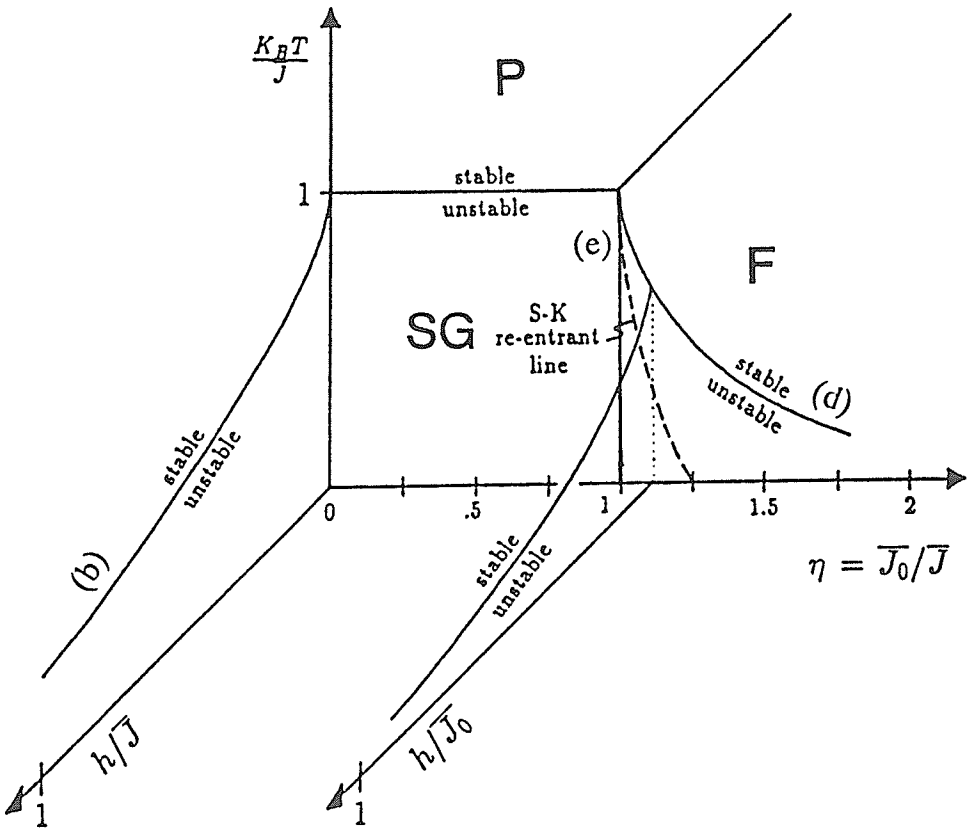

Fig.2.2-3: The AT instability lines (b) and (d) in the phase diagram of the S-K model. The area below the AT lines represents the unstable solutions in the S-K model, and corresponds to replica-symmetry breaking.

symmetry. (we write $q_{\alpha\beta}$ here instead of $y_{\alpha\beta}$ in order to conform with the notation which has become standard in the literature). The simplest $n \times n$ $q_{\alpha\beta}$ matrix for the SK solution has to be reconstructed in a space $n \times n$, although there exists no general way to find it. Among several schemes to break the replica symmetry (Binder and Young, section IV.B, and references therein), the ansätze proposed by Parisi has been most successful. The detailed description of Parisi's method to parameterize the $n \times n$ matrix $q_{\alpha\beta}$ was given in his papers (1979, 1980a, 1980b), and also in the review articles (Binder and Young, 1986, section IV B; Fischer and Hertz, 1991, section 3.4). The procedures are summarized bellow, and schematically shown in Figure 2.2-4.

Parisi's order parameter matrix $q_{\alpha\beta}$ has the following hierarchical structure. We start with the matrix $q_{\alpha\beta}$ in the SK form, in which all off diagonal elements are assigned the same value $q(m_0)$, and all the diagonal elements are taken to be zero. As a first step (step1), we break the $n \times n$ matrix into $n/m_1 \times n/m_1$ blocks of size $m_1 \times m_1$ where m_1 and n/m_1 are all integers. In the off diagonal blocks, nothing is changed, but in the diagonal blocks we replace $q(m_0)$ is replaced by $q(m_1)$. As the second step (step2), one subdivides each of the $m_1 \times m_1$ blocks, which are all along the diagonal, into $m_1/m_2 \times m_1/m_2$ subblocks, each of size $m_2 \times m_2$, and in each of these, along the diagonal, we replace $q(m_1)$ by $q(m_2)$. This can be repeated k times (step k), provided that each m_i can be evenly divided by m_{i+1}, which requires that

$$n \equiv m_0 \geq m_1 \geq \ldots m_k \geq 1. \tag{2.70}$$

The $n \times n$ order parameter matrix $q_{\alpha\beta}$ now contains corresponding order parameters $q(m_0), q(m_1), \ldots, q(m_k)$.

The procedure above makes sense for n a positive integer and k finite; however we must take limit $n \to 0$ when calculating the free energy. In order to calculate the matrix $q_{\alpha\beta}$ for $n = 0$, Parisi (1980) suggested that it is not evident that the m_i must remain as integers. In doing so, he further assumed that for noninteger

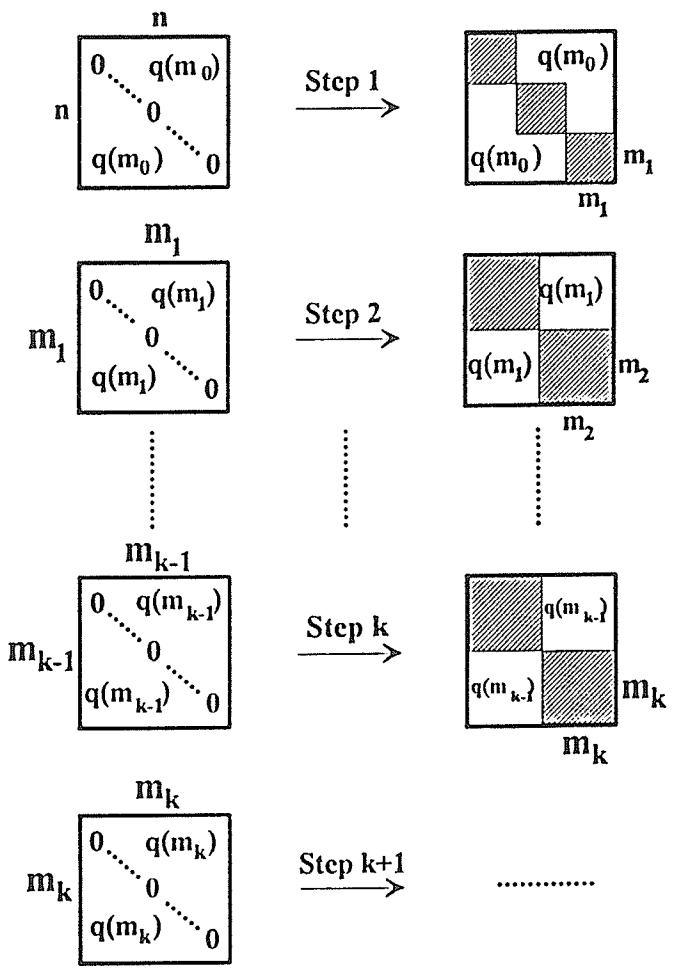

Figure 2.2-4: Construction of the matrix $q_{\alpha\beta}$ for Parisi's replica symmetry breaking scheme.

n, m_i can be an arbitrary real number, but has to satisfy the following condition

$$0 \leq m_i \leq 1, \qquad i = 0, \ldots, k. \tag{2.71}$$

In the limit of an infinite number of steps $k \to \infty$, m_i is replaced by a continuous variable x, and $q(m_i)$ in the matrix $q_{\alpha\beta}$ becomes Parisi's order parameter function $q(x)$ defined on the unit interval $0 \leq x \leq 1$. In other words, there are an infinite number of order parameters $q(x)$ for the spin glass state when the replica symmetry is broken. Note that the SK solution corresponds to the $k = 0$ stage of Parisi's scheme, or equivalently to assuming that $q(x)$ is independent of x.

Several novel results were obtained with Parisi's order parameter function $q(x)$ (Binder and Young 1986, section IV B; Fischer and Hertz 1991, section 3.4), although the general solution for $q(x)$ is unknown (except for T close to T_{SG} and $\overline{J_0}$):

(i) The equilibrium susceptibility becomes

$$\chi = \lim_{n \to 0} \frac{1}{k_B T} \left[1 - \frac{1}{n(n-1)} \sum_{\alpha\beta} q_{\alpha\beta} \right] = \frac{1}{k_B T} \left(1 - \int_0^1 q(x) dx \right). \tag{2.72}$$

In zero field, χ becomes constant for $T < T_{SG}$,

$$\chi = \frac{1}{\overline{J}}. \tag{2.73}$$

A *constant* susceptibility below T_{SG} is one of the striking features of the Parisi solution, and is reminiscent of field-cooled magnetization measurements (see Figure 1-19).

(ii) As shown in Figure 2.2-3, the phase boundary (line (e)) between the spin glass phase (SG) and the ferromagnetic phase (F) is predicted to be vertical. Thus the reentrant spin glass behaviour (dashed line), predicted by the SK theory, does not occur in the Parisi solution.

(iii) The entropy at zero temperature $S(0)$ is evaluated numerically for a finite number k in Eq.(2.71). Parisi found $S(0)$ = -0.16 with k=0 (SK results), S(0)

= -0.01 for k=1 and S(0) = -0.004 for k=2 (Parisi, 1980b). The entropy S(0) approaches zero fairly quickly with increasing k, and it is likely that $S(0) = 0$ for $k \to \infty$. Therefore it seems that the Parisi solution cures the negative entropy problem of the SK model.

The stability of the Parisi solution was discussed further by Fischer and Hertz (1991). Two families of eigenvectors, each now with a spectrum of eigenvalues, were found when the Hessian matrix was diagonalized. One spectrum has all finite and positive eigenvalues, while the other has eigenvalues which tend to be close to zero; however, there are no negative eigenvalues. Thus the AT instability has been removed.

The physical meaning of replica symmetry breaking can be seen from the following relationship (Binder and Young 1986, section IV.E)

$$\frac{dx}{dq} \equiv P(q) \tag{2.74}$$

where $P(q)$ given by Eq.(2.38) is the probability distribution of an overlap function $q^{ll'}$ between different thermodynamic states l, l'. $x(q)$ is the inverse function of the order parameter function $q(x)$. Therefore Eq.(2.74) shows that the replica symmetry breaking leads to broken ergodicity. As we have discussed earlier in section 2.1.3, the infinite number of thermodynamic states ("valleys") can be described by the Parisi order parameter function $q(x)$. Below the AT instability line, broken ergodicity occurs, and many different thermodynamic states, separated by energy barriers, with equal minima, are available. For a finite system these barriers will be finite. As $N \to \infty$, the barrier heights appear to diverge and so do the relaxation times (Binder and Young 1986, Section IV.D). Grest et al. (1983, see also Soukoulis et al., 1983a, and 1983b) further suggested that below T_{SG} the number of minima increases as T decreases. With small changes in applied field, minima disappear and reappear in other regions of the free energy surface. Whenever the system finds itself at the nearest local minimum, it will eventually relax

into a more stable state or true ground state by hopping over free energy barriers via thermal activation (see Figure 2.1-4). Since the destruction of energy minima implies irreversibility, while minima-hopping implies slow relaxation, Grest et al. deemed it reasonable *to associate the onset of replica-symmetry-breaking with the onset of irreversibility*, such as magnetic hysteresis, remanence, and time effects.

2.2.2 Vector Model

While the Sherrington-Kirkpatrick model serves as a good starting point to understand spin glass behavior, its predictions are probably inadequate because the model considers Ising spins, whereas experimental spins are probably Heisenberg-like vector spins. In this section we will discuss, briefly, a version of the SK model introduced by Gabay and Toulouse (1981) that considers N classical vector spins. Each spin $\vec{S}_i$ has m components $S_{i\mu}(\mu = 1, ..., m)$ which satisfy the following normalization condition:

$$\sum_{\mu=1}^{m} {S_{i\mu}}^2 = m. \tag{2.75}$$

They interact via independent random interactions J_{ij} (over infinite range) which are distributed according to the Gaussian distribution given by Eq.(2.43). In the presence of an external magnetic field H_0 applied along the $\mu = 1$ direction, the Hamiltonian of the model is

$$H = -\sum_{(ij)} J_{ij} \sum_{\mu} S_{i\mu} S_{j\mu} - h \sum_{i} S_{i1}. \tag{2.76}$$

For m component vector spins, the order parameter can be categorized as follows:

(a) Transverse order parameter

$$q_T{}^{\alpha\beta} \equiv \left\langle \left\langle {S_{i\mu}}^{\alpha} {S_{i\mu}}^{\beta} \right\rangle_T \right\rangle_J, \quad \mu \neq 1, \quad \alpha \neq \beta; \tag{2.77}$$

(b) Longitudinal order parameter

$$q_L{}^{\alpha\beta} \equiv \left\langle \left\langle {S_{i1}}^{\alpha} {S_{i1}}^{\beta} \right\rangle_T \right\rangle_J, \quad \alpha \neq \beta; \tag{2.78}$$

(c) Quadrupolar order parameter

$$q_\mu{}^{\alpha\alpha} = \left\langle \langle S_{i\mu}{}^{\alpha} S_{i\mu}{}^{\alpha} \rangle_T \right\rangle_J \tag{2.79}$$

where $\alpha, \beta = 1, \ldots, n$ are replica labels, and the external field is in the $\mu = 1$ direction.

By analogy with the procedure used in solving the SK model in the previous section, and with the use of the replica technique, the Parisi solution for the m-component vector spin glass in a field was obtained (Gabay et al.,1982; Elderfield and Sherrington, 1982; and Cragg et al., 1982); we only discuss the new phase diagram predicted by this model.

The phase diagram in the vector model is presented in Figure 2.2-5 (Gabay and Toulouse, 1981, $\overline{J}$ and k_B are set to 1 for calculation convenience, thus $T_{SG}(h = 0) = 1.$). Comparison of Figure 2.2-5 and Figure 2.2-3 in the SK model shows that there are two more transition lines (a) and (c), called Gabay-Toulouse(GT) lines, above the AT instability lines (b) and (d).

(i) In the case of $\overline{J_0} = 0$ and finite field h, the GT line (a) in the $h - T$ plane can be approximately represented by (Elderfield and Sherrington, 1982; Gabay et al., 1982)

$$T_{GT} = 1 - \frac{m^2 + 4m + 2}{4(m+2)^2} h^2 + \quad higher \ \ orders \ \ in \ \ h. \tag{2.80}$$

To the lowest order in h, the GT transition temperature $T_{GT}(h)$ has the following behaviour

$$\delta T \equiv T_{SG}(h = 0) - T_{GT}(h \neq 0) \propto h^{\psi_{GT}} \qquad \text{with} \quad \psi_{GT} = 2. \tag{2.81}$$

The GT line (a) in Figure 2.2-5 separates the paramagnetic phase (q_T= 0) from a lower temperature phase in which the transverse spin components are frozen into random directions ($q_T \neq 0$), and thus describes the onset of transverse spin glass ordering (TSG). The longitudinal order parameter q_L is non-zero on both sides

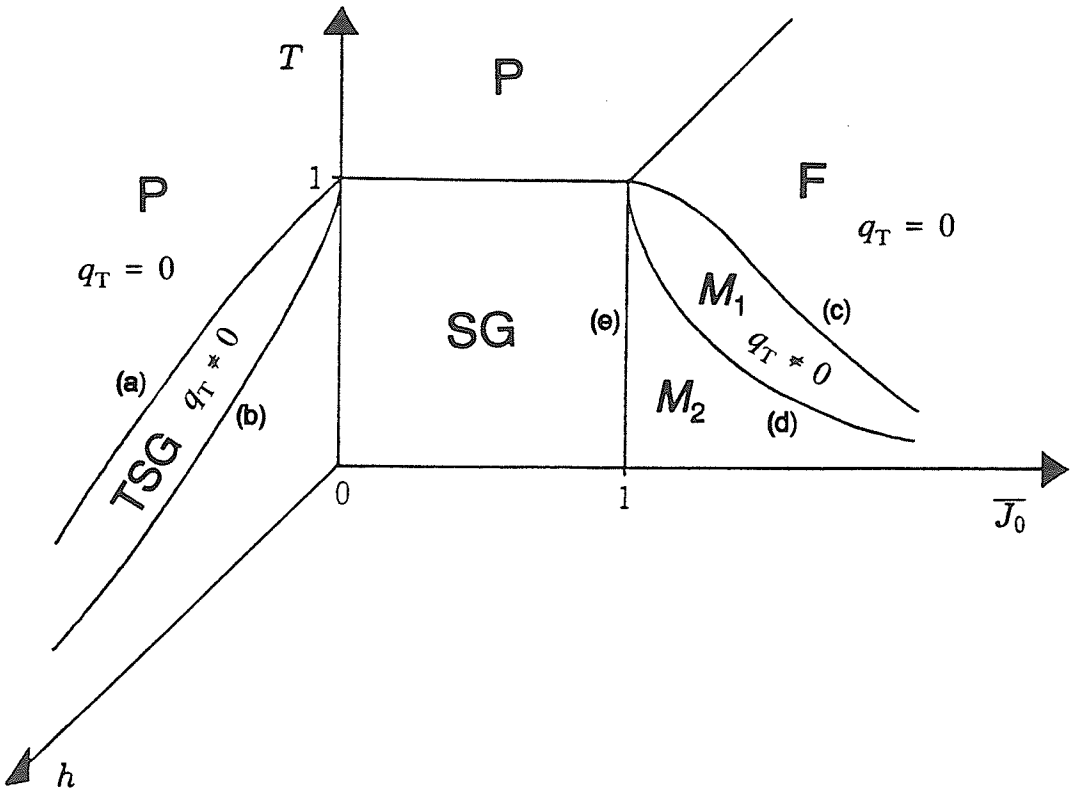

Figure 2.2-5: The phase diagram of the vector model. Curves (a) and (c) are GT lines, while curves (b) and (d) are AT lines in the vector model representing the onset of strong irreversibility. TSG is a transverse spin glass phase. The mixed phases M_1 and M_2 are *canted ferromagnetic phases*. Note that the "re-entrant" transition line in the S-K model no longer exists.

of the transition due to polarization by the finite field. Upon lowering the temperature further, line (b) is encountered, which is recognized as the m-component analogy of the A-T instability line, corresponding to replica symmetry breaking. For small h, the position of the AT line is defined by (Cragg et al., 1982)

$$(1 - T_{AT})^3 = \frac{(m+1)(m+2)}{8} h^2, \quad \text{for} \quad T_{AT} \leq 1 \tag{2.82}$$

and

$$T_{SG}(h = 0) - T_{AT}(h \neq 0) \propto h^{\psi_{AT}} \qquad \text{with} \quad \psi_{AT} = 2/3. \tag{2.83}$$

Gabay and Toulouse (1981) originally claimed that there was no replica symmetry breaking just below the GT line, but this is now known to be incorrect. The proof of replica symmetry breaking below the GT line was given by Cragg et al. (1982) by studying the eigenvalues of the Hessian matrix. They found that the replica symmetry breaking occurs simultaneously with the onset of transverse spin-glass ordering below the GT line. Above the GT line, similar to the Ising case, there is only one stable solution. For any finite m, the replica symmetric solution is unstable below the GT line.

These conclusions were confirmed by the Parisi-type solution obtained by Elderfield and Sherrington (1982) and Gabay et al. (1982). The Parisi solution in the vector model showed: (a) $\chi = \overline{J}^{-1}$ a constant, for all $T \leq T_{SG}$, just as for the Ising case. (b) The breaking of replica symmetry at the GT line has only a weak effect on the longitudinal order parameter, in the sense that $q_L(x)$ is only weakly dependent on x. As we already know that the replica symmetry breaking marks the onset of irreversibility, *the GT line is associated with weak irreversibility of the longitudinal susceptibility.* The longitudinal order parameter has been strongly changed at the AT line. We therefore see that a vestige of the AT line (line (b) and (d) in Figure 2.2-5) remains in the vector model, but instead of being a sharp line it represents *a crossover region below which strong irreversibility occurs in the longitudinal spin components.* Strong irreversibility of the transverse spin com-

ponents ($q_T(x)$) is very different from its SK value after crossing the GT line. It seems fair to say that the GT transition would be detected by the onset of irreversible behavior in the transverse susceptibility, which is not an easy experiment to do.

(ii) In the case of $\overline{J_0} \neq 0$ and $h = 0$ (ferromagnetic ordering allowed), the phase diagram is shown in the $\overline{J_0} - T$ plane of Figure 2.2-5. The existence of paramagnetic (P), spin-glass (SG), and ferromagnetic (F) phases was recognized in the SK model ($m = 1$). As in the SK model, the phase boundary to separate spin-glass from ferromagnet (line (e)) is drawn vertical again at $\overline{J_0}/\overline{J} = 1$ based on Parisi's solution for vector spins. Line (c) is another GT line, which separates the ferromagnetic phase F (with $q_T = 0, q_L \neq 0$) from a lower temperature mixed phase M_1 (with $q_T \neq 0, q_L \neq 0$). The collinear ferromagnetic phase F (with no transverse ordering) gives way to a canted ferromagnetic phase M_1 in which the transverse spin components are frozen into random orientations but the longitudinal spin components are still ordered ferromagnetically. Line (d) is another AT line for m-component spins indicating the crossover into a mixed phase M_2 which has the same type of spin configuration as mixed phase M_1, i.e $q_T \neq 0, q_L \neq 0$, but with the onset of the strong longitudinal irreversibility.

2.3 Critical Theory of Magnetic Phase Transition

Phase transitions are an important class of physical phenomena, known as critical phenomena, which are classified according to how the various quantities of interest vary near the critical point. According to Ehrenfest's classification, a phase transition occurs whenever there is a discontinuity in a derivative of the Gibbs function G (Eq.(2.88)), with the order of the transition defined by the lowest order derivative in which the discontinuity occurs. For a magnetic system the thermodynamic equations can be obtained from the relations established for

an ideal gas system by simply making the substitutions (Stanley 1971, chapter 2)

$$\begin{cases} V & \rightarrow & -M \\ P & \rightarrow & H \end{cases} \tag{2.84}$$

where P is the pressure and V the volume of the gas system, M is the magnetization and H is the magnetic field. The analogous differentials of the four state functions for a magnetic system thus are

$$dU = TdS + HdM \tag{2.85}$$

$$dF = -SdT + HdM \tag{2.86}$$

$$dE = TdS - MdH \tag{2.87}$$

$$dG = -SdT - MdH \tag{2.88}$$

where U is the internal energy, and the three other state functions are the enthalpy E, the Gipps potential G, and Helmholtz free energy F. The thermodynamic parameters which characterize a magnetic system are now (H, M, T), instead of (P, V, T) for an ideal gas system. The isothermal susceptibility is

$$\chi_T \equiv \left(\frac{\partial M}{\partial H}\right)_T = -\left(\frac{\partial^2 G}{\partial H^2}\right)_T \tag{2.89}$$

while the adiabatic susceptibility is

$$\chi_S \equiv \left(\frac{\partial M}{\partial H}\right)_S = -\left(\frac{\partial^2 E}{\partial H^2}\right)_S . \tag{2.90}$$

In this regard ferromagnets display second-order phase transitions since their susceptibilities (Eq.(2.89)) (and specific heats) evaluated in zero field and as a function of temperature, diverge as the Curie temperature is approached, while, as we show next, the spin glass phase transition appears to be an even higher order phase transition since the zero-field susceptibility shows no comparable divergence.

2.3.1 Critical Point Exponents

The study of critical phenomena focuses on the values of a set of indices, called critical-point exponents. In studying critical phenomena in phase transitions, one often uses a reduced temperature

$$t \equiv \frac{T - T_c}{T_c} \tag{2.91}$$

to measure the difference in temperature from the critical temperature T_c. If a general function $f(t)$ is positive and continuous for sufficiently small, positive values of t near the critical point, the limit (if it exists)

$$\lambda \equiv \lim_{t \to 0} \frac{\ln f(t)}{\ln t} \tag{2.92}$$

is called the critical-point exponent associated with the function $f(t)$. As a short-hand notation, one frequently writes

$$f(t) \sim t^{\lambda} \tag{2.93}$$

to denote the fact that λ is the critical point exponent for $f(t)$.

It is important to point out that the relation $f(t) \sim t^{\lambda}$ does not imply the relation

$$f(t) = At^x \qquad (x = \lambda). \tag{2.94}$$

In general we may find a more complicated functional expression such as

$$f(t) = At^x(1 + Bt^y + \ldots). \qquad (y > 0). \tag{2.95}$$

Note that the definition Eq.(2.92) of a critical-point exponent does not distinguish the functional forms Eq.(2.94) and (2.95).

The critical-point exponent plays an important role in the study of phase transitions, for the following two reasons: the critical behavior is dominated by the leading term when the temperature is sufficiently near the critical point; there exists a large number of relations among the critical exponents which arise from

fundamental thermodynamic and statistical mechanical considerations and thus transcend any particular system.

The following table summarizes the definitions of the critical-point exponents for magnetic systems (Stanley 1971, chapter 3).

Table 2.1: Definitions of critical-point exponents for a magnetic system. $t \equiv T/T_c - 1$

Exponent	Definition	Conditions			Quantity
		t	H	M	
α'	$C_H \sim (-t)^{-\alpha'}$	< 0	0	0	specific heat at constant magnetic field
α	$C_H \sim (t)^{-\alpha}$	> 0	0	0	specific heat at constant magnetic field
β	$M \sim (-t)^{\beta}$	< 0	0	$\neq 0$	zero-field magnetization
γ'	$\chi_T \sim (-t)^{-\gamma'}$	< 0	0	$\neq 0$	zero field isothermal susceptibility
γ	$\chi_T \sim t^{-\gamma}$	> 0	0	0	zero field isothermal susceptibility
δ	$H \sim \lvert M \rvert^{\delta} sgn(M)$	0	$\neq 0$	$\neq 0$	critical isotherm

The rigorous relations among the exponents are a set of inequalities given by Stanley (1971, chapter 4):

$$\alpha' + 2\beta + \gamma' \geq 2 \tag{2.96}$$

$$\alpha' + \beta(\delta + 1) \geq 2 \tag{2.97}$$

$$\alpha'(\delta + 1) \geq (2 - \alpha')(\delta - 1) \tag{2.98}$$

$$\gamma' \geq \beta(\delta - 1). \tag{2.99}$$

It should be noted that in real system these relations are often obliged equalities rather than inequalities.

2.3.2 Scaling Theory

The scaling theory for magnetic systems is capable of providing the functional relations among the critical-point exponents (in fact the inequalities among exponents become equalities) if independent critical-point exponents are restricted in number, and also makes specific predictions about the form of the equation of state. The theory (also called the static scaling law or homogeneous function approach) involves making a simple assumption concerning the basic form of a thermodynamic potential, for which thus far no rigorous justification has yet been given. Therefore the results of this section rest on an unproved assumption. However both the predicted relations among critical-point exponents and the form of the magnetic equation of state from scaling appear to be supported by most experiment work.

A function $f(\vec{r})$ is defined to be homogeneous if for all values of the parameter λ

$$f(\lambda\vec{r}) = g(\lambda)f(\vec{r})$$

where the n-dimensional vector $\vec{r}$ represents the n-tuple $(x_1, x_2, \ldots, x_n)$, and the scaling function $g(\lambda)$ must be of the form (Stanley, 1971)

$$g(\lambda) = \lambda^p.$$

The parameter p is generally called the degree of homogeneity. A two variable homogeneous function can be written as

$$f(\lambda x, \lambda y) = \lambda^p f(x, y).$$

It has been shown (Stanley 1971, chapter 11) that a two variable generalized homogeneous function has the form

$$f(\lambda^a x, \lambda^b y) = \lambda f(x, y) \tag{2.100}$$

where a and b are arbitrary values.

The *static scaling hypothesis* states that the Gibbs potential $G(T, H)$ or $G(t, H)$ is a generalized homogeneous function:

$$G(\lambda^{a_t} t, \lambda^{a_H} H) = \lambda G(t, H) \tag{2.101}$$

where t is called the reduced temperature, and a_t and a_H are unspecified parameters. By differentiating both sides of Eq.(2.101) with respect to H, and using Eq.(2.88)

$$\lambda^{a_H} M(\lambda^{a_t} t, \lambda^{a_H} H) = \lambda M(t, H). \tag{2.102}$$

Based on Eq.(2.102) all critical exponents defined in Table 2.1 can be expressed in terms of a_H and a_t (Stanley 1971, chapter 11):

$$\beta = \frac{1 - a_H}{a_t} \tag{2.103}$$

$$\delta = \frac{a_H}{1 - a_H} \tag{2.104}$$

$$\gamma = \gamma' = \frac{2a_H - 1}{a_t} \tag{2.105}$$

$$\alpha = \alpha' + \frac{2a_t - 1}{a_t}. \tag{2.106}$$

Thus the inequalities among these exponents in Eq.(2.96) to Eq.(2.99) become equalities and

$$\gamma' = \beta(\delta - 1) \tag{2.107}$$

is called the *Widom equality.*

The magnetic equation of state can be derived as follows. Recall Eq.(2.102)

$$M(t, H) = \lambda^{a_H - 1} M\left(\lambda^{a_t} t, \lambda^{a_H} H\right)$$

and let $\lambda = |t|^{-1/a_t}$; then Eq.(2.102) becomes

$$M(t, H) = |t|^{(1-a_H)/a_t} M\left(\frac{t}{|t|}, H/|t|^{a_H/a_t}\right). \tag{2.108}$$

Using Eqs.(2.103) and (2.104) to eliminate the scaling parameters a_H and a_t in favor of the critical-point exponents β and δ, Eq.(2.108) becomes

$$M(t, H) = |t|^{\beta} M\left(\pm 1, \frac{H}{|t|^{\beta\delta}}\right).$$

Noticing that the function on the right-hand side is only a function of $H/|t|^{\beta\delta}$ and the sign of $T - T_c$, one can define a function of a single variable $H/|t|^{\beta\delta}$:

$$F_{\pm}\left(\frac{H}{|t|^{\beta\delta}}\right) = M\left(\pm 1, \frac{H}{|t|^{\beta\delta}}\right), \tag{2.109}$$

and therefore

$$\begin{aligned} M(t,H) &= |t|^{\beta} F_{\pm}\left(\frac{H}{|t|^{\beta\delta}}\right) \\ &= |t|^{\beta} F_{\pm}\left(\frac{H}{|t|^{\gamma+\beta}}\right), \end{aligned} \tag{2.110}$$

with $t \equiv \frac{T-T_c}{T_c}$. This equation is known as the scaling equation of state of a magnetic system. It is also common to write Eq.(2.110) as

$$m = F_{\pm}(h) \tag{2.111}$$

where $m = M/|t|^{\beta}$ and $h = H/|t|^{\gamma+\beta}$ are the scaled magnetization and scaled magnetic field respectively.

The scaling equation for the isothermal susceptibility can be derived by differentiating Eq.(2.110) with respect to field H (Ho. et al., 1981a)

$$\begin{aligned} \chi(t,H) &= \left(\frac{\partial M}{\partial H}\right)_T = |t|^{-\gamma} \dot{F}_{\pm}\left(\frac{H}{|t|^{\gamma+\beta}}\right) \\ &= H^{-\gamma/(\gamma+\beta)} \left(\frac{H}{|t|^{\gamma+\beta}}\right)^{\frac{\gamma}{\gamma+\beta}} \dot{F}_{\pm}\left(\frac{H}{|t|^{\gamma+\beta}}\right) \\ &= H^{(1/\delta)-1} G_{\pm}\left(\frac{H}{|t|^{\gamma+\beta}}\right) \end{aligned} \tag{2.112}$$

where we have used the Widom relation $\gamma = \beta(\delta - 1)$ and defined $G(x) = x^{\frac{\gamma}{\gamma+\beta}} \dot{F}(x)$. This susceptibility, measured in fixed field H, has a maximum at $|t_m|$ when

$$\left(\frac{\partial \chi}{\partial t}\right)\Big|_{|t|=|t_m|} = 0, \quad i.e. \quad \dot{G}\left(\frac{H}{|t|^{\gamma+\beta}}\right)\Big|_{|t|=|t_m|} = 0 \tag{2.113}$$

This latter condition is satisfied if the argument of the function $G(x)$ is a constant, i.e.

$$\frac{H}{|t_m|^{\gamma+\beta}} = const. \tag{2.114}$$

Thus the static scaling hypothesis predicts the following two power law relations concerning the susceptibility

$$|t_m| \propto H^{\frac{1}{\gamma+\beta}} \tag{2.115}$$

$$\chi(|t_m|, H) \propto H^{(1/\delta)-1} \tag{2.116}$$

and (from Table 2.1)

$$\chi(t, 0) \propto t^{-\gamma} \qquad T > T_c \tag{2.117}$$

$$M(\epsilon, 0) \propto (-\epsilon)^{\beta} \qquad T < T_c \tag{2.118}$$

Eq.(2.115) indicates that the peak temperature $|t_m|$ in $\chi(t, H)$ increases with increasing field along a "cross-over" line given by Eq.(2.115), and $(\gamma+\beta)$ is thus called the "cross-over" exponent. As Eq.(2.116) shows, the peak amplitude $\chi(|t_m|, H)$ decreases with increasing field ($\delta > 1$). This prediction has been verified through ac susceptibility measurements.

2.3.3 Critical Analysis in Mean-Field Theory: The Effective Field Approach

The critical analysis presented in this section will be limited to a model, called the effective field model, within the context of the MFT. This model, which was first discussed in detail by Southern (1976), considered the SK-like system described by the following Ising Hamiltonian for arbitrary spin S

$$H = -\sum_{(ij)} J_{ij} S_i S_j - h \sum_i S_i \tag{2.119}$$

where $h = g\mu_B H_a$, and each S_i has $2S + 1$ components (i.e, $-S \leq S_i \leq +S$, and $S = 1/2$ in the SK model). In order to calculate the magnetization m and the order parameter q defined in Eq.(2.63) and Eq.(2.64), the following exact relation was used

$$< S_i >_T = \langle S B_S [S\beta (h + H_i)] \rangle_T \tag{2.120}$$

for the thermal average (Roshko and Williams 1984), where $B_s(x)$ is the Brillouin function defined as

$$B_s(x) = \frac{2S+1}{2S}\coth\left(\frac{2S+1}{2S}x\right) - \frac{1}{2S}\coth\left(\frac{x}{2S}\right). \tag{2.121}$$

The $H_i = \sum_j J_{ij}S_j$ is the effective RKKY field acting on spin S_i due to all the other spins. For a Gaussian distribution of J_{ij} (as in the SK model) the following set of coupled equations was obtained (Roshko and Williams, 1984, see also Kornik, 1990)

$$\begin{aligned} m &= \langle\langle S_i\rangle_T\rangle_J \\ &= \frac{1}{\sqrt{2\pi}}\int_{-\infty}^{+\infty} d\alpha \exp\left(-\frac{1}{2}\alpha^2\right) S B_S\left[\beta S\left(\overline{J_0}m + \overline{J}q^{1/2}\alpha + h\right)\right] \qquad (2.122) \\ q &= \left\langle \langle S_i\rangle_T{}^2 \right\rangle_J \\ &= \frac{1}{\sqrt{2\pi}}\int_{-\infty}^{+\infty} d\alpha \exp\left(-\frac{1}{2}\alpha^2\right) S^2 B_S{}^2\left[\beta S\left(\overline{J_0}m + \overline{J}q^{1/2}\alpha + h\right)\right] \qquad (2.123) \end{aligned}$$

where $\overline{J_0}$ and $\overline{J}$ represent the mean value and the width of the Gaussian J_{ij} distribution respectively. Notice that Eq.(2.122) and Eq.(2.123) become identical to Eq.(2.61) and Eq.(2.62) of the SK model for S = 1/2.

The effective-field approach has the dual advantage of not only avoiding the nonphysical low temperature behavior associated with the replica-trick solutions of the SK model, but can also be extended directly beyond the $S = 1/2$ case to include arbitrary spin and finite applied field. However it should be pointed out that while this approach does not use the replica technique, the possibility still exists that its solutions may suffer from instabilities analogous to those associated with replica symmetry breaking in the SK model below the de Almeida-Thouless line. Furthermore Binder and Young (1986, section IV A and C) have argued that one important term, called the Onsager reaction field term, should be *excluded* in $H_i = \sum_j J_{ij}S_j$.

(A) Critical behavior in ferromagnets and spin glasses

As with the SK model, the coupled equations Eq.(2.122) and Eq.(2.123) along with the associated expression for the susceptibility can be solved numerically. This leads to three distinct phases which were recognized in the SK model: a ferromagnetic ground state for $\overline{J_0}/\overline{J} \geq 1.25$, a spin glass ground state with for $\overline{J_0}/\overline{J} \leq 1.0$ and an intermediate "reentrant" region for $1.0 < \overline{J_0}/\overline{J} < 1.25$. When the argument of the Brillouin function in Eq.(2.122) and Eq.(2.123) is small, asymptotic expressions for m and q can be derived by expanding the Brillouin function and evaluating the appropriate integrals.

In a ferromagnetic ground state, the asymptotic expression for m (Roshko and Williams, 1985) yields asymptotic values of the mean-field critical-point exponents: γ =1, $\beta = 1/2$, and $\delta = 3$ satisfying $\gamma = \beta(\delta - 1)$. The zero field susceptibility $\chi(0,t)$ for $T > T_c$ is given by

$$\chi^F(0,t) \approx \frac{S(S+1)}{3t}, \tag{2.124}$$

and the scaling equation for the nonlinear susceptibility ${\chi_{NL}}^F$ can be written as (Yeung et al., 1987)

$${\chi_{NL}}^F(h,t) = \chi(0,t) - \chi(h,t) = t^{-\gamma} G\left(\frac{h^2}{t^{2\gamma+2\beta}}\right) \tag{2.125}$$

where the reduced temperature $t = |(T - T_c)/T_c|$. Therefore the leading critical divergence for a ferromagnetic system occurs in the linear term (even though all of the higher order terms still diverge), viz, $\chi(0,t) \sim t^{-\gamma}$, with $\gamma = 1$ in MFT. This is not the case for spin glasses where the zero-field susceptibility is continuous through the spin glass temperature T_{SG}. This is important from an experimental point of view, since the non-linear response is typically much weaker, and hence the corresponding divergence is more difficult to observe than the linear response.

In spin glasses, the order parameter is non-zero. The expansion for both m and q can be made (Roshko and Williams, 1985), and the asymptotic expression

for m results in the zero field susceptibility

$$\chi^{SG}(0,t) \approx \frac{S(S+1)}{3(t+1-\eta)} \tag{2.126}$$

where $t = |(T - T_{SG})/T_{SG}|$ and $\eta = \overline{J_0}/\overline{J}$. The zero field susceptibility is finite at $T = T_{SG}$. To leading order, a symmetric divergence was found for the nonlinear susceptibility χ_{NL} (Roshko and Williams, 1985) in spin glass systems around T_{SG}

$$\chi_{NL} \sim |t|^{-1} h^2, \qquad as \ T \to {T_{SG}}^{\pm}. \tag{2.127}$$

The scaling function for the non-linear susceptibility in spin glasses can be expressed as (Yeung et al., 1987, Roshko and Williams, 1985)

$${\chi_{NL}}^{SG}(h,t) = \chi(0,t) - \chi(h,t) = t^{\beta'} F\left(\frac{h^2}{t^{\gamma'+\beta'}}\right) \tag{2.128}$$

Therefore the leading divergence in the susceptibility occurs in the much smaller nonlinear term in spin glasses.

(B) Corrections to scaling theory in the ferromagnetic phase

We have obtained the asymptotic values for the critical-point exponents ($\gamma = 1$, $\beta = 1/2$, $\delta = 3$) in the ferromagnetic regime by using an effective-field model. Table 2.2 shows the comparison between the theoretical predictions of the critical exponents and the experimental results of some crystalline ferromagnets and amorphous ferromagnets. (Kaul, 1985)

As shown in Table 2.2, the experimental results are in general close to the predictions from a more realistic 3-D Heisenberg model (Le Guillou and Zinn-Justin, 1980), and quite different from the mean field (or effective field) values. The amorphous ferromagnets tend to have larger critical exponents than the crystalline ferromagnets. As we will show in Chapter IV, the critical exponents of the bond disordered ferromagnets are even more influenced by the exchange bond distribution and the magnetic field. (In principle the true critical-point exponents should be field and temperature independent). The experimental value of the order

parameter exponent $\beta(T)$ often remains constant below T_c until reduced temperatures between $0.05 \leq t \leq 0.1$ are reached, below which $\beta(T)$ falls; the exponent $\delta(H)$ decreases with increasing field and the susceptibility exponent γ also shows a complicated temperature dependence, sometimes with *anomalously large values.* (Kornik et al., 1990, and reference therein) The effective critical exponents, called effective Kouvel-Fisher exponents, defined as follows (Kaul, 1985):

$$\gamma^*(T) = (T - T_c)\chi(T)\frac{d\chi^{-1}}{dT} = -\frac{d\ln\chi(T)}{d\ln t} \tag{2.129}$$

$$\beta^*(T) = (T - T_c)M^{-1}\frac{dM}{dT} = \frac{d\ln M}{d\ln t} \tag{2.130}$$

with $t = |(T - T_c)/T_c|$, are often used to describe the temperature dependence of the critical exponents.

Table 2.2: Comparison of the theoretical and experimental values of the critical exponents. (Kaul, 1985)

	β	γ	δ
Mean-Field-Theory	0.5	1.0	3.0
3-D Heisenberg model	0.365±0.003	1.386±0.004	4.80±0.04
Fe	0.389±0.005	1.333	4.35±0.05
Co	0.435±0.025	1.225±0.025	3.35±0.35
Ni	0.378±0.004	1.34±0.01	4.58±0.05
$Fe_{10}Ni_{70}B_{19}Si_1$	0.42±0.02	1.35±0.04	4.49±0.05
$Fe_{20}Ni_{60}P_{14}B_6$	0.39±0.02	1.33±0.05	4.45±0.07
$Fe_{92}Zr_8$	0.620±0.003	1.92±0.02	5.82±0.06

(a) The exponent $\beta(T)$

Just below the Curie temperature T_c, the expansions of the Brillouin function in Eq.(2.122) and (2.123) yield (Kornik et al., 1990)

$$m(0,t) \approx t^{1/2}(1-t)\left[\frac{(1-t)^2-\eta^2}{(1-t)^2+2\eta^2}\right]^{1/2}\left[\frac{10S^2(S+1)^2}{3(2S^2+2S+1)}\right]^{1/2} \tag{2.131}$$

where $t = |(T - T_c)/T_c|$ and $\eta = \overline{J}/\overline{J_0} < 1.0$. To the leading order, this gives an asymptotic value of $1/2$ for β. However, there are other noncritical factors

which produce a temperature dependence in $\beta^*(T)$. By using Eq.(2.131), $\beta^*(T)$ in Eq.(2.130) can be calculated for different η and the results are shown in Figure 2.3-1(a) (Kornik et al., 1990). For a pure ferromagnet ($\eta = 0$), the exponent $\beta^*(T)$ decreases monotonically with increasing t, in agreement with experimental measurements on both amorphous and crystalline ferromagnets (Kaul, 1985). For a disordered ferromagnet ($0 < \eta \leq 1$), as Figure 2.3-1(a) shows, with increasing disorder η, the decrease of the effective exponent $\beta^*(T)$ with increasing t is initially suppressed, also in agreement with experimental observations (Kaul, 1985). Moreover, the effective-field model calculations indicate that, when the disorder becomes quite strong ($\eta \geq 0.5$), $\beta^*(T)$ should initially exhibit a marked increase with increasing t, passing through a maximum before decreasing as the temperature is lowered further. Such an effect has not, as yet, been observed experimentally. In fact the experimentally observed $\beta^*(T)$ shows a minimum in the vicinity of $t = 0.1$ (Kaul, 1985).

According to Eq.(2.115), the exponent β for $T > T_c$ can also be obtained through susceptibility measurements. From the complete solution of the coupled equations (2.122) and (2.123), the susceptibility $\chi(h,t)$ can be numerically calculated as a function of the reduced temperature t in various fixed fields h. Figure 2.3-2 shows the results for $\eta = 0.5$ (Kornik et al., 1990). The numerical relations from the SK model agree exactly with the scaling predictions from Eq.(2.115) and Eq.(2.116). The dotted line in Figure 2.3-2 of section 2.3-2 represents the cross-over line, satisfying Eq.(2.115). The effective cross-over exponents $\tilde{\gamma}(t) + \tilde{\beta}(t)$ can be obtained by calculating the local slope of $\log|t_m|$ vs $\log h$, from which $\tilde{\beta}(t)$ as a function of $|t_m|$ can then be extracted, since the exponent $\tilde{\gamma}(t) \equiv 1$ in the effective field model; the results are displayed in Figure 2.3-1(b) (Kornik et al., 1990). A comparison of Figure 2.3-1(a) and Figure 2.3-1(b) indicates that, while the corrections to scaling induced in the order parameter exponent as a function of reduced temperature t and disorder η are generally similar in sign and magnitude above

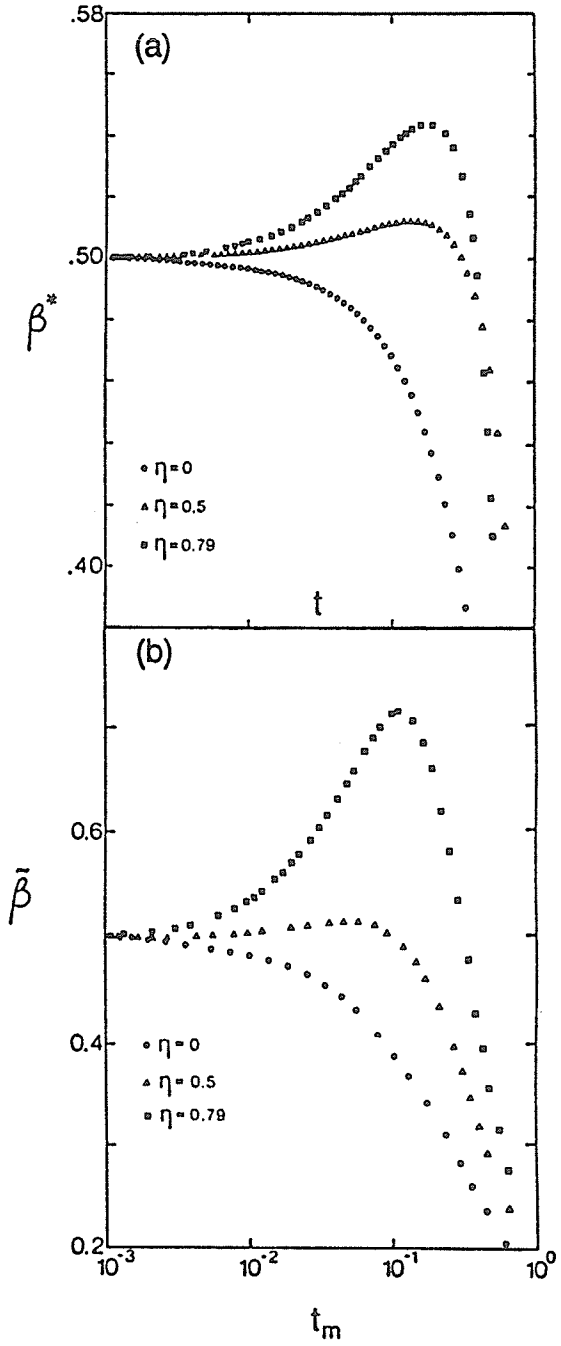

Figure 2.3-1: (a) Effective exponent β^* deduced from the temperature dependence of the spontaneous magnetization below T_c, as a function of reduced temperature t and disorder η. (b) Effective exponent $\tilde{\beta}$ deduced from the cross-over exponent in Figure 2.3-2, plotted as a function of susceptibility peak temperature t_m. From Kornik et al. (1990).

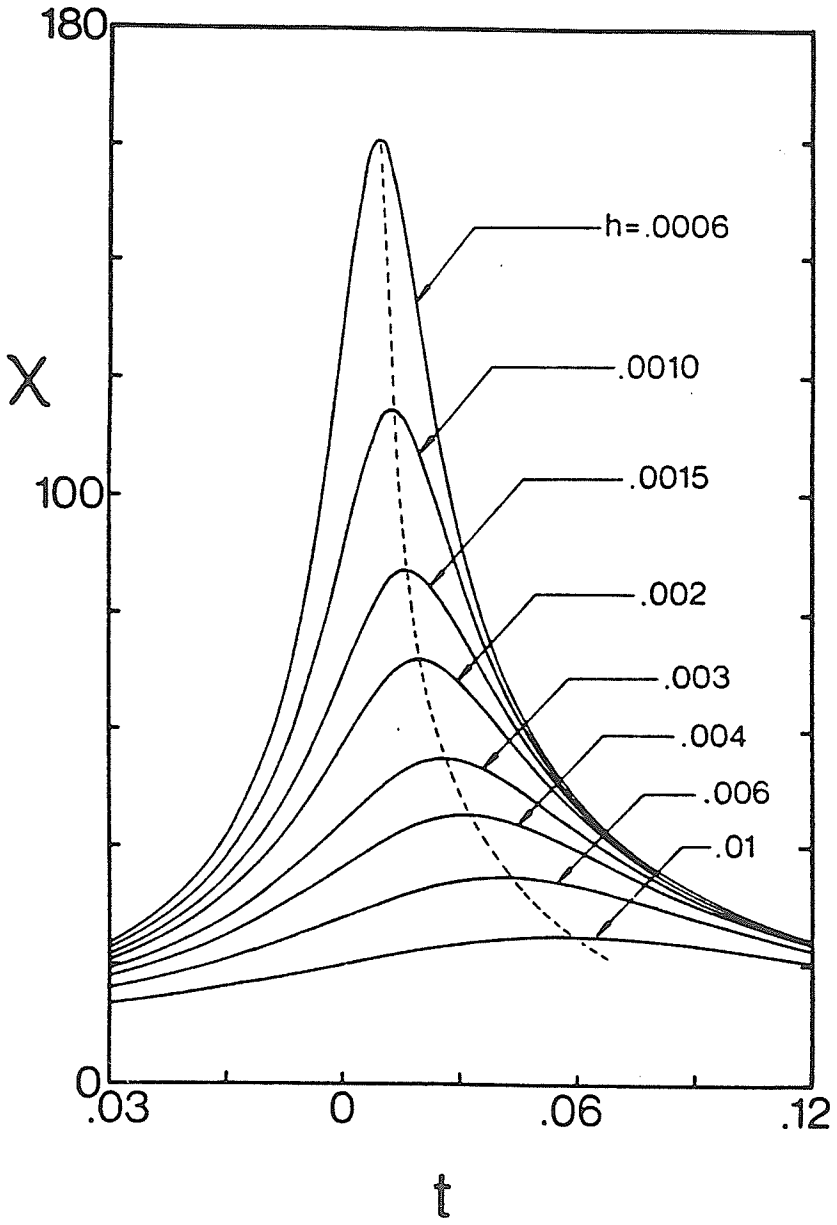

Figure 2.3-2: Temperature dependence of the numerical susceptibility $\chi(h,t)$ in various fixed fields h, for $\eta = 0.5$. The dotted line represents the *cross-over* line. From Kornik et al. (1990).

and below T_c , the corrections found from the behavior along the cross-over line are larger at a given reduced temperature, particularly as η approaches unity and the limit of stability of the ferromagnetic ground state is approached.

(b) The exponent $\delta(h)$

This exponent is most often deduced from the field dependence of the magnetization along the critical isotherm ($T = T_c$) using $m(h, t = 0) \sim h^{1/\delta}$ (Table 2.1). However, this exponent can also be found from the field dependence of the susceptibility peak amplitude along the cross-over line, using Eq.(2.116). Figure 2.3-3(a) shows the behavior of the model exponent $\delta^*(h)$ extracted from the double logarithmic plot of the numerical solution for $m(h, t = 0)$ as a function of h by solving the coupled equations (2.122) and (2.123). Figure 2.3-3(b) illustrates the behavior of the corresponding exponent $\tilde{\delta}(h)$, but obtained from the cross-over line (Kornik et al., 1990)

For the pure ferromagnet($\eta = 0$), both $\delta^*(h)$ and $\tilde{\delta}(h)$ are relatively featureless, simply increasing monotonically with increasing field h. As can be seen from these figures, weak disorder initially suppresses this increase in $\delta^*(h)$ and $\tilde{\delta}(h)$, so that the effective exponent remains close to its asymptotic value 3.0 over a wider range of reduced fields than it does in a pure ferromagnet. For strong disorder, however, $\delta^*(h)$ and $\tilde{\delta}(h)$ develop structure, and pass through minima before increasing again at higher fields, The latter behavior, such as $\tilde{\delta}(h, \eta)$ decreasing with increasing η and $\tilde{\delta}(h, \eta)$ decreasing with increasing h for large η, imitates the systematics of the variation in $\tilde{\delta}(h, \eta)$ reported experimentally from measurements along the cross-over line on a number of randomly substituted crystalline systems with bond disorder (Ho et al., 1981a, 1981b)

Finally, it should be pointed out that the corrections to scaling in $\tilde{\delta}(h)$ are not more pronounced along the cross-over line compared with those found for δ^*(h) along the critical isotherm. This contrasts with the behavior reported for $\tilde{\beta}(T)$. However, comparison of Figures 2.3-3 (a) and (b) reveals that these deviations

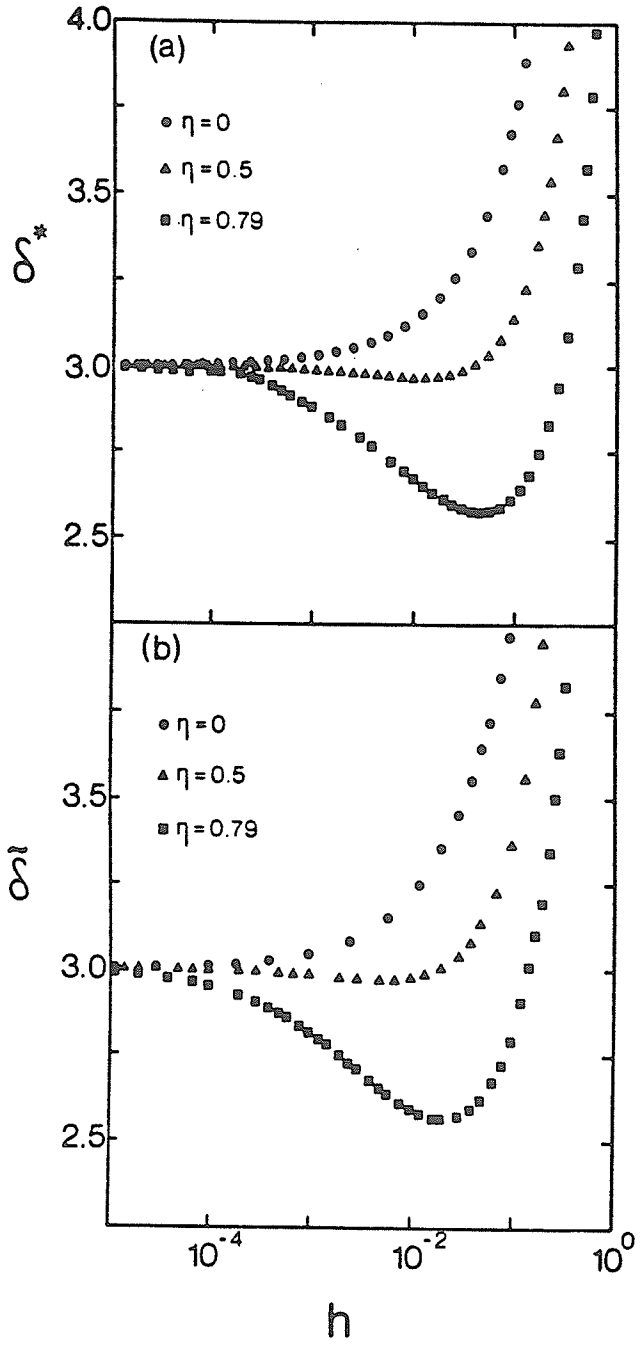

Figure 2.3-3: (a) Effective exponent δ^* deduced from the field dependence of the magnetization along the critical isotherm $t = 0$. (b) Effective exponent $\tilde{\delta}$ deduced from the field dependence of the susceptibility peak amplitude along the cross-over line. From Kornik et al. (1990).

do set in at a lower field along the cross-over line; this complements the behavior discussed earlier in connection with $\tilde{\beta}(T)$ since at a given reduced field h, the cross-over line is further removed from the critical point in the $(h-t)$ plane than is the critical isotherm.

(c) The exponent $\gamma(T)$

The effective field model predicts $\tilde{\gamma}(T) = \gamma^*(T) \equiv 1$, that is, temperature independent, which is in strong disagreement with experimental observations on disordered systems. The temperature dependence of γ has been explained by a correlated molecular field theory (Kornik et al. 1990, and reference therein). We will defer our detailed discussion about γ to Chapter IV.

2.4 Equilibrium and Nonequilibrium Dynamics in Spin Glasses

Investigation of spin glass dynamic behaviour in the mean-field theory has been summarized by Binder and Young (1986, Section IV.D) and Fischer and Hertz (1991, Chapter 5). The SK model appears to have a broad spectrum of relaxation times, which diverge as $N \to \infty$ below the AT line. In this section, we will discuss the dynamics of spin glasses from other theoretical points of view, which provide a more physical explanation for nonequilibrium behaviour in spin glasses, and we show the extent to which predictions of these models agree both qualitatively and quantitatively with the experimental observations.

2.4.1 Droplet Scaling Theory

The droplet scaling theory was extensively developed by Fisher and Huse for both ferromagnets (Huse and Fisher, 1987) and spin glasses (1988a, 1988b). The system they considered contains Ising spins ($S_i = \pm 1$) with short range nearest-neighbour interactions. The main feature of their model is clusters or droplets of coherently flipped spins enclosed by a "domain wall". These droplets only oc-

cur for temperatures below the ordering temperature. Figure 2.4-1(a) depicts a droplet of a "down" domain embedded in the "up" magnetized phase in a Ising ferromagnet, in which only a pair (up or down) of equilibrium states can be found. For Ising spin glasses with finite-range interactions, Fisher and Huse argued that at any given temperature below T_{SG} the spin glass also has only two pure equilibrium states Γ and $\overline{\Gamma}$ (1988b) in zero field which are simply related by global spin reversal, in contrast with the picture of an infinite number of equilibrium states in the MFT Parisi solution. As shown in Figure 2.4-1(b), a droplet in an Ising spin glass is a cluster of spins in the $\overline{\Gamma}$ state enclosed by a "domain wall" outside which the state is Γ. The macroscopic dynamic properties are determined by these low-lying excitation-droplets. A schematic picture of the domain walls present in the ground state of an Ising spin glass is shown in Figure 2.4-2.

(i) Equilibrium Dynamics of Droplet Fluctuations in Random Ising Ferromagnets

In the droplet theory of Ising ferromagnets (Huse and Fisher, 1987), Fisher and Huse argued that the long-time equilibrium dynamics of long-range ordered Ising ferromagnets are dominated by the creation and annihilation of long-lived droplet fluctuations. Two types of disordered ferromagnets are considered: *random-exchange disorder* and *random field disorder.* One important dynamic quantity which they computed is the spatial average of the temporal autocorrelation function $\overline{C(t)}$

$$\overline{C(t)} \equiv \langle C_i(t) \rangle_c = \left\langle \langle S_i(0) S_i(t) \rangle_t - \langle S_i \rangle_t^2 \right\rangle_c \tag{2.132}$$

where $< \ldots >_t$ denotes the infinite time average, and $< \ldots >_c$ is the configuration (spatial) average. Clearly the time dependence of $\overline{C(t)}$ in the limit $t \to \infty$ will be mostly affected by those long-lived spins (droplets).

According to Huse and Fisher (1987), the free energy F_D of a droplet fluctu-

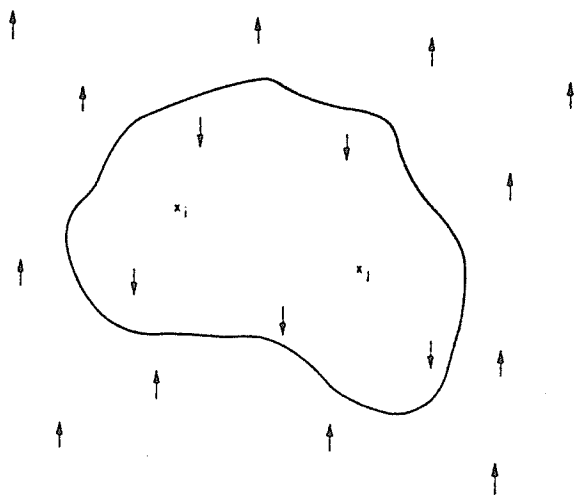

Figure 2.4-1(a): A droplet fluctuation in an Ising ferromagnet. The droplet (down domain) surrounded by a domain wall (solid line) is imbedded in the "up" phase. From Huse and Fisher (1987).

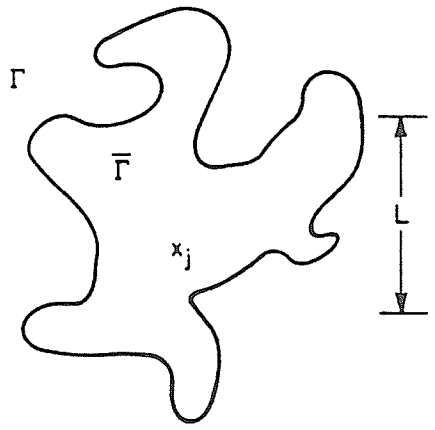

Figure 2.4-1(b): Schematic picture of a droplet of length scale L in an Ising spin glass. Outside the droplet the spins are aligned as in the ground state Γ, while inside the droplet the spins are reversed, as in the ground state $\overline{\Gamma}$. The surface of the droplet is actually fractal, as vaguely suggested by this drawing. From Fisher and Huse (1988a).

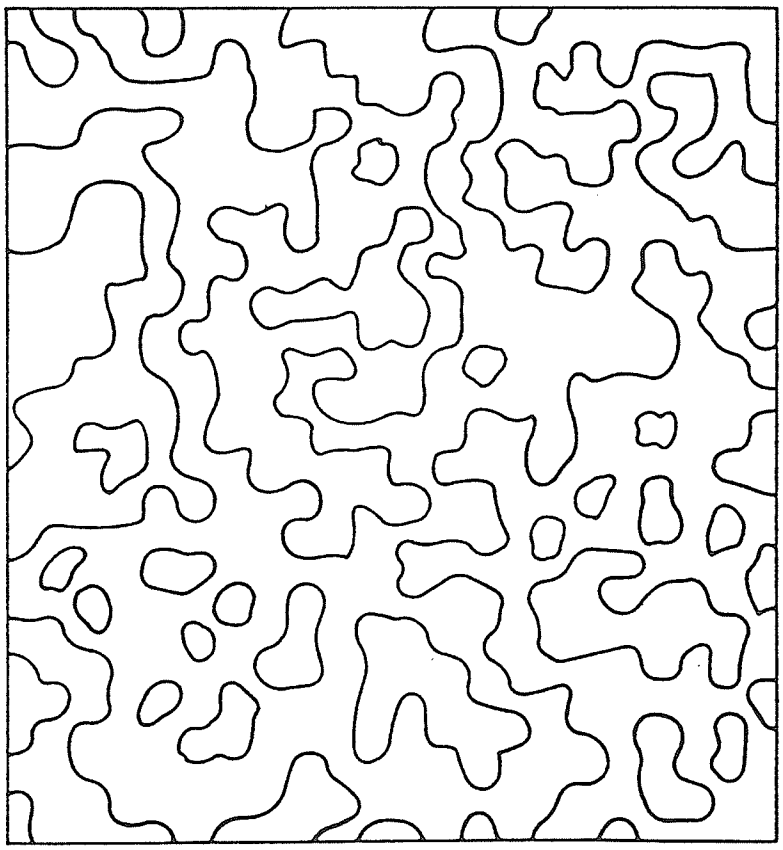

Figure 2.4-2: Schematic picture of the domain walls present in the ground-state configuration of an Ising spin glass in a uniform magnetic field. The domain walls separate regions between Γ and $\bar{\Gamma}$ states. From Fisher and Huse (1988a).

ation consists of the free energy of the domain wall and the free energy cost of flipping the interior (spins) of the domain when the system is subject to a random or uniform field. In order to create or annihilate a droplet, a free energy barrier B_D has to be surmounted, and the lifetime of the droplet fluctuation τ_D is activated according to

$$\tau_D \sim \exp(B_D/T) \tag{2.133}$$

Thus for long times t, only those long-lived droplets with $\tau_D \geq t$ contribute significantly to $C_i(t)$ and the long time dynamics are dominated by *rare* droplets.

For simplicity Huse and Fisher (1987) considered a roughly circular or spherical droplet of radius r, which has a free energy F_D given by

$$F_D = A_d \sigma r^{d-1} \tag{2.134}$$

where σ is the average surface tension and A_d is the surface area of a unit circle or sphere in d dimensions. Huse and Fisher suggested that the activation barrier B_D is proportional to r^{d-1},

$$B_D \cong b(f) r^{d-1}, \tag{2.135}$$

with f to be defined as a ratio of the actual free energy to the average free energy of a droplet. Thus the lifetime for a droplet is given by

$$\tau_D \sim \exp\left(b(f) r^{d-1}/T\right), \qquad (f < 1). \tag{2.136}$$

For a given f, the radius of the long-lived droplets can be obtained using $\tau_D \approx t$, and hence

$$r^{d-1} \approx \frac{T \ln(t/t_0)}{b(f)} \tag{2.137}$$

where t_0 is a microscopic time. Eq.(2.136) and Eq.(2.137) indicate that the lifetimes of the droplets which dominate the long time dynamics of $\overline{C(t)}$ are exponentially rare in lnt, and the spatially averaged autocorrelation function becomes

$$\overline{C(t)} \sim t^{-x(T)} \tag{2.138}$$

that is, a power-law decay of the autocorrelation at long times for a *random-exchange system.* The exponent $\overline{x(T)}$ will depend on the temperature T, and on nonuniversal details of the system.

For random-field systems, an extra term due to the random fields acting over the entire interior of the droplet has to be added in Eq.(2.134), while Eq.(2.135) and Eq.(2.136) still keep the same form, viz, the radius of the long-lived droplets varies as a function of $\ln t$. The spatially averaged temporal correlation function is

$$\overline{C(t)} \sim \exp(-k(\ln t)^y) \tag{2.139}$$

where $y = (d-2)/(d-1)$ and k depends on the details of the distribution of the random-field free energy, and on the temperature. The decay described in Eq.(2.139) is slower than that in Eq.(2.138). Notice that Eq.(2.138) can be included in Eq.(2.139) by setting $y = 1$. This is not surprising since in both cases, the relaxation times of the long-lived droplets are exponentially rare in $\ln t$. The exponent y simply reflects the nature of the randomness.

(ii) Dynamics of Droplets in Spin Glasses

Since the properties of droplets in spin glasses have not been directly calculated, Fisher and Huse (1988a) made the following scaling ansätz for the droplet.

In a d-dimensional lattice, the free energy of a droplet of length scale L (see Figure 2.4-1(b)) will scale as

$$F_L \sim L^\theta \tag{2.140}$$

The upper bound of the exponent θ is shown to be $\theta \leq \frac{d-1}{2}$, different from the limit in Ising ferromagnets(Eq.(2.134)). Large droplets will have large free energies, and there is a distribution $\rho_L(F_L)$ of F_L

$$\rho_L(F_L) \approx \frac{1}{\Upsilon L^\theta} \tilde{\rho}\left[\frac{F_L}{\Upsilon L^\theta}\right] \tag{2.141}$$

which has weight down to zero energy. The droplets with free energy $F_L \leq T$ are thermally active droplets which will dominate much of the equilibrium dynamics of spin glasses.

Because of randomness, the large-droplet excitations can have complicated shapes, and the broad distribution of free energies of the droplets will make their surfaces fractal (see Figure 2.4-1(b)) with surface area A_L scaling as

$$A_L \sim L^{d_s} \tag{2.142}$$

where the exponent $(d-1) < d_s < d$.

This simple scaling ansätz can make a variety of predictions for static and dynamic magnetic properties in finite-range interaction spin glasses; we focus here only on the dynamics of the magnetization.

(A) Equilibrium dynamics

As mentioned earlier, the equilibrium behaviour will be dominated by the creation and annihilation of the thermally active droplets. The natural scaling ansätz for an energy barrier of a spin glass droplet of scale L is

$$B_L \sim L^{\psi} \tag{2.143}$$

where the exponent ψ satisfies $\theta \leq \psi \leq (d-1)$. The barrier to create a droplet of length scale L is just $F_L + B_L$. Like the droplet free energies, droplet barriers also have a broad distribution, $\Phi_L(B_L)$, and for large L

$$\Phi_L(B_L) \simeq \frac{1}{\Delta L^{\psi}} \tilde{\Phi}\left[\frac{B_L}{\Delta L^{\psi}}\right] \tag{2.144}$$

where Δ sets the overall free-energy scale of the barriers.

The characteristic lifetime τ_L is exponential activated

$$\tau_L \sim \tau_0 e^{B_L/T} \tag{2.145}$$

where τ_0 is a characteristic microscopic time scale for creation and annihilation of a small droplet on a scale of order one (for instance one spin droplet).

The spatially averaged autocorrelation function, defined in Eq.(2.132), in the equilibrium spin glass state is dominated by the thermally active droplets, and has an extremely slow logarithmic decay

$$\overline{C(t)} \sim q_{EA} \frac{T}{\Upsilon} \left[\frac{\Delta}{T \ln(t/\tau_0)} \right]^{\theta/\psi}, \qquad \theta/\psi \leq 1 \tag{2.146}$$

where $q_{EA} \equiv \left\langle \langle S_i \rangle_t^{\,2} \right\rangle_c = \frac{1}{V} \sum_i \langle S_i \rangle_t^{\,2}$ is the Edwards-Anderson order parameter. The equilibrium magnetization will thus decay (Fisher and Huse, 1988b)

$$m_{eq}(t) \sim \frac{H}{(\ln t)^{\theta/\psi}} \tag{2.147}$$

(B) Nonequilibrium dynamics

According to Fisher and Huse (1988b), nonequilibrium dynamics is characterized by the growth of droplets or domains. Consider a thermoremanent magnetization measurement where the sample is cooled from a high temperature in the paramagnetic phase to a temperature $T_m < T_{SG}$ in a finite field H_c, and, after a wait time t_w at T_m, the field H_c is removed. Since there are only a pair of equilibrium states Γ and $\overline{\Gamma}$, for the spin glass at temperature T_m in zero field, immediately after the field removal, we can decompose the random spin configuration into domains (or individual spins) which are in either Γ or $\overline{\Gamma}$. The system will try to lower its free energy by decreasing the amount of interface between Γ and $\overline{\Gamma}$ states, thus leading to domain growth. A logarithmic growth law was predicted by Fisher and Huse (1988b), and the characteristic length scale of a domain at time t is

$$R_t \sim \left[\frac{T \ln t}{\Delta(T)} \right]^{1/\psi} \tag{2.148}$$

where $\Delta(T)$, introduced in Eq.(2.144), sets the free-energy scale of the barriers to be surmounted during the growth of the domain. The growth of domains causes the nonequilibrium magnetization to decay as

$$m_{neq}(t) \sim \left[\frac{\Delta}{(T \ln t)} \right]^{\lambda/\psi} \tag{2.149}$$

where λ is a nonequilibrium exponent in the range of $d/2 \leq \lambda \leq d$. Since $\theta \leq (d-1)/2$, so $\lambda > \theta$; the nonequilibrium decay is faster than the equilibrium decay m_{eq} given in Eq.(2.147). Such a crossover from equilibrium to nonequilibrium relaxation can be observed in the wait time experiment described above.

During the wait time t_w, the domains of length scale

$$R_w \equiv R_{t_w} \sim \left[\frac{T \ln t_w}{\Delta(T)}\right]^{1/\psi} \tag{2.150}$$

are formed. When the magnetization decay $m(t)$ is measured after the field removal ($t = 0$), in the early epoch $\ln t \ll \ln t_w$, one will only detect the relaxation which occurs on much smaller length scales $L_t \sim \left[\frac{T \ln t}{\Delta(T)}\right]^{1/\psi} \ll R_{t_w}$, and thus observe a quasiequilibrium relaxation (Eq.(2.147)), whereas in the late epoch $\ln t \gg \ln t_w$, the faster nonequilibrium decay (Eq.(2.149)) due to the growth of domains will be measured. The crossover time ($\ln \tau_c$) depends on t_w as well as on the cooling field H_c. For normally small fields H_c, $\ln \tau_c \sim \ln t_w$; however for a strong field, $\ln \tau_c \sim \frac{\Delta}{T} \xi_H{}^{\psi} \ll lnt_w$ and is *independent* of t_w (Fisher and Huse, 1988b). (ξ_H is called magnetic correlation length, which is inversely proportional to the field H (Fisher and Huse, 1988a)).

(C) Temperature cycling experiments

Fisher and Huse (1988b) designed a temperature cycling experiment in which the system is quenched to a temperature $T_1 < T_{SG}$, and after a wait time t_{w1}, the temperature is changed to $T_2 < T_{SG}$, and after a further wait time t_{w2}, relaxation is probed. They argued that the two states $\Gamma(T_1)$ at T_1 and $\Gamma(T_2)$ at T_2 are indistinguishable within a characteristic length scale $L_{\Delta T_{12}}$ called the overlap length:

$$L_{\Delta T_{12}} \sim |T_1 - T_2|^{-\left[\frac{d_s}{2} - \theta\right]^{-1}} \tag{2.151}$$

where $\Delta T_{12} \equiv |T_1 - T_2|$.

At the end of the wait time t_{w2}, we must compare three characteristic length scales: the domain size R_{w1} after t_{w1}, the overlap length $L_{\Delta T_{12}}$ imposed by ΔT_{12},

and the domain size R_{w2} after t_{w2}. The final domain size R_w after t_{w2} should be determined by

$$R_w = max(R_{w2}, min(L_{\Delta T_{12}}, R_{w1})) \tag{2.152}$$

The choice of *min* in Eq.(2.152) is because a new overlap length is forced on the system when the temperature is changed by ΔT_{12}. At T_2 one must consider the new state $\Gamma(T_2)$.

An interesting result of Eq.(2.152) is that for a temperature ΔT_{12} such that

$$R_{w2} \ll L_{\Delta T_{12}} \ll R_{w1} \tag{2.153}$$

then $R_w = L_{\Delta T_{12}}$. The temperature change then imposes a smaller crossover length scale $L_{\Delta T_{12}} \ll R_{w1}$, which should cause double crossover in the magnetization decay, so that experimentally two inflection points should be observed with the earlier inflection point corresponding to ΔT_{12}.

2.4.2 A Mesoscopic Theory of Aging in Spin Glasses

The aging in spin glasses has been described in Chapter I as the wait time dependence of the magnetization (see Figure 1-22). In order to explain aging in spin glasses, Koper and Hilhorst (1988) devised a theory which postulates that a spin glass state can be decomposed into a collection of domains, or regions of correlated spins; the aging can then be explained by the dynamics (growth and breaking-up) of the domains.

The mesoscopic domain picture postulated by Koper and Hilhorst can be outlined as following:

(i) A domain is defined as a region where the spins are correlated with each other and the correlation is a function of temperature T and field H; the domain is called a (T, H)-domain. The two types of domains, (T_1, H_1) and (T_2, H_2), are nearly identical up to an overlap length $l(T_1 - T_2, H_1 - H_2)$, which is *inversely* proportional to the temperature and field difference $\Delta T = |T_1 - T_2|$ $\Delta H = |H_1 - H_2|$, so that l diverges as $(T_2, H_2) \rightarrow (T_1, H_1)$. The two domains (T_1, H_1) and (T_2, H_2) are distinguishable beyond their overlap length $l(T_1 - T_2, H_1 - H_2)$. One can always find a (T_2, H_2)-domain in a (T_1, H_1)-domain and vice versa.

(ii) For a system in equilibrium at (T, H), there exists a single infinite (T, H)-domain. However, one also finds a distribution of (T_1, H_1)-domains centered around $l(T_1 - T, H_1 - H)$ in addition to the infinite (T, H) domain. For a *nonequilibrium* system, the size s of a (T_1, H_1)-domain will vary with time t, and there will be a size distribution $p(s, t; T_1, H_1)$ at time t for (T_1, H_1)-domains.

(iii) At the moment when the system is quenched to $T_m < T_{SG}$ in a field H_c, all domain sizes are zero, and all domains start to grow. However the (T_m, H_c)-domain will grow without limit; other $(T_1, H_1) \neq (T_m, H_c)$-domains will grow until they reach the overlap length $l(T_1 - T_m, H_1 - H_c)$, and then will subsequently break up into domains of this maximum size. The growth and the break up of domains is governed by a certain law.

(iv) The magnetic relaxation within a domain is described by a linear response relation.

For a reasonably small magnetic field, the linear response is valid. The time dependence of magnetization $M(t)$ to a time-dependent field $H(t)$ has the general relation

$$M(t) = M(0) + N\chi_{eq}\int_0^t dt' G(t,t')\dot{H}(t') \tag{2.154}$$

where χ_{eq} is the equilibrium dc susceptibility in zero field and N is the number of spins in the sample. The response function $G(t,t')$ represents the response at time t to a unit change in field H at time t' and $\dot{H}(t')$ is the rate of field change. If another response function $R(t,t')$ is defined by

$$R(t,t') \equiv 1 - G(t,t') \tag{2.155}$$

then Eq.(2.154) can be rewritten as

$$M(t) = N\chi_{eq}\left(H(t) - \int_0^t dt' R(t,t')\dot{H}(t')\right) \tag{2.156}$$

The response function $R(t,t')$ has the properties

$$\begin{cases} R(t,t) = 1 \ (G(t,t) = 0)) \\ \lim_{t-t'\to\infty} R(t,t') = 0 \\ \lim_{t\to\infty} R(t,t-\tau) \equiv R_{eq}(\tau) \end{cases} \tag{2.157}$$

where $R_{eq}(\tau)$ is the equilibrium relaxation function.

In a thermoremanent magnetization measurement, we perform a field jump after a certain wait time t_w at a measurement temperature T_m:

$$H(t) = \begin{cases} H_c & (t \le t_w) \\ 0 & (t > t_w) \end{cases} \tag{2.158}$$

Substituting Eq.(2.158) into Eq.(2.156), we obtain the relaxation of the magnetization

$$\Delta M(t) = N\chi_{eq}H_c R(t,t_w) \qquad (t > t_w) \tag{2.159}$$

Koper and Hilhorst made a reasonable assumption that $R(t,t')$ takes the form

$$R(t,t') = R_{eq}(t-t')F(t,t') \tag{2.160}$$

where $R_{eq}(t-t')$ is the relaxation function for an infinite domain in equilibrium, and $F(t,t')$ is a cutoff reflecting the *finite* domain size, and describes the deviation of the response function when the system is out of equilibrium. The function $F(t,t')$ satisfies

$$\begin{cases} F(t,t)=1 \\ \lim_{t\to\infty} F(t,t-\tau)=1 \qquad (\tau \text{ fixed}) \end{cases} \tag{2.161}$$

Koper and Hilhorst chose a power law for the equilibrium relaxation $R_{eq}(t-t')$:

$$R_{eq}(\tau)=\left(1+\frac{\tau}{t_0}\right)^{-\alpha} \cong \left(\frac{\tau}{t_0}\right)^{-\alpha} \tag{2.162}$$

where the time constant t_0 is generally small, representing a microscopic relaxation time for a single spin flip, and α is in the range 0.05 to 0.2.

For an equilibrium domain of size s, a plausible choice for $F(t,t')$ is

$$F(t,t')=e^{-(t-t')/\tau_{max}(s)} \tag{2.163}$$

where $\tau_{max}(s)$ is the maximum relaxation time in the relaxation spectrum of a size s domain, and $\tau_{max}(s) \simeq t_1\left(\frac{s}{a}\right)^z$, where t_1 is a microscopic time, z is a constant, and a is the typical spin spacing.

During the equilibration of a nonequilibrium system after the field H_c is removed, the domain size s will vary with time $s=s(t'')$. The response function in Eqs.(2.160) and (2.163) is changed into a form $F(t,t',s(t''))$ for a domain with size s. The relaxation function for the system $R(t,t')$ is now a weighted sum over all $R(t,t',s(t''))=R_{eq}(t-t'')F(t,t',s(t''))$:

$$R(t,t')=\int D\left[s(t'')\right] f\left[T(t),H(t),s(t'')\right] R(t,t',s(t'')) \tag{2.164}$$

where $f\left[T(t),H(t),s(t'')\right]$ is the weight function for an $s(t'')$ domain, which represents the probability distribution for (T,H)-domains of size s. By specifying the rules for domain growth and break up, and redefining $F(t,t',s(t''))$, Eq.(2.164) can be calculated; and Koper and Hilhorst showed that, for a *small field* jump

(Eq.(2.158)), the magnetization relaxation $\Delta M(t)$ in Eq.(2.159) becomes

$$\Delta M(t_w+\tau) = N\chi_{eq}H_c(1+\frac{\tau}{t_0})^{-\alpha}\exp\left[-\frac{{t_2}^{pz}}{t_1(1-pz)}\left\{(t_w+\tau)^{1-pz}-{t_w}^{1-pz}\right\}\right] \tag{2.165}$$

where t_2 is a microscopic time and p is a constant.

The relaxation function Eq.(2.165) shows the specific wait time dependence of the TRM. As shown in Figure 2.4-3, a plot of $\Delta M/H_c$ as a function of $\log\tau$ produces an inflection point which corresponds to a maximum in the relaxation rate $S(\tau) \sim \frac{d\Delta M}{d\log\tau}$, at τ_m (Figure 2.4-3(b)) (Koper and Hilhorst, 1988). A crossover occurs at τ_m from the slow power law *equilibrium* decay to a more rapid *nonequilibrium* decay imposed by the function F. This inflection point τ_m is shown by Koper and Hilhorst to be wait-time dependent with $\tau_m \cong t_w$, which agrees with experimental observations.

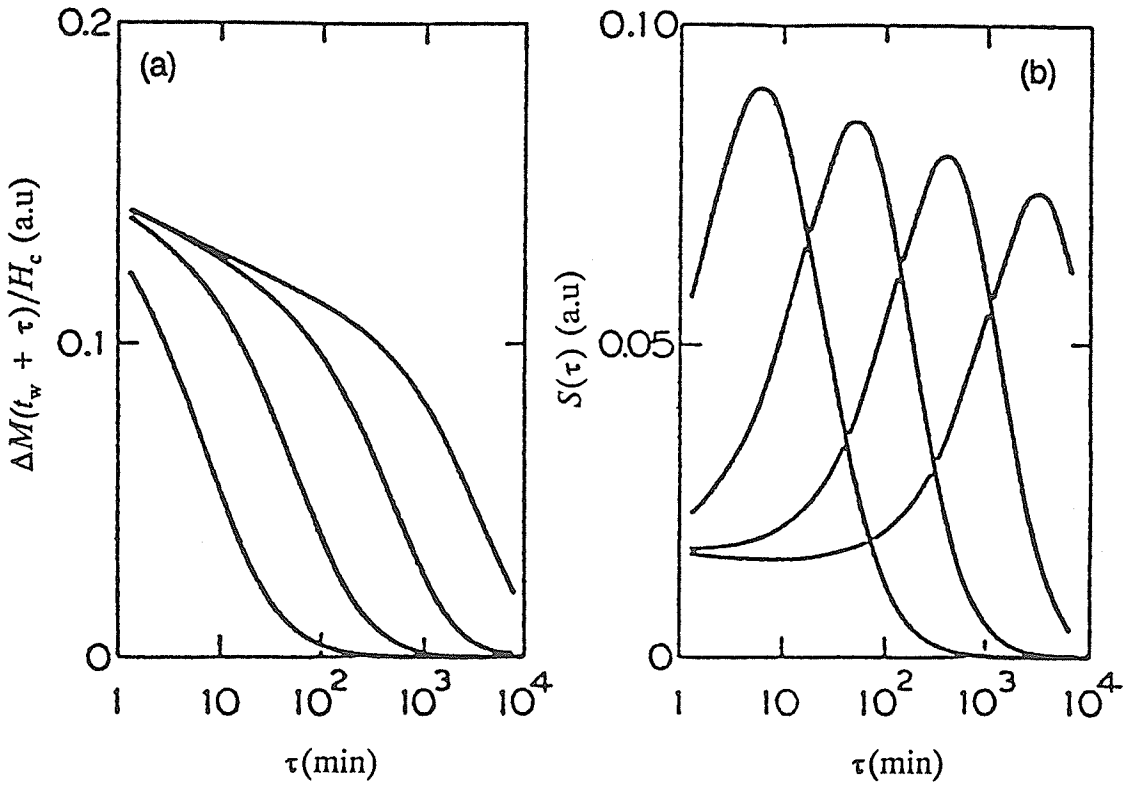

Figure 2.4-3: Theoretical curves for (a) the relaxation of the thermoremanent magnetization $\Delta M(t_w + \tau)/H_c$ as a function of time τ (Eq.(2.165)); (b) the relaxation rate $S(\tau)$ as a function of time τ, for small field jumps H_c and wait times t_w = 10, 10^2, 10^3, 10^4 min (from left to right). From Koper and Hilhorst (1988).

2.4.3 Percolation Model for Magnon Relaxation

Very recently, a new model for magnetization relaxation, based on the relaxation of quantized excitations (magnons) within finite domains, has been presented by Chamberlin and co-workers (Chamberlin and Haines, 1990; Chamberlin and Holtzberg, 1991). The salient feature of this model is that it can provide a very good fit to magnetization relaxation data over about eight decades of observation time ($10^{-4} - 10^{4}$ sec.).

Chamberlin defined a domain as a dynamically correlated region where all spins have the same average excitation energy, and then assumed that all spins (or excitations or magnons) will share a common relaxation rate ω_s. A domain D_s contains s spins, and there exists a distribution n_s for various finite domain sizes. The probability that a given spin belongs to a domain will be sn_s. If all s spins in D_s have the same relaxation rate ω_s, assuming linear response, the net magnetization relaxation of the system will be the probability sn_s times the probability that this domain D_s has not reached the equilibrium state $e^{-\omega_s t}$, summed over all domains (Chamberlin and Haines, 1990).

$$M(t) \propto \sum_s sn_s \cdot e^{-\omega_s t} \tag{2.166}$$

Chamberlin assume that a given spin is dynamically correlated to at least one of its neighbours with random probability p. When p is less than the critical concentration p_c for bond percolation there are only finite domains in the system. When p is above p_c the system contains an infinite domain (backbone) as well as domains of finite size. The domain size distribution n_s can then be predicted specifically from percolation theory (Chamberlin and Haines, 1990):

$$n_s \propto s^{-\theta} \exp\left[-(C's)^{\xi}\right] \tag{2.167}$$

where s is the number of spins, $\theta = -\frac{1}{9}$ and $\xi = \frac{2}{3}$ are size-scaling exponents, and $C' \propto |p - p_c|^{1/\sigma}$ with $\sigma = 0.45$. For activated relaxation of a quantized system at

temperature T, the relaxation rate (the transition rate that spins flip) is

$$\omega_s \propto e^{-\delta E/k_B T} \tag{2.168}$$

where δE is the energy change of the magnon relaxation. Chamberlin and Haines only consider the relaxation of quantized dispersive excitations, in which the energy of an individual magnon Δ is distributed throughout all the s spins in the domain. Thus an average energy-level spacing per particle is

$$\delta E = \Delta/s. \tag{2.169}$$

The magnon energy Δ only depends on the average interaction between spins, and is independent of domain size s. For weakly interacting spins ($\Delta \approx 0$), the average energy-level spacing δE is thus inversely proportional to the size of the domain, the smaller the domain, the larger the δE.

Substituting Eq.(2.167)-(2.169) into Eq.(2.166) and converting $\sum_s$ into a integration leads to

$$M(t) = M_i \int_0^\infty x^{10/9} \exp(-x^{2/3}) \exp\left(-t\omega_\infty e^{-C/x}\right) dx \tag{2.170}$$

where the integration variable $x = C's$, M_i is proportional to the initial magnetization, ω_∞ is the relaxation rate of the largest domain, and $C = C'\Delta/k_B T \propto \delta E$ is defined as a correlation coefficient which is small for weakly interacting spins or high temperatures.

Consider a magnetic sample which is cooled in finite field H from the paramagnetic regime to a given low temperature; the finite field is reduced to zero after a certain wait time t_w and the relaxation starts. Two types of domain relaxation processes should be identified: the domains *aligned* with the magnetic field, which have low initial energy, will increase their energy after H is removed, resulting in $C \propto \delta E > 0$, while *antialigned* domains will decrease their energy from the initially higher excitation level causing $C \propto \delta E < 0$. The observed relaxation curve

may probably contain both relaxation processes, and may possibly be divided into these two relaxation regimes. Thus it is useful to express Eq.(2.170) as two specific equations which separately describe the relaxation of aligned (Eq.(2.171)) and antialigned (Eq.(2.172)) domains:

$$M(t) = M_i \int_0^\infty x^{10/9} \exp(-x^{2/3}) \exp\left(-t\omega_- e^{-C/x}\right) dx, \quad C > 0 \quad (2.171)$$

$$M(t) = M_i \int_0^\infty x^{10/9} \exp(-x^{2/3}) \exp\left(-t\omega_+ e^{-C/x}\right) dx, \quad C < 0 \quad (2.172)$$

where both ω_- and ω_+ are the relaxation rate of the largest domain; however ω_-, corresponding to $\delta E > 0$, represents the fastest relaxation rate, whereas ω_+ is the slowest relaxation rate according to Eq.(2.168) (Note that $|\delta E| (\propto \frac{1}{s})$ is small in both cases).

The experimental test for the percolation model was done by Chamberlin and Haines (1990) on the AuFe system and by Chamberlin and Holtzberg (1991) on a simple EuS Heisenberg ferromagnet. Figure 2.4-4(a) shows the magnetic relaxation for a concentrated Au-11.9 at.%Fe spin glass at three temperatures above the spin glass temperature $T_m = 39$ K. The solid curves are the best fits using Eq.(2.171) only, which implies the relaxation at higher temperatures $T > T_m$ is dominated by "aligned" domains; the insert in Figure 2.4-4(a) shows that Eq.(2.171) works better than the commonly used simple power (Eq.(1.9)) (solid curves). For temperatures below T_m, the addition of Eq.(2.171) and Eq.(2.172) is required in order to produce the best fit over eight decades (Figure 2.4-4(b)), which indicates that when the sample is field cooled to a lower temperature, both aligned and antialigned domains appear. They also found that increasing the wait time t_w produces a decrease in C due to domain growth, which confirms the relation $C \propto \delta E \propto \frac{1}{s}$. The magnetic relaxation over $10^{-4} - 10^2$ seconds for a Au-19.8 at.% Fe ferromagnet was best fitted by Eq.(2.171) plus Eq.(2.172), plus a constant baseline which is necessary for this strong ferromagnet.

The functional test on a EuS ferromagnet in Figure 2.4-5 also displays two

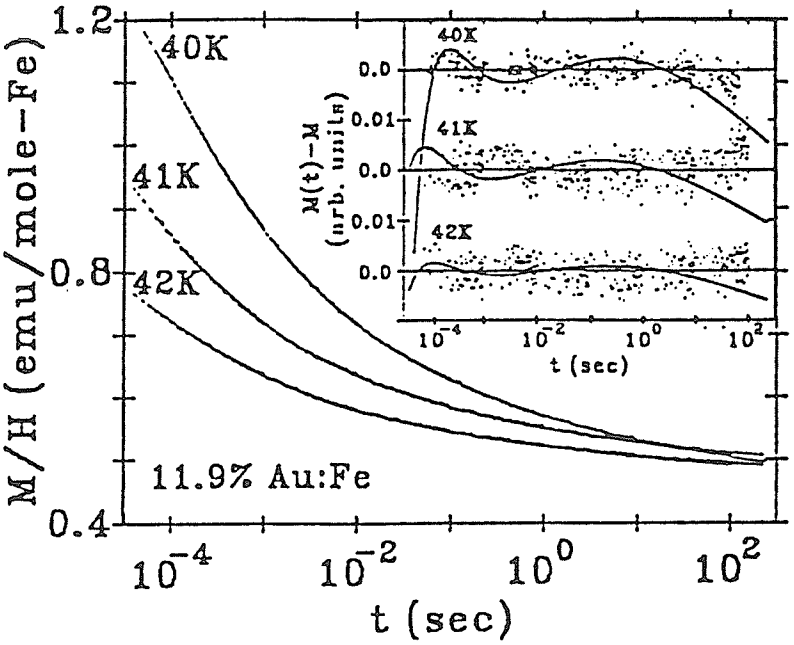

Figure 2.4-4(a): Magnetic relaxation of Au-11.9 at% Fe at three temperatures above T_m. The solid curves are the best fits using Eq.(2.171). The insert shows the difference between Eq.(2.171) and the data; a commonly used simple power function (solid curves) can not represent the data at both short and long times. From Chamberlin and Haines (1990).

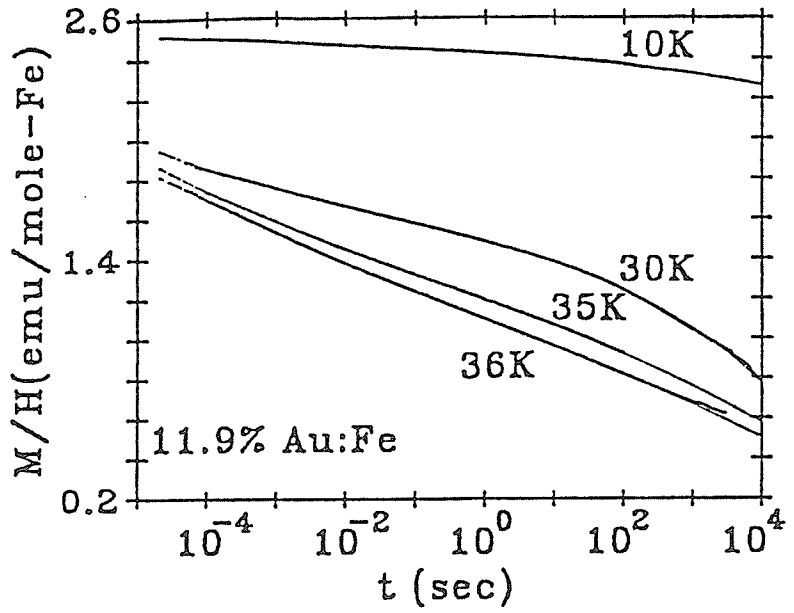

Figure 2.4-4(b): Magnetic relaxation of Au-11.9 at% Fe at four temperatures below T_m. The solid curves are the best fits using Eq.(2.171) *plus* Eq.(2.172). From Chamberlin and Haines (1990).

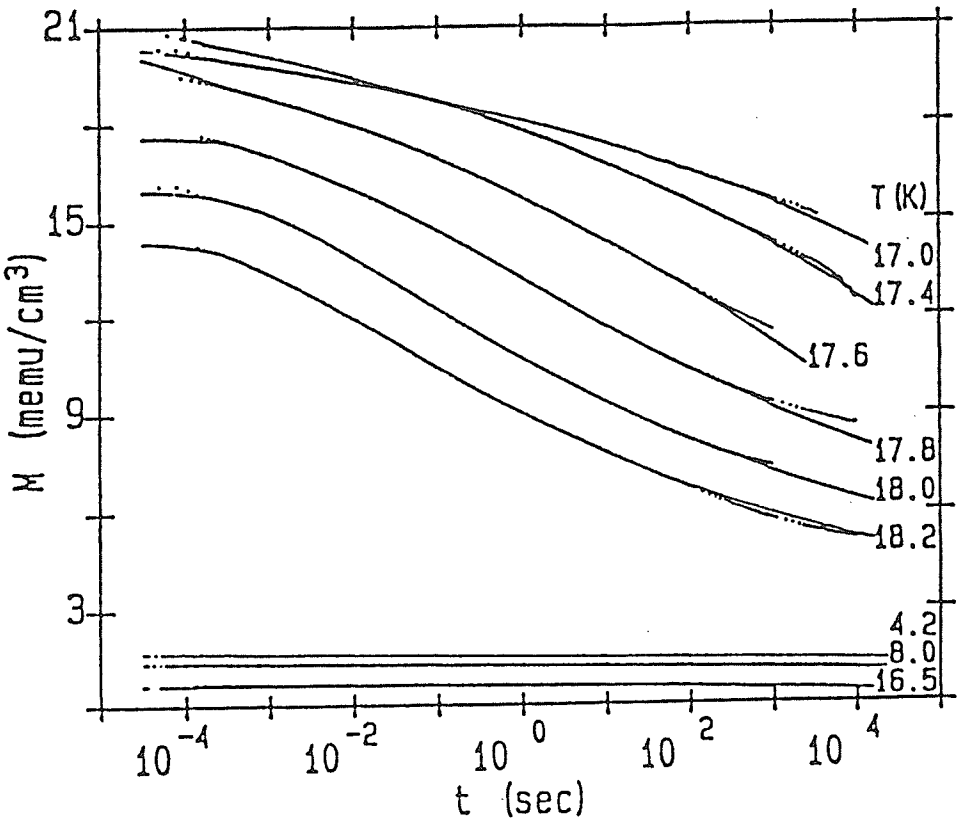

Figure 2.4-5: Magnetic relaxation of a ferromagnet EuS after removing H = 9 Oe. Above T_B = 17.75 K, *S*-shaped curvature indicates "aligned" relaxation, whereas for $T < T_B$ the best fit can only be achieved using Eq.(2.172), indicative of "antialigned" behavior. From Chamberlin and Holtzberg (1991).

temperature regimes. For higher temperatures $T > T_B = 17.75$ K, Eq.(2.171) itself provides an excellent fit for the S-shaped curves, while fitting the low temperature data requires Eq.(2.172) indicating a crossover from aligned to antialigned domains in the ferromagnet EuS.

Finally, it is worthwhile pointing out that, with mathematical approximations to Eq.(2.171) and Eq.(2.172), several empirical functions can be obtained (Chamberlin and Haines, 1990). For $C\omega_- t \gg 1$, Eq.(2.171) becomes a simple power law $M(t) \sim t^{-\alpha}$, whereas for $C\omega_+ t \leq 1$, Eq.(2.172) becomes a stretched-exponential $M(t) \sim \exp\left(-t^{\beta}\right)$. Furthermore, because the percolation model is based on general geometric considerations, the functions should give excellent agreement with relaxations in any random system with dispersive excitations (Chamberlin and Holtzberg, 1991, and reference therein).

Chapter III

Experimental Apparatus and Sample Preparation

3.1 AC SQUID Susceptometer/Magnetometer

Magnetic phase transitions in disordered magnets often occur at temperatures below 300K, which requires the use of cryogenic techniques to maintain the samples at low temperatures. Furthermore, since re-entrant ferromagnets or spin glasses often produce very weak magnetic signals, a state-of-the art, high resolution SQUID (Superconducting QUantum Interference Devices) probe, which provides an extremely sensitive means of detecting changing in magnetic flux, was used in our investigations. A major portion of my thesis research was devoted to designing and constructing an AC susceptometer/magnetometer consisting of a conventional ^{4}He cryostat which operates at temperatures between 1.5K and 300K, a multi-function SQUID probe and controled electronics, a low level ac impedance bridge with a discrete selection of measurement frequencies at ν = 16, 32, 80 or 160 Hz. A detailed description of this system will be given in the following sections.

3.1.1 The ^{4}He Cryostat

The ^{4}He cryostat basically consists of a vacuum system, and a cryogenic core immersed in a liquid helium bath. The physical configuration of the cryostat is shown in Figure 3-1, and the flow diagram of pumping system is summarized schematically in Figure 3-2. The cryogenic insert contains mainly the sample chamber and a rf-SQUID (Figure 3-1), both of which will be described next.

To initially cool the cryostat from room temperature to 77K, the helium dewar is pumped, with a mechanical pump MP2 (Alcatel Model 2033), flushed with N_2 gas a few times to reduce the partial pressure of air, and then filled with N_2 gas to slightly over one atmosphere. The vacuum space of the helium dewar is flushed

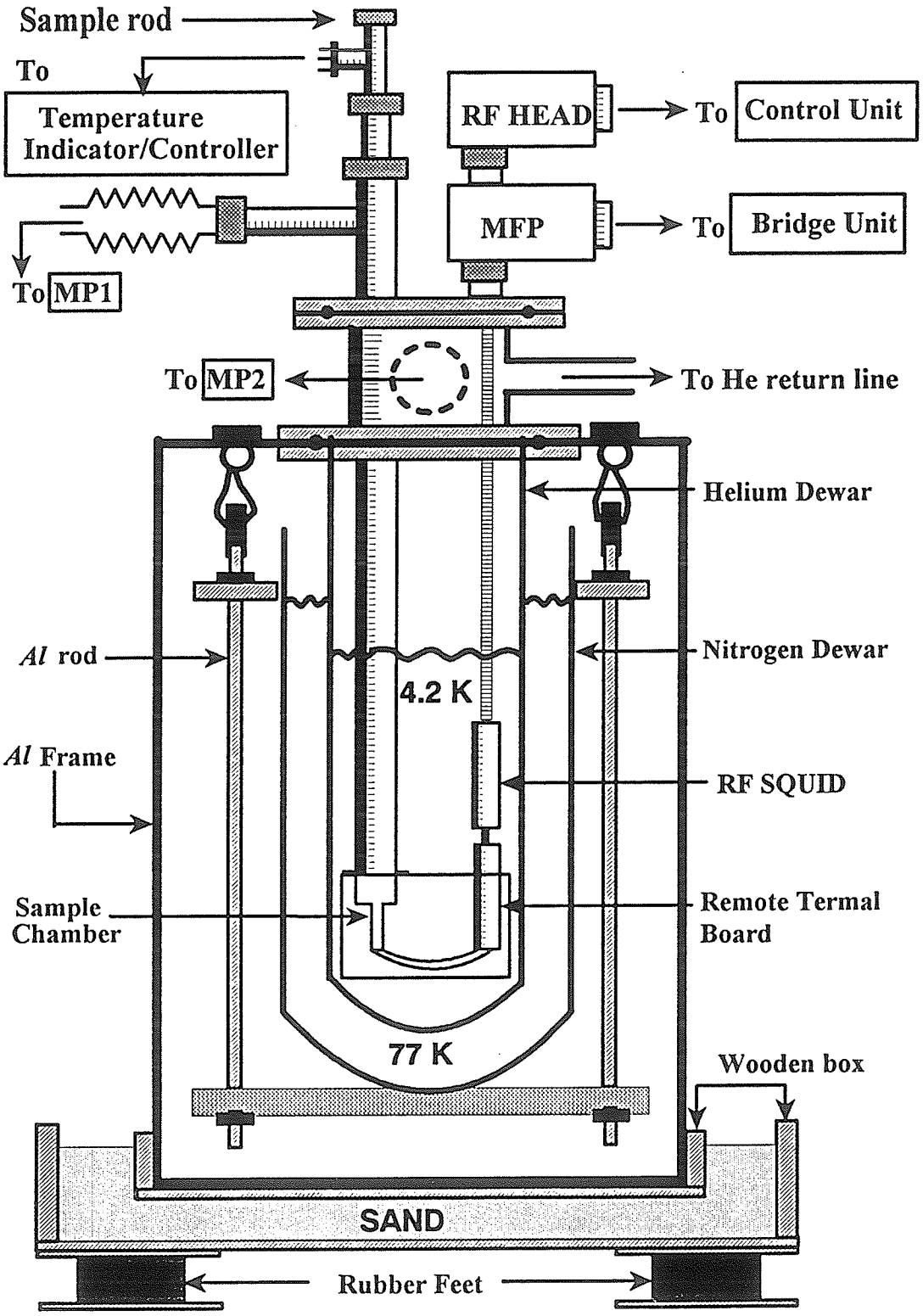

Figure 3-1: ^{4}He Cryostat.

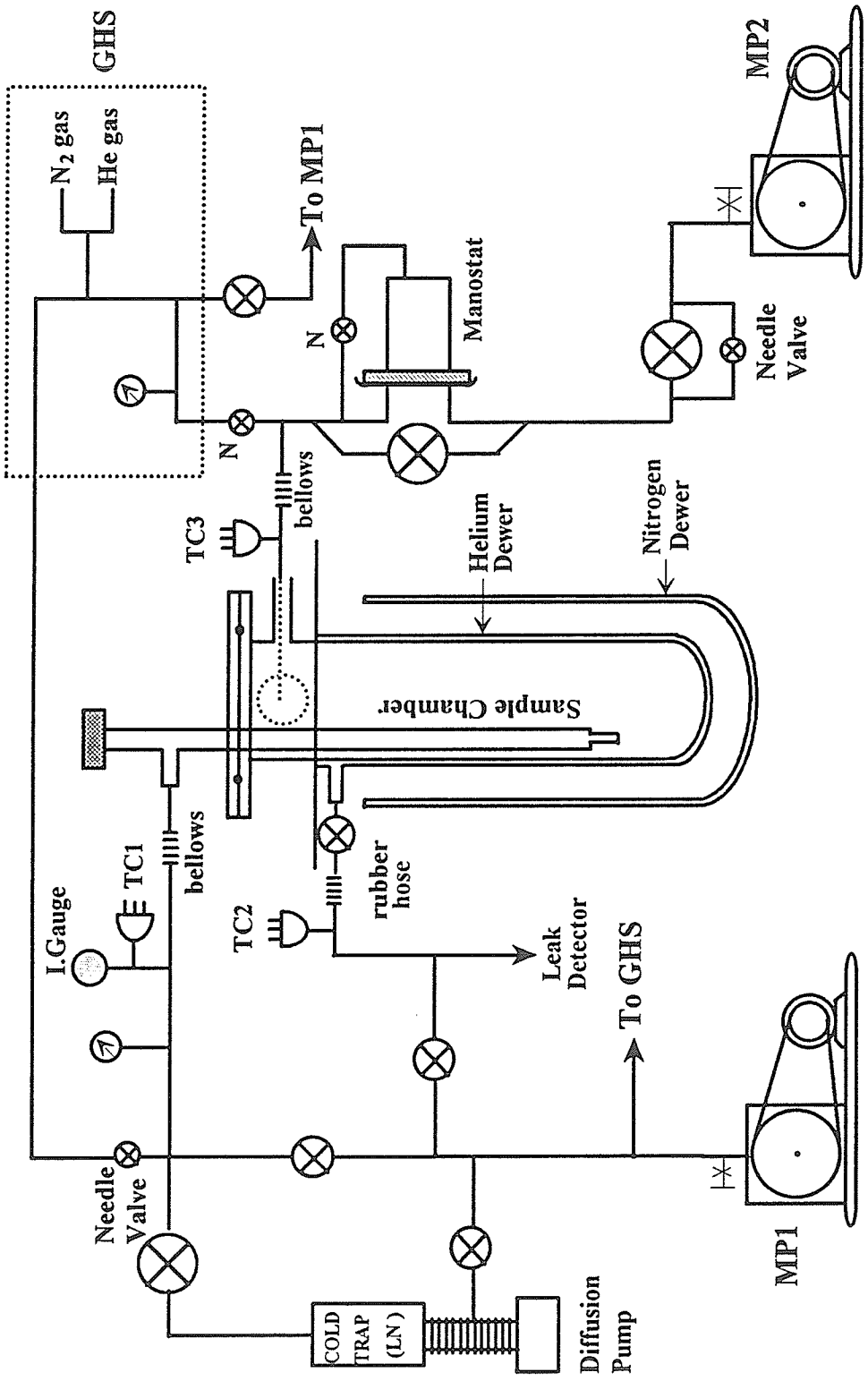

Figure 3-2: Flow diagram of pumping lines.

(with air) and pumped with the mechanical pump MP1 (Sargent Welch model 1402), flushed with air several times, and then sealed under a partial vacuum ($7 \sim 8\mu$). After the sample rod is inserted into the sample chamber (SC), the mechanical pump MP1 together with an oil vapour diffusion pump, are used to reduce the partial pressure of air in the sample chamber by flushing with N_2 gas a few times. The pressure of the sample chamber was measured with a thermocouple gauge TC1 and an ionization gauge I (Model 270 Gauge Controller, Granille-Phillips).When the pressure of the SC is about 1×10^{-4} Torr, liquid nitrogen is transferred into the nitrogen dewar and the sample begins to cool. The SC is pumped continuously until the temperature of the sample reaches 250K, where the outgassing of the sample (due mostly to the G.E. varnish and Ag paint used to glue sample to the sample rod) becomes insignificant; then $\sim 200\mu$ N_2 of exchange gas is leaked into the SC to speed up the cooling process. It is important to cool the system slowly towards 77K, since most of the significant contraction of materials occurs between 300K and 77K. The total cooling time for our cryostat from 300K to 100K is about 4 hours. As the system cools, the pressure inside the helium dewar drops below one atmosphere; and more N_2 exchange gas must be added to the dewar to maintain a pressure of one atmosphere. When the temperature of the sample reaches around 100K, the N_2 exchange gas in both the SC and the helium dewar are replaced by ^{4}He exchange gas via the mechanical pumps MP1 and MP2 respectively; and the gas handling system (GHS) (labeled on Figure 3-2); liquid helium can then be transferred into the helium dewar in order to cool the sample to 4.2K

Sample temperatures between 1.5K and 4.2K can be achieved and controlled by pumping on the ^{4}He bath through a manostat using the pump MP2, since the boiling point of the helium bath decreases with a reduction in its vapour pressure. Figure 3-3 shows the detailed structure of the manostat. When both the main valve and the needle value are open, the helium bath is pumped directly by the

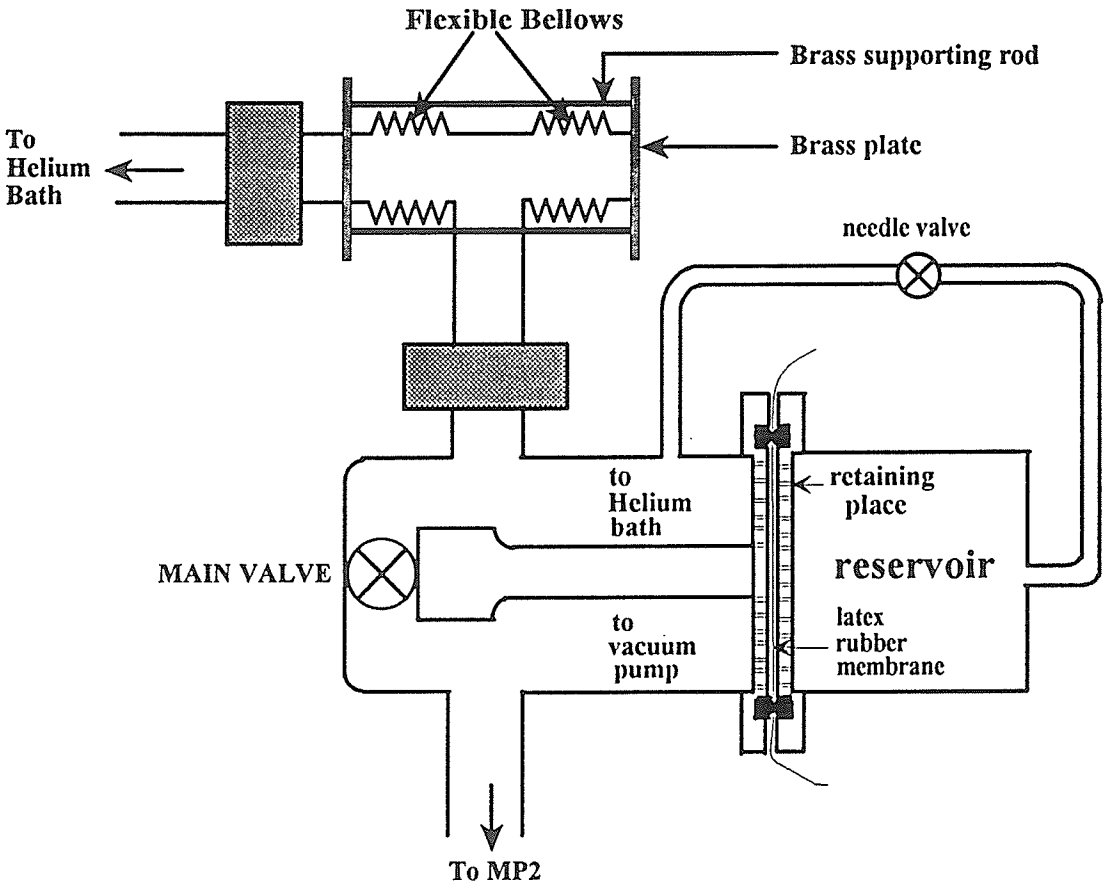

Figure 3-3: Manostat.

pump MP2. When the desired temperature is reached, both valves are closed, trapping a constant reference pressure P_{ref} in the reservoir of the manostat. If the pressure of the helium bath P_{bath} rises above the reference pressure, the latex rubber membrane is pushed open (against the reservoir) and the over pressure in the helium bath is reduced by the pump MP2. If $P_{bath} < P_{ref}$, the helium bath is sealed off from the pump by the latex rubber membrane. Thus constant temperatures below 4.2K are reached by maintaining a constant pressure $P_{bath}(=P_{ref})$ via the manostat.

Although the cryostat is capable of controlling temperatures below 4.2K, a temperature reservoir with $T < 4.2$ K does not provide the optimal environment for operating an rf-SQUID, due partly to the degradation of the critical current stability below 4.2 K, and partly to vibrations caused by the boiling of the helium bath below 4.2K. The main sources of noise at the SQUID detector are (a) electromagnetic or radio frequency (RF) interference from external sources which will be discussed in next section, and (b) mechanical vibrations. The mechanical vibrations from ground are reduced by resting the frame of the cryostat (see Figure 3-1) in a wooden box filled with sand, which in turn rests on four rubber feet (approximately 4″ high and 8″ in diameter). The cryostat is isolated from the vibrations caused by the mechanical pumps by means of flexible bellows or rubber hoses on the pumping lines, as shown in Figures 3-1, 3-2 and 3-3.

A more detailed illustration of the operational core of the cryostat insert is shown in Figure 3-4. A thin walled (1/16″) aluminum can, 4″ high and $4\frac{5}{8}$″ OD and covered with lead sheet to provide shielding from stray magnetic noise, encloses the SQUID remote terminal board, sample chamber and pick up coils. The can is bolted to a brass plate which is suspended by six 1/4″ OD thin wall stainless steel supporting tubes, approximately 32″ long, from the top plate of the cryostat. Two copper radiation shields are soldered onto the supporting rods to reduce liquid helium boiling caused by radiation.

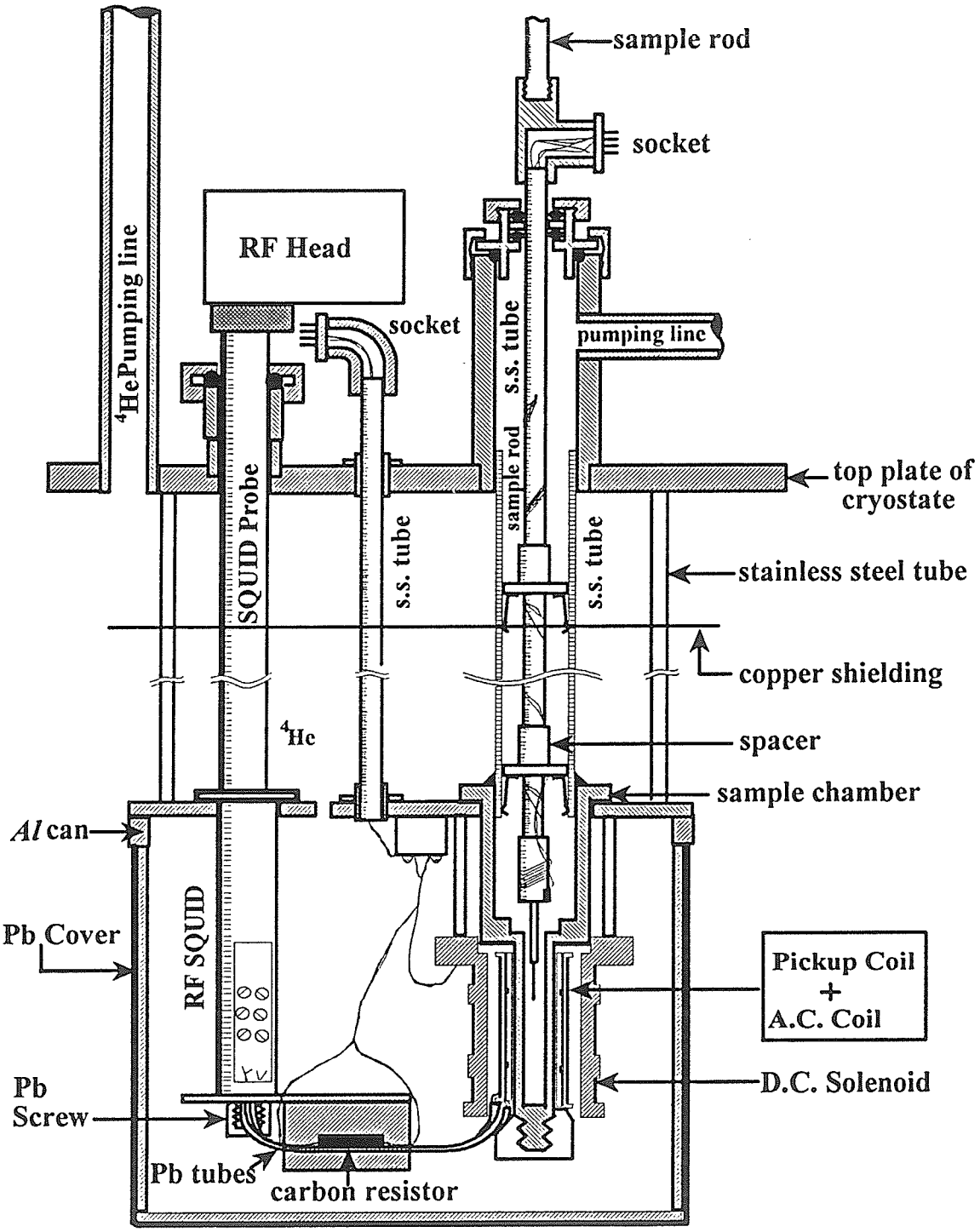

Figure 3-4: Insert of ^{4}He Cryostat.

The sample chamber (see Figure 3-5) was machined from a solid rod of Emerson and Cumming 1266 Stycast epoxy, and glued with 1266 Stycast epoxy to one end of a one meter length of 3/4″ OD stainless steel tube of thickness 0.020″. The other end of the stainless steel tube was hard soldered onto a brass tube (see Figure 3-4) on the cryostat top plate, which contains both the pumping part and an O-ring sealed connector for removing the sample rod. The seal for the sample rod was a double O-ring seal (see Figure 3-4), which allowed the sample rod to be moved up and down within the sample space, without breaking the vacuum.

The sample rod essentially consists of 1/4″ OD low thermal conductivity stainless steel tube approximately 1 meter long and of wall thickness 0.010″, with a silver sample block attached to one end. Four brass spacers were soldered onto the stainless steel tube to center the sample rod with respect to the sample space, and four springs mounted on each spacer provided thermal grounding with the walls of the sample tube to reduce heat leaks from the room temperature end of the sample rod into the 4.2K helium bath. As shown in detail in Figure 3-5, the sample block consists of a 99.99 % pure silver block of high thermal conductivity, which was soldered to one end of a thin walled 1/8″ OD stainless steel tube; the other end of the tube was connected to the sample rod with a brass screw arrangement, thus permitting the demounting of the sample block for repairs. A 25Ω heater was made by winding 36-gauge manganin wire in one noninductive layer around the large diameter portion (7mm OD) of the silver block. The heater was then soaked with G.E varnish to ensure good thermal contact with the silver block and was covered with masking tape. The temperature of the silver block was measured with a calibrated silicon diode (model DT-470-SD-13 Lake Shore Cryotronics) which is glued with G.E varnish to a flat surface (purposely machined to provide good thermal contact) near the bottom of the cylinder, and as close as possible to the location of a sample. The temperature was controlled with a Model 520 Cryogenic Temperature Indicator/Controller (Lake Shore Cryotronics). The

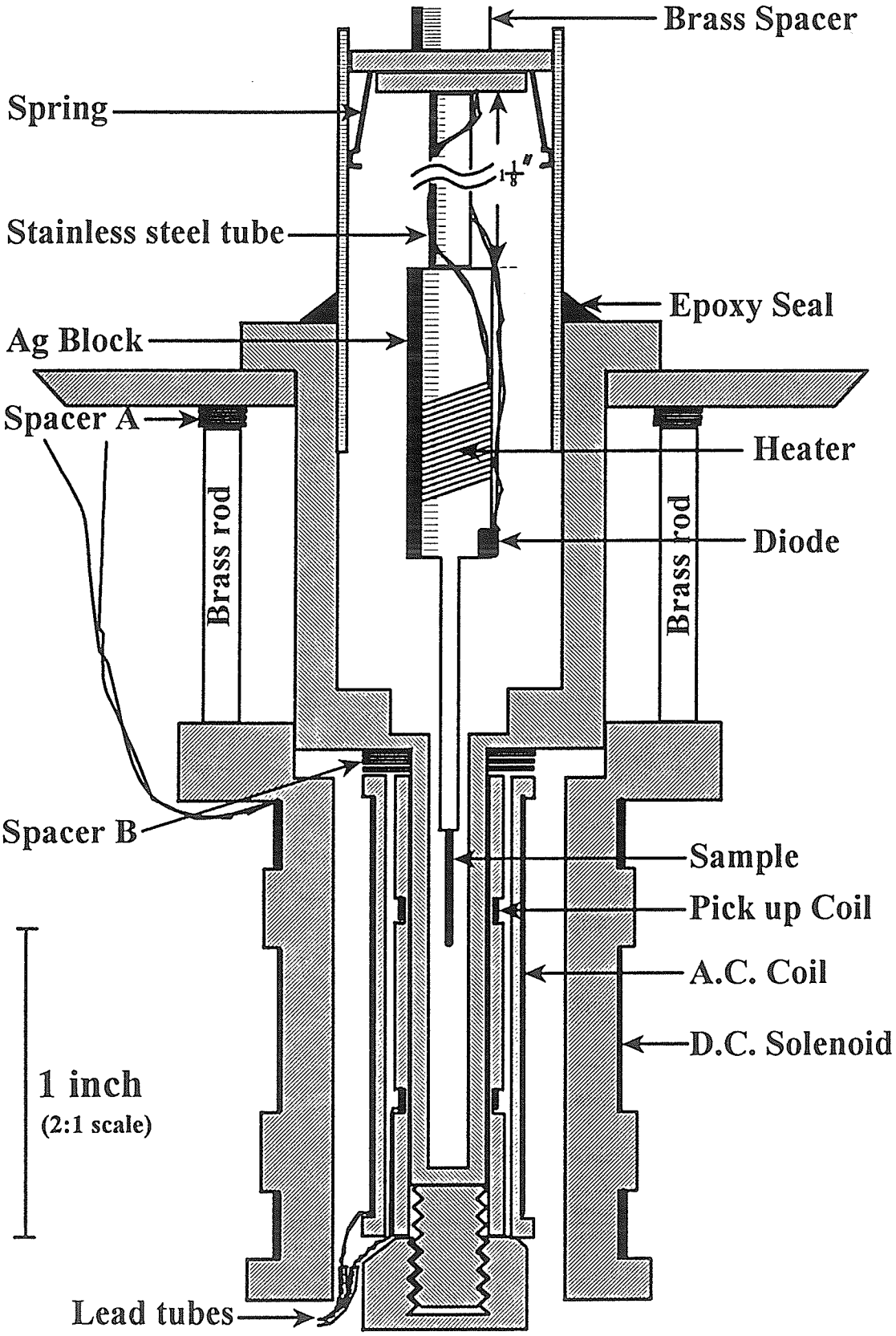

Figure 3-5: Configuration of the pick up coil, A.C Coil, D.C. solenoid and the Ag sample block.

magnetic sample is attached with G.E varnish and high-purity silver paint (from SPI Supplies, West Chester PA) to the end of the 7/8″ long pin at the bottom of the Ag block (0.060″ OD) (the mechanical strength is provided by the G.E varnish, while high-purity silver paint provides good thermal contact between the sample and the silver pin). The heater and diode are connected by long lengths of #32 gauge copper wires to a vacuum sealed electrical socket at the room temperature end of the sample rod (Figure 3-4). The copper wires are wrapped around the stainless steel portion of the sample rod and anchored with G.E. varnish to reduce any heat leaks or selfheating. It is worthwhile to point out that the heat leak along the sample rod has a very profound effect on the temperature control. In fact, tests indicated that without springs on the brass spacers, the heat leak by itself can warm the sample to well above 77K; thus the springs were an essential ingredient of the design. The low thermal conductivity stainless steel tube also plays an important role in decoupling the room temperature end of the sample rod from its low temperature end.

Temperatures between 15 and 300K can be controlled with extreme long term temperature stability (±5 mK) when the sample chamber (SC) is pumped down to $\sim 2 \times 10^{-5}$ Torr. Temperatures between 1.5 and 4.2K are controlled by the manostat, as discussed earlier with sufficient He exchange gas (200μ or more) inside the SC. It is quite tricky to control the sample temperature between 4.2 and 15K, since this requires just the right amount of He exchange gas to counteract the heat leak along the sample rod from the room temperature end. In this regime, the temperature of the sample is stabilized by a balance between the cooling power from the 4.2K helium bath outside the SC and the heating power from the heater (see Figure 3-4). The pressure inside the SC over this temperature range is typically less than 1 micron.

In the magnetic relaxation experiments, which in theory require an instantaneous "temperature quench", an appropriate amount (~ 50 μ) of He exchange gas

is inserted in the SC to initiate the cooling procedure and then gradually pumped out as the desired temperature is approached (in order to minimize overshooting). The final pressure in the SC is determined by the location of the desired measurement temperature T_m with respect to the various temperature ranges discussed above. If $15 \leq T_m \leq 25$K, it is better to keep a little extra He exchange gas in the SC, and to pump it out after the T_m is stabilized if the heater current is too high.

The 0.060″ diameter Ag pin, to which the sample is attached, is centered inside the sample chamber with only 0.045″ clearance with the inner wall of the sample chamber (see Figure 3-5); nevertheless, the sample can still be heated up to as high as 300K by the heater when the sample chamber is pumped down to 2×10^{-5} Torr (using a Sargent Welch model 1402 mechanical pump and an oil vapour diffusion pump). Obviously, the degree of coupling between the sample and the 4.2 K helium bath outside the sample can be controlled by varying the amount of exchange gas in the sample chamber.

3.1.2 The Magnetization/Susceptibility Measurement System

The magnetometer/susceptometer utilizes a Superconducting QUantum Interference Device (SQUID) as a sensor for measuring magnetic flux. The first section summarizes the basic operating principles of the device, followed by a detailed description of the measurement system used here.

(i) rf-SQUID

The SQUID design is based on the London concept (1950) of fluxoid quantization in a superconductor and on Josephson tunneling effects (1962, 1965) through a non-superconducting "weak link" between two superconductors. The device can be used to detect magnetic flux with an unprecedented sensitivity approaching 0.1 aW$_b$ (=10^{-19} W$_b$), and to measure voltage or current with a resolution limited only by thermal noise in the source resistance (Lounasmaa, 1974). The heart of a

SQUID probe consists of a toroid of superconducting metal (usually Nb) containing single or double Josephson junctions (oxide layers). There are two types of SQUID: a dc-biased SQUID with double Josephson junctions in a superconducting ring, and the more commonly used rf-biased SQUID with a single Josephson junction mounted on a superconducting ring. The name "Superconducting QUantum Interference Device" comes from the fact that the quantum interference phenomena can be observed on a macroscopic scale in the SQUID, by analogy to the optical interference pattern of single or double slits. In the following, we will briefly describe the operating principles of the rf-SQUID.

As shown in Figure 3-6, an rf-SQUID contains a thick superconducting ring with a single Josephson junction as a weak link of length $2a$. The resistanceless current in a superconductor below its critical temperature is formed by, according to the well known BCS theory (Bardeen, Cooper and Schrieffer, 1957a, 1957b), the motion of pairs of electrons, called Cooper pairs which become attracted to each other via the interaction with the atoms on the lattice sites, despite their strong Coulomb repulsion. These Cooper pairs behave as bosons of zero net spin, mass $m = 2m_e$ and charge $q = -2 \mid e \mid$, and are in a single macroscopic quantum state which can be described by a single valued wave function. The coherence of the Cooper pair wave function is preserved over laboratory-scale dimensions, so that their mean-free-path becomes infinite and the electrical resistance becomes zero. We now consider the situation where a non-zero external magnetic field $\vec{B}_{ext}$ is applied to this superconducting ring. For a pure superconducting ring without a weak link (a=0), the magnetic fluxoid ϕ', as defined by London (1950), can be expressed as (Lounasmaa, 1974)

$$\phi' = \phi + \left(\frac{m_e}{2\rho_s e^2}\right) \oint \vec{j}_s \cdot \vec{dl} = n\phi_o, \qquad n = 0, \pm 1, \pm 2, \cdots, \tag{3.1}$$

where ϕ is the magnetic flux threading through the hole of the superconducting ring, ρ_s is the density of Cooper electron pairs, and $\phi_o = h/(2 \mid e \mid) = 2.068 \times$

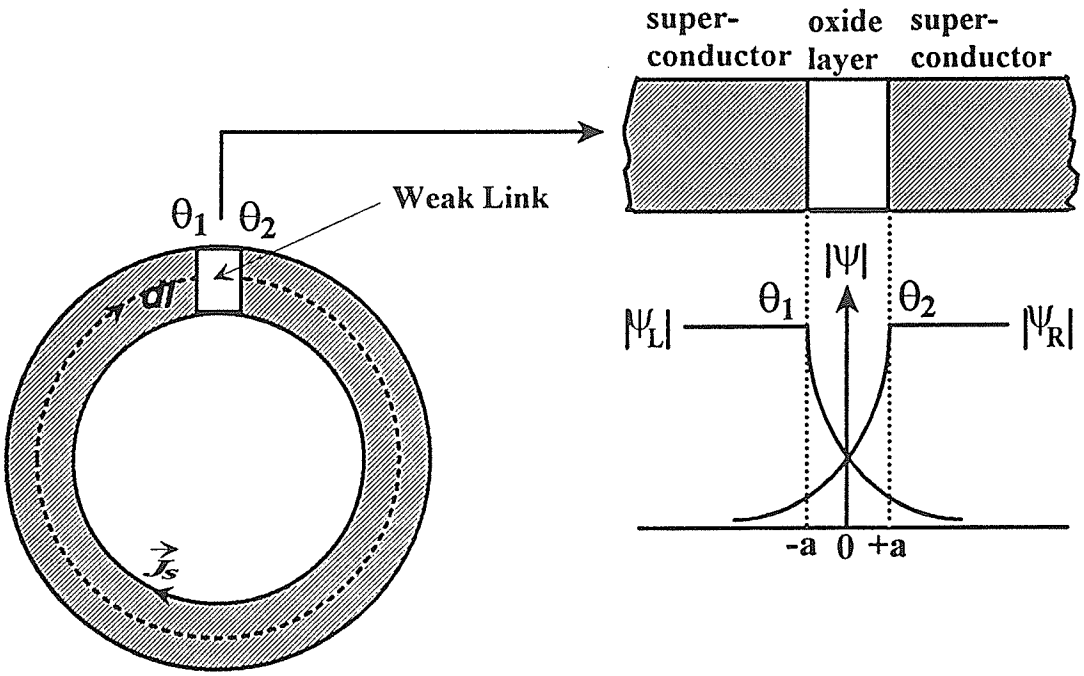

Figure 3-6: SQUID toroid: a superconducting ring with weak link.

10^{-15}Wb $= 2.068 \times 10^{-7}$ G cm^2 is the flux quantum or fluxon. $\vec{j_s}$ is the supercurrent density circulating only within a thin inner surface (see Figure 3-6) layer of depth $\sim \lambda_L$ (λ_L is called the London penetration depth, with a typical value of 0.1 μm). The magnetic field inside the bulk of the superconducting ring is zero (Meissner effect), which is achieved by supercurrents circulating along the inner and outer surfaces of the ring. Therefore, the path of integration in $\oint \vec{j_s} \cdot \vec{dl}$ can always be chosen in such a way that $\oint \vec{j_s} \cdot \vec{dl} = 0$ and Eq.(3.1) states that the flux through the hole of a superconducting ring is quantized in units of ϕ_o. For a hole of radius $r \cong 1$ mm, one flux quantum ϕ_o is equivalent to a change of magnetic field inside the hole of ~ 10 μG.

In a superconducting ring with a weak link (Figure 3-6), the path integral $\oint \vec{j_s} \cdot \vec{dl}$ is no longer zero since there will be a finite current $\vec{J_s} = \sigma \vec{j_s}$ crossing the weak link as the Cooper pairs tunnel through the weak link barrier (the Josephson tunnelling effects), where σ is the cross-sectional area of the weak link. The circulating current J_s is given by (Lounasmaa, 1974)

$$J_s = -J_c(0) \sin\left(\frac{2\pi\phi}{\phi_o}\right) \tag{3.2}$$

where $J_c(0) = (2 \mid e \mid \rho_s \hbar \sigma / m_e \lambda) \exp(-2a/\lambda)$ is the critical current which depends only on the properties of the weak link, such as a, σ, and the characteristic constant of the oxide barrier λ. By taking account of the magnetic flux ϕ_J passing through the area of the weak link, Eq(3.2) becomes

$$J_s = -J_c(0) \frac{|\sin(\pi\phi_J/\phi_o)|}{\pi\phi_J/\phi_o} \sin\left(\frac{2\pi\phi}{\phi_o}\right) \tag{3.3}$$

which has the same form as the optical Fraunhofer diffraction from a single slit. Since $\phi_J \ll \phi$, the diffraction pattern from a SQUID (Eq.(3.3)) is "modulated" by the diffraction occuring at the weak link. In the case where there exists an external applied magnetic field $\vec{B}_{ext}$, it is convenient to express the total flux through the hole in the superconducting ring as

$$\phi = \phi_{ext} + LJ_s, \tag{3.4}$$

where ϕ_{ext} denotes the magnetic flux produced by $\vec{B}_{ext}$ and L is the self-inductance of the ring. By substituting Eq(3.2) into Eq(3.4), we have

$$\phi + LJ_c \sin\left(\frac{2\pi\phi}{\phi_o}\right) = \phi_{ext}. \tag{3.5}$$

Eq(3.5) indicates that the flux ϕ oscillates periodically about the straight line $\phi = \phi_{ext}$ with a period of one flux quantum ϕ_o, as Figure 3-7 shows. $\phi = \phi_{ext}$ when $\phi = \frac{n}{2}\phi_o, n = 0, 1, 2, \cdots$. The effects of the weak link can be clearly seen in the following expression

$$\frac{d\phi}{d\phi_{ext}} = \frac{1}{1 + (2\pi LJ_c/\phi_o)\cos(2\pi\phi/\phi_o)}. \tag{3.6}$$

In the extreme weakly superconducting limit, $2\pi LJ_c \ll \phi_o, \phi \approx \phi_{ext}$, and the external flux penetrates the hole almost freely. In the strong superconducting limit $2\pi LJ_c \gg \phi_o, \frac{d\phi}{d\phi_{ext}} \approx 0$, and the superconducting ring acts as a bulk superconductor with no flux through the hole. For the operation of a SQUID, the weak link is adjusted so that $2\pi LJ_c \geq \phi_o$. Figure 3-7 shows the change in ϕ as a function of ϕ_{ext} for $2\pi LJ_c = \phi_o, 3\phi_o, 5\phi_o$. The flux through the hole increases initially with increasing ϕ_{ext} until point P, where $d\phi/d\phi_{ext} = \infty$ is reached. An unstable situation then arises; the fluxoid ϕ' in Eq.(3.1) increases by one ϕ_o and the flux ϕ through the hole jumps discontinuously from point P to point Q. With a further increase in ϕ_{ext}, ϕ changes from Q to R and a new "transition" occurs from R to S while ϕ' changes by another fluxon ϕ_o. When ϕ_{ext} is decreased, ϕ follows a different path from S to S', and then jumps to R'; therefore there is hysteresis.

Operationally, it is possible to use the SQUID in a digital fashion, simply counting the number of flux quanta through the device to determine the unknown flux ϕ_{ext}. By introducing a weak link into a superconducting ring (Figure 3-6), we are able to measure a fraction of one fluxon ϕ_o according to Eq.(3.5). For maximum sensitivity a rf-SQUID is, however, inductively coupled to a LC resonant circuit which is driven at RF frequency (normally 20 MHz). The A.C voltage

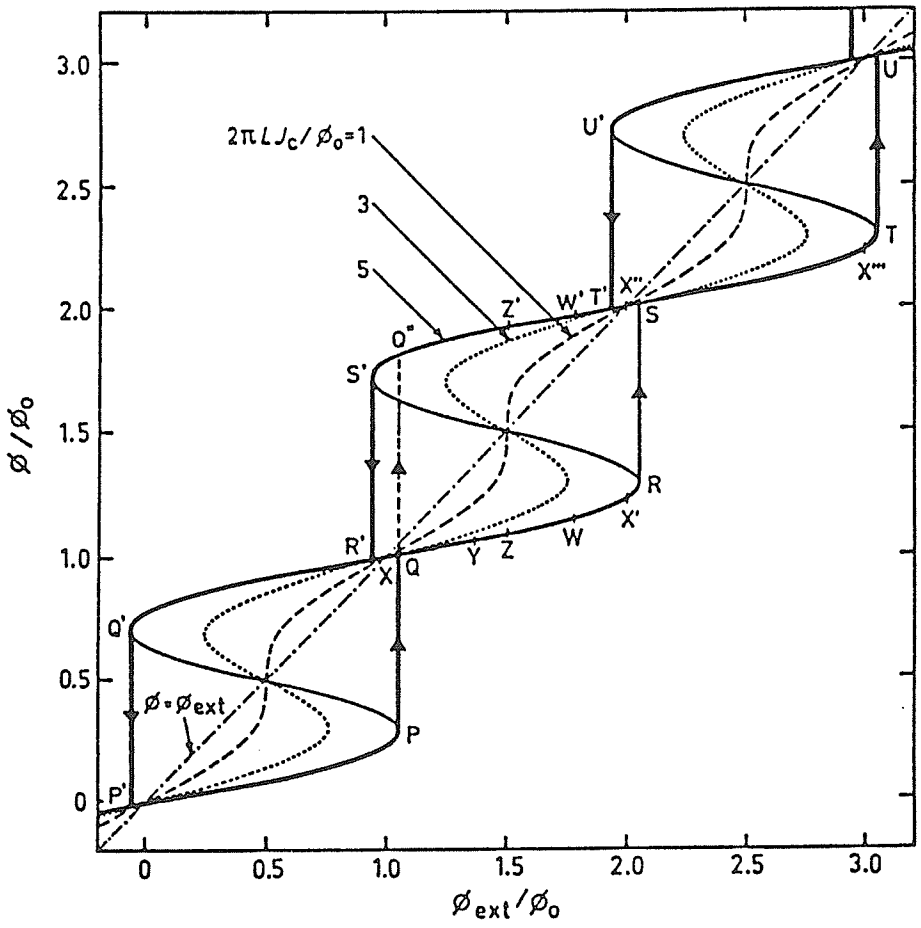

Figure 3-7: ϕ/ϕ_o as a function of ϕ_{ext}/ϕ_o in three cases: $2\pi LJ_c = \phi_o$, $3\phi_o$, and $5\phi_o$. Vertical lines with arrows correspond to discontinuous changes of one flux quantum in the fluxoid ϕ' and to somewhat smaller changes in the flux ϕ. From Lounasmaa (1974).

across this circuit, which is induced by the change of magnetic flux through the superconducting toroid, is then amplified and detected. A detailed discussion of the operating principles of the rf-SQUID can be found in the book by Lounasmaa (1974, Chapter 7) and the thesis by Kornik (1990).

(ii) Details of the Measurement System

A schematic diagram of the AC SQUID Susceptometer/Magnetometer system is shown in Figure 3-8 and the pick up coil geometry is shown in detail in Figure 3-5 on a 2:1 scale. The pick up coils (primary and secondary), and the D.C. field solenoid are all wound on 1266 Stycast clear epoxy formers and designed to fit concentrically about the bottom of the sample chamber. The use of epoxy avoids any skin-depth problems associated with metals particularly in an A.C. driving field.

The pick-up coils (secondary) were wound from 0.006″ diameter NbTi superconducting wire. Each coil of the astatic pair (Figure 3-5) consists of 8 turns wound on a diameter of 0.274″ and is separated by 0.625″ center-to-center. The coaxial A.C. field coil (primary) is wound in a single layer on a diameter of 0.41″, with 213 ± 5 turns using 0.006″ NbTi wire.

The D.C. low field coil is wound from copper wire on a specially designed epoxy former which can provide a uniform magnetic field over the volume of the sample and the astatic pair of pick-up coils. The basic idea was to produce a wider range of a uniform magnetic field than normally afforded by a solenoid, by adding two compensating coils at each end of the main solenoid so that the usual rapid drop off points in the field profile are delayed relative to the centre of the solenoid (see Figure 3-10(a)). The magnetic field along the central axis produced by a solenoid shown in Figure 3-9

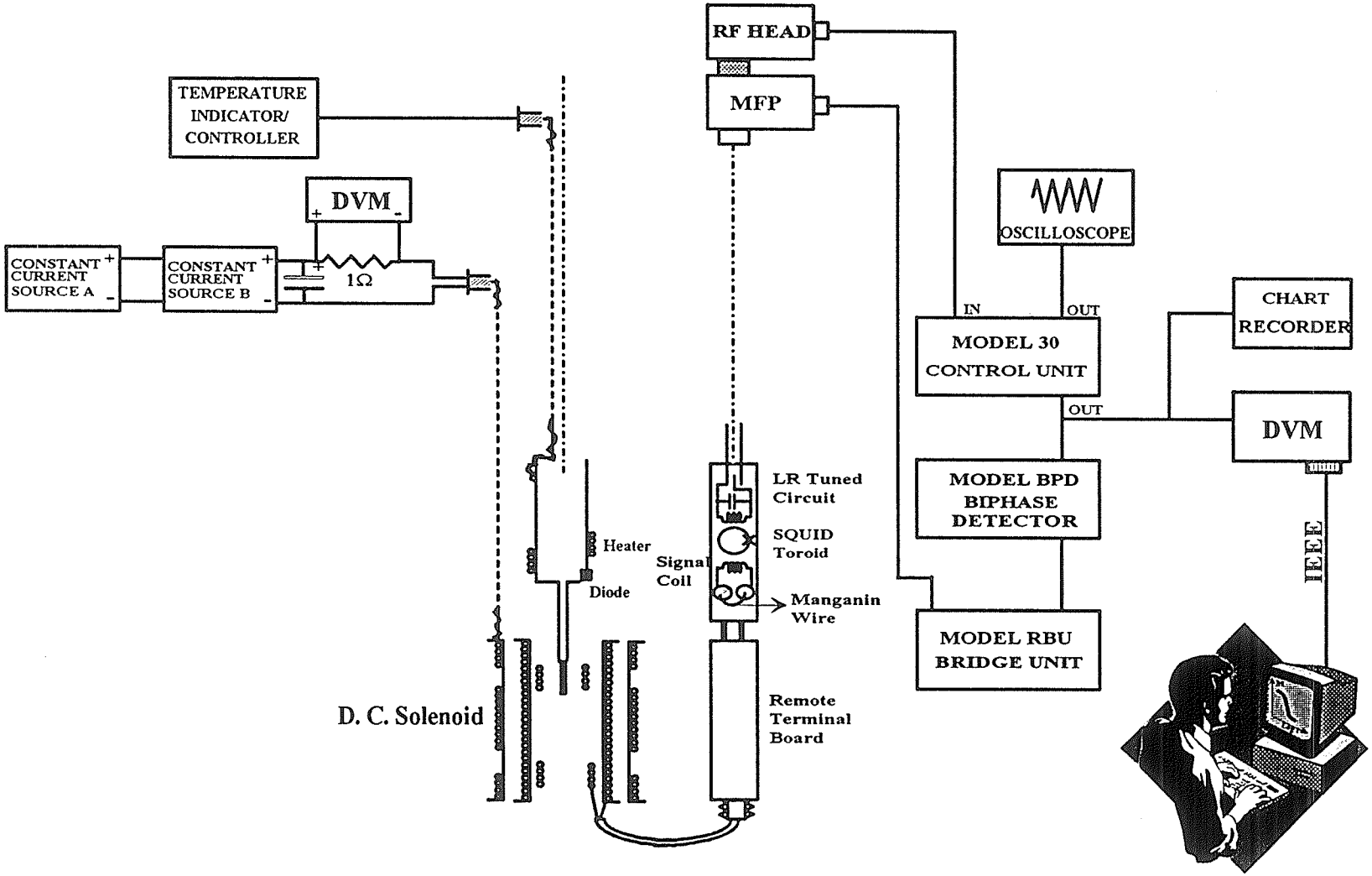

Figure 3-8: Electronic block diagram of the AC SQUID Susceptometer/Magnetometer.

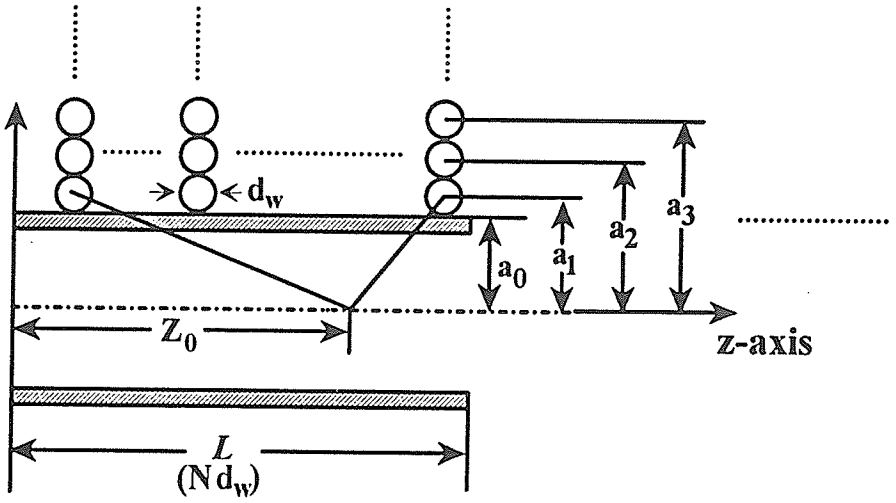

Figure 3-9: A solenoid with multilayer windings.

can be calculated using

$$B(Z_o) = C \sum_{i=1}^{m} \left[\cos\left(\tan^{-1}\left(\frac{a_i}{Z_o} \right) \right) + \cos\left(\tan^{-1}\left(\frac{a_i}{L - Z_o} \right) \right) \right] \qquad (3.7)$$

where $C = \frac{\mu_o NI}{2L} = \frac{\mu_o I}{2d_w}$, N is the number of turns per layer, d_w is the diameter of the wire, m is the number of layers, and we have made the approximation that the current I is concentrated along the axis of the wire. Using Eq.(3.7), we were able to generate various total field profiles of the solenoid as a function of the parameters N, d_w, m, the diameter of the solenoid, and the spacer thickness separating the compensating coils and the main coil (see Figure 3-5). The computer program for the calculation is given in the Appendix C. The final design of the solenoid consisted of a single layer central portion of 68 turns and two compensating solenoids consisting of 3 layers of 24 turns per layer, all of which are wound from 32-gauge (0.008″ OD) copper wire on a common diameter (1.1024″) epoxy former. The two epoxy spacers are 0.246″ wide and separated by 0.849″ center-to-center. The calculated and measured magnetic field profiles along the central axis of the solenoid are displayed in Figure 3-10 (a) and (b) respectively. The location of the pick-up coils, as well as the approximate size of the sample, are both marked in Figure

3-10. The magnetic fields at the two members of the astatic pair are almost the same, so that changes in magnetic flux due to changes in the D.C. static field are effectively cancelled by the two coils. The field produced by the solenoid is 46 Oe/A.

The windings of the pick-up coils and the DC solenoid were all saturated with the 1266 Stycast epoxy to enhance the mechanical rigidity and prevent turn-jumping. The correct relative positions of the sample, pick-up coils and D.C. solenoid are set by adjusting the thickness of the spacers A and B (see Figure 3-5). The long superconducting leads from both the astatic pair secondary and the A.C. primary coils were twisted tightly, enclosed inside Pb tubing, and connected to the appropriate terminals on the SQUID remote terminal board. The superconducting Pb tubing provides good RF and magnetic shielding when the magnetic flux is transferred from the pick-up coils into the SQUID. A small Teflon box containing a carbon resistor was designed (although never used) to heat the superconducting leads momentarily into a normal state to eliminate any large persistent currents in the superconducting coils, as well as to reduce any vibrations from the lead tubing.

When the lead can in Figure 3-4 is cooled to 4.2K in the local Earth's field, it reproducibly traps a field of ~ 0.3 Oe (down) which can be cancelled at the sample location by passing the appropriate current I_0 through the D.C. copper solenoid. In order to determine I_0, we heated the magnetic sample into its paramagnetic regime and then measured the change in magnetic moment ΔM corresponding to change in temperature $\Delta T \sim 5 - 10K$, and varying the current I through the solenoid until $\Delta M \cong 0$. The current I_0, which backs off the trapped field was $I_0 =$ 0.006505 A.

The D.C. solenoid is connected to two constant current sources (Figure 3-8) which are connected in parallel, and the current through the solenoid is read directly across a 1 Ω standard temperature insensitive (oil-immersed) resistor

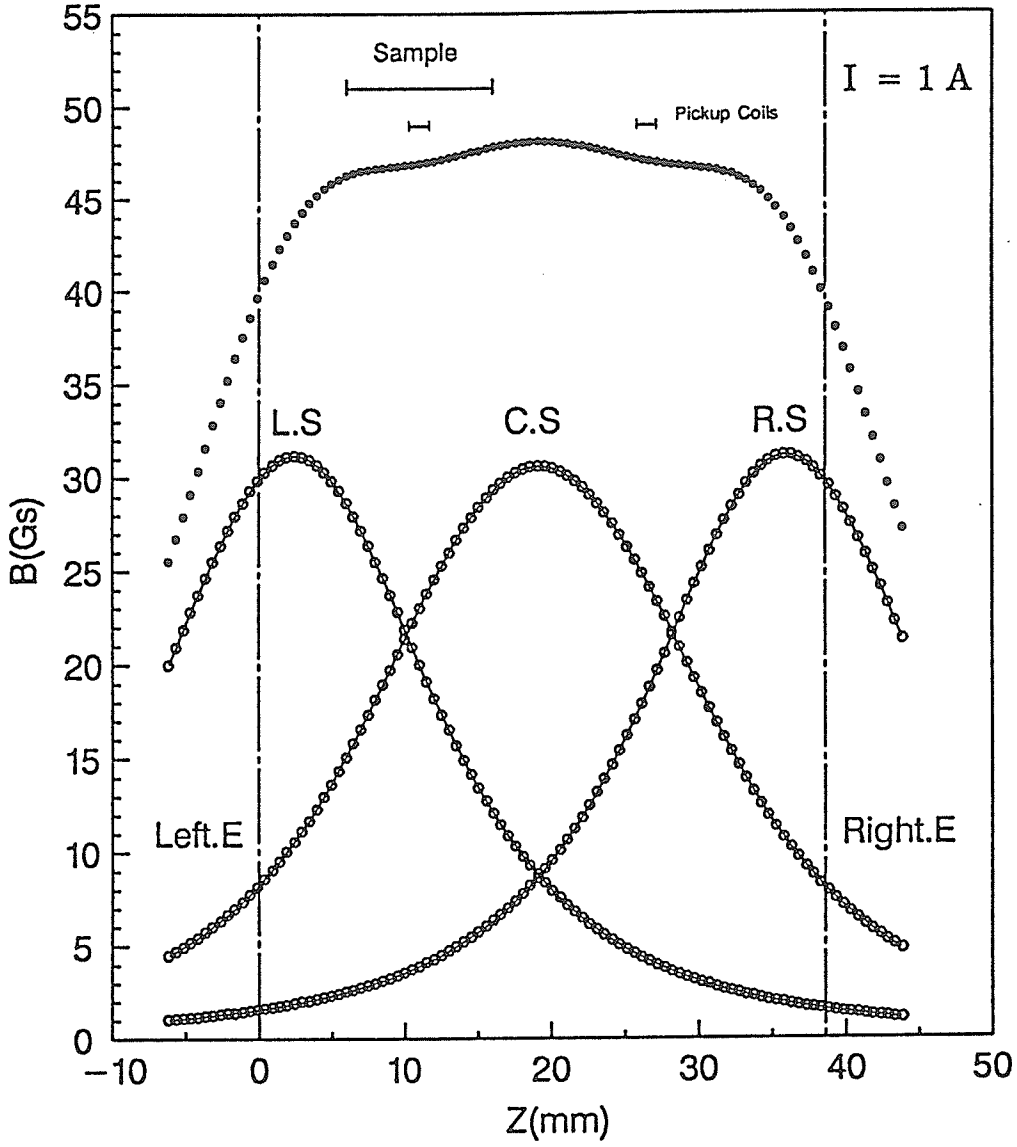

Figure 3-10(a): The calculated (using Eq.(3.7)) magnetic field profile along the central axis of the D.C solenoid, for a current $I = 1$ A. The field profiles produced by the left solenoid (L.S.), central solenoid (C.S) and right solenoid (R.S) are also shown in the figure. Two vertical lines mark the ends of the winding. Both location and size of the pickup coils, as well as the sample are also indicated.

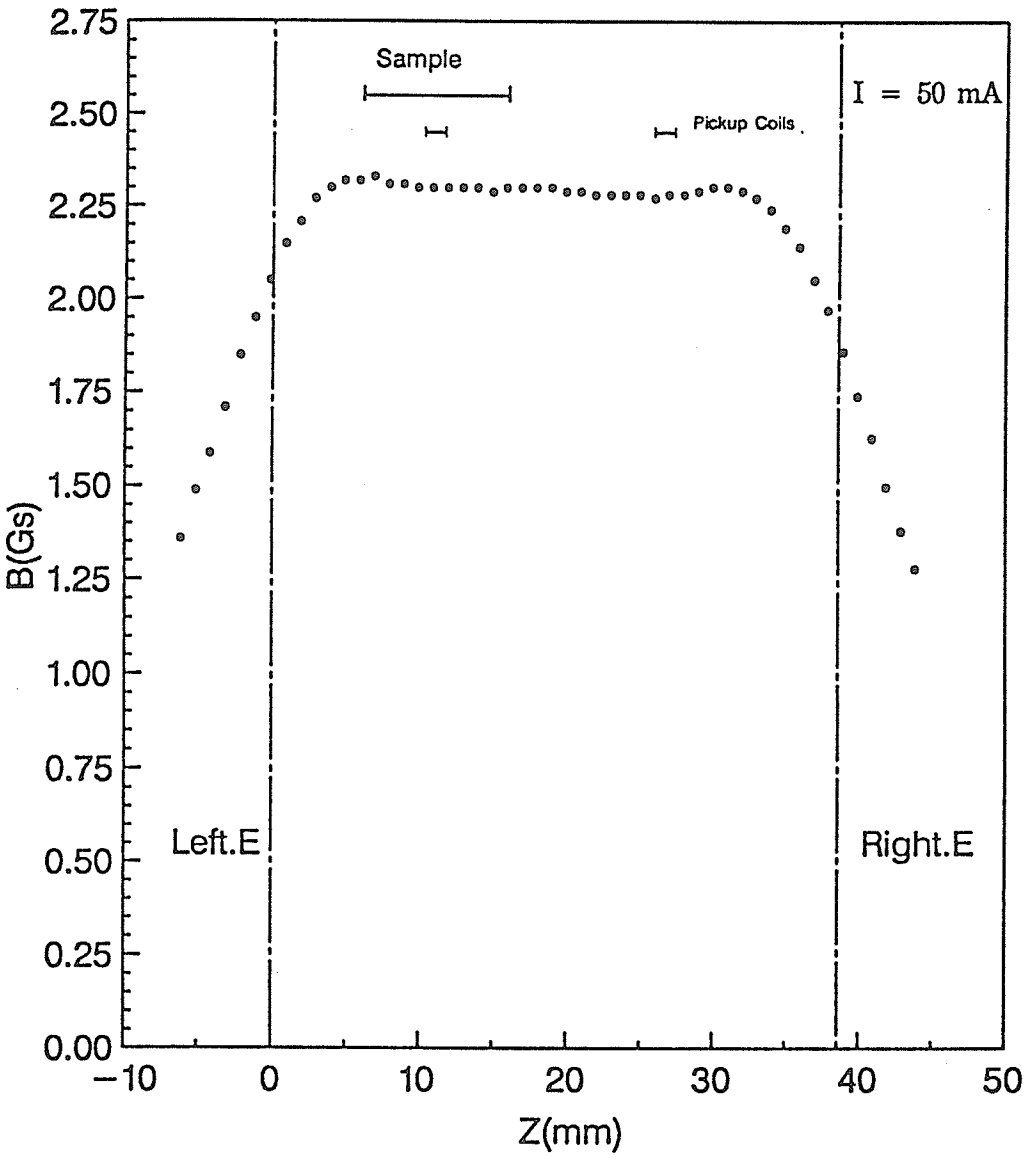

Figure 3-10(b): The measured magnetic field profile along the central axis of the D.C solenoid, for a current I = 50 mA. Two vertical lines mark the ends of the winding. Both location and size of the pickup coils, as well as the sample are also indicated.

(Gambrell-Croydon 12223/469) with a high precision RACAL-DANA model 5003 digital voltmeter (RACAL-DANA Instruments Inc.). The home-made constant current source A (see Yeung, 1988) provides a continuously variable current ($0 \leq I \leq 1$ A) and is used for measurements requiring a continuous field sweep (such as magnetic isotherms), while the constant current source B (Model TC-602-CR Princeton Applied Research) is a discretely variable sources of both current and voltage, with a maximum capacity of 2 A and extreme stability over extended time intervals; it is thus essential when measuring isokaps (constant field curves) and magnetic relaxations.

We have mentioned previously that one of the major sources of interference in the SQUID system is electromagnetic interference, primarily in the RF band ($\sim$ 20 MHz). Since the D.C. solenoid is coupled rather tightly to the pick-up coils (Figure 3-5), any noise picked up by the D.C. solenoid will be transmitted directly into the SQUID through the pick-up coils and degrade its operation. By putting a large capacitor (50 μF, sometimes up to 3 such capacitors are necessary) in parallel with the D.C. solenoid, we were able to filter out much of the most significant RF noise, but were still unable to completely remove low frequency (60Hz) interference. In order to achieve the optimal working environment for the SQUID, all cables connected with the sample rod, the D.C. solenoid and the SQUID probe were all properly grounded and RF shielded, all leads were tightly twisted and the superconducting leads from the pick-up coils were enclosed in a superconducting Pb tube sealed with a Pb screw at the remote terminal board (see Figure 3-4). The SQUID probe itself is also protected from RF interference with a superconducting NbTi shielding. Furthermore, a manganin resistive shunt is put across the signal coil input to the SQUID to help filter the RF interference.

The SQUID electronic components of the AC SQUID susceptometer/ magnetometer consist of a Multi-Functional Probe (MFP) with RF head, a model 30 SQUID Control Unit, a model BPD Bi-phase detector and a model RBU Preci-

sion Low-Level A.C. Impedance Bridge Unit, all manufactured by BTi, San Diego. In the magnetometer configuration, only the RF head and the Control Unit are used, and the AC primary coil is disconnected from the SQUID to minimize source of RF noise. The magnetic flux in the astatic pair of pick-up coils, which is caused by the presence of the sample in the top pick up coil, is coupled directly into the signal coil in the SQUID probe, and then detected by the SQUID. The voltage output of the Model 30 Control Unit varies linearly with the change in magnetic flux in the pick-up coils. The output voltage from the Control Unit, which is thus proportional to the magnetic moment M of the sample, can be measured with a RACAL-DANA model 5003 digital voltmeter (DVM). In magnetic relaxation experiments, the decay of the sample magnetization (in volts) was collected directly from the RACAL-DANA 5003 DVM by an IBM PC (Datatrain-286) via an IEEE interface bus. a computer program for the data-acquisition, as well as the graphic display of the magnetization M as a function of log t, was written in Quick Basic 4.5 for use with the IEEE interface bus, and is listed in the Appendix C.

In the susceptometer configuration, the Multi-Function Probe, the model BPD Bi-phase Detector and the model RBU Bridge Unit are used in conjunction with the RF Head and the Model 30 Control Unit. A simplified circuit diagram is shown in Figure 3-11. The SQUID is used as a null detector for the Low-Level A.C. Impedance Bridge Unit which takes advantage of the exceptional sensitivity of the SQUID to permit measurements of ac resistance(R), self-inductance(L), and mutual inductance (M) with a resolution of 0.001% at extremely low power dissipation levels. The balancing mutual inductance, of nominal value m_{nom} = 1 μH, is sealed within the Multi-Function Probe, and the configuration of the unknown impedance Z in the susceptometer is shown in the insert in Figure 3-11. It can be proved (Appendix A) that the mutual inductance between the astatic pair of pick-up coils (secondary) and the AC coil (primary) when the magnetic sample is inserted into one member of the astatic pair is proportional to the AC

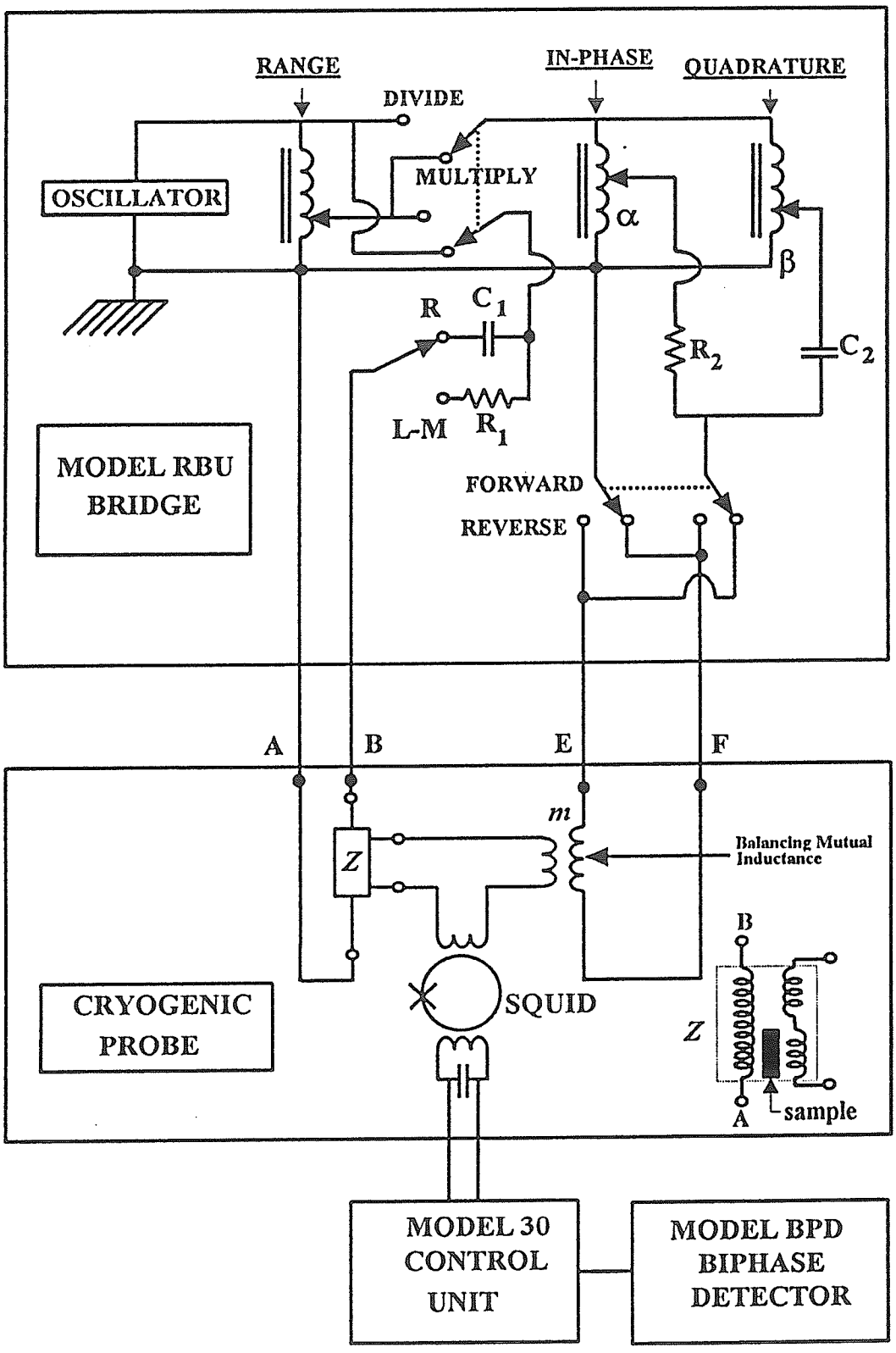

Figure 3-11: Simplified circuit diagram of RLM system.

susceptibility χ_{AC} of the sample, i.e.

$$\chi_{AC} \propto m \tag{3.8}$$

or

$$\chi'_{AC} + i\chi''_{AC} \propto m' + im''. \tag{3.9}$$

The real component χ'_{AC} is in phase with the AC magnetic field produced by the primary coil, and the imaginary component χ''_{AC} is $\pi/2$ out of phase (or in quadrature) with the AC driving field, and represents a frequency-dependent energy dissipation.

As shown in Figure 3-11, the model RBU Impedance Bridge allows both the real (m') and the imaginary (m'') parts of the mutual inductance to be measured. The AC primary coil is driven by a sine wave oscillator through a ratio transformer. The frequency of the AC field may be selected to be ν = 16, 32, 80 or 160 Hz, and the amplitude of the AC field generated by the superconducting primary coil was calculated to be $\sim$ 7 mOe. The range DIVIDE/MULTIPLY switch allows the high sensitivity range of the bridge to be greatly expanded; although the DIVIDE mode is always usable, maximum sensitivity may necessitate going to the MULTIPLY mode. Unlike the DC resistance bridge, the AC impedance bridge has to be balanced in both amplitude and phase. The unbalanced mutual inductance arising in the pick up coils is balanced by changing the balancing mutual inductor m via two adjustable ratio transformers $\underline{\alpha}$ and $\underline{\beta}$ which are *in phase* and *in quadrature.* Therefore,

$$\alpha \propto m' \propto \chi'_{AC} \tag{3.10}$$

and

$$\beta \propto m'' \propto \chi''_{AC}. \tag{3.11}$$

The FORWARD/REVERSE switch, which reverses the two leads connected to the balancing coil (thus changing the sign of α and β), is sometimes required in

order to achieve phase balancing, (a balance will only be possible in one position, which is determined empirically). The true balancing of the bridge is only achieved when *both* the IN-PHASE and the QUADRATURE null-meter on the Bi-Phase Detector are brought into a null condition by adjusting the real component α and the imaginary component β simultaneously and independently. The balancing of α should not affect the balancing of β, and vice versa.

3.1.3 Calibration of the AC SQUID Susceptometer/Magnetometer

We used a paramagnetic oxide Gd_2O_3 to calibrate the system. A cylindrical sample holder was machined out of aluminum, with dimensions 0.56 mm ID $\times$ 1 mm OD $\times$ 8 mm long, chosen to simulate the volume of a typical magnetic sample used in this study. This aluminum holder was filled with 4.8 mg of Gd_2O_3 powder (Aldrich Chemical Co., Wisconsin), and was sealed with an aluminum cap using Stycast 1266 epoxy. The magnetization was measured at several fixed temperatures T = 4.2, 20, 30, 40 K, a static field H_a= 10 Oe, by extracting the sample from the pick-up coils. The magnetic moment of Gd_2O_3 for a given field H and temperature T can also be calculated from to the following formula

$$M = \frac{N{\mu_{eff}}^2 H}{3k_B(T-\theta)} \tag{3.12}$$

where the Boltzmann constant $k_B = 1.38 \times 10^{-16}$ erg/K, the Curie-Weiss temperature θ = -13 K, the effective magnetic moment of Gd $\mu_{eff} = (7.70 \pm 0.04)\mu_B$ and the number of Gd atoms per gram $N = 3.32 \times 10^{21}$ atoms/gm. Comparison with the measured values (in Volts) gave the following calibration factor:

$$1 \ Volts \approx 1.5 \times 10^{-5} \ emu \tag{3.13}$$

Gd_2O_3 was also used to obtain a calibration factor for the ac susceptibility. In this case, 71.5 mg of Gd_2O_3 powder was sealed into a cylindrical sample holder with 0.080″ OD and 0.055″ ID, and 0.433″ in length, machined from 1266 Stycast epoxy.

The real part of the AC susceptibility χ' was measured (in arbitrary units) with the bridge as described in the previous section, and the calculated susceptibility was obtained from Eq.(3.12) as M/H

$$\chi = \frac{N{\mu_{eff}}^2}{3k_B(T-\theta)} \tag{3.14}$$

with the parameters listed above. The calibration factor for the real part of susceptibility $\alpha(\propto \chi')$ was

$$1 \ a.u \ in \ \alpha = 0.035 \ emu/Oe \tag{3.15}$$

3.2 Sample Preparation

Three bond disordered magnetic systems, NiMn, AuFe, CrFe and one canonical ferromagnet PdFe, were prepared for the current investigation.

3.2.1 NiMn System

A total of 5 NiMn alloys was prepared, Mn concentrations ranging from 22.0 to 26.9 at%. Table 3.1 summarizes a number of the important parameters related to sample preparation, shape and heat treatment. All the samples were fabricated by arc melting appropriate amounts of the X and Y pure elements on the water cooled copper hearth of a Ti-gettered argon arc furnace using a tungsten electrode. The 99.997% pure Ni foil and 99.99% pure Mn flake (both obtained from Aldrich Chemical Co., Milwaukee) were melted into solid ingots, which were repeatedly inverted and remelted ($\sim$ 7 times) in order to achieve homogeneity. The ingots were then placed in a Vycor quartz tube, evacuated to 10^{-5} Torr, and given an homogenizing anneal at a temperature $T_h = 900°$C for $t_h = 3$ days, and then cooled slowly to room temperature. The alloys were etched in a solution of dilute nitric acid (HNO_3:H_2O = 1:5 in Volume) in order to eliminate surface contamination. As

shown in Table 3.1, the true composition of the alloys C_{true}, which were estimated from the melting losses, and later confirmed by an EDAX (Energy Dispersion Analysis of X-ray) concentration analysis, are less than the C_{nom}; the melting losses were attributed predominantly to Mn vaporization due to its low boiling temperature (1962°C, as compared to 2732°C for Ni). The large Mn melting losses introduced considerable difficulty into the preparation procedure for the NiMn alloys, particularly since the magnetic character may be altered dramatically with only a little change in Mn composition. Large ingots are always helpful, while extra pure Mn was purposely added in preparing the small ingots.

Table 3.1: NiMn alloys

C_{nom} ($at\%$)	X + Y	C_{true} ($at\%$)	samples $a \times b \times c$ (mm^3)	m (mg)	D $\left(\frac{g.Oe}{emu}\right)$	T_{dis} (^0C)	t_{dis} (d)	t_q (s)
27.0	99.997% Ni foil + 99.99%Mn flake	26.9	9.90×0.43×0.42	20.7	—	900	3	1
23.0	99.997% Ni foil + 99.99% Mn flake	22.5	9.45×0.50×0.26(A)	8.3	0.467	900	3	1
			15.9×1.00×0.22(B)	25.3	0.278	900	3	1
25.0	99.997% Ni foil + Ni-26.9 at% Mn master alloy	24.0	6.00×1.00×1.00(A)	40.5	4.76	900	3	20
			10.2×1.10×0.95(B)	82.7	1.3	900	3	1
			16.0×2.60×0.30(C)	96.8	0.4	900	3	1
			9.70×0.28×0.23	4.6	—	900	3	1
23.5	Ni-22.5 at% Mn + Ni-24.0 at% Mn master alloy	22.0	10.01×0.45×0.20	8.7	0.315	900	3	1
23.5	99.99% Mn flake + Ni-22.0 at% Mn master alloy	23.6	10.0×0.45×0.19	7.8	0.272	900	3	1
			9.72×0.20×0.18(A)	2.6	—	900	3	1
			10.0×0.30×0.13(B)	3.3	—	900	3	1

The ingots were cold rolled into sheets (typical $\sim$ 0.2 mm thick), and a number of strips were spark-cut from the sheet; the final dimensions of the samples

are listed in Table 3.1. The NiMn system undergoes an atomic order-disorder transformation at about 500°C for Mn compositions ~ 25 at%, with a strongly ferromagnetic atomically ordered Ni_3Mn phase ($T_c \approx 700$ K) (see Figure 4.1.1-2; Hansen, 1958). In order to generate an atomically disordered state, the samples were encapsulated in small quartz tubes (≈ 12 mm long, 10 mm OD) under an argon atmosphere (160 Torr), the sealed tubes were placed inside a furnace at T_{dis} = 900°C for t_{dis} = 3 days, and then quenched rapidly by fracturing the tubes in water. The approximate total quenching time t_q for each sample is listed in Table 3.1. Table 3.1 also lists the mass of each sample and the calculated demagnetizing factors D used in the susceptibility data analysis.

3.2.2 AuFe System

Two AuFe alloys containing nominally 10.0 and 17.0 at% Fe, were prepared by argon arc-melting as described in the previous section; Table 3.2 lists some important parameters. Both the 99.99% pure Au wire and the 99.99% pure Fe wire were obtained from Aldrich Chemical Co., Milwaukee. Total melting losses indicated that the true concentration C_{true} was (at worst) within ± 0.3 at% of the nominal value for the 17.0 at% Fe alloy, and within ± 0.5 at% for the 10.0 at% Fe alloy. Both ingots were placed in a Vycor quartz tube, evacuated to 10^{-5} Torr, given a homogenizing anneal for 3 days at T_h = 900°C, and then cooled slowly to room temperature. The Au-10.0 at % Fe ingot was cold rolled into a 0.85 mm thick plate, and the sample was spark cut (with a copper blade) from the plate. The Au-17.0 at% Fe ingot was cold rolled into a 0.08 mm thin sheet, and two samples were cut with scissors. The final dimensions of the samples listed in Table 3.2 were obtained with the use of sand paper. A solution of Aqua-Regia (HNO_3:HCl = 1:4 in volume) was used to eliminate surface contamination.

These samples were again encapsulated in small quartz tubes under an argon atmosphere (160 Torr), the sealed tubes were placed inside a furnace at T_{dis} =

900°C for t_{dis} = 3 days, and then quenched rapidly by fracturing the tubes in water. The approximate total elapsed quenching time t_q was about 1 second. It is worthwhile to point out that the cold working should be minimized after quenching since it could significantly change the original magnetic properties for AuFe samples (Crane and Claus, 1980). An EDAX analysis was consistent with a high degree of homogeneity.

Table 3.2: AuFe alloys

C_{nom} $(at\%)$	X + Y	C_{true} $(at\%)$	samples $a \times b \times c\ (mm^3)$	m (mg)	T_{dis} (^0C)	t_{dis} (d)	t_q (s)
17.0	99.99% Au wire + 99.99%Fe wire	17.0	10.4×0.80×0.08(A)	11.6	900	3	1
			10.1×0.22×0.08(B)	2.9	900	3	1
10.0	99.99% Au wire + Au-17.0 at% Fe master alloy	10.0	5.16×0.89×0.85	73.9	900	3	1

3.2.3 CrFe System

A total of 6 CrFe alloys with nominal Fe concentrations 17, 20, 21, 22, 23, 24 at% were prepared by arc-melting as described in section 3.2.1. First, a master alloy containing nominally 24 at% Fe was prepared from 99.99 % pure Cr flakes and 99.99 % pure Fe wire (both supplied by Aldrich Chemical Co., Milwaukee). Melting losses were attributed predominantly to Cr, and indicated that the true composition of the master alloy was 24.0 ± 0.3 at% Fe. The master alloy was given an homogenizing anneal at T_h = 1160°C for t_h = 4 days and cooled naturally. The high annealing temperature and the longer annealing time were required by the location of the liquid-solid transformation line, which occurs at ~ 1700°C (as compared to 1200°C in NiMn). When cold-rolling of the ingot was attempted, however, the ingot fractured into several pieces. Five small ingots, each weighing

$\sim$ 2 gm, were obtained by spark-cutting the master alloy ingot, and these ingots were used to make the 17, 20, 21, 22, 23 at% Fe alloys separately by dilution with pure Cr. The ingots were etched with a solution of HCl(20 cc) + HNO_3(10 cc) + glycerol(30 cc) + few drops H_2O_2. An homogenizing anneal at 1160° C for 4 days was applied to all 5 alloys. Melting losses, which placed the true compositions of each alloy within (at worst) $\pm$ 1 at% of their nominal values, were insufficient to alter the intended magnetic character.

The final sample shapes were obtained by spark cutting and sanding; the dimensions are listed in Table 3.3, along with several other relevant parameters. To generate a disordered magnetic state, the samples were encapsulated in small quartz tubes under an argon atmosphere (160 Torr), the sealed tubes were placed inside a furnace at $T_{dis} = 1160°C$ for $t_{dis} = 4$ days, and then quenched rapidly by fracturing the tubes in water. The approximate total elapsed quenching time t_q was about 1 second.

Table 3.3: Cr-Fe alloys

C_{nom} $(at\%)$	X + Y	C_{true} $(at\%)$	samples $a \times b \times c\ (mm^3)$	m (mg)	T_{dis} (^0C)	t_{dis} (d)	t_q (s)
17.0	99.99% Cr + Cr-24.0 at% Fe master alloy	17.0	7.51×0.45×0.44	11.3	1160	4	1
22.0	99.99% Cr + Cr-24.0 at% Fe master alloy	22.0	8.37×0.42×0.41	11.4	1160	4	1

3.2.4 An Pd-1.4 at% Fe Sample

A ferromagnetic PdFe alloy containing nominally 1.4 at% Fe was prepared by arc-melting 99.999% pure Pd sponge (Johnson-Mathey, London) and 99.998% pure Fe wire (Aldrich Chemical Co., Milwaukee) both of which had been pre-melted

into buttons. The small melting loss indicated the true composition of the alloy was 1.4 $\pm$ 0.3 at% Fe. The ingot was cold-rolled into a thin sheet of thickness $\sim$ 0.2 mm (no homogenizing anneal was done for this button) and a number of strips were spark-cut from the sheet. A solution of HCl(30cc) + HNO_3(10cc) + H_2O(10cc) + a few drops H_2O_2 was used to eliminate surface contamination of both pure Pd and the Pd-1.4 at% alloy. A needle shaped sample ($\sim$ 10.0 $\times$ 0.2 $\times$ 0.05 mm^3 and m = 1.2 mg) was sealed in a Vycor quartz tube under argon atmosphere (160 Torr), annealled for 36 hours at 1000°C and quenched rapidly ($\sim$ 1 s) in water.

Chapter IV

Data Analysis and Discussion

The primary goal of our experiments is to investigate the magnetic properties of disordered ferromagnets, particularly those which exhibit a reentrant sequence, and, through comparison with the behaviour of pure spin glasses, to verify the existence of orientationally random spin freezing in the reentrant phase. Four systems, NiMn, AuFe, and CrFe, and PdFe were chosen for the present investigation, and emphasis was placed primarily on critical phenomena and magnetic relaxation.

4.1 The NiMn System

We first discuss our measurements of ac susceptibility, static magnetization and thermoremanent relaxation for disordered NiMn alloys with Mn concentrations from 22.0 to 27.0 at.%.

4.1.1 Experimental Magnetic Phase Diagram

As mentioned previously, spin frustration is caused by competition between a ferromagnetic interaction($J > 0$) and an antiferromagnetic($J < 0$) interaction. According to Carr (1952) and Sato (1955), both types of interactions are present in NiMn alloys: *a ferromagnetic interaction* between nearest-neighbour Ni-Ni and Ni-Mn spins, and *a direct antiferromagnetic interaction* between nearest-neighbour Mn-Mn spins. For small concentrations of Mn, the ferromagnetic interaction is dominant and NiMn exhibits ferromagnetism. As the Mn composition increases to about 25 at.%, there are still no Mn-Mn nearest-neighbors, provided the system is in the atomically ordered Ni_3Mn state as shown in Figure 4.1.1-1. Such a state is naturally formed when the NiMn system is cooled slowly through the order-disorder transformation line from $900°C$ to room temperature, according to its

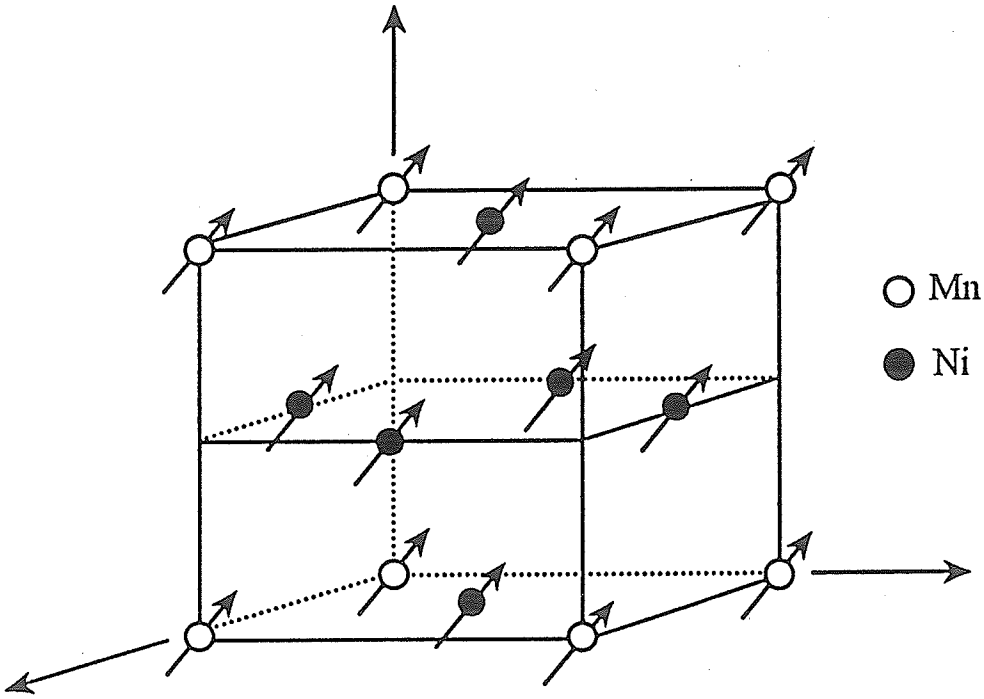

Figure 4.1.1-1: FCC structure of ordered strongly ferromagnetic Ni_3Mn with *Mn* located at the corners of the cell and *Ni* at the face-centers of the cell.

phase diagram Figure 4.1.1-2. When the alloy is quenched very rapidly from $900°C$ to room temperature, atomically disordered NiMn can form, in which an appreciable fraction of Ni (or Mn) is replaced by Mn (or Ni) randomly at the lattice sites, and nearest-neighbor Mn-Mn antiferromagnetic interaction is now possible. Thus a spin glass state can occur in disordered NiMn alloys at low temperature. Marcinkowski and Brown (1961) studied the Ni_3Mn order-disorder transformation in detail and obtained a lattice constant $a = 3.589 \pm 0.001A°$ in both ordered and disordered states. The magnetic moment distribution in NiMn was studied by neutron diffraction. Cable and Child (1974) showed that the individual moments are 3.5 μ_B/Mn and 0.58 μ_B/Ni at 5 at.% Mn. Both moments decrease with increasing Mn content, and attain values of 1.1 μ_B/Mn and 0.3 μ_B/Ni for 20 at.% Mn.

Unusual magnetic behavior in disordered NiMn alloys was discovered by Kouvel et al. (1958 and 1959). They found a pronounced maximum at low temperatures when magnetization was measured as a function of temperature, together with a displaced magnetic hysteresis loop. These unusual properties were attributed to the coexistence of ferromagnetism and antiferromagnetism at low temperatures. After the discovery of spin glass freezing, extensive work on disordered NiMn was done by Kouvel and co-workers again in order to construct a complete magnetic phase diagram (Abdul-Razzaq and Kouvel, 1984, 1987; Aitken et al., 1982). Magnetization was measured as a function of temperature under both zero field cooled (solid curves) and field cooled (dashed curves) conditions for Mn concentrations ranging from 23 to 27 at.%, and these results are summarized in Figure 4.1.1-3. For Mn concentrations $x \geq 24$ at.%, the ZFC curves show a typical spin glass maximum at the spin glass freezing temperature T_g and strong irreversibility below T_g. (difference between solid line and dashed line). For the alloys with $x =$ 23 and 23.5 at.% Mn, the curves in Figure 4.1.1-3 show a temperature independent plateau which separates the high temperature paramagnetic region from a

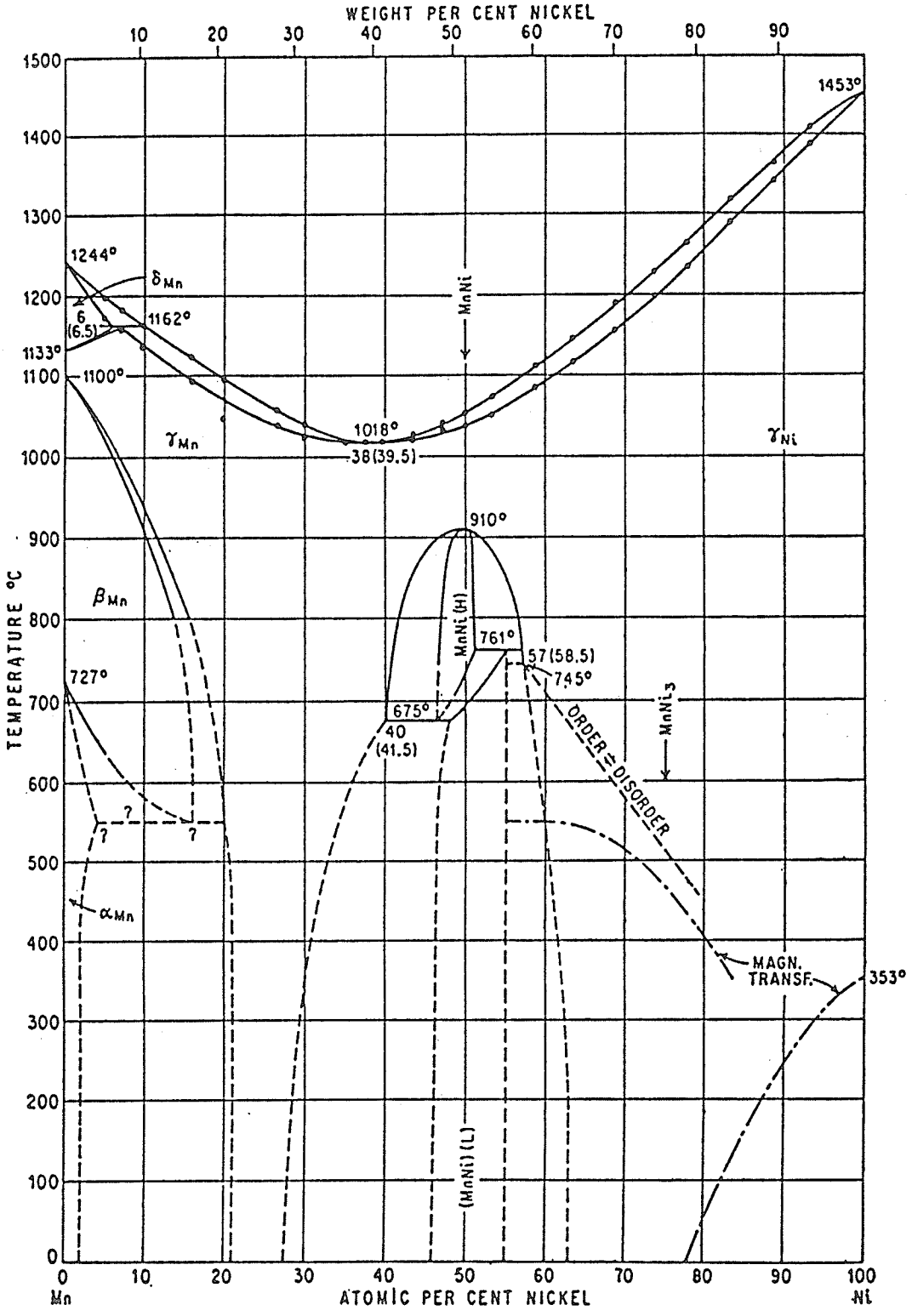

Figure 4.1.1-2: The phase diagram of NiMn. From Hansen (1958).

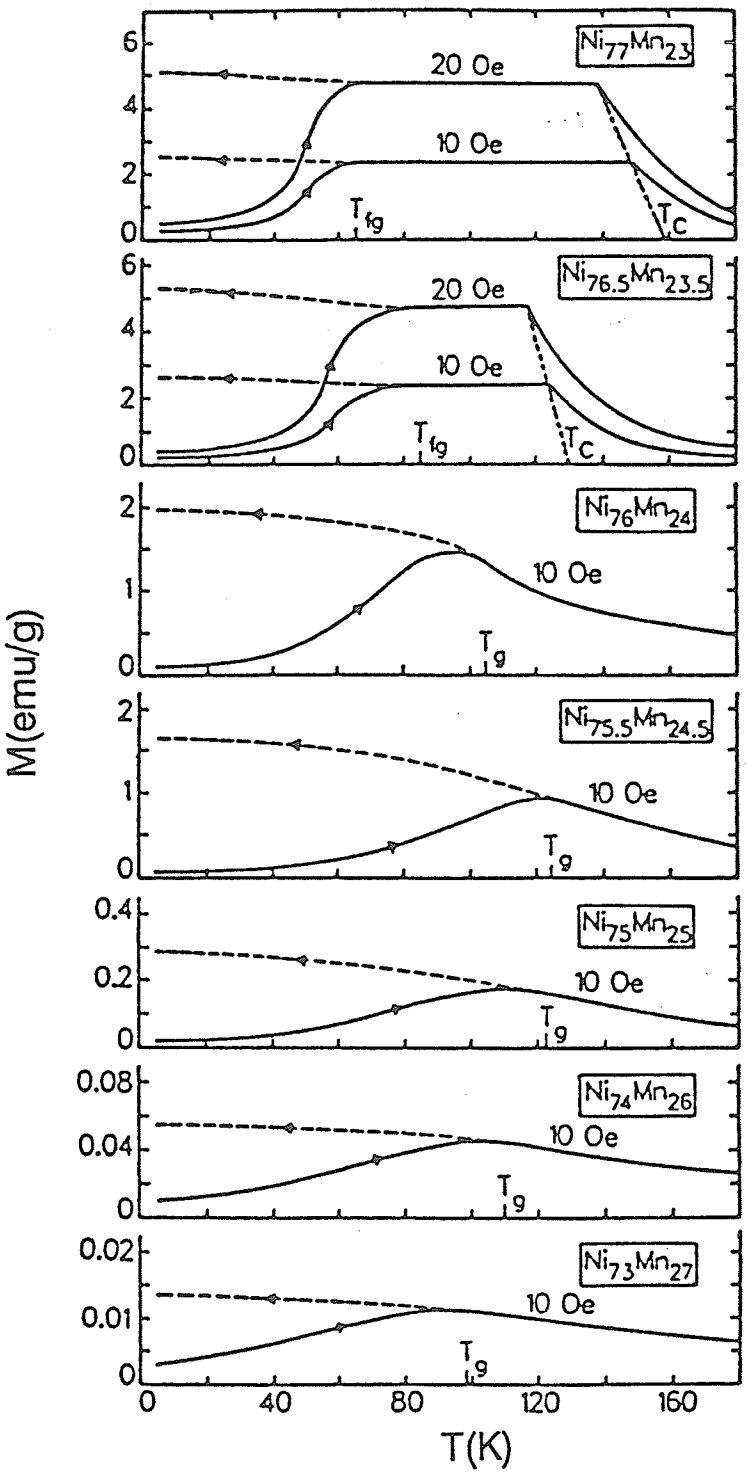

Figure 4.1.1-3: Magnetization vs temperature for various NiMn alloys, initially zero-field cooled to 4.2 K, upon warming (solid curves) and cooling (dashed curves) in a constant magnetic field. From Abdul-Razzaq and Kouvel (1987).

low temperature "reentrant" phase with irreversibility. The temperature independent plateau is produced 'artificially' by the large demagnetization factor of their samples($M_{max} = H_a/D$ at the plateau, $H_i = H_a - DM \geq 0$), and such behavior is often used to signal the occurrence of ferromagnetism (spontaneous magnetization). The kink-point temperature extrapolated to zero field (dotted line in Figure 4.1.1-3) gives T_c. The temperature at which the ZFC and FC curves separate is defined to be T_{fg} , below which system is suggested to be in the reentrant spin glass state with remanence, irreversibility, magnetic hysteresis etc.

Based on their measurements, a magnetic phase diagram of NiMn (Figure 4.1.1-4) was constructed by plotting T_c, T_{fg} and T_g as a function of Mn concentration. The multi-critical point (MCP), $x = 23.9$, occurs at the intersection of the T_c, T_{fg}, and T_g lines. When $x \leq 23.9$, sequential reentrant behaviour, from paramagnetism to ferromagnetism to a "ferro-spin-glass", is possible and for $x > 23.9$, the system experiences a typical pure spin glass transition. Notice that the transition line between the pure SG and mixed FSG states is drawn vertically, in agreement with the predictions of the vector model (Section 2.2.2). This is based on their measurements of the spontaneous magnetization as a function internal field H_{int}. According to the vector model, a longitudinal spontaneous magnetization sets in in the mixed FSG state whereas there is no spontaneous magnetization in the pure spin glass state. Kouvel et al. found no spontaneous magnetization for $x \geq 24$ at.%. However the initial slope of the M vs H_{int} plot increases rapidly and appears to be diverging as x approaches a value *just under* 24, very close to the location of the MCP (In fact, when x reaches 23.5, the M vs H_{int} plot merges tangentially with the M axis, giving a finite intercept around 11 emu/g, representing a spontaneous ferromagnetic moment.) After examining the variation of the spontaneous ferromagnetic moment of the 23 and 23.5 at.% samples as the temperature is further decreased below T_c, Kouvel et al. suggested that the temperature for the onset of SG ordering, which perhaps marks the actual GT reentrant transition

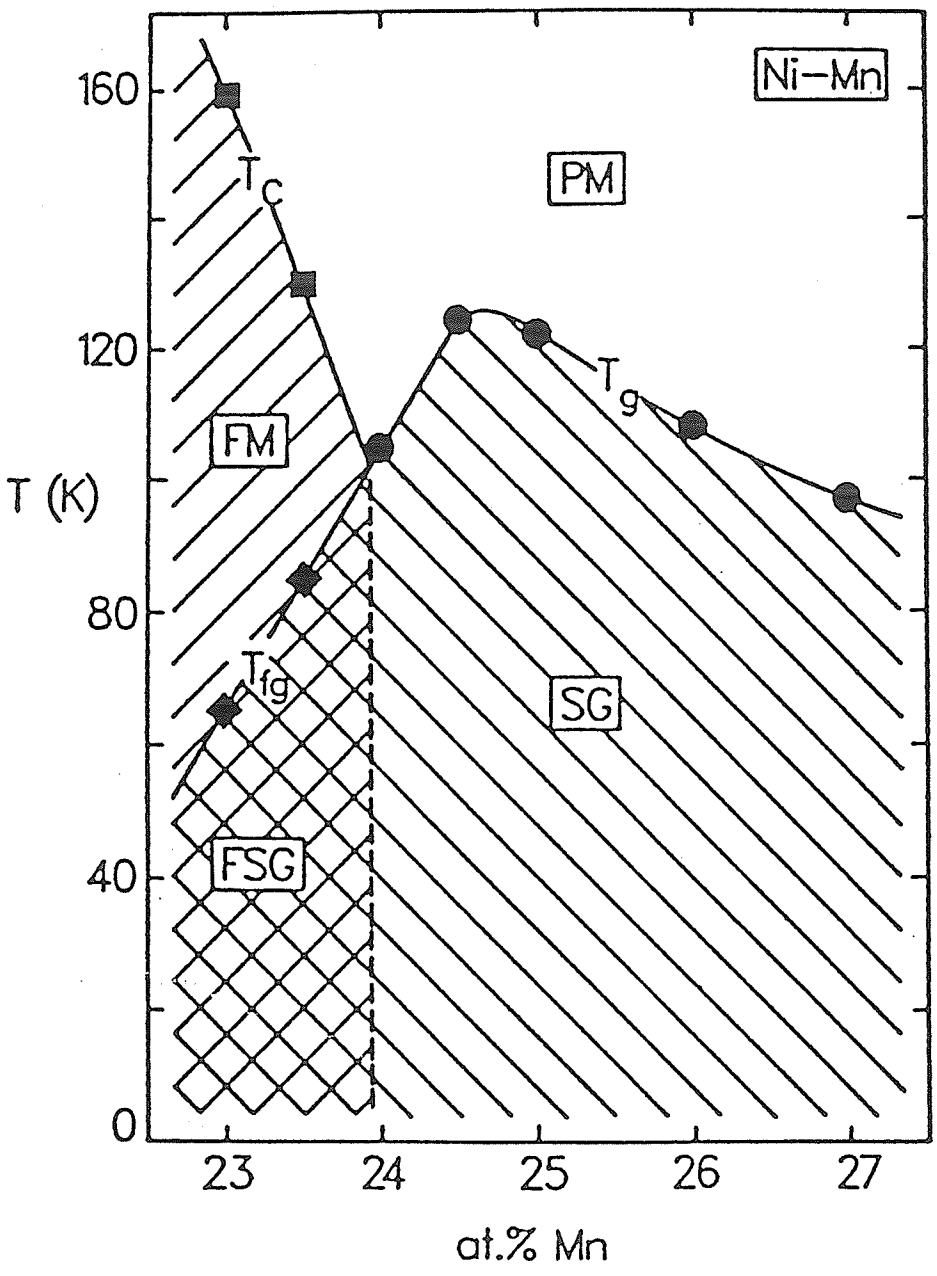

Figure 4.1.1-4: Magnetic phase diagram for disordered NiMn, showing ferromagnetic (FM), reentrant, ferro-spin-glass (FSG), spin glass (SG), and paramagnetic (PM) regimes. The T_c, T_{fg}, and T_g lines (and the vertical line between FSG and SG) all meet at a multicritical point (23.9 at%Mn, 102 K). From Abdul-Razzq and Kouvel (1987).

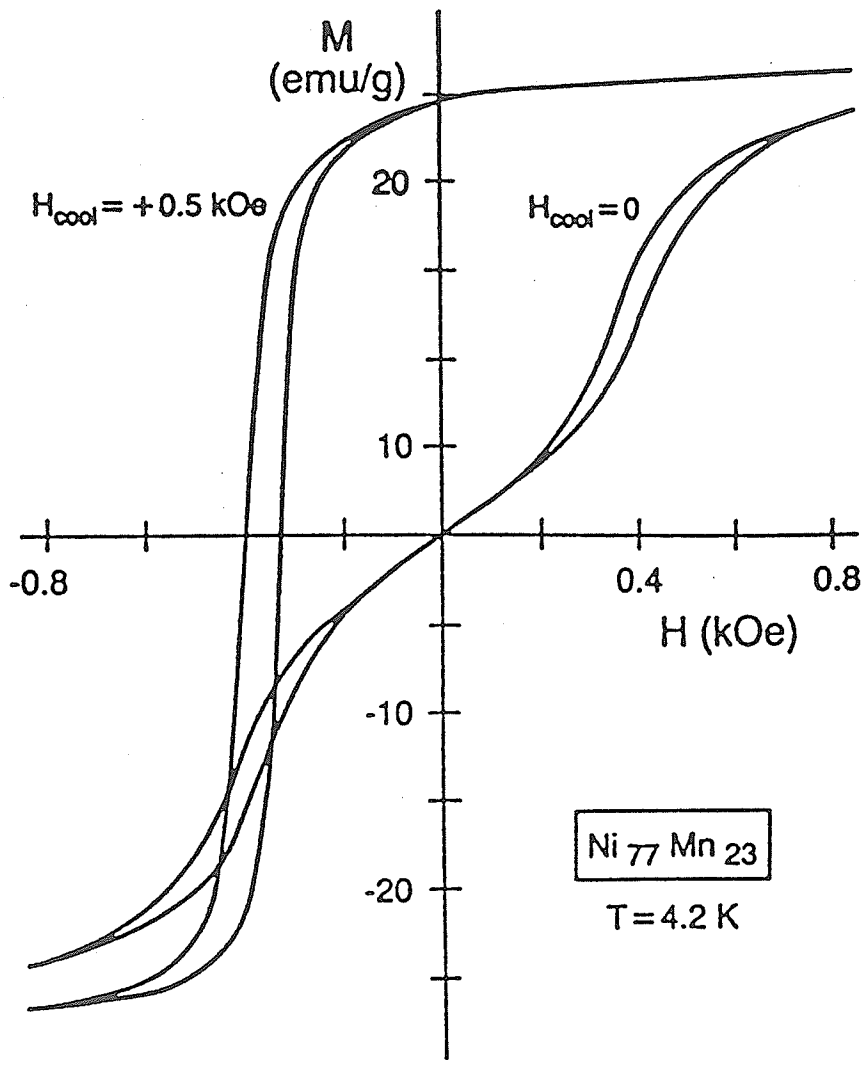

Figure 4.1.1-5: Magnetic hysteresis loops for $Ni_{77}Mn_{23}$ cooled to 4.2 K in zero field and in +0.5 kOe. From Abdul-Razzq and Kouvel (1984).

line, probably lies significantly above the temperature T_{fg}.

NiMn shows displaced magnetic hysteresis loops for both reentrant ferromagnets and spin glasses from 22 to 27 at.% Mn (Abdul-Razzaq and Kouvel 1984; Kouvel and Abdul-Razzaq 1985; Aitken et al., 1982). Figure 4.1.1-5 shows the hysteresis loop for Ni-23 at.% Mn, which was obtained after cooling the sample from above T_{fg} in both zero field as well as in a field of 0.5 kOe to 4.1 K (Abdul-Razzaq and Kouvel, 1984). Cooling the sample in a field sufficiently strong to saturate the thermoremanent magnetization(TRM) resulted in a displaced hysteresis loop which was asymmetric with respect to the origin such that both remanences were positive. A ferro-spin-glass domain model was developed which was capable of reproducing the displaced hysteresis loops (Kouvel et al., 1987; Kouvel and Abdul-Razzaq, 1985)

4.1.2 Spurious Reentrant Behavior in $Ni_{76}Mn_{24}$: the Effects of Short-Range Order

It was Kouvel's magnetization measurements, and in particular the sharpness of the demag-limited plateau, (Figure 4.1.1-3) which inspired our intensive study of the NiMn system. Our investigation begins with $Ni_{76}Mn_{24}$ which, according to the phase diagram in Figure 4.1.1-4, is a spin glass close to the multi-critical point. Since reentrant systems are also ferromagnetic, the magnetic impurity component of their composition is frequently rather high (typically 15 at.% in AuFe, 20 at.% in CrFe, and 20 at.% in NiMn), so that metallurgical influences may have a profound effect on the magnetic properties. The metallurgical influences are especially pronounced in the NiMn system since the alloys undergo an order-disorder transformation to a strongly ferromagnetic Ni_3Mn phase as mentioned earlier. In this section, we show that the presence of short-range atomic order in NiMn can produce structure in the susceptibility which mimics that usually associated with "reentrant" systems, even though no long-range ferromagnetic order is apparently

present, and we suggest an essential criterion which distinguishes such systems from genuine "reentrant" ones.

An alloy of NiMn containing nominally 25 at.% was prepared following the procedure described in section 3.2.1 and three samples **A**, **B** and **C** were fabricated from the original ingot; the dimensions of the samples are listed in Table 3.1. In order to control the amount of short range order present in the samples, each sample was deliberately quenched at a different rate, t_q, as listed in Table 3.1: (a) Sample **A** was subjected to a *slow quench*, (b) Sample **B** represented an *intermediate quench*, with a quenching interval of approximately 1 second. (This is also the lower limit on the quenching interval imposed by the physical proximity of the furnace and the bath.) (c) Sample **C** was submitted to a *rapid quench.* This quenching process was nominally identical to that of Sample **B**; however, since Sample **C** was thinner and the ratio of its surface area to its volume was larger, its effective quenching rate was considerably more rapid.

The curves labeled (a), (b), and (c) in Figure 4.1.2-1 show the temperature dependence of the real part of the complex susceptibility of samples **A**, **B**, and **C** measured at 2400 Hz in zero static magnetic field, and appropriately corrected for demagnetizing effects [1], $\chi'_{true} = \chi'_{meas}/(1 - D\chi'_{meas})$. Curve ($b'$) provides a typical illustration of the effect of a finite static field (H_a = 6.1 Oe) for sample **B**. In each case, the sample was cooled from room temperature to 77K in zero field, and the susceptibility was measured upon warming. The uncorrected susceptibilities (χ'_{meas}) were all well below the maximum value (D^{-1}) imposed by the geometry of the samples, and hence the artificial structure normally encountered

[1]The demagnetizing factors employed in the current analysis were D_A = 4.76 gm-Oe/emu, D_B = 1.3 gm-Oe/emu, and D_C = 0.4 gm-Oe/emu. A comparison of the uncorrected high frequency and low frequency data indicated that calculations which approximated these rectangular samples by an ellipsoidal geometry overestimated the value of the demagnetizing factor, in agreement with the data tabulated by Bozorth (Bozorth, 1951). Although a suitable reduction has been incorporated into the values listed above, it should be emphasized that, since the measured susceptibilities are all so small, the data in Figure 4.1.2-1 are relatively insensitive to the details of these modifications.

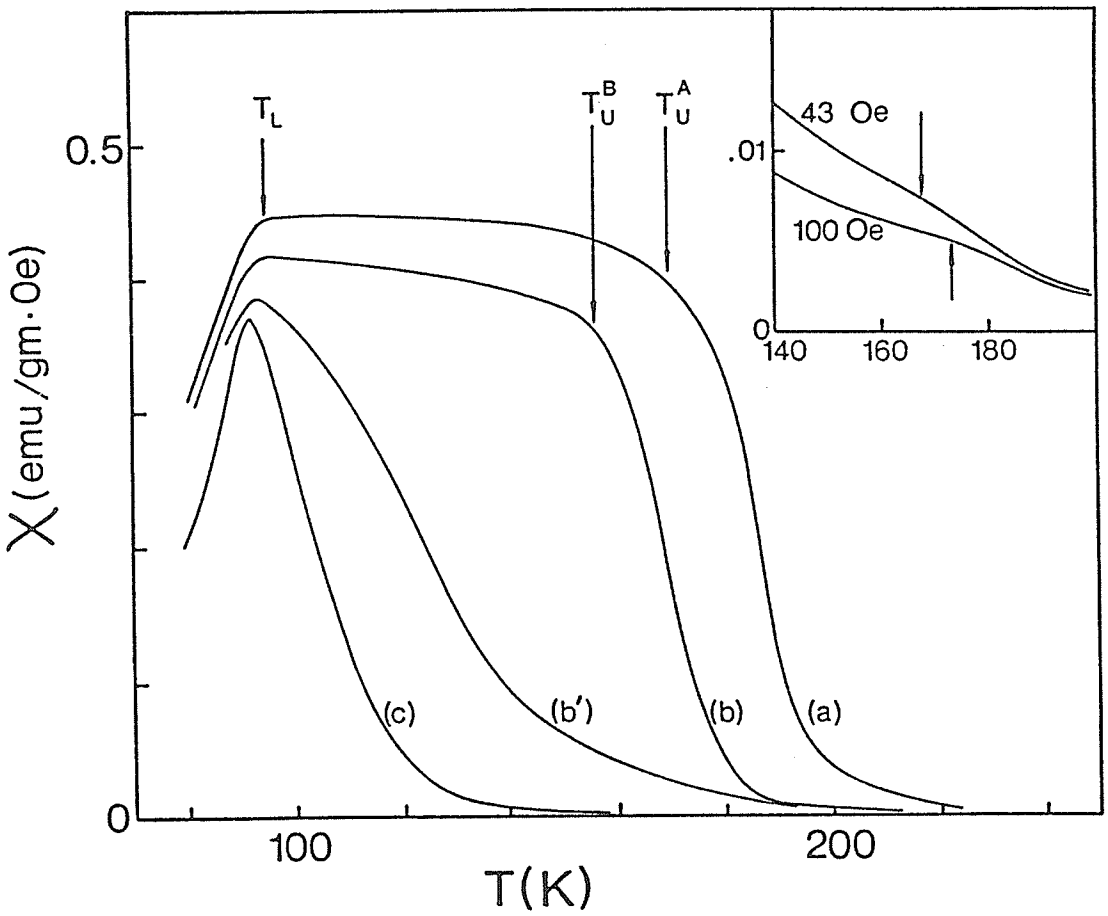

Figure 4.1.2-1: Temperature dependence of the true susceptibility measured at 2400 Hz for (a) Sample A (slow quench), $H_a = 0$ Oe, (b) sample B (intermediate quench), $H_a = 0$ Oe, (b') sample B (intermediate quench), $H_a = 6.1$ Oe, (c) sample C (rapid quench), $H_a = 0$ Oe. The insert shows the weak convexity in two of the higher field isokaps, $H_a = 43$ Oe and $H_a = 100$ Oe, for sample B.

in demagnetization-limited measurements of the susceptibility was avoided.

It is clear from Figure 4.1.2-1 that the magnetic response of the system is influenced significantly by the effective rate at which the quench is done. Curves (a) and (b), which represent a slow and intermediate quench, exhibit several superficial features which are highly suggestive of reentrant behaviour: there are apparently two well-defined "transitions", an upper "transition" at T_U and a lower "transition" at T_L, separated by a plateau with a very weak temperature dependence. A comparison of these curves shows that a reduction in quenching rate enhances the magnetic response at all temperatures and shifts the upper "transition" to higher temperatures (from ${T_U}^B = 160$ K to ${T_U}^A = 180$ K), while the lower "transition" ($T_L \cong 94$ K) suffers no apparent displacement in temperature. Moreover, as curve (b') shows, the superposition of a static magnetic field quenches the high temperature knee (in much the the same way as the Hopkinson peak in a ferromagnet is suppressed by the application of a static field) and reveals further structure in the vicinity of both " transitions". The structure associated with the lower "transition" is clearly visible in curve (b') as a single distinct peak, while the structure in the neighbourhood of the upper "transition" is considerably more subtle and difficult to resolve. The insert in Figure 4.1.2-1 shows the position of an extremely weak convexity in two of the higher field isokaps (a term suggested by Professor B.R. Coles to denote a curve of constant field.) for sample **B**, which becomes more distinct and appears to shift upward in temperature with increasing field. By contrast, the rapid quenching process alters the magnetic state of the system dramatically (curve (c)): the upper "transition" vanishes completely and the system is transformed into a spin glass with a freezing temperature $T_{SG} = 90$K (defined by the susceptibility cusp) which is approximately at the same location as the temperature T_L of the former "reentrant" transition. Thus the behavior of $Ni_{76}Mn_{24}$ closely resembles that observed in $Au_{86}Fe_{14}$, which, as will be discussed in section 4.2.1 (Figure 4.2.1-4), can also be converted from a reentrant

ferromagnet to a spin glass by changing the annealing temperature (Crane and Claus, 1981).

In order to gain further insight into the nature of the magnetically ordered states associated with the apparently reentrant version of the system, the susceptibility of sample **B** was remeasured at a much slower frequency with the SQUID susceptometer described in Chapter III. Figure 4.1.2-2 shows the real part of the true complex susceptibility, in various static applied magnetic fields H_a between 0.3 Oe and 20 Oe, plotted as a function of temperature. With the exception of the 0.3 Oe data, which was measured after cooling the sample to 4.2 K in the trapped field of the lead container, an identical experimental technique was employed to extract each isokap: the sample was heated to 180 K in the paramagnetic regime to remove any remanence, cooled in zero field to 20 K where both the a.c. field and the static magnetic field were applied, and then warmed incrementally in these fields. For purposes of comparison, the susceptibility of the same sample measured at 2400 Hz has been reproduced in this figure as the solid curve.

The trapped-field data appear to confirm the existence of sequential "transitions": there is a high temperature knee at $T_U \cong 155$ K and a prominent low temperature maximum at $T_L = 94$ K, separated by a region of somewhat weaker temperature dependence. While the high temperature behavior is essentially unaffected by the change in excitation frequency, there is a noticeable loss of magnetic response for temperatures below 170 K associated with the higher frequency measurement, particularly in the vicinity of the lower "transition", thus establishing the existence of a substantial irreversible component in the magnetic susceptibility. There is, however, no detectable shift in the temperature T_L at which the lower "transition" occurs. As before, the superposition of a static magnetic field reveals the presence of a single distinct peak in the neighbourhood of the lower "transition", reminiscent of that observed at a "direct" paramagnetic-spin glass transition, which is systematically suppressed in both amplitude and temperature

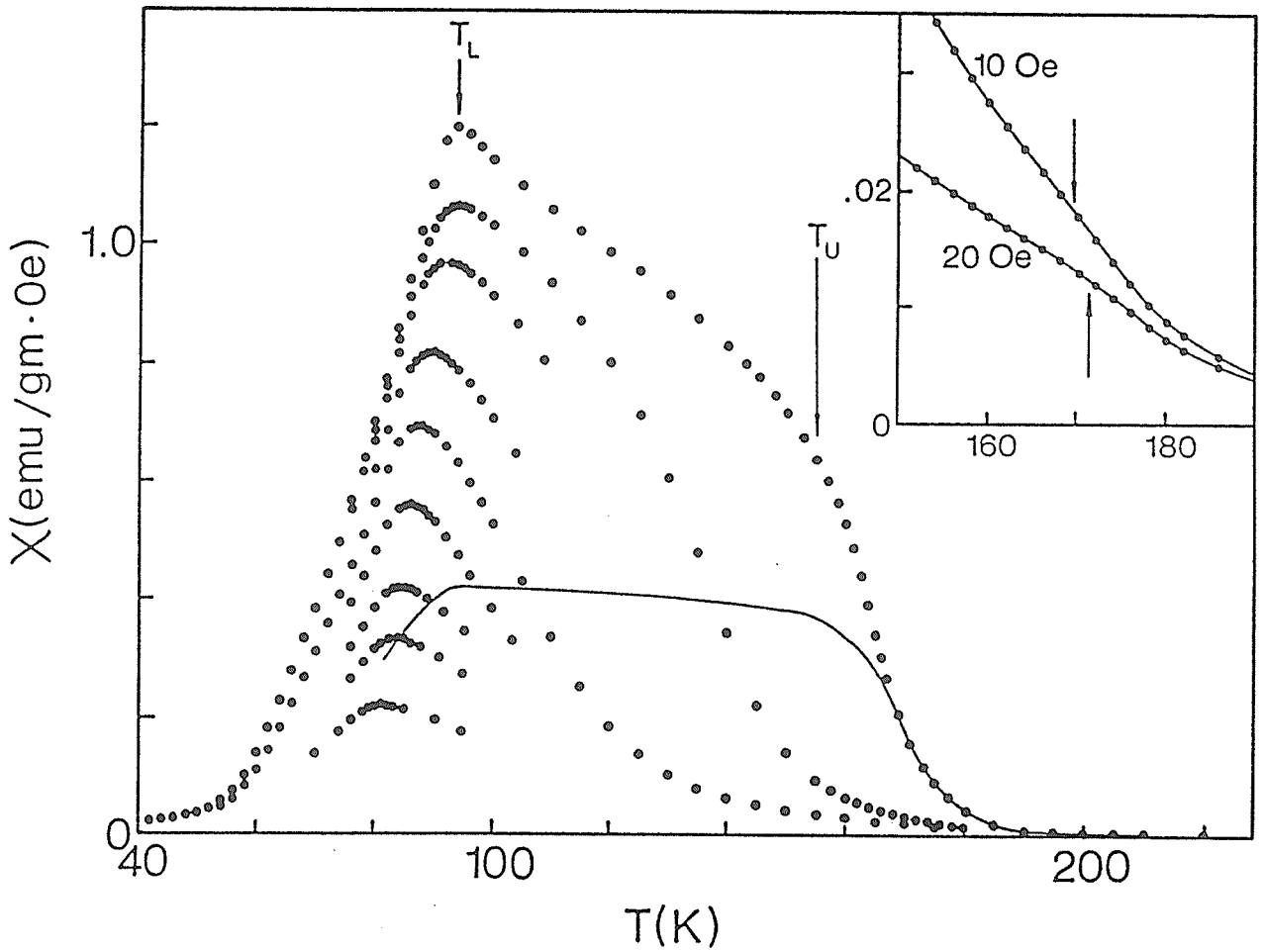

Figure 4.1.2-2: Temperature dependence of the true susceptibility of sample B measured at 16 Hz(dots) in the following static magnetic fields (in order of decreasing peak amplitude): H_a = 0.3, 4.5, 6.3, 8.6, 10.4, 12.3, 14.6, 16.4, 20.6 Oe. The solid curve reproduces the zero-field susceptibility of the same sample measured at 2400 Hz.

with increasing field. These low frequency measurements also continue to exhibit the weak structure observed in the vicinity of the upper "transition" at 2400 Hz. The arrows in the insert in Figure 4.1.2-2 mark the location of an extremely weak shoulder in both the 10 Oe and 20 Oe isokaps; although the anomaly remains broad and extremely difficult to resolve, there is sufficient definition to confirm the high frequency systematics: the shoulder is suppressed and appears to shift upward in temperature with increasing field.

Figure 4.1.2-3 shows a selection of representative, demagnetization-corrected magnetic isotherms for Sample **B**, measured with the SQUID susceptometer at a variety of temperatures between 67.5 K and 140 K, and plotted as a function of the internal field $H_i = H_a - DM$. All the isotherms were obtained after first zero field cooling the sample from the paramagnetic regime ($T > 170$K) to the desired temperature and then sweeping the static applied field H_a incrementally from 0.3 Oe to 40 Oe (corresponding to an internal field range $0 \leq H_i \leq 30$ Oe) in approximately 50 steps. At all the temperatures shown here, the shape of the isotherms, particularly at low fields, is influenced to a greater or lesser extent by the presence of an irreversible, time dependent component in the magnetic response. Consequently, for temperatures $T \leq 86$ K, the leading field dependence is roughly linear rather than quadratic as expected on the basis of general symmetry arguments, while, for temperatures between 88 K and 115 K, the isotherms are characterized by an anomalous upward curvature at low fields ($H_i < 1$ Oe). The details of this anomaly are shown in the inserts in Figure 4.1.2-3 on a magnified scale; the anomaly develops around 88 K, achieves its maximum amplitude at 94 K (which is also the temperature T_L of the peak in the trapped field isokap in Figure 4.1.2-2), and then gradually dissipates. (A similar anomalous structure is also observed in FeZr in the neighbourhood of the reentrant transition (Ma 1990).) At temperatures above 120 K, the shape of the isotherms becomes progressively less anomalous and the initial curvature gradually assumes its "natural" quadratic

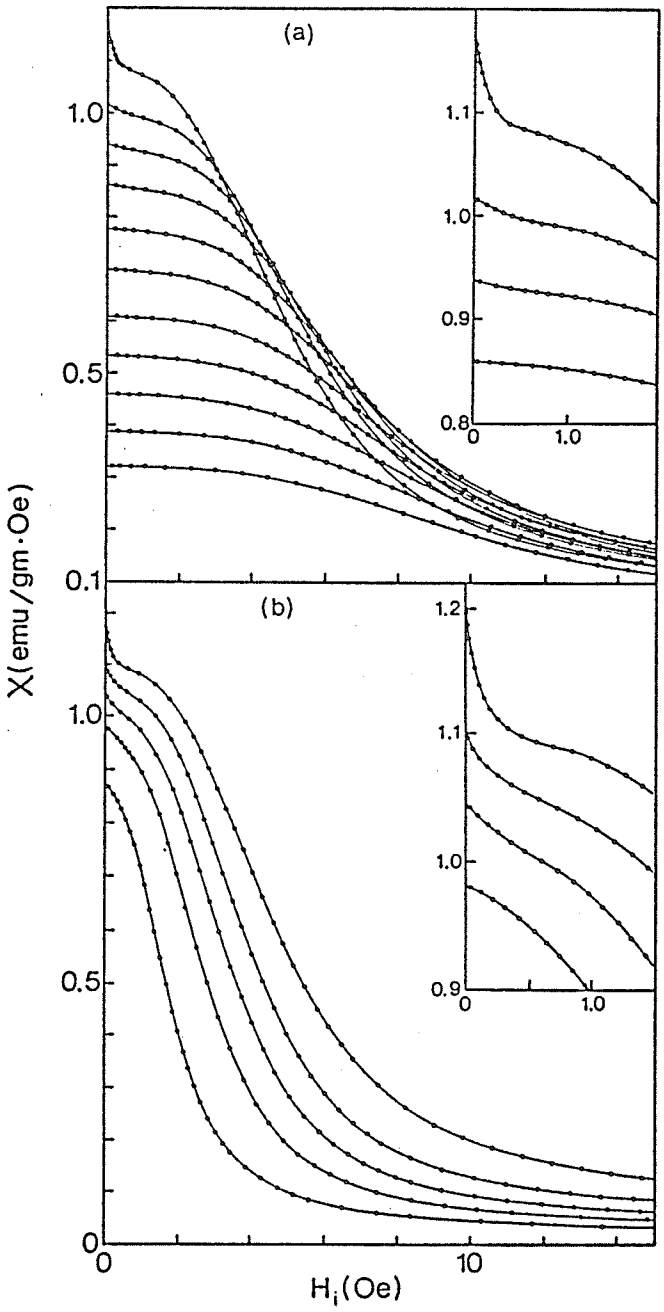

Figure 4.1.2-3: (a) Magnetic isotherms for sample B measured at 16 Hz and plotted as a function of internal field for the following temperatures (in order of increasing vertical intercept): T = 67.5, 70.0, 72.5, 75.0, 77.5, 80.0, 82.0, 84.0, 86.0, 88.0, 92.0 K. The insert shows the low-field behaviour of the top four isotherms on an expanded scale. (b) Magnetic isotherms as a function of internal field for sample B measured at 16 Hz for the following temperatures (in order of decreasing vertical intercept): T = 94, 106, 115, 125, 140 K. The insert shows the low-field behaviour of the top four isotherms on an expanded scale.

form as the paramagnetic regime is approached.

The zero field susceptibility of samples A and B measured at 2400 Hz (curves (a) and (b) in Figure 4.1.2-1) exhibits a temperature-dependent structure which conforms to the universally accepted image of a "reentrant" system which undergoes sequential phase transitions. The measurements performed at low frequencies support the interpretation of "multiple transitions" (see the trapped field isokaps in Figure 4.1.2-2), although they also indicate that time dependent effects play a significant role in shaping the reentrant profile at 2400 Hz. [2] However, the nature of the magnetically ordered states associated with the two transitions is far from obvious. As mentioned earlier, the peaks which are generated in the vicinity of the lower "transition" by the application of successively larger static magnetic fields (see Figure 4.1.2-2) are not only superficially reminiscent of those observed in both "pure" spin glasses as well as in other reentrant systems, but also display systematics which are quantitatively consistent. In particular, a double-logarithmic plot of the peak heights $\chi(H_a, T_{PEAK})$ as a function of applied field H_a does not yield simple power law behaviour, but instead exhibits the same continuous curvature as analogous plots in the spin glass phase of the PdMn system (the latter have been modelled successfully using numerical simulations based on a simple mean theory (Roshko, Williams and Gash, 1984)).

The lower "transition" thus possesses considerable spin glass character and may be tentatively associated with the onset of a low temperature "reentrant" spin glass phase. This identification is supported by two further observations: (a) While critical behaviour does not appear to manifest itself directly in the susceptibility (double logarithmic plots, such as the one referred to above, do not

[2]It should be pointed out that this interpretation would become even more compelling had the measurements been performed under demagnetization-limited conditions, since the zero field susceptibility then acquires an artificial temperature independent plateau. While such measurements are routinely accepted as evidence for the reentrant character of a system, and the temperatures at which the plateau terminates are identical with the critical temperatures, they tend to exaggerate the reentrant features and may even disguise the true nature of the magnetic state.

yield well-defined critical exponents), there is anomalous structure in the nonlinear components of the susceptibility (specifically in the initial slope of the isotherms shown in the inserts in Figure 4.1.2-3) which suggests a potentially critical divergence in the amplitude of the leading field dependent term as $T \rightarrow T_L$ from above and below. Nonlinear critical singularities are also a characteristic of the direct paramagnetic-spin glass transition both above and below T_{SG} (Zastre, Roshko, and Williams 1985). However, in the present instance, the leading field dependence in the vicinity of T_L is clearly much faster than the usual H_i^2 dependence and the low field structure of the isotherms is too complicated to permit a meaningful quantitative critical analysis. (b) The similarity between the reentrant transition temperature ($T_L = 94$ K), and the ordering temperature of the spin glass ($T_{SG} =$ 90 K) which is formed when the system is subjected to an extremely rapid quench, suggests that the essential ingredients of the exchange bond distribution which are necessary for the formation of the spin glass must also be present to a substantial degree in the "reentrant" version of the system.

The upper transition is far more difficult to characterize. Its location with respect to the lower spin glass transition (T_L) is certainly typical of the paramagnetic to ferromagnetic transition in the normal reentrant sequence, and the accompanying structure observed in the isokaps (see the inserts in Figures 4.1.2-1 and 4.1.2-2) is vaguely reminiscent of the critical peaks associated with a direct paramagnetic-ferromagnetic transition. (This structure does not appear to be an artifact of the experimental method since it is present in two sets of data which were acquired independently using different measurement techniques.) However, ferromagnetic critical peaks are well defined entities, with a field dependent amplitude $\chi(H_i, T_{max})$ and temperature $T_{max}(H_i)$ which obey critical power laws of the form $\chi(H_i, T_{max}) \propto H_i^{(1/\delta)-1}$ (Eq.(2.116) and $\mid T_{max}(H_i) - T_c \mid \propto H_i^{(\gamma+\delta)^{-1}}$, (Eq.(2.115)) while the structure observed here, although exhibiting similar systematics, clearly lacks sufficient resolution to establish the existence of critical

behaviour unequivocally. These features lead us to conclude that there is no genuine long-range ferromagnetism present in this system, and consequently that the upper transition (T_U) does not represent a cooperative thermodynamic phase transition from a paramagnetic phase to a ferromagnetic phase. Nevertheless, there is undoubtly evidence for incipient ferromagnetism, probably due to regions of the atomically ordered Ni_3Mn phase which were not completely removed by the quenching process, on a scale which is however, insufficient to support the formation of well defined critical peaks. Thus the transition (T_U) is most likely a cluster glass (or superparamagnetic) transition, although the weak shoulder -like structure implies that the clusters may be close to ferromagnetic percolation on a large scale.

In summary, we have shown that the presence of short range order can produce anomalies in the temperature dependence of the susceptibility which mimic those observed in critically reentrant systems and thus may lead to a misdiagnosis of the magnetic state of the system. More importantly, the present investigation illustrates the necessity for a comprehensive asymptotic (low field and low reduced temperature) critical analysis in order to properly establish the magnetic character of the two transitions in a potentially reentrant system. As an essential ingredient of such an analysis, one would expect to observe well-defined critical peaks in the vicinity of the upper transition, with a set of critical exponents which would be sensitive to the details of the exchange bond distribution, and hence to the degree of short-range order in the material. In fact, the presence of critical peaks, in itself, would serve as a valuable criterion for a preliminary identification of a critically ferromagnetic upper transition. In the present instance, this criterion is clearly not satisfied, in spite of the suggestive structure of the zero field susceptibility. In the neighbourhood of the lower transition, the critical analysis must focus on the nonlinear components of the susceptibility in order to establish the spin glass character of the reentrant phase. The system investigated here exhibits

all the symptoms of a reentrant transition at T_L = 94 K into a spin glass phase, including an anomalously rapid temperature dependence in the leading nonlinear term near T_L, although time effects (probably related to the relaxation of large ferromagnetic clusters) preclude a proper critical analysis.

4.1.3 The Ferromagnetic Critical Analysis of A Genuinely Reentrant $Ni_{77.5}Mn_{22.5}$ Alloy

An alloy of NiMn containing nominally 23 at.% Mn was prepared by arc melting as discussed in section 3.2.1 of chapter III. Two samples were assembled from the quenched strips, each consisting of a bundle of parallel strips with contiguous surfaces electrically insulated from each other with masking tape. Sample A comprised 3 strips with average dimensions and a calculated demagnetizing factor listed in Table 3.1. This sample was used to investigate the response of the system in relatively small static fields ($H_a \leq 200Oe$). Sample B contained 4 strips with average dimensions and average demagnetizing factor also given in Table 3.1. This larger sample was reserved exclusively for the ferro-magnetic critical analysis, which required an enhanced signal amplitude, particularly at higher fields ($H_a \geq 200$ Oe).

Figure 4.1.3-1 shows the temperature dependence of the real part of the true complex susceptibility of sample A, measured in several static magnetic fields $H_a \leq 43$ Oe, and appropriately corrected for demagnetizing effects. With the exception of the solid curve in part (a) of this figure, which represents the zero field response of the system at 2400 Hz measured with the phase-locked magnetometer, all of the data in Figure 4.1.3-1 were acquired with the SQUID susceptometer, at an excitation frequency of 16 Hz. An identical experimental procedure was employed to obtain each isokap: the sample was first heated to a reference temperature T_R = 250 K in the paramagnetic regime to eliminate any remanence, then cooled in zero net field to T = 15 K where both the a.c. field and the static magnetic field

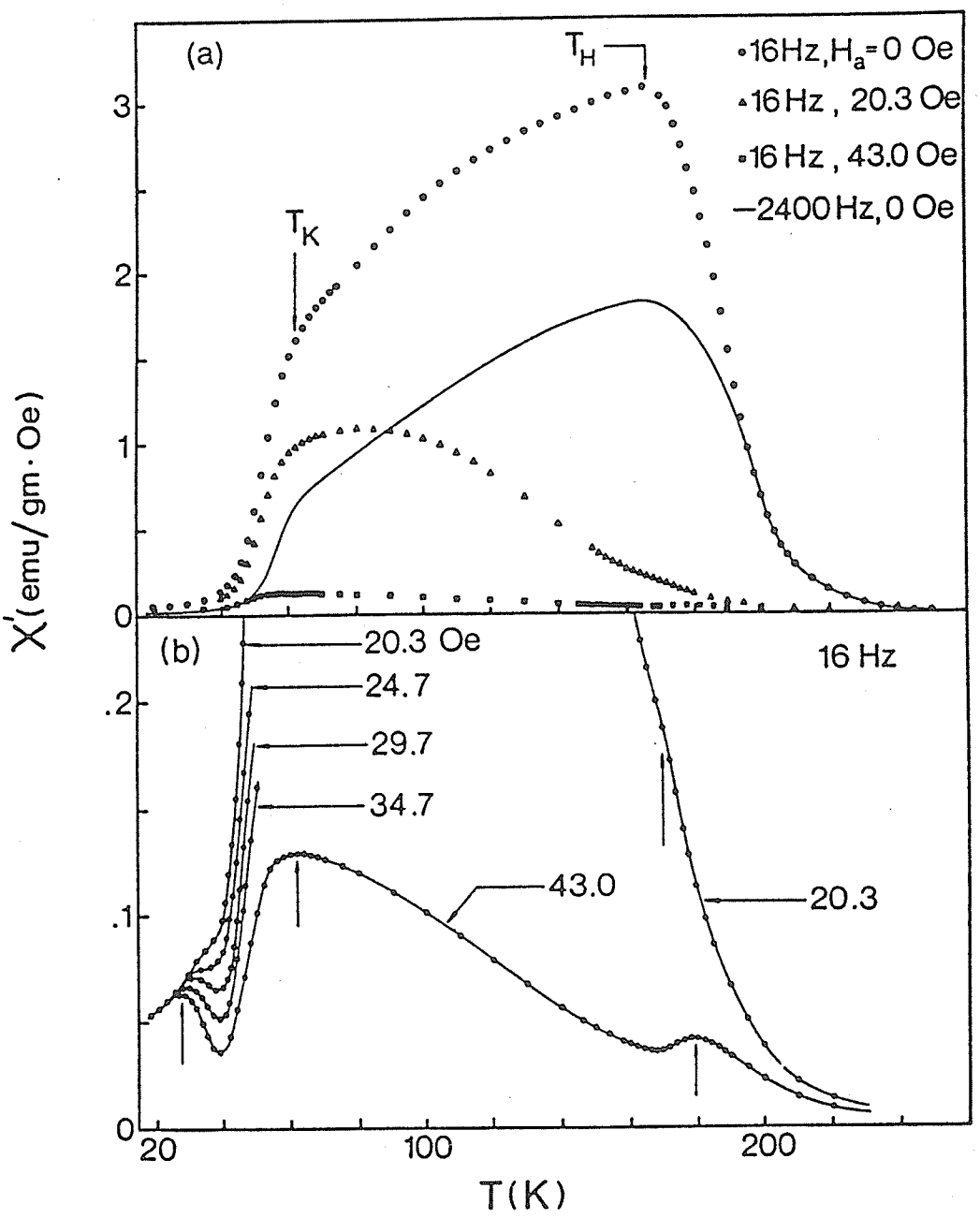

Figure 4.1.3-1: (a) The temperature dependence of the real part of the true susceptibility $\chi'(T, H_a)$ in various static magnetic fields H_a at excitation frequencies of omega = 16 Hz (discrete data points) and ω = 2400 Hz (solid curve). (b) Details of some of the 16 Hz isokaps in part (a) on a magnified vertical scale. Each isokap is identified by the value of the static field H_a, and the vertical arrows indicate the location of some of the structure.

were applied, and the susceptibility was subsequently measured upon warming.

The susceptibility in zero static field exhibits features which are suggestive of reentrant behaviour with sequential transitions. There is a distinct principal (Hopkinson) maximum at $T_H = 165K$ and a more diffuse knee at $T_K = 60K$, which separate the magnetic response into three regimes, tentatively designated as follows: a "paramagnetic phase" for $T > T_H$, a "ferromagnetic phase" for $T_K < T < T_H$, and a "reentrant phase" for $T < T_K$. A comparison of the zero field data at 16 Hz and 2400 Hz shows that, while there is a noticeable loss of response associated with the higher excitation frequency, indicating the presence of a broad spectrum of relaxation times in the susceptibility below 190 K, the values of the two "characteristic" temperatures T_H and T_K are essentially unaffected by the change in excitation frequency. It should be pointed out here that the demagnetizing factors of the samples employed in the present investigation are sufficiently small that the artificial temperature independent plateau normally encountered in demagnetization limited measurements of the magnetization and susceptibility has been avoided. While such structure is routinely accepted as evidence for a divergence in the true susceptibility and hence for a spontaneous magnetization (and, in fact, has been used to establish the location of the magnetic phase boundaries of the NiMn system, Abdul-Razzaq and Kouvel, 1987), the data in Figure 4.1.3-1 show that true susceptibility is finite everywhere, and furthermore, that the reentrant "transition" in NiMn becomes a considerably more subtle effect when the influence of sample geometry is minimized.

The superposition of a static magnetic field collinear with the alternating field suppresses the principal Hopkinson maximum, and reveals multiple structure in the isokaps. Figure 4.1.3-1(b) illustrates the details of this structure on a magnified, vertical scale. The structure consists of three peaks, (observed for the first time in NiMn) one which emanates from the vicinity of the Hopkinson maximum, and two at lower temperatures which appear to be correlated with the onset

of the reentrant phase. The high temperature peak in Figure 4.1.3-1(b) (which is really only a shoulder in $H_a = 20.3$ Oe) displays a systematic suppression in amplitude and upward shift in temperature with increasing static field which are typical of ferromagnetic critical peaks, and provides some preliminary justification for regarding the upper transition as one from paramagnetism to long-range ferromagnetism. The two "reentrant" peaks are similarly suppressed in amplitude, but are shifted downward in temperature; the extent to which these peaks may also be a manifestation of critical behaviour is discussed later.

Figure 4.1.3-2(a) shows the details of the field and temperature dependence of the high temperature ferromagnetic peak, in fifteen static magnetic fields H_a between 40 Oe and 704 Oe. The measurements were performed on sample **B**, using the phase-locked magnetometer, and an excitation frequency of 2400 Hz[3]. For purposes of comparison, Figure 4.1.3-2(b) shows a set of ferromagnetic critical peaks generated numerically within the reentrant phase of a mean, effective field model (Eq.(2.122) and (2.123)) using a Gaussian exchange bond distribution with a first moment to second moment ratio of $\overline{J_o}/\overline{J} = 1.1$ and an impurity spin $S = 5/2$, for several reduced applied fields $h \equiv g\mu_B H_a/k_B T_c$ between 0.0002 and 0.003. (For a system of finite size, $h \rightarrow H_i = H_a - DM$ = the internal field). Based on the ferromagnetic scaling theory discussed in section 2.3 in chapter II, the model peak heights $\chi(h, t_m)$ and reduced peak temperatures t_m obey simple power law dependences as a function of reduced field h:

$$\begin{aligned} t_m &\propto h^{(\gamma+\beta)^{-1}} \\ \chi(h, t_m) &\propto h^{(1/\delta)-1} \end{aligned}$$

where $t_m = |(T_m - T_c)/T_c|$ is the reduced peak temperature, and the critical

[3]The magnetometer cryostat was designed to accept the bulkier samples which could not be accommodated within the working volume of the SQUID susceptometer, and which were necessary to achieve sufficient sensitivity to perform an accurate critical analysis. However, a comparison of the data obtained at the two excitation frequencies showed that static fields $H_a \geq 40Oe$ were sufficient to essentially quench the time dependent component of the magnetic response in the vicinity of the ferromagnetic transition. Consequently the critical structure, and the associated critical analysis, are essentially frequency independent.

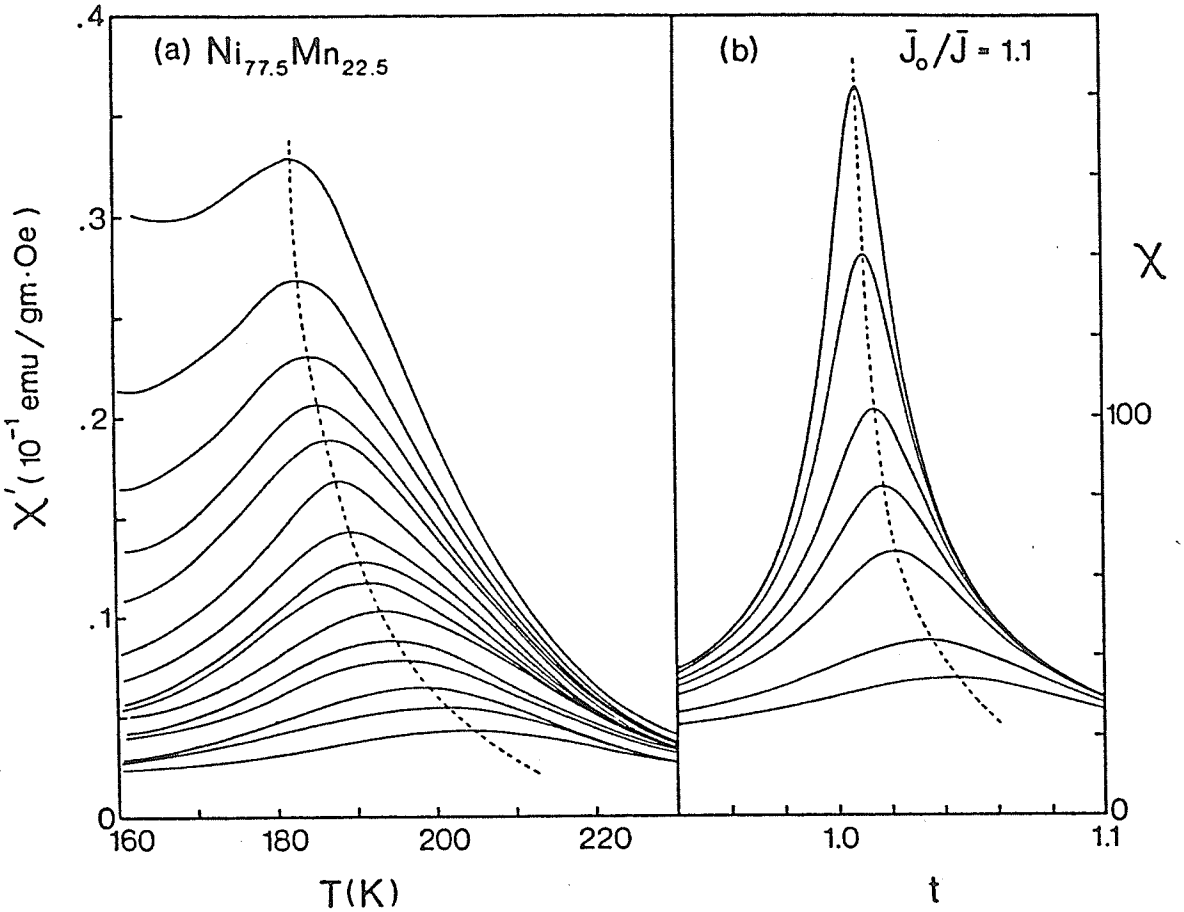

Figure 4.1.3-2: (a) A set of fifteen representative experimental ferromagnetic critical peaks measured at $\omega = 2400$ Hz in the following static fields H_a (in order of decreasing peak amplitude): 40.1, 50.1, 60.2, 70.1, 80.2, 100.2, 120.2, 140.0, 159.4, 200.4, 250.2, 300.0, 400.6, 501.5, and 704.0 Oe. The dashed curve is the locus of the maxima. (b) A set of representative model ferromagnetic critical peaks for $\bar{J}_0/\bar{J} = 1.1$ and $S = 5/2$, for the followed reduced fields h (in order of decreasing peak amplitude): 0.0002, 0.0003, 0.0005, 0.0007, 0.0010, 0.0020, and 0.0030.

exponents γ, β, and δ are related through the Widom equality $\gamma = \beta(\delta - 1)$. Such power laws have been confirmed numerically (Roshko and Williams, 1984), although the model necessarily yields mean field values for the exponents ($\gamma = 1, \beta = 1/2, \delta = 3$) which are not typical of real systems.

The first step in the experimental critical analysis was to establish the value of the ferromagnetic Curie temperature T_c, and since no rigorous criterion exists which correlates T_c with any particular feature of the zero field susceptibility in Figure 4.1.3-1(a), an indirect approach was necessary. According to Eq.(2.115), the critical peak temperature $T_m \rightarrow T_c$ as $h \rightarrow 0$, and Figure 4.1.3-3 shows a plot of the peak temperatures T_m as a function of internal field $H_i^{(\gamma+\beta)^{-1}}$, assuming a 3-D Heisenberg value (Le Guillou and Zinn-Justin 1980) for the exponent $(\gamma + \beta)^{-1} = 0.57$. At each peak temperature, the magnetization was evaluated by integrating the measured susceptibility with respect to the applied field, $M = \int_0^{H_a} \chi'_{meas}(T_m, H_a) dH_a$, and the internal field was then determined from the relation $H_i = H_a - DM$. The straight line in Figure 4.1.3-3 represents a fit to the asymptotic low field data, and the extrapolation to $H_i = 0$ gives a value of $T_c = 166.6 \pm 1.5K$, which lies just above the Hopkinson maximum.

In order to determine the critical exponent γ, which describes the temperature dependence of the zero field susceptibility, through $\chi'(H_i = 0, t) \propto t^{-\gamma}$ (Eq.(2.117)), a double logarithmic plot of $\chi'(0, t)$ as a function of reduced temperature t was constructed, using the value of T_c obtained above. As shown in Figure 4.1.3-4(a), this plot exhibits continuous curvature for all temperatures $T > T_c$, with a local slope which increases monotonically as a function of temperature. The straight line in this figure, which represents the mean field Curie-Weiss behaviour for $\gamma = 1$, has been included in order to emphasize the anomalous characteristics of the zero field susceptibility in this system which unlike other strongly disordered ferromagnets, shows no tendency to approach the mean field regime

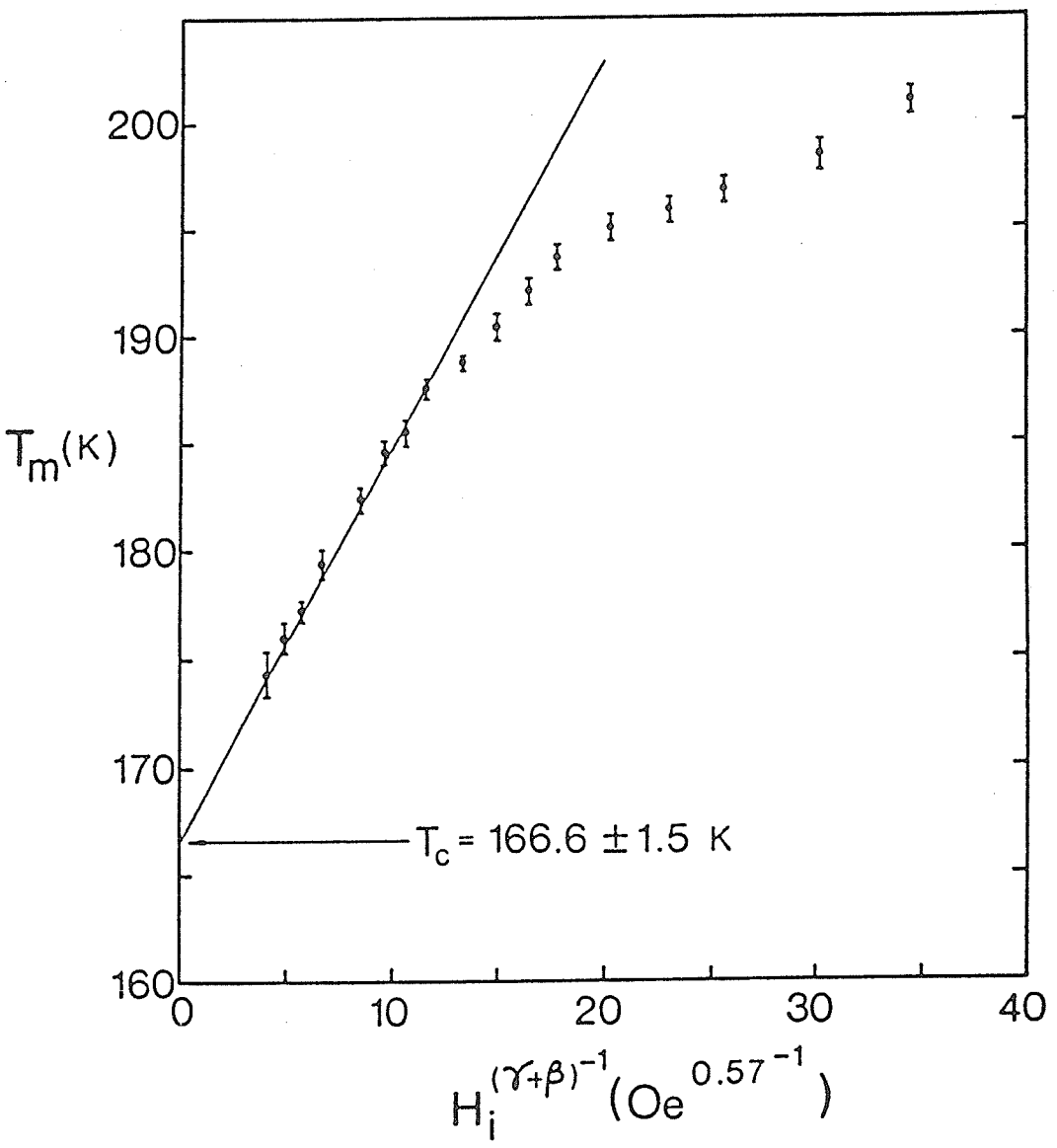

Figure 4.1.3-3: A plot of the experimental ferromagnetic critical peak temperatures $T_m(K)$ as a function of $H_i^{1/(\gamma+\beta)}$, where H_i is the internal field. The extrapolation of the straight line through the low field data to $H_i = 0$ yields the Curie temperature T_c.

for $T \gg T_c$. [4]. This latter behaviour, when translated into the language of an effective Kouvel-Fisher exponent (Kaul 1985)

$$\gamma^*(t) \equiv -\frac{\partial \ln \chi'(0,t)}{\partial \ln t}$$

means that γ^* assumes values which are so high ($\gamma^* \sim 10$) that it can no longer be regarded as a legitimate critical exponent (at least at temperatures well above T_c). Anomalously high values for the exponent γ^* have also been recorded in the PdMn (Ho et al., 1981b) and FeZr (Reisser et al., 1988) systems, and appear to be a characteristic of extensive exchange bond disorder. While such effects are also expected to occur in the present system, which lies reasonably close to the multicritical point where $\overline{J} \cong \overline{J_0}$, the situation here is undoubtedly complicated further by the tendency to form localized regions of the atomically ordered Ni_3Mn phase, which must contribute at least in part to the anomalous behaviour of $\chi'(0,t)$ (although the preparation techniques employed in the present investigation should produce optimal conditions with a minimum of short range order). Nevertheless, as the insert in Figure 4.1.3-4(a) shows, the Kouvel-Fisher analysis does yield reasonable values for $\gamma^*(t)$ for reduced temperatures $t \leq 0.15$ and furthermore, the exponent assumes its 3-D Heisenberg value $\gamma^* = 1.38$ at $t = 0.116$ ($T = 186$ K) which coincides with the inflection point in the zero field susceptibility.

According to Eq.(2.116), the field dependence of the critical peak amplitude is governed exclusively by the exponent δ, and Figure 4.1.3-4(b) shows a double logarithmic plot of the critical peak heights $\chi'(H_i, T_m)$ as a function of internal field H_i. The plot reveals two regimes corresponding to different values of δ^*: an asymptotic low field regime ($H_i < 40$ Oe) with $\delta^*_{LF} = 5.0 \pm 0.3$, which agrees with

[4]While it may be tempting to dismiss it as a pathological property of this particular sample, perhaps related to an excessive degree of short range order generated by a flaw in the preparation procedure, it should be pointed out that it is a consistent, reproducible feature of all samples of a similar geometry obtained from the same ingot, using a technique designed to minimize the formation of atomically ordered Ni_3Mn islands. It is also not an artifact of the experimental measurement technique, since it is also a characteristic of zero field SQUID measurements performed independently at the lower excitation frequency of 16 Hz.

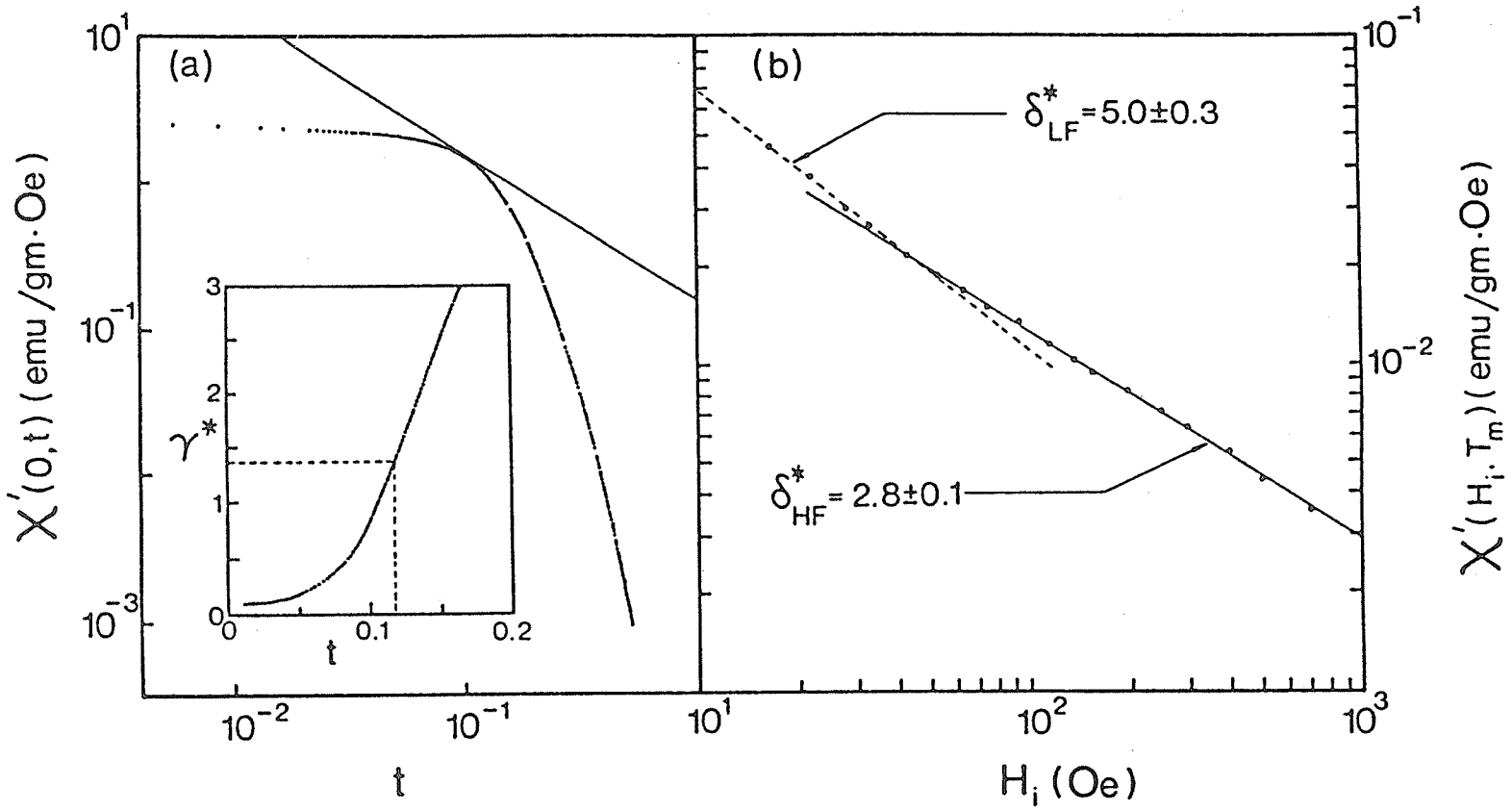

Figure 4.1.3-4: (a) A double-logarithmic plot of the zero-field susceptibility $\chi'(0,t)$ at ω = 2400 Hz as a function of reduced temperature t. The straight line represents the mean-field Curie-Weiss law for γ =1. The insert shows the effective Kouvel-Fisher exponent γ^* obtained from the measured zero-field susceptibility, and the dashed lines correspond to γ^* = 1.38 and t = 0.116. (b) A double-logarithmic plot of the measured ferromagnetic critical peak heights $\chi'(H_i, T_m)$ as a function of internal field H_i.

the 3-D Heisenberg model prediction of $\delta = 4.8$ within experimental error, and a high field regime ($H_i > 40$ Oe) with $\delta^*_{HF} = 2.8 \pm 0.1$, which is essentially the mean field prediction $\delta = 3$. The existence of two regimes is a feature of other bond disordered systems (Ho et al. 1981a,b), and the variation of δ^* with internal field is consistent with numerical calculations based on the effective field Ising model. According to our discussion in section 2.3.3 (Figure 2.3-3), the effective exponent δ^* should decrease with increasing field for large values of $\eta = \overline{J}/\overline{J_o}$ which corresponds to large exchange bond disorder.

The reentrant transition is accompanied by a double-peaked structure in the susceptibility (see Figure 4.1.3-1); both components are suppressed in amplitude and shifted downward in temperature by the application of successively higher static magnetic fields. Each isokap in Figure 4.1.3-1(b) is also characterized by a temperature interval, commencing below the low temperature peak and terminating roughly midway between the minimum and the higher temperature peaks, over which the magnetic response is time-dependent and irreversible: when the temperature is increased incrementally and then stabilized, the magnetization (which can be monitored simultaneously with the susceptibility in the SQUID system) continues to relax upward while the susceptibility relaxes downward. The higher temperature (reversible) peak is quite broad and asymmetric and, for a given field, has an amplitude which is considerably larger than that of the corresponding ferromagnetic critical peak; this component is typical of all reentrant systems while, as mentioned earlier, the low temperature (irreversible) peak is not universal. The behaviour of the low temperature peak is illustrated in detail in Figure 4.1.3-5, in a variety of static magnetic fields and at both excitation frequencies. The systematics of the two sets of data are qualitatively similar, although there is clearly a substantial reduction in response associated with the higher excitation frequency, which reflects the presence of a broad spectrum of relaxation times.

The multiple reentrant structure in the susceptibility is reminiscent of the t-

wo reentrant phase boundaries predicted by vector spin models of isotropic bond disordered ferromagnets discussed in section 2.2.2. Guided by the theoretical predications about the field dependence of the GT and AT critical temperatures $T_{GT}(0) - T_{GT}(H_a) \sim {H_a}^2$ (Eq.(2.81)) and $T_{AT}(0) - T_{AT}(H_a) \sim {H_a}^{2/3}$ (Eq.(2.83)), the temperatures of the two peaks were plotted as a function of applied field H_a and extrapolated to $H_a = 0$, yielding ${T_P}^U = 86 \pm 2$ K for the upper peak and ${T_P}^L = 46 \pm 1$K for the lower peak, and then double-logarithmic plots of reduced peak temperature $t_P = 1 - T_P(H_a)/T_P(0)$ versus H_a were then constructed. While the upper peak displayed *no* simple power-law dependence, the field dependence of lower peak temperature measured at an excitation frequency of $\omega = 2400$ Hz was well described by ${H_a}^{\psi}$ with $\psi = 0.58 \pm 0.10$ (see the insert in Figure 4.1.3-5), which agrees, within the experimental error, with both the AT exponent $\psi = 2/3$ and with Monte Carlo calculations $\psi_{MC} \simeq 0.55 - 0.7$ (Bhatt and Young, 1985).

Numerical simulations (Kornik et al., 1989), based on the mean field Ising model in connection with the ferromagnetic critical analysis, have shown that the reentrant ferromagnetic-spin glass phase boundary is characterized by critical singularities in the nonlinear components of the susceptibility, both above and below the reentrant transition temperature. The direct paramagnetic-spin glass transition is also distinguished by similar nonlinear singularities (see Figure 1-9), and hence evidence for critical behaviour in the vicinity of the reentrant phase boundary of $Ni_{77.5}Mn_{22.5}$ was sought in the leading field dependent terms in the susceptibility. Figure 4.1.3-6(a) shows a set of representative demagnetization-corrected susceptibility isotherms measured at $\omega = 16$ Hz for various temperatures between 46 and 160 K, plotted as a function of internal field over the range $0 \leq H_i \leq 25$Oe. The gradual increase in the low field curvature of these isotherms as the temperature increases suggests a corresponding enhancement in the nonlinear components of the susceptibility, and a plot of these isotherms as a function of ${H_i}^2$ is indeed characterized by an initial slope $a_2(T)$ which increases with increasing

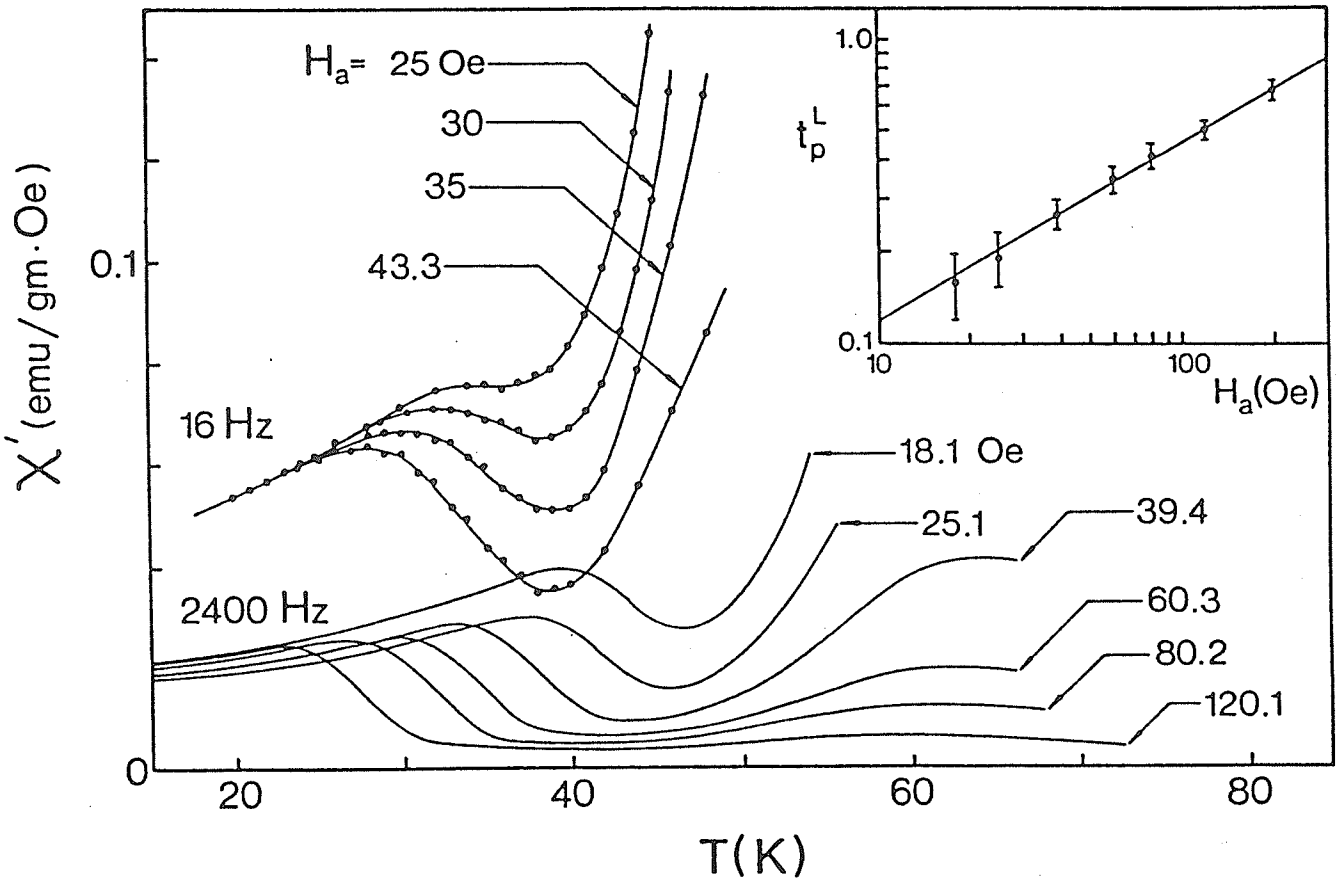

Figure 4.1.3-5: A comparison of the field and temperature dependence of the lowest-temperature component of the triple-peaked structure in Fig.4.1.3-1(b) at the two excitation frequencies ω = 16 Hz and ω = 2400 Hz, in various static magnetic fields H_a. The insert is a double-logarithmic plot of the reduced peak temperature at 2400 Hz as a function of applied static field H_a, and the straight line yields the exponent ψ.

temperature, while its range of validity along the field axis continuously decreases (see Figure 4.1.3-6(b)). Moreover, as the insert in Figure 4.1.3-6(b) shows, the initial slope (which represents the amplitude of the leading quadratic term in the nonlinear susceptibility) does indeed exhibit an anomalous peak, as expected, at $T = 60$ K, which is also the temperature T_K of the reentrant knee in the zero field susceptibility (see Figure 4.1.3-1(a)). A similar anomaly has also been observed in a reentrant (PdFe)Mn alloy (see Figure 1-10) (the variation in $a_2(t)$ with reduced temperature t in (PdFe)Mn is comparable to that observed here, to within a factor of 2), and the model simulations indicate that, in both instances, it is the longitudinal manifestation of the transverse nonlinear critical singularity.

The preceding analysis of the low field response of $Ni_{77.5}Mn_{22.5}$ shows a system which is predominantly a soft ferromagnet at "high" temperatures ($60K < T < 170K$), with a Curie temperature $T_c = 166.6 \pm 1.5$ K, which undergoes a transition, below about 60 K, to a highly irreversible state with spin glass characteristics. The effective exponent δ^*, obtained from the field dependence of the ferromagnetic critical peak heights, exhibits an asymptotic low field value ($\delta^*_{LF} = 5.0 \pm 0.3$) which is consistent with a 3-D Heisenberg picture, while, at higher fields, a crossover occurs to a (mean field) regime characterized by a much lower value of the exponent ($\delta^*_{HF} = 2.8 \pm 0.1$). While similar behaviour has been observed in a number of other ferromagnetic systems with nominally reentrant characteristics, including PdMn (Ho et al. 1981b), PdNi (Wang et al., 1990), and (PdNi)Mn (Hall et al., 1984), where it appears to be correlated with the width of the exchange bond distribution, becoming more pronounced as the tricritical point is approached, it is not typical of all reentrant systems. In particular, AuFe (Kleiman et al., 1982), FeZr (Saito et al., 1986), and (PdFe)Mn (Kunkel and Williams, 1988) can be described quite adequately (over a comparable range of fields) by only a single value of δ^*. Nevertheless, as discussed in section 2.3.3 double logarithmic plots for calculated susceptibility peak heights $\chi(h, t_m)$ versus reduced field h display a similar

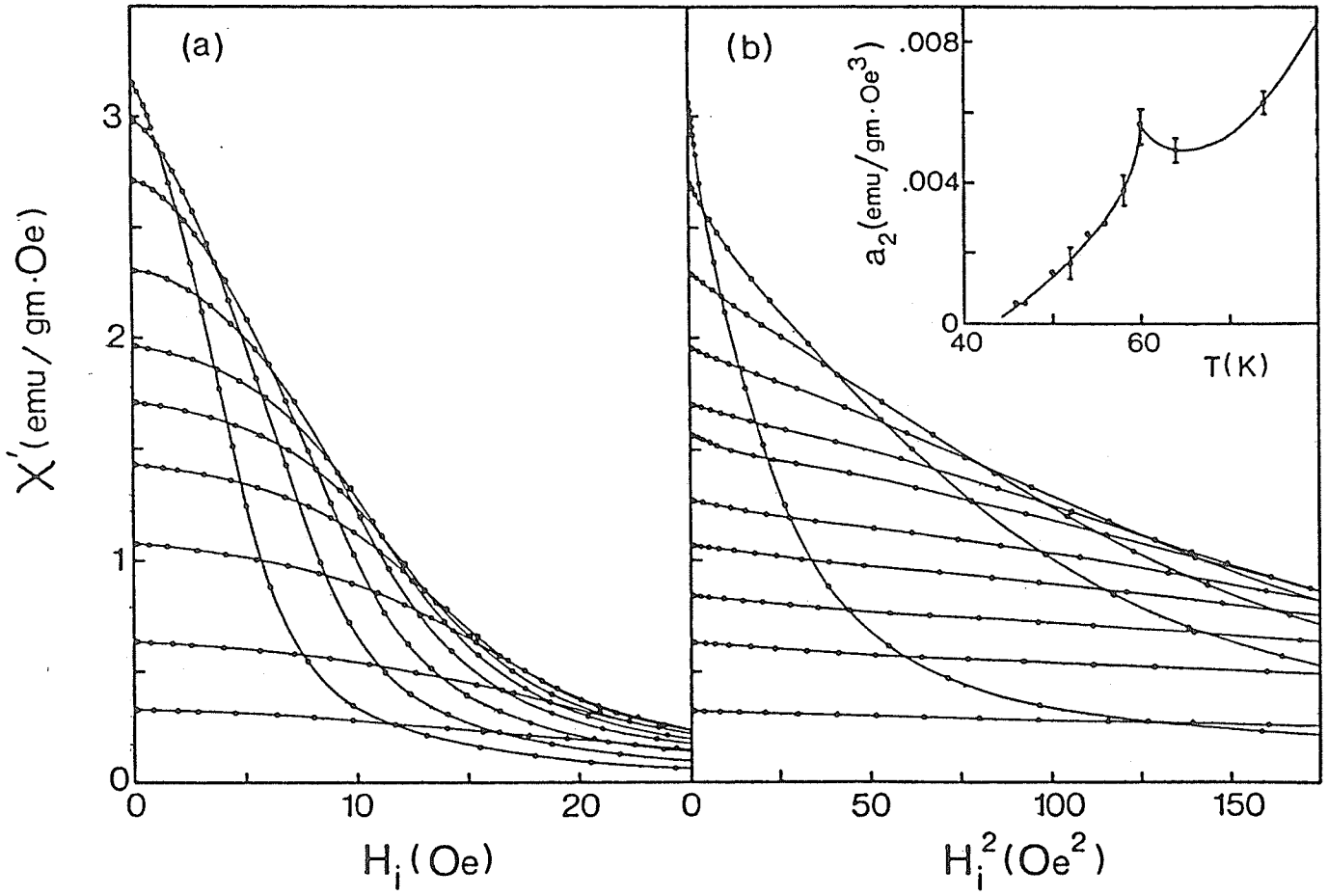

Figure 4.1.3-6: (a) A set of representative susceptibility isotherms measured at ω = 16 Hz as a function of internal field H_i for the following temperatures (in order of increasing vertical intercept): T = 46, 50, 54, 58, 64, 74, 90, 115, 140, and 160 K. (b) A set of isotherms plotted as a function of H_i^2 for T = 46, 50, 54, 58, 60, 64, 74, 90, 115, 140 and 160 K. The insert shows the anomaly in the temperature dependence of the amplitude of the leading nonlinear (quadratic) term.

systematic variation of δ^* with field h. As Figure 2.3-3 shows, the true value of the model critical exponent ($\delta = 3.0$) is observed only in the asymptotic limit $h \rightarrow 0$; as h increases, the plots exhibit curvature, with a local slope which indicates a progressively decreasing value of δ^*, and this effect becomes more pronounced as $\overline{J_o}/\overline{J} \rightarrow 1^+$ and the disorder increases. (The model predicts a curvature of opposite sign for a pure ferromagnet with $\overline{J}/\overline{J_o} = 0$).

The behaviour of the zero field susceptibility in Figure 4.1.3-4(a) is unusual. While values of the Kouvel-Fisher exponent γ^* as high as ~ 3 have been observed in other reentrant systems (Ho et al. 1981b) close to the tricritical point, this behaviour is typically accompanied by a maximum in the temperature dependence of γ^* (Saito et al., 1986) (or equivalently, by an inflection point in $\log\chi'(0,t)$ versus $\log t$) so that, at higher reduced temperatures, the exponent shows a tendency to approach its mean field value $\gamma = 1$. Nevertheless, in spite of the anomalous high temperature ($T \gg T_c$) properties of $\chi'(0,t)$ and $\gamma^*(t)$ (which raises some doubts concerning the eligibility of γ^* as a proper critical exponent in this regime), γ^* does assume its 3-D Heisenberg value ($\gamma = 1.38$) at a temperature close to the inflection point in the zero field susceptibility, which coincidentally also marks the onset of noncritical processes (such as domain formation) which effectively disguise the existence of a spontaneous magnetization and suppress the critical divergence of the susceptibility. (In fact, it is the proximity of the domain-related Hopkinson maximum which accounts for the abrupt flattening of the temperature dependence of γ^* as $t \rightarrow 0$ below the inflection point.)

The low field dynamic response in the neighbourhood of the reentrant transition reveals some rather intriguing multiple structure which appears to support the sequential transition hypothesis. Numerical simulations based on a mean field Sherrington-Kirkpatrick-like Ising model (Kornik et al., 1989) with a single critically reentrant F-SG phase boundary, show that the reentrant transition is accompanied by a susceptibility peak within the reentrant SG phase with the same sys-

tematic suppression in amplitude and shift to lower temperatures with increasing field which is observed in the experimental peaks. This similarity in systematics, coupled with the observation that the upper and lower peaks are distinguishable on the basis of weak versus strong irreversibility, respectively, and with the AT-like exponent which describes the field dependence of the lower peak temperature, provide compelling evidence that the two reentrant susceptibility peaks are manifestations of the two orthogonal spin freezing processes permitted for Heisenberg spin systems: (a) a critical spin glass ordering of the transverse spin components along a GT line coincident with the location of the upper peak, and (b) the onset of strong longitudinal irreversibility along an AT line defined by the position of the lower peak.

Further evidence in favour of genuine critical behaviour at the reentrant transition is provided by the anomaly observed in the temperature dependence of the leading nonlinear term in the susceptibility isotherms in the vicinity of the reentrant knee $T_K = 60$ (see insert in Figure 4.1.3-6(b)) [5]. For "pure" spin glasses, in which the order parameter couples directly to the nonlinear components of the magnetic response, nonlinear anomalies are the primary source of evidence for critical behaviour. If the reentrant transition is indeed a genuine cooperative effect with elements of spin glass order, it should exhibit similar nonlinear characteristics. As discussed in section 2.3.3, this expectation is indeed confirmed by numerical calculations performed in the vicinity of the reentrant phase boundary of an SK-like Ising model, which predicts a critically divergent anomaly in the nonlinear susceptibility both above and below the reentrant temperature (Eq.(2.127)). Moreover, Katori and Suzuki (1985) have predicted that the longitudinal susceptibility in vector spin systems should exhibit a complementary nonlinear anomaly in

[5] A temperature-dependent nonlinear susceptibility also precludes thermally activated blocking processes as the primary mechanism for the formation of the reentrant phase, since superparamagnetic system are typically characterized by a temperature-independent nonlinear susceptibility (Fiorani et al.,1986)

response to transverse spin freezing. The structure in Figure 4.1.3-6(b) supports this hypothesis, and its nonsingular nature is consistent with the weak coupling anticipated between the transverse order parameter and the non-conjugate longitudinal field.

4.1.4 The Reentrant Instability Boundaries in a Reentrant $Ni_{78}Mn_{22}$ Alloy

In this section, we present measurements of the real and imaginary components of the complex frequency-dependent susceptibility of a good reentrant ferromagnet $Ni_{78}Mn_{22}$, as a function of field and temperature. We show the triple-peaked structure in the temperature dependence of the a.c. susceptibility in fixed static field, and we attempt to correlate the low temperature components of the multiple-peaked structure with the GT and AT instability boundaries.

Figure 4.1.4-1, and 4.1.4-2 shows the temperature dependence of the real part of the true complex susceptibility, measured in several static magnetic fields $H_a \leq$ 43 Oe, and appropriately corrected for demagnetizing effects. All of the data were acquired with the SQUID susceptometer, at an excitation frequency of 16 Hz. To obtain each isokap, the sample was first heated to a reference temperature $T_R = 250K$ in the paramagnetic regime to eliminate any remanence, then cooled in zero net field to $T = 4.2$ K where both the a.c. field and the static magnetic field were applied; the susceptibility was subsequently measured upon warming.

The susceptibility in zero static field (Figure 4.1.4-1) has a distinct principal (Hopkinson) maximum at $T_H = 175K$ and a more diffuse knee at $T_K = 52K$. The superposition of a static magnetic field collinear with the alternating field suppresses the principal Hopkinson maximum, and reveals the usual *triple-peaked* structure in the isokaps. Figure 4.1.4-2 illustrates the details of this structure.

The imaginary component χ'' of the complex susceptibility is plotted in Figure 4.1.4-3 and 4.1.4-4 as a function of temperature, for the same set of static fields as

in Figure 4.1.4-1 and 4.1.4-2. The reentrant structure in χ' is closely accompanied by a complementary structure in the absorption (or loss) signal χ'', although, for a given value of the applied field H_a, the two peaks in χ'' are shifted toward each other in temperature relative to the locations of their counterparts in χ'. Further comparison of Figure 4.1.4-2 and 4.1.4-4 also reveals quantitative differences in shape and definition between the two sets of peaks: the higher temperature peak is considerably more symmetric in χ'', while the lower temperature peak is resolvable in weaker applied fields in χ'. No counterpart in χ'' was observed within experimental error for the highest temperature ferromagnetic peak in χ'.

Further evidence for irreversibility in the reentrant phase is provided by comparing the magnetic response under field-cooled and zero-field-cooled conditions. Figure 4.1.4-5 shows the temperature dependence of the real and imaginary components of the susceptibility measured in a static field $H_a = 35$ Oe after cooling in zero field (solid curve) and in the measuring field (dashed curve). For temperatures below approximately 35 K, both χ' and χ'' are extremely sensitive to the cooling field, and, in particular, when the system is cooled in the measuring field, the lowest temperature peak is completely quenched. By contrast, field cooling has only a weak effect on the remaining structural features.

Figure 4.1.4-6 summarizes the field dependence of the various reentrant susceptibility peaks in Figures 4.1.4-1 to 4.1.4-4. As discussed previously, in vector models of bond disordered systems, spin-glass ordering of the transverse spin components occurs at the Gabay- Toulouse (GT) line, followed by longitudinal spin freezing and the onset of strong irreversibility at the de Almeida-Thouless (AT) line. For "pure" spin glasses, with a symmetric bond distribution (the ratio of the mean value $\overline{J_0}$ to the dispersion $\overline{J}$ is $\overline{J_0}/\overline{J} = 0$), the field dependence of the GT transition line is given by $T_{GT}(0) - T_{GT}(H_a) \sim {H_a}^2$ while, for the AT transition line, $T_{AT}(0) - T_{AT}(H_a) \sim {H_a}^{2/3}$. In the ferromagnetic regime ($\overline{J_0} > \overline{J}$), the GT and AT lines are associated with the formation of the reentrant phase,

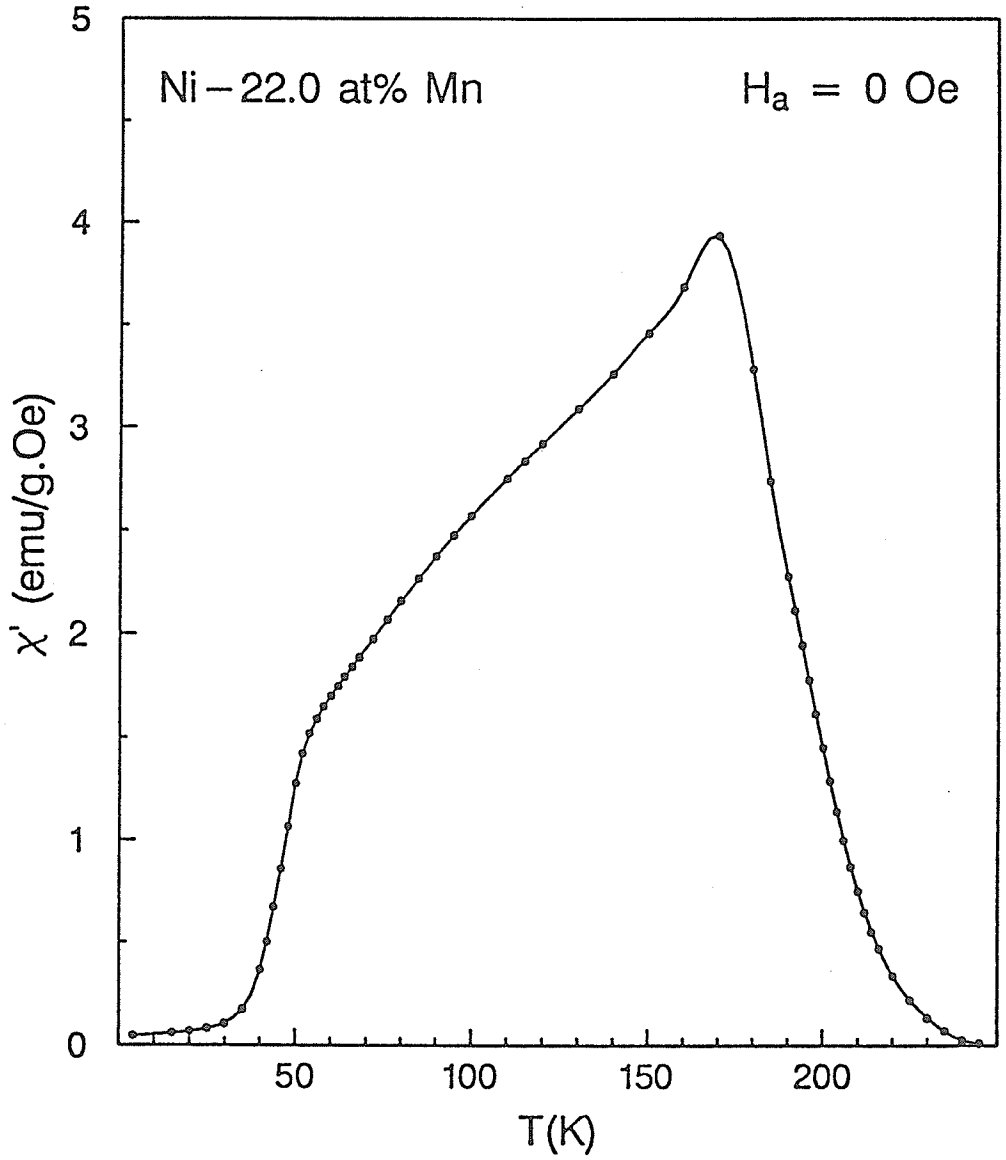

Figure 4.1.4-1: The temperature dependence of the real component χ' of the susceptibility in zero static magnetic field.

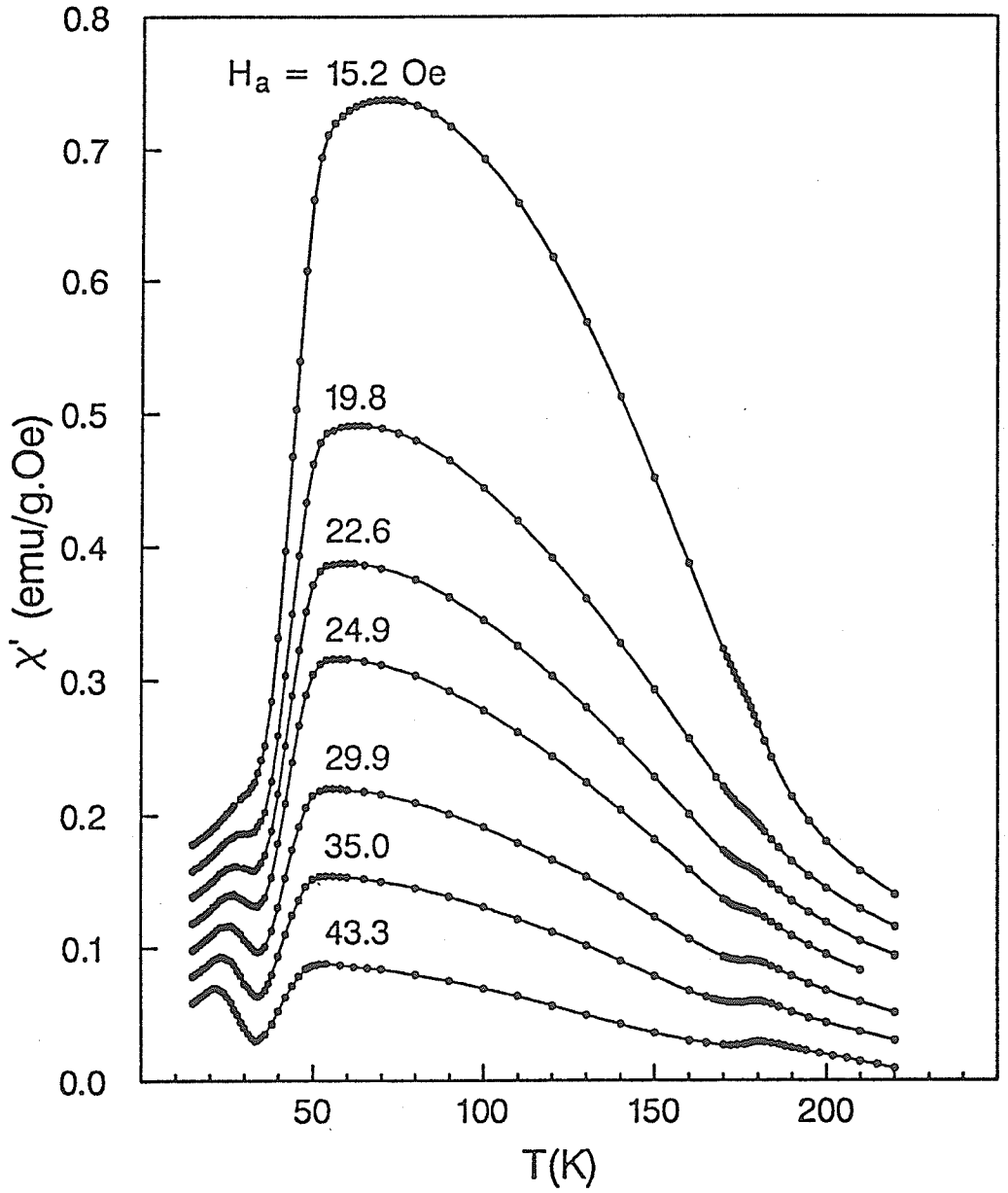

Figure 4.1.4-2: The temperature dependence of the real component χ' of the susceptibility in various static magnetic fields. (With the exception of the highest field data, successive curves have been displaced vertically by + 0.02 emu/gm Oe, for purposes of clarity.)

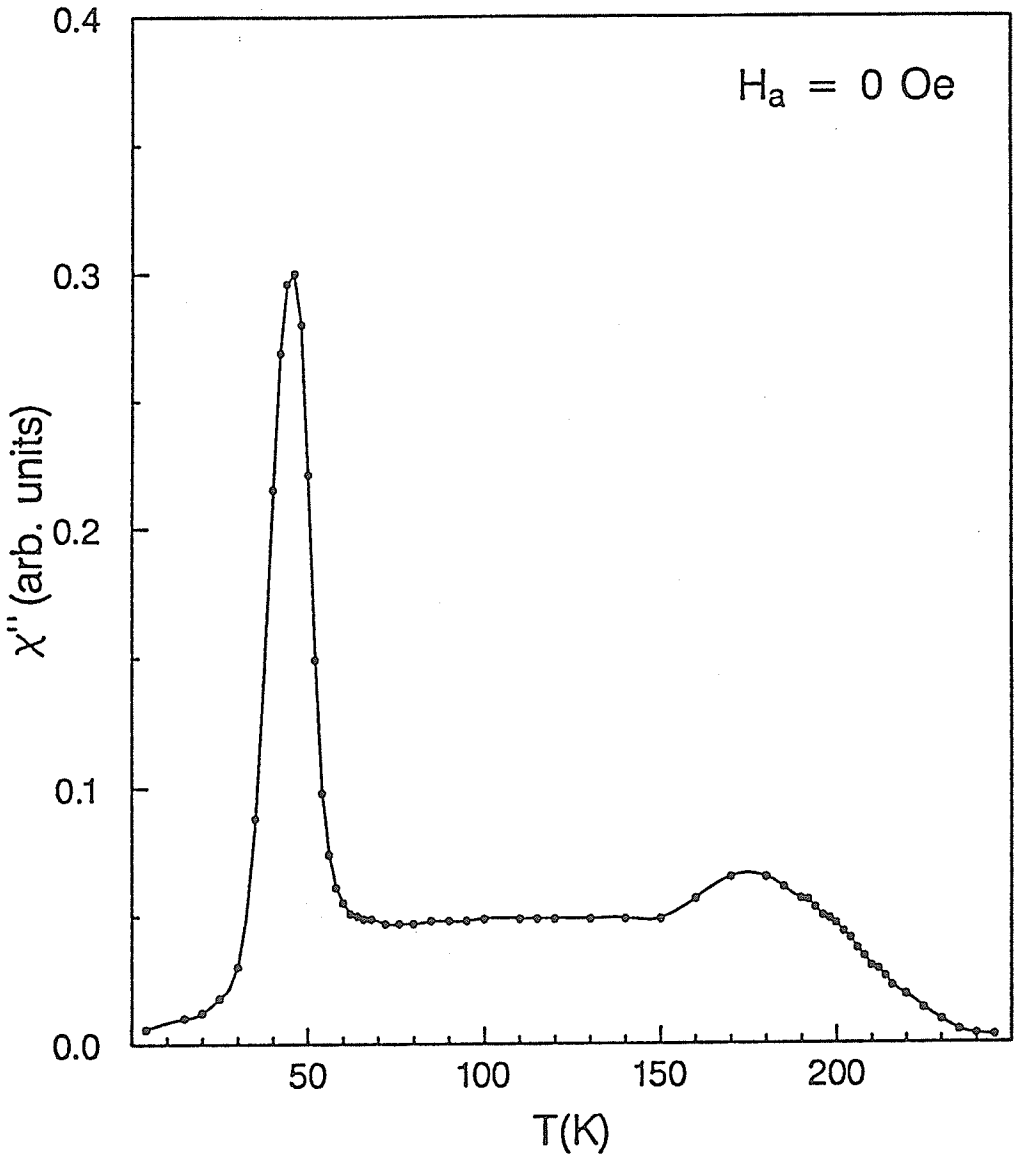

Figure 4.1.4-3: The temperature dependence of the imaginary component χ'' of the susceptibility in zero static magnetic field.

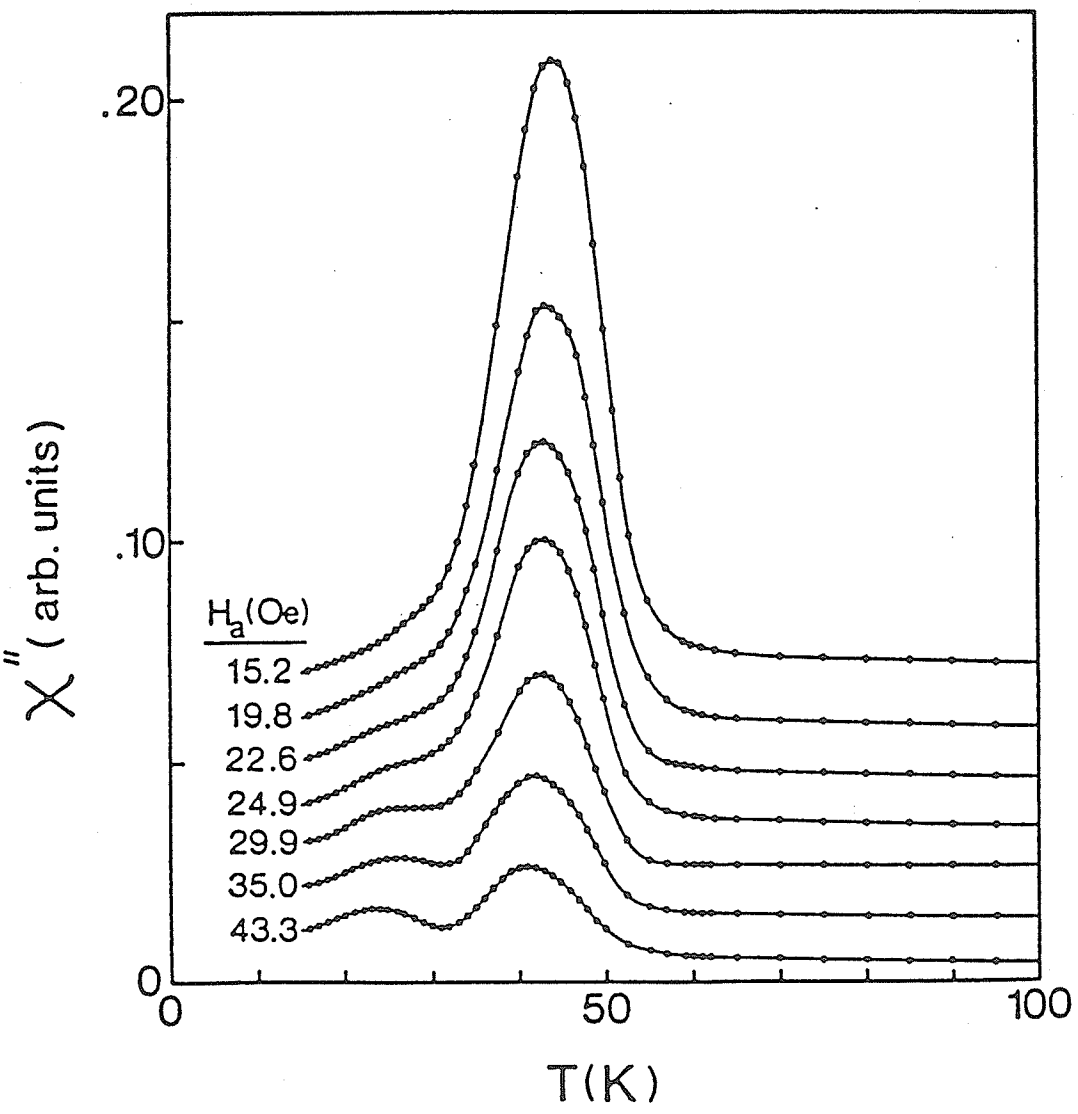

Figure 4.1.4-4: The temperature dependence of the imaginary component χ'' of the susceptibility in various static magnetic fields. (With the exception of the highest field data, successive curves have been displaced vertically by + 0.01 a.u.)

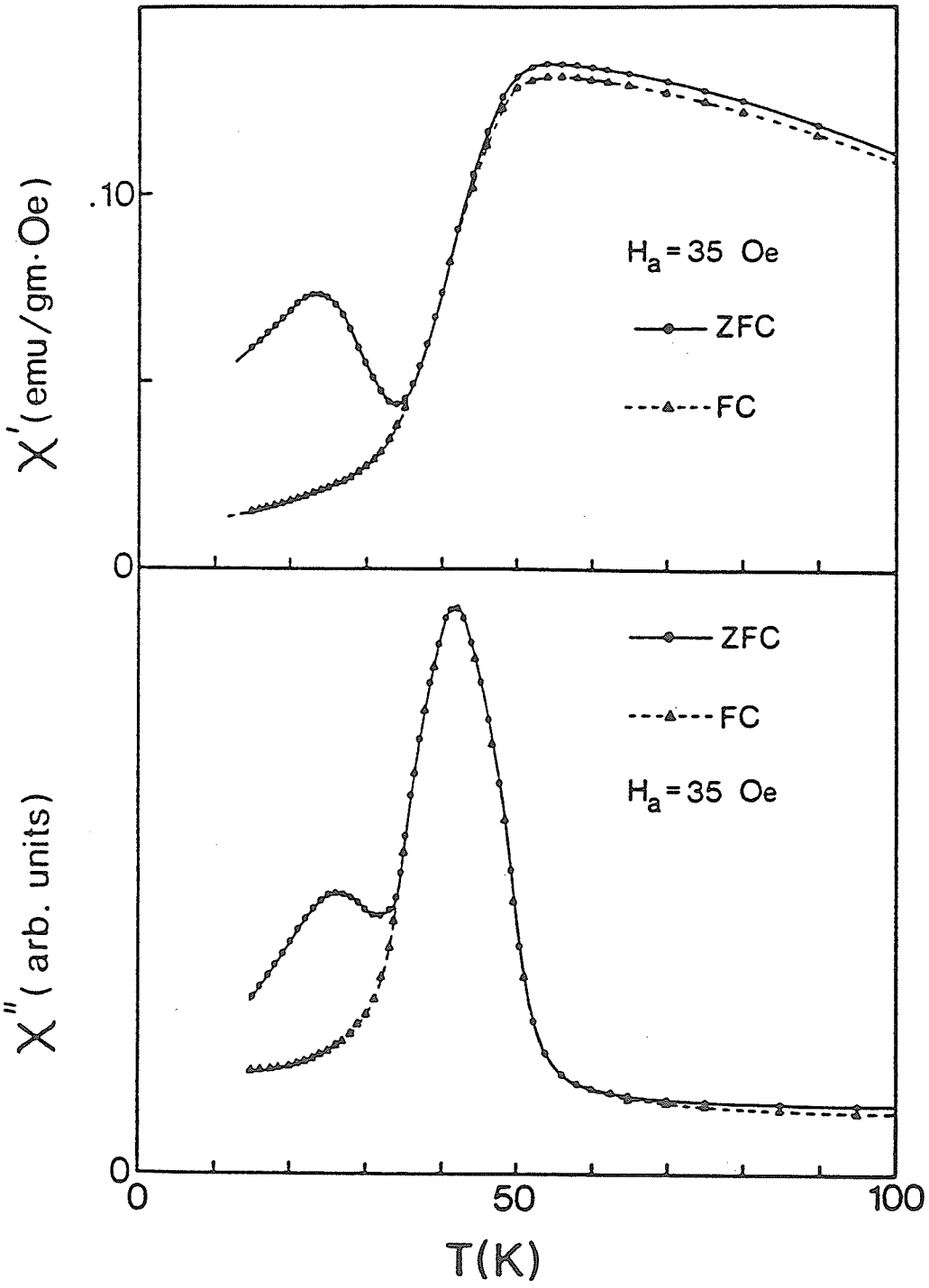

Figure 4.1.4-5: The real and imaginary components $\chi'$and χ'' under field-cooled (FC) and zero-field-cooled (ZFC) conditions in an external field H_a = 35 Oe.

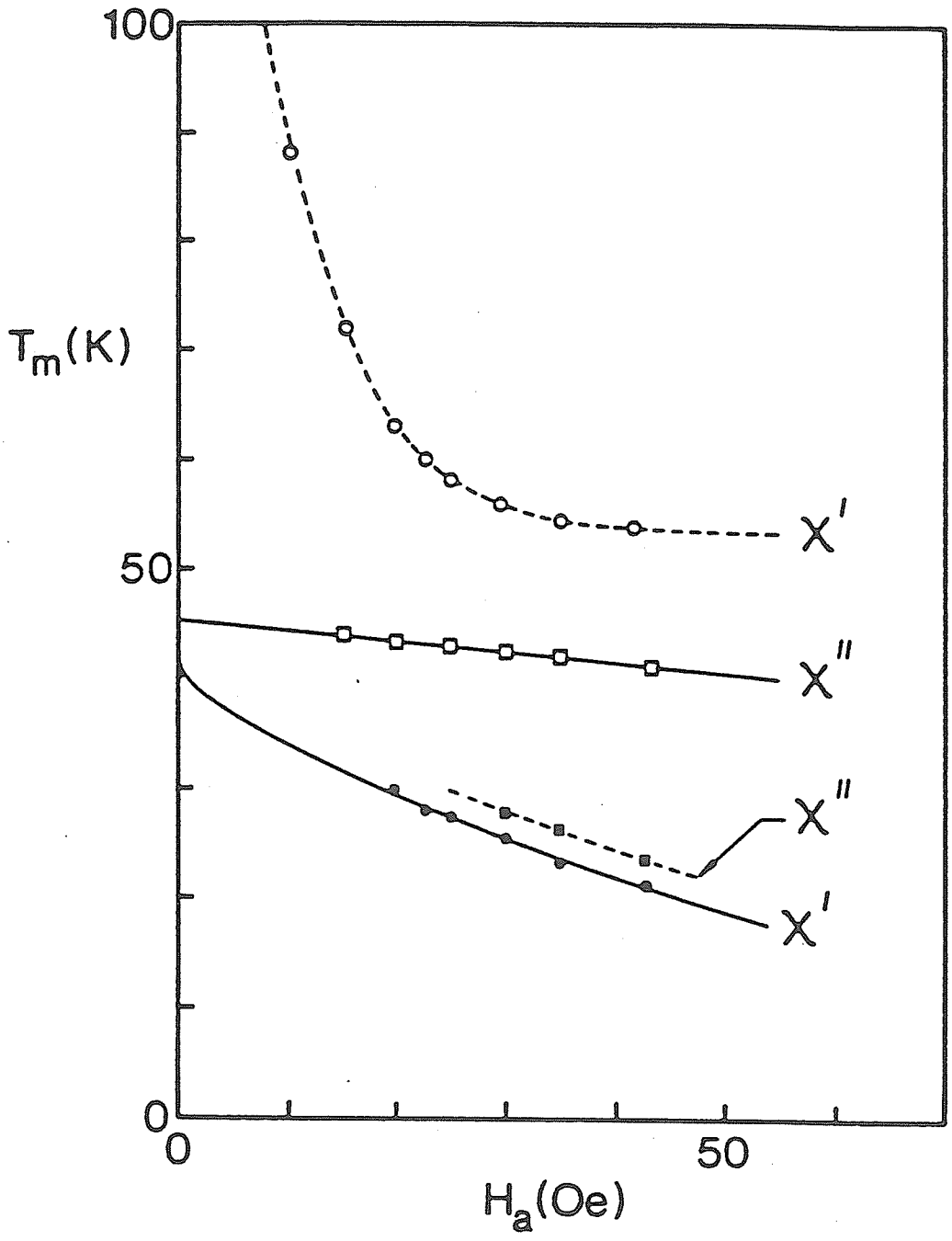

Figure 4.1.4-6: The applied field dependence of the peak temperature T_m for the various reentrant peaks in Figs.4.1.4-2 and 4. The solid lines are theoretical curves. (Error bars are approximately the size of the data points.)

which is essentially a canted ferromagnet with transverse spin-glass freezing and a longitudinal spontaneous magnetization. The behaviour of the reentrant critical line $T_{GT}(H_a)$ was investigated theoretically (Dubiel et al., 1987) within the ferromagnetic regime of a mean-field reentrant isotropic vector model; the calculations showed that, *close* to the critical point ($\overline{J_0} \geq \overline{J}$), the ferromagnetic state is strongly distorted and the critical temperature T_{GT} varies linearly as a function of external field: $T_{GT}(0) - T_{GT}(H_a) \sim H_a$.

Guided by these theoretical predictions, double logarithmic plots of reduced peak temperature as a function of applied field were constructed (with suitable choices for the zero-field "critical" temperatures) for each of the reentrant peaks in Figure 4.1.4-6. The high-temperature peak in χ' (open circles) obeys no simple power law. By contrast, the high-temperature peak in χ'' (open squares) varies linearly with applied field (solid straight line), as predicted for the reentrant GT line near the tricritical point. While there is insufficient data to reliably establish power law behaviour for the low-temperature peak in χ''(solid squares), the low-temperature peak in χ' (solid squares) is well described by a power law with an exponent reminiscent of the AT line, and the associated solid curve in Figure 4.1.4-6 represents a plot of $T_m(H_a) = T_m(0)(1 - CH_a{}^{\psi})$ with $\psi_{AT} = 0.66 \pm 0.05$, $T_m(0) = 41.5$ K, and $C = 0.039 \pm 0.002$. This analysis thus establishes a correlation between the structure observed in the complex dynamic susceptibility and the critical phase boundaries in the vector model phase diagram, with the high-temperature peak in χ'' a manifestation of the reentrant GT critical line, and the low-temperature peak in χ' the signature of the AT line. This identification is further reinforced by the comparison of the FC and ZFC data in Figure 4.1.4-5, which demonstrates that, like the GT and AT lines, the upper and lower peaks are also differentiated on the basis of weak and strong irreversibility, respectively.

4.1.5 The Critical Analysis of Nearly Tricritical $Ni_{76.4}Mn_{23.6}$

In this section, we present measurements of the low frequency complex dynamic susceptibility (both real and imaginary components) of a reentrant NiMn ferromagnet located very close to the multicritical point ($c_m \cong 24$ at.% Mn), as a function of both temperature (4.2K $\leq$ T $\leq$ 170K) and magnetic field ($0 \leq H_a \leq$ 46 Oe).

Figure 4.1.5-1 summarizes the temperature dependence of the real part χ' of the complex dynamic susceptibility, measured at an excitation frequency $\omega = 16$ Hz and appropriately corrected for demagnetizing effects, in a variety of representative static biasing fields between $H_a = 0$ Oe and $H_a = 45.0$ Oe. Each isofield was obtained by following an identical experimental procedure: the sample was cooled in zero magnetic field from a temperature $T = 170$ K (well within the paramagnetic regime) to $T = 4.2$ K, where both the excitation field and the static field were applied to the sample, and the susceptibility was then measured upon incremental warming. The magnetic response in zero static biasing field (Figure 4.1.5-1(a)) consists of a single, relatively sharp peak, superficially reminiscent of that observed in typical spin glass systems. However, this resemblance is deceptive and, as Figure 4.1.5-1(b) shows, the magnetic response in finite static biasing fields exhibits triple-peaked structure characteristic of reentrant ferromagnetism, with all the attendant systematics described earlier. Some elements of the structure associated with the dynamic response (Figure 4.1.5-1(b)) are particularly sensitive to the cooling conditions, and this is illustrated in Figure 4.1.5-2, which shows the differential susceptibility at 16 Hz measured upon warming in a static biasing field H_a=25 Oe, after cooling in various static fields H_c between $0 \leq H_c \leq 25$ Oe. For temperatures below approximately 55K, the presence of the cooling field inhibits the dynamic response, systematically suppressing and ultimately quenching the lowest temperature peak while the higher temperature peaks are not affected by different cooling fields. Figure 4.1.5-3 summarizes the variation of the three

peak temperatures T_p with internal field H_i. A rough extrapolation of these three curves to $H_i = 0$ (dashed lines in Figure 4.1.5-3) indicated that the system possesses three distinct "characteristic" temperatures, consistent with three sequential "transitions".

Figures 4.1.5-4 and 4.1.5-5 show the imaginary component χ'' of the complex dynamic susceptibility plotted as a function of temperature, for the same set of static biasing fields as in Figure 4.1.5-1(a) and (b). In contrast to Figure 4.1.5-1(a), the imaginary part of the ac susceptibility χ'' in zero field shows (Figure 4.1.5-4) a triple-peaked structure: the highest temperature peak occurs around 130 K, close to the high temperature knee ($\sim$ 130 K) in Figure 4.1.5-1(a), corresponding to the ferromagnetic transition, and the lowest temperature peak at 68 K correlates with the onset of the reentrant phase (although nothing unusual can be seen in χ' (Figure 4.1.5-1(a)) at this temperature). The very weak maximum around 100 K is situated at the temperature of the principle maximum in Figure 4.1.5-1(a). A comparison of Figure 4.1.5-5 and Figure 4.1.5-1(b) shows that with the application of a finite field, the two lower temperature peaks in χ' are accompanied by a complementary dual-peaked structure in the absorption (or loss) signal χ'', with similar field dependent and time dependent systematics, while the highest temperature peak in χ', attributed to ferromagnetic critical fluctuations, has no apparent counterpart in χ''.

While several features of the magnetic response in Figures 4.1.5-1 through 4.1.5-5 are consistent with a picture of reentrant ferromagnetism, the extreme proximity of the system to the multicritical point, and the attendant breadth of the exchange bond distribution, are expected to yield anomalous ferromagnetic critical properties. Following the same analytical techniques as those described in detail in section 4.1.3, a preliminary estimate for T_c was obtained by plotting the critical peak temperatures T_p as a function of $H_i^{1/(\gamma+\beta)}$, and extrapolating to $T_p \rightarrow T_c$ as $H_i \rightarrow 0$, assuming a 3-D Heisenberg value of $(\gamma+\beta)^{-1} = 0.57$; this

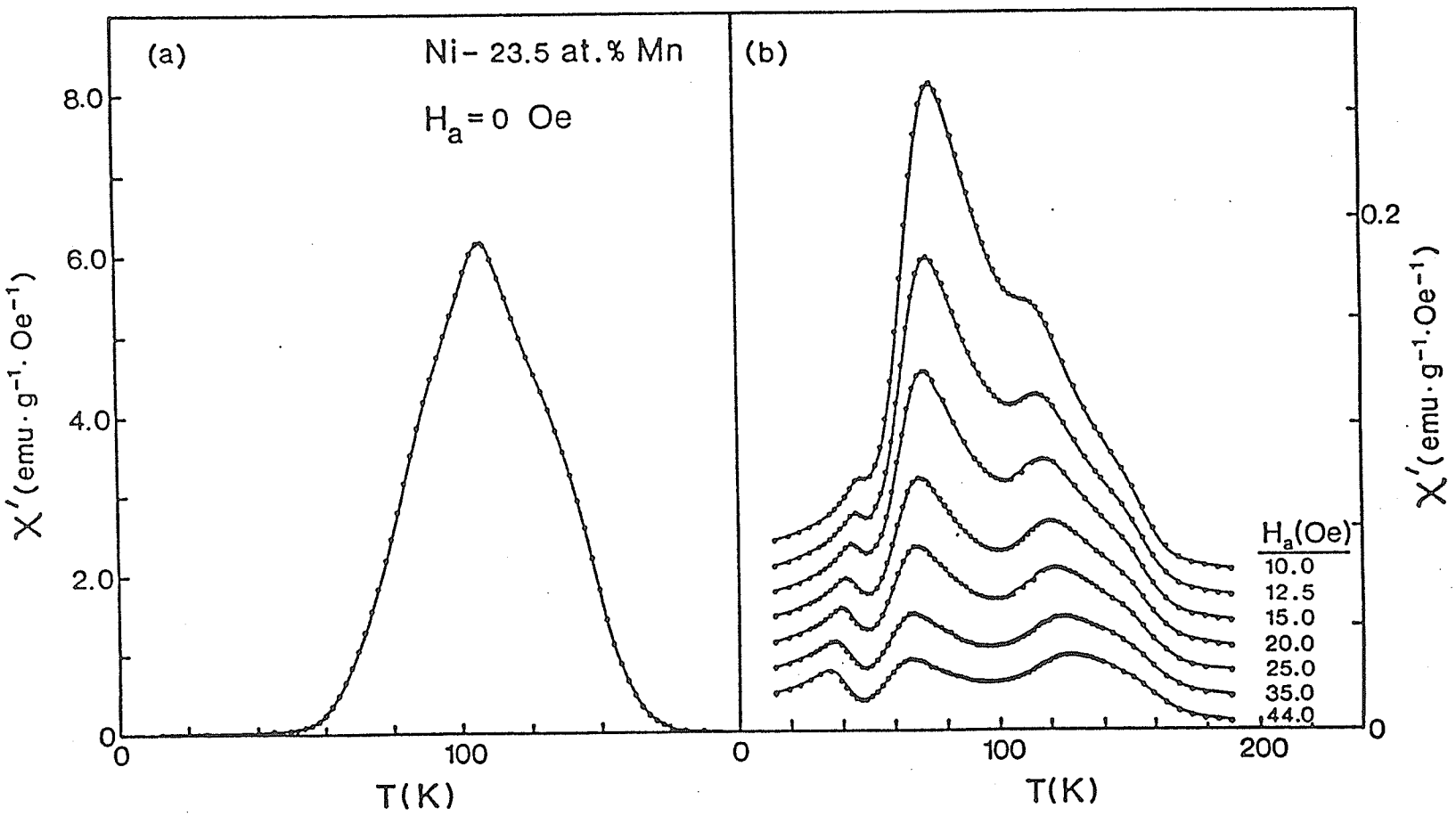

Figure 4.1.5-1: (a) Temperature dependence of the real part χ' of the dynamic susceptibility in zero static biasing field. (b) Temperature dependence of χ' in several representative static biasing fields H_a between 10 Oe and 44 Oe. For purposes of clarity, successive isofields have been separated vertically by +0.01 emu/gm-Oe, so that the vertical scale applies only to the 44 Oe isofield.

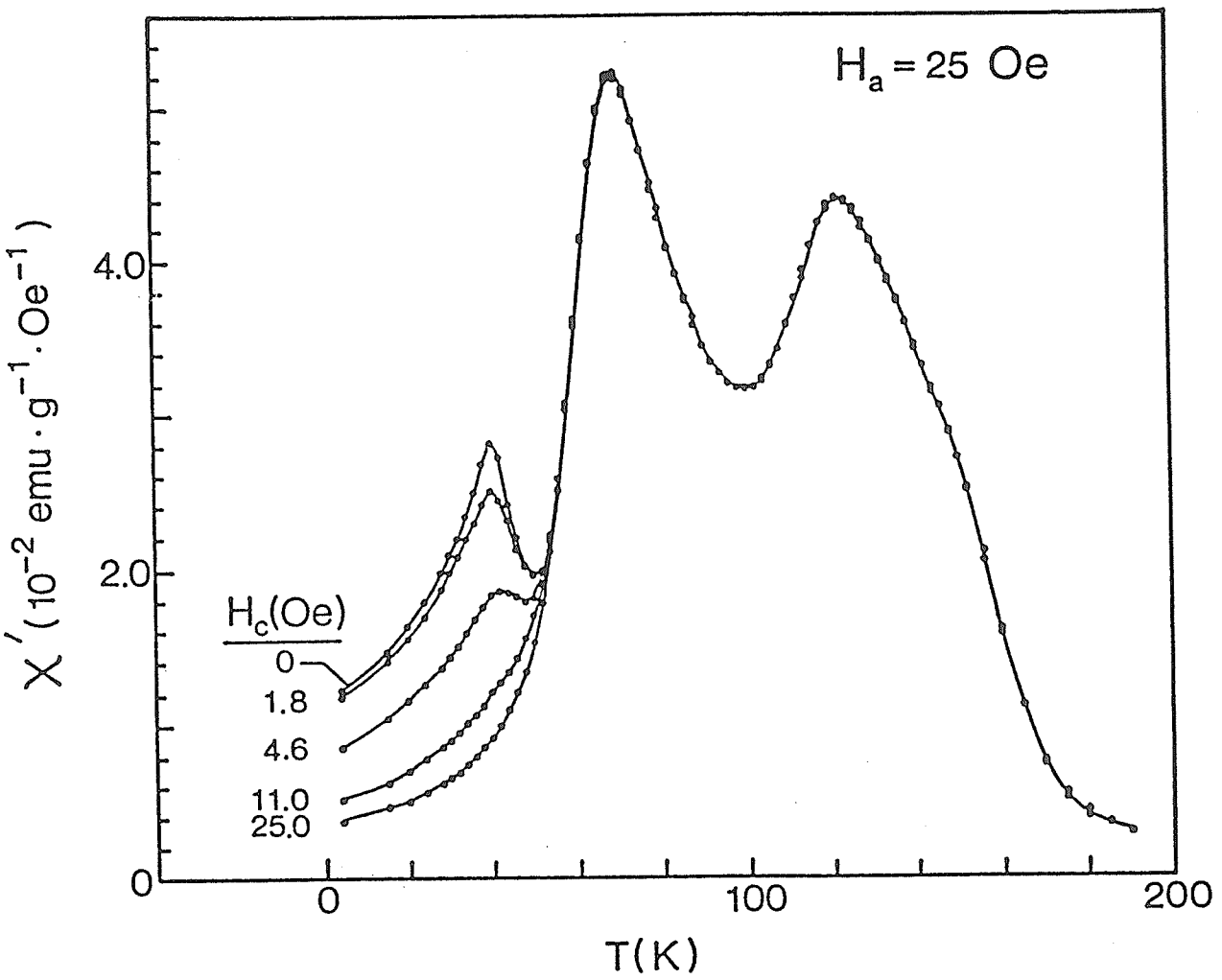

Figure 4.1.5-2: Temperature dependence of the real susceptibility χ' measured in a static biasing field H_a = 25 Oe, after cooling in various static fields H_c between 0 Oe and 25 Oe.

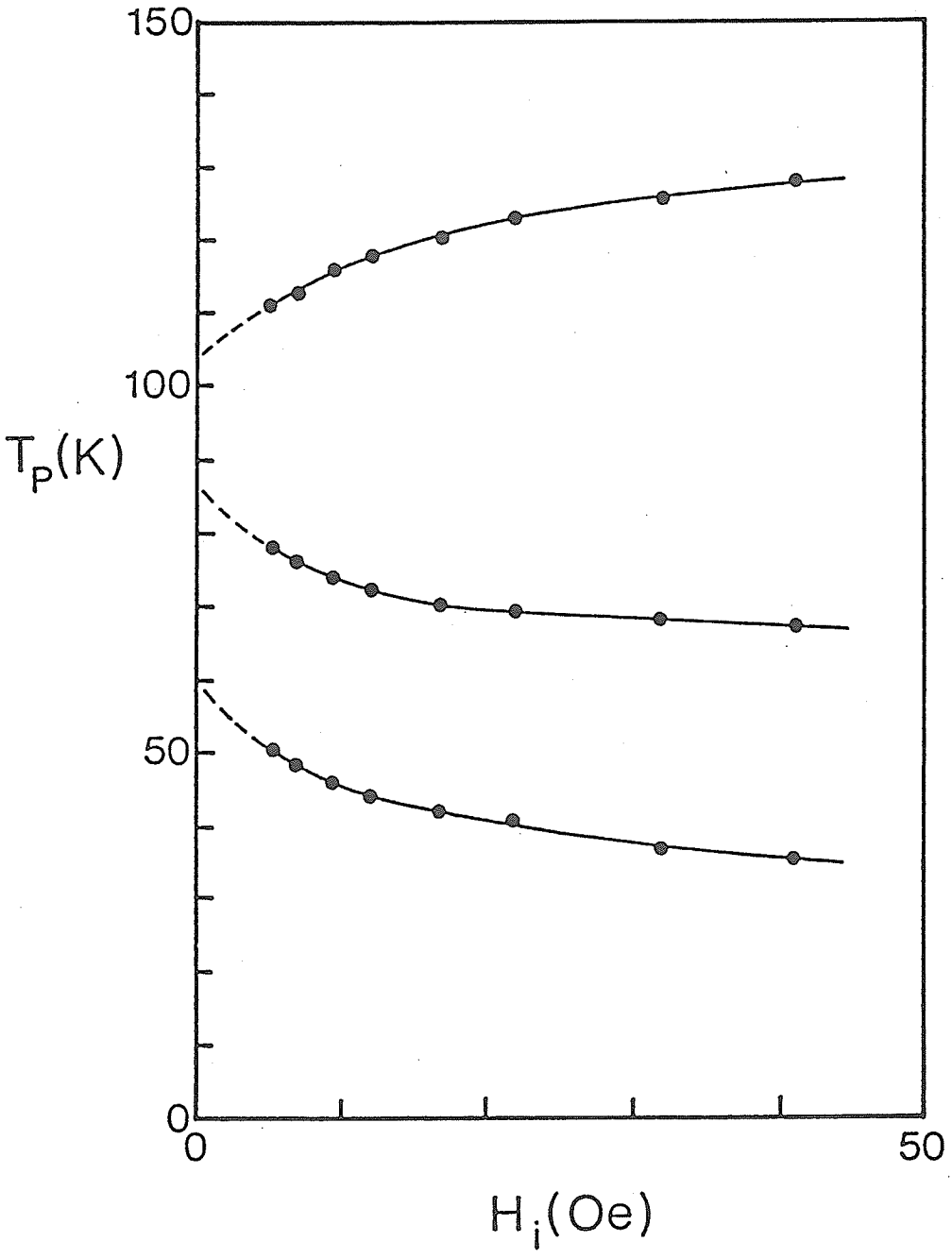

Figure 4.1.5-3: Internal field dependence of the temperatures of the three peaks in χ'. The dashed lines are an extrapolation to zero internal field.

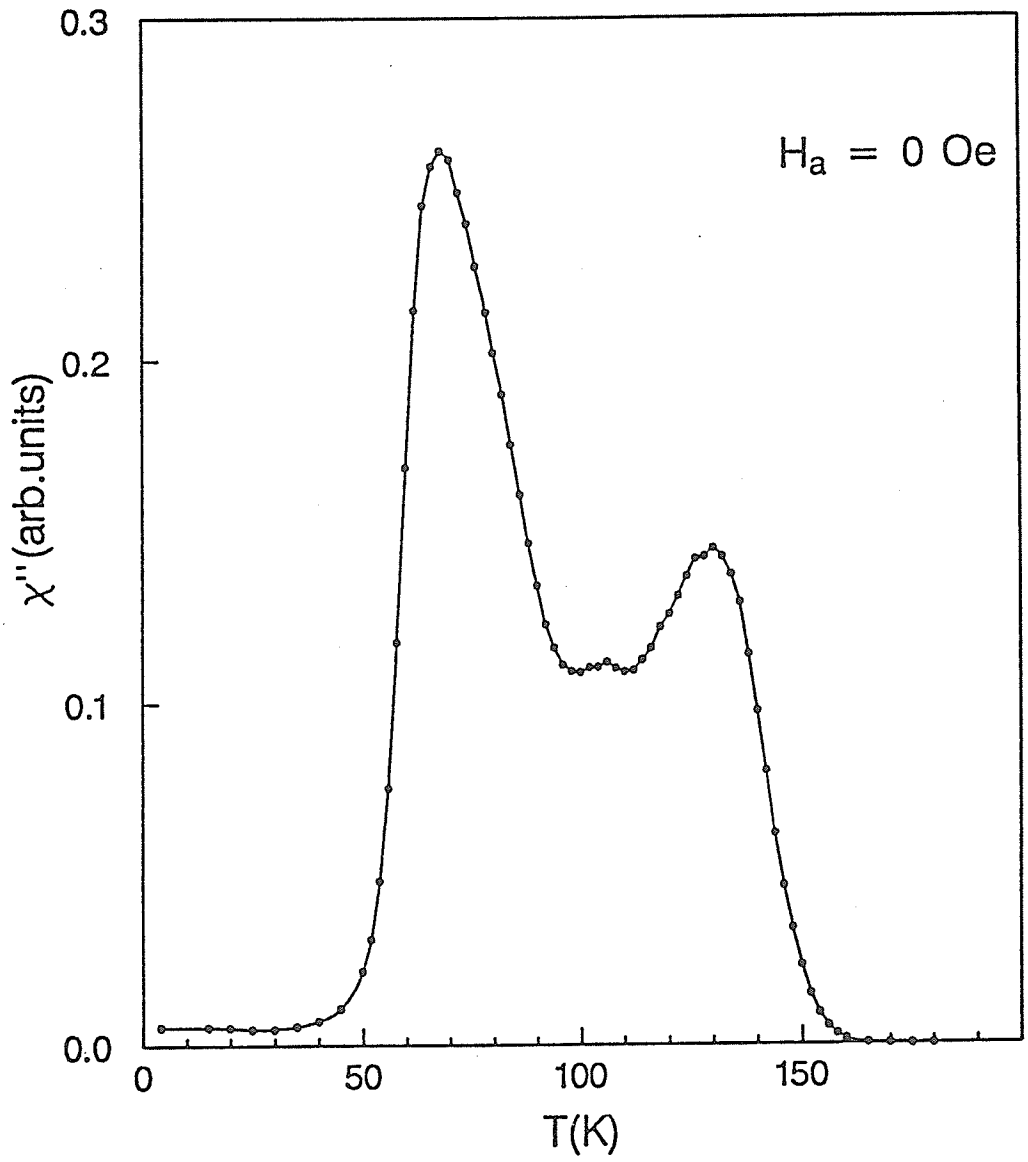

Figure 4.1.5-4: The temperature dependence of the imaginary part χ'' of the susceptibility in zero static magnetic field.

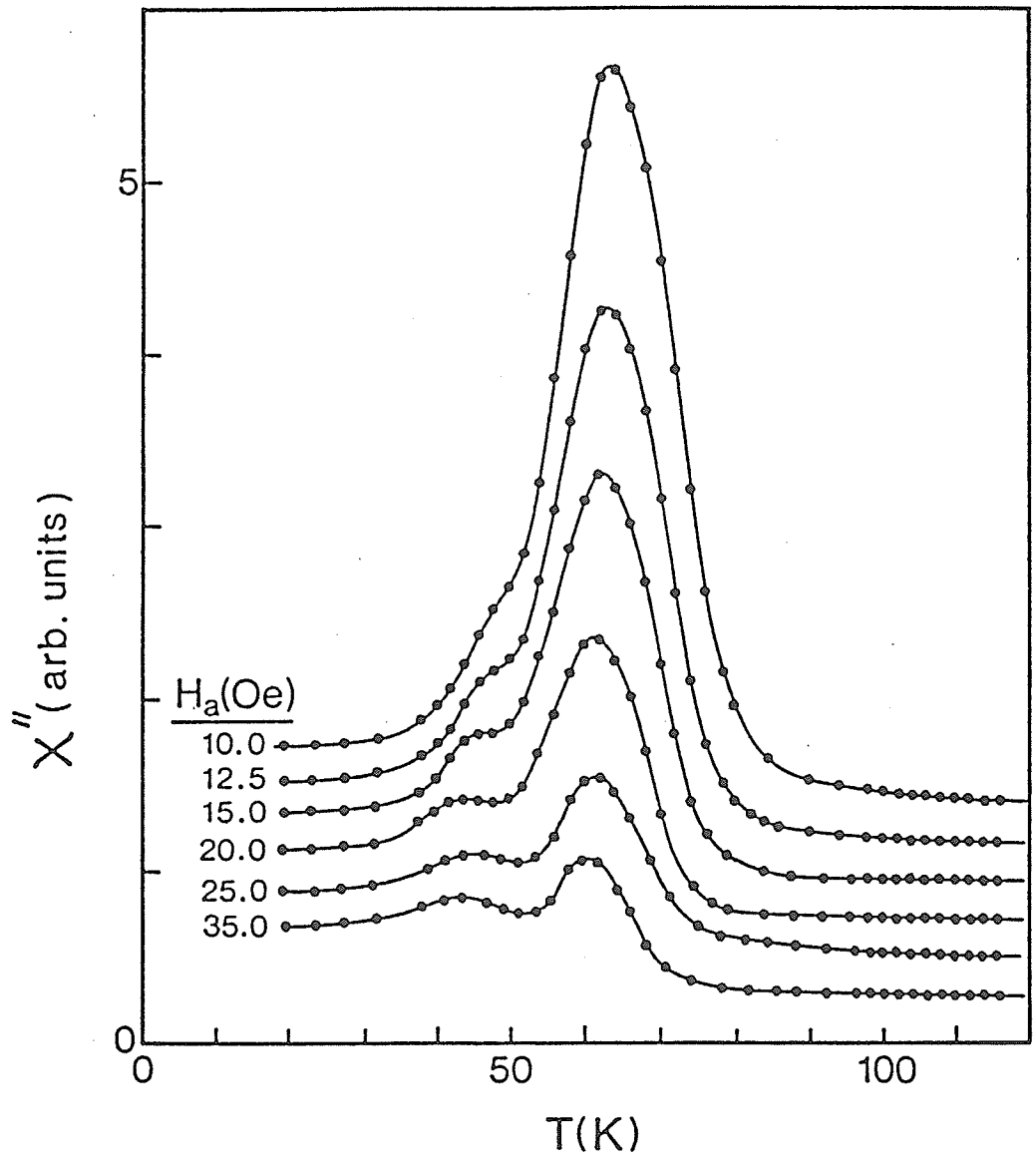

Figure 4.1.5-5: Temperature dependence of the imaginary component χ'' of the dynamic susceptibility in several representative static biasing fields H_a between 10 Oe and 35 Oe. With the exception of the 35 Oe isofield, successive isofields have been separated vertically by + 0.02 a.u. for purposes of clarity.

estimate was subsequently refined until a linear double logarithmic plot of reduced peak temperature t_p verses H_i was achieved. The result is shown in Figure 4.1.5-6. The analysis yielded a critical temperature $T_c = (104 \pm 2)$ K (just below the principal maximum in the zero field susceptibility), and an inverse crossover exponent $(\gamma + \beta)^{-1} = 0.47 \pm 0.07$, which is lower than the 3-D Heisenberg prediction. This latter behaviour is consistent with numerical Ising model simulations (Kornik et al., 1990), which show that, as the system approaches the tricritical point and the ratio $\overline{J_o}/\overline{J}$ (the mean value to the width of the exchange bond distribution) approaches unity (the limit of stability of the ferromagnetic ground state), the size of the critical region in the h-t plane becomes vanishingly small and essentially inaccessible experimentally, so that, even in relatively small laboratory fields, the corrections to scaling are significant and reduce the effective exponent $(\gamma + \beta)^{-1}$ below its true asymptotic critical value.

The behaviour of the critical exponent δ, which governs the internal field dependence of the critical peak amplitudes, also reflects the proximity of the multicritical point. Figure 4.1.5-7(a) shows a double logarithmic plot of the critical peak heights $\chi'(H_i, T_p)$ as a function of internal field H_i. The plot reveals two distinct regimes corresponding to different values of δ: an asymptotic low field regime ($H_i < 15$ Oe) with $\delta_{LF} = 5.6 \pm 0.3$, as before reminiscent of the 3-D Heisenberg prediction of δ=4.8 (Le Guillou and Zinn-Justin, 1980), and a high field regime ($H_{int} > 15$ Oe) with $\delta_{HF} = 2.9 \pm 0.1$, which is essentially the mean field prediction δ=3.

The temperature dependence of the zero field susceptibility above T_c is described by the exponent γ, according to $\chi'(0, t > 0) \sim t^{\gamma}$ (Eq.(2.117)), and Figure 4.1.5-7(b) shows a double logarithmic plot of $\chi'(0, t > 0)$ as a function of reduced temperature t with $T_c = 104$ K. The two straight lines in this figure represent the mean field Curie-Weiss prediction, γ=1, for purposes of comparison. While several features of this plot, particularly the inflection point, which translates into

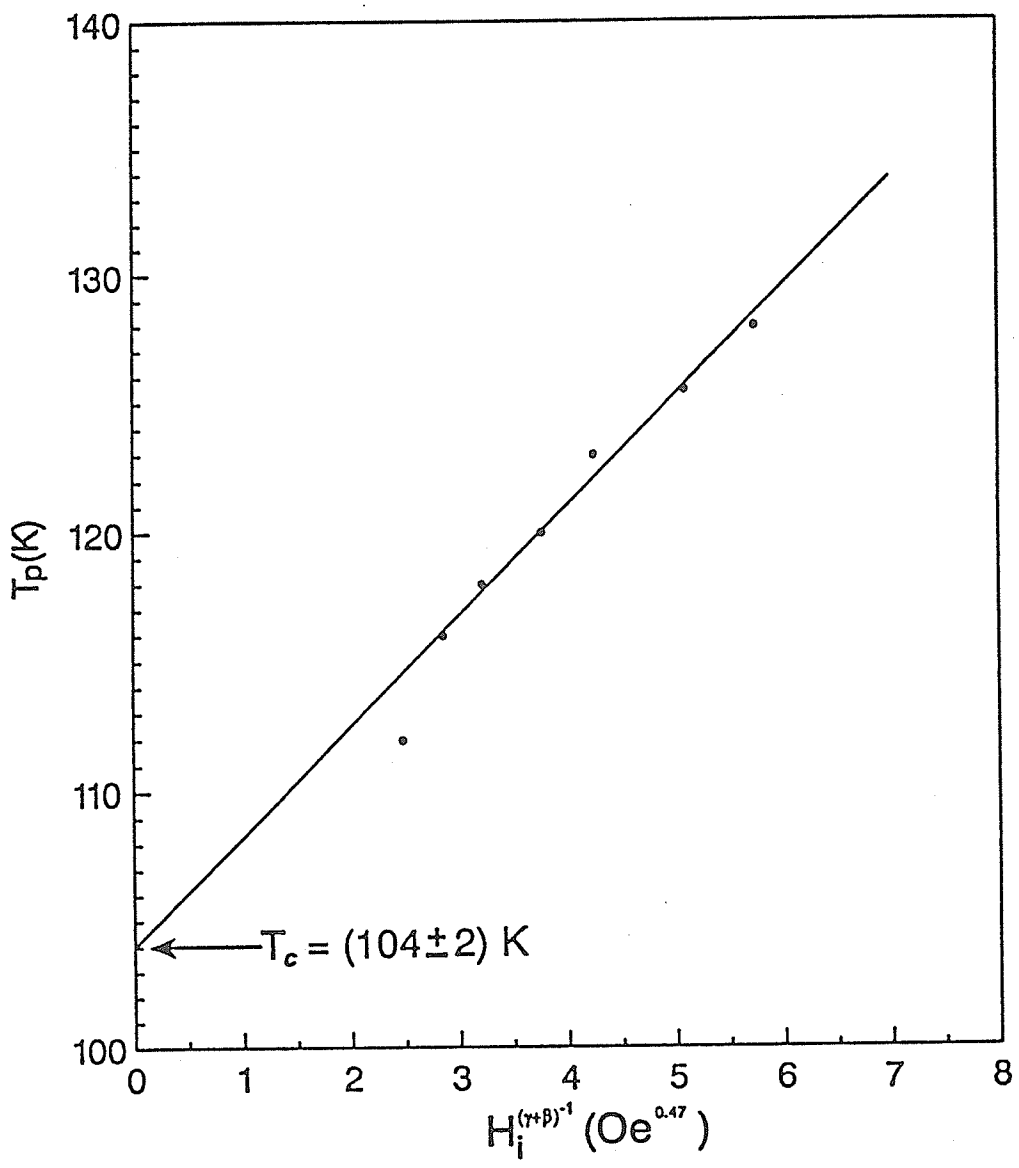

Figure 4.1.5-6: A plot of the experimental ferromagnetic critical peak temperatures $T_p(K)$ as a function of $H_i^{1/(\gamma+\beta)}$, where H_i is the internal field. The extrapolation of the straight line through the low field data to $H_i = 0$ yields the Curie temperature T_c.

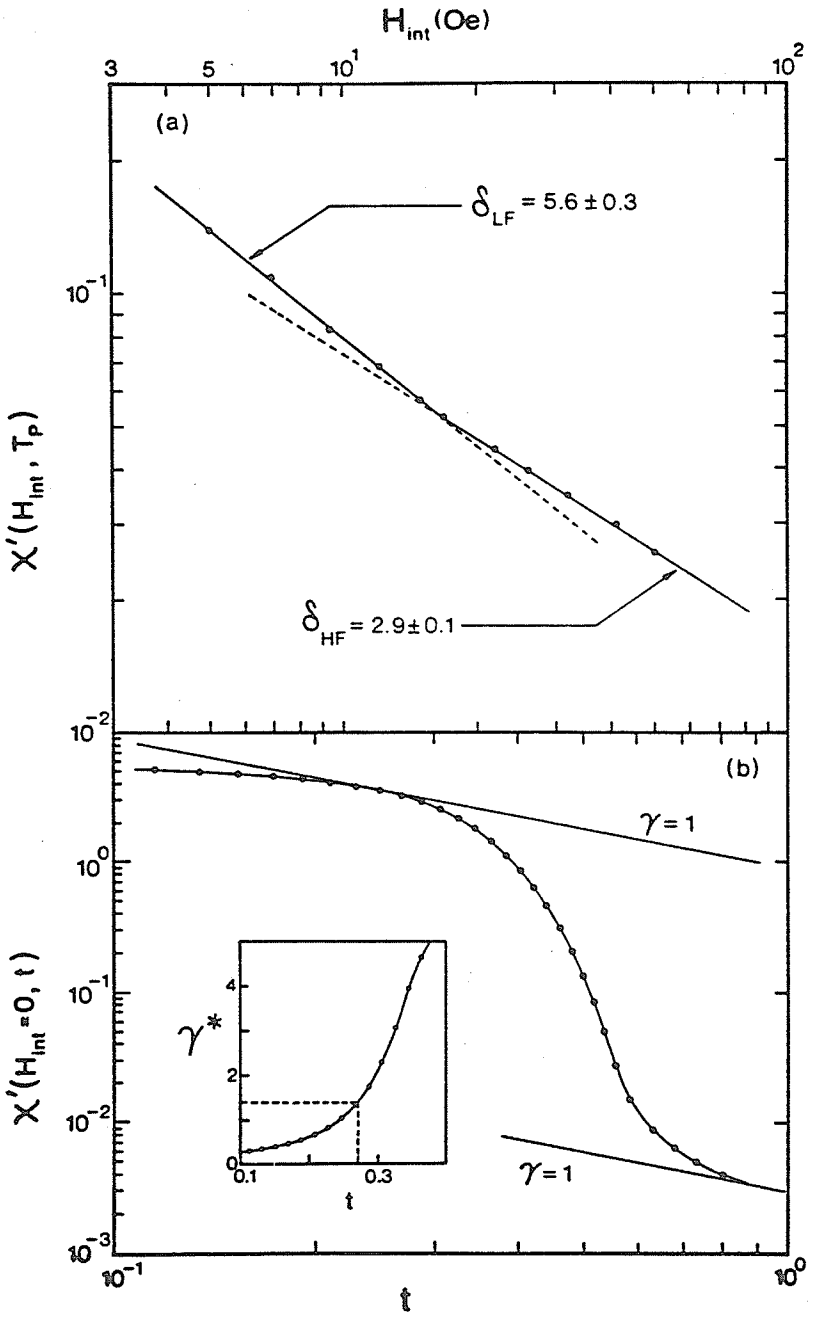

Figure 4.1.5-7: (a) Double logarithmic plot of the ferromagnetic critical peak heights $\chi'(H_i, T_p)$ as a function of internal field H_i. (b) Double logarithmic plot of the zero-field susceptibility $\chi'(H_i=0,t)$ as a function of reduced temperature t. The straight lines represent the mean-field Curie-Weiss law for $\gamma = 1$. The insert shows the effective Kouvel-Fisher exponent γ^* over a restricted temperature interval, and the dashed horizontal line identifies the 3-D Heisenberg value $\gamma^* = 1.38$.

a distinct maximum in the temperature dependence of the effective Kouvel-Fisher exponent γ^* near t $\approx$ 0.5, and the asymptotic approach to the mean field limit for $T \gg T_c$, are typical of bond disordered ferromagnets, and are successfully replicated by correlated molecular field models (Fähnle, 1987), the curvature is unusually pronounced in the present system, leading once again to values of the effective exponent as high as $\gamma^* \sim 10$ in the neighbourhood of the inflection point. Such effects are expected to be particularly dramatic in the present system, which lies extremely close to the multicritical point. Nevertheless, an inspection of the insert in Figure 4.1.5-7(b), which shows the behaviour of the effective exponent over a restricted reduced temperature interval ($t \leq 0.4$), reveals that γ^* does assume its 3-D Heisenberg value $\gamma^* = 1.38$ (Le Guillou and Zinn-Justin, 1980) at a reduced temperature $t = 0.27$ (dashed lines in the insert), close to the inflection point in the zero field susceptibility (see Figure 4.1.5-1(a)), below which noncritical processes (such as domain formation) dominate the magnetic response and suppress the critical singularity in $\chi'(0, t > 0)$.

4.1.6 Thermoremanent Relaxation in Two "Pure" Spin Glasses: $Ni_{76}Mn_{24}$ and $Ni_{73.1}Mn_{26.9}$

In the preceding analysis, we have concentrated on the critical analysis of both the ferromagnetic and spin-glass transitions in reentrant NiMn using complex dynamic susceptibility measurements. While the analysis exploits the systematics of the highest temperature component of the triple-peaked structure (see Figures 4.1.3-1, 4.1.4-2 and 4.1.5-1(b)) to establish the presence of ferromagnetic critical fluctuations, the two lower temperature peaks suggest that the ferromagnetic phase is not the stable ground state, but subsequently evolves into a spin glass-like phase with strong irreversibility. Although we have provided some evidence (based primarily on the field dependence of the two "reentrant" peak temperatures) for a possible correspondence between the "reentrant" susceptibility peaks and the

Gabay-Toulouse (GT) and de Almeida-Thouless (AT) instability lines which characterize vector spin models of bond disordered ferromagnets, the correlation is difficult to justify rigorously since these models are currently incapable of replicating the dual reentrant structure observed in the susceptibility, and consequently we turned our attention to thermoremanent relaxation effects as a possible mechanism for gaining further insight into the nature of the spin configuration within the reentrant phase and its relationship to that in the ferromagnetic and "pure" spin glasses phases.

(a) $Ni_{76}Mn_{24}$

The $Ni_{76}Mn_{24}$ alloy is located close to the multicritical point ($c_m \cong 24$ at.%) and, as discussed in section 4.1.2, is a concentrated cluster spin glass, with no evidence of ferromagnetic critical peaks and with susceptibility isofields consisting of a single peak which is systematically suppressed in amplitude and shifted downward in temperature with increasing field. Figure 4.1.6-1 shows the temperature dependence of the static magnetization measured under both field cooled (FC) and zero field cooled (ZFC) conditions, in a static applied field $H_a = 1.0$ Oe. The sample exhibits a typical spin glass peak at $T_{SG} = 85$ K, and below about 85 K, the FC and ZFC curves diverge and time effects become appreciable.

The decay of the thermoremanent magnetization was measured at a variety of temperatures T_m between $56 \leq T_m \leq 76$ K. Figure 4.1.6-2 shows all the "low" temperature thermoremanent relaxation isotherms, plotted on a logarithmic time scale. Each isotherm was obtained by following an identical experimental procedure: the sample was first warmed to a reference temperature $T_R = 140$ K, well within the paramagnetic regime, in order to eliminate any remanent magnetization, then cooled in a static field $H_c = 1.0$ Oe to a predetermined measuring temperature T_m within the ordered phase (the cooling time t_c was essentially independent of T_m, and consistently between $t_c = 975 \pm 45$ s) and, after a wait time t_w

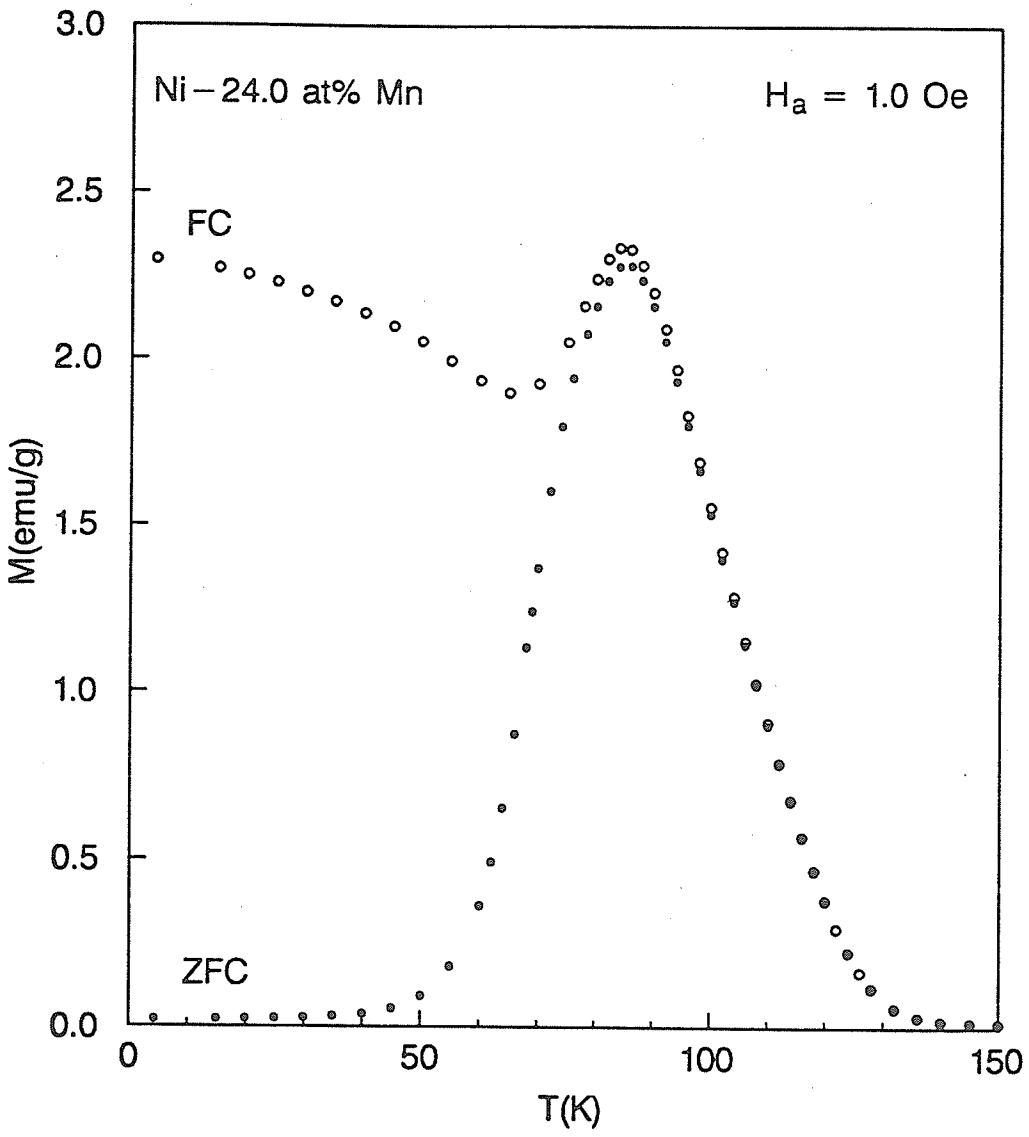

Figure 4.1.6-1: Temperature dependence of the FC and ZFC magnetization of the Ni-24.0 at% Mn spin glass measured in an applied field H_a = 1 Oe.

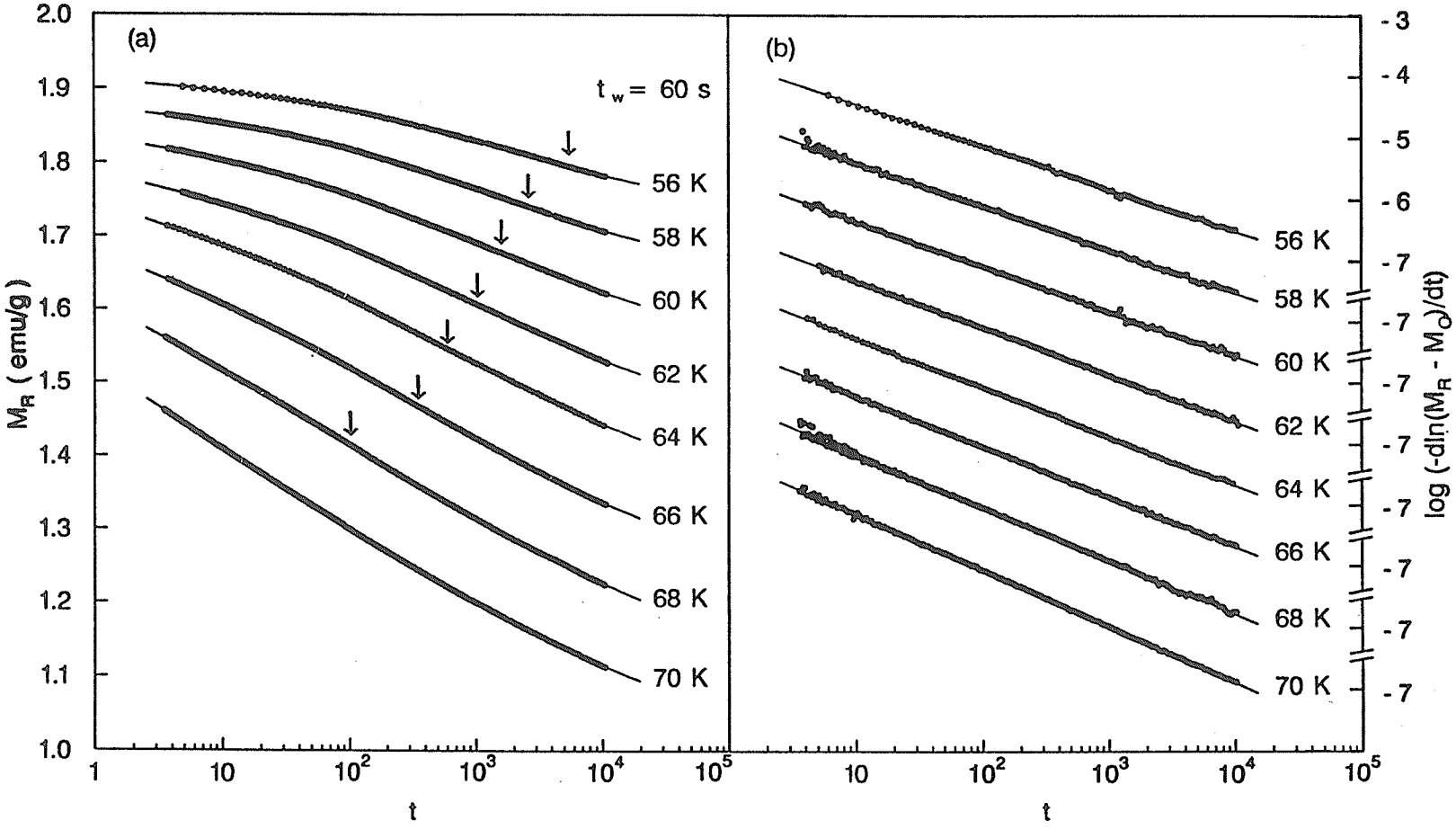

Figure 4.1.6-2: (a) A set of "low" temperature relaxation isotherms in the spin glass phase all corresponding to a wait time t_w = 60 s. Solid lines represent the best fits to Eq.(4.1). The vertical arrows mark the locations of the inflection points. (b) Double-logarithmic plots of $-d\ln(M_R - M_0)/dt$ as a function of t for the isotherms in (a).

= 60 s had elapsed at constant temperature T_m, the field was abruptly removed, and the decay of the thermoremanent magnetization was recorded over nearly four decades of observation time 4 s$< t \leq 10^4$ s. The sample was then warmed in zero field to the reference temperature T_R in order to establish the zero of magnetization. The most prominent feature of the relaxation curves in Figure 4.1.6-2(a), when viewed on a logarithmic time scale, is the inflection point (vertical arrows), which propagates from longer to shorter observation times with increasing temperature, leading to a gradual and systematic change in curvature from concave down at low temperatures to concave up at high temperatures. (The locations of the inflection points t_{infl} in Figure 4.1.6-2(a) were established by plotting the local slope of the isotherms, or relaxation rate, $S(t) \equiv -\partial M_R/\partial \ln t$, on a logarithmic time scale, thus generating well-defined maxima centered at log t_{infl}.) In order to generate the most suitable functional description of the relaxation isotherms in Figure 4.1.6-2(a), the data were compared with some of the more common theoretical representations of spin glass relaxation, individually and in combination; the simplest formulation which was capable of accurately reproducing all the structural features of the experimental data, over the *entire* observational time window, consisted of the superposition of a stretched exponential and a constant term,

$$M_R(t) = M_o + M_1 exp[-(t/\tau)^{1-n}], \tag{4.1}$$

and the solid curves in Figure 4.1.6-2(a) are the best fits to Eq.(4.1). Figure 4.1.6-2(b) shows that double logarithmic plots of $-d/dt[ln(M_R - M_o)]$ as a function of t yield excellent straight lines, as expected, and Table 4.1-1 summarizes the values of the various best fit parameters. For purposes of comparison, the total aging time $t_{age} = t_w + t_c$ and t_{infl} are also listed in the table. The time independent component of the remanence M_o is an essential ingredient, and large in comparison with pure spin glasses (Nordblad et al., 1986; Chamberlin, 1984), accounting for approximately 75-95% of the magnitude of the total signal, and decreases

monotonically with increasing temperature. The large value of M_o is a further indication that the $Ni_{76}Mn_{24}$ is a concentrated spin glass. The exponent n exhibits canonical spin glass behavior (Hoogerbeets et al.,1986) , approaching unity as $T \rightarrow T_{SG}$, and the characteristic time τ (which locates the inflection point in the stretched exponential , and hence the maximum in the relaxation rate) agrees with t_{infl}, within experimental error. The uncertainties in t_{infl} reflect the scatter in the numerical derivative of the raw data. A comparison of the wait time t_w with t_{infl} for each isotherm, shows that the inflection point does not coincide with t_w, contrary to other studies (see Figures 1-22 and 1-23 in chapter I). Such behavior is probably caused by the large cooling intervals ($T_R - T_m \sim 100K$) imposed in our experiments, and correspondingly long cooling times t_c. A detailed discussion will be given in the next section.

Table 4.1-1: $Ni_{76}Mn_{24}$ Spin Glass Parameters for Eq.(4.1)

T(K)	t_w(s)	$t_w + t_c$ (s)	t_{infl} (s)	τ (s)	n	M_o(emu/g)
56	60	1050	5000±2000	2551±226	0.69±0.01	1.74±0.01
58	60	1050	2500±1000	1917±53	0.70±0.01	1.66±0.01
60	60	1080	1800±500	1666±61	0.74±0.01	1.56±0.01
62	60	1050	1000±400	1213±38	0.76±0.01	1.46±0.01
64	60	1080	600±400	736±31	0.79±0.01	1.35±0.01
66	60	1050	350±200	370±6	0.82±0.01	1.24±0.01
68	60	1050	100±50	74±3	0.87±0.01	1.10±0.01
70	60	1080	<3	2.2±0.4	0.91±0.01	0.96±0.01

The stretched exponential representation fails to describe the relaxation for higher temperatures between $72 \leq T_m \leq 76K$. In this region, double logarithmic plots of $-d/dt[ln(M_R - M_o)]$ as a function of t, (M_o =0) still yield straight lines, but with an nonphysical value of the slope $n > 1$, which corresponds to an increasing TRM. However, the superposition of a simple power-law and a constant term,

$$M_R(t) = M_o + M_1 t^{-m}, \tag{4.2}$$

provided a good description of these high temperature data, as shown by the solid lines in Figure 4.1.6-3(a), over 4 decades of observation time. Double logarithmic plots of $-dM_R/dt$ versus t yield excellent straight lines, as shown in Figure 4.1.6-3(b). Table 4.1-2 lists the best fit values of the parameter M_o, which decreases with increasing temperature, and m, which is weakly temperature dependent.

Table 4.1-2: $Ni_{76}Mn_{24}$ Spin Glass Parameters for Eq.(4.2)

T(K)	t_w(s)	m	M_o(emu/g)
72	60	0.08±0.01	0.61±0.01
74	60	0.10±0.01	0.60±0.01
76	60	0.10±0.01	0.53±0.01
76	7200	0.09±0.01	0.48±0.01
100	60	0.15±0.01	0.09±0.01

A significant feature of all the relaxation isotherms at low temperatures ($T_m \leq$ 72 K) is their dependence on the wait time t_w for which the system is held at constant temperature prior to changing the field. As a typical illustration of this nonequilibrium character, Figure 4.1.6-4(a) shows a comparison of four relaxation curves, all measured at the same temperature T_m = 66 K, but for different wait times t_w = 60 s, 360 s, 900, and 1800 s; the age dependent behavior of the relaxation is readily apparent in this figure as a shift in the location of the inflection point, or the maximum in the relaxation rate $S(t) \equiv -\partial M_R/\partial lnt$ shown in Figure 4.1.6-4(b), towards longer observation times with increasing wait time. Similar behavior was found at T_m =68 K (Figure 4.1.6-5) and T_m = 70 K (Figure 4.1.6-6). Although strong aging effects were observed at low temperatures, no wait time dependence was found at temperatures higher than 72 K, as illustrated in Figure 4.1.6-3 where the open circles show the relaxation at T_m = 76 K with t_w = 7200 s. This is consistent with the fact that the high temperature data can be modelled by a simple power law indicative of thermal equilibrium, as pointed out in chapter

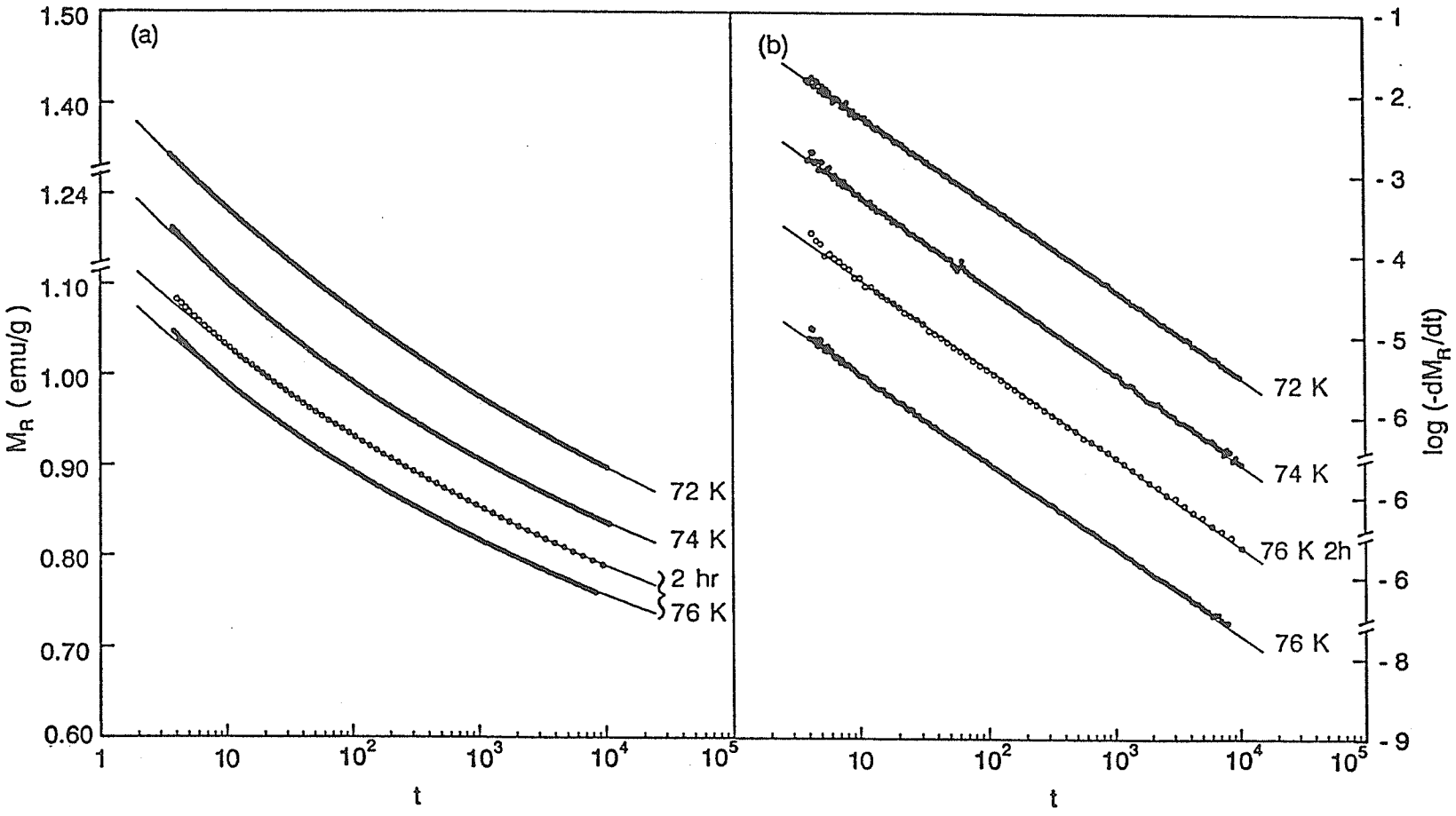

Figure 4.1.6-3: (a) Thermoremanent relaxation isotherms corresponding to wait times t_w = 60 s (solid circles) and t_w = 7200 s (open circles) at three "high" temperatures. No obvious wait time dependence was observed in this regime. Solid lines represent the best fits to Eq.(4.2). (b) Double-logarithmic plots of $-dM_R/dt$ as a function of t for the isotherms in (a).

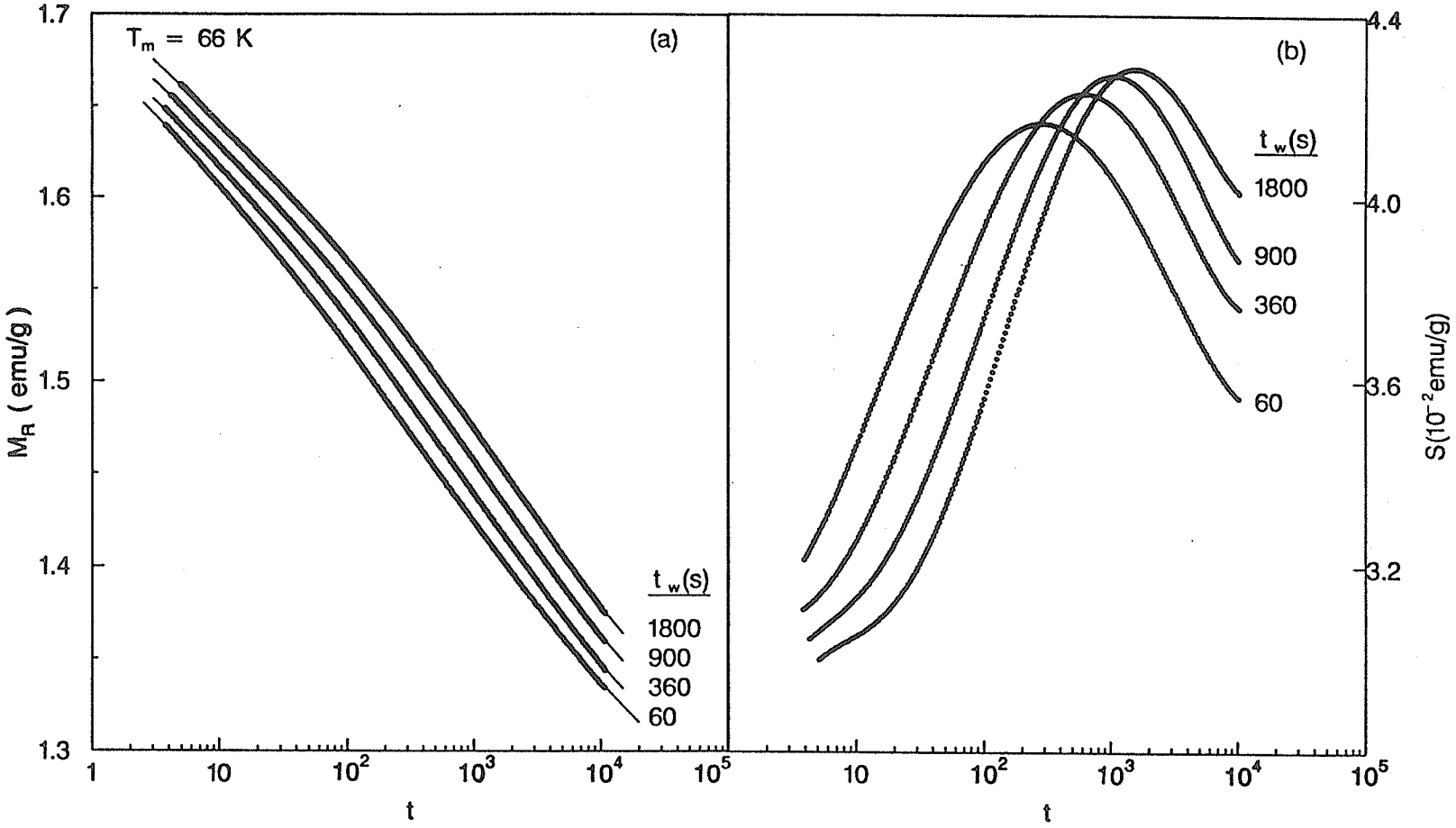

Figure 4.1.6-4: (a) The decay of the thermoremanent magnetization M_R at a measurement temperature T_m = 66 K for wait times t_w = 60, 360, 900, 1800 s. The solid curve for t_w = 60 s is the fit to Eq.(4.1), while the solid curves for t_w > 60 s are the best fits to Eq.(4.3). (b) The numerically calculated relaxation rate $S(t) \equiv -dM_R/d\ln t$ for the relaxation curves in (a), plotted on a logarithmic scale.

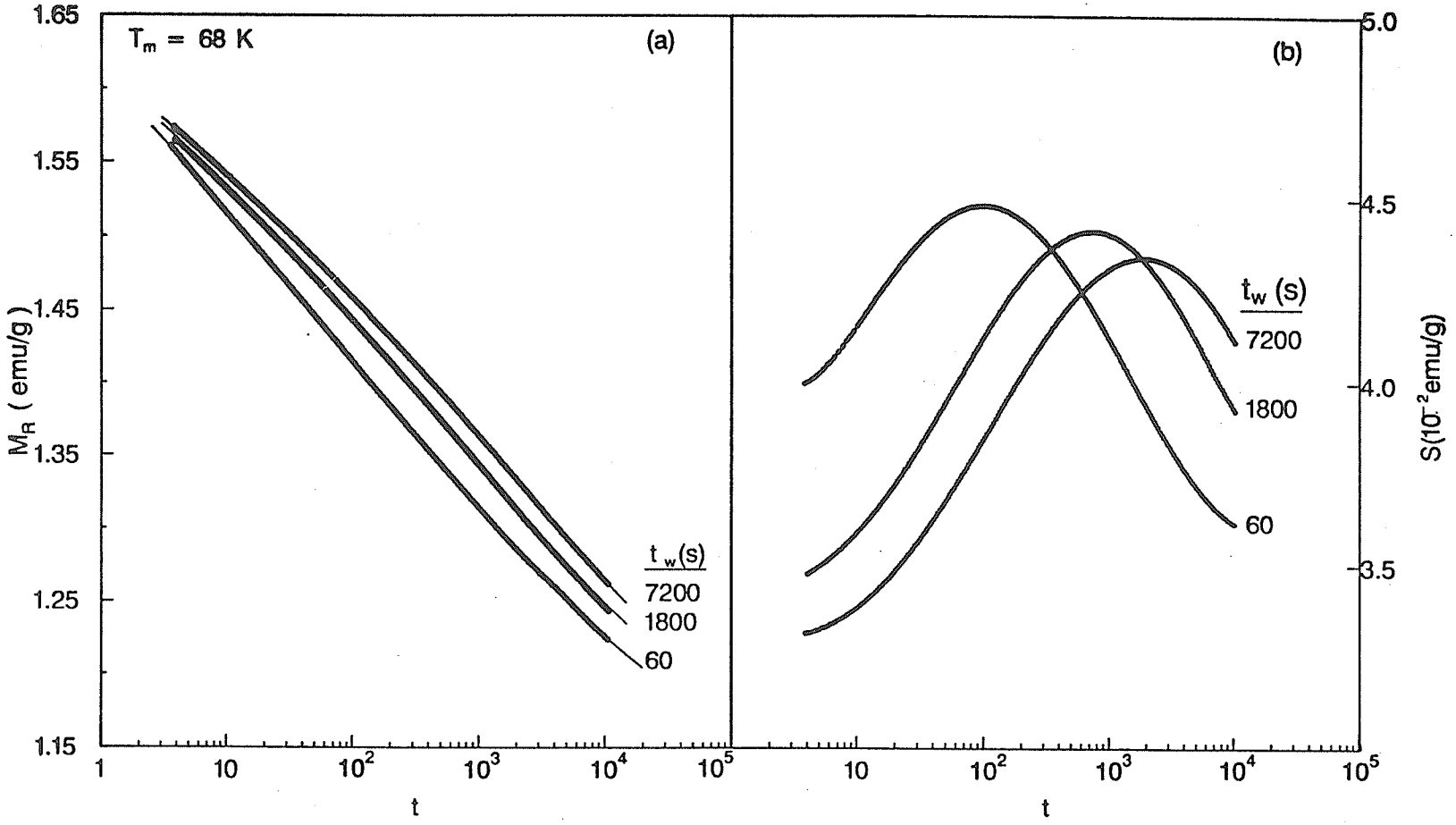

Figure 4.1.6-5: Same as in Figure 4.1.6-4, but for a measurement temperature T_m = 68 K, and wait times t_w = 60, 1800, 7200 s.

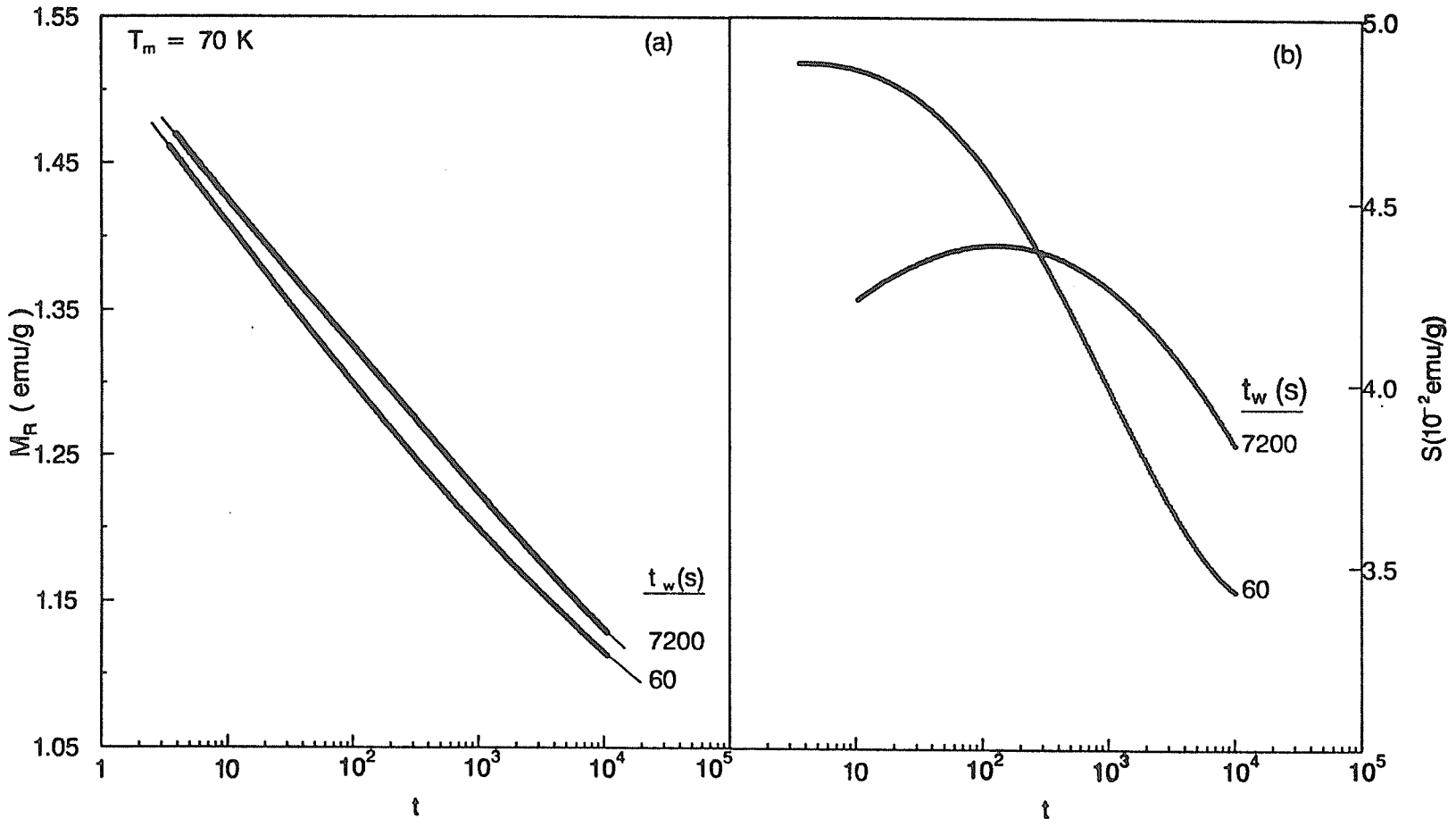

Figure 4.1.6-6: Same as in Figure 4.1.6-4, but for a measurement temperature T_m = 70 K, and wait times t_w = 60, 7200 s.

I. It is also consistent with the fact that the $Ni_{76}Mn_{24}$ is a concentrated spin glass with short-range ferromagnetic clusters present in the system. In the next section, we show that the simple power-law Eq.(4.2) is also an appropriate function for describing the relaxation in the high temperature ferromagnetic regime. However, vector models of spin glasses suggest that it may also represent the weakly irreversible behaviour expected between the GT and AT lines.

Attempts to apply the analytical representation in Eq(4.1) to the TRM curves for longer wait times $t_w > 60$ s revealed that the superposition of the stretched exponential and a constant was only able to describe the data over a limited range; there were systematic deviations at short observation times, with the range of validity becoming progressively narrower for longer and longer wait times t_w. Such behavior is consistent with previous investigations (Nordblad et al.,1987b), which suggest that the applicability of the stretched exponential is restricted to experimental time intervals in the immediate vicinity of the effective experimental age of the system, where the relaxation rate is dominated by the influence of the aging process, but it is incompatible with the short time($t \ll t_w$) equilibrium response, which is expected to be a weak power law decay (Nordblad et al., 1987b; see also chapter I). Guided by these suggestions, the superposition of a constant and the product of a stretched exponential and a power law

$$M_R(t) = M_o + M_1 t^{-m} exp[-(t/\tau)^{1-n}] \tag{4.3}$$

was applied to the longer wait time relaxation curves. The function, shown by the solid line in Figures 4.1.6-4, 4.1.6-5 and 4.1.6-6 for $t_w > 60s$, and for $T_m =$ 66, 68, and 70 K, represents the data over the entire observation time window. The best fit parameters are listed in Table 4.1-3, and reveal weakly temperature dependent exponents m (~ 0.05) and n(~ 0.7), while τ no longer coincides with the location of the inflection points in the relaxation isotherms, as expected. The theoretical justification for Eq.(4.3) can be linked to the mesoscopic picture of

growth and fragmentation of spin glasses domains which was discussed in section 2.4.2 (Eq.(2.165)).

Table 4.1-3: $Ni_{76}Mn_{24}$ Spin Glass Parameters for Eq.(4.3)

$T(K)$	t_w(s)	$t_w + t_c$ (s)	t_{infl} (s)	τ (s)	m	n	M_o(emu/g)
66	360	1350	700±300	1500±181	0.02±0.01	0.77±0.01	1.25±0.01
66	900	1860	1000±300	4100±60	0.05±0.01	0.67±0.01	1.28±0.01
66	1800	2790	2000±1000	5384±80	0.06±0.01	0.62±0.01	1.29±0.01
68	1800	2760	800±300	3651±80	0.04±0.01	0.74±0.01	1.14±0.01
68	7200	8160	2000±1000	8437±124	0.05±0.01	0.70±0.01	1.15±0.01
70	7200	8130	150±100	9058±331	0.09±0.01	0.63±0.01	1.07±0.01

(b) $Ni_{73.1}Mn_{26.9}$

To complete the characterization of the pure spin glass relaxation, we measured the relaxation isotherms in $Ni_{73.1}Mn_{26.9}$ which lies well above the multicritical point ($c_m \cong 24.0$ at.%) and hence should be a good spin glass, according to the magnetic phase diagram in Figure 4.1.1-4. Figure 4.1.6-7 shows a typical spin glass cusp at $T_{SG} = 78$ K in the ZFC magnetization, and a significant difference below T_{SG} between the FC and ZFC curves, due to strong irreversibility. The magnetization in $Ni_{73.1}Mn_{26.9}$ is also substantially reduced compared with the magnetization of $Ni_{76}Mn_{24}$. The decay of the thermoremanent magnetization was measured at temperatures $50 \leq T_m \leq 75$ K in a cooling field $H_c = 5$ Oe, and the relaxation isotherms were acquired by a technique similar to that described earlier, with a reference temperature $T_R = 100$ K. Figure 4.1.6-8 shows these isotherms for a wait time $t_w = 60$ s, plotted on a logarithmic time scale, together with the fits using the stretched exponential function Eq.(4.1) (solid curves). Table 4.1-4 lists the best fit parameters of Eq.(4.1), which are typical of spin glasses. In contrast to the concentrated $Ni_{76}Mn_{24}$ spin glass, the value of M_o is comparable to the total decay of the relaxation, and approaches zero within the uncertainty,

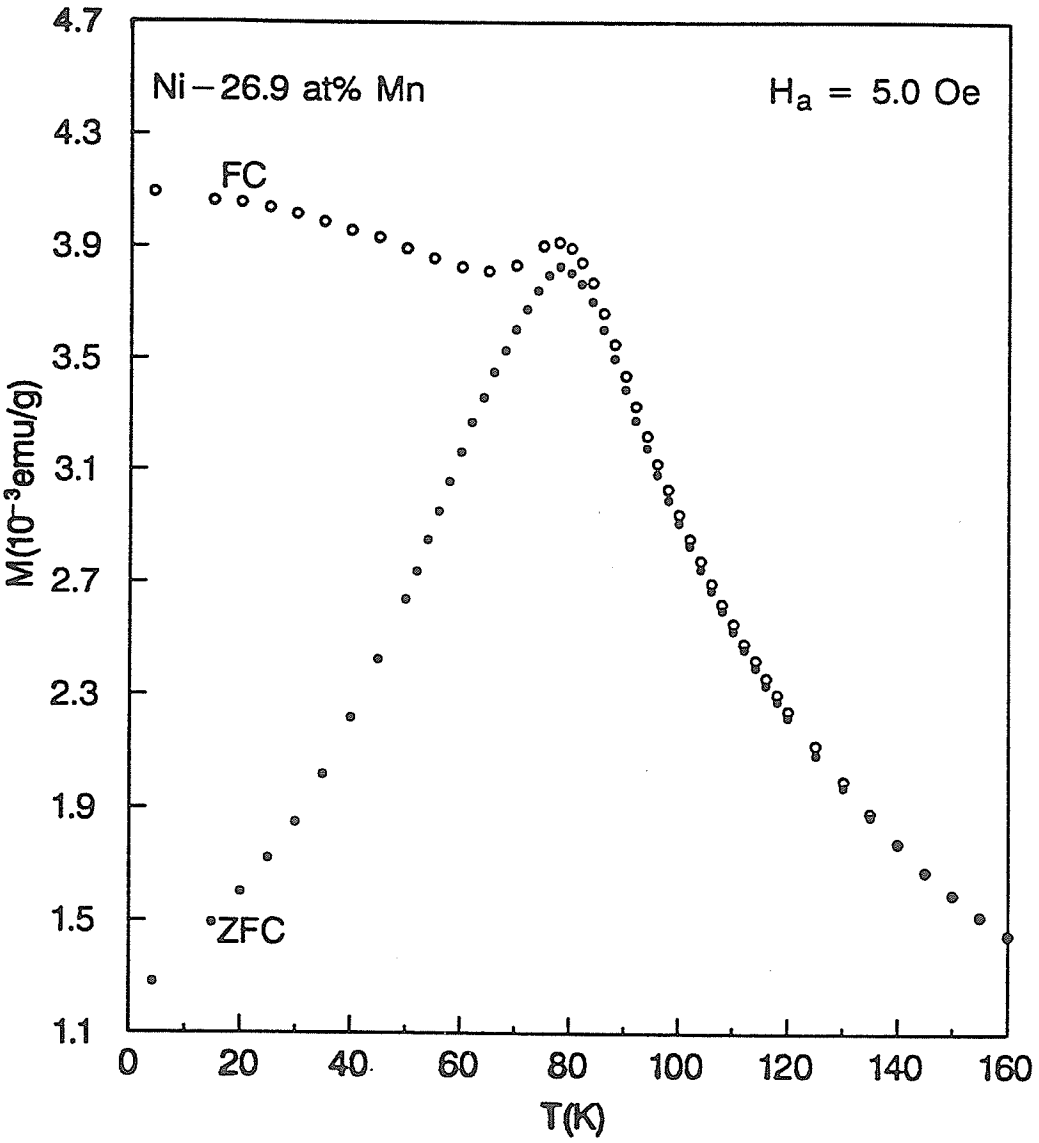

Figure 4.1.6-7: The temperature dependence of the field cooled (FC) and zero field cooled (ZFC) static magnetization of the Ni-26.9 at% Fe spin glass measured in an applied field H_a = 5.0 Oe.

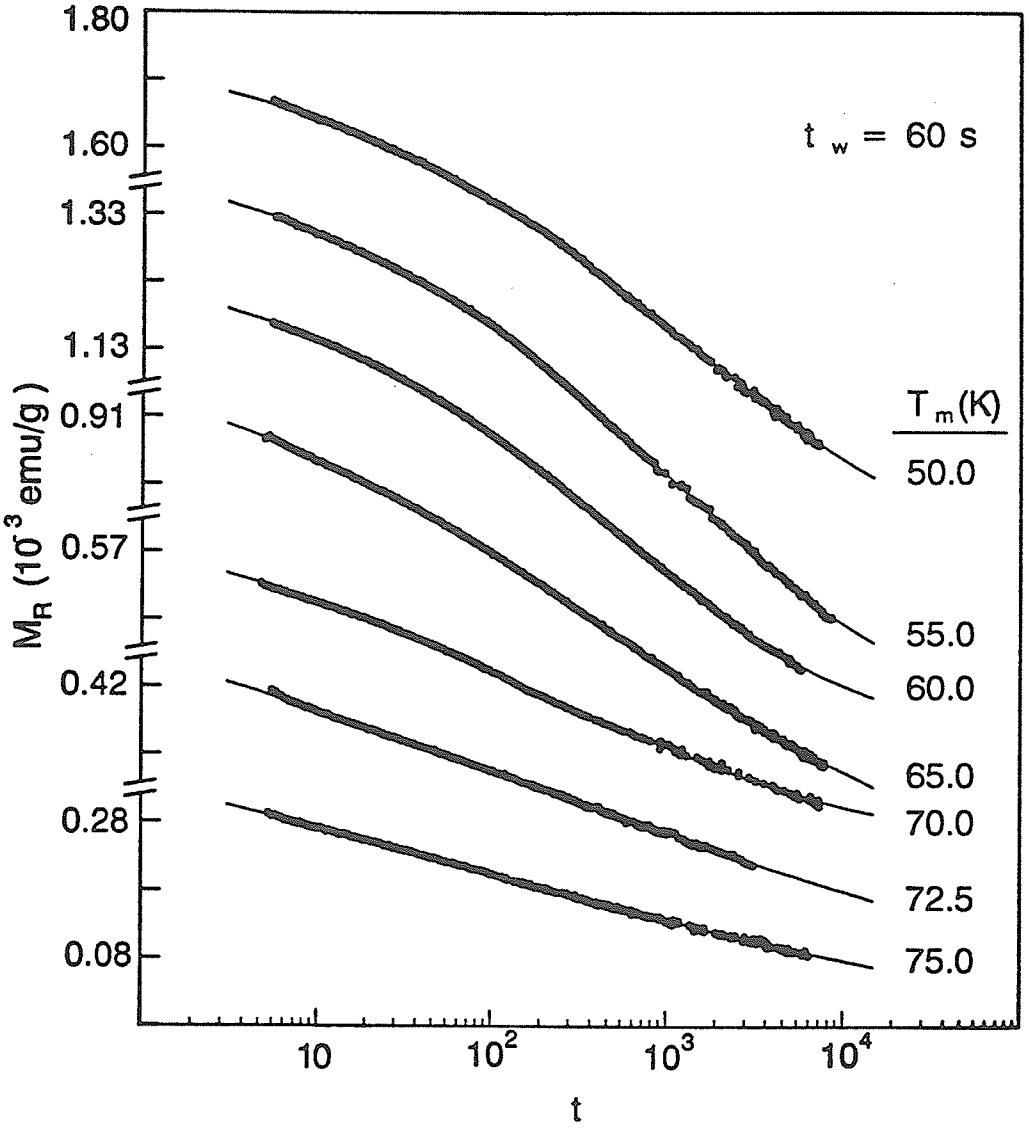

Figure 4.1.6-8: Decay of the thermoremanent magnetization M_R for t_w = 60 s at several measurement temperatures T_m within the spin glass phase. Solid curves are the best fits to Eq.(4.1).

at temperatures close to T_{SG}. However, as before, a similar discrepancy exists between t_{infl} and t_{age} due to the large cooling intervals from T_R to $T_m(\sim 35$ K), and long cooling times $t_c \sim 15$ min.

Table 4.1-4: $Ni_{73.1}Mn_{26.9}$ Spin Glass Parameters for Eq.(4.1)

T(K)	t_w(s)	$t_w + t_c$ (s)	t_{infl} (s)	τ (s)	n	$M_o(10^{-3}$ emu/g)
50	60	960	5000±2000	1491±51	0.66±0.01	1.03±0.02
55	60	900	2500±1000	1258±29	0.66±0.01	0.61±0.01
60	60	840	1800±500	655±6	0.65±0.01	0.57±0.01
65	60	840	1000±400	690±11	0.74±0.01	0.27±0.01
70	60	810	600±400	259±9	0.75±0.01	0.14±0.01
72.5	60	870	350±200	215±26	0.87±0.02	0.05±0.03
75	60	780	100±50	106±18	0.86±0.02	0.02±0.01

4.1.7 Thermoremanent Relaxation in a $Ni_{76.4}Mn_{23.6}$ Reentrant Ferromagnet

Having established a quantitative picture of pure spin glass relaxation in NiMn, we now turn our attention to a reentrant NiMn ferromagnet. In this section, we present a detailed study of the relaxation of the low field thermoremanent magnetization, over four decades of observation time (1 s $< t \leq 10^4$ s); the temperature interval includes portions of both the ferromagnetic and reentrant phases in the $Ni_{76.4}Mn_{23.6}$ alloy located very close to the multicritical point ($c_m = 24$ at.% Mn). We show that, within the limitations of an analysis based on the approximate stretched exponential representation, the reentrant phase in $Ni_{76.4}Mn_{23.6}$ and the spin glass phase in $Ni_{76}Mn_{24}$ show essentially identical relaxation dynamics.

The sample used for this investigation has already been characterized by the ac susceptibility measurements presented in section 4.1.5. In order to perform the magnetization measurements, two needle shaped samples **A** and **B**, with dimensions listed in Table 3.1 were used. We also found that re-annealing an old sample which had been allowed to age at room temperature yielded unpredictable and in-

consistent magnetic behaviour, and consequently, the two needles used here were fabricated directly from the cold rolled sheet which had never been annealled.

The onset of strong irreversibility within the reentrant phase can be seen in the temperature dependence of the FC and ZFC static magnetization. Figure 4.1.7-1 shows the difference between the ZFC (open circles) and FC data (solid circles) due to the time-dependent component, as measured in a field of 0.5 Oe ; for purposes of comparison, the susceptibility isofield measured in a static biasing field $H_a = 25$ Oe (Figure 4.1.5-2) has also been reproduced in this figure (triangles). In the FC static magnetization, the two phases are clearly distinguishable by their temperature dependence, which is plateau-like in the ferromagnetic regime ($60 < T < 95$K), and concave downward in the reentrant phase ($T \leq 60$K). In the ZFC magnetization, the crossover is visible as a weak shoulder below the principal maximum, near 60K. The vertical arrows mark the three characteristic temperatures which identify the extrapolated location of the three susceptibility peaks (Figure 4.1.5-3) in the limit of zero internal field (the dashed lines indicate the correspondence); the crossover from weak to strong irreversibility is readily apparent in M_{FC} as a change in curvature near 60K, which coincides with the lowest characteristic temperature.

Figure 4.1.7-2(a) shows a sequence of twelve low field thermoremanent relaxation isotherms of sample A obtained over a temperature interval $40K \leq T \leq 95K$ which spans both the reentrant and ferromagnetic phases. All the relaxation isotherms were measured in a cooling field $H_c = 1$ Oe, for a wait time $t_w = 60$ s and a reference temperature $T_R = 170$ K, well within the paramagnetic regime. The relaxation curves in Figure 4.1.7-2(a) show the similar gradual and systematic change in curvature as those of $Ni_{76}Mn_{24}$, with the data at intermediate temperatures exhibiting an inflection point. Although the latter structure is rather subtle when viewed from the perspective of Figure 4.1.7-2(a), it is readily apparent in the derivative of the relaxation curves, and Figure 4.1.7-2(b) shows the numerically cal-

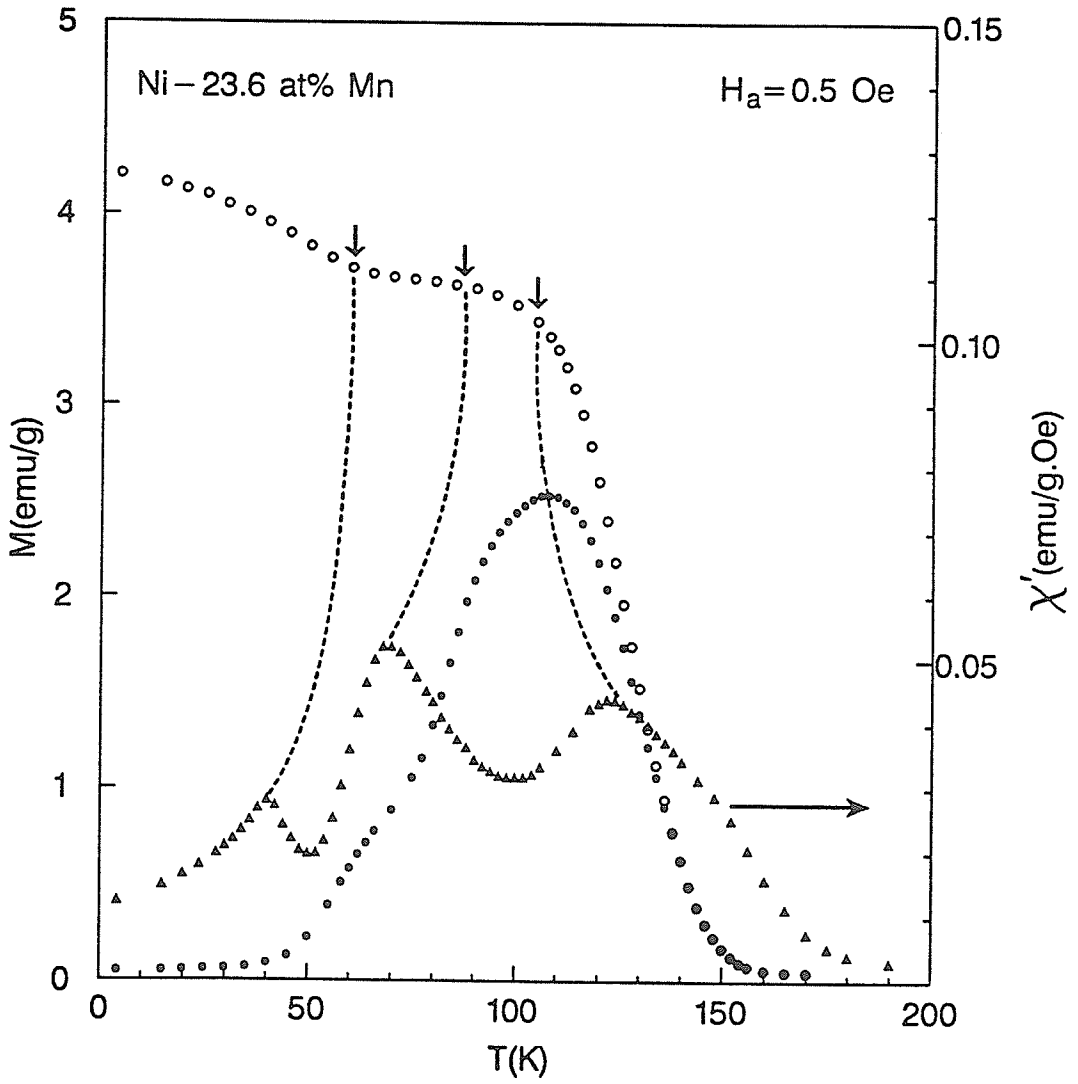

Figure 4.1.7-1: The field cooled (FC) and zero field cooled (ZFC) static magnetization of the Ni-23.6 at% Mn reentrant ferromagnet measured in an applied field H_a = 0.5 Oe, and a ZFC susceptibility isofield (triangles) from Fig.4.1.5-2. The vertical arrows mark the three zero field characteristic temperatures from Fig.4.1.5-3, and the dashed lines indicate the correspondence with each susceptibility peak.

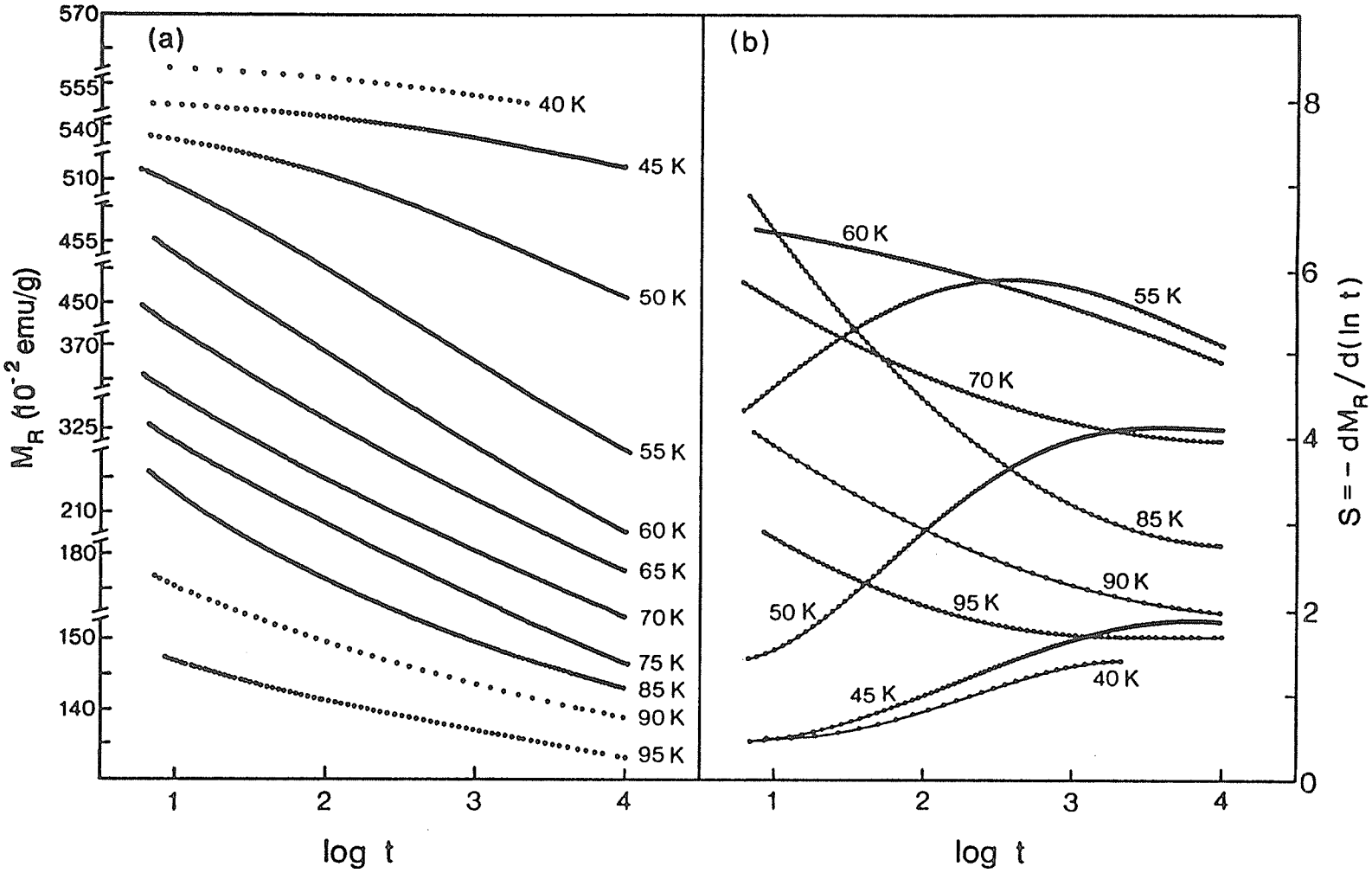

Figure 4.1.7-2: (a) Decay of the thermoremanent magnetization M_R at several temperatures T_m between 40K and 95K, all for a wait time t_w = 60 s. (b) The relaxation rate $S(t)$ for each of the isotherms in (a). Note the maximum in the 55K isotherm.

culated relaxation rate $S(t)$ of some of the isotherms in Figure 4.1.7-2(a), plotted on a logarithmic time scale. In this representation, the inflection point translates into a maximum in the relaxation rate, and a comparison of the various isotherms suggests that the maximum propagates with increasing temperature from long to short times like the crest of a wave, passing rapidly through the experimental time window at temperatures near $T_m = 55$K.

Since much of this behaviour is at least qualitatively reminiscent of spin glass relaxation as described in the previous section, the analysis of the reentrant data focused initially on those functional forms which were employed previously to characterize the thermoremanent decay in the pure spin glass phase. Two distinct relaxation regimes were identified: (a) For temperatures $T_m \leq 60$K (i.e. within the reentrant phase), the data are accurately described over the entire experimental time window by Eq.(4.1), the superposition of a stretched exponential and a constant term. The quality of the fits is shown by the excellent straight lines in Figure 4.1.7-3(a), which shows double logarithmic plots of $-d/dt[\ln(M_R(t) - M_0]$ as a function of time t, and Table 4.1-5 summarizes the values of the best fit parameters as well as other relevant parameters. As for the $Ni_{76}Mn_{24}$ sample, the time independent component of the remanence (M_0) is large, accounting for approximately 90-95% of the magnitude of the total signal, and decreases monotonically with increasing temperature, thus resembling the behaviour of a ferromagnetic spontaneous magnetization. By contrast, the temperature dependence and magnitude of the exponent n and the characteristic time τ are both typical of pure spin glasses (Nordblad et al., 1986; Chamberlin, 1984) and, in particular, the variation of τ with temperature is consistent with the experimental systematics described in the previous paragraph, viz, a picture in which a fixed observation time window samples different portions of a stretched exponential curve as the characteristic time τ passes through the window. (b) For temperatures $65K \leq T_m \leq 95K$ (i.e. within the ferromagnetic phase), the stretched exponential description fails, and

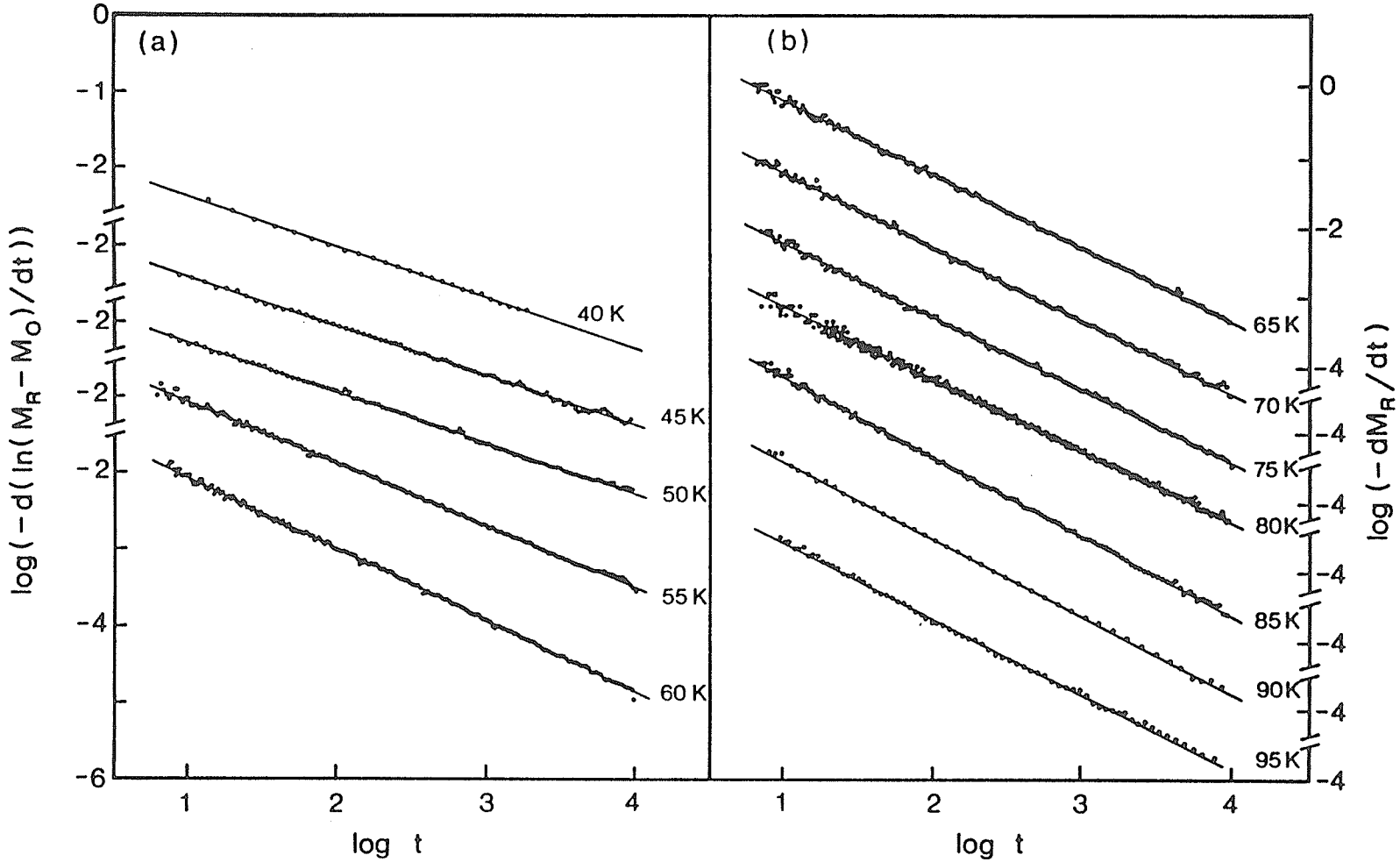

Figure 4.1.7-3: (a) Double-logarithmic plots of $-dln\ (M_R - M_0)/dt$ as a function of t for isotherms within reentrant phase (40 K $\leq T_m \leq$ 60 K). (b) Double-logarithmic plots of $-dM_R/dt$ as a function of t for isotherms within the ferromagnetic regime (65 K $\leq T_m \leq$ 95 K).

the functional form of the relaxation changes to Eq.(4.2), the superposition of a simple power law and a constant term. As shown by the straight lines in Figure 4.1.7-3(b), double logarithmic plots of $-dM_R/dt$ versus t, this function provides an excellent description over three decades of observation time, with a weakly temperature dependent exponent m (see Table 4.1-6 for a list of the best fit values of the parameters M_0 and m). Both the functional form of the decay and the magnitude of the exponent are symptomatic of relaxation at thermal equilibrium (Nordblad et al.,1987b).

Table 4.1-5: $Ni_{76.4}Mn_{23.6}$ **(Sample A)** Reentrant Phase Parameters for Eq.(4.1)

T(K)	t_w(s)	$t_w + t_c$ (s)	t_{infl} (s)	τ (s)	n	M_o(emu/g)
40	60	1110	8020±2110	3906±730	0.64±0.01	5.52±0.01
45	60	1050	5000±1440	4316±136	0.64±0.01	5.39±0.01
50	60	1080	2220±300	2437±59	0.68±0.01	5.08±0.01
55	60	1020	477±40	539±6	0.81±0.01	4.56±0.01
60	60	1080	2.4±1	3.8±0.7	0.92±0.01	3.80±0.01

Table 4.1-6: $Ni_{76.4}Mn_{23.6}$ **(Sample A)** Ferromagnetic Phase Parameters for Eq.(4.2)

T(K)	t_w(s)	m	M_o(emu/g)
65	60	0.05±0.01	3.37±0.01
70	60	0.06±0.01	2.65±0.01
75	60	0.05±0.01	1.93±0.02
80	60	0.05±0.01	1.33±0.02
85	60	0.13±0.01	1.67±0.01
90	60	0.11±0.01	1.40±0.01
95	60	0.12±0.01	1.15±0.01

As mentioned in the previous section, the decay of the thermoremanent magnetization in pure spin glasses is sensitive to the wait time t_w, and the wait time dependence of the TRM decay for this reentrant system was specifically examined

in sample B at six temperatures, three in each ordered phase. An identical procedure to that described earlier was employed here to acquire the decay at various wait times t_w, and Figure 4.1.7-4 shows the thermoremanent relaxations, all for a wait time $t_w = 60$ s, plotted on a logarithmic time scale. The functional forms which are compatible with the new relaxation isotherms confirm our aforementioned conclusions: (a) the reentrant isotherms (top 3 curves) are all accurately described, over the entire experimental time window, by Eq.(4.1) with parameters typical of spin glasses (see Table 4.1-7); (b) the ferromagnetic isotherms (bottom 3 curves) behave as simple power laws Eq.(4.2), with a weakly temperature dependent exponent m (see Table 4.1-8). Figure 4.1.7-5 shows double logarithmic plots of $-d/dt[ln(M_R - M_o)]$, for the reentrant isotherms, and $-dM_R/dt$, for the ferromagnetic isotherms, as a function of t.

As observed in the pure NiMn spin glasses, the decay in the reentrant phase exhibits a significant wait time dependence, as illustrated in Figure 4.1.7-6 and 4.1.7-7 for $T_m = 55$ and 60 K respectively, while no apparent wait time effects were observed in the ferromagnetic relaxation isotherms, as shown in Figure 4.1.7-8, indicating that aging processes, which dominate the decay in the reentrant phase and are responsible for the stretched exponential time dependence, are essentially absent within the ferromagnetic phase. This conclusion is consistent with the behaviour of the dynamic susceptibility in Figure 4.1.5-2, which exhibits virtually no sensitivity to the cooling conditions for temperatures $T_m > 65$K (field cooling is expected to produce a state which is considerably closer to thermal equilibrium than that generated by zero field cooling). In contrast to the $Ni_{76}Mn_{24}$ spin glass, the pure stretched-exponential plus a constant (Eq.(4.1)) is capable of describing the relaxation isotherms of $Ni_{76.4}Mn_{23.6}$ for wait times $t_w > 60$ s in the reentrant phase over the entire observation time window, as shown by the solid curves in Figure 4.1.7-4, 4.1.7-6 and 4.1.7-7. Table 4.1-7 summarizes the best fit parameters; both the exponent n and M_o show typical spin glass values, and τ agrees with t_{infl}

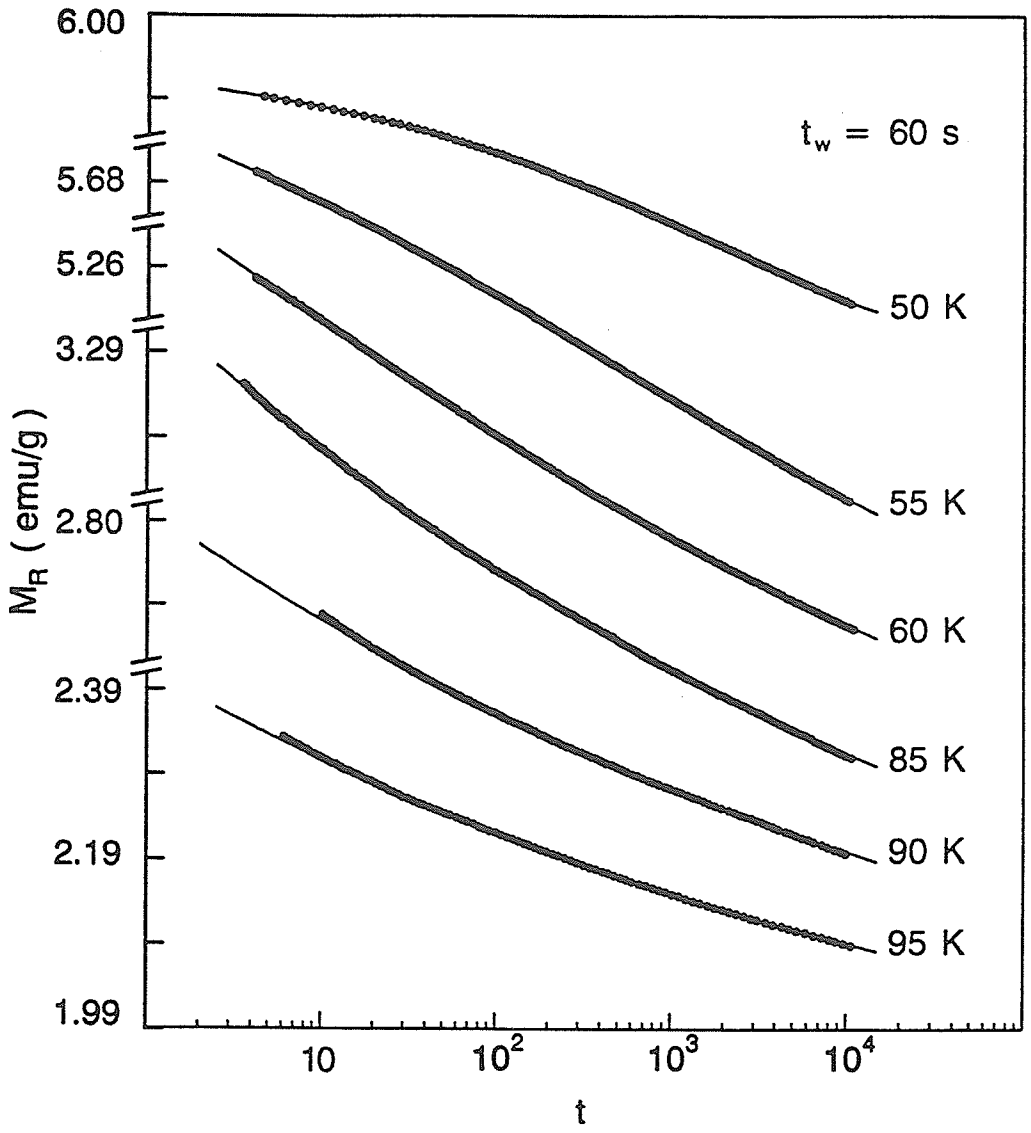

Figure 4.1.7-4: Decay of the thermoremanent magnetization M_R measured for sample B at several selected T_m between 40K and 95K, all for a wait time t_w = 60 s. Solid curves for T_m = 50, 55, 60 K are the fits to Eq.(4.1) and solid curves for T_m = 85, 90, 95 K are the best fits to Eq.(4.2).

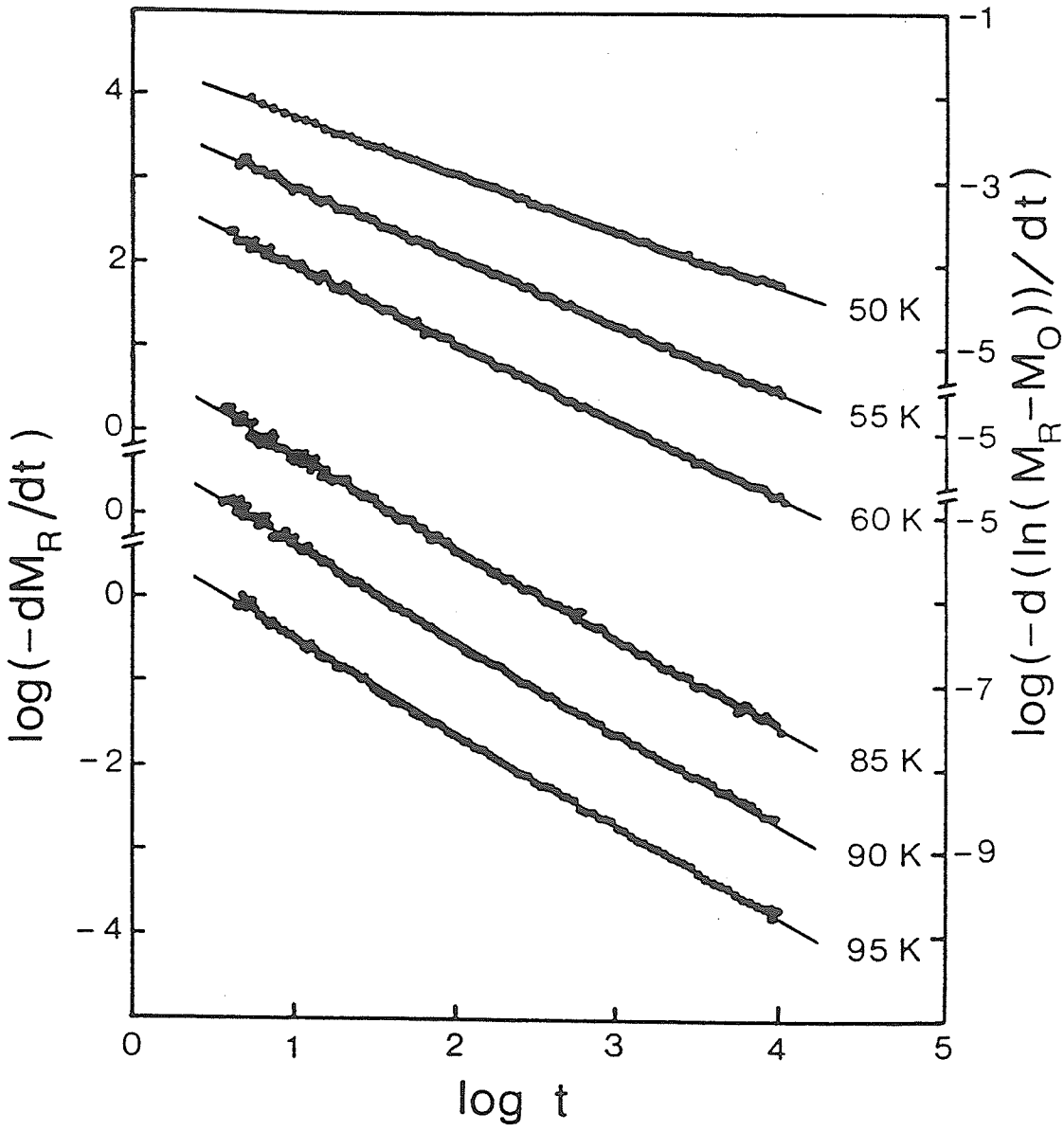

Figure 4.1.7-5: Double-logarithmic plots of $-dln\ (M_R - M_0)/dt$ (top 3 curves, right hand scale) and $-dM_R/dt$ (bottom 3 curves, left hand scale) as a function of t for isotherms in Fig.4.1.7-4.

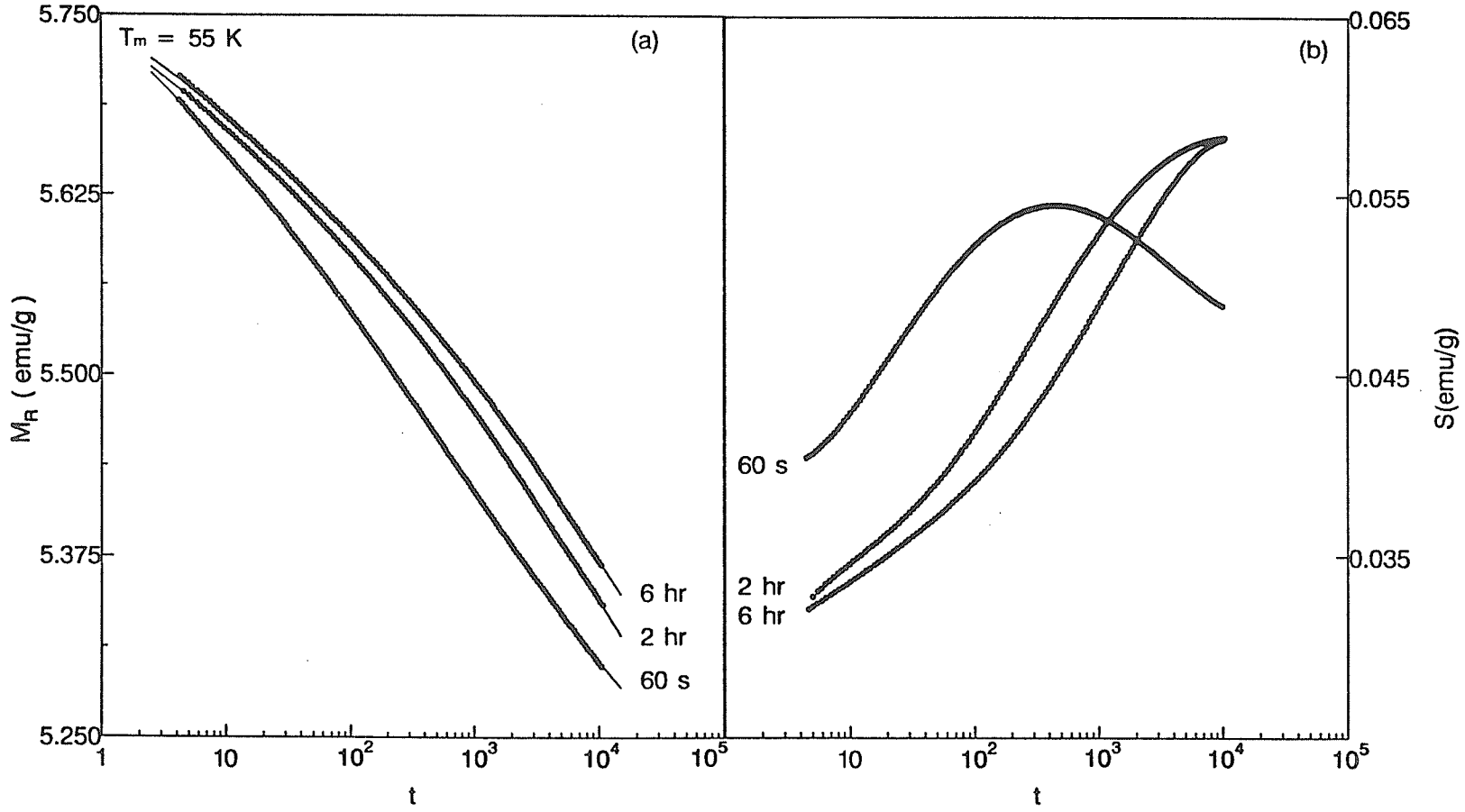

Figure 4.1.7-6: (a) The decay of the thermoremanent magnetization M_R at a measurement temperature T_m = 55 K for wait times t_w = 60 s, 2 hours, and 6 hours. The solid curves are the best fits to Eq.(4.1). (b) The numerically calculated relaxation rate $S(t)$ for the relaxation curves in (a), plotted on a logarithmic scale.

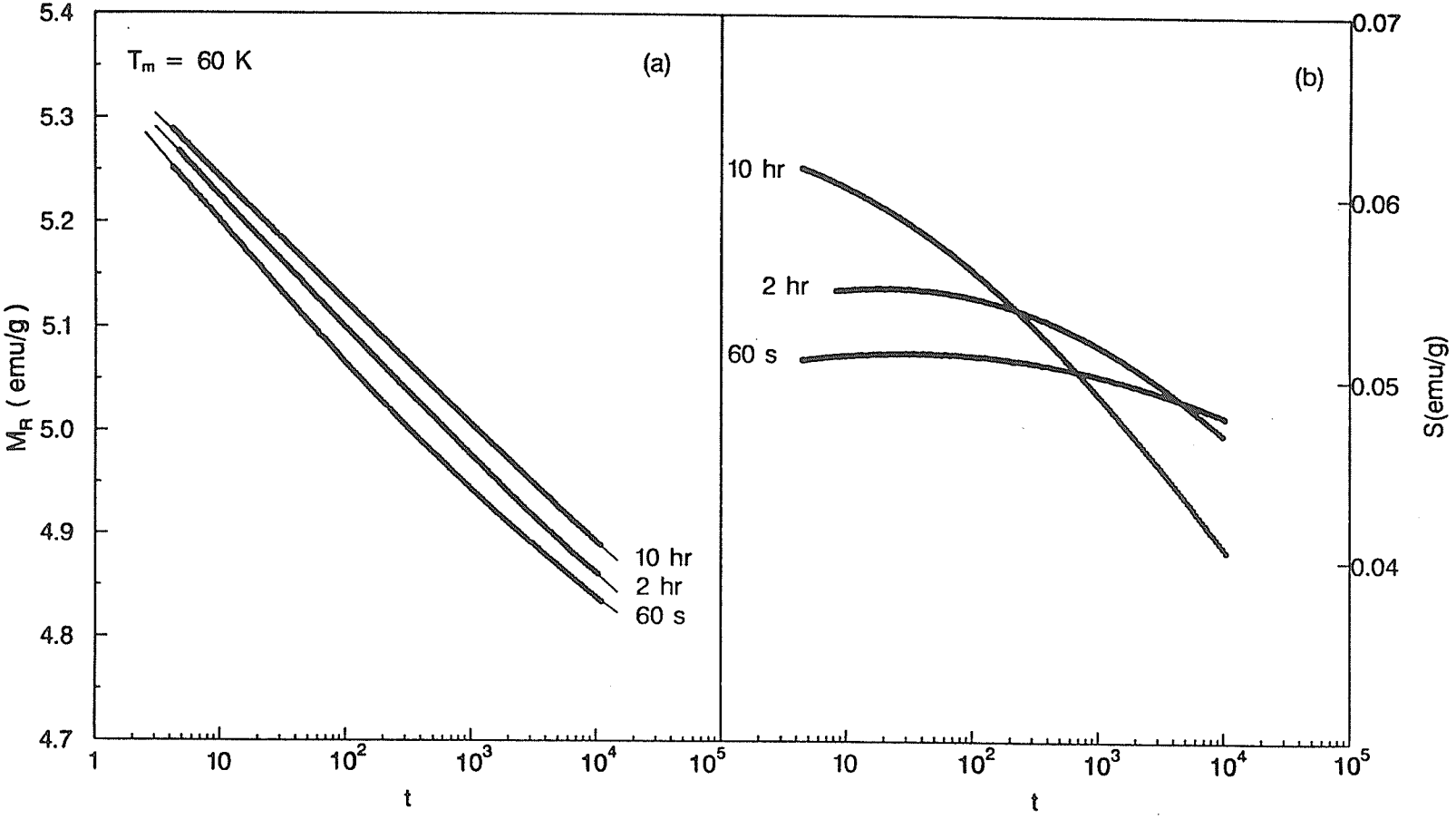

Figure 4.1.7-7: Same as in Fig.4.1.7-6, but for T_m = 60 K and wait times t_w = 60 s, 2 hours, and 10 hours.

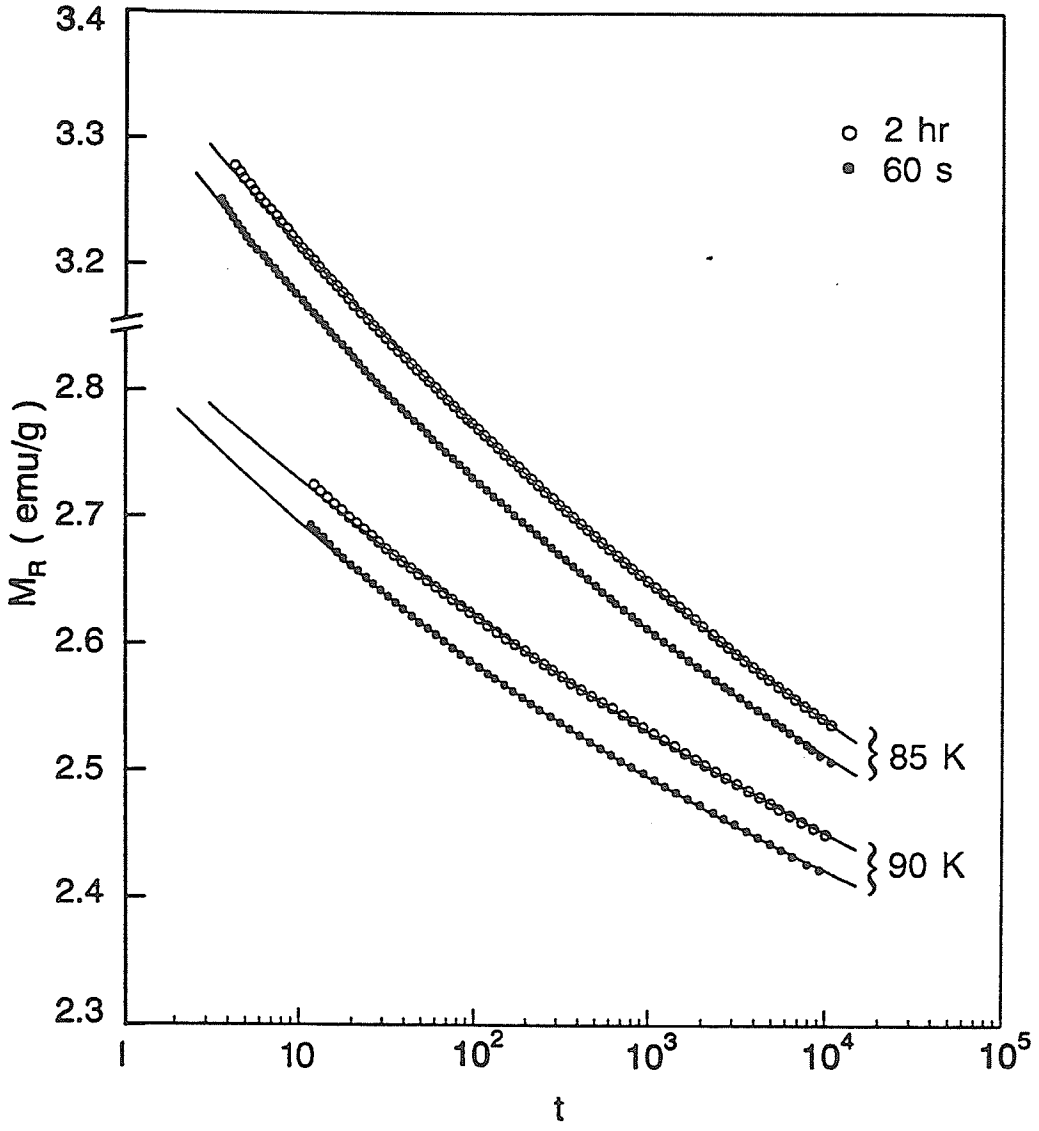

Figure 4.1.7-8: An illustration of the influence of the wait time t_w on the "high" temperature relaxation isotherms at T_m = 85 and 90 K within the ferromagnetic phase. Solid curves are the best fits to Eq.(4.2).

within experimental error.

Table 4.1-7: $Ni_{76.4}Mn_{23.6}$ (Sample B) Reentrant Phase Parameters for Eq.(4.1)

T(K)	t_w(s)	$t_w + t_c$ (s)	t_{infl} (s)	τ (s)	n	M_o(emu/g)
50	60	1110	3000±1500	2041±87	0.68±0.02	5.59±0.01
55	60	1020	600±300	603±15	0.81±0.02	5.16±0.01
55	7200	8130	$>10^4$	$(1.354\pm0.42)\times 10^5$	0.85±0.01	4.72±0.04
55	21600	22620	$>10^4$	$(1.03\pm1.05)\times 10^6$	0.86±0.01	4.48±0.13
60	60	1050	<4	0.32±0.21	0.92±0.01	4.61±0.01
60	7200	8220	20±15	20±9	0.92±0.01	4.45±0.03
60	36000	36960	40±30	32±14	0.94±0.01	4.30±0.07

Table 4.1-8: $Ni_{76.4}Mn_{23.6}$ (Sample B) Ferromagnetic Phase Parameters for Eq.(4.2)

T(K)	t_w(s)	m	M_o(emu/g)
85	60	0.08±0.01	2.33±0.01
85	7200	0.06±0.01	2.08±0.01
90	60	0.09±0.01	2.08±0.02
90	7200	0.06±0.01	1.90±0.03
95	60	0.08±0.01	1.82±0.01

The preceding analysis of thermoremanent relaxation dynamics in sections 4.1.6 and 4.1.7 offers novel and compelling evidence for the equivalence of the reentrant and spin glass phases: under comparable experimental conditions, the thermoremanent decay in both phases is dominated by nonequilibrium, age-dependent processes, and describable by a common relaxation function (for $t_w > 60$ s), which has been linked, theoretically, to a mesoscopic picture of growth and fragmentation of spin glass domains (section 2.4.2). Nevertheless, some specific features of the current study require further comment: (i) While the locations of the inflection points in the NiMn relaxation isotherms in Figures 4.1.6-2(a) ($Ni_{76}Mn_{24}$ spin glass) and 4.1.7-2(a) (reentrant ferromagnet) are approximately coincident with

the effective experimental age of the system, $t_{age} = t_w + t_c \sim 10^3$ s, in accordance with theoretical expectations (section 2.4.1), they also clearly exhibit a systematic, temperature dependent shift towards progressively longer observation times as the measurement temperature T_m is decreased. (A similar trend is clearly apparent in some of the authoritative relaxation studies, by Lundgren and co-workers, on CuMn, by Nordblad et al.(1987b), who show that t_{infl} varies monotonically from $t_{infl} < t_w$ at high temperatures to $t_{infl} > t_w$ at low temperatures.) This ability to discriminate, experimentally, between the various isotherms on the basis of the age of the system (t_{infl}), in spite of the constraints imposed on the current experimental procedure by the comparatively large cooling intervals $T_R - T_m \simeq 100$K and correspondingly long cooling times $t_c \simeq 15$ m (far removed from the ideal "temperature quench"), which effectively suppress the temperature dependence of t_c, simply indicates that the system is essentially in equilibrium over a significant portion of the cooling interval, and that the aging process does not commence until the system has been cooled through some effective reference temperature T_R^* which lies well below T_R (for the spin glass, the onset of nonequilibrium behaviour occurs just below the principal maximum in $M(T)$, while for the reentrant ferromagnet, the absence of nonequilibrium effects throughout the ferromagnetic phase suggests that T_R^* is located close to the ferromagnetic-reentrant phase boundary). Furthermore, from the tendency for t_{infl} to eventually exceed all of the obvious experimental time constants, at the lower measurement temperatures, it is evident that slow cooling rates accelerate the aging process so that, while t_w remains an appropriate measure of the evolution of the system at constant temperature T_m (in fact, $t_w = 60$ s represents a lower bound on all of the experimentally observable inflection points, as expected), the parameter t_c (or, more accurately, t_c' , if properly reckoned from the instant the system passes through T_R^* until it reaches T_m) considerably underestimates the influence of the cooling process. (A comparable trend develops in some of the CuMn relaxation data of Nordblad et al. (1986) at the

lowest measurement temperature, $T_m = 21$ K, where longer cooling times $t_c \sim 200$ s also yield $t_{infl} > (t_w + t_c)$, even for comparatively long wait times $t_w \sim 10t_c$). (ii) A "pure" stretched exponential is insufficient to provide a complete description of the NiMn relaxation isotherms in either the reentrant or spin glass phases, but must be supplemented by a time-independent term which decreases with increasing temperature T_m. This constant component is also an ingredient of other empirical representations of remanent relaxation in systems such as CuMn (Nordblad et al.,1986) and AuFe (Chamberlin and Haines, 1990), where it exhibits similar temperature dependent systematics (Nordblad et al.,1986). While the presence of this component in the reentrant NiMn ferromagnet is certainly consistent with vector models (section 2.2.2) which predict a longitudinal ferromagnetic spontaneous magnetization to coexist with transverse spin glass freezing within the reentrant phase, its physical significance in the "pure" spin glass phase is less transparent. However, the sharp theoretical phase boundary which separates the ferromagnetic regime ($m \neq 0, q \neq 0$) from the spin glass regime ($m = 0, q \neq 0$) in zero field (section 2.2.2 and Toulouse,1980), must vanish in finite field (Toulouse, 1980), so that the distinction between the ferromagnetic and spin glass phases is blurred, and the crossover becomes a more gradual, continuous process; consequently, it is not surprising if finite field measurements on a concentrated spin glass like $Ni_{76}Mn_{24}$, with its extreme proximity to the multicritical point and with a substantial ferromagnetic bias to its bond distribution, exhibit some features in common with its ferromagnetic neighbors (even though its critical properties are distinctly not ferromagnetic).

It is also instructive to compare the viscous properties of the reentrant NiMn ferromagnet described above, with a recent study by Chamberlin and Haines (1990) of thermoremanent relaxation in the $Au_{1-x}Fe_x$ system (see section 2.4.3.). Although the AuFe study did not explicitly include reentrant ferromagnets, a number of intriguing similarities nevertheless emerge from this comparison: (a)

the existence of two distinct relaxation regimes is also a characteristic of AuFe alloys within the cluster glass region of the magnetic phase diagram ($x \cong 0.12$): for temperatures *above* the maximum in the ZFC magnetization (which defines the transition temperature T_{CG}), the relaxation curves are concave up and represented by a relaxation function which reduces to a simple power law $M_R(t) \sim t^{-\alpha}$ in the limit of long observation times, while, below T_{CG}, the curvature of the data is inverted, necessitating the introduction of a further relaxation function which reduces to the Kohlrausch-Williams-Watts stretched exponential $M_R(t) \sim exp(-t^{\beta})$ in a similar limit. Thus the validity of the "power law" and "stretched exponential" descriptions of the reentrant NiMn data is a consequence of the comparatively more "restricted" experimental time window (1 s $< t \leq 10^4 s$) employed in the current investigation, while the absence of a well-defined inflection point (which is known to be a nonequilibrium manifestation of aging) below T_{CG} in the AuFe study, is related to the relatively long cooling times employed in this study ($t_{eff} \sim 10^3 s$), which yield a response closer to true thermal equilibrium. (b) Within the ferromagnetic phase of the AuFe system, the relaxation exhibited several complex features which required not only the superposition of the two relaxation functions mentioned above, but also the introduction of a constant base line, in order to achieve a satisfactory description of these more concentrated samples. This time independent component of the remanence is also an essential ingredient of the current analysis in NiMn, (see Tables 4.1-1 to 4.1-8 for values of the parameter M_o), particularly in the reentrant phase, and supports the hypothesis that the reentrant phase is a hybrid of two ordered spin configurations: longitudinal ferromagnetism, which generates the large static remanence, and spin glass freezing, which is responsible for the stretched exponential thermoremanent decay with its age-dependent characteristics. However for a spin glass $Ni_{73.1}Mn_{26.9}$ the magnitude of the remanent constant M_o is comparable to the size of the decay and eventually approaches zero.

4.2 The AuFe System

4.2.1 Introduction

The AuFe system is perhaps the most extensively investigated disordered system. Transition temperatures obtained from experiments by Cannella and Mydosh (1972), Coles et al. (1978) and Sarkissian (1981) have been compiled into the magnetic phase diagram shown in Figure 4.2.1-1. At very low Fe concentrations the alloy behaves as an isolated impurity system with a Kondo temperature of about 0.3 K. The concentration range 0.5-8 at % Fe corresponds to archetypal spin glass behaviour at low temperatures due to the freezing of good local Fe moments which are coupled through the RKKY interaction (section 2.1.1). As the Fe concentration is increased above 8 at.%, ferromagnetically coupled clusters of Fe moments appear and form a cluster glass (CG) at low temperatures, with superparamagnetism at high temperatures. At a critical percolation composition $C_p = 15.7 \pm 0.5$ at.% Fe (Sarkissian, 1981), an infinite ferromagnetic cluster can be found and long-range ferromagnetism occurs. It should be emphasized that, even after the percolation concentration 15.7 at % Fe is exceeded, a significant fraction of the iron moments will still not be in the infinite cluster, yielding the possibility of coexisting long-ranged ferromagnetism and cluster glass behaviour between 16 and 28 at % Fe, and hence potentially reentrant behaviour. Above 28 at % Fe, there is only long range ferromagnetism.

There are significant uncertainties concerning the magnetic phase diagram due to the extreme sensitivity of the magnetic properties to the metallurgical state of the system. In order to produce a random AuFe system one has to water quench the alloy from high temperature. Various heat treatments can change the degree of atomic Fe clustering dramatically, thereby affecting the magnetic ordering temperature. Crane and Claus (1980, 1981) have studied the effects of annealing

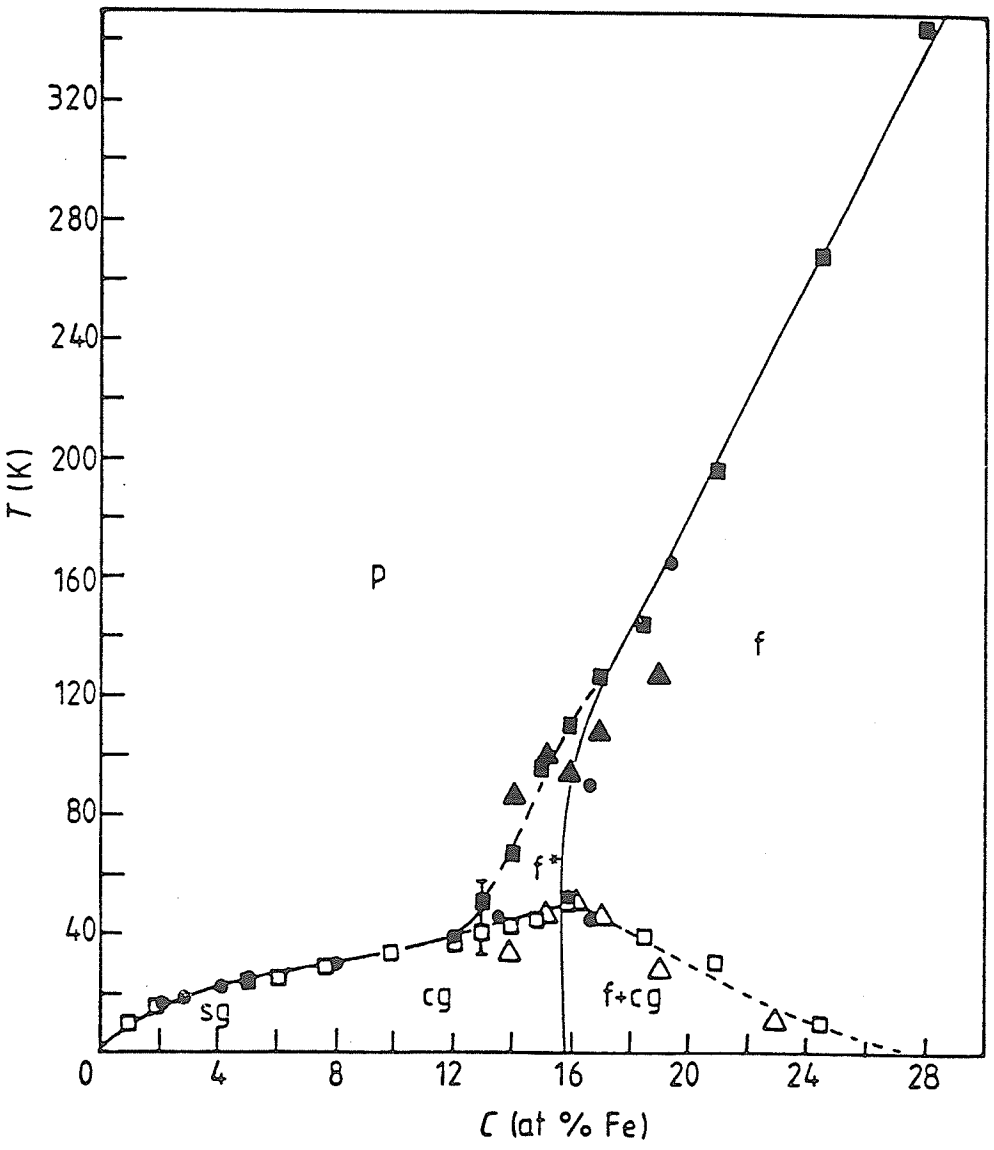

Figure 4.2.1-1: Magnetic phase diagram of AuFe. The various regimes are paramagnetic (p), ferromagnetic (f), spin glass (sg), cluster glass (cg) and quasi-critical (f*). From Sarkissian (1981).

temperature on the magnetic ordering temperature and spontaneous magnetization for Au-14 and 15 at.% Fe samples. Figure 4.2.1-2 shows the ac susceptibility measured as a function of temperature for a Au-15 at.% Fe sample which was annealed at various temperatures T_A. In the state quenched from the lowest annealing temperature $200°C$, the interaction between large ferromagnetic clusters causes the sample to order ferromagnetically at a high temperature $T_c = 108$ K. Increasing the annealing temperature reduces the degree of atomic clustering. The sample becomes more and more random with fewer and fewer ferromagnetic clusters. At $T_A = 480°C$, the Curie temperature is reduced to $T_c = 60$ K. When the annealing temperature is increased further above $535°C$, the magnetic ordering temperature *increases* again. Crane and Claus concluded that the highest degree of disorder in Au-15 at.% Fe sample is obtained by quenching from $550°C$, and that quenching from a higher temperature produces an inhomogeneous state and should be avoided. They pointed out that the reversal of this trend for $T_A > 550°C$ is due to a vacancy-enhanced diffusion during the quenching process (Crane and Claus, 1980). The annealing temperature is so high that one is no longer able to quench-in a high temperature equilibrium state. Significant diffusion takes place during the quenching process and one ends up with a quenched-in state with a larger degree of clustering than that obtained from $550°C$.

Similar metallurgical behaviour has been found in Au-14 at % Fe. According to Figure 4.2.1-3, quenching from higher temperature can reduce the magnetic ordering temperature dramatically and also suppress the height of the susceptibility maximum. In fact, quenching from above about $300°C$ can change the system from a ferromagnet into a spin glass. Strong evidence for such a transformation as a function of annealing temperature is shown in Figure 4.2.1-4, which shows the inverse susceptibility and spontaneous magnetization as a function of temperature for various quenched states (Crane and Claus, 1981). In the states quenched from $281°C$ and $287°C$, the susceptibility diverges at T_{C1}=61.5 K and 58 K respective-

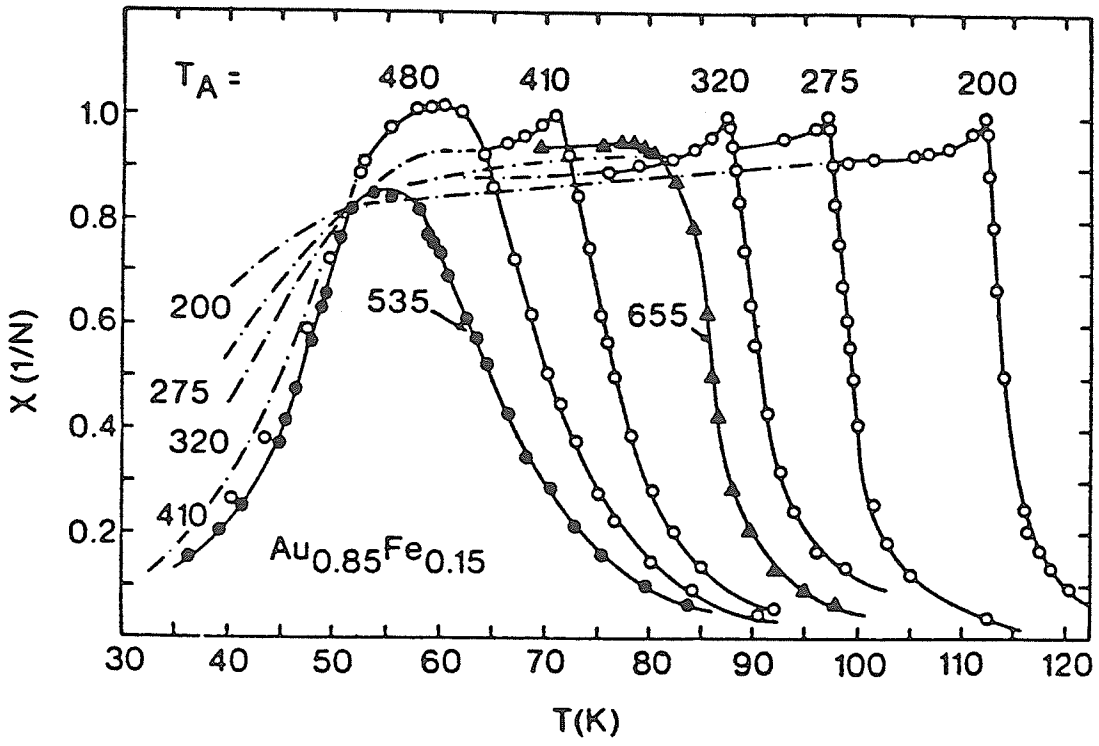

Figure 4.2.1-2: ac susceptibility in units of the reciprocal demagnetization factor vs. temperature, for a Au-15 at% Fe alloy, quenched from various annealing temperatures T_A. From Crane and Claus (1980).

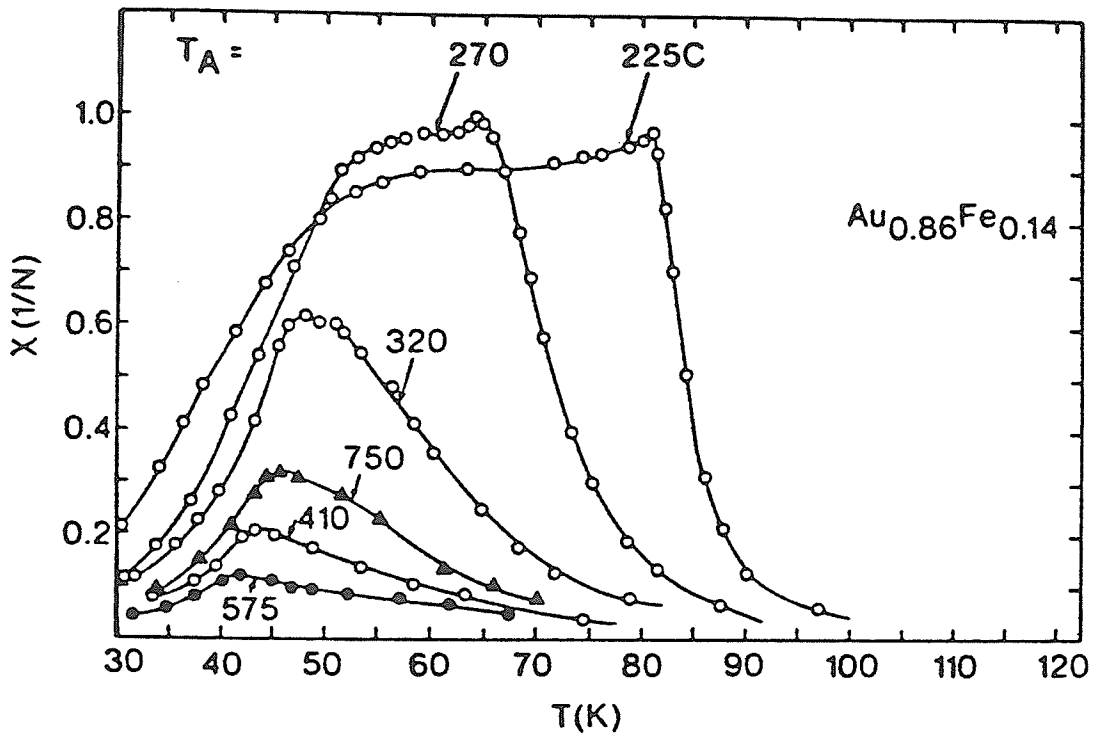

Figure 4.2.1-3: ac susceptibility in units of the reciprocal demagnetization factor vs. temperature, for a Au-14 at% Fe alloy, quenched from various annealing temperatures T_A. From Crane and Claus (1980).

ly, and a spontaneous magnetization develops (solid squares) which indicates the onset of ferromagnetism. Below a second critical temperature T_{C2}= 51 K and 54 K for 281°C and 287°C respectively, the spontaneous magnetization disappears, corresponding to a transition into a spin-glass-like state. When the sample was annealed at 300°C and 311°C the susceptibility remain finite at all temperatures. The broad minimum in $1/\chi$ probably indicates a direct transition from paramagnetic to spin glass state. Ferromagnetism is absent in these two states.

Extensive studies of the dynamic response of AuFe in the critical concentration regime $8 \leq c \leq 28$ at.% Fe have been conducted by Sarkissian (1981). Sarkissian measured the real component of the ac susceptibility $\chi'(\omega)$ as a function of field, temperature, frequency and amplitude of the ac driving field. All specimens were subjected to an homogenizing annealing at 900°C for three days, followed by water quenching.

The ac susceptibility was measured in zero dc biasing field as a function of temperature using an excitation frequency of 340 Hz, and very small (about 10^{-6} RMS Oe) alternating fields. These results are shown in Figure 4.2.1-5, and 4.2.1-6 for alloys above and below the critical percolation concentration $C_p = 15.7 \pm 0.5$ at.% Fe. In alloys close to and above C_p, with an infinite cluster, the transition to a ferromagnetic state shows a very sharp peak at T_c. This peak is extremely sensitive to the amplitude of the ac field. As the alternating field was increased, the peak was suppressed and shifted to lower temperatures. Another distinct characteristic of the $\chi'(\omega)$ curves for $c \geq 16$ at %Fe alloys at lower temperatures is the rapid drop, creating a very marked shoulder, which is attributed to the freezing of the finite clusters. Below the critical concentration 16.0 at % Fe the temperature dependence of $\chi'(\omega)$ only shows a rounded maximum (Figure 4.2.1-6). Absence of the sharp peak at high temperatures indicates that finite clusters dominate the magnetic response. With Fe concentrations below about 10 at.%, the nearest-neighbour ferromagnetic Fe-Fe coupling becomes impossible. The domi-

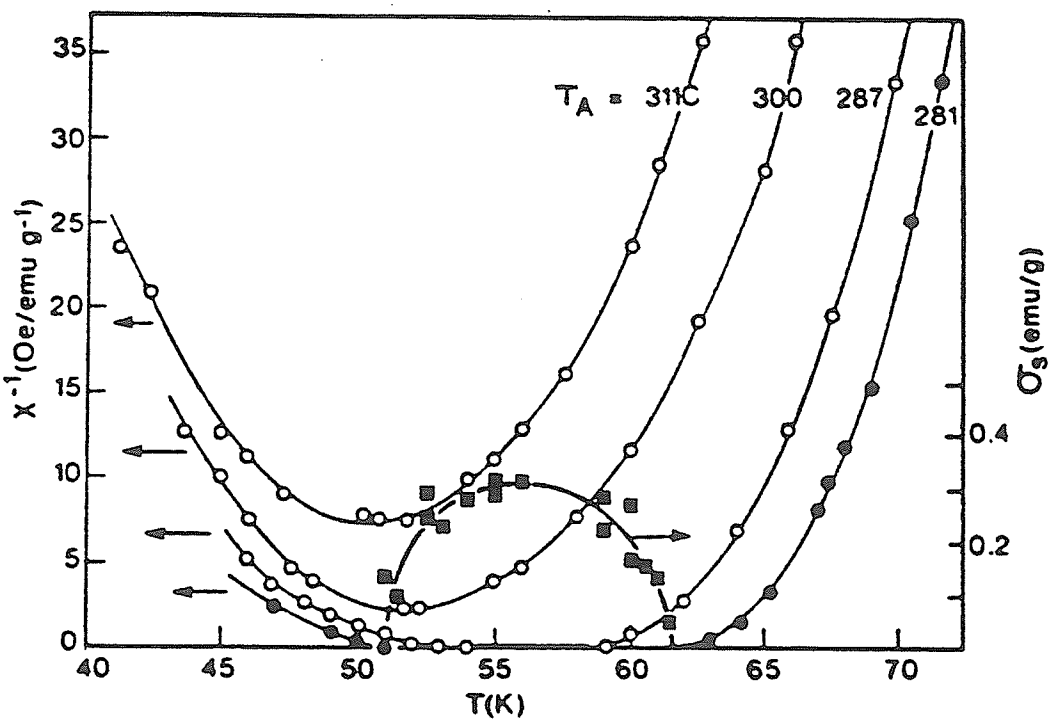

Figure 4.2.1-4: ○ ● inverse susceptibility, scale on left, ■ spontaneous magnetization, scale on right for a Au-14 at% Fe sample quenched from various annealing temperatures. From Crane and Claus (1981).

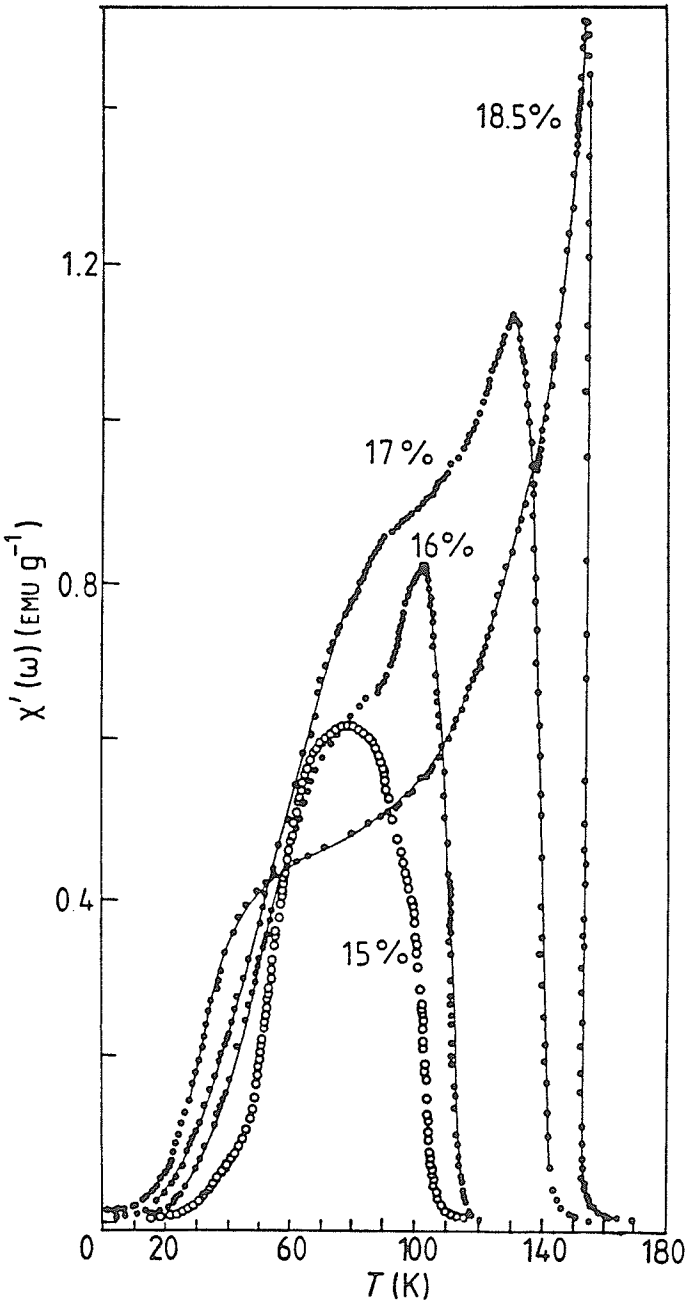

Figure 4.2.1-5: ac susceptibility χ' as a function of temperature for AuFe alloys close to the percolation concentration. From Sarkassian (1981).

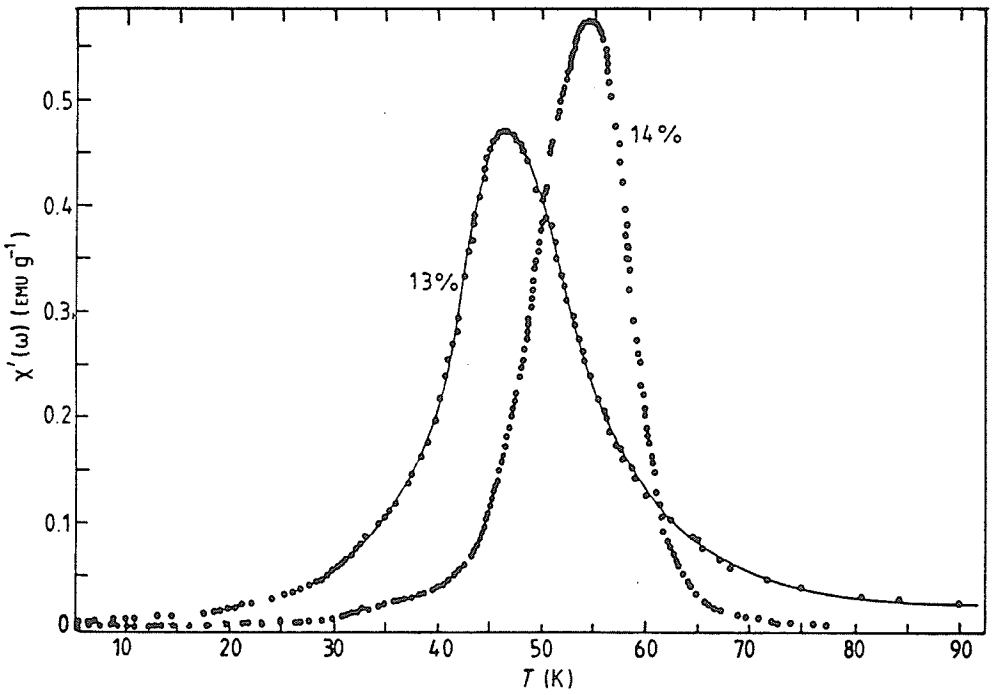

Figure 4.2.1-6: ac susceptibility as a function of temperature for AuFe alloys below the percolation concentration. From Sarkassian (1981).

nant RKKY interaction between isolated Fe moments causes a typical spin glass cusp at a freezing-temperature T_{SG}. The cusp becomes rounded with the application of magnetic field. Critical behaviour in a spin glass Au-0.97 at.% Fe was examined by Chikazawa et al. (1983). The temperature dependence of the nonlinear susceptibility $\chi_2(t)$ shows a sharp peak near $T_{SG} = 8.9$ K.

In a finite dc biasing field, there is considerable structure in the susceptibility versus temperature measurements. Figure 4.2.1-7(a) shows the temperature dependence of the susceptibility $\chi'(\omega)$ in different steady fields for a Au-15 at.% Fe alloy (Kleiman et al., 1982). Three distinct peaks are present in non-zero dc fields: the highest temperature peaks were recognized as ferromagnetic critical peaks, with the peak temperature increasing and peak amplitude decreasing as the steady field is increased. The lower temperature peaks are also suppressed in amplitude, but shifted downward in temperature exhibiting a reentrant spin glass behaviour.

Critical analyses have been performed by Maartense and Williams (1978), who measured the ac susceptibility of a reentrant ferromagnet Au-22 at.% Fe at an excitation frequency f=2400 Hz, as a function of both applied field and thermal history. High temperature critical point exponent analysis yielded the exponents $\gamma = 1.51$ and $\delta = 3.6$ for quenched thin samples. Aging for 1500h at room temperature increases the Curie temperature by $\sim$ 70K, while, aging between 100 and $300°C$ causes T_c to fall again (by $\sim$ 50 K). Both γ and the magnetic moment of Fe (μ_{eff}) were unchanged by such heat treatment, but δ increased to 3.9. This behaviour was ascribed to the occurrence of short-range order, rather than the formation of large magnetic clusters. An analysis of the ferromagnetic component of the triple-peaked structure of the Au-15 at.% Fe sample, shown in Figure 4.2-7(a) yielded a simple power-law dependence for $\chi(h, t_m)$ vs h_{int} (Eq.2.116) with $\delta = 3.4 \pm 0.15$. However, the double logarithmic plot of $\chi(0, T > T_c)$ against reduced temperature showed considerable curvature, similar to that found in Ni-

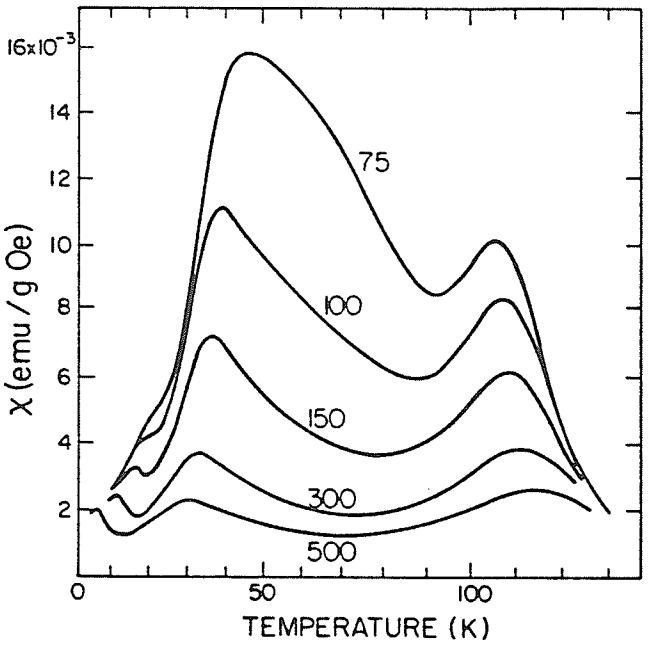

Figure 4.2.1-7 (a): ac susceptibility of Au-15.0 at.% Fe, measured in various static biasing fields, plotted against temperature. The static biasing field (in Oe) is marked against each curve. From Kleiman et al. (1982).

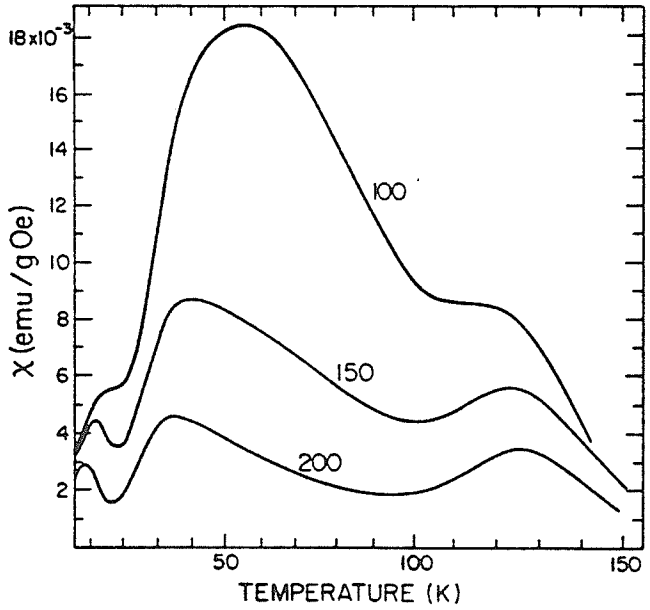

Figure 4.2.1-7 (b): ac susceptibility of Au-15.0 at.% Fe, measured in various static biasing fields, plotted against temperature for the *aged* sample. The data taken at 200 Oe has been shifted downwards by one scale unit for clarity. From Kleiman et al. (1982).

23.6 at % Mn (section 4.1.5), due to the absence of long range ferromagnetic order. An analogous set of scaling equations (Eq.2.128) was applied to the intermediate peak, but no scaling-like relationship was found. Strong aging affects were also found in this sample. Figure 4.2.1-7(b) shows the ac susceptibility measured on a sample aged at room temperature for 190 hours. Aging causes these peaks to become considerably broader, and demands a much higher field to resolve them, indicating enhancements of short range order (increasing the number of nearest neighbour Fe impurities). The zero field susceptibility in the aged sample is generally reduced in magnitude compared with the quenched specimen, but the weak temperature independent "plateau" is broadened.

4.2.2 Low Field Thermoremanent Relaxation in a Pure Spin Glass: $Au_{90}Fe_{10}$

In contrast to NiMn, the critical properties of the ferromagnetic and spin glass transitions in AuFe have been the subject of considerable attention in the literature, and may be regarded as well established; however, with the exception of the early work by Guy (1978), the viscous properties of AuFe have received surprisingly little attention, particularly within the reentrant ferromagnetic configuration. Consequently, the current investigation focused exclusively on measurements of the thermoremanent relaxation, and exploited the results of the earlier critical investigations only to aid in choosing appropriate concentrations as good candidates for spin glass and reentrant ferromagnetic behaviour.

In this section we present TRM relaxation measurements in a $Au_{90}Fe_{10}$ "pure" spin glass. The sample preparation was described in section 3.2.2, and the dimensions of the sample are listed in Table 3.2. An EDAX analysis was consistent with a high degree of homogeneity.

Figure 4.2.2-1 shows the temperature dependence of the low field static magnetization of the $Au_{90}Fe_{10}$ sample, measured in $H_a = 5$ Oe under both FC and

ZFC conditions. The spin glass exhibits the canonical cusp-like structure at T_{SG} = 32 K, indicative of random spin freezing, and the gradual bifurcation of the M_{FC} and M_{ZFC} curves below T_{SG} symptomatic of irreversibility. The decay of the thermoremanent magnetization was measured over four decades of observation time (6 s$< t \leq 10^4$ s), and Figure 4.2.2-2 summarizes the features of this decay at various measurement temperatures T_m between 18 and 30 K for $t_w = 60$ s. Each relaxation isotherm in Figure 4.2.2-2 was obtained by following an identical procedure to that described in section 4.1.6, with an applied cooling field of $H_c = 5.0$ Oe and a reference temperature of $T_R = 50$ K (The cooling procedure was again very reproducible and yielded cooling times consistently close to $t_c = 500$ s). On a logarithmic time scale, the relaxation isotherms exhibit well defined inflection points (marked by arrows) for the isotherms with $T_m \leq 28$ K, and all are well described by the superposition of a stretched exponential and a constant term as shown by the solid curves. The best fit parameters are listed in Table 4.2-1, along with a number of other relevant experimental parameters. The inflection point t_{infl} was established from the maximum in a plot of the relaxation rate $S(t) \equiv -\partial M_R/\partial \ln t$ as a function of log t, and as shown in Figure 4.2.2-2, exhibits a systematic shift with T_m, so that, at high temperatures ($T_m > 24$ K), a discrepancy develops between t_{infl} and the effective age $t_{age} = t_w + t_c$ of the system, which is probably a manifestation of limitations imposed by the finite cooling rate. The magnitude of the exponent n is typical of canonical spin glasses, and exhibits a slight increase with measurement temperature for $T_m/T_{SG} > 0.8$.

The nonequilibrium age-dependent behaviour was examined in detail at a representative temperature $T_m = 22$K, and the wait time dependence of the isotherms is shown in Figure 4.2.2-3(a). The inflection points coincide, within experimental error (see Table 4.2-2), with the effective age of the system, so that $t_{infl} \cong t_w + t_c$, and, as before,this age dependent behavior translates into a maximum in the relaxation rate $S(t)$ at $t_m = t_{infl} = t_w + t_c$ which propagates towards longer ob-

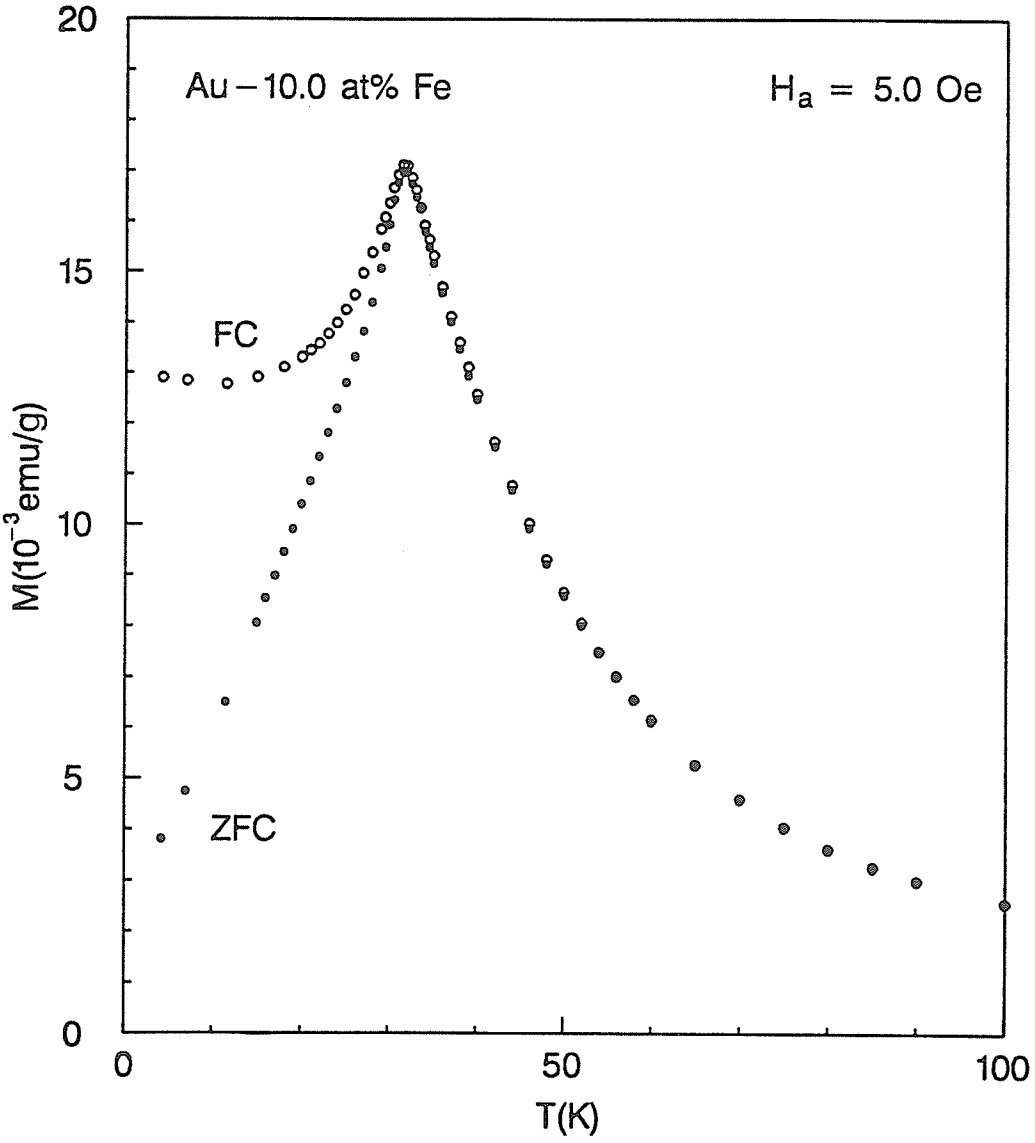

Figure 4.2.2-1: The temperature dependence of the field cooled (FC) and zero field cooled (ZFC) static magnetization of the Au-10.0 at% Fe spin glass measured in an applied field H_a = 5 Oe.

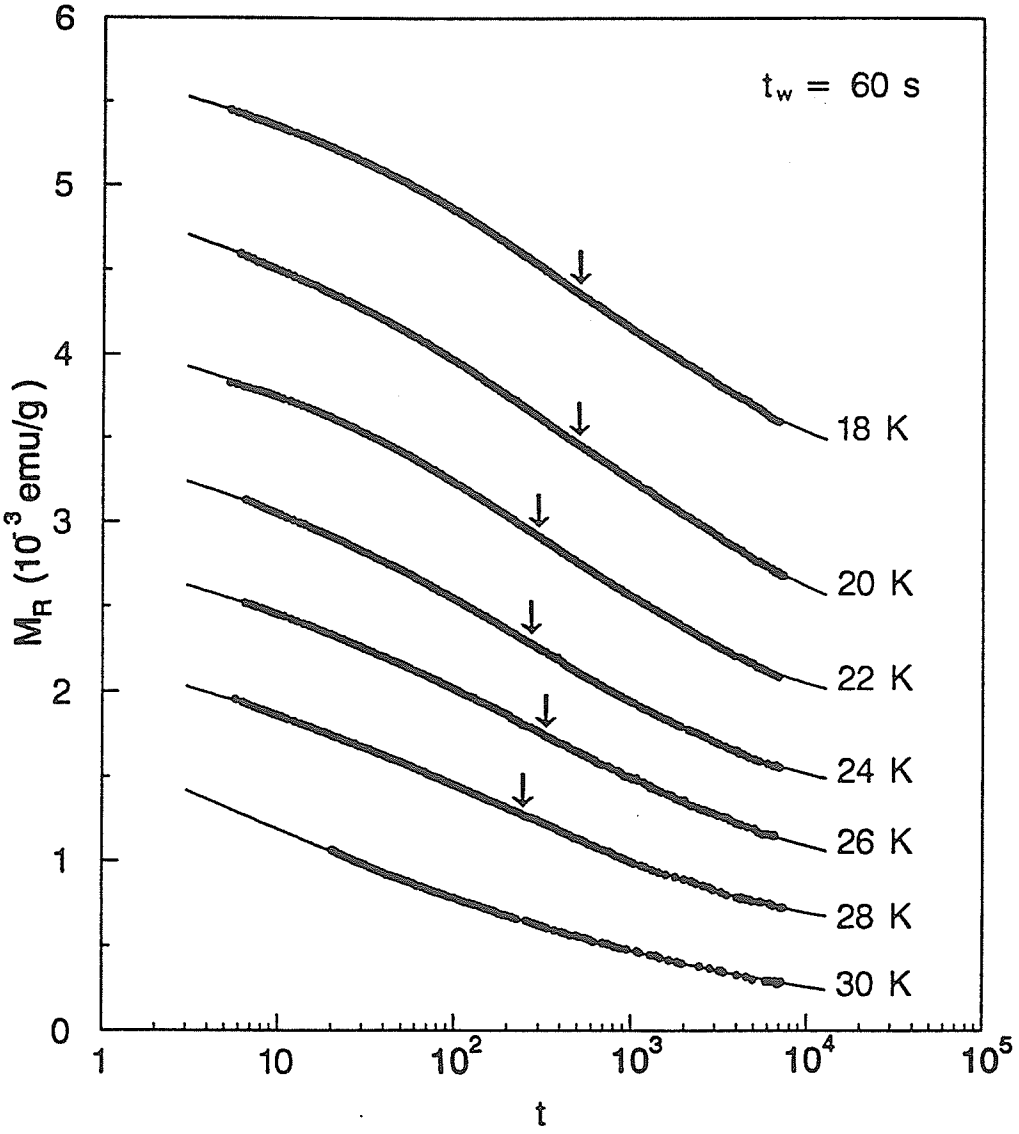

Figure 4.2.2-2: A set of relaxation isotherms all corresponding to a wait time t_w = 60 s. The vertical arrows mark the locations of the inflection points. Solid curves are the best fits to Eq.(4.1).

servation times with increasing t_w, as shown in Figure 4.2.2-3(b). Attempts to fit these curves to the pure stretched exponential in Eq.(4.1) revealed that this representation was inadequate for large wait times $t_w > 60$ s, and only provided a good description over a limited time interval which became progressively narrower as the wait time increased, so that systematic deviations developed at short times. However, the *product* of the stretched exponential and simple power law Eq.(4.3) was able to provide a complete description (solid lines in Figure 4.2.2-3(a)) of the isotherms over the entire observation time interval, and the best fit parameters are listed in Table 4.2-2.

Table 4.2-1: $Au_{90}Fe_{10}$ Spin Glass Parameters for Eq.(4.1)

T(K)	t_w(s)	$t_w + t_c$ (s)	t_{infl} (s)	τ (s)	n	$M_o(10^{-3}$ emu/g)
18	60	540	500±200	730±20	0.68±0.01	3.26±0.02
20	60	510	500±200	630±20	0.71±0.01	2.31±0.02
22	60	510	300±100	440±10	0.67±0.01	1.91±0.02
24	60	570	290±100	290±6	0.70±0.01	1.39±0.01
26	60	780	350±100	330±10	0.72±0.01	0.93±0.02
28	60	630	250±100	180±10	0.73±0.01	0.60±0.01

Table 4.2-2: $Au_{90}Fe_{10}$ Spin Glass Parameters for Eq.(4.3)

T(K)	t_w(s)	$t_w + t_c$ (s)	t_{infl} (s)	τ (s)	m	n	$M_o(10^{-3}$emu/g)
22	240	720	600±200	993±50	0.02±0.01	0.61±0.01	1.91±0.01
22	1200	1680	2000±500	2664±21	0.05±0.01	0.45±0.01	2.04±0.01
22	1800	2280	2000±500	2592±42	0.06±0.01	0.40±0.01	2.22±0.01
22	3600	4050	4000±1000	4866±116	0.05±0.01	0.41±0.01	2.17±0.01

A fascinating feature of our current investigation of AuFe is our observation of the memory behaviour of the spin glass relaxation, which was first observed in a canonical Cu-5.0 at.% Mn spin glass by Lundgren et al. (1986a, see Figure

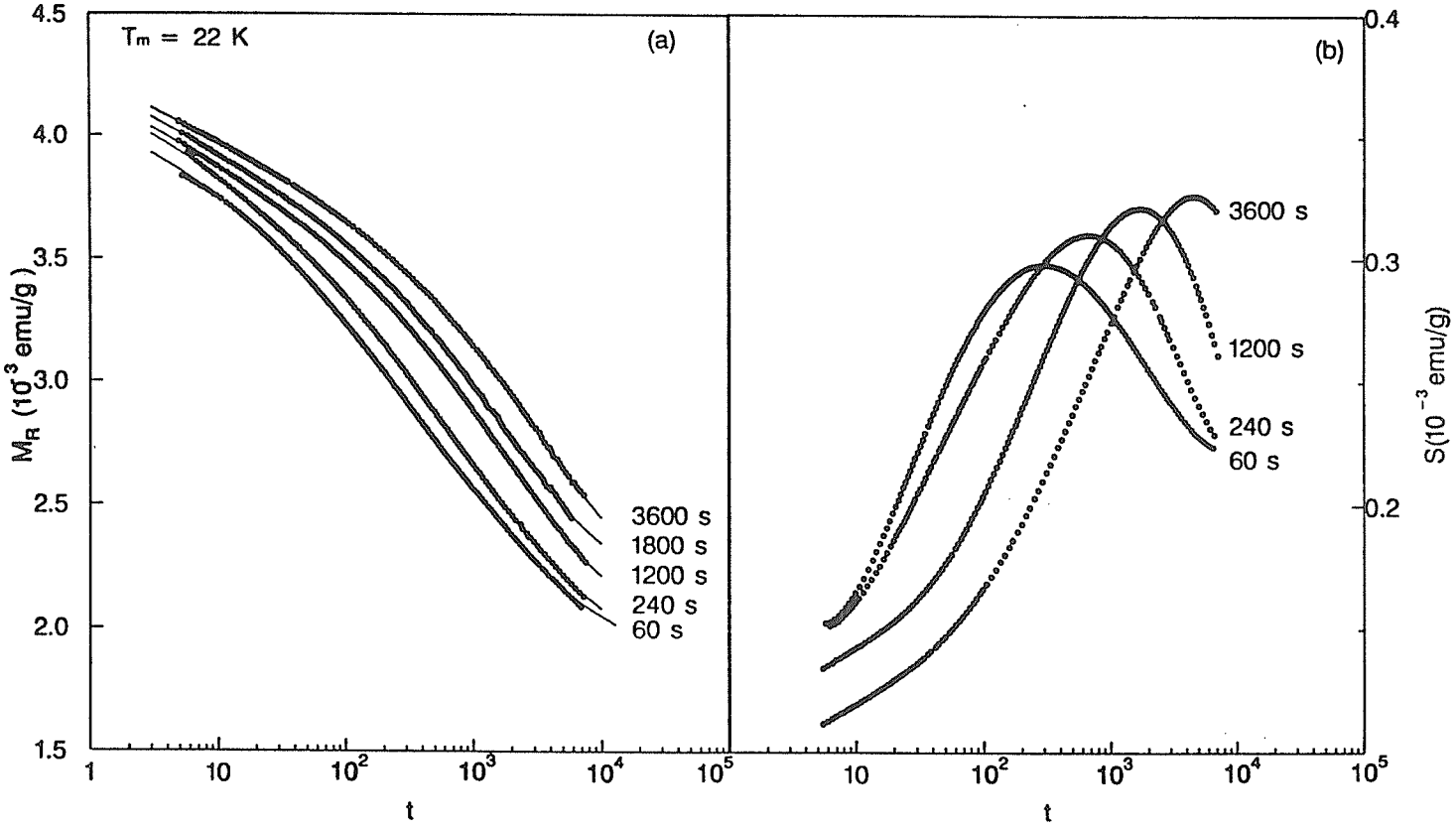

Figure 4.2.2-3: (a) The decay of the thermoremanent magnetization M_R at a typical measurement temperature T_m = 22 K for wait times t_w = 60, 240, 1200, 1800, 3600 s. The solid curves for t_w > 60 s are the best fits to Eq.(4.3). (b) The numerically calculated relaxation rate $S(t)$ for four of the five relaxation curves in (a), plotted on a logarithmic scale.

1-26). The existence of macroscopically long relaxation times in any spin glass ultimately implies that the decay of the thermoremanent magnetization depends on the history of the sample and should thus display a memory for past events. The fundamental principles governing the memory function which controls the relaxation of the magnetization are based on linear response theory. According to the detailed investigations on the field dependence of the remanent magnetization in a Cu-5.0% Mn spin glass, by Nordblad et al. (1987a), at low fields (< 10 Oe) the isothermal remanent magnetization (IRM) M_{IRM} has a linear field dependence regardless of wait time and observation time, whereas the thermoremanent magnetization M_{TRM} has a nonlinear field dependence. In ZFC magnetization measurement, in which the sample is cooled in zero field to a measurement temperature T_m (below T_{SG}) after which a small external field is applied, the change of the magnetization may be expressed (Lundgren et al., 1986a) as

$$M_{ZFC}(t_w, t) = h \cdot p(t_w, t) \tag{4.4}$$

according linear response theory, where $p(t_w, t)$ is called the response function, which depends on the wait time t_w at T_m due to the age dependence of spin glasses. In an isothermal remanent magnetization measurement, the sample is similarly cooled in zero field to T_m, where a small field pulse is applied after an initial wait time t_{w1} and removed after a wait time t_{w2}, as shown in Figure 4.2.2-4(a). The validity of the linear response of the relaxation implies that the principle of superposition applies (Lundgren et al., 1986a; and reference therein), and thus the relaxation of the IRM can be written as a sum of responses caused by a positive field change at t_{w1} and a negative field change at t_{w2} (Figure 4.2.2-4(b)), viz

$$M_{IRM}(t_w, t) = h \cdot p\left(t_{w1}, t + (t_{w2} - t_{w1})\right) - h \cdot p\left(t_{w2}, t\right). \tag{4.5}$$

The memory of the field change experienced by the system may not be erased by a subsequent field reversal. The duration of the field pulse is $t_{w2} - t_{w1}$ and t is

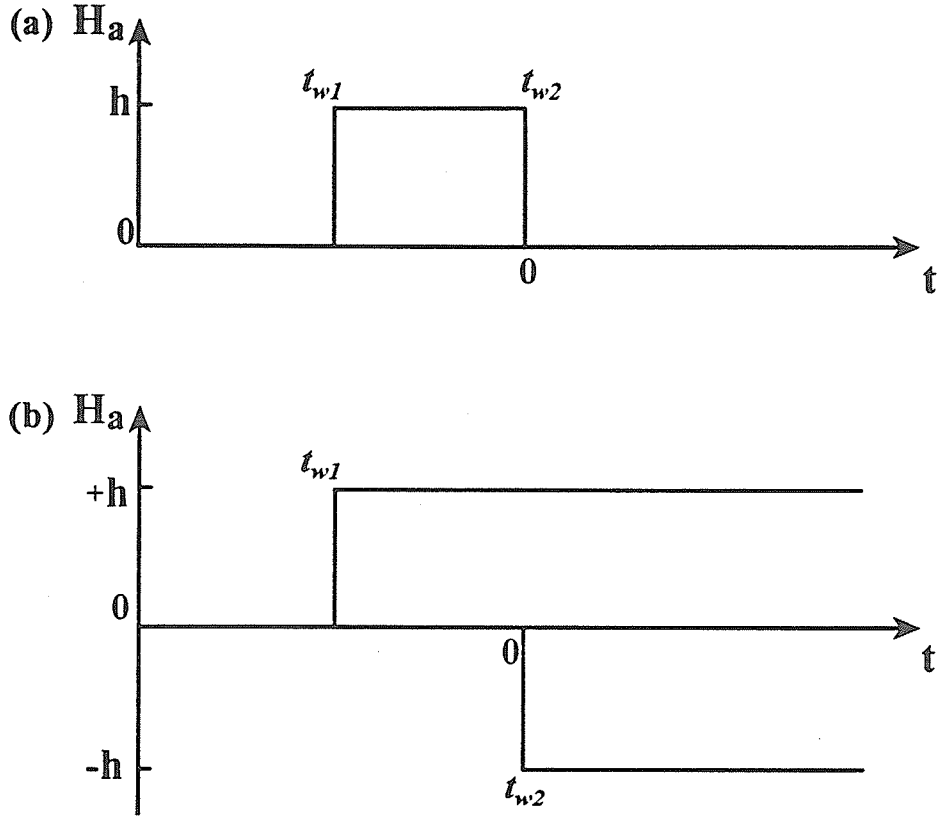

Figure 4.2.2-4: (a) Field pulse in isothermal-remanent magnetization (IRM) measurements. (b) Equivalent scheme for the field cycling in IRM measurements based on the principle of superposition. From Lundgren et al. (1986a).

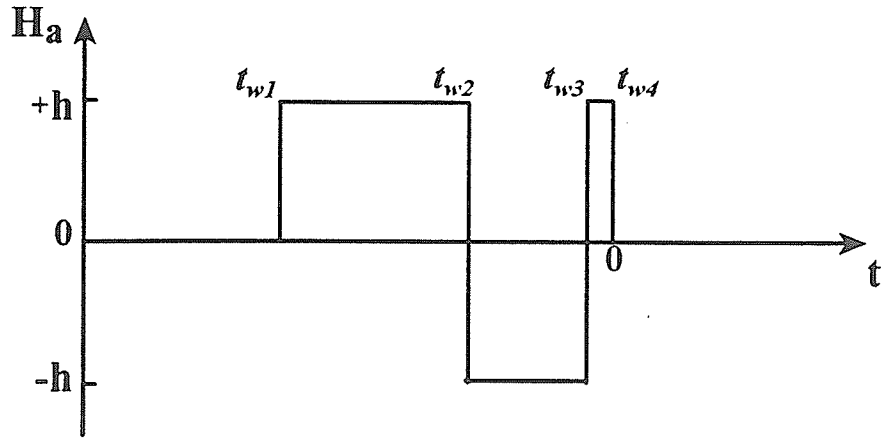

Figure 4.2.2-5: The sequence of field pulses used to test the memory function $M_{mem}(t)$ of Eq.(4.6). The t_{wi}'s refer to the wait times at constant temperature prior to the *i-th* field change. By definition, t equals zero at t_{w4}. From Lundgren et al. (1986a).

defined to be zero at the final change of the field. For an arbitrary sequence of step changes of the field, the above equation can be generalized following the theme of superposition, and the memory function M_{mem} can be generally written as

$$M_{mem}(t) = \sum_{i=1}^{n} \Delta h_i p\left(t_{wi}, t + (t_{wn} - t_{wi})\right), \tag{4.6}$$

where Δh_i is the field change at the wait time t_{wi} and where all the t_{wi} are *negative.* For the sequence of field changes shown in Figure 4.2.2-5, Eq.(4.6) becomes

$$\begin{aligned} M_{mem}(t) &= hp\left(t_{w1}, t + (t_{w4} - t_{w1})\right) - 2hp\left(t_{w2}, t + (t_{w4} - t_{w2})\right) \\ &\quad + 2hp\left(t_{w3}, t + (t_{w4} - t_{w3})\right) - hp\left(t_{w4}, t\right) \end{aligned} \tag{4.7}$$

Guided by the above discussion, we conducted the memory behaviour experiments on $Au_{90}Fe_{10}$ at $T_m = 22$ K. As a first step, we measured the IRM relaxation in order to define to the response function, according to Eq.(4.4). The sample was cooled in zero field from $T_R = 50$ K to 22 K, and after a wait time $t_w = 60$ s, a field of $H_a = 5$ Oe was applied and the relaxation of the IRM was recorded over the time interval 2 s$\leq t <$ 3000 s. After recording, the sample was warmed in H_a = 5 Oe to $T = 60$ K in the paramagnetic regime, and the field was then removed in order to establish the true zero of the relaxation. The result is shown in Figure 4.2.2-6. From our earlier experience in fitting TRM relaxation data, we are able to accurately represent $M_{ZFC}(t)$ by the following function (solid curve in Figure 4.2.2-6):

$$M_{ZFC}(-60, t) = hp(-60, t) = 9.248 - 2.087 Exp\left(-\left(\frac{t}{309.49}\right)^{1-0.631}\right). \tag{4.8}$$

Having established the response function for the wait time $t_w = 60$ s, we then measured the memory behavior at $T_m = 22$ K, and the results are illustrated in Figure 4.2.2-7 to 4.2.2-10 for various pulse sequences. The sample was first cooled in zero field from the reference temperature $T_R = 50$ K to $T_m = 22$ K ($t_c \sim 480s$), and, after a initial wait time $t_{w1} = 60$ s, subjected to the sequence of field reversals

depicted above each figure; the relaxation was then recorded after the field was finally turned off at $t_{w4} \equiv 0$. The observed remanent magnetization reflects the sequence of field reversals experienced in the past, and the principle features can be reproduced numerically by employing Eq.(4.7). Due to a lack of knowledge concerning the response functions for all the different wait times t_{wi}(i= 1, 2, 3, 4), we made the reasonable approximation in Eq.(4.7) that:

$$p(t_{wi}, t) \cong p(-60, t), \qquad \text{for all } i = 1, 2, 3, 4, \tag{4.9}$$

so Eq.(4.7) simply reduces to

$$\begin{aligned} M_{mem}(t) &= M_{ZFC}(-60, t - t_{w1}) - 2.0 M_{ZFC}(-60, t - t_{w2}) \\ &\quad + 2.0 M_{ZFC}(-60, t - t_{w3}) - M_{ZFC}(-60, t) \end{aligned} \tag{4.10}$$

The solid curves in Figure 4.2.2-7 to 4.2.2-10 are the calculated memory functions using Eq.(4.10), and presented on an absolute scale . The astonishing resemblance between the solid curves and the oscillating remanent magnetization (ORM) (especially in Figure 4.2.2-8), recorded in zero applied field, support the validity of the principle of superposition, as well as the linear response assumption. The memory function M_{mem} simply reflects the historical events in the past, and the memory of the field pulses may not be erased. It is worthwhile to point out that no adjustable parameters are required to calculate the memory function for the sequence of pulses with n=4 in this experiment (If n is an odd number, so there are an odd number of terms in Eq.(4.7), the true zero in M_{ZFC} has to be well defined in order for M_{mem} to represent the ORM correctly. In latter case, the constant term in Eq.(4.7) may become an adjustable parameter.) The discrepancy between the solid curves and the observed ORM may be attributed to the approximation in Eq.(4.9).

For purposes of completeness, we also tested the droplet model developed by Fisher and Huse (section 2.4.1). According to our discussion in section 2.4.1, if

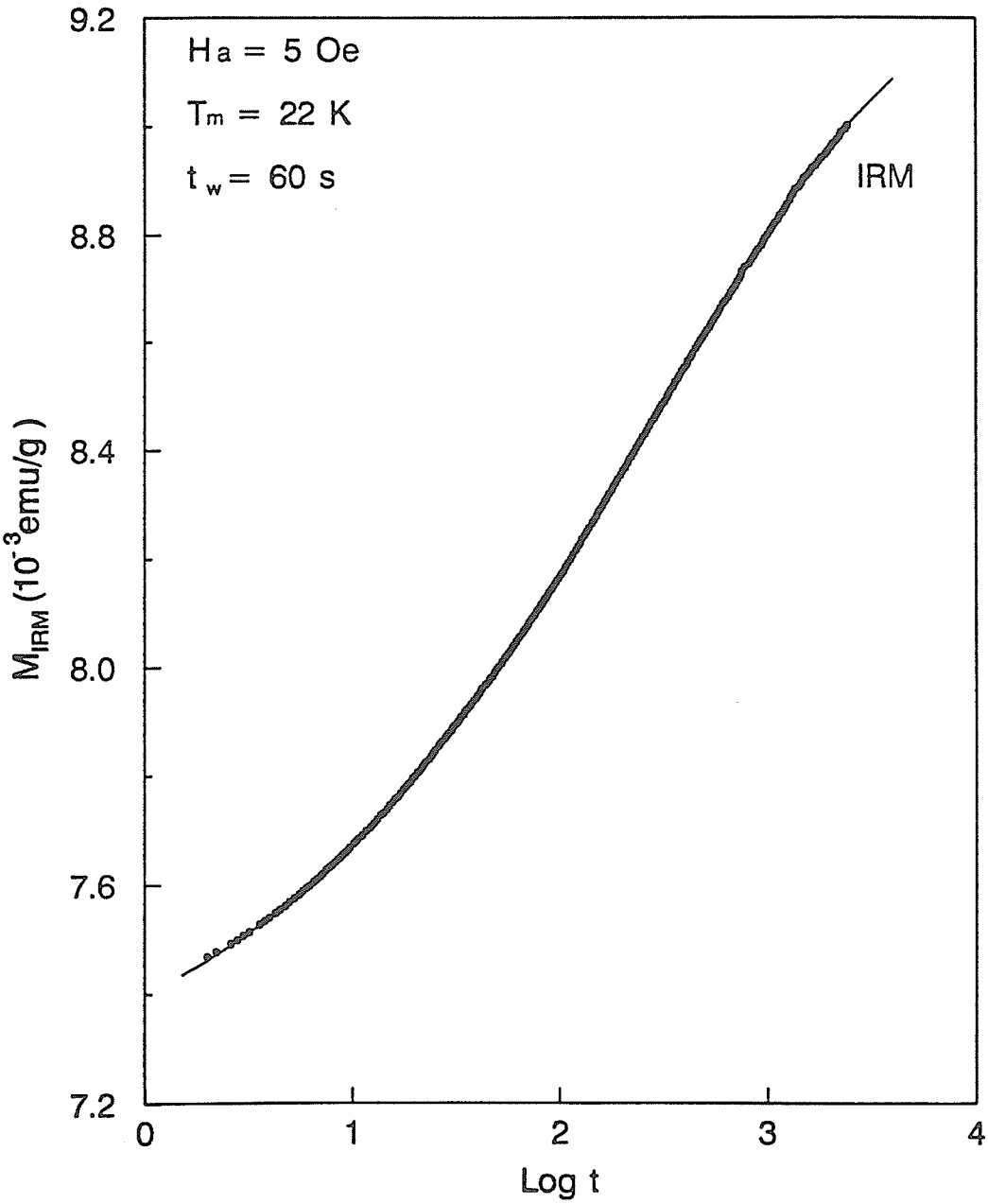

Figure 4.2.2-6: The relaxation of the isothermal remanent magnetization (IRM) at a measurement temperature T_m = 22 K. The sample was cooled in zero field to T_m and after a wait time t_w = 60 s, a field of H_a = 5 Oe was applied.

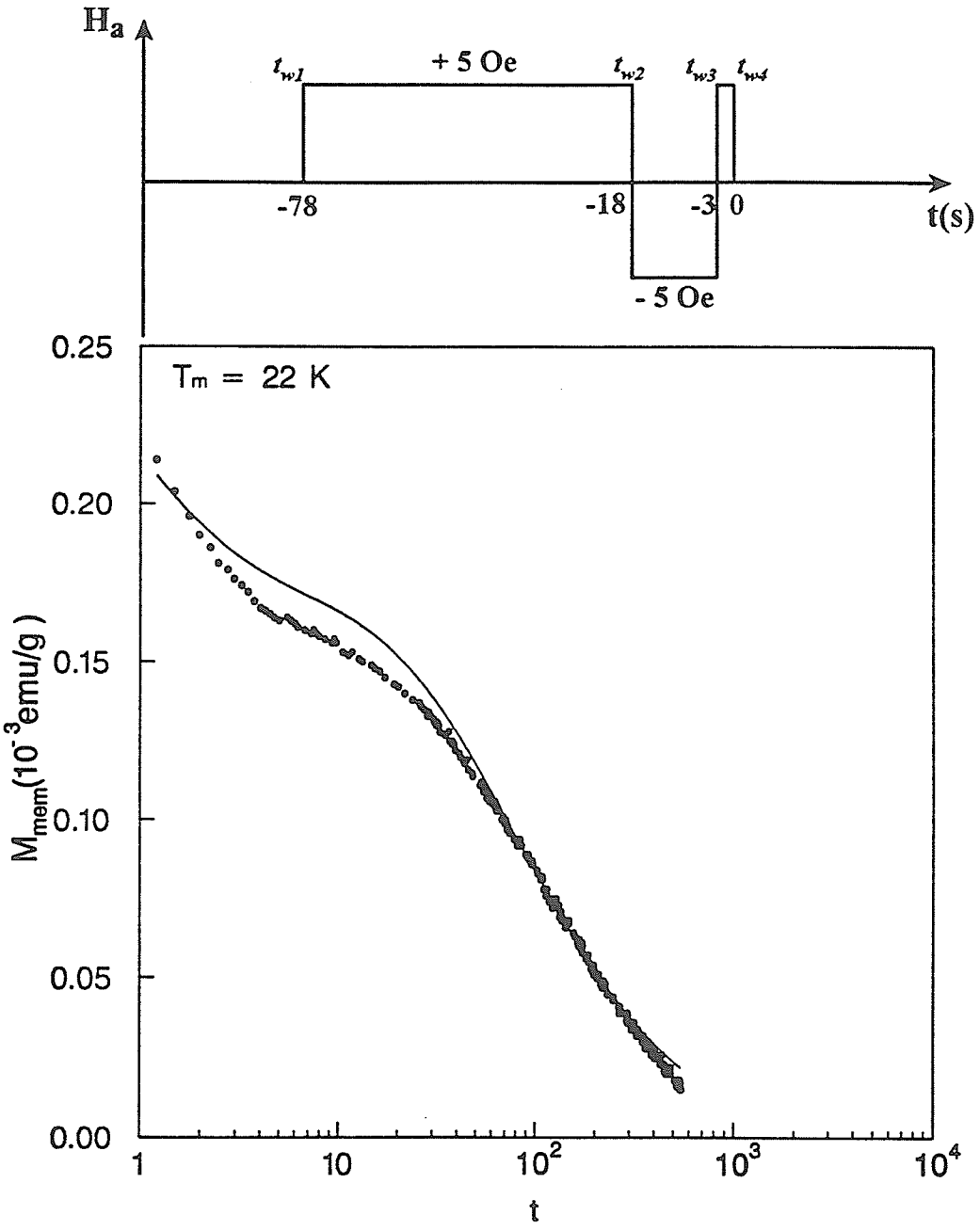

Figure 4.2.2-7: The memory effect: the time dependence of the thermoremanent magnetization M_{mem} after the sample was cooled in zero field to the measurement temperature T_m = 22 K and then subjected to the sequence of field pulses shown above the figure.

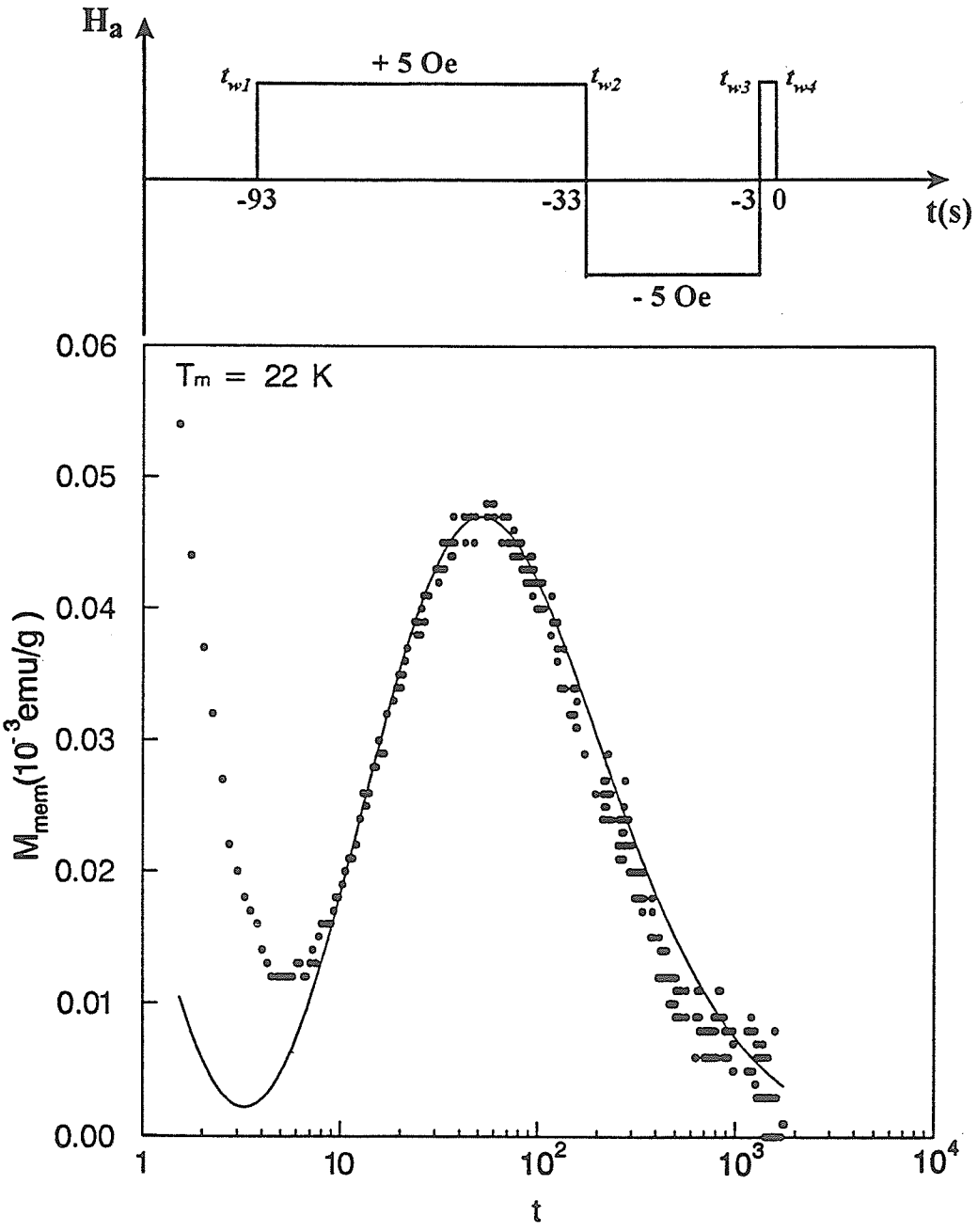

Figure 4.2.2-8: Same as Figure 4.2.2-7, but for a different sequence of field pulses.

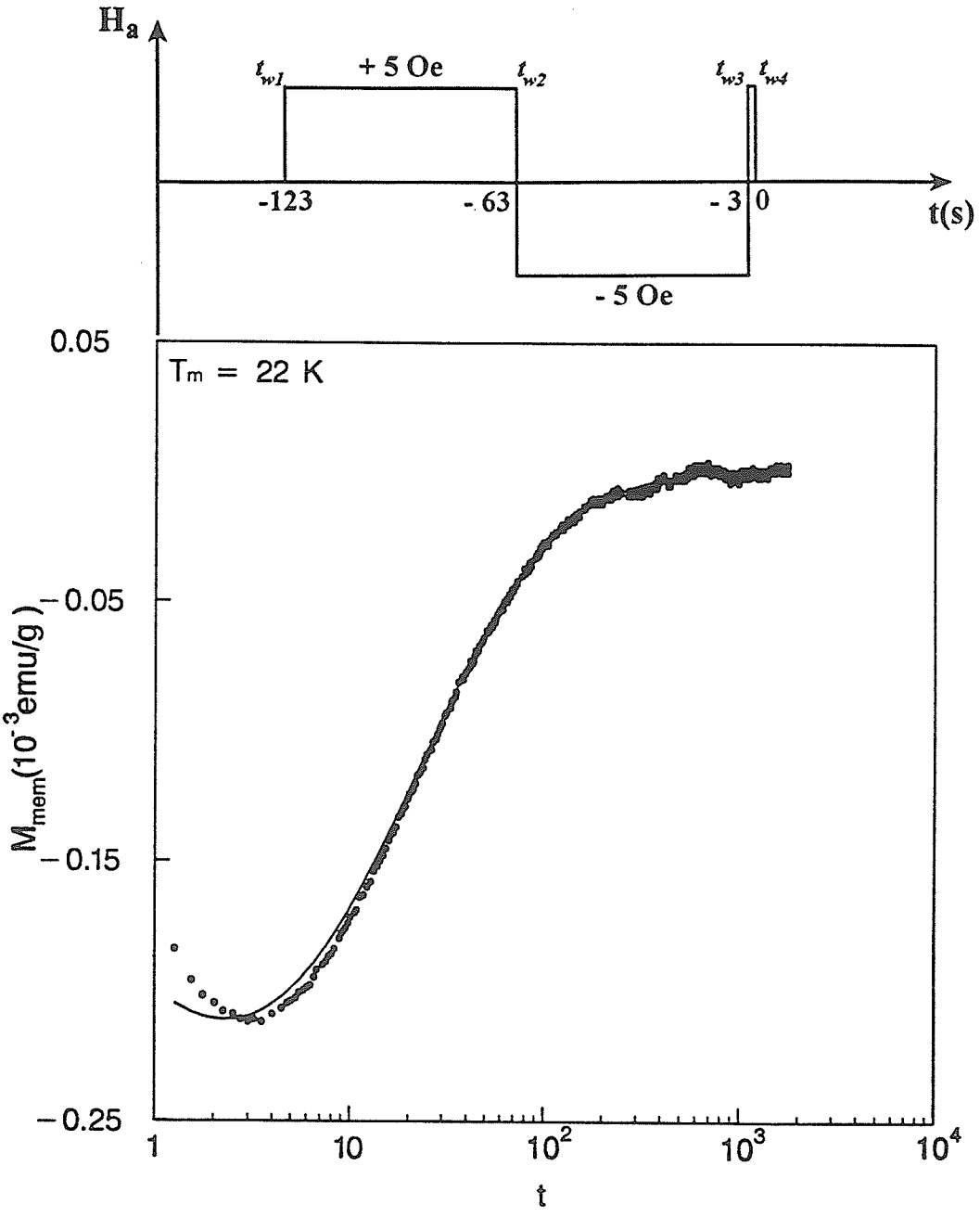

Figure 4.2.2-9: Same as Figure 4.2.2-7, but for a different sequence of field pulses.

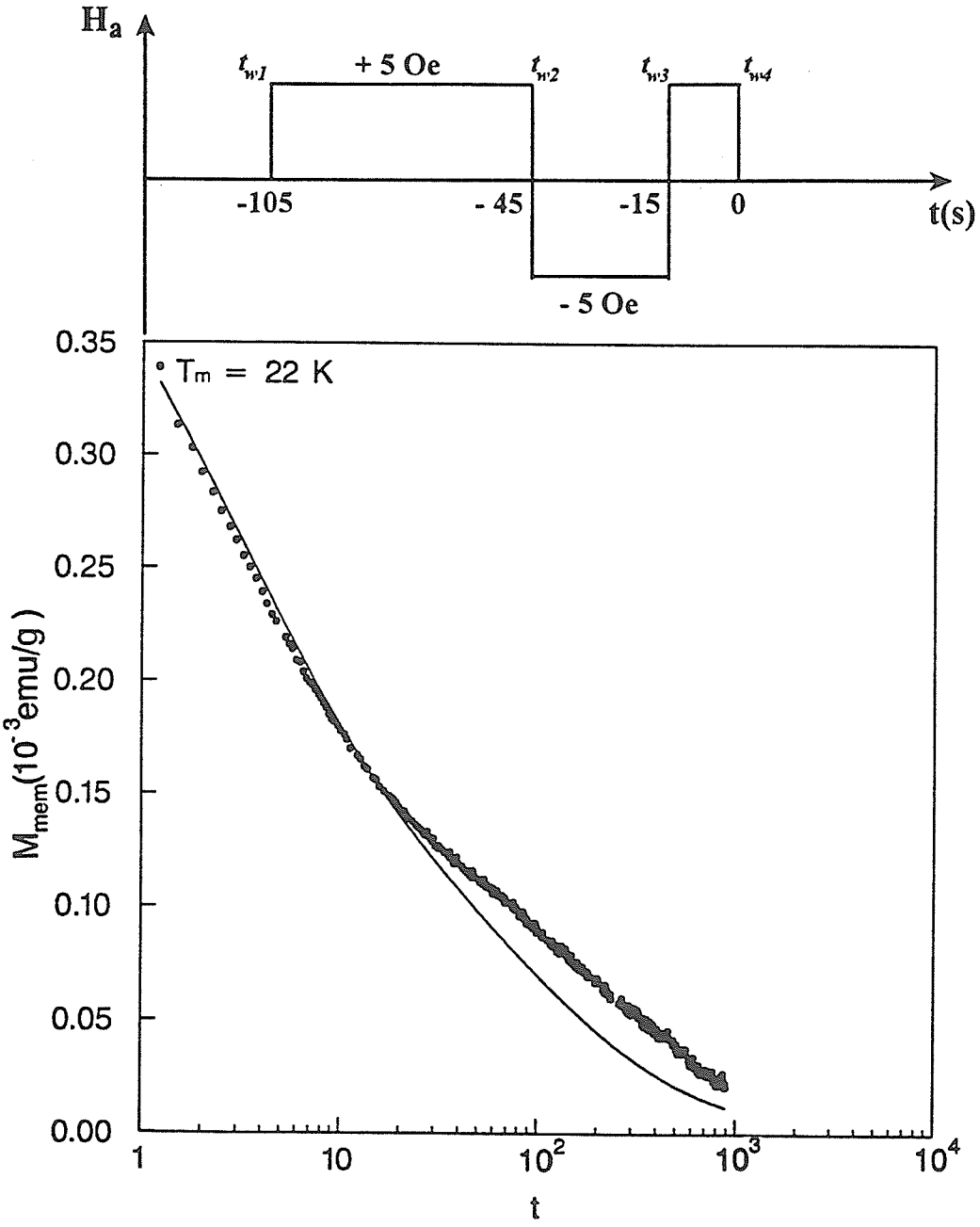

Figure 4.2.2-10: Same as Figure 4.2.2-7, but for a different sequence of field pulses.

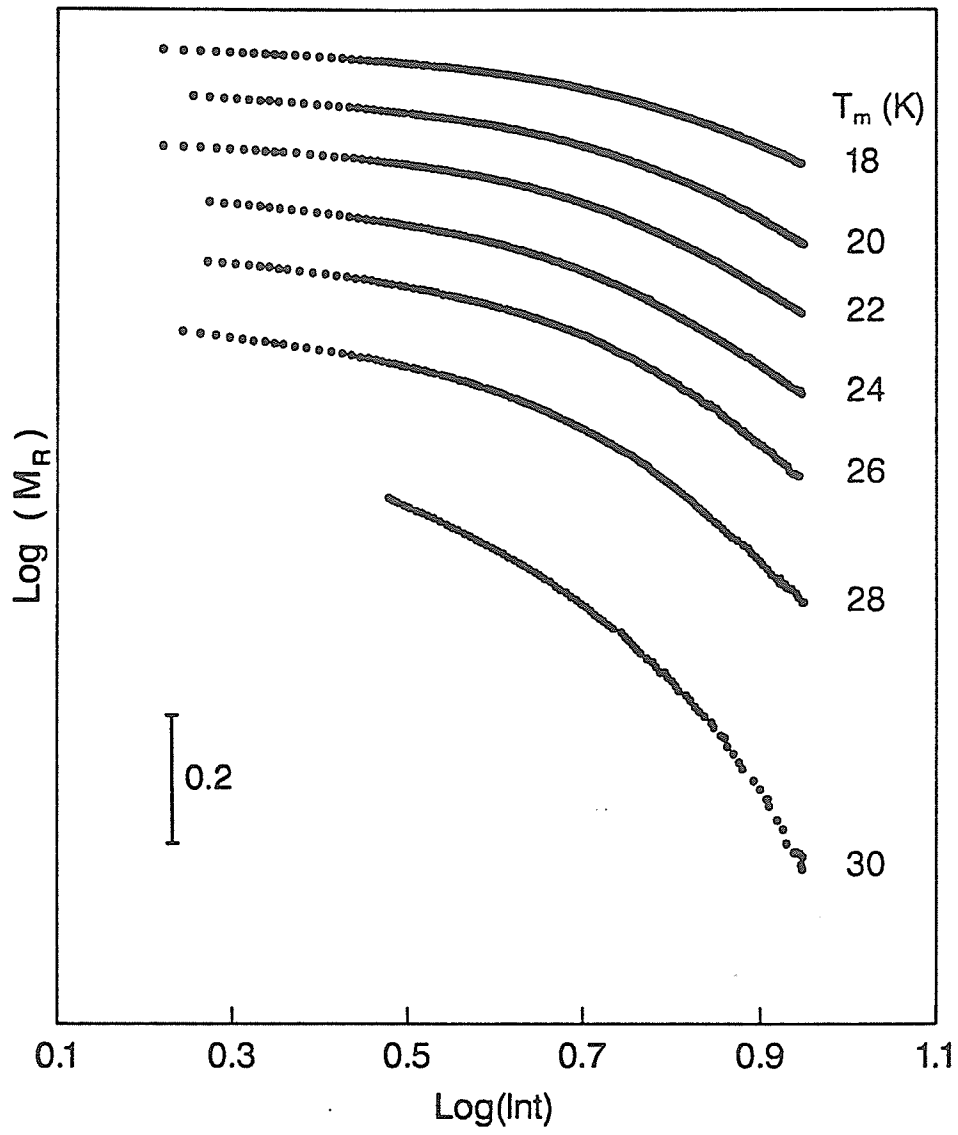

Figure 4.2.2-11: Double logarithmic plots of M_R as a function of *ln t* for the isotherms in Figure 4.2.2-2.

a spin glass is subjected to an ideal quench from infinite temperature to a temperature $T < T_{SG}$ in zero magnetic field, then, after a time t_w has elapsed, the system will consist of domains of typical linear dimension $L(t_w)$ within which the spin configuration is locally equivalent to one of the two pure equilibrium states Γ and $\overline{\Gamma}$ characteristic of the temperature T. Two temporal relaxation regimes are distinguishable: an "early epoch" ($lnt \ll lnt_w$) when relaxation occurs on length scales $L \ll L(t_w)$ through activated equilibrium droplet fluctuations, and the equilibrium magnetization $m_{eq}(t)$ decays as $m_{eq}(t) \sim (lnt)^{-\theta/\psi}$ (Eq.(2.147)), and a "late epoch" ($lnt \gg lnt_w$) where the dynamics are a consequence of activated nonequilibrium domain growth and the decay is governed by a nonequilibrium exponent $\lambda > \theta$ which leads to a more *rapid* logarithmic power law, $m_{neq}(t) \sim (lnt)^{-\lambda/\psi}$ (Eq.(2.149)). Thermoremanent relaxation measurements allow both regimes to be observed in the same experiment, and, on a logarithmic time scale, the relaxation curves should exhibit a crossover between the two limiting relaxation regimes. A double logarithmic plot of M_{TRM} vs. $ln\ t$ is shown in Figure 4.2.2-11 for all relaxation isotherms with $T_m \leq 30$ K, and the results are qualitatively in agreement with the predictions of the Fisher-Huse model. The negative slope of the curves changes from a low value ($\propto -\theta/\psi$) to a higher value ($\propto -\lambda/\psi$), with increasing $ln\ t$, which agrees with $\lambda > \theta$. However, the curvature is continuously changing, and there is no extended temperature interval which corresponds to well defined linear behaviour, so that the above conclusions are valid only asymptotically at best.

4.2.3 TRM Relaxation in a Reentrant Ferromagnetism: $Au_{83}Fe_{17}$

Having established the characteristics of TRM relaxation in a pure AuFe spin glass, we now turn our attention to relaxation in a reentrant ferromagnet.

An alloy of AuFe containing nominally 17 at.% Fe was prepared by arc melting as described in section 3.2.2, total melting losses indicated that the true concentra-

tion was (at worst) within ±0.3 at.% of the nominal value. Two samples **A** and **B** specified in Table 3.2 were prepared from the cold rolled sheet. An EDAX analysis was consistent with a high degree of homogeneity and negligible clustering.

Figure 4.2.3-1 shows the temperature dependence of the low field static FC and ZFC magnetizations in $H_a = 0.5$ Oe. The reentrant ferromagnet exhibits multiple structure (identified by the vertical arrows in Figure 4.2.3-1) consistent with the dynamic measurements described in section 4.2.1, and thus with the formation of a ferromagnetically ordered state below about $T_c \cong 100$ K, which subsequently collapses near $T \cong 40$ K into a low temperature reentrant phase, within which the temperature dependence of the FC and ZFC magnetization mimic those in the pure spin glass phase.

The characterization of the thermoremanent relaxation in the reentrant $Au_{83}Fe_{17}$ ferromagnet proceeded by adapting the experimental and analytical techniques developed for the $Au_{90}Fe_{10}$ spin glass. The tendency for residual relaxation effects to persist well above the peak in the ZFC magnetization (see Figure 4.2.3-1) necessitated the choice of a comparatively high reference temperature $T_R =$ 140 K for establishing the zero level of magnetization, so that, as usual, the reentrant study was severely constrained by the anomalously large cooling intervals $T_R - T_m$ (~100 K for the reentrant phase) and correspondingly long cooling times t_c (typically ~1000 s), which, as before, allowed the cooling process to assume a dominant role in defining the age of the system. Figures 4.2.3-2 and 4.2.3-3 summarize the thermoremanent decay for a sequence of representative measurement temperatures T_m spanning virtually the entire ordered phase ($15K \leq T_m \leq 115$ K), for a wait time $t_w = 60$ s. The low temperature isotherms in Figure 4.2.3-2 were obtained from sample **A**, with a cooling field $H_c = 2$ Oe, while the "high" temperature isotherms in Figure 4.2.3-3 were obtained from sample **B** with a cooling field $H_c = 4$ Oe. The necessity to introduce a second needle-shaped sample(**B**) arose when oscillations developed in the relaxation isotherms of sample **A** for tem-

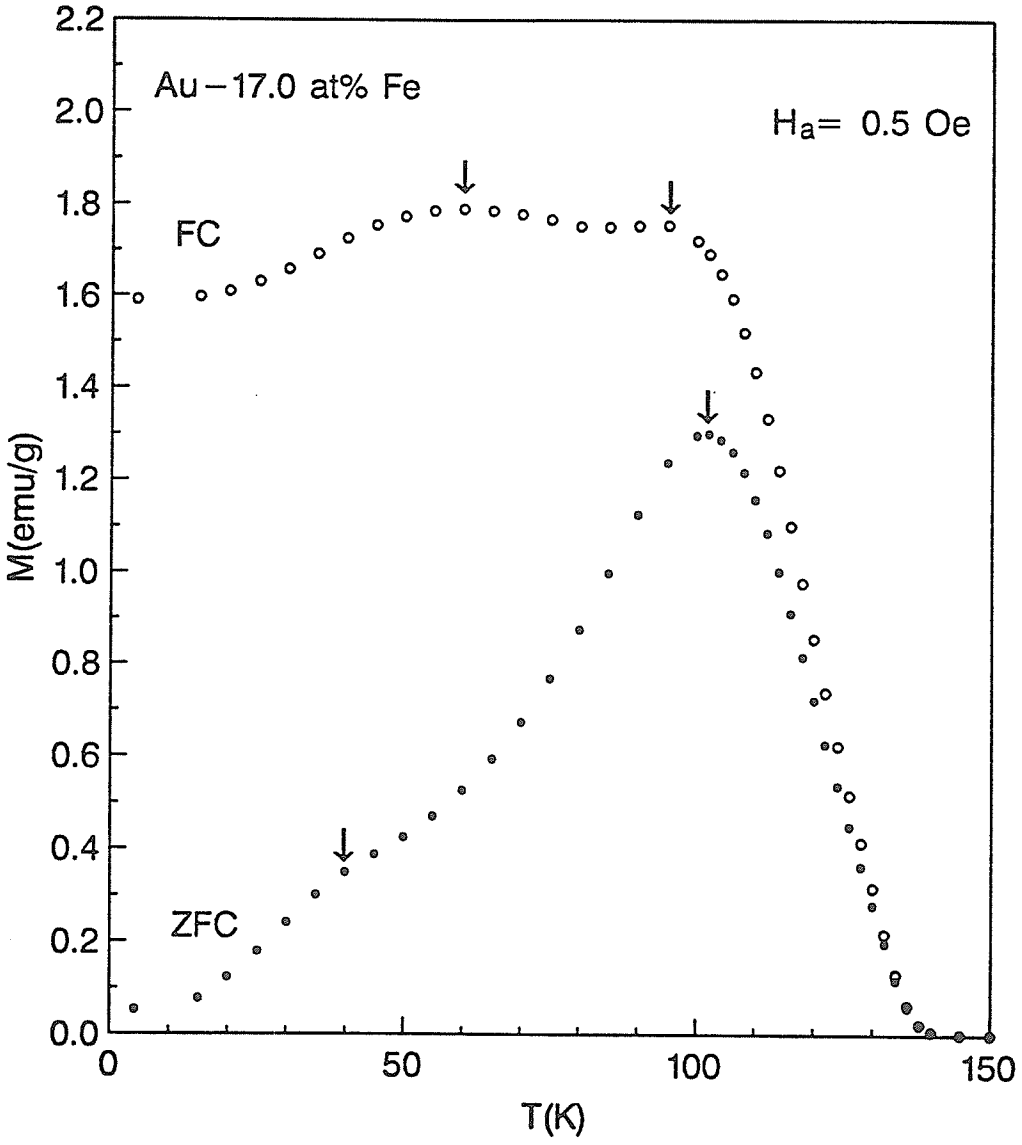

Figure 4.2.3-1: Temperature dependence of the field cooled (FC) and zero field cooled (ZFC) static magnetization of the Au-17.0 at% Fe reentrant ferromagnet measured in an applied field H_a = 0.5 Oe.

peratures $T_m > 25$ K, which were traced to temperature instabilities due to its width ($\sim$ 1 mm). While the structure of these isotherms (particularly at the lower temperatures) is much broader and considerably more subtle than that associated with "pure" spin glass relaxation (undoubtedly a consequence of the comparatively slow cooling rates), there is nevertheless an unmistakable, progressive change in curvature throughout both figures, similar to that observed in reentrant NiMn, from concave down to concave up with increasing measurement temperature T_m. Furthermore, quantitative analysis of the isotherms revealed that, as with NiMn, two distinct types of relaxation behaviour are possible, corresponding to two distinct temperature regimes each of which coincides with one of the two ordered phases which characterize the reentrant sequence. The isotherms in Figure 4.2.3-2 and 4.2.3-3 have been grouped accordingly in order to reflect this dichotomy. (a) Figure 4.2.3-2 presents the low temperature reentrant regime with $T_m < 30$ K, where the isotherms all possess inflection points (marked by the arrows) and exhibit a wait time dependence indicative of nonequilibrium processes. These curves are describable analytically by the superposition of a pure stretched exponential and a constant term as in Eq.(4.1). (b) Figure 4.2.3-3 shows the high temperature (ferromagnetic) regime with $T_m \geq 30$ K, where aging effects are negligible and where the decay is incompatible with a stretched exponential representation, but is consistent with a weak power-law dependence (Eq.(4.2)) symptomatic of relaxation from a fully equilibrated field cooled state. Figure 4.2.3-4 shows the wait-time dependence for selected isotherms in each of the two relaxation regimes, and Tables 4.2-3 and 4.2-4 list all the relevant experimental parameters, including the best fit values of the constants M_o, n, τ, and m in Eq.(4.1) and (4.2).

Based on a comparison with the relaxation dynamics of a pure spin glass, as defined by Figure 4.2.2-2 and Table 4.2-1, the magnitude and variation of the stretched exponential parameters n and τ in Table 4.2-3 are completely consistent with orientationally random spin freezing within the low temperature reentran-

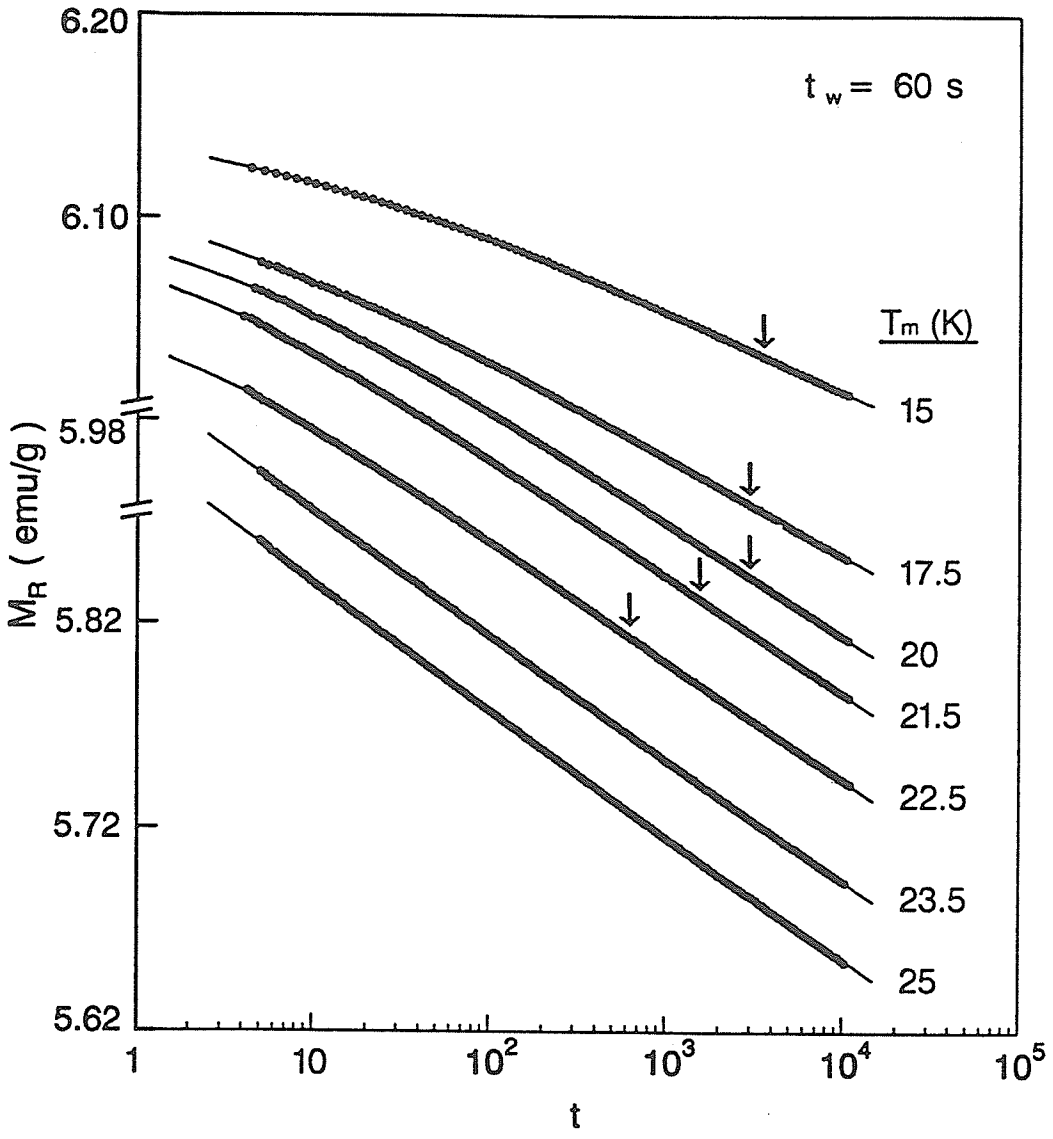

Figure 4.2.3-2: Decay of the thermoremanent magnetization M_R at several representative temperatures T_m within the reentrant phase of the Au-17.0 at% Fe ferromagnet, for a wait time t_w = 60 s. The vertical arrows mark the locations of the inflection points. Solid curves are the best fits to Eq.(4.1).

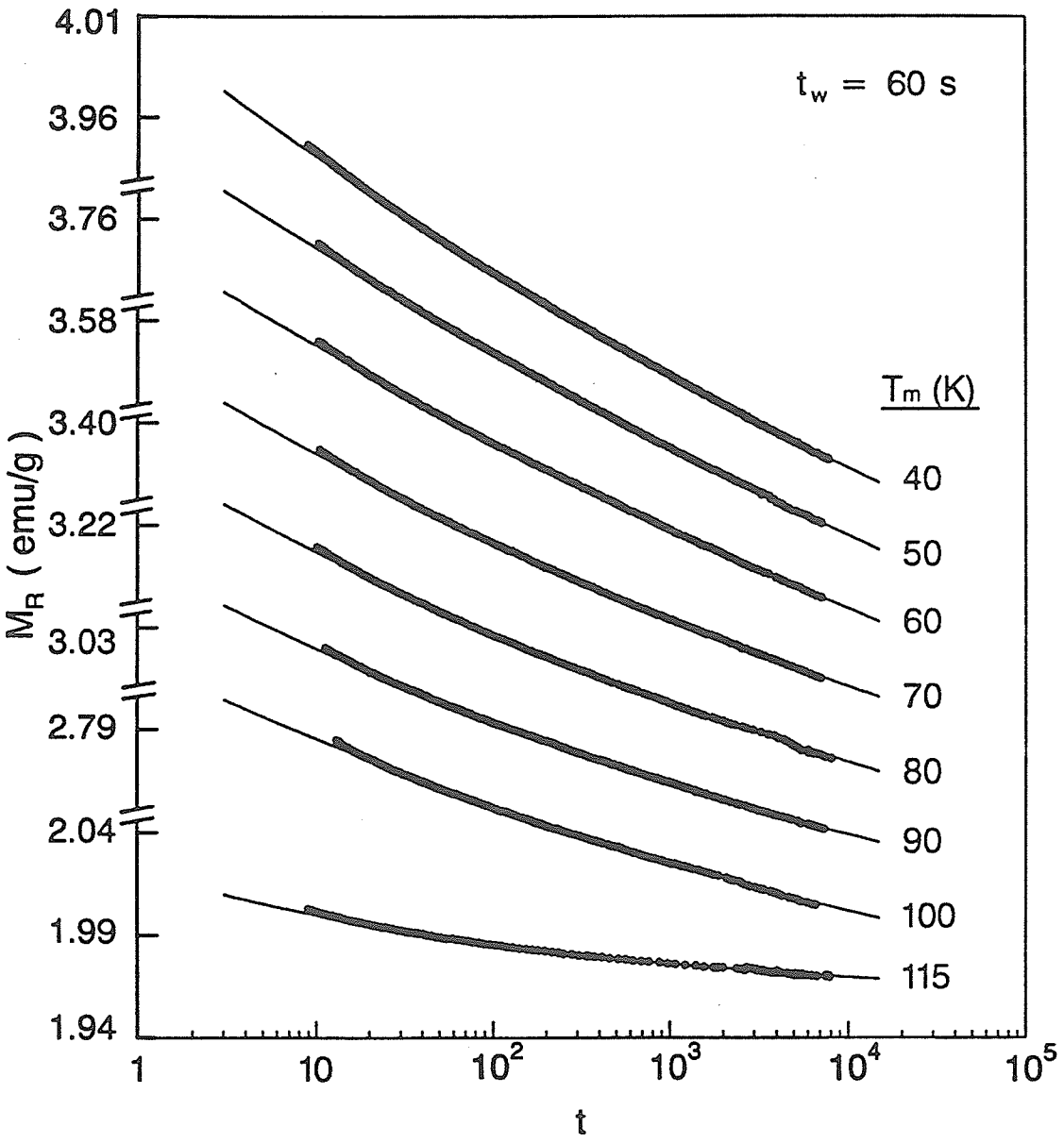

Figure 4.2.3-3: Decay of the thermoremanent magnetization M_R for t_w = 60 s at several representative temperatures T_m within the ferromagnet phase of the Au-17.0 at% Fe ferromagnet. Solid curves are the best fits to the simple power law in Eq.(4.2).

t regime and thus support the conclusions of the NiMn study. Moreover, the constraints imposed on the experimental cooling rates by the necessity to cool the system over relatively large temperature intervals $T_R - T_m$ are responsible for systematic discrepancies similar to those observed in NiMn. The experimental cooling technique is unable to distinguish between cooling intervals differing by $\Delta(T_R - T_m)/T_m \sim 0.1$, the nominal experimental age $t_w + t_c$ of the system is essentially independent of measurement temperature T_m within the reentrant phase. However, the location of the inflection point $t_{infl} = \tau$ (see vertical arrows in Figures 4.2.3-2 and 4.2.3-4(a)), and hence the true age of the system, exhibits an inverse correlation with T_m, shifting from $t_{infl} > t_w + t_c$ to $t_{infl} < t_w + t_c$ with increasing measurement temperature. This behaviour is entirely consistent with the absence of aging observed throughout the ferromagnetic phase (Figure 4.2.3-4(b)), and, as in NiMn, merely confirms that the system is continuously in equilibrium throughout the initial portion of the cooling interval. Thus aging processes do not commence until the system has been cooled through some effective reference temperature T_R^* which lies well below T_R but close to the ferromagnetic-reentrant phase boundary.

A test of the Fisher-Huse model similar to that performed for $Au_{90}Fe_{10}$ was also attempted for the reentrant $Au_{83}Fe_{17}$ alloy. The relaxation isotherms in the low temperature reentrant phase in Figure 4.2.3-5 again exhibit an increase in negative slope from short times to long times, which qualitatively agrees with the model. The relaxation isotherms in the high temperature ferromagnetic phase in Figure 4.2.3-6 are clearly not unique straight lines as would be expected for a system relaxing from equilibrium, but rather exhibit similar curvature to those in Figure 4.2.3-5. Nevertheless the double logarithmic plot of M vs. $ln\ t$ for the highest temperature $T_m = 115$ K isotherm does yield a good straight line, which indicates the possibility of yet a third relaxation regime above T_c which perhaps represents the "true" ferromagnetic equilibrium relaxation.

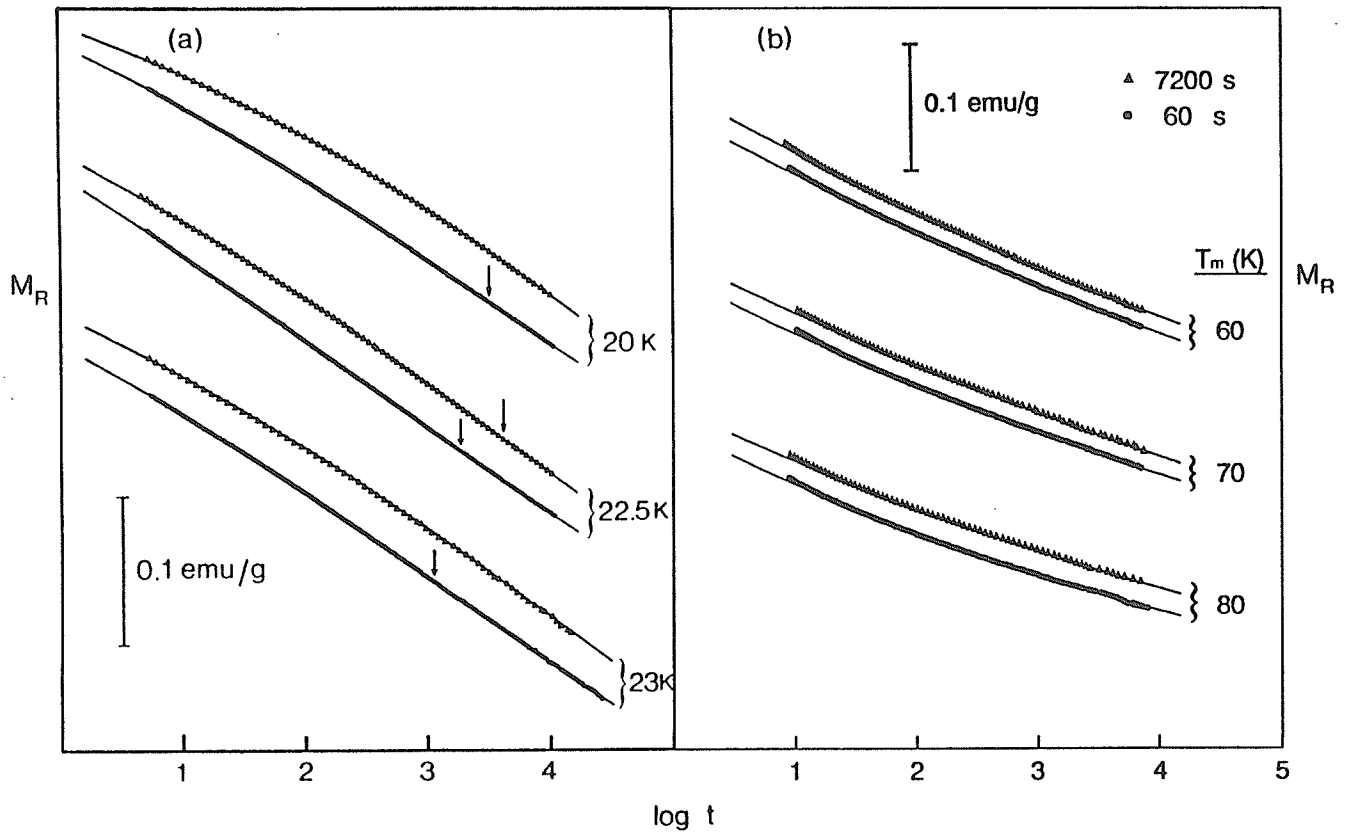

Figure 4.2.3-4: An illustration of the influence of the wait time t_w on (a): the relaxation isotherms within the reentrant phase. The vertical arrows mark the locations of the inflection points, and the zero magnetization levels of the relaxation curves have been shifted by arbitrary amounts for clarity of presentation, so that only the scale of the relaxation has been indicated in the lower left of the figure. Solid curves are the best fits to Eq.(4.1) (b): the relaxation isotherms within the ferromagnet phase. As in figure (a) only the scale of the relaxation has been indicated. Solid curves are the best fits to Eq.(4.2).

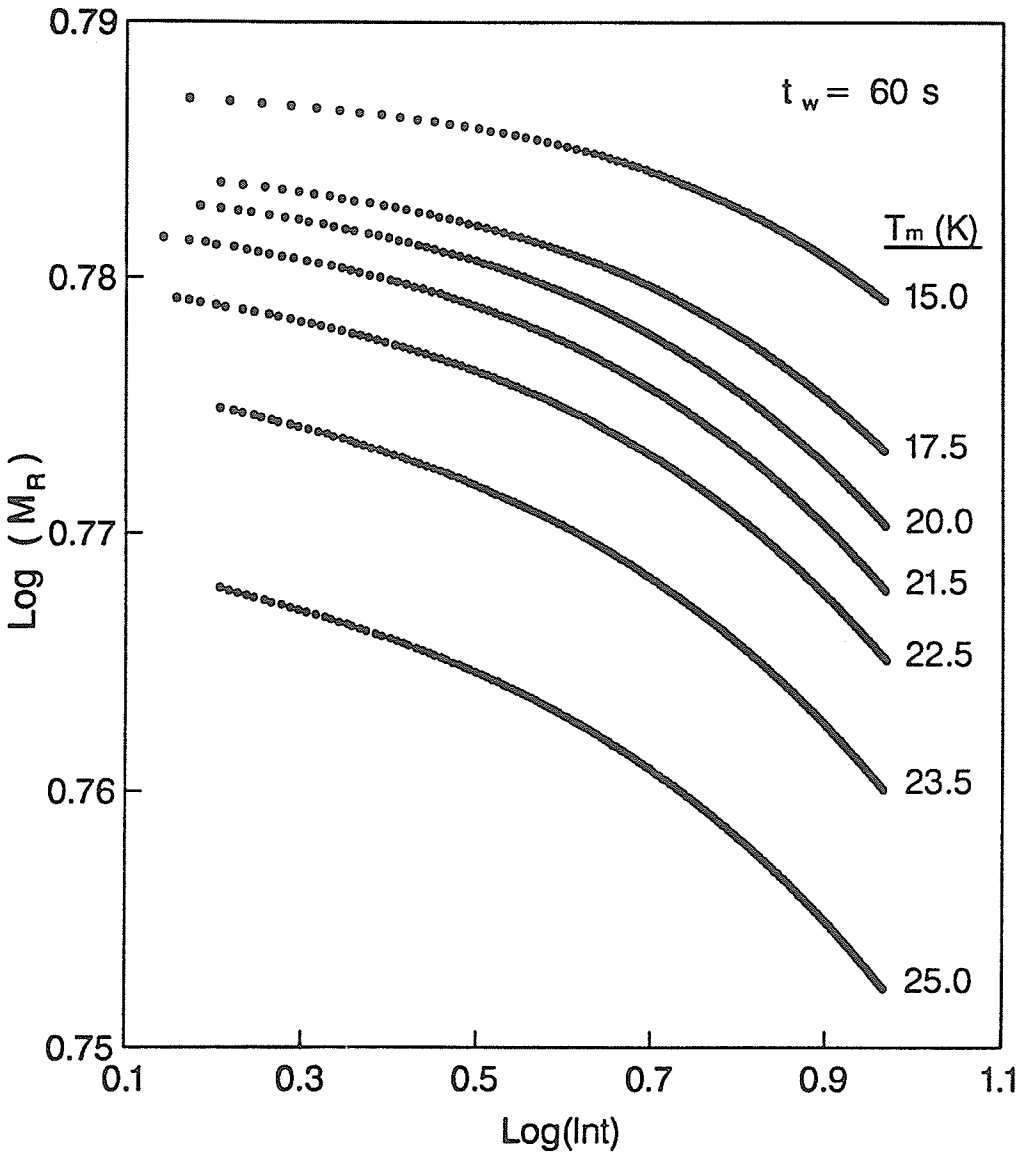

Figure 4.2.3-5: Double logarithmic plots of M_R as a function of *ln t* for the isotherms in Figure 4.2.3-2.

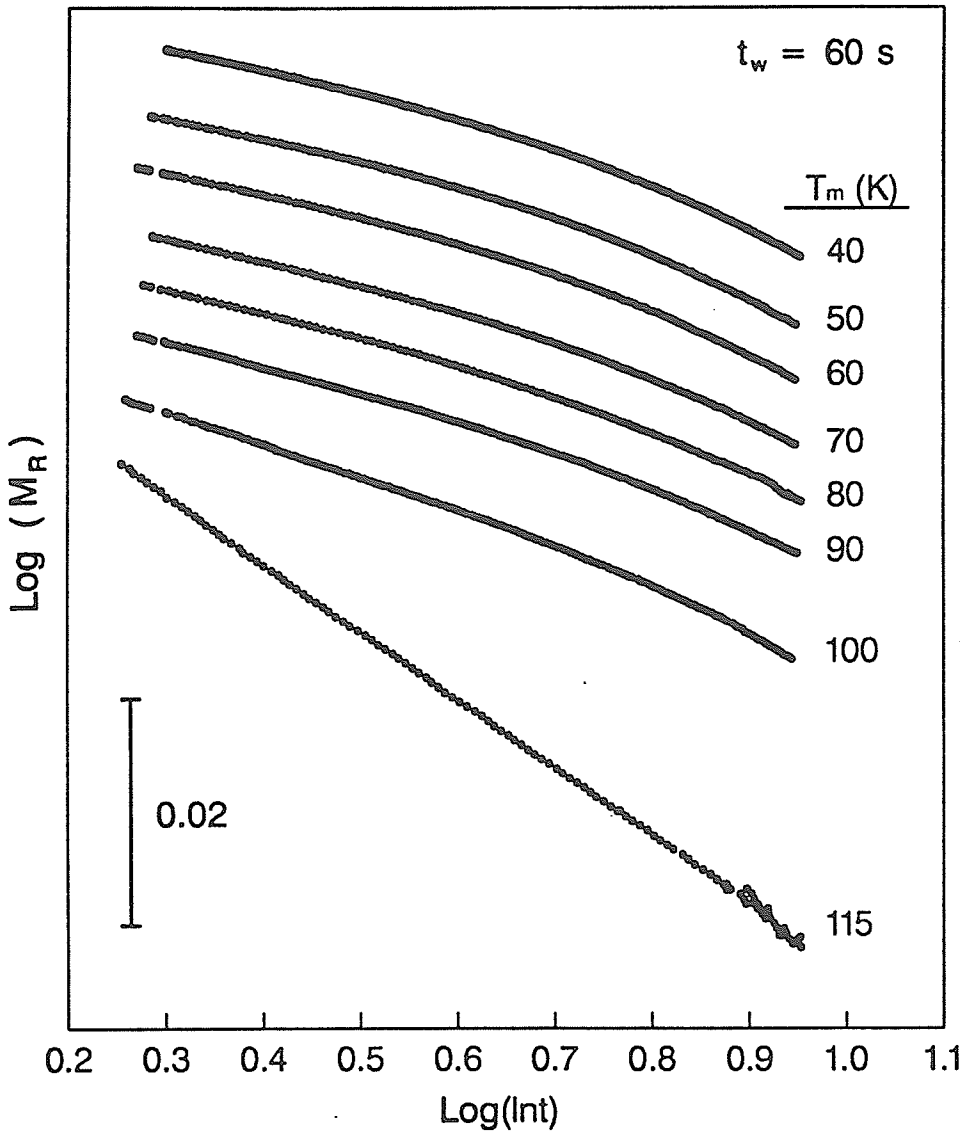

Figure 4.2.3-6: Double logarithmic plots of M_R as a function of *ln t* for the isotherms in Figure 4.2.3-3. The zero magnetization levels of the relaxation curves have been shifted by arbitrary amounts for clarity of presentation, so that only the vertical scale has been indicated in the lower left of the figure.

Table 4.2-3: $Au_{83}Fe_{17}$ Reentrant Phase Parameters for Eq.(4.1)

T(K)	t_w(s)	$t_w + t_c$ (s)	t_{infl} (s)	τ (s)	n	M_o(emu/g)
15	60	900	3500±1000	2900±200	0.77±0.01	5.96±0.01
17.5	60	900	3000±1000	2500±200	0.83±0.01	5.84±0.01
20	60	960	2000±1000	2300±300	0.88±0.01	5.73±0.01
20	7200	8220	$>10^4$	$(1.9\pm0.7)\times 10^5$	0.87±0.01	5.49±0.05
21.5	60	1200	1500±600	1800±400	0.91±0.01	5.64±0.02
22.5	60	1260	1200±300	1000±70	0.92±0.01	5.59±0.03
22.5	7200	8250	4000±1000	4800±600	0.89±0.01	5.41±0.04
23.0	60	1160	1000±1000	900±100	0.93±0.01	5.56±0.02
23.0	7200	8220	$>10^4$	$(5.4\pm0.3)\times 10^4$	0.89±0.01	5.53±0.06
23.5	60	1200	<10	7.0±2.0	0.96±0.01	5.36±0.05

On the basis of both Monte Carlo simulations (Ogielski, 1985) and critical fractal-cluster model calculations (Lundgren et al.,1986b), to be characterized the zero field equilibrium ($t_w = \infty$) relaxation in spin glasses is expected to be characterized by a slow power law decay below T_{SG}. This expectation is supported by both static and dynamic measurements of the relaxation rate S in various canonical spin glass systems (Lundgren et al.,1986b). According to our discussion in section 2.4.1, a weak power decay is also predicted for random ferromagnets from the droplet scaling theory. The long-time behaviour of the spatially averaged temporal autocorrelation function Eq.(2.132) is dominated by droplet excitations with anomalously long relaxation times which, in random ferromagnets, are exponentially rare in ln t, yielding a power-law decay Eq.(2.138)

$$\overline{C(t)} \sim t^{-x(T)}.$$

Moreover, Fisher and Huse (1987) have pointed out that the region of validity of the predicted asymptotic equilibrium decay Eq.(2.138) *expands* to include progressively shorter observation times as the bond disorder becomes more extreme, so that nearly tricritical ferromagnets should represent the best experimental candi-

dates for assessing the applicability of Eq.(2.138). Since these are precisely the conditions which favour reentrant ferromagnetism, it follows that the behaviour of the relaxation isotherms within the ferromagnetic phase of both the reentrant $Au_{83}Fe_{17}$ and reentrant $Ni_{76.4}Mn_{23.6}$ alloys (viz., a weak power law decay with an exponent $m \sim .04 - .08$, and negligible wait time effects) may be interpreted as direct confirmation of the theoretical predictions.

Table 4.2-4: $Au_{83}Fe_{17}$ Ferromagnetic Phase Parameters for Eq.(4.2)

T(K)	t_w(s)	m	M_o(emu/g)
40	60	0.05±0.01	3.38±0.01
45	60	0.05±0.01	3.28±0.01
50	60	0.04±0.01	2.94±0.03
55	60	0.04±0.01	2.91±0.02
60	60	0.04±0.01	2.76±0.02
60	7200	0.04±0.01	2.76±0.02
65	60	0.06±0.01	2.74±0.01
70	60	0.06±0.01	2.60±0.01
70	7200	0.04±0.01	2.60±0.02
75	60	0.08±0.01	2.53±0.01
80	60	0.07±0.01	2.36±0.01
80	7200	0.06±0.01	2.35±0.01
85	60	0.06±0.01	2.23±0.02
90	60	0.08±0.01	2.09±0.01
100	60	0.08±0.01	1.69±0.01
115	60	0.18±0.01	0.36±0.01

4.3 The CrFe System

4.3.1 Introduction

Pure chromium is considered a typical itinerant antiferromagnet with a Néel temperature T_N of about 313 K. The antiferromagnetic phase of chromium and its alloys has been satisfactorily explained in terms of the existence of a spin density wave (SDW) within the itinerant electron system (Antonoff, 1977). The spin density wave state may be recognized as a new type of ground state of the conduction

electron gas. This state has the property that the expectation value of the total conduction electron spin density operator, relative to an axis of quantization $\vec{\epsilon}$,varies with position $\vec{R}$ as follows (Overhauser, 1959):

$$\vec{s} = bN\vec{\epsilon}\cos(\vec{q}\cdot\vec{R}) \tag{4.11}$$

where b is a dimensionless amplitude and N is the number of atoms per unit volume. This static spin density wave allows the total charge density of the gas to remain spatially uniform. Such a collective excited state may be visualized as the sum of two spin density waves, one of electrons with spins parallel to $\vec{\epsilon}$ and the other with antiparallel spins, which are equal in magnitude but out of phase. Paramagnetic solute spins will interact with a spin density wave through the ordinary s-d exchange interaction. A solute spin $\vec{S}_j$ at lattice site $\vec{R}_j$ will experience an effective field $\vec{H}_j$ defined by the interaction Hamiltonian between the paramagnetic solute spin $\vec{S}_j$ and the conduction electron spin density wave $\vec{s}$ at $\vec{R}_j$

$$H_{eff} = -J_{sd}\vec{S}_j\cdot bN\vec{\epsilon}\cos(\vec{q}\cdot\vec{R}_j) = -\vec{S}_j\cdot\vec{H}_j \tag{4.12}$$

and

$$\vec{H}_j = -J_{sd}bN\vec{\epsilon}\cos(\vec{q}\cdot\vec{R}_j) \tag{4.13}$$

where J_{sd} is the exchange interaction between the spin $\vec{S}_j$ of solute atoms and s conduction electrons. A given solute spin will be polarized up or down depending on its location relative to the phase of the spin density wave. A long-range coherence of the solute spins occurs below a critical temperature, which causes antiferromagnetism. It should be appreciated that the wave vector $\vec{q}$ will generally be incommensurate with reciprocal lattice vectors. In fact pure chromium is recognized as an incommensurate antiferromagnet below the Néel temperature.

CrFe has been investigated extensively by Burke and Rainford and their coworkers (Burke and Rainford, 1978; Burke and Rainford, 1983; Burke et al., 1983; Palumbo et al., 1983; Shapiro et al., 1981). Most of the previous studies involved

neutron scattering, and a detailed phase diagram (Figure 4.3.1-1) was assembled by Burke et al. (1983), based on neutron scattering and low-field magnetization (Figure 4.3.1-1). Adding Fe to antiferromagnetic Cr results in a decrease of T_N, and the addition of more than 2-3 at.% Fe is sufficient to change the system from incommensurate (I) to commensurate (C) antiferromagnetic order (Burke and Rainford, 1978). This anomalous behaviour is thought to be due to the interaction between the antiferromagnetic spin density wave and local Fe moments, which coexist with the SDW. However, no consensus has yet been reached about the most basic aspects of this process, in particular, the nature of the Fe moment, the strength of the interaction and the magnetic defect surrounding an Fe atom in Cr (Burke and Rainford, 1983, and references therein).

When the Fe concentration is increased further (C $\geq$ 7%), the magnetic properties become complicated by ferromagnetically nearest-neighbour Fe-Fe interactions. Neutron diffuse scattering experiments show clustering effects in the alloys with Fe concentration above 2.4 at.%. At Fe concentration of 14.2 at.% the linear dimension of the clusters (correlated assemblies of Fe moments) is about 6.3 A° and the clusters contain about 110 atoms, and coexist with the SDW (Burke and Rainford, 1983, and references therein). Magnetization measurements indicate a spin-glass-like transition connected with a freezing of ferromagnetic clusters at very low temperatures. According to the phase diagram (Figure 4.3.1-1), antiferromagnetic order disappears at a critical concentration $C_A = 16.0 \pm 0.5$ at.% (Burke and Rainford, 1978), and there is no region of overlapping ferromagnetism and antiferromagnetism. For Fe concentrations in the range 10-16 at.%, the system can experience a sequential transition from paramagnet to antiferromagnet to a spin-glass-like state in which the superparamagnetic blocking of ferromagnetic clusters occurs.

The ferromagnetic critical concentration C_F is $C_F = 19.0 \pm 0.5$ at.% (Figure 4.3.1-1), above which long range ferromagnetic order sets in. Complex magnetic

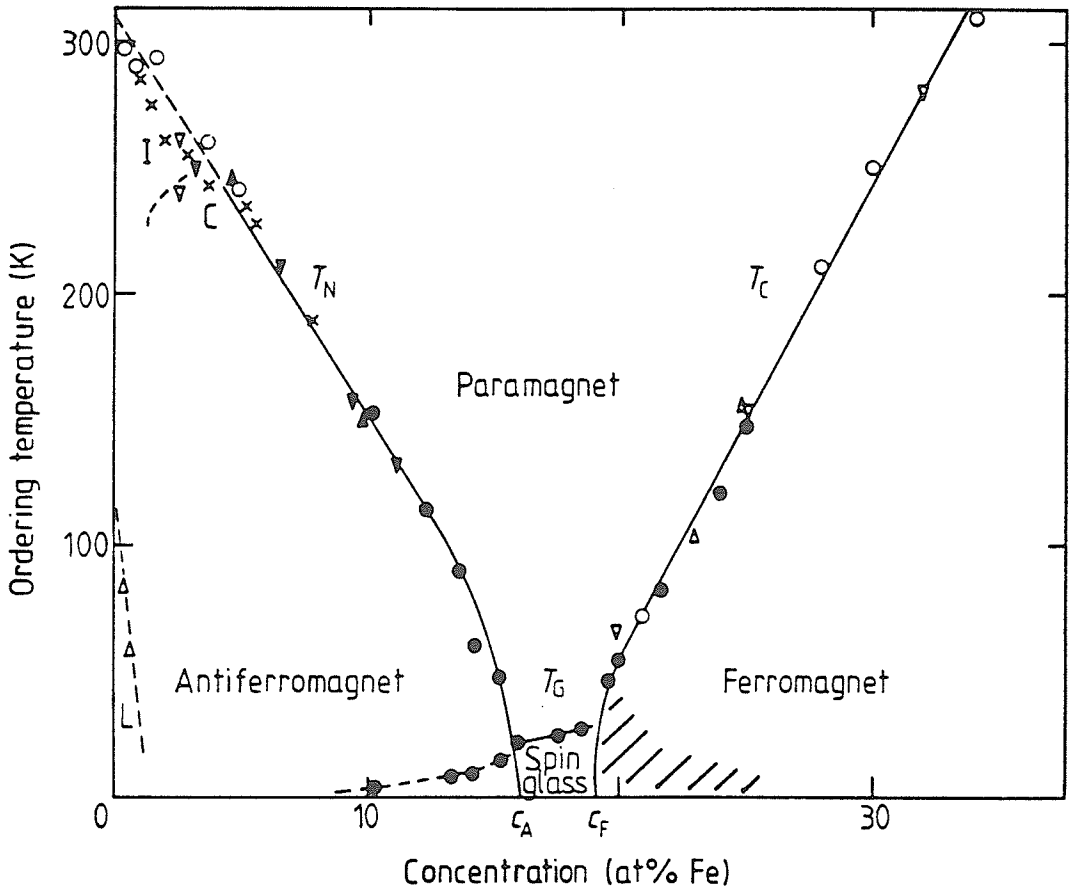

Figure 4.3.1-1: Magnetic phase diagram for CrFe. Complex magnetic properties are observed in the hatched region. From Burke et al (1983).

properties were observed in the hatched region for $19.0 \leq c < 25.0$ at.%, where a possible reentrant (sequential) transition is expected. Spin-glass behaviour occurs in the narrow concentration range between 16 and 19 at.% Fe where long-range order cannot be supported. Figure 4.3.1-2 shows the a.c susceptibility of a spin glass Cr-17.5 at.% Fe and nearly multicritical reentrant ferromagnet Cr-19.5 at.% Fe (Burke et al., 1983). Both curves show a sharp asymmetric peak at 30 K, indicating the onset of spin glass freezing. Closer examination of the 19.5 at.% Fe data reveals a slight shoulder between 40 and 60 K which is absent in the 17.5 at.% Fe curve. The "kink" temperature ($\sim$ 44 K) appears to correlate well with the Curie temperature $T_c = 45$ K from neutron scattering results.

Figure 4.3.1-3 shows both zero field cooled (ZFC) and field cooled (FC) magnetization of the spin glass Cr-17.5 at.% Fe. The ZFC magnetization shows a somewhat rounded peak at 24K, and the separation between the FC and ZFC data below the peak temperature is due to a time dependent component in the magnetization. The isothermal remanent magnetization (IRM) increases logarithmically as shown in the insert in Fig 4.3.1-3. It should be noted that the approximate addition of the thermoremanent (TRM) and ZFC magnetizations produces a nearly constant FC magnetization below the peak temperature and the TRM disappears above the peak temperature. Hysteresis loops obtained after field cooling also show a displacement with respect to the hysteresis of zero field cooled loops. The low field magnetization as a function temperature for three reentrant ferromagnets with c=19.9, 20.8 and 25.0 at.% Fe is shown in Figure 4.3.1-4. The magnetization increases rapidly with decreasing temperature until the demagnetizing limit is reached at the "kink point" temperatures (arrows). The magnetization remains at the demagnetization limit (H_a/D) as the temperature is decreased further, and then drops quickly, heralding the onset of a low temperature spin glass like phase.

Palumbo et al. (1983) have studied the TRM and IRM relaxation of various CrFe alloys. While these studies exploited the viscous properties of the remanent

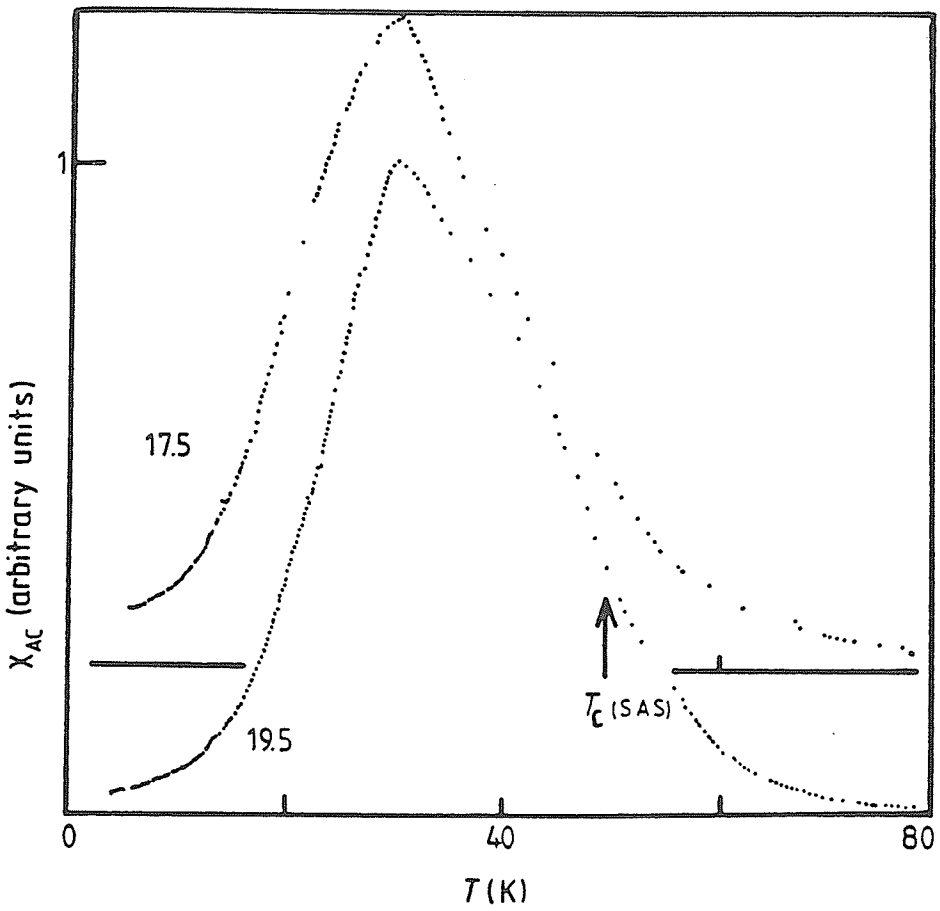

Figure 4.3.1-2: AC susceptibility of Cr-17.5 at.% Fe ($c < c_F$) and ferromagnetic Cr-19.5 at.% Fe as a function of temperature. The two curves have been displaced for clarity. The Curie temperature for the 19.5 at.% alloy is shown by an arrow. Alloy concentrations (at.% Fe) are indicated. From Burke et al. (1983).

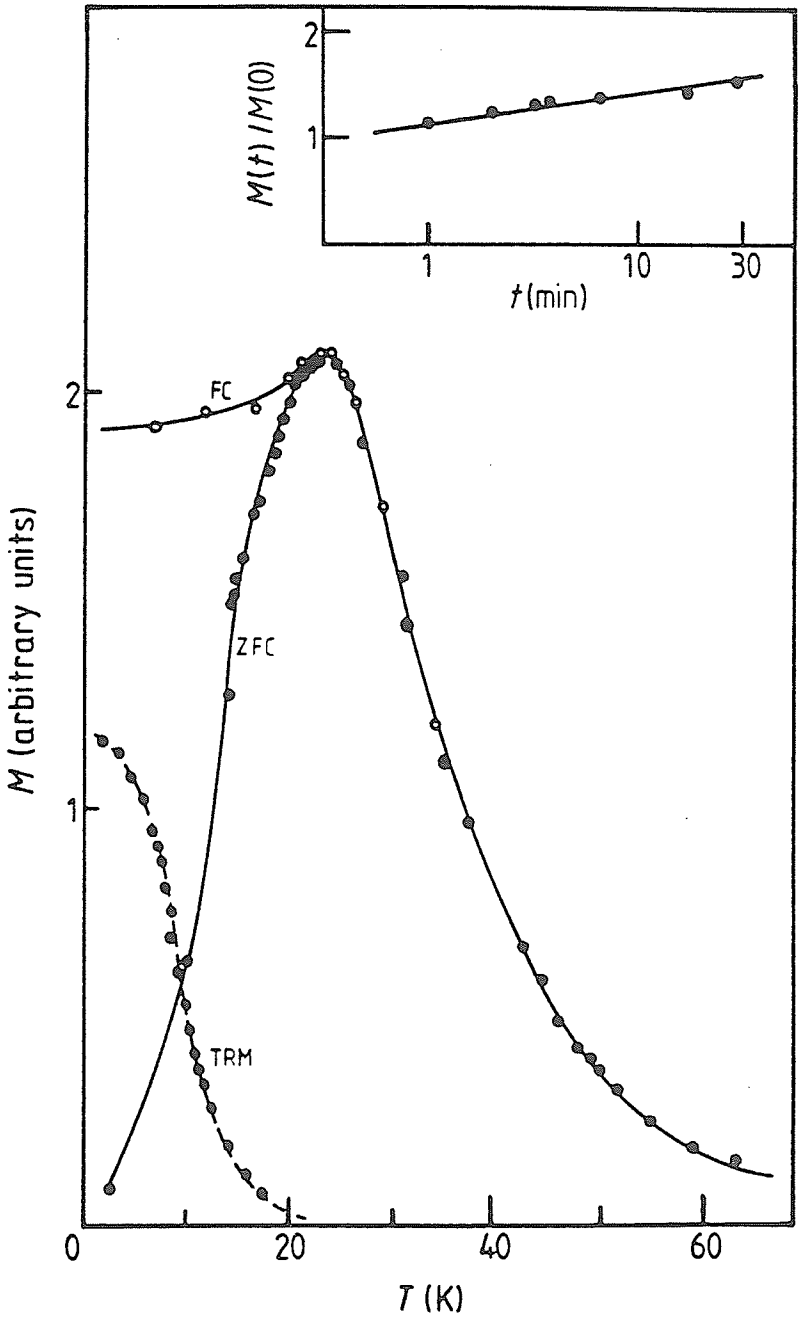

Figure 4.3.1-3: Low-field magnetization of Cr-17.5 at.% Fe in an applied field of 35 Oe as a function temperature. Zero-field-cooled (ZFC), field-cooled (35 Oe) (FC) magnetization and thermoremanent magnetization (TRM) in arbitrary units are shown. The inset shows the increase in ZFC magnetization at a temperature of 4.2 K with time in a constant applied field of 35 Oe. From Burke et al. (1983).

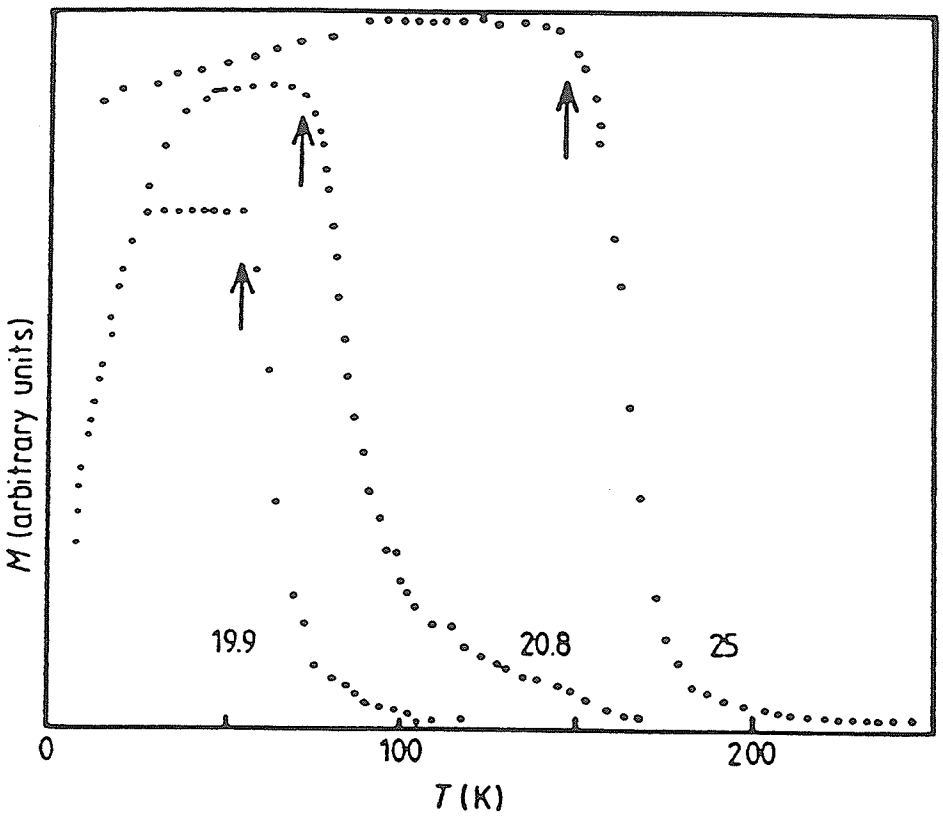

Figure 4.3.1-4: Low-field magnetization of ferromagnetic Cr-19.9 at.% Fe, Cr-20.8 at.% Fe and Cr-25 at.% Fe alloys. Magnetization in an applied field of 10 Oe is shown as a function temperature. Curie temperatures determined by neutron SAS are indicated by arrows. Alloy concentrations (at.% Fe) are indicated. From Burke et al. (1983).

magnetization to establish the locations of the de Almeida-Thouless instability boundaries $T_{AT}(H)$ in the various regimes of the magnetic phase diagram, the relaxation measurements were confined to very short observation times t <300 s, and hence the temporal perspective was far too narrow to permit an appreciation of the structural complexities which characterize the decay, or to formulate an unambiguous functional representation for the decay, which was indistinguishably consistent with both a power law or a logarithmic time dependence. In the following two subsections, we present detailed measurements of the low field thermoremanent relaxation in the spin glass and reentrant ferromagnetic configurations of CrFe over a broad experimental time window and we show that the TRM relaxation within the pure spin glass phase exhibits nonequilibrium, age-dependent behaviour, similar to that in NiMn and AuFe, and that the reentrant ferromagnetic configuration is accompanied by a crossover from equilibrium dynamics at high temperatures to nonequilibrium dynamics at low temperatures. We also present temperature cycling experiments, done for the first time in the CrFe system, which provide experimental support for the droplet scaling theory of Fisher and Huse (section 2.4.1)

4.3.2 Low Field Thermoremanent Relaxation in the Spin Glass $Cr_{83}Fe_{17}$

An alloy of CrFe containing nominally 17.0 at.% Fe was prepared by arc melting, (melting losses, which placed the true compositions within $\pm$ 1 at.% of the nominal values, were insufficient to alter the intended magnetic character) and a rod shaped sample with rectangular cross section (dimensions given in Table 3.3) was spark cut from the ingot.

Figure 4.3.2-1 shows the temperature dependence of the low field static FC and ZFC magnetizations of the $Cr_{83}Fe_{17}$ spin glass measured in H_a = 1.84 Oe. While the data in Figure 4.3.2-1 exhibits the single peaked structure characteristic of a spin glass and the usual bifurcation of the FC and ZFC curves below T_{SG} symptomatic of irreversibility, there are some subtle difference in shape which

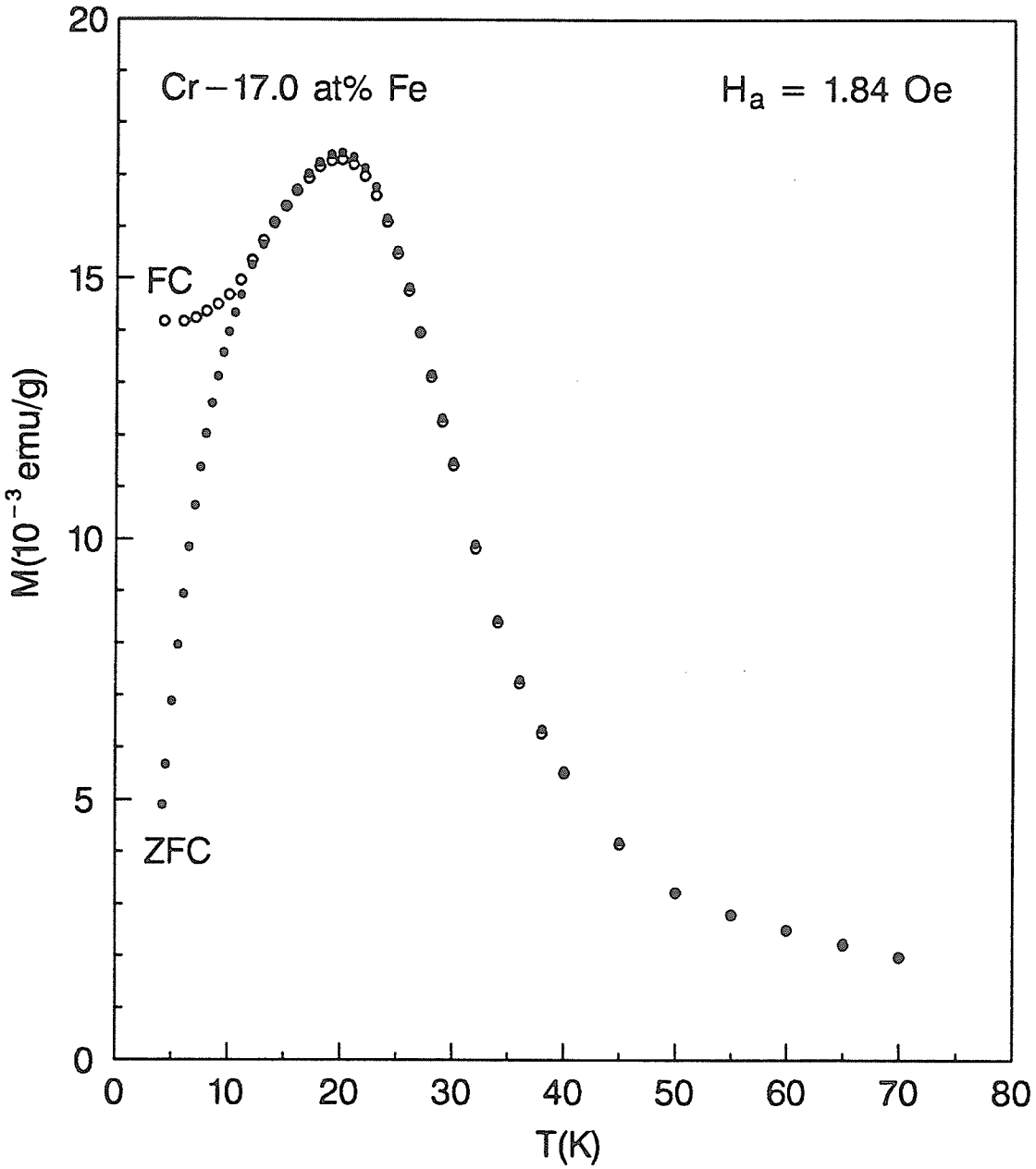

Figure 4.3.2-1: The temperature dependence of the field cooled (FC) and zero field cooled (ZFC) static magnetization of the Cr-17.0 at% Fe spin glass measured in an applied field H_a = 1.84 Oe.

distinguish this CrFe spin glass from the canonical $Au_{90}Fe_{10}$ spin glass (Figure 4.2.2-1). In particular, the peak is more rounded and asymmetric (in agreement with the earlier work by Burke et al.(1983)), and the FC and ZFC curves coalesce well below the peak.

The TRM relaxation was recorded over 6 s $< t <$ 10^4 s after cooling the sample in a field $H_c = 4.6$ Oe from $T_R = 30$ K, with typical cooling times $t_c \cong 300$ s. Figure 4.3.2-2 shows the relaxation isotherms at various temperature T_m below T_{SG}, for a wait time $t_w = 60$ s. On a logarithmic time scale, the relaxation isotherms in Figure 4.3.2-2 show systematic changes in curvature similar to that observed in NiMn (Figure 4.1.6-2) and AuFe (Figure 4.2.2-2(a)) spin glasses, with perhaps the most clearly defined inflection points, which, as before, shift monotonically with increasing measurement temperature from $t_{infl} > t_w + t_c$ to $t_{infl} < t_w + t_c$. The solid lines in Figure 4.3.2-2 are the best fits using the superposition of a pure stretched exponential and a constant (Eq.(4.1)), and the best fit parameters are listed in Table 4.3-1, along with t_{infl} which is estimated from plots of the relaxation rate $S(t)$ as a function of log t. The constant term M_o decreases with increasing temperature, and the exponent n has typical spin glass values.

Table 4.3-1: $Cr_{83}Fe_{17}$ Spin Glass Parameters for Eq.(4.1)

T(K)	t_w(s)	$t_w + t_c$ (s)	t_{infl} (s)	τ (s)	n	$M_o(10^{-3}$emu/g)
4.2	60	240	$>10^4$	(4.33±4.99)× 10^5	0.86±0.01	15.93±1.13
6	60	360	>4000	4590±189	0.77±0.01	11.48±0.08
7	60	360	1100±300	1226±16	0.73±0.01	7.65±0.04
8	60	300	220±100	294±20	0.73±0.01	3.62±0.03
9	60	420	100±20	89±1	0.72±0.01	1.68±0.03
10	60	560	<2	4.7±0.5	0.80±0.01	0.35±0.01

The age dependent nonequilibrium behaviour in the spin glass state is vividly illustrated in Figure 4.3.2-3. Figure 4.3.2-3(a) shows the relaxation isotherms at

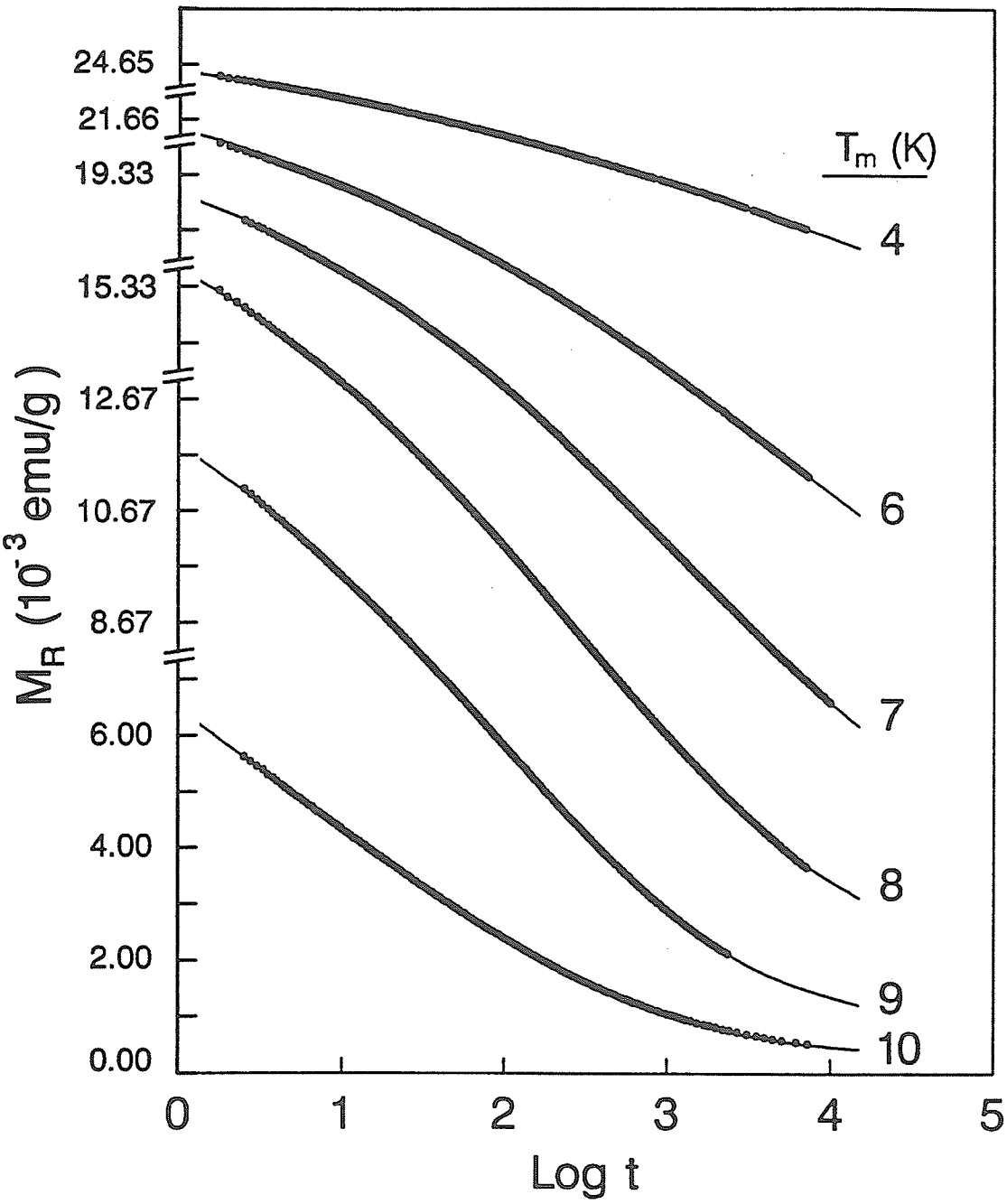

Figure 4.3.2-2: Decay of the thermoremanent magnetization M_R at several temperatures T_m within the spin glass phase, all for a wait time t_w = 60 s. Solid curves are the best fits to Eq.(4.1).

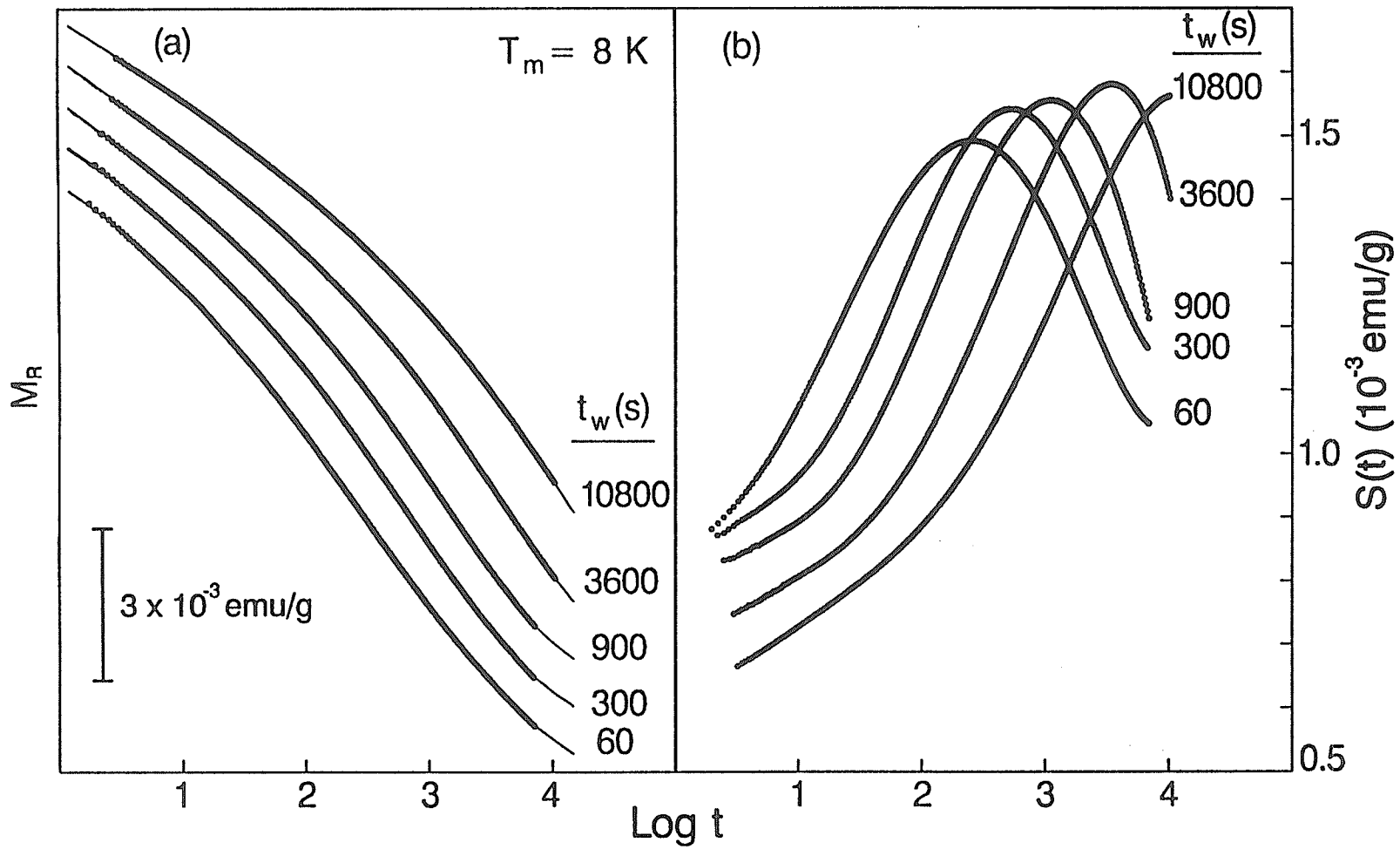

Figure 4.3.2-3: (a) Decay of the thermoremanent magnetization M_R at a typical measurement temperature T_m = 8 K for wait times t_w = 60, 300, 900, 3600, 10800 s. The solid curves for t_w > 60 s are the best fits to Eq.(4.3). (b) The numerically calculated relaxation rate *S(t)* for the isotherms in (a).

one typical measurement temperature $T_m = 8$ K for a series of wait times t_w ranging from 1 minute to 3 hours, and the propagation of the inflection point towards longer observation times with increasing t_w is clearly apparent in Figure 4.3.2-3(b), which plots the relaxation rate $S(t)$ as a function of log t. Guided by our experience in analyzing the $Au_{90}Fe_{10}$ spin glass data, we have successfully fit the relaxation isotherms over the entire experimental time window (solid curves in Figure 4.3.2-3(a)) to a function consisting of the product of a power law and a stretched exponential superinposed on a constant term Eq.(4.3). By contrast, the pure stretched exponential fit (Eq.(4.1)) is valid only over a limited time interval which excludes progressingly more short time data as t_w increases. The theoretical justification of Eq.(4.3) is, as before, provided by the mesoscopic domain model of Koper and Hilhorst (section 2.4.2), which shows that it is a consequence of probing two timescales simultaneously: intradomain dynamics and domain growth. Table 4.3-2 summarizes the best fit values of the parameters M_o, m, n, and τ. The inflection points t_{infl} coincide with the effective age of the system $t_w + t_c$.

Table 4.3-2: $Cr_{83}Fe_{17}$ Spin Glass Parameters for Eq.(4.3)

T(K)	t_w(s)	$t_w + t_c$ (s)	t_{infl} (s)	τ (s)	m	n	$M_o(10^{-3}$ emu/g)
8	300	600	550±150	1220±30	0.04±0.01	0.60±0.01	4.16±0.05
8	900	1230	1200±300	2210±10	0.06±0.01	0.52±0.01	4.55±0.03
8	1800	2100	2200±600	3400±50	0.05±0.01	0.52±0.01	4.11±0.04
8	3600	3960	3600±600	5780±60	0.06±0.01	0.49±0.01	4.20±0.03
8	10800	11160	$>10^4$	$(3.68\pm0.42)\times10^4$	0.04±0.01	0.60±0.01	1.73±0.32

Our current investigation of the spin glass $Cr_{83}Fe_{17}$ also included temperature cycling experiments which provide fascinating evidence for the existence of the overlap length introduced in the droplet scaling theory and the mesoscopic domain theory discussed in sections 2.4.1 and 2.4.2 respectively. Experiments of this type, which probe the influence of temperature variations, including temperature shifts,

temperature cycling, and temperature fluctuations, on the aging process were first conducted on the spin glass Cu-10 at.% Mn (Figure 1-27) by Sandlund et al.(1988) and Lundgren (1988) (see also Nordblad et al.,1987c), and the results were in qualitative agreement with the physical picture described in these two theories. According to the discussion in section 2.4.1, two important features of the non-equilibrium dynamics of spin glasses discussed within these theories are: (a) the aging process involving the non-equilibrium growth of domains, within which equilibrium spin glass order exists; and (b) the overlap length, $l_{\Delta T}$, which determines the maximum length scale below which the spin correlations corresponding to T and $T+\Delta T$ domains are indistinguishable. The overlap length decreases rapidly with increasing values of ΔT according to Eq.(2.151)

$$l_{\Delta T} \sim (\Delta T)^{-2/(d_s-2\theta)} \propto 1/\Delta T.$$

At a constant temperature T, the domains of correlated spins grow without limit, and the characteristic size of a domain R_{t_w} increases with age (or wait time t_w at T) of the system according to Eq.(2.150)

$$R_{t_w} \sim \left[\frac{T \ln t_w}{\Delta(T)}\right]^{1/\psi}.$$

A cross-over occurs at $lnt \sim lnt_w$ from quasi-equilibrium relaxation within domains at short time scales ($lnt \ll lnt_w$) to non-equilibrium dynamics attributed to the growth of domains at long time scales ($lnt \gg lnt_w$). If a temperature shift ΔT is imposed on the system after a wait time t_w at constant temperature T, a new domain corresponding to the temperature $T+\Delta$T starts to grow and the relevant size of this domain at $T+\Delta T$ is equal to $min(R_w, l_{\Delta T})$ according to Eq.(2.152). In a temperature cycling experiment the temperature is immediately reduced back to T after reaching $T+\Delta T$, and two different domains with sizes $l_{\Delta T}$ and R_w may coexist in the system provided that $l_{\Delta T} \leq R_w$ ($R_{w2} < l_{\Delta T}$ in Eq.(2.152) since there is no wait time after the temperature is reduced back to T). Experimentally

another "crossover" (or inflection point in M_{TRM} vs. log t), corresponding to $l_{\Delta T}$, may appear in the magnetization relaxation curves at short times ($lnt \ll lnt_w$).

The temperature cycling experiment was performed at a measuring temperature T_m = 8 K using the following procedure: The sample was cooled in a field H_c = 4.6 Oe from T_R = 30 K to T_m = 8 K. After a long wait time t_w = 10800 s (3 hours) at T_m, a positive temperature cycling $T_m \Rightarrow T_m + \Delta T \Rightarrow T_m$ was performed (this typically lasts for about 100 s, with essentially no extra wait time permitted at $T_m + \Delta T$), and when T_m was recovered the applied field was abruptly removed and the decay of the magnetization was recorded over 4 decades(1 s $< t \leq 10^4$ s). The duration of the temperature cycling was thus negligible compared to the wait time. When the recording was complete, the sample was warmed to the high temperature paramagnetic regime to establish the true zero of the decay.

Figure 4.3.2-4 shows these relaxation isotherms for ΔT =+0.5, +0.8, +0.85, +0.9, and +1.0 K, and the very subtle multiple structure in these isotherms becomes apparent when the local slope, or relaxation rate $S(t)$, is plotted as function of log t in Figure 4.3.2-5(a). For small values of ΔT ($\sim$ +0.5 K), the overlap length is large and the relaxation rate curve is only weakly affected, as compared with the undisturbed curve ΔT = 0.0 K, with only a weak shoulder at short times. When ΔT is large enough (ΔT $\sim$ 0.8, 0.85, 0.9) to guarantee $l_{\Delta T} < R_{t_w=10800}$, some domains will fracture into smaller domains, whereas other domains remain intact. The relevant domain size at $T_m + \Delta T$ is $l_{\Delta T}$, and the domain growth continues from that scale. When T_m is recovered after the temperature cycling, the coexistence of the two domain sizes $l_{\Delta T}$ and R_{t_w} thus results in two maxima (inflection points in Figure 4.3.2-4), corresponding to the two crossovers from quasiequilibrium to non-equilibrium relaxation, at about t_{infl}^1 = 200 s and $t_{infl}^2 = 10^4$ s respectively for the relaxation rate curves in Figure 4.3.2-5(a). For a large value of ΔT($\sim$ 1.0 K), the overlap length is so small that only one maximum, corresponding to $l_{\Delta T}$ is found at short times within the obser-

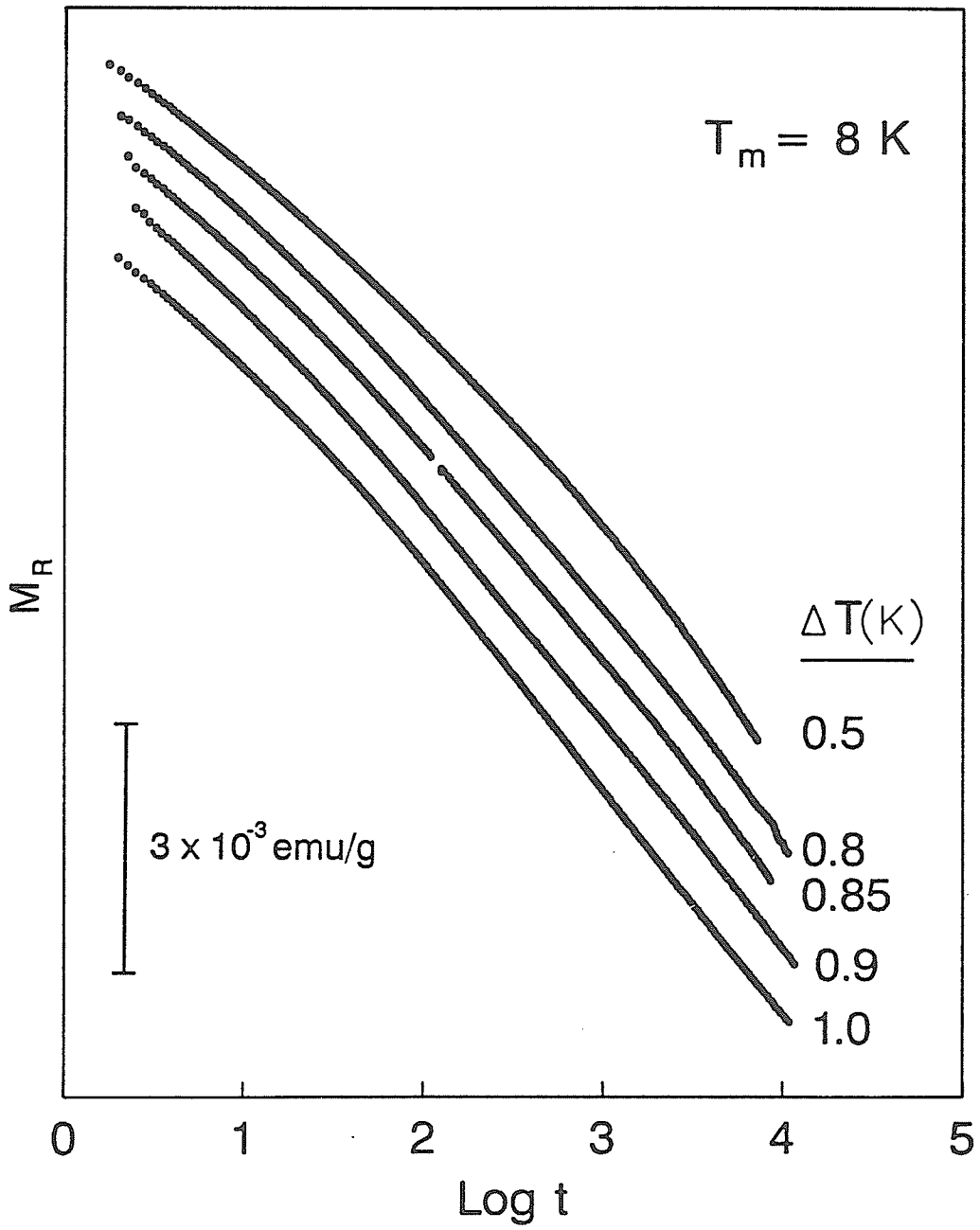

Figure 4.3.2-4: Decay of the thermoremanent magnetization M_R at a typical measurement temperature T_m = 8 K for a positive *temperature cycling* ΔT = 0.5, 0.8, 0.85, 0.9, 1.0 K. All curves have been initially aged for 10800 s at T_m = 8 K.

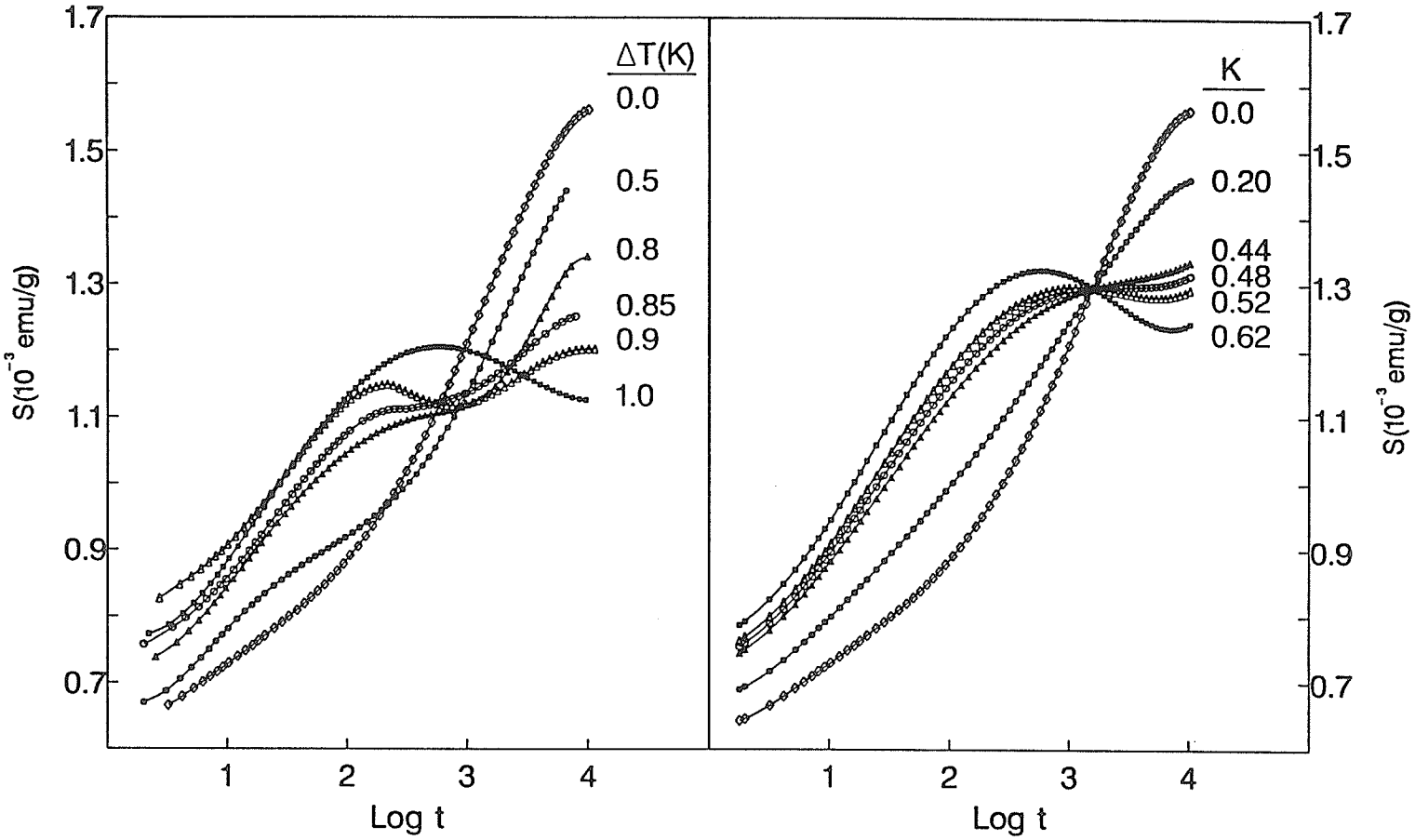

Figure 4.3.2-5: (a) The numerically calculated relaxation rate *S(t)* for the relaxation isotherms in Fig.4.3.2-4. (b) The reproduced relaxation rate *S(t)* corresponding to (a), using Eq.(4.14) with suitable choices for the fraction factor k of the domain at t_w = 60 s.

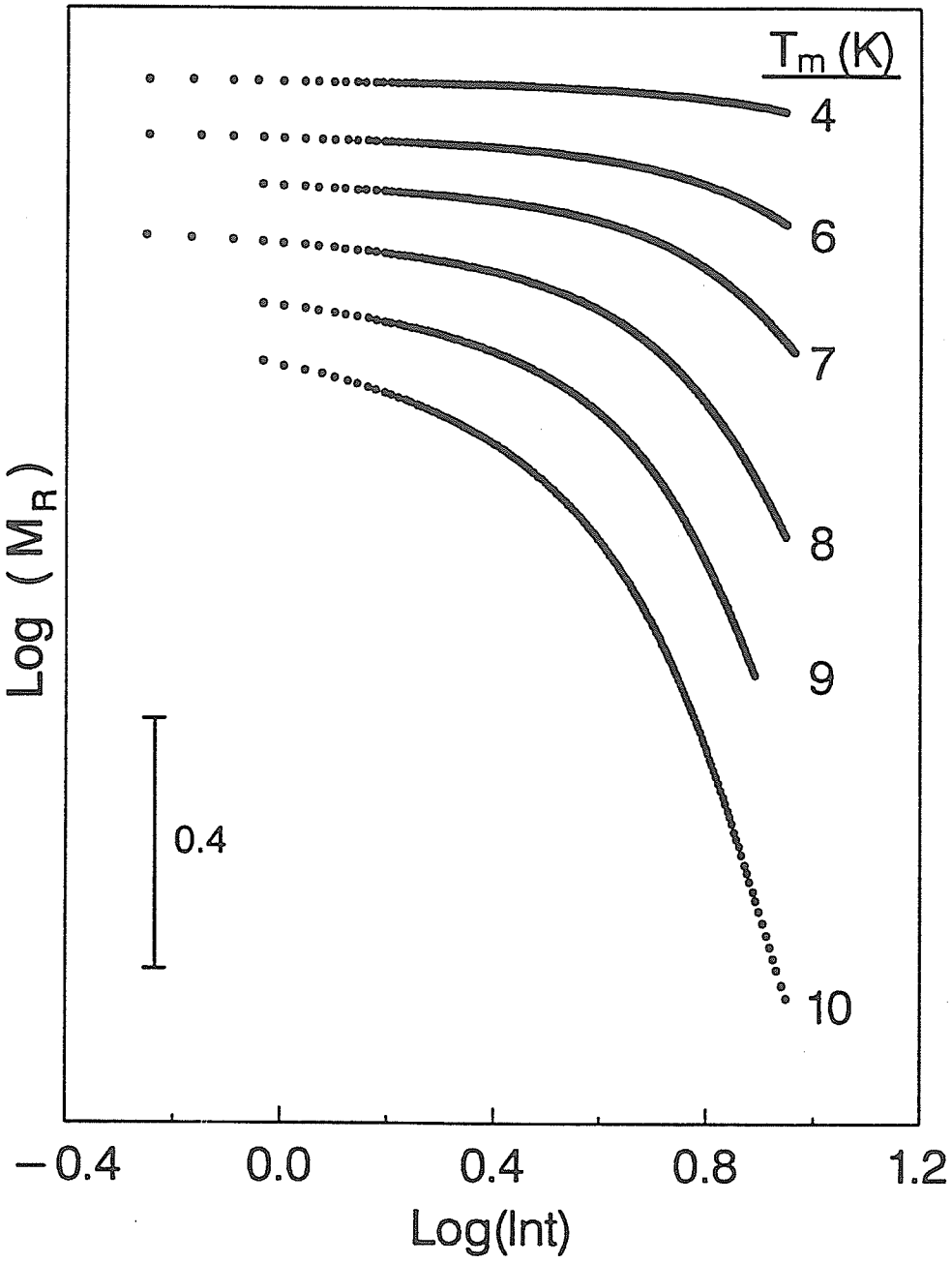

Figure 4.3.2-6: Double logarithmic plots of M_R as a function of *ln t* for the isotherms in Figure 4.3.2-2.

vation time window. The decrease in the peak amplitude with decreasing ΔT in Figure 4.3.2-5(a) indicates that there exists a threshold value of ΔT below which the peak at earlier times disappears. This threshold value ΔT_o corresponds to the value of ΔT at which the overlap length equals the domain size, i.e. $l_{\Delta T} = R_{t_w}$. Within the regime of $\Delta T < \Delta T_o$, the growing domains R_{t_w} are *unaffected* by the temperature cycling and the relaxation curves should be identical to the relaxation curve for R_{t_w} ($t_w = 10800$ s) (or $\Delta T = 0$). The threshold value ΔT_o is temperature dependent (Sandlund et al., 1988), and is less than 0.5 K for $T_m = 8$ K (see Figure 4.3.2-5(a)) in this experiment. The experimental relaxation rate curves $S(t)$ for the temperature cycling experiments in Figure 4.3.2-5(a) can also be decomposed by using the two undisturbed relaxation rate curves $S_1(t)$ and $S_2(t)$:

$$S(t) = kS_1(t) + (1-k)S_2(t) \tag{4.14}$$

where $S_1(t)$ is the relaxation rate at T_m for $t_w = 0$ s, and $S_2(t)$ is the relaxation rate at T_m for $t_w = 10800$ s. The parameter k is a factor which represents the fraction of the domain with at $t_w = 0$ s in the system. In this experiment we represent $S_1(t)$ by the measured relaxation rate curve at $t_w = 60$ s in Figure 4.3.2-3(b), and both $S_1(t)$ and $S_2(t)$ are accurately represented by a 5th order polynomial function. With suitable choices of k the shape of the experimental relaxation rate curves can be reproduced, as shown in Figure 4.3.2-5(b).

Figure 4.3.2-6 shows double logarithmic plots of M_{TRM} vs ln t for all the isotherms in order to test the validity of the Fisher-Huse predictions. The results are very similar to those in the $Au_{90}Fe_{10}$ spin glass (See Figure 4.2.2-11), with the slope increasing from a small negative value to a higher negative value with increasing time, thus agreeing qualitatively with the model.

4.3.3 The Low Field Thermoremanent Relaxation in a Reentrant Ferromagnet: $Cr_{78}Fe_{22}$

An alloy of CrFe containing nominally 22.0 at.% Fe was prepared by arc melting, (as before, melting losses, which placed the true compositions within ± 1 at.% of the nominal values, were insufficient to alter the intended magnetic character) and a rod shaped sample with rectangular cross section, of dimensions specified in Table 3.3, was spark cut from the ingot.

Figure 4.3.3-1 shows the temperature dependence of the low field static FC and ZFC magnetization measured in $H_a = 0.51$ Oe. The multiple structure (marked by the vertical arrows) in Figure 4.3.3-1 is consistent with a paramagnetic-ferromagnetic transition at $T_c = 80$ K, followed by a reentrant collapse below about $T_K \cong 30$ K, with evidence of irreversibility ($M_{FC} > M_{ZFC}$) throughout both ordered phases (i.e. for all $T < T_c$).

The characterization of the relaxation dynamics in the $Cr_{78}Fe_{22}$ ferromagnet employed virtually identical experimental and analytical procedures to those described previously, and essentially supported the conclusions reached in the preceding studies of reentrant NiMn and AuFe. The principal features of the thermoremanent decay are illustrated in Figure 4.3.3-2 for a sequence of representative measurement temperatures T_m spanning the entire ordered phase, with all isotherms corresponding to an identical cooling field $H_c = 0.46$ Oe, and to a wait time of $t_w = 60$ s. While the structure of these isotherms is much broader and considerably more subtle than that associated with the "pure" spin glass relaxation in Figure 4.3.2-2, there is nevertheless a clear, systematic change in curvature from concave-down to concave-up with increasing temperature, with inflection points visible in some of the intermediate isotherms (vertical arrows in Figure 4.3.3-2(a)), which translate into distinct maxima in the relaxation rate $S(t)$, as shown for the isotherm $T_m = 20$ K. Furthermore, as in reentrant NiMn and AuFe, quantitative analysis reveals the presence of two distinct types of dynamic behaviour, which occupy two distinct thermal regimes. (a) A low temperature regime T_m <35 K (the isotherms in Figure 4.3.3-2(a)) where the thermoremanent decay is sensitive

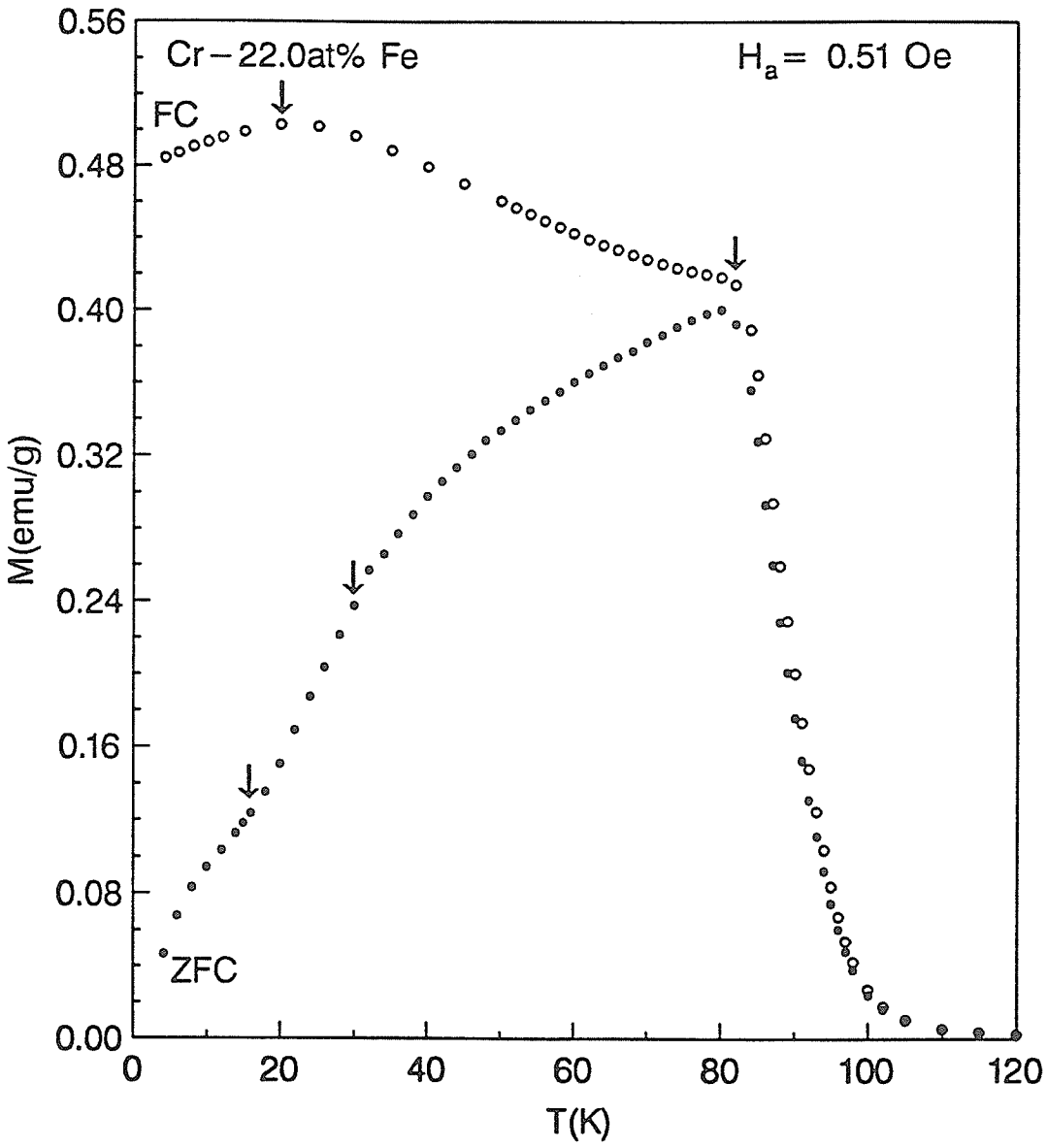

Figure 4.3.3-1: Temperature dependence of the field cooled (FC) and zero field cooled (ZFC) static magnetization of the Cr-22.0 at% Fe reentrant ferromagnet measured in an applied field H_a = 0.51 Oe. The vertical arrows mark the principal structure features.

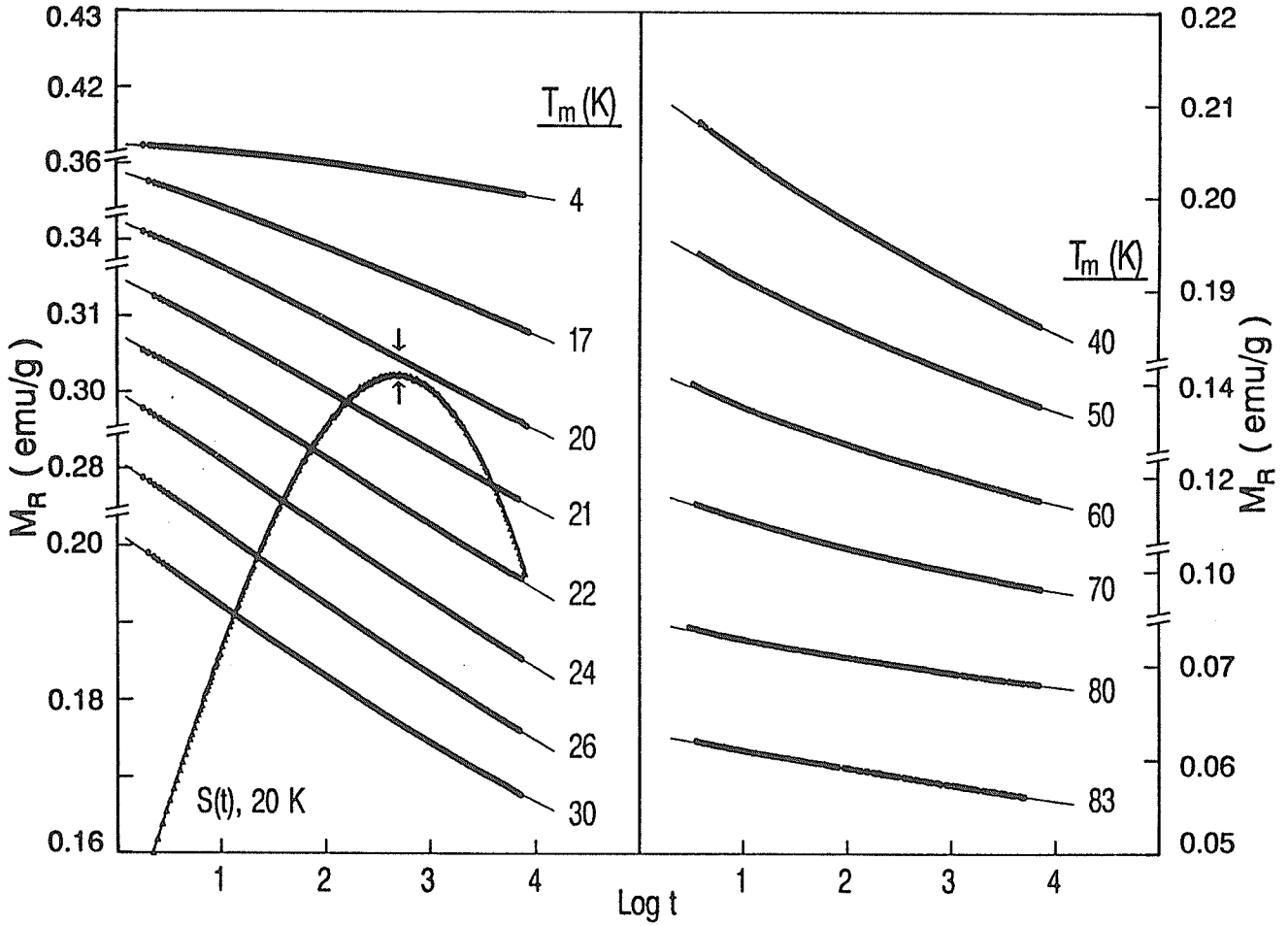

Figure 4.3.3-2: (a) Decay of the thermoremanent magnetization M_R at several representative temperatures T_m within the reentrant phase, for a wait time t_w = 60 s, and the relaxation rate $S(t)$ for T_m = 20 K.The arrows mark the location of the inflection point for T_m = 20 K. Solid curves are the best fits to Eq.(4.1). (b) Decay of the thermoremanent magnetization M_R for t_w = 60 s at several representative temperatures T_m within the ferromagnet phase. Solid curves are the best fits to Eq.(4.2).

to the age of the system and where all the isotherms are accurately described by the superposition of a pure stretched exponential and a constant (Eq.(4.1)) with parameters typical of pure spin glasses. (b) A high temperature regime $40K \leq T_m \leq 83K$ (the isotherms in Figure 4.3.3-2(b)) where aging effects are negligible and where the decay is incompatible with the stretched exponential representation but is consistent with a weak power law dependence of the form given in Eq.(4.2). The solid curves in Figure 4.3.3-2 illustrate the quality of the fits in the two relaxation regimes, and Tables 4.3-3 and 4.3-4 summarize the values of some of the best fit parameters in Eq(4.1) and (4.2) respectively.

Table 4.3-3: $Cr_{78}Fe_{22}$ Reentrant Phase Parameters for Eq.(4.1)

T(K)	t_w(s)	$t_w + t_c$ (s)	t_{infl} (s)	τ (s)	n	$M_o(10^{-3}$emu/g)
4.2	60	810	5000±2000	3086±144	0.74±0.01	404±1
15	60	780	>1400	1732±625	0.91±0.01	348±2
17	60	720	>8000	(1.05±0.45)× 10^4	0.92±0.01	305±3
20	60	810	700±500	469±22	0.88±0.01	302±1
20	7200	7890	4000±3000	3707±1818	0.90±0.01	246±4
21	60	840	500±400	296±18	0.92±0.01	256±1
22	60	930	500±400	412±104	0.92±0.01	243±6
22	7200	7890	>7000	7839±7386	0.93±0.01	233±10
23	60	810	200±100	171±10	0.93±0.01	225±2
23	10800	11520	>8000	(0.87±1.12)× 10^4	0.97±0.01	142±22
24	60	870	20±10	20±5	0.94±0.01	223±3
26	60	1020	10±7	10±2	0.93±0.01	211±2
30	60	1020	<2	0.7±0.4	0.93±0.01	151±1

Evidence for the nonequilibrium age-dependent character of the reentrant phase is shown in Figures 4.3.3-3 and 4.3.3-4. Figure 4.3.3-3 shows the relaxation isotherms at three temperatures below $T_K = 30$ K for different wait times t_w. Although the change in structure is extremely subtle in this perspective due to the very gentle curvature of the isotherms, the aging effect is readily apparent in Figure 4.3.3-4 where the relaxation rate $S(t)$ is plotted as a function of log t.

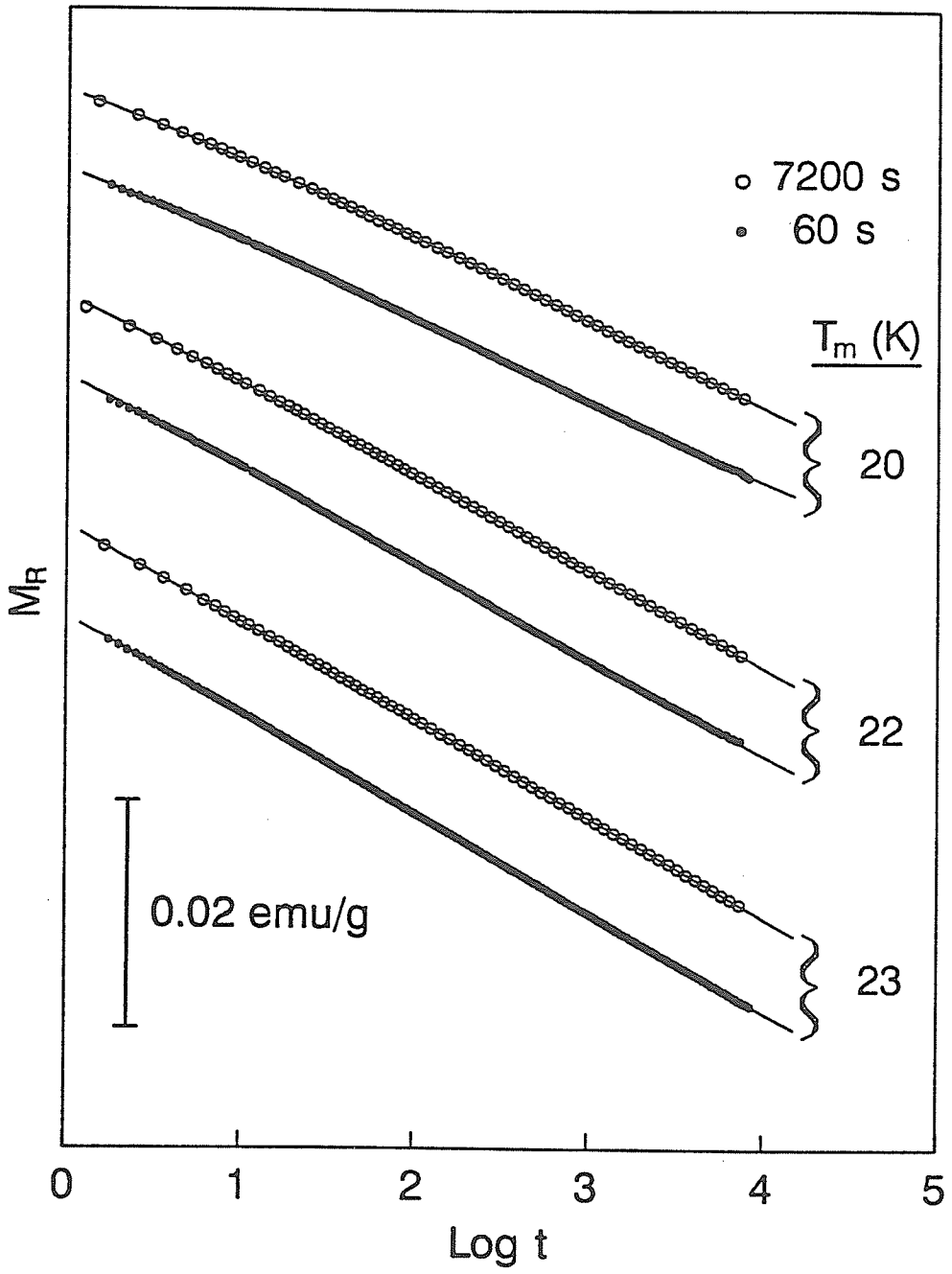

Figure 4.3.3-3: An illustration of the influence of the wait time t_w on three typical relaxation isotherms within the reentrant phase. Curves with open circles are for t_w = 7200 s. The zero magnetization levels of the relaxation curves have been shifted by arbitrary amounts for clarity of presentation, so that only the scale of the relaxation has been indicated in the lower left of the figure. Solid curves are the best fits to Eq.(4.1).

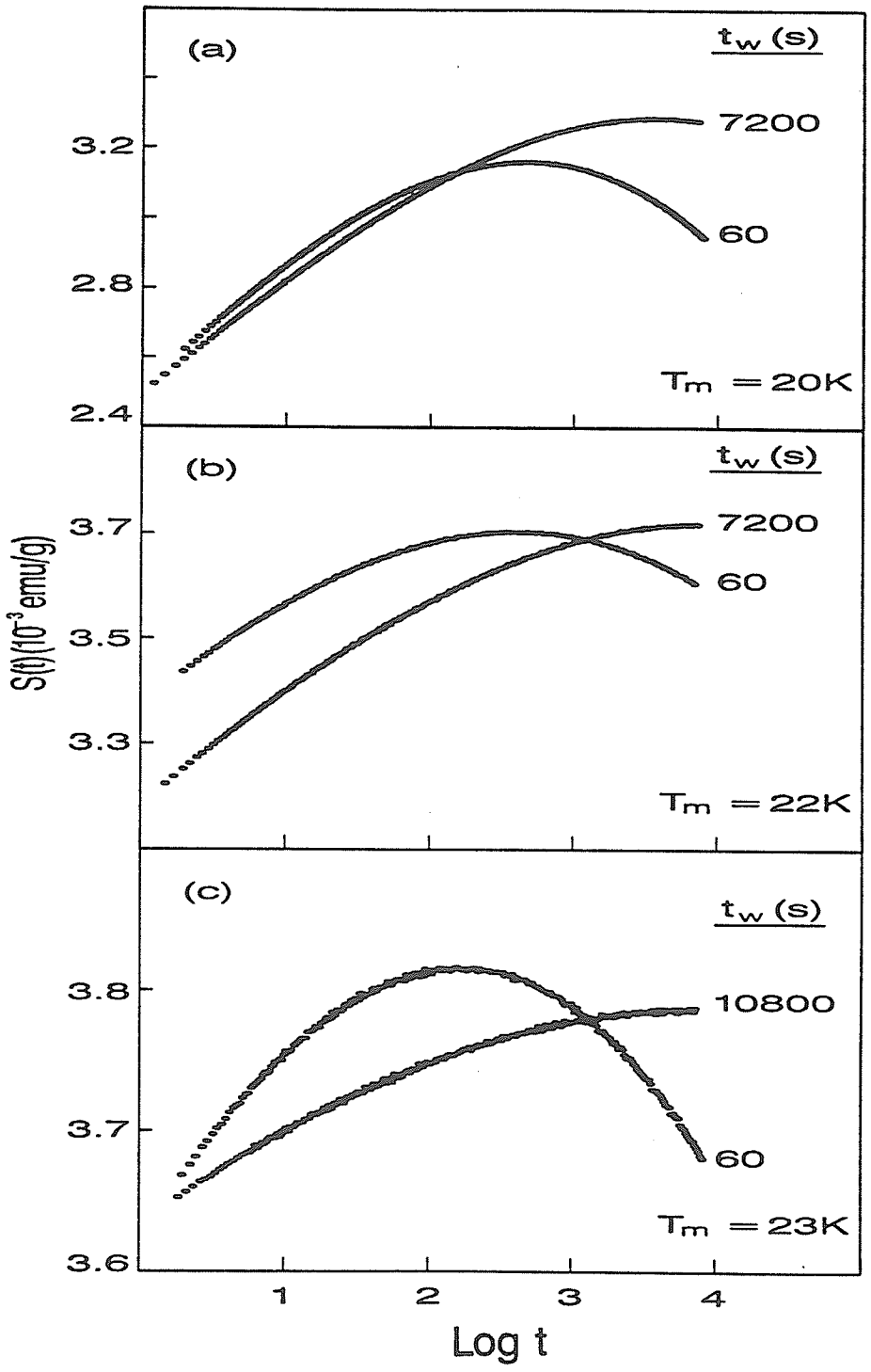

Figure 4.3.3-4: The numerically calculated relaxation rate *S(t)* for the isotherms in Fig.4.3.3-2 to show the influence of the wait time.

The inflection points, or equivalently the maxima in $S(t)$, move towards longer observation times with increasing t_w.

Table 4.3-4: $Cr_{78}Fe_{22}$ Ferromagnetic Phase Parameters For Eq.(4.2)

T(K)	t_w(s)	m	M_o(emu/g)
40	60	0.05±0.01	142±1
40	7200	0.05±0.01	81±1
50	60	0.06±0.01	109±1
60	60	0.06±0.01	100±1
70	60	0.08±0.01	90±1
80	60	0.05±0.01	56±1
83	60	0.02±0.01	39±6

The test of the Fisher-Huse model, a double logarithmic plot of M_{TRM} vs ln t, is shown in Figure 4.3.3-5(a) and 4.3.3-5(b) for the reentrant phase and the ferromagnetic phase respectively. The behaviour in the low temperature reentrant phase is very similar to that in the pure spin glass phase of $Cr_{83}Fe_{17}$ (Figure 4.3.2-6), the slope increasing with increasing ln t. The isotherms in the high temperature ferromagnetic phase also show curvature similar to that observed in the ferromagnetic state in reentrant $Au_{83}Fe_{17}$ (see Figure 4.2.3-6); however, no straight line is observed for $Cr_{78}Fe_{22}$ even at the highest temperature $T_m = 83$ K, above T_c (It is possible that this temperature is not high enough).

The preceding analysis shows that the reentrant ferromagnetic configuration of NiMn, AuFe and CrFe is characterized by a temperature driven crossover from equilibrium to nonequilibrium dynamics, and indicates that the two relaxation regimes are correlated with the two sequential ordered phases, with the equilibrium behaviour essentially confined to the high temperature ferromagnetically ordered state, and with the onset of nonequilibrium effects coinciding with the ferromagnetic collapse and the formation of the low temperature reentrant phase. Furthermore, the similarity between the reentrant and pure spin glass phases, with

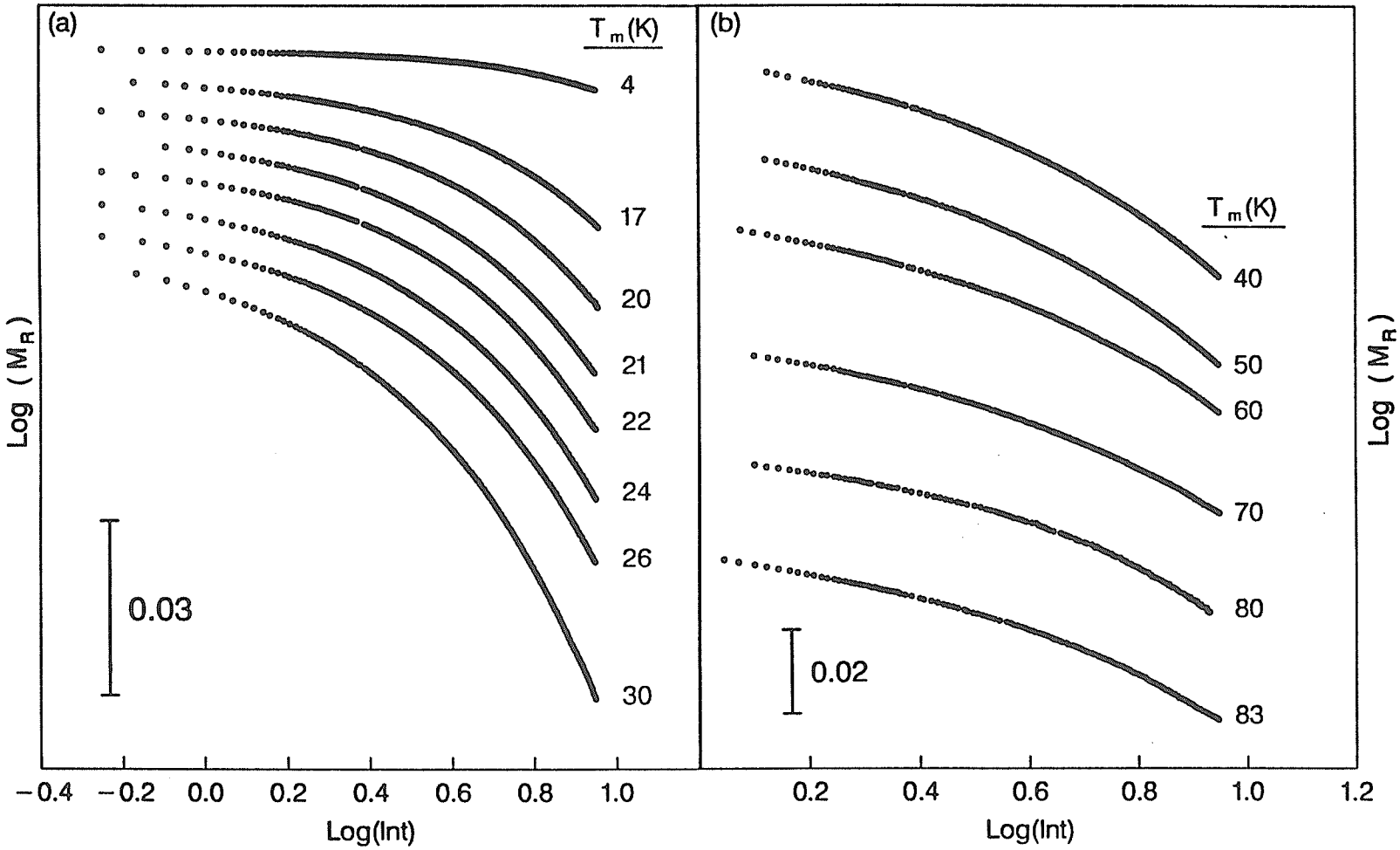

Figure 4.3.3-5: Double logarithmic plots of M_R as a function of *ln t* for the isotherms in Figure 4.3.3-2. The zero magnetization levels of the relaxation curves have been shifted by arbitrary amounts for clarity of presentation, so that only the scale of the relaxation has been indicated in the lower left of the figure.

respect to their nonequilibrium properties as well as to the functional description of the thermoremanent relaxation, provides compelling evidence for orientationally random spin freezing within the reentrant state. The magnitude of the time independent component M_o of the remanence in the reentrant phase accounts for approximately 90-95% of the total signal. Coupled with its tendency to decrease with increasing temperature, this behaviour lends support to the Gabay-Toulouse picture (section 2.2.2) of the reentrant state as a mixed phase in which a ferromagnetic longitudinal spontaneous magnetization coexists with transverse spin glass freezing.

4.4 Thermoremanent Relaxation in a Canonical Ferromagnet: Pd-1.4 at.% Fe

As mentioned in section 2.1.1, Pd based alloys (such as PdFe, PdCo, and PdMn) are characterized by "giant moments". The strong exchange interaction between $4d$ conduction electrons in Pd enhances the paramagnetic susceptibility of the Pd host, and the presence of localized magnetic impurities, such as Fe, Mn, and Co, in the Pd matrix polarizes of the itinerant $4d$ conduction electrons surrounding each impurity atom which is consequently of large amplitude and long range. The interaction between these "giant moments" yields long-range ferromagnetism at quite low magnetic impurity concentrations. In the PdFe system, the percolation limit for ferromagnetism is about 0.1 at.% Fe, according to the magnetization measurements by Chouteau and Tournier (1971). The ferromagnetic state begins to weaken below 0.1 at.% Fe, until, below approximately 100-ppm Fe, the system becomes a spin glass, and exhibits the typical spin glass cusp in the low frequency ac susceptibility measured as a function of temperature. (Peters et al., 1984). Extensive studies have been conducted on the PdFe system, including static magnetization (Crangle, 1960), electrical resistivity (Coles et al., 1965), specific heat (Veal and Rayne, 1964), Mössbauer effect (Craig et al., 1965)

and a.c. susceptibility (Wang, 1990). Figure 4.4-1 summarizes the results of these measurements (Mydosh et al., 1968).

In the current work, we focus on the magnetic relaxation behaviour, in order to provide a comparison between reentrant ferromagnets and a canonical ferromagnet. For this purpose, an alloy of Pd-1.4 at.% Fe was chosen, based on the detailed critical analyses performed by Wang (1990) which describe this particular concentration as a "perfect" ferromagnet with a Curie temperature $T_c = 55.6 \pm 0.1$ K, and critical indices $\delta = 4.0 \pm 0.1$, $(\gamma + \beta)^{-1} = 0.54 \pm 0.02$, and $\gamma = 1.36 \pm 0.05$. For higher and lower Fe concentrations, the exponents are decidedly less canonical (Wang, 1990).

The temperature dependence of the static FC and ZFC magnetizations of the Pd-1.4 at.% Fe sample, measured in $H_a = 5.0$ Oe, is shown in Figure 4.4-2. Unlike the reentrant ferromagnets studied earlier, the Pd-1.4 at.% Fe system shows a very sharp transition in the vicinity of $T_c \cong 52.3$ K (identified by the location of inflection point in the paramagnetic portion of the curve), and no indication of a further sudden drop-off at low temperatures. The bifurcation of the FC and ZFC magnetization data below about 52 K indicates the presence of irreversibility, and consequently of viscous behaviour.

The relaxation of the TRM was measured between 3 s $\leq t <$ 7200 s after cooling the sample in a static field $H_c = 5.0$ Oe from a reference temperature $T_R =$ 60 K, with typical cooling times $t_c \cong 750$ s. The relaxation is plotted as a function of log t at several measurement temperatures $T_m \leq 51$ K, and for a wait time $t_w =$ 60 s, in Figure 4.4-3. The relaxation data are clearly quite noisy, particularly when compared with the data for the other reentrant ferromagnets described earlier. This is due to the fact that the amplitude of the decay is very weak and, is comparable to the size of the background decay (see Figure B in Appendix B). As a result, the smoothing capacitor C in Figure 3-8 was not used for data acquisition in order not to distort the curve, and hence this sample was subjected to more RF

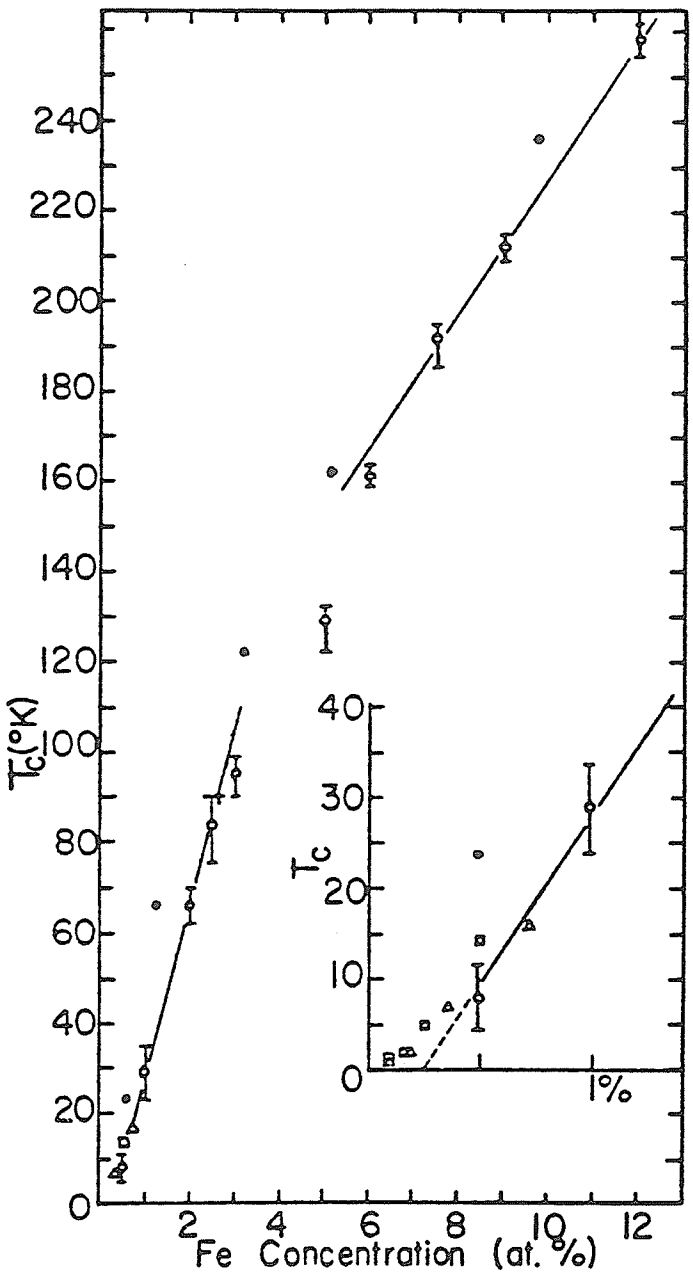

Figure 4.4-1: Variation of the magnetic-ordering temperature T_c with Fe concentration in PdFe. The inset shows the concentration range below 1 at% Fe on a magnified scale. From Mydosh et al. (1968).

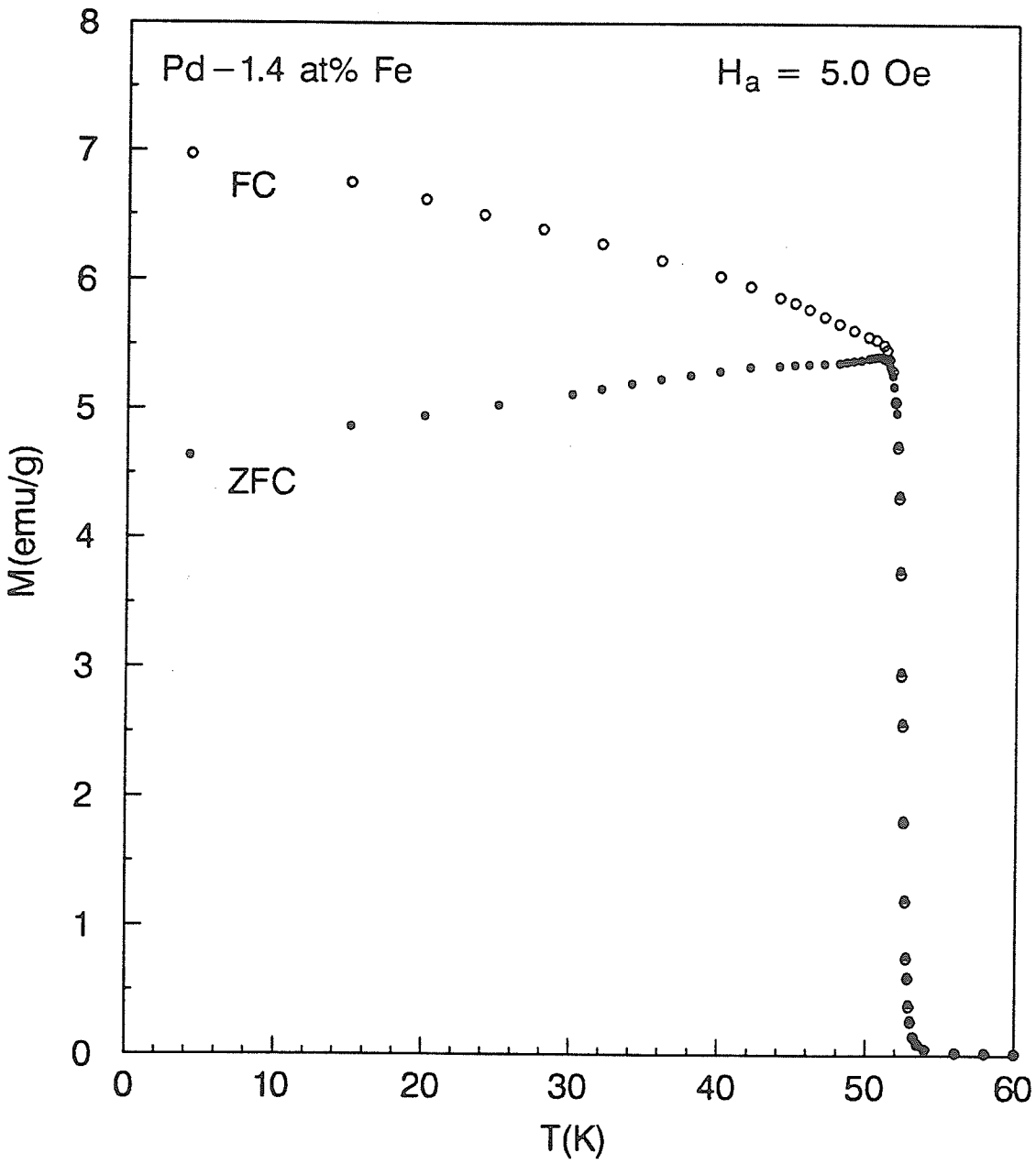

Figure 4.4-2: The temperature dependence of the field cooled (FC) and zero field cooled (ZFC) static magnetization of the canonical Pd-1.4 at% Fe ferromagnet measured in an applied field H_a = 5.0 Oe.

noise during the data acquisition process. (The noise may also be related to the Barkhausen effect which is magnetic noise due to jerky, discontinuous domain wall jumps.) The relaxation isotherms in Figure 4.4-3 are clearly not purely logarithmic functions of t, although there is some evidence, in the "low" temperature isotherms $T_m \leq 40$ K, of straight line behaviour for 30 s$< t <10^4$ S, with deviation at short observation times. This logarithmic component seems to disappear at higher temperatures ($T_m \geq 45$ K). Guided by the experience in NiMn, AuFe and CrFe as well as by the theoretical predictions (section 2.4), we were able to describe all the relaxation data by the superposition of a constant and a simple power-law (Eq.(4.3)), and the solid lines in Figure 4.3-3 show the quality of the fits with the best fit parameters listed in Table 4.4-1. The constant term M_o decreases with increasing temperature, while the exponent m tends to increase from $m \sim 0.03$ to $m = 0.57$ at higher temperatures. (as compared with $m \sim 0.05$ for reentrant ferromagnets). This power-law behaviour in PdFe provides compelling evidence to support our interpretation that the high temperature, age-independent relaxation isotherms observed in all the reentrant systems investigated here are a symptom of ferromagnetic ordering, particularly in view of recent studies (Luo et al., 1990) which claim that the stretched-exponential is a fundamental component of the equilibrium relaxation of all spin glasses, and not merely a consequence of nonequilibrium aging effects.

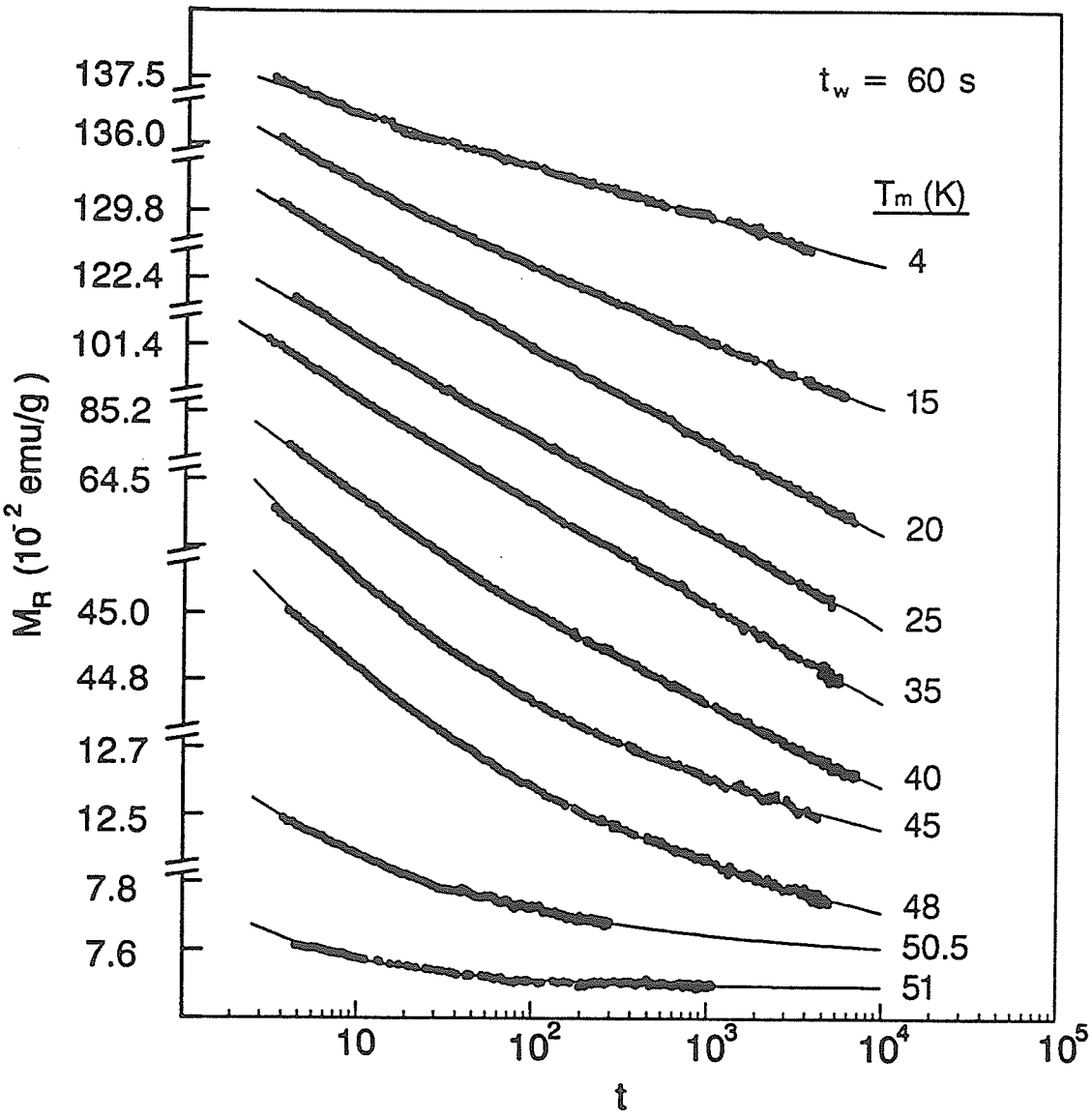

Figure 4.4-3: Decay of the thermoremanent magnetization M_R at several temperatures T_m below T_c, all for a wait time t_w = 60 s. Solid curves are the best fits to the simple power law function Eq.(4.3).

Table 4.4-1: Pd-1.4 at.% Fe Ferromagnetic Parameters for Eq.(4.2)

T(K)	t_w(s)	m	M_o(emu/g)
4.2	60	0.03±0.01	1.350±0.003
15	60	0.05±0.01	1.335±0.003
20	60	0.01±0.01	1.169±0.010
25	60	0.01±0.01	0.963±0.003
35	60	0.02±0.01	0.929±0.006
40	60	0.07±0.01	0.826±0.003
45	60	0.18±0.01	0.631±0.001
48	60	0.18±0.01	0.438±0.001
50.5	60	0.31±0.01	0.121±0.001
51	60	0.57±0.02	0.075±0.001

Chapter V

Conclusions

Measurements of the frequency dependent susceptibility, the static magnetization and the relaxation of the thermoremanent magnetization have been used to study the behaviour of several glassy magnetic systems (NiMn, AuFe, CrFe) close to, and on both the spin glass and ferromagnetic sides of, the multicritical point in the magnetic phase diagram.

On the spin glass side, the most striking feature is the nonequilibrium nature of the frozen state: the relaxation isotherms exhibit an inflection point on a logarithmic time scale, which depends on the wait time which is allowed to elapse at constant temperature before the system is probed by removing the field, and which propagates towards longer observation times with increasing system age. For short wait times ($t_w \leq 60s$), the behaviour is well-described by the superposition of a constant and a stretched exponential:

$$M_R(t) = M_o + M_1 exp[-(t/\tau)^{1-n}]$$

while for longer wait times ($t_w > 60$ s), it is necessary to introduce an additional power law factor in order to account for the gradual emergence of the equilibrium decay for observation times $t \ll t_w$:

$$M_R(t) = M_o + M_1 t^{-m} exp[-(t/\tau)^{1-n}]$$

Temperature cycling experiments yield multiple structure in the relaxation rate which confirms the instability of the spin glass state to arbitrarily small changes in temperature, as measured by the overlap length scale $l_{\Delta T}$, and thus help to establish the validity of the mesoscopic domain picture of Fisher and Huse. The observation of the memory effect, in which a sequence of field reversals induces

oscillations in the thermoremanent decay, indicates the presence of extremely long relaxation times in spin glasses and proves the applicability of the linear response principle.

On the ferromagnetic side, where the system exhibits so-called reentrant behaviour, measurements of the a.c. susceptibility yield ferromagnetic critical peaks in the vicinity of the paramagnetic-ferromagnetic phase boundary. However, analysis of the critical exponent behaviour is consistent with extensive bond disorder, and yields values for δ^* and γ^* which are far from canonical. At low temperatures, near the reentrant transition, the a.c. susceptibility exhibits a dual-peaked structure and evidence of strong irreversibility, particularly in the lower-temperature peak. While a weak non-divergent anomaly is observed in the coefficient of the leading term in the nonlinear susceptibility, there is insufficient evidence to categorically confirm the existence of critical behaviour at this transition. Nevertheless, a distinct crossover is observed on the relaxation dynamics, from equilibrium behaviour within the high temperature, ferromagnetically ordered phase, described by a weak power law:

$$M_R(t) = M_o + M_1 t^{-m}$$

to nonequilibrium, age-dependent behaviour within the low temperature, reentrant phase, indicating that there is significant orientational disorder in the frozen spin configuration, and supporting the hypothesis of a collapse of the ferromagnetic state into a spin glass-like phase.

Appendix A:

The mutual inductance between the secondary astatic pick-up coil and the primary A.C. field coil can be calculated by considering the total magnetic flux Φ through the pick-up coil (see Fig.3-8), which includes the contribution from both the applied magnetic field H_a and the magnetization of the sample M_s, i.e;

$$\begin{aligned}\Phi &= C_1 H_a + C_2 M_s \\ &= C_1(H_{DC} + h_{AC}) + C_2({M_s}^{DC} + {M_s}^{AC}),\end{aligned}$$

where C_1 and C_2 are constants related to the pick-up coil geometry. ${M_s}^{DC}$ and ${M_s}^{AC}$ are the magnetizations produced by the D.C. field H_{DC} and the A.C. field H_{AC} respectively. At each experimental point, both the D.C. field and the temperature are fixed, thus $\Delta H_{DC} = \Delta {M_s}^{DC} = 0$. For a change of A.C driving field Δh_{AC}, the change of the mutual inductance becomes

$$\Delta\Phi = C_1 \Delta h_{AC} + C_2 \Delta {M_s}^{AC}.$$

Therefore the mutual inductance between the primay A.C coil and the secondary pick-up coil m is given by

$$\begin{aligned} m &\equiv \frac{\Delta\Phi}{\Delta h_{AC}} \\ &= C_1 + C_2 \frac{\Delta {M_s}^{AC}}{\Delta h_{AC}} \\ &= C_1 + C_2 \chi_{AC}\end{aligned}$$

Appendix B:

In order to measure the background decay, we put *one* capacitor, which is usually required to filter out RF noise, across the DC solenoid (Fig.3-8) and withdrew the sample from the pick-up coil. After turning off the field from 5 Oe to zero, the background relaxation (mostly induced by this capacitor) was recorded over 10 minutes. As shown in Figure B, the capacitive background decay approaches zero after 200 seconds. The solid line in this figure represents the best fit to a $6th$ order polynomial described as expression

$$M = Ax^6 + Bx^5 + Cx^4 + Dx^3 + Ex^2 + Fx + G$$

where $x = Log_{10}t$, and the coeficients are

$$\begin{aligned} A &= -2.60693 \times 10^{-2}, \quad B = 2.233994 \times 10^{-1} \\ C &= -7.22601 \times 10^{-1}, \quad D = 1.000000 \\ E &= -2.36408 \times 10^{-1}, \quad F = -8.14544 \times 10^{-1} \\ G &= 6.574132 \times 10^{-1}. \end{aligned}$$

The background correction is required when the decay from the sample is small (usually for spin glass samples, such as Au-10.0 at% Fe). The subtraction of the background decay from the total decay can be made using the equation above. If the size of the decay from the sample is comparable to the magnitude of the background decay, the capacitor is removed from the circuit.

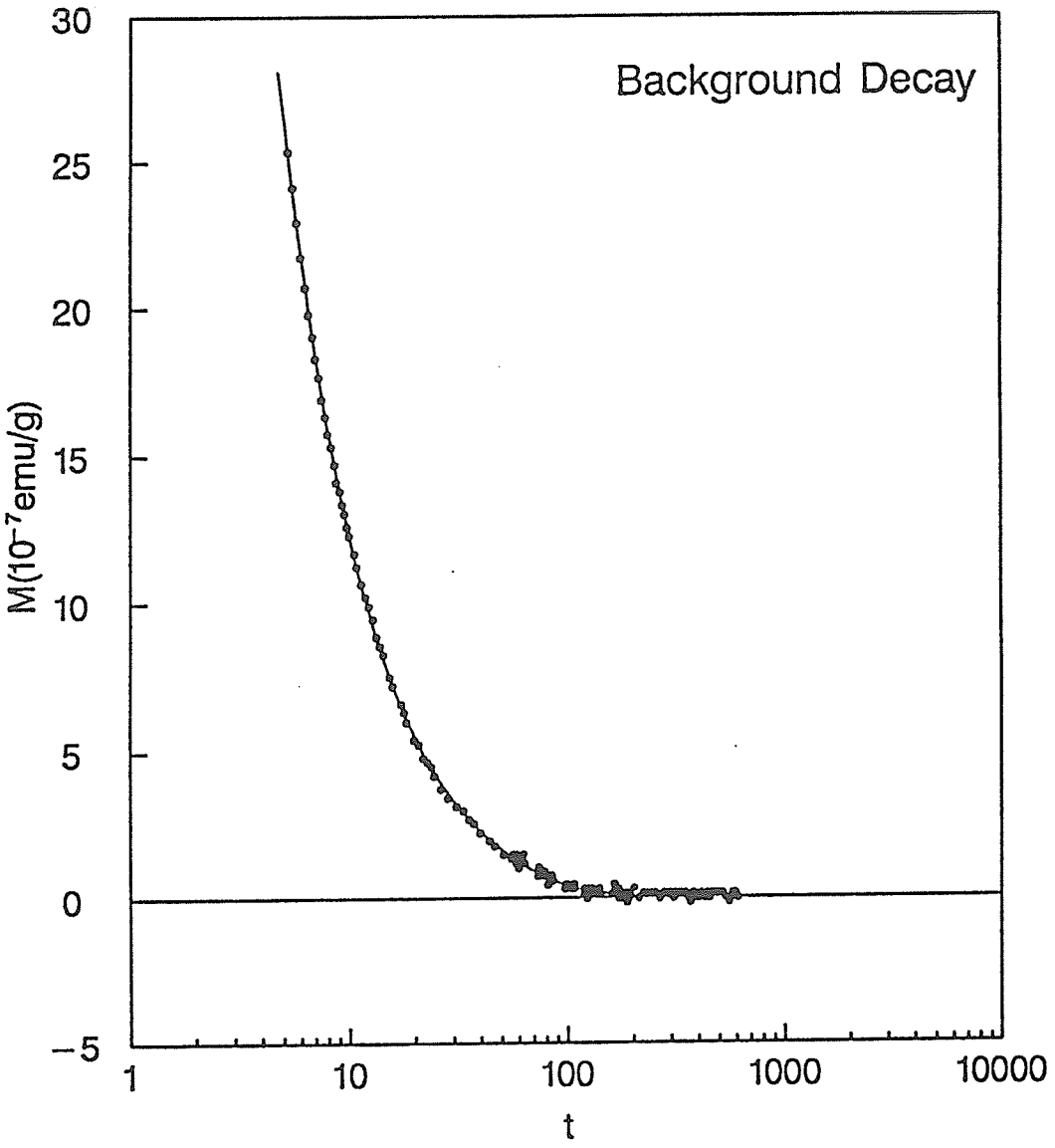

Figure B: Background relaxation of the SQUID Magnetometer, measured after removing the sample from the pick-up coil and turning off the field from 5 Oe to zero. *One* capacitor was put across the D.C solenoid (Figure 3-8). The solid curve represents the best fit to a *6th* order polynomial with coefficients listed in the text.

Appendix C:

```
C*************************************************************************************************
C  FORTRON PROGRAM TO CALCULATE (BASED ON EQ.(3.7)) FIELD PROFILE OF THE DC
C  SOLENOID WHICH CONSISTS OF 3 COAXIAL SOLENOIDS, ALL WOUND WITH A FORMER OF
C  RADIUS A0, WIRE OF DIAMETER DW, AND WITH CURRENT II.THE COIL DIMENSIONS ARE
C  GIVEN IN TERMS OF DW.
C NTOT = TOTAL LENGTH OF THE SOLENOID IN TERMS OF DW.
C NYC  = # OF LAYERS ON CENTRE SOLENOID.
C NYE  = # OF LAYERS ON END SOLENOIDS.
C NXE  = # OF TURNS ON END SOLENOIDS.
C NXS = SPACE BETWEEN ADJACENT SOLENOIDS IN TERMS OF DW.
C   CALCULATES PROFILE FROM ZSTART TO ZEND FOR ZN POINTS.
C   USE MKS UNITS. FIELD IS IN GAUSS. ORIGIN IS AT LEFT END OF THE FIRST SOLENOID.
C*************************************************************************************************
C
      INTEGER NTOT,NYC,NXE,NYE,J,ZN,NXC
      REAL NXS
      REAL CONV,MU,L,A0,DW,II,ZSTART,ZEND,C,A,ZZ,ZZZ,BBB,XE,XC,XS
      REAL Z0(300),BZ(3,300)
      MU=1.257E-6
      CONV=1.0E+4
C*****************************SOLENOID DATA*************************************
C
      II=1.0
      A0=1.400E-2
      DW=2.032E-4
      NTOT=189
      NYC=1
      NXE=24
      NYE=3
      NXS=31.0
C*************************PROFILE RANGE DATA*************************************
      ZSTART=-0.242*2.54*1E-02
      ZEND=4.385E-02
      ZN=100
C*************************DEFINE CONSTANTS*************************************
      C=CONV*MU*II/(2*DW)
      L=NTOT*DW
      XE=NXE*DW
      NXC=NTOT-2*(NXE+NXS)
      XC=NXC*DW
      XS=NXS*DW
      A=A0-DW/2
C********CALCULATE FIELD PROFILE FOR LEFT,CENTER,AND RIGHT SOLENOIDS************
C
      ZZ=(ZEND-ZSTART)/(ZN-1)
      ZZZ=ZSTART-ZZ
      DO 10 J=1,ZN
        ZZZ=ZZZ+ZZ
        Z0(J)=ZZZ
 10   CONTINUE
C
      DO 20 J=1,ZN
        ZZZ=Z0(J)
         BZ(1,J)=BB(NYE,A,XE,ZZZ,DW)*C
        ZZZ=Z0(J)-(L-XE-XS-XC)
         BZ(2,J)=BB(NYC,A,XC,ZZZ,DW)*C
        ZZZ=Z0(J)-(L-XE)
         BZ(3,J)=BB(NYE,A,XE,ZZZ,DW)*C
        BBB=BZ(1,J)+BZ(2,J)+BZ(3,J)
```

```
      WRITE(6,*)Z0(J),BBB,BZ(1,J),BZ(2,J),BZ(3,J)
 20   CONTINUE
      STOP
      END
C*************************************************************************************************
C
      REAL FUNCTION BB(M,A0,L,Z,DW)
      INTEGER M,J
      REAL A0,L,Z,DW,A,ALPH1,ALPH2
      BB=0.0
      DO 40 J=1,M
       A=A0+J*DW
       ALPH1=ATAN2(A,Z)
       ALPH2=ATAN2(A,(L-Z))
       BB=BB+COS(ALPH1)+COS(ALPH2)
 40   CONTINUE
      RETURN
      END
```

```
'PROGRAM: Data_Acquisition_in_Magnetic_Relaxation_Measurements
'*************************************************************************************************
'File        : record.bas
'Description : Used with Hewlett-Packard Interface Bus(HPIB) to record voltages from DVM (RACAL-DANA
'             5003) as a function of time. The HP-IB Command Library for Quick Basic 4.5 has to be
'             preloaded. M(v) as a function of log t is displayed  on the screen while the data is recorded. The
'             program will shift all RESETs and RF interferences to make a smoother curve.
'Author      : Wenxin Ruan
'Created     : April 25, 1991                    Last Update :  Aug. 20, 1992
'*************************************************************************************************
'
'Time axis scales are: 1--10--100--1000--10000-100000 seconds
'#1 file: raw data file.
'#2 file: data file after smoothing.
'VSTEP  : output voltage step between two consecutive points while recording data.
'JSTEP  : criterion for justifying RF inteference or RESET.
'DELTA  : The voltage change in order for DVM to recognize the magnetic is turned off. Make a good guess!
'
'data format in #1 and #2 files:
'            ***Time(seconds)***    ***Magnetization(Volts)***                                    '
'
'
'Begin_Program
DECLARE SUB INITIALIZE (ISC&, DVM&)
DECLARE SUB DVMSETUP (DVM&)
DECLARE SUB TAKEREADINGS (DVM&)
'
' Copyright Hewlett-Packard Co., 1986, 1989
'
'************************************Main*****************************************
REM $INCLUDE: 'QBSETUP'
CALL INITIALIZE(ISC&, DVM&)
CALL DVMSETUP(DVM&)
```

```
CALL TAKEREADINGS(DVM&)
END

'**********************************Initialize DVM*******************************
SUB INITIALIZE (ISC&, DVM&) STATIC
SHARED PCIB.ERR, PCIB.BASERR, NOERR
'"INPUT "Enter Select Code: ", ISC&
 ISC& = 7
'INPUT "Enter bus address of VOLTMETER: ", DVM&
 DVM& = 26
 DVM& = ISC& * 100 + DVM&
 CALL IORESET(ISC&)
 IF PCIB.ERR <> NOERR THEN ERROR PCIB.BASERR
 CALL IOTIMEOUT(ISC&, 5!)
 IF PCIB.ERR <> NOERR THEN ERROR PCIB.BASERR
 CALL IOCLEAR(DVM&)
 IF PCIB.ERR <> NOERR THEN ERROR PCIB.BASERR
 CALL IOCLEAR(ISC&)
 IF PCIB.ERR <> NOERR THEN ERROR PCIB.BASERR
 CALL IOREMOTE(DVM&)
 IF PCIB.ERR <> NOERR THEN ERROR PCIB.BASERR
 CALL IOREMOTE(ISC&)
 IF PCIB.ERR <> NOERR THEN ERROR PCIB.BASERR
END SUB

'************************************Set DVM************************************
SUB DVMSETUP (DVM&) STATIC
SHARED PCIB.ERR, PCIB.BASERR, NOERR
 CODES1$ = "Z I2 T1 F1"
 CLS : LOCATE 25, 1:
 PRINT "R0=AUTO  R3=.1V  R4=1V  R5=10V  R6=100V  R7=1000V"
 INPUT "Select Voltage Range for DVM setting >>>>>>", CODES2$
 CODES$ = CODES1$ + CODES2$
 CALL IOOUTPUTS(DVM&, CODES$, LEN(CODES$))
 IF PCIB.ERR <> NOERR THEN ERROR PCIB.BASERR
END SUB

'*****************************Record Magnetization*****************************
SUB TAKEREADINGS (DVM&) STATIC
SHARED PCIB.ERR, PCIB.BASERR, NOERR
 TIME$ = "06:45:00"
 VSTEP! = .0001: JSTEP = .05
 CLS
 INPUT "Store raw data in file ? ", RAWDATA$
 OPEN "A", #1, RAWDATA$
 PRINT : INPUT "Store smoothed data in file ? ", SMDATA$
 OPEN "A", #2, SMDATA$
 PRINT :
 PRINT : PRINT "Readings are formatted as:  Time (s)   Magnetization(V)"
 PRINT : PRINT "Input parameter for plotting....?"
 PRINT : INPUT "(YMIN,YMAX & # OF DVISIONS)"; YMIN!, YMAX!, NDVIY&
 XMIN! = 0!: XMAX = 5!: NDVIX& = 5
 CLS : LOCATE 25, 1: PRINT "Press END to exit"
 PRINT : PRINT "Press any key to begin reading..."

'EXIT>>>>>>
  KG$ = INKEY$
  IF KG$ = CHR$(0) + "O" THEN 2000: 'EXIT,press END

'Start sampling*****
1000 X$ = INKEY$: IF X$ = "" THEN 1000
  TZERO1! = TIMER
```

```
'Define display window
  CLS : LOCATE 25, 1: PRINT "Press END to stop readings and save data": LOCATE 1, 1
  CLS : SCREEN 11
  WINDOW (XMIN!, YMIN!)-(XMAX!, YMAX!)
  LINE (XMIN!, YMIN!)-(XMAX!, YMAX), , B
   DELTAX! = (XMAX! - XMIN!) / NDVIX&
   DELTAY! = (YMAX! - YMIN!) / NDVIY&
  'Draw X ticks....
    FOR I = 1 TO NDVIX& - 1
    LINE (XMIN! + I * DELTAX!, YMIN!)-(XMIN + I * DELTAX!, YMIN! + DELTAY! / 20)
    NEXT I
  'Draw Y scale....
    FOR I = 1 TO NDVIY& - 1
    LINE (XMIN!, YMIN! + I * DELTAY!)-(XMIN + DELTAX! / 30, YMIN! + I * DELTAY!)
    NEXT I
   LOCATE 28, 1: PRINT YMIN!
   LOCATE 1, 1: PRINT "+"; YMAX!
   LOCATE 14, 3: PRINT "M(V)"
   LOCATE 1, 33: PRINT "M(V) vs Log(t)"; SPC(20); SMDATA$
   LOCATE 3, 1: PRINT 1; SPC(10); 10; SPC(11); 100; SPC(10); 1000; SPC(10); 10000
   LOCATE 27, 5: PRINT "press END to stop reading and save data...."

'Define time zero*****
   DO
    CALL IOENTER(DVM&, READING!)
    INITIAL! = READING!
    SUM! = 0!
     FOR S = 1 TO 1
      CALL IOENTER(DVM&, READING!)
      SUM! = SUM! + READING!
     NEXT S
    AVRD! = SUM! / 1!
    DELTA! = ABS(INITIAL! - READING!)
   IF DELTA! < .3 THEN 1030 ELSE 1500:   'Turning off field
1030 PRINT #1, USING "########.###"; -(TIMER - TZERO1!); SPC(5); AVRD!
     COMLOGT1! = LOG(ABS(TIMER - TZERO1!)) / LOG(10!)
     PSET (COMLOGT1!, AVRD!)

'EXIT>>>>>>
   KG$ = INKEY$
   IF KG$ = CHR$(0) + "O" THEN 2000: 'EXIT,press END
  LOOP

'Turn off field*****t=0.0 s
'Record data as much as possible before 10 sec.!
1500  TZERO2! = TIMER
   DO
    CALL IOENTER(DVM&, READING!)
    REAL.T! = ABS(TIMER - TZERO2!)
     IF REAL.T! >= .95 AND REAL.T! <= 1! THEN
      COMLOGT! = LOG(REAL.T!) / LOG(10!)
      LINE (COMLOGT!, YMIN!)-(COMLOGT!, YMAX!)
     END IF
     IF REAL.T > 10! THEN 1600 ELSE 1520
1520 PRINT #1, USING "########.###"; REAL.T!; SPC(5); READING!
    PRINT #2, USING "########.###"; REAL.T!; SPC(5); READING!
     IF REAL.T! >= .1 THEN
       COMLOGT! = LOG(REAL.T!) / LOG(10!)
       PSET (COMLOGT!, READING!)
     END IF
'EXIT>>>>>>
  KG$ = INKEY$
```

```
  IF KG$ = CHR$(0) + "O" THEN 2000: 'EXIT,press END
  LOOP

'Press RESET*****
 1600  CALL IOENTER(DVM&, READINGI!)
       PRINT #1, USING "########.###"; TIMER - TZERO2!; SPC(5); READINGI!
       PRINT #2, USING "########.###"; TIMER - TZERO2!; SPC(5); READINGI!
       COMLOGT! = LOG(ABS(TIMER - TZERO2!)) / LOG(10!)
       PSET (COMLOGT!, READINGI!)
       LINE (COMLOGT!, YMIN!)-(COMLOGT!, YMAX!)
       II& = 1: IJ& = 1
    DO
'EXIT> > > > > >
   KG$ = INKEY$
   IF KG$ = CHR$(0) + "O" THEN 2000: 'EXIT,press END
     CALL IOENTER(DVM&, READING1!)
     REAL.T1! = ABS(TIMER - TZERO2!)
     DELTA.A! = READINGI! - READING1!
'EXIT> > > > > >
1650 KG$ = INKEY$
    IF KG$ = CHR$(0) + "O" THEN 2000: 'EXIT,press END

'Saveing data.....
      IF II& = IJ& * 1000 THEN
       CLOSE #1: CLOSE #2
       OPEN "A", #1, RAWDATA$: OPEN "A", #2, SMDATA$
       IJ& = IJ& + 1
      END IF
      CALL IOENTER(DVM&, READING2!)
      REAL.T2! = ABS(TIMER - TZERO2!)
      DELTA.B! = READING1! - READING2!
'Draw x scale to indicate time zone....
      IF REAL.T2! > = 9.97 AND REAL.T2! < = 10! THEN
        XSCALE! = LOG(REAL.T2!) / LOG(10!)
        LINE (XSCALE!, YMIN!)-(XSCALE!, YMAX!)
      ELSEIF REAL.T2! > = 98! AND REAL.T2! < = 100! THEN
        XSCALE! = LOG(REAL.T2!) / LOG(10!)
        LINE (XSCALE!, YMIN!)-(XSCALE!, YMAX!)
      ELSEIF REAL.T2! > = 990! AND REAL.T2! < = 1000! THEN
        LINE (XSCALE!, YMIN!)-(XSCALE!, YMAX!)
        XSCALE! = LOG(REAL.T2!) / LOG(10!)
      ELSEIF REAL.T2! > = 7200! AND REAL.T2! < = 7240! THEN
        XSCALE! = LOG(REAL.T2!) / LOG(10!)
        LINE (XSCALE!, YMIN!)-(XSCALE!, YMAX!)
      ELSEIF REAL.T2! > = 9900! AND REAL.T2! < = 10000! THEN
        XSCALE! = LOG(REAL.T2!) / LOG(10!)
        LINE (XSCALE!, YMIN!)-(XSCALE!, YMAX!)
      END IF
'Re-adjust recording step! Too small of VSTEP will cause huge data files!!!
      IF REAL.T2! > = 30! AND REAL.T2! < = 100! THEN
        VSTEP! = .001
      ELSEIF REAL.T2! > 100! AND REAL.T2! < = 1000! THEN
        VSTEP! = .004
      ELSEIF REAL.T2! > 1000! THEN
        VSTEP! = .006
      END IF

'If no RF attack!!!
      IF ABS(DELTA.A!) < JSTEP! AND ABS(DELTA.B!) < JSTEP! THEN
        IF ABS(DELTA.A!) > = VSTEP! THEN
          PRINT #1, USING "########.###"; REAL.T1!; SPC(5); READING1!
          PRINT #2, USING "########.###"; REAL.T1!; SPC(5); READING1!
```

```
          COMLOGT! = LOG(REAL.T1!) / LOG(10!)
          PSET (COMLOGT!, READING1!)
          READINGI! = READING1!
          II& = II& + 1
        END IF
'One RF attack!!!
      ELSEIF ABS(DELTA.B!) < JSTEP! THEN
        IF ABS(DELTA.B!) > = VSTEP! THEN
          SHIFT.R2! = READING2! + DELTA.A!
          PRINT #1, USING "#######.###"; REAL.T2!; SPC(5); READING2!
          PRINT #2, USING "#######.###"; REAL.T2!; SPC(5); SHIFT.R2!
          COMLOGT! = LOG(REAL.T2!) / LOG(10!)
          PSET (COMLOGT!, SHIFT.R2!)
          READING1! = READING2!
          II& = II& + 1
          GOTO 1650
        ELSE
          GOTO 1650
        END IF
'Another RF attack!!!
      ELSE
        DELTA.A! = DELTA.A! + DELTA.B! - .5 * VSTEP!
        READING1! = READING2!
        PRINT #1, USING "#######.###"; REAL.T2!; SPC(5); READING2!
        II& = II& + 1
        GOTO 1650
      END IF
1900 LOOP
'finish recording*****
2000   PRINT #1, USING "#######.###"; 999!; SPC(5); READING2!
      PRINT #2, USING "#######.###"; 999!; SPC(5); READING2!
      PRINT "Saving data...";
      CLOSE #1
      CLOSE #2
      PRINT "Done."
      PRINT : PRINT : PRINT
END SUB
'End_Program.
```

References

Abdul-Razzaq, W., and Kouvel, J. S., 1984, *J. Appl. Phys.* **55**, 1623.

Abdul-Razzaq, W., and Kouvel, J. S., 1987, *Phys. Rev.* B **35**, 1764.

Aitken, R. G., Cheung, T. D., Kouvel, J. S., and Hurdequint, H., 1982, *J. Magn. Magn. Mate.* **30**, L1.

Alba, M., Ocio, M., and Hammann, J., 1986, *Europhys. Letters* **2**, 45.

Antonoff, M. M., 1977, *Physica* **91B**, 193.

Bardeen, J., Cooper, L. N., and Schrieffer, J. R., 1957a, *Phys. Rev.* **106**, 162.

Bardeen, J., Cooper, L. N., and Schrieffer, J. R., 1957b, *Phys. Rev.* **108**, 1175.

Beck, P. A., 1978, *Prog. Mater. Sci.* **23** 1.

Bhatt, R. N., and Young, A. P., 1985, *Phys. Rev. Lett.* **54**, 924.

Binder, K., and Young, A. P., 1986, *Rev. Mod. Phys.* **58**, 801.

Boerstoel, B. M., Zwart, J. J., and Hansen, J., 1972, *Physica* **57**, 397.

Bontemps, N., and Orbach, R., 1988, *Phys. Rev.* B **37**, 4708.

Bozorth, R. M., 1951, *Ferromagnetism* p.968, New York: Van Nostrand.

Brodale, G. E., Fisher, R.A, Fogle, W. E., Phillips, N. E., and Curen, J. Van, 1983, *J. Magn. Magn. Mater.* **31-34**, 1331.

Burke, S. K., Cywinski, R., D, J. R., and Rainford, B.D., 1983, *J. Phys.* F **13**, 451.

Burke, S. K., and Rainford, B. D., 1978, *J. Phys.* F **8**, L239.

Burke, S. K., and Rainford, B. D., 1983, *J. Phys.* F **13**, 441.

Cable J. W., and Child, H. R., 1974, *Phys. Rev.* B **10**, 4607.

Cannella V., and Mydosh, J. A., 1972, *Phys. Rev.* B **6**, 4220.

Carr Jr., W. J., 1952, *Phys. Rev.* B **85**, 590.

Chamberlin, R. V., 1984, *Phys. Rev.* B **30**, 5393.

Chamberlin, R. V., 1985, *J. Appl. Phys.* **57**, 3377.

Chamberlin, R. V., and Haines, D. N., 1990, *Phys. Rev. Lett.* **65**, 2197.

Chamberlin, R. V., and Holtzberg, F., 1991, *Phys. Rev. Lett.* **67**, 1606.

Chamberlin, R. V., Mozurkewich, G., and Orbach, R., 1984, *Phys. Rev. Lett.* **52**, 867.

Chikazawa, S., Taniguchi, S., Matsuyama, H., and Miyako, Y., 1983, *J. Magn. Magn. Mate.* **31-34**, 1355.

Chouteau, G., and Tournier, R., 1971, *J. de. Physique* Colloque **C1**, C1-1002.

Coles, B. R., Sarkissian, B. V. B., and Taylor R. H., 1978, *Phil. Mag.* B **37**, 489.

Coles, B. R., Waszink, J. H., and Loran, J., 1965, in *Proceedings of the International Conference on Magnetism, Nottingham, England,* (The Institute of Physics and The Physical Society) 165.

Cragg, D. M., Sherrington, D., and Gabay, M., 1982, *Phys. Rev. Lett.* **49**, 158.

Craig, P. P., Perisho, R. C., Segnan, R., and Steyert, W. A., 1965, *Phys. Rev.* **138**, A1460.

Crane, S., and Claus, H., 1980, *Solid State Commun.* **35**, 461.

Crane, S., and Claus, H., 1981, *Phys. Rev. Lett.* **46**, 1693.

Crangle, J., 1960, *Phil. Mag.* **5**, 335.

Crangle, J., and Scott, W. R., 1965, *J. Appl. Phys.* **36**, 921.

Daybell, M. D., 1973, in *Magnetism V*, p.121, edited by Rado, G. T., and Suhl, H., Academic Press, New York.

de Almeida, J. R. L., and Thouless, D. J., 1978, *J. Phys.* A **11**, 983.

Dubiel, S. M., Fischer, K. H., Sauer, Ch., and Zinn, W., 1987, *Phys. Rev.*, B **36**, 360.

Edwards, S. F., and Anderson, P. W., 1975 *J. Phys.* F **5**, 965.

Elderfield, D., and Sherrington D., 1982 *J. Phys.* F **15**, L513.

Fähnle, M. J., 1987, *J. Magn. Magn. Mate.* **65**, 1.

Ferré, J., Rajchenbach, J., and Maletta, H., 1981, *J. Appl. Phys.* **52**, 1697.

Fiorani, D., Dormann, J. L., Tholence, J. L., Bessais, L., and Villers, D., 1986, *J. Magn. Magn. Mate.* **54-57**, 173.

Fischer, K. H. 1983, *Physica Status Solidi* B **116**, 357.

Fischer, K. H. 1985, *Physica Status Solidi* B **130**, 13.

Fischer, K. H., and Hertz, J. A., 1991 *Spin Glasses*, Cambridge University Press, Cambridge.

Fisher, D. S., and Huse, D. A., 1988a *Phys. Rev.* B **38**, 386.

Fisher, D. S., and Huse, D. A., 1988b *Phys. Rev.* B **38**, 373.

Fogle, W. E., Boyer, J. D., Phillips, N. E., and Curen, J. V., 1981, *Phys. Rev. Lett.* **47**, 352.

Ford, P. J., and Mydosh, J. A., 1976, *Phys. Rev.* B **14**, 2057.

Gabay, M., and Toulouse, G., 1981, *Phys. Rev. Lett.* **47**, 201.

Gabay, M., Garel, T., and De Dominicis C., 1982 *J. Phys.* C **15**, 7165.

Granberg, P., Svedlindh, P., Nordblad, P., Lundgren, L., 1986, in *Lecture Notes in Physics* Vol. **38**, 40.

Granberg, P., Svedlindh, P., Nordblad, P., Lundgren, L. , and Chen, H. S., 1987, *Phys. Rev.* B **35**, 2075.

Granberg, P., Sandlund, L., Nordblad, P., Svedlindh, P., and Lundgren, L., 1988,

Phys. Rev. B **38**, 7097.

Granberg, P., Lundgren, L., and Nordblad, P., 1990, *J. Magn. Magn. Mate.* **92**, 228.

Grest, G. S., Soukoulis, C.M., and Levin, K., 1983, in *Magnetic Phase Transitions*, edited by Ausloos, M.,, and Elliott, R. J., Springer-Verlag Press, Berlin Heidelberg.

Guy, C. N., 1978, *J.Phys.* F **8**, 1309.

Hall, N. G., Roshko, R. M., and Williams, G., 1984, *J. Phys.* F **14**, 711.

Hansen, M., 1958, *Constitution of Binary Alloys*, 938-941, McGraw Hill, New Y-ork.

Ho, S. C., Maartense, I., and Williams, G., 1981a, *J. Phys.* F **11**, 699.

Ho, S. C., Maartense, I., and Williams, G., 1981b, *J. Phys.* F **11**, 1107.

Holtzberg, F., Tholence, J. L., and Tournier, T., 1977, in *Amorphous Magnetism II*, edited by Levy, R. A., and Hasegawa (Plenum, New York), 155.

Hoogerbeets, R., Luo, Wei-Li, and Orbach, R., and Fiorani, D., 1985, *Phys. Rev. Lett.* **55**, 111.

Hoogerbeets, R., Luo, Wei-Li, and Orbach, R., 1986, *Phys. Rev.* B **34**, 1719.

Huang, C. Y., 1985, *J. Magn. Magn. Mate.* **51**, 1.

Huck, B., Landes, J., Stasch, R., and Hesse, J., 1988, *J. de. Physique.* Colloque **C8**, C8-1141.

Huse, D. A., and Fisher, D. S., 1987 *Phys. Rev.* B **35**, 6841.

Josephson, B. D., 1962, *Phys. Lett.* **1**, 251.

Josephson, B. D., 1965, *Adv. Phys.* **14**, 419.

Katori, M., and Suzuki, M., 1985, *Progs. Theor. Phys.* **74**, 1175.

Kaul, S. N., 1985, *J. Magn. Magn. Mate.* **53**, 5.

Kim, D. J., and Schwartz, B. B., 1968, *Phys. Rev. Lett.* **20**, 201.

Kirkpatrick, S., and Sherrington, D., 1978, *Phys. Rev.* B **17**, 4384.

Kittel, C., 1963, *Quantum Theory of Solids*, John Wiley & Sons, Inc., New York.
Kittel, C., 1968, *Solid State Physics* **22**, 1.

Kleiman, R. N., Maartense, I., and Williams, Gwyn, 1982, *Phys. Rev.* B **26**, 5241.

Koper, G. J. M., and Hilhorst H. J., 1988, *J. Phys. France* **49**, 429.

Kornik, K. R., 1990, *Magnetic Studies of an Effective Field Model and Several Potentially Re-entrant Palladium Alloys*, M.Sc Thesis: University of Manitoba.

Kornik, K. R., Kunkel, H.P., Roshko, R. M., and Williams, G., 1990, *Solid State Commun.* **76**, 993.

Kornik, K. R., Roshko, R. M., and Williams, G., 1989, *J. Magn. Magn. Mate.* **81**, 323.

Kouvel, J. S., Graham Jr., C. D., and Becker, J. J., 1958, *J. Appl. Phys.* **29**, 518.

Kouvel, J. S., Graham Jr., C. D., and Jacobs, I. S., 1959, *J. de. Physique.* **20**, 198.

Kouvel, J. S., Abdul-Razzaq W., and Ziq, Kh., 1987, *Phys. Rev.* B **35**, 1768.

Kouvel, J. S., and Abdul-Razzaq W., 1985, *J. Magn. Magn. Mate.* **53**, 139.

Kunkel, H. P., and Williams, G., 1988, *J. Magn. Magn. Mate.* **75**, 98.

Lange, S., Abd-Elmeguid, M. M., and Micklitz, H., 1990 *Phys. Rev.* B **41**, 6907.

Le Guillou, J. C., and Zinn-Justin, J., 1980, *Phys. Rev.* B **21**, 3976.

London, F., 1950, *Superfluids* **1**, 48, Wiley & Sons, Chichester.

Lounasmaa, O.V., 1974, *Experimental Principles and Methods Below 1 K*, Academic Press, New York.

Lundgren, L., 1988, *J. de Physique* Colloque **C8**, C8-1001.

Lundgren, L., Nordblad, P., and Sandlund, L., 1986a, *Europhys. Letters* **1**, 529.

Lundgren, L., Nordblad, P., and Svedlindh, P., 1986b, *Phys. Rev.* B **34**, 8164.

Lundgren, L., Svedlindh, P., and Beckman, O., 1982, *Phys. Rev.* B **26**, 3990.

Lundgren, L., Svedlindh, P., and Beckman, O., 1983, *J. Magn. Magn. Mate.* **31-34**, 1349.

Lundgren, L., Svedlindh, P., Nordblad, P., and Beckman, O., 1983, *Phys. Rev. Lett.* **51**, 911.

Lundgren, L., Nordblad, P., Svedlindh, P., and Beckman, O., 1985, *J. Appl. Phys.* **57**, 3371.

Luo, Wei-Li, Hoogerbeets, R., Orbach, R., and Bontemps, N., 1988, *J. de Physique* Colloque **C8**, C8-1151.

Luo, Wei-Li, Lederman, M., Orbach, R., Bontemps, N., and Nahoum, R., 1990, *Phys. Rev.* B **41**, 4465.

Ma, H., 1990, *A.C. Susceptibility and Magnetoresistivity measurements on Amorphous FeZr Alloys*, M.Sc Thesis: University of Manitoba.

Maartense, I., and Williams, Gwyn, 1978, *Phys. Rev.* B **17**, 377.

Marcinkowski, M. J., and Brown, N., 1961, *J. Appl. Phys.* **32**, 375.

Martin, Douglas L., 1980, *Phys. Rev.* B **21**, 1902.

Meschede, D., Steglich, F., Felsch, W., Maletta, H., and Zinn, W., 1980, *Phys. Rev. Lett.* **44**, 102.

Meyer, C., Hartmann-Boutron, F., Gros, Y., and Campbell, I. A., 1985, *J. Magn. Magn. Mate.* **46**, 254.

Schwartz, Brian. B., 1976, in *Magnetism: Selected Topics*, Chapter III, edited by Foner, Simon, Chapter III, Gordon and Breach Science Publishers, New York.

Shapiro, S. M., Fincher, Jr., Palumbo, A. C., and Parks, R. D.; 1981, *Phys. Rev.* B **24**, 6661.

Sherrington, D., and Kirkpatrick, S., 1975, *Phys. Rev. Lett.* **35**, 1792.

Soukoulis, C. M., Grest, G. S., and Levin, K., 1983a, *Phys. Rev.* B **28**, 1510.

Soukoulis, C. M., Levin, K., and Grest, G. S., 1983b, *Phys. Rev.* B **28**, 1495.

Southern, B. W., 1976, *J. Phys.* C **9**, 4011.

Stanley, H.E., 1971, *Introduction to Phase Transitions and Critical Phenomena*, Oxford University Press, New York.

Street, R., and Woolley, J. C., 1949, *Proc. Phys. Soc. London* A **62**, 562.

Svedlindh, P., Granberg, P., Nordblad, P., Lundgren, L., and Chen, H. S., 1987, *Phys. Rev.* B **35**, 268.

Tholence, J. L., and Tournier, R., 1974, *J. de. Physique.* Colloque C4 C4-229.

Toulouse, G., 1980, *J. Phys.(Paris) Lett.* **41**, L-447.

van Hemmen, J. L., and Nieuwenhuys, G.J., 1986, *Europhys. Letters* **2**, 797.

Veal, B. W., and Rayne, J. A., 1964, *Phys. Rev.* **135**, A442.

Verbeek, B. H., Nieuwenhuys, G. J., Stocker, H., and Mydosh, J. A., 1978, *Phys. Rev. Lett.* **40**, 586.

Violet, C. E., and Borg, R. J., 1983 *Phys. Rev. Lett.* **51**, 1073.

Violet, C. E., and Borg, R. J., 1984 *Phys. Rev. Lett.* **52**, 2098.

Wang, Z., Kunkel, H., and Williams, G., 1990, *J. Phys.* Condens. Matter **2**, 4173.

Wang, Z., 1990, *Magnetic and Electrical Properties of Dilute PdNi, PdFe, and (PdFe)Mn alloys*, Ph.D Thesis: University of Manitoba.

White, R.M., 1983, *Quantum Theory of Magnetism*, Springer-Verlag Berlin Heidelberg.

Wohlfarth, E.P., 1980, *Ferromagnetic Materials, a handbook on the properties of magnetic ordered substance*, Edited by Wohlfarth, E. P, North-Holland Pub., New York. Heidelberg.

Yeung, I., Roshko, R.M., and Williams, G., 1987, *J. Magn. Magn. Mate.* **68**, 39.

Yeung, I., Ruan, W., and Roshko, R.M., 1988, *J. Magn. Magn. Mate.* **74**, 59.

Yeung, W.T.I., 1988, *D.C. Magnetization Measurements on Two PtMn Spin Glasses*, M.Sc. Thesis: University of Manitoba.

Zastre, E., Roshko, R.M., and Williams, G., *Phys. Rev.* B **32**, (1985) p.7597.